

NOTE TO USERS

This reproduction is the best copy available.

UMI[®]

**Mineralogy, petrology, and isotope geochemistry of magmatic rocks
from the Western Alps, Ernici and Roccamonfina, Italy:
Constraints on mantle enrichment processes**

by

Jennifer P. Owen, B.Sc. (Hon)

A thesis submitted to
the Faculty of Graduate Studies and Research
in partial fulfillment of
the requirements for the degree of
Doctor of Philosophy

Ottawa-Carleton Geoscience Centre

Department of Earth Sciences

Carleton University

Ottawa, Ontario

Canada

January, 2006

© Jennifer P. Owen, 2006



Library and
Archives Canada

Bibliothèque et
Archives Canada

Published Heritage
Branch

Direction du
Patrimoine de l'édition

395 Wellington Street
Ottawa ON K1A 0N4
Canada

395, rue Wellington
Ottawa ON K1A 0N4
Canada

Your file *Votre référence*
ISBN: 0-494-13396-1
Our file *Notre référence*
ISBN: 0-494-13396-1

NOTICE:

The author has granted a non-exclusive license allowing Library and Archives Canada to reproduce, publish, archive, preserve, conserve, communicate to the public by telecommunication or on the Internet, loan, distribute and sell theses worldwide, for commercial or non-commercial purposes, in microform, paper, electronic and/or any other formats.

The author retains copyright ownership and moral rights in this thesis. Neither the thesis nor substantial extracts from it may be printed or otherwise reproduced without the author's permission.

AVIS:

L'auteur a accordé une licence non exclusive permettant à la Bibliothèque et Archives Canada de reproduire, publier, archiver, sauvegarder, conserver, transmettre au public par télécommunication ou par l'Internet, prêter, distribuer et vendre des thèses partout dans le monde, à des fins commerciales ou autres, sur support microforme, papier, électronique et/ou autres formats.

L'auteur conserve la propriété du droit d'auteur et des droits moraux qui protègent cette thèse. Ni la thèse ni des extraits substantiels de celle-ci ne doivent être imprimés ou autrement reproduits sans son autorisation.

In compliance with the Canadian Privacy Act some supporting forms may have been removed from this thesis.

Conformément à la loi canadienne sur la protection de la vie privée, quelques formulaires secondaires ont été enlevés de cette thèse.

While these forms may be included in the document page count, their removal does not represent any loss of content from the thesis.

Bien que ces formulaires aient inclus dans la pagination, il n'y aura aucun contenu manquant.


Canada

ABSTRACT

Mineralogical and geochemical data from lamprophyres from the Western Alps, northern Italy, and volcanic rocks from Roccamonfina and Ernici, central-southern Italy, are used to investigate mantle enrichment processes. The lamprophyres are classified as minettes, spessartites, and kersantites, whereas the volcanic rocks from Roccamonfina and Ernici include a potassic series (KS) and an ultrapotassic series (HKS). The lamprophyres and the KS and HKS rocks have high concentrations of LREE and strongly fractionated LREE/HREE and LILE/HFSE ratios similar to many subduction-related rocks. Incompatible trace element ratios and Sr, Nd, and Pb isotopic data support metasomatism by a slab-derived fluid in the Alpine mantle, and by a carbonate-rich melt beneath the Apennines. High B contents in rocks from Roccamonfina and Ernici constrain subduction-related metasomatism to the past 5 Ma in central-southern Italy.

Isotopic data from rocks from the Western Alps, Roccamonfina, and Ernici fall on a previously-defined, two-component mixing line between a depleted, mantle end-member and an enriched, crust-like end-member. The lamprophyres from the Western Alps best represent the enriched end-member, while rocks from Roccamonfina and Ernici have moderately enriched signatures that lie between those of the Roman and Campanian Provinces. The geodynamic model favoured for the origin of the two isotopic end-members involves a widespread, isotopically-depleted asthenosphere variably contaminated by pelagic sediments subducted during closure of the Tethyan Ocean. Incompatible trace element and K_2O contents of rocks from Roccamonfina and Ernici are attributed to source enrichment during Apennine subduction.

ACKNOWLEDGEMENTS

Many thanks go to my supervisor Keith Bell for inviting me to work on this interesting and thought-provoking thesis. I appreciate his superb editing, ability to look at the big picture, and most of all his encouragement to always question scientific "truths" that others often take for granted.

I am grateful to Angelo Peccerillo for recommending the study localities, as well as insightful discussions on Italian magmatism and funding for field work. Georgio Martinotti is thanked for helping collect samples from the Western Alps, and Vittorio Zanon is thanked for his driving skills, language translation, and good company during field work at Roccamonfina and Ernici. Lab work at Carleton University could not have been completed without the assistance of Mike Jackson for thin section preparation, Peter Jones for electron microprobe analyses, and Ineke de Jong for isotope geochemistry. Brian Cousens and John Blenkinsop are thanked for their patience in teaching me the finer points of mass spectrometry. I would also like to thank Giusy Lavecchia and André LaLonde for helpful suggestions and constructive criticism, and Don Hogarth for valuable input on mineralogy and petrography.

Finally, I would like to thank my family and friends for their love and support throughout my time at Carleton. My friends Andrea, Heidi, Sara, Wanda, Sean, Alana, and John were always there when I needed them. Special thanks to Robin and his family for inviting me into their lives. Most of all, thanks to my parents Alan and Linda, sister Kate, aunt Judith, and grandparents Ross, Ruby, John and Fran for inspiring me to work hard and achieve my goals.

TABLE OF CONTENTS

	Page
Abstract	ii
Acknowledgments	iii
Table of Contents	iv
List of Tables	xiv
List of Figures	xvi
List of Plates	xxiii
List of Appendices	xxvi
CHAPTER 1: INTRODUCTION	
1.1 Overview of Italian magmatism	1
1.2 Introduction to magmatic rocks of the Western Alps, Roccamonfina, and Ernici	1
1.3 Tectonic setting of Italian magmatism	4
1.4 Overview of lamprophyres: mineralogy, geochemistry and mode of occurrence	5
1.5 Overview of world-wide potassic and ultrapotassic rocks	7
1.6 Radiogenic isotope geochemistry of lamprophyres, potassic rocks, and ultrapotassic rocks	11
1.7 Purpose of study	15
CHAPTER 2: GEODYNAMIC EVOLUTION OF THE WESTERN MEDITERRANEAN	
2.1 Introduction	16

2.2	Alpine Tectonics	18
2.2a	Mesozoic paleogeography	18
2.2b	Eo-Alpine deformation (135 – 60 Ma)	20
2.2c	Meso-Alpine deformation (60 – 30 Ma)	21
2.2d	Neo-Alpine deformation (30 – 7 Ma)	23
2.2e	Summary of main Alpine tectonic features	24
2.3	Extensional basin formation	25
2.3a	Introduction	25
2.3b	Phase I: late Oligocene – middle Miocene	26
2.3c	Phase II: middle Miocene – Quaternary	29
2.3d	Summary of main tectonic features of basin formation	30
2.3e	Geodynamics of basin formation	31
2.4	Apennine tectonics	34
2.4a	Introduction	34
2.4b	Structure	35
2.4c	Controls on tectonic evolution	36
2.4d	The Adriatic microplate	38
2.4e	Summary of main Apennine tectonic features	39

CHAPTER 3: CENOZOIC ITALIAN MAGMATIC PROVINCES

3.1	Introduction	41
3.2	Northern Italy	43
3.2a	Tertiary Periadriatic Province	43

3.2b	Veneto Province	45
3.3	Central Italy	46
3.3a	Tuscan Province	46
3.3b	Roman Province	50
3.3c	Southern Latium Transition Zone	52
3.3d	Campanian Province	53
3.3e	Internal Apennines Zone	54
3.3f	Vulture	55
3.3g	Pietre Nere	56
3.4	Southern Italy	57
3.4a	Aeolian Islands	57
3.4b	Tyrrhenian Sea	57
3.4c	Etna	59
3.4d	Iblean Plateau	60
3.4e	Pantelleria	60
3.5	Sardinia	61
3.6	Summary of main geochemical features of Cenozoic Italian magmatism	62

CHAPTER 4: PREVIOUS ISOTOPIC WORK

4.1	Introduction	63
4.2	The early years (1966 – 1980): discovery of regional isotopic trends	63
4.3	The 1980s and 1990s: end-member signatures in a geodynamic context	68

4.4	Recent work (2000-2005): an additional end-member and a new geodynamic context	74
-----	--	----

CHAPTER 5: GEOLOGY OF THE STUDY AREAS

5.1	Introduction	77
5.2	Western Alps	77
5.2a	Location and field work	77
5.2b	Geological setting	78
5.2c	Previous work on the petrology and geochemistry of dykes from the Western Alps	80
5.3	Roccamonfina	82
5.3a	Location and field work	82
5.3b	Geological setting	83
5.3c	Previous work on the petrology and geochemistry of KS and HKS volcanic rocks from Roccamonfina	88
5.4	Ernici	90
5.4a	Location and field work	90
5.4b	Geological setting	92
5.4c	Previous work on the petrology and geochemistry of KS and HKS volcanic rocks from Ernici	94

CHAPTER 6: PETROGRAPHY AND MINERAL CHEMISTRY

6.1	Introduction	96
6.2	Petrography	96
6.2a	Western Alps	96
6.2a.i	Minettes	100

6.2a.ii	Spessartites	104
6.2a.iii	Kersantite	108
6.2b	Roccamonfina	108
6.2b.i	Potassic series (KS)	111
6.2b.ii	Ultrapotassic series (HKS)	115
6.2c	Ernici	117
6.2c.i	Potassic series (KS)	117
6.2c.ii	Ultrapotassic series (HKS)	122
6.3	Mineral chemistry	126
6.3a	Calculation of mineral formulae	126
6.3a.i	Olivine	126
6.3a.ii	Pyroxene	126
6.3a.iii	Amphibole	127
6.3a.iv	Mica	129
6.3a.v	Feldspar	129
6.3a.vi	Feldspathoids	130
6.3b	Western Alps	131
6.3b.i	Olivine	131
6.3b.ii	Pyroxene	131
6.3b.iii	Amphibole	133
6.3b.iv	Mica	137
6.3b.v	Feldspar	138
6.3b.vi	Feldspathoids	140

6.3b.vii	Summary of mineral chemistry	140
6.3c	Roccamonfina and Ernici	142
6.3c.i	Olivine	142
6.3c.ii	Pyroxene	144
6.3c.iii	Crystal structure simulation of clinopyroxene from Ernici	153
6.3c.iv	Amphibole	159
6.3c.v	Mica	160
6.3c.vi	Feldspar	162
6.3c.vii	Feldspathoids	164
6.3c.viii	Summary of mineral chemistry	166

CHAPTER 7: WHOLE-ROCK GEOCHEMISTRY

7.1	Introduction	168
7.2	Major element geochemistry	168
7.2a	Western Alps	168
7.2b	Roccamonfina	173
7.2c	Ernici	176
7.2d	Comparison between Roccamonfina and Ernici	180
7.2e	CIPW normative compositions of samples from Roccamonfina and Ernici	184
7.3	Degree of mantle fertility in the Western Alps and central-southern Italy based on major element geochemistry	186
7.4	Trace element geochemistry	190
7.4a	Introduction	190

7.4b	Western Alps	191
	7.4b.i Compatible elements	191
	7.4b.ii Incompatible elements	191
7.4c	Roccamonfina	195
	7.4c.i Compatible elements	195
	7.4c.ii Incompatible elements	195
7.4d	Ernici	198
	7.4d.i Compatible elements	198
	7.4d.ii Incompatible elements	199
7.4e	Comparison of trace element data from Roccamonfina and Ernici	203
7.4f	Can the samples from Roccamonfina and Ernici be considered primitive?	203
7.4g	Incompatible trace element data from the Western Alps, Roccamonfina and Ernici compared to other Italian magmatic rocks	206
7.5	Evidence for a crustal component in the mantle of the Western Alps and central-southern Italy	211
	7.5a Introduction	211
	7.5b Incompatible trace element patterns	212
	7.5b.i Significance of negative Nb, Ta and Ti anomalies in incompatible trace element diagrams	215
	7.5c Tectonic discrimination diagrams using HFSE	222
	7.5d Ce/Pb and Nb/U ratios as sediment tracers	224
	7.5e Boron and beryllium systematics	225
	7.5e.i Geochemical behavior of B and Be	227

7.5e.ii	B and Be data from Roccamonfina and Ernici	229
7.5e.iii	Comparison of B-Be data from Roccamonfina and Ernici with the Sunda arc	234
7.5f	Nature of the metasomatising agent: hydrous fluid or silicate melt?	237
7.6	Summary of whole-rock geochemistry	243
7.6a	Western Alps	243
7.6b	Roccamonfina and Ernici	244

CHAPTER 8: ISOTOPE GEOCHEMISTRY

8.1	Introduction	246
8.2	Radiogenic isotope systems	247
8.2a	Rb-Sr	247
8.2b	Sm-Nd	247
8.2c	U-Th-Pb	248
8.3	Isotopic data	249
8.3a	Western Alps	249
8.3b	Roccamonfina and Ernici	257
8.4	Regional isotopic trends and end-member reservoirs	264
8.4a	Introduction	264
8.4b	The depleted end-member	266
8.4b.i	What are FOZO, LVC and EAR?	268
8.4c	The enriched end-member	272
8.5	Geochemical signature of ITEM	275

CHAPTER 9: GEODYNAMIC INTERPRETATION OF ITALIAN ISOTOPIC MIXING

9.1	Introduction	285
9.2	Seismic tomography	287
9.2a	Introduction	287
9.2b	Tomographic images of the Alpine mantle	288
9.2c	Evidence for slab break-off beneath the Alpine orogen	290
9.2d	Tomographic images of the Apennine mantle	292
9.3	Origin of the depleted isotopic end-member in Italian magmatic rocks	294
9.3a	Introduction	294
9.3b	Geodynamic models for the origin of FOZO in the Adriatic mantle	295
9.3c	Geodynamic model for the origin of FOZO in the Tyrrhenian mantle	306
9.3d	Geodynamic model for the origin of LVC-EAR in the Western Mediterranean mantle	310
9.3e	Evaluation of geodynamic models for the depleted end-member in Italian magmatic rocks	312
9.4	Origin of the ITEM isotopic component in Italian magmatic rocks	316
9.4a	Evaluation of geodynamic models for the ITEM end-member in Italian magmatic rocks	323
9.5	An integrated model for the origin of the enriched and depleted end-members involved in Italian isotopic mixing	323
9.6	Summary of major geodynamic events that influenced the geochemistry of Italian magmatic rocks in chronological order	329

CHAPTER 10: CONCLUSIONS

10.1	Western Alps	331
10.2	Roccamonfina and Ernici	333
10.3	Geodynamic implications of Italian isotopic mixing	336

REFERENCES	339
-------------------	------------

LIST OF TABLES

	Page
1.1 Geochemical and geological characteristics of Group I, Group II, and Group III ultrapotassic rocks	8
3.1 Summary of the volcanic landforms, geochemistry, and rock types of central Italy	47
3.2 Summary of the volcanic landforms, geochemistry, and rock types of southern Italy	58
6.1 Essential and accessory mineralogy of samples from the Western Alps	98
6.2 Essential and accessory minerals of studied volcanic rocks from Roccamonfina	112
6.3 Essential and accessory minerals of studied volcanic rocks from Ernici	118
6.4 Summary of main chemical features of silicate minerals from Western Alps lamprophyres	141
6.5 Summary of the main chemical features and petrogenetic indicators from silicate minerals from Roccamonfina and Ernici	167
7.1 Major element geochemistry of the Western Alps lamprophyres	169
7.2a Major element geochemistry for samples from Roccamonfina	174
7.2b Major element geochemistry for samples from Ernici	174
7.3 Trace element concentrations of lamprophyres from the Western Alps	192
7.4 Trace element concentrations of KS and HKS volcanic rocks from Roccamonfina	196
7.5 Trace element concentrations of KS and HKS volcanic rocks from Ernici	200
7.6 B and Be contents and B/Be ratios of sedimentary and igneous rocks	228
7.7 B and Be concentrations and B/Be ratios of KS and HKS volcanic rocks from Roccamonfina and Ernici	230
8.1 Isotopic data from the Western Alps	251

8.2	Isotopic data from Roccamonfina and Ernici	258
A.1	References for published Sr, Nd, and Pb isotopic ratios used in regional diagrams	373
B.1	Western Alps sample localities	375
B.2	Roccamonfina sample localities	376
B.3	Ernici sample localities	377
C.1	Lamprophyre classification based on predominant felsic and mafic silicate mineralogy	378
F.5.a	Elution chart for Rb-Sr column	438
F.5.b	Elution chart for REE column	438
F.5.c	Elution chart for 0.50 ml Pb column	439
F.5.d	Elution chart for 0.20 ml Pb column	439
G.1	Reported precision and accuracy of standard MRG used for major element analysis	444
G.2	Reported precision and accuracy of standard MRG used for trace element analysis	444
G.3	Loading procedures for Sr, Nd, and Pb for TIMS analysis	447
G.4	Running conditions for TIMS	447
H.1	Further subdivisions of fields A, B, and C on the Total Alkalis-Silica diagram	448

LIST OF FIGURES

	Page	
1.1	Location map of the Western Alps, Roccamonfina, and Ernici	1
1.2	Sr-Nd isotopic compositions of lamprophyres and ultrapotassic rocks	12
1.3	Pb isotopic compositions of lamprophyres and ultrapotassic rocks	13
2.1	Internal and external units of the Alpine chain in Western Europe	17
2.2	Extensional basins in the Western Mediterranean	27
2.3	Paleogeographic reconstruction of slab rollback in the Western Mediterranean	33
2.4	Map of the Northern Apennine, central-southern Apennine, and Calabrian arcs	37
3.1	Cenozoic magmatic provinces of Italy	42
3.2	Tectonic map of the Alps showing the distribution of Tertiary magmatic rocks along the Periadriatic Lineament	44
3.3	K ₂ O/Na ₂ O vs. Q for Italian magmatic rocks	51
4.1	Regional trend in ⁸⁷ Sr/ ⁸⁶ Sr for Italian magmatic rocks	64
5.1	Simplified tectonic map of the Western Alps showing sample localities	79
5.2	Geologic map of Roccamonfina volcano showing sample localities	84
5.3	Geologic map of Ernici showing sample localities	93
6.1	Ternary Ca ₂ Si ₂ O ₆ (Wo) – Mg ₂ Si ₂ O ₆ (En) – Fe ₂ Si ₂ O ₆ (Fs) diagram for clinopyroxene from Western Alpine minettes	132
6.2	Classification for calcic amphibole from the Western Alps with Ca _B ≥ 1.50; (Na+K) _A ≥ 0.50; Ti < 0.50	134
6.3	Classification for calcic amphibole from the Western Alps with Ca _B ≥ 1.50; (Na+K) _A < 0.50; Ca _A < 0.50	134
6.4	Classification for sodic-calcic amphibole from the Western Alps with (Na+K) _A ≥ 0.50; (Ca+Na) _B ≥ 1.00; 0.50 < Na _B < 1.50	136

6.5	Ternary KAlSi_3O_8 (Or) – $\text{NaAlSi}_3\text{O}_8$ (Ab) – $\text{CaAl}_2\text{Si}_2\text{O}_8$ (An) diagram for feldspars from lamprophyres from the Western Alps	139
6.6	Comparison of MnO and CaO abundance (wt%) in olivine from the HKS and KS rocks of Roccamonfina and Ernici	145
6.7	Ternary $\text{Ca}_2\text{Si}_2\text{O}_6$ (Wo) – $\text{Mg}_2\text{Si}_2\text{O}_6$ (En) – $\text{Fe}_2\text{Si}_2\text{O}_6$ (Fs) diagram for pyroxene from the Roccamonfina KS and HKS rocks.	146
6.8	Ternary $\text{Ca}_2\text{Si}_2\text{O}_6$ (Wo) – $\text{Mg}_2\text{Si}_2\text{O}_6$ (En) – $\text{Fe}_2\text{Si}_2\text{O}_6$ (Fs) diagram for pyroxene from the Ernici KS and HKS rocks	146
6.9	Fe^{3+} vs. Al^{3+} for clinopyroxene from Roccamonfina and Ernici	149
6.10	Q-J diagram for clinopyroxene from Roccamonfina and Ernici	150
6.11	Al^{3+} vs. Si^{4+} for clinopyroxene from Roccamonfina and Ernici	152
6.12	Calculated Vcell and VM1 for clinopyroxene phenocryst cores from the HKS and KS rocks of Ernici	155
6.13	Relation between AlM1 and VM1 for clinopyroxene from Ernici	157
6.14	Lack of relation between AlM1 and Vcell for clinopyroxene from Ernici	157
6.15	Crystal chemical effects of common substitutions on the V_{cell} and V_{M1} of clinopyroxene	158
6.16	Crystal structure effects of alkaline (low $a\text{SiO}_2$, high $a\text{CaO}$) and subalkaline (high $a\text{SiO}_2$, low $a\text{CaO}$) melts on clinopyroxene	158
6.17	Ternary KAlSi_3O_8 (Or) – $\text{NaAlSi}_3\text{O}_8$ (Ab) – $\text{CaAl}_2\text{Si}_2\text{O}_8$ (An) diagram for HKS and KS feldspars from Roccamonfina	163
6.18	Ternary KAlSi_3O_8 (Or) – $\text{NaAlSi}_3\text{O}_8$ (Ab) – $\text{CaAl}_2\text{Si}_2\text{O}_8$ (An) diagram for HKS and KS feldspars from Ernici	163
7.1	K_2O vs. SiO_2 for mafic dykes along the Periadriatic Line	172
7.2	Total alkali-silica (TAS) diagram for samples from Roccamonfina and Ernici	175
7.3	Plot of Alkali Index (A.I.) versus Al_2O_3 (wt%) for subalkali basalt samples from Ernici	179

7.4	Division of the basalt-rhyolite series into low-K, medium-K, and high-K types	179
7.5a	K ₂ O vs. SiO ₂ diagram for samples from Roccamonfina and Ernici	181
7.5b	Na ₂ O vs. SiO ₂ diagram for samples from Roccamonfina and Ernici	181
7.5c	MgO vs. SiO ₂ diagram for samples from Roccamonfina and Ernici	181
7.5d	Fe _{total} (FeO+Fe ₂ O ₃) vs. SiO ₂ diagram for samples from Roccamonfina and Ernici.	181
7.6	SiO ₂ vs. (K ₂ O+Na ₂ O)/Al ₂ O ₃ comparison of data from KS and HKS volcanic rocks from Roccamonfina and Ernici with Tuscan lamproites, the Sisco lamproite, and Italian kamafugites	183
7.7	Fe ₂ O ₃ vs. TiO ₂ comparison of data from rocks of Roccamonfina, Ernici, and the Western Alps with Tuscan lamproites, Italian kamafugites, MORB, and intraplate mafic potassic/ultrapotassic rocks	187
7.8a	CaO vs. Na ₂ O comparison of data from samples from the Western Alps, Roccamonfina and Ernici with Tuscan lamproites and Italian kamafugites	189
7.8b	CaO vs. Al ₂ O ₃ comparison of data from samples from the Western Alps, Roccamonfina and Ernici with Tuscan lamproites and Italian kamafugites	189
7.9	Chondrite-normalized REE diagram for lamprophyres from the Western Alps	193
7.10	Chondrite-normalized extended multi-element (spider) diagram for lamprophyres from the Western Alps	193
7.11	REE diagram for KS and HKS samples from Roccamonfina	197
7.12	Chondrite-normalized extended multi-element (spider) diagram for samples from Roccamonfina	197
7.13	REE diagram for KS and HKS samples from Ernici	201
7.14	Chondrite-normalized extended multi-element (spider) diagram for samples from Ernici	201
7.15	Comparison of the incompatible trace element patterns of samples from the HKS and KS series at Roccamonfina and Ernici	204

7.16	Average chondrite-normalized incompatible element concentrations for lamprophyres from the Western Alps, calc-alkaline volcanic rocks from the Eastern Alps, Sisco, Orciatico, and Torre Alfina	207
7.17	Incompatible trace element data of samples from Roccamonfina and Ernici, the Roman Province, the Campanian Province, Vesuvius, and Vulture	209
7.18	Incompatible trace element data of samples WA 104 and WA 105 from the Western Alps (minettes), sample ER 110 (phonotephrite), and the Orciatico lamproite	209
7.19	Average chondrite-normalized REE concentrations for minette, kersantite, and spessartite samples from the Western Alps compared with average upper continental crust	213
7.20	Incompatible trace element data from rocks from Roccamonfina and Ernici compared with the upper continental crust, the lower continental crust, average n-MORB, and average OIB	213
7.21	Incompatible trace element patterns of rocks from Roccamonfina, Vesuvius, and Vulture using the element order of McCulloch and Gamble (1991)	218
7.22a	Nb (ppm) vs. K ₂ O (wt%) for rocks of Roccamonfina and Ernici	221
7.22b	TiO ₂ (wt%) vs. K ₂ O (wt%) for rocks of Roccamonfina and Ernici	221
7.23	Th/Yb vs. Ta/Yb tectonic discrimination diagram for data from Roccamonfina, Ernici, and the Western Alps, along with assorted magmatic rocks from Italy	223
7.24	(Th x 100)/Zr vs. (Nb x 100)/Zr tectonic discrimination diagram for data from Roccamonfina, Ernici, and the Western Alps, along with assorted magmatic rocks from Italy	223
7.25	Ce/Pb vs. Ce plotted on a log-log scale for samples from the Western Alps, Roccamonfina, and Ernici	226
7.26	Nb/U vs. Nb plotted on a log-log scale for samples from the Western Alps, Roccamonfina, and Ernici	226
7.27	B and Be data from Roccamonfina and Ernici as well as the range of values for various sedimentary and igneous rock types	232

7.28	B (ppm) vs. K ₂ O (wt%) for KS and HKS samples from Roccamonfina and Ernici	233
7.29	Be (ppm) vs. K ₂ O (wt%) for KS and HKS samples from Roccamonfina and Ernici	233
7.30	B-Be data from Roccamonfina and Ernici compared to rocks from the Sunda arc, Indonesia	235
7.31	B-Be and K ₂ O contents of samples from Roccamonfina and Ernici compared to rocks from the Sunda arc, Indonesia	235
7.32	Ba/Nb vs. Zr/Nb diagram for samples from the Western Alps, Roccamonfina, and Ernici	239
7.33	Ce/Sr vs. Th/Ta comparison of rocks from the Western Alps, Roccamonfina and Ernici with Tuscan lamproites and KS and HKS rocks from the Roman and Campanian Provinces	241
8.1	Nd-Sr anti-correlation diagram for samples from the Western Alps, as well as rocks from the Tertiary Periadriatic Province, central Europe, and the Tuscan Province in central Italy	254
8.2	Pb-Pb diagram for samples from the Western Alps, as well as rocks from the Tertiary Periadriatic Province, central Europe, and the Tuscan Province in central Italy	256
8.3	Nd-Sr isotope ratio diagram for KS and HKS rocks from Roccamonfina and Ernici	260
8.4	⁸⁷ Sr/ ⁸⁶ Sr vs. ²⁰⁶ Pb/ ²⁰⁴ Pb ratios for HKS and KS rocks from Roccamonfina and Ernici	262
8.5	⁸⁷ Sr/ ⁸⁶ Sr vs. ²⁰⁷ Pb/ ²⁰⁴ Pb ratios for HKS and KS rocks from Roccamonfina and Ernici	262
8.6	Sr-Nd anti-correlation diagram for volcanic rocks from Roccamonfina and Ernici, the Roman Province, and the Campanian Province	263
8.7	Nd-Sr anti-correlation diagram for Italian magmatic rocks showing the mantle end-members DMM, EMI, EMII, and HIMU, as well as FOZO, EAR, LVC, and the crustal end-member ITEM	265
8.8	Pb-Sr diagram for Italian magmatic rocks showing the mantle end-members DMM, EMI, EMII, and HIMU, as well as FOZO, LVC, and the crustal end-member ITEM	267

8.9	$^{207}\text{Pb}/^{204}\text{Pb}$ vs. $^{206}\text{Pb}/^{204}\text{Pb}$ diagram for Italian magmatic rocks showing the mantle end-members DMM, EMI, EMII, and HIMU, as well as FOZO, LVC, and the crustal end-member ITEM	274
8.10	K_2O (wt%) vs. $^{87}\text{Sr}/^{86}\text{Sr}$ ratios for studied lamprophyres from the Western Alps, as well as samples from Venturelli et al. (1984)	276
8.11	K_2O (wt%) vs. $^{87}\text{Sr}/^{86}\text{Sr}$ ratios for KS and HKS samples from Roccamonfina and Ernici	276
8.12	K_2O (wt%) vs. $^{87}\text{Sr}/^{86}\text{Sr}$ ratios for samples from Roccamonfina, Ernici, and the Western Alps, along with additional data from the Western Alps (Venturelli et al., 1984)	277
8.13	TiO_2 (wt%) vs. $^{87}\text{Sr}/^{86}\text{Sr}$ ratios for lamprophyres from the Western Alps and KS and HKS volcanic rocks from Roccamonfina and Ernici	277
8.14	Th (ppm) vs. $^{87}\text{Sr}/^{86}\text{Sr}$ for lamprophyres from the Western Alps as well as KS and HKS volcanic rocks from Roccamonfina and Ernici	280
8.15	La (ppm) vs. $^{87}\text{Sr}/^{86}\text{Sr}$ for lamprophyres from the Western Alps as well as KS and HKS volcanic rocks from Roccamonfina and Ernici	280
8.16	Ba (ppm) vs. $^{87}\text{Sr}/^{86}\text{Sr}$ for lamprophyres from the Western Alps and KS and HKS volcanic rocks from Roccamonfina and Ernici	282
8.17	Ba/La vs. $^{87}\text{Sr}/^{86}\text{Sr}$ for lamprophyres from the Western Alps as well as rocks from Roccamonfina and Ernici, Tuscan lamproites, Italian kamafugites, and rocks from the Roman and Campanian Provinces	282
9.1	Simplified tectonic plate boundaries in the Italian region and locations of rocks with the strongest depleted and enriched isotopic signatures	286
9.2	Tomographic model of Piromallo and Morelli (2003)	289
9.3	Tomographic model of Bijwaard and Spakman (2000)	293
9.4	Model I: schematic of horizontal stretching of the downgoing Apennine slab in the Calabrian	296
9.5	Model II: schematic of lateral slab detachment beneath Italy	296
9.6	Model III: schematic of SE-directed rollback of the Ionian oceanic lithosphere	300

9.7	Model IV: schematic of a window in the Adriatic slab below central-southern Italy	300
9.8	Hypothetical evolution of the Apennine chain and Tyrrhenian basin from 16 Ma to the present day	305
9.9a	SW-NE schematic cross-section of a slab window beneath central-southern Italy	307
9.9b	NW-SE schematic cross-section of a slab window beneath central-southern Italy	307
9.10	Interpretive transect showing a degassed mantle plume trapped in the Mediterranean transition zone	308
9.11a	Late Cretaceous position of the proposed mantle plume beneath the Western Mediterranean	315
9.11b	Mid-Late Tertiary position of the mantle plume head beneath the Western Mediterranean	315
9.12	Present-day crustal-scale cross-section, late Cretaceous reconstruction, and present-day simplified cross-section of the Western Alps	321
9.13	Paleogeographic reconstruction of the European margin of the Western Mediterranean in the late Oligocene	325

LIST OF PLATES

	Page
5.1 The Santa Croce KS lava dome at Roccamonfina	87
5.2 Volcanic centres in the Media Valle Latina at Ernici	91
6.1 Porphyritic texture (sample WA 100)	101
6.2 Equigranular texture (sample WA 102)	101
6.3 Disequilibrium texture in a phlogopite phenocryst (sample WA104)	101
6.4 Complete replacement of possible olivine by talc (sample WA 104)	101
6.5 Quartz xenocryst rimmed by epidote, augite, and orthoclase (sample WA100)	102
6.6 Globular structure composed of augite, orthoclase, and albite (sample WA 100)	102
6.7 Reversely zoned diopside phenocryst (sample WA 100)	103
6.8 Concentrically zoned, euhedral diopside phenocryst (sample WA 102)	103
6.9 Partially resorbed, zoned phlogopite phenocryst (sample WA 102)	103
6.10 Normally zoned, kinked phlogopite (sample WA 102)	103
6.11 Reversely zoned, partially resorbed phlogopite (sample WA 104)	103
6.12 Disequilibrium texture, phlogopite megacryst (sample WA 104)	103
6.13 Heavily-altered, euhedral magnesiohornblende phenocrysts (sample WA 101)	106
6.14 Highly-chloritized magnesiohornblende phenocrysts (sample WA 103)	106
6.15 Heavily-altered magnesiohastingsite phenocryst (sample WA 103)	107
6.16 Actinolite alteration of tschermakite megacryst (sample WA 101)	107
6.17 Globular structure rimmed by amphibole filled by talc (sample WA 107)	107
6.18 Rings of Fe-S-Si alteration products (sample WA 107)	107

6.19	Phlogopite, quartz, dolomite and albite (sample WA106)	109
6.20	Kinked phlogopite surrounded by dolomite (sample WA106)	109
6.21	Phlogopite, albite, dolomite and quartz (sample WA 106)	110
6.22	Normally zoned, euhedral phlogopite with apatite (sample WA 106)	110
6.23	Dolomite surrounded by phlogopite and quartz (sample WA 106)	110
6.24	Quartz surrounded by phlogopite with abundant apatite (sample WA 106)	110
6.25	Trachytic texture of plagioclase phenocrysts with zoned, euhedral diopside phenocryst (KS sample RC107)	114
6.26	Sieve-textured, plagioclase phenocryst with phlogopite and diopside (KS sample RC106)	114
6.27	Anhedral, olivine phenocryst with reaction rim (KS sample RC110)	114
6.28	Leucite and zoned clinopyroxene phenocrysts in a leucite-dominated groundmass (HKS sample RC100)	116
6.29	Leucite and plagioclase groundmass (HKS sample RC 113)	116
6.30	Cross-shaped and star-shaped leucite crystals in a glassy groundmass (HKS sample RC 117)	116
6.31	Weak alignment of small euhedral plagioclase (HKS sample RC123)	116
6.32	Glassy groundmass with irregular amygdules and euhedral to subhedral phenocrysts of diopside (KS sample ER 113)	120
6.33	Analcime-rich KS sample ER 109 with phenocrysts of biotite and clinopyroxene	120
6.34	Reversely zoned, euhedral diopside phenocryst (KS sample ER109)	121
6.35	Normally zoned diopside in a groundmass of plagioclase and analcime (KS sample ER 121)	121
6.36	Olivine phenocryst with Fe-rich rim (KS sample ER 121)	121
6.37	Euhedral, plagioclase (bytownite) phenocrysts (KS sample ER 109)	121

6.38	Analcime-rich KS sample ER 117 with reversely zoned diopside, unzoned diopside, and groundmass plagioclase	121
6.39	Analcime-rich KS sample ER 117 showing phlogopite phenocryst	121
6.40	Equigranular texture of leucite and diopside (HKS sample ER 105)	124
6.41	Partially resorbed, olivine phenocryst with reaction rim (HKS sample ER 118)	124
6.42	Large phlogopite and abundant euhedral to subhedral leucite phenocrysts (HKS sample ER 110)	124
6.43	Enlarged view of HKS sample ER 110 showing leucite phenocryst with acicular inclusions of apatite	124
6.44	Euhedral, normally zoned diopside phenocryst (HKS sample ER 118)	125
6.45	Complex, irregular zoning in diopside phenocryst (HKS sample ER 118)	125
6.46	Partially resorbed olivine (forsterite) phenocryst (HKS sample ER 104)	125
6.47	Groundmass olivine (fayalite), diopside, and leucite (HKS sample ER 118)	125

LIST OF APPENDICES

	Page	
A	Isotope references	373
B	Sample localities	375
C	Lamprophyre classification	378
D	Mineralogy and texture of samples from Roccamonfina and Ernici	379
E	Microprobe analyses	405
F	Sample preparation	434
G	Analytical methods	440
H	Total Alkalis-Silica diagram sub-divisions	448
I	CIPW normative compositions	449

CHAPTER 1

INTRODUCTION

1.1 Overview of Italian magmatism

The Cenozoic igneous rocks of Italy have been studied extensively since the early 1900's, due in part to their unusual mineralogical and geochemical characteristics and in part to active volcanoes such as Vesuvius, Stromboli, Vulcano and Etna. Plio-Quaternary magmatism has produced a wide variety of mantle-derived rock types, including lamprophyres in the Western Alps, lamproites in Tuscany, kamafugites and carbonatites along the axis of the Apennine chain, ultrapotassic and potassic rocks in central Italy, calc-alkaline rocks in the Aeolian Islands, and sodic rocks in Sicily and Sardinia (Chapter 3). Mantle-derived Italian volcanic rocks have trace element signatures that range from intraplate to orogenic affinity, and radiogenic isotope compositions that extend from mantle to crustal values. The extreme geochemical variability of the volcanic rocks suggests that the mantle beneath Italy is chemically and mineralogically heterogeneous over relatively short distances (< 100 km) (Peccerillo and Panza, 1999).

1.2 Introduction to magmatic rocks of the Western Alps, Roccamonfina, and Ernici

This thesis focuses on the geochemistry of lamprophyre dykes from the Western Alps, and potassic and ultrapotassic volcanic rocks from Roccamonfina and Ernici in central-southern Italy (Figure 1.1). The lamprophyres from the Western Alps are located within the high-grade metamorphic rocks of the Alpine chain, while the potassic and ultrapotassic rocks from Roccamonfina and Ernici are located within the intermediate

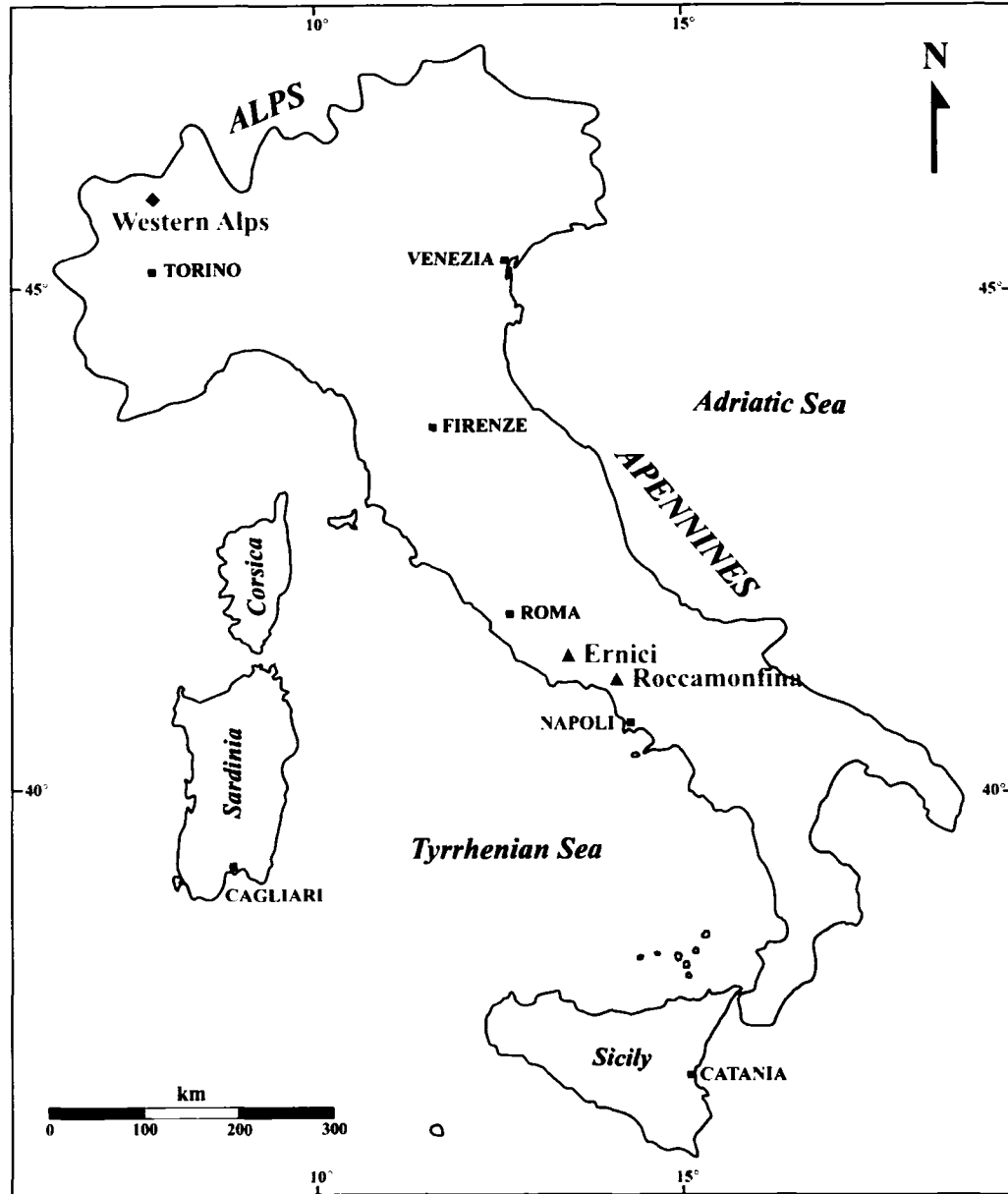


Figure 1.1. Location of the Western Alps, Roccamonfina, and Ernici in relation to some major Italian cities, the Alpine chain in northern Italy, and Apennine chain in peninsular Italy.

units of the Apennine chain. The lamprophyres are considerably older than the potassic and ultrapotassic volcanic rocks from Roccamonfina and Ernici, yet previous work has indicated that these areas may be isotopically related (Vollmer, 1976; Hawkesworth and Vollmer, 1979; Bell et al., 2003). By studying magmatic rocks that outcrop in the Alpine and Apennine chains, it may be possible to pinpoint the influence of each orogeny on the geochemistry of the Italian mantle.

The lamprophyre dykes from the Western Alps belong to a group of Eocene to Oligocene tholeiitic, calc-alkaline, shoshonitic, and ultrapotassic rocks that occur along a linear zone within the Alpine chain. Published isotopic data from the numerous mafic dykes and plutons in the Alps indicate that the mantle beneath the Western Alps may be isotopically different from the mantle beneath the Central and Eastern Alps (Kagami et al., 1985). High $^{87}\text{Sr}/^{86}\text{Sr}$ ratios (> 0.715) of ultrapotassic lamprophyres from the Western Alps (Venturelli et al., 1984) overlap with the $^{87}\text{Sr}/^{86}\text{Sr}$ ratios of several Tuscan lamproites (Conticelli, 1998), which suggests the possibility of a common, highly enriched mantle source region in north-central Italy. Despite the geographic and geodynamic importance of primitive rocks from the Western Alps, detailed studies of the mineral chemistry, major element, trace element, and isotope geochemistry of the dykes are lacking. The main purpose of studying lamprophyres from the Western Alps is to determine their geochemical signature and compare the data to other Alpine magmatic rocks as well as Plio-Quaternary volcanic rocks of peninsular Italy.

Roccamonfina and Ernici are located in one of the only regions in Italy where both potassic and ultrapotassic rock types occur. Studies of the geographic distribution of potassium-rich rocks in Italy have determined that volcanic rocks near Rome are

dominantly ultrapotassic in composition, while volcanic rocks in the Naples area are mainly potassic (Conticelli and Peccerillo, 1992). Roccamonfina and Ernici are located in a magmatic transition zone situated between Rome and Naples, where potassic (potassic trachybasalt, shoshonite, latite, and trachyte) and ultrapotassic (leucitite, tephrite, phonotephrite, tephriphonolite, and phonolite) rock types overlap in both space and time. Previous isotopic work has suggested that the ultrapotassic and potassic rock series reflect two different enrichment processes in the mantle (Rogers et al., 1985; Peccerillo, 1985). The main purpose of studying the potassic and ultrapotassic rocks from Roccamonfina and Ernici is to quantify the chemical differences between the two rock series and constrain the origin of potential contaminants that may have affected the chemistry of the mantle in central-southern Italy.

1.3 Tectonic setting of Italian magmatism

The unusual geochemistry of the mantle beneath Italy reflects the complex tectonic evolution of the Western Mediterranean. During the Cenozoic, the Western Mediterranean has been dominated by the interaction of the Alpine-Betic (Cretaceous-Miocene) and the Apennine-Maghrebides (late Oligocene-Pleistocene) collisional systems (Chapter 2). Subduction of oceanic lithosphere and limited amounts of continental lithosphere during one or both orogenies may be responsible for variable metasomatism of the Italian mantle (Thompson, 1977; Di Girolamo, 1978; Rogers et al., 1985; Beccaluva et al., 1991; Peccerillo, 1992). However, while many Italian volcanic rocks have trace element signatures that are comparable to those of world-wide subduction-related rocks, some features of Italian magmatism do not seem to fit a

convergent margin tectonic setting (Chapter 7). Opponents to subduction cite the presence of kamafugites and carbonatites in central Italy, rock types that have not been previously found in a subduction-related environment (Stoppa and Lavecchia, 1992). An alternative to a subduction scenario is an intraplate tectonic setting in which the mantle is enriched by deep-seated fluids or melts (Cundari, 1980; Vollmer et al., 1981; Stoppa and Lavecchia, 1992). Although the magmatic and tectonic differences between a convergent margin and an intraplate setting might seem clear, inconsistencies in tomographic images of subducted slabs and problems with the timing of volcanism have resulted in continued debate over the present-day tectonic setting of peninsular Italy.

Current discussion is focused on the identification of deep vs. shallow mantle enrichment processes. Shallow processes include slab dehydration related to subduction during the Alpine or Apennine orogeny, while deep processes include asthenospheric upwelling or mantle plumes. Unfortunately, volcanic rocks that are chemically similar to those from Italy have been found in both active island arcs (e.g. Sunda arc, Indonesia; Gertisser and Keller, 2003) and in intraplate continental settings where they are commonly associated with either active rifting (e.g. Toro-Ankole, East African Rift; Barberi et al., 1982) or perhaps even hotspot activity (e.g. Leucite Hills, USA; Mirnejad, 2002). Fortunately, new isotopic data (Chapters 4 and 8) may help to constrain both the tectonic setting and mantle enrichment processes involved in Italian volcanism.

1.4 Overview of lamprophyres: mineralogy, geochemistry and mode of occurrence

The term lamprophyre is derived from the Greek *lampros porphyros* meaning "glistening porphyry" (Gümbel, 1874) in reference to the large, lustrous biotite

phenocrysts that occur at the type locality of Fichtelgebirge, Germany. Most lamprophyres form dykes, sills, plugs, or stocks that are characterized by unusual intrusive features such as offsetting, segmentation, and banded or zoned internal structures. Lamprophyres commonly occur in dyke swarms or sill complexes, some of which can include hundreds to thousands of members (Rock, 1991). They are volatile-rich and carry essential amphibole and/or mica, along with significant amounts of minerals rich in F, Cl, SO₃, CO₂, and H₂O, such as carbonates, halides, sulphates, and zeolites (Rock, 1991). Alkali feldspar, phlogopite, amphiboles, and pyroxenes are characterized by high Ba, Fe³⁺, Al and/or Ti contents. Late-stage or subsolidus alteration of primary minerals is developed to an extreme degree in lamprophyres, due to their high volatile contents. Minerals normally considered secondary (e.g. chlorite, epidote, and serpentine) are almost as abundant as primary magmatic phases (Rock, 1991).

Lamprophyres commonly show a panidiomorphic texture in which many of the amphibole, mica, or pyroxene phenocrysts are euhedral. Bent, zoned mica, and felsic globular structures composed of carbonate, feldspars, chlorite, and/or epidote are characteristic (Rock, 1991). The major element geochemistry of lamprophyres is extremely variable, ranging from silica-oversaturated to strongly silica-undersaturated and from sodic to ultrapotassic. Trace elements are equally variable, although most lamprophyres contain high concentrations of large ion lithophile elements (LILE) such as K, Rb, Sr, and Ba, and low values of heavy rare earth elements (HREE), Sc, and Y.

Lamprophyres can be difficult to chemically discriminate based on whole-rock and mineral chemistry alone, and as a result the classification of many lamprophyres is largely based on texture, mode of occurrence, and tectono-magmatic association. Only a

few igneous rock types, including calc-alkaline granitoid plutons, shoshonite suites, alkaline syenite-gabbro plutons, and carbonatite-ijolite-nephelinite complexes, are associated with lamprophyres. Lamprophyres are found at both convergent margins in association with calc-alkaline plutons and shoshonites, and in intraplate tectonic settings with alkaline plutons and carbonatite complexes. A compilation of the global distribution and igneous associations of lamprophyres is given in Rock (1991). The lamprophyres from the Western Alps in northern Italy are associated in space and time with calc-alkaline granitoid plutons related to the Alpine orogeny (Chapter 5).

1.5 Overview of world-wide potassic and ultrapotassic rocks

Potassic rocks are characterized by high contents of K_2O (2-3 wt%) and other incompatible elements, combined with high K_2O/Na_2O ratios (> 1) and high $Mg/(Mg+Fe)$, Ni, and Cr. Ultrapotassic magmas, as defined by Foley et al. (1987), have $K_2O/Na_2O > 2$, $K_2O > 3$ wt%, and $MgO > 3$ wt.%. The $K_2O > 3$ wt% constraint avoids rocks that have high K_2O/Na_2O ratios but low total alkalis (virtually all kimberlites), and $MgO > 3$ wt% includes mafic but excludes sialic rocks. Potassic rock types include potassic trachybasalt, shoshonite, latite, and trachyte, while ultrapotassic rocks can be described in terms of three major chemical end-member groups (Foley et al., 1987): Group I (lamproites), Group II (kamafugites), and Group III (Roman-type plagioclites). Table 1.1 summarizes the geochemical and geological characteristics of the three ultrapotassic rock groups.

Potassic rocks range from slightly silica-oversaturated to slightly silica-undersaturated, and typically have high Al_2O_3 (14-20 wt%), low TiO_2 (< 1.2 wt%), and

	Group I Lamproites	Group II Kamafugites	Group III Plagioclitites
Major elements	Low Al ₂ O ₃ , CaO, Na ₂ O High K ₂ O/Al ₂ O ₃ (> 0.70) Variable TiO ₂ Extremely high K/Na	Low Al ₂ O ₃ , Na ₂ O High CaO Low SiO ₂ (< 45 wt%) Variable K ₂ O/Al ₂ O ₃	High Al ₂ O ₃ Low TiO ₂ Low K ₂ O/Al ₂ O ₃ compared to groups I and II
Trace elements	Most extreme incompatible elements and LREE enrichment Variable Nb, Ta, Zr Often negative Sr anomaly	Incompatible elements relatively anomaly-free High Nb, Ta, Zr No negative Sr anomaly	Negative anomalies for Ti, Nb, Ta, Zr, Ba
Volatiles	High H ₂ O, low CO ₂ Highest F (0.2-0.6 wt%)	High CO ₂ , high H ₂ O High or moderate F	Moderate H ₂ O Low to moderate CO ₂ Moderate F
Tectonic setting	Continental mild extension	Continental rift	Collisional setting
Ultramafic xenoliths	Depleted types (dunite, harzburgite) > fertile types (spinel lherzolite)	Pyroxenite, mica-bearing xenoliths > lherzolite, harzburgite	Dominantly pyroxenite, including mica-bearing types
Primitive magma character	High K/Al Low Ca, Al, Na Extremely high Mg-number (often 70-85) Variable SiO ₂ (~43-53 wt%)	Low SiO ₂ High Ca/Al	High Al ₂ O ₃ No extreme Mg-number (≤ 70)
Source redox condition	? reduced source	? oxidized source	? oxidized source

Table 1.1. Typical geochemical and geological characteristics of Group I, Group II, and Group III ultrapotassic rocks (Foley, 1992a).

high CaO (10-12 wt%) (Peccerillo, 1992). Moderately high K₂O contents, high K₂O+Na₂O (> 5 wt%), and high concentrations of incompatible elements distinguish potassic rocks from more common sub-alkaline rock types. The mineralogy of potassic rocks is dominated by diopsidic to salic clinopyroxene, plagioclase, olivine, biotite, and sanidine. Potassic rocks are commonly associated with calc-alkaline volcanic rocks along convergent plate boundaries (e.g. Sunda arc, Indonesia, and Aeolian arc, Italy), where they display a fractionated LILE/HFSE trace element signatures typical of subduction-related magmatism. Potassic rocks are also found in rift-related tectonic settings (e.g. East African Rift) (Barberi et al., 1982).

Group I ultrapotassic rocks (lamproites) are ultramafic to intermediate in composition, and are characterized by low CaO (< 8 wt%), Al₂O₃ (< 11 wt%) and Na₂O (< 2 wt%) contents. Lamproite mineralogy consists mainly of Mg-rich olivine, Al-poor diopside, Ti-rich phlogopite, sanidine, and potassian richterite. Minor and accessory phases include priderite, wadeite, perovskite, ilmenite, and enstatite, while the Al and Na-poor nature of Group I rocks prevents the crystallization of plagioclase, nepheline, and hauyne. Lamproites show the highest overall abundance of incompatible trace elements compared to other ultrapotassic rock types, particularly for Ba, Rb, K, Nb, and La. Group I rocks occur both in stable continental areas (Western Australia, Gausberg, Leucite Hills) and in orogenic areas associated with calc-alkaline or shoshonitic rocks. Lamproites associated with relatively recent orogenesis are found in southeastern Spain, Corsica, and Tuscany, and are characterized by marked negative anomalies of Nb, Ti, and Ba, similar to those of upper crustal rocks. Ultramafic mantle xenoliths found in lamproites are dominantly dunite and harzburgite.

Group II rocks (kamafugites) are named from the katungite – mafurite – ugandite series of the East African Rift. Although the Toro-Ankole rocks of Uganda are the type members of this group, kamafugites are also present at San Venanzo, Polino, Colle Fabbri, Cupaello, and Grotta del Cervo in central Italy. Group II rocks are distinguished by low SiO_2 (< 46 wt.%) and high CaO (up to 18 wt%), but generally lower $\text{K}_2\text{O}/\text{Al}_2\text{O}_3$ than Group I. Kalsilite, melilite, Mg-rich olivine, and diopside are common; monticellite, phlogopite, and perovskite may be present. Kamafugites from East Africa have high Nb, Ta, and Ti concentrations that closely resemble those of intraplate sodic alkaline rocks, while kamafugites from Italy are characterized by depletions in Ba, Nb, and Ti (Foley et al., 1987). Group II rocks occur dominantly in rift environments, as typified by the Toro-Ankole volcanics of the East African rift zone where kamafugites are found in association with carbonatites (Nixon and Hornung, 1973). Ultramafic nodules from the East African rift valley include clinopyroxenite and glimmerite; orthopyroxene and garnet are notably absent (Lloyd, 1981).

Group III rocks make up the strongly silica-undersaturated leucitite, leucite tephrite, phonotephrite, tephriphonolite, and phonolite series (collectively referred to as plagiroleucitites by Foley et al., 1987). Roman Province volcanic rocks are the type members of this group, which also includes the chemically similar leucite-bearing volcanics of the Sunda arc, Indonesia. Group III ultrapotassic rocks are commonly associated with potassic volcanic rocks, and are found in close proximity to shoshonitic rocks in both the Roman Province and the Sunda arc. Group III ultrapotassic rocks contain high Al_2O_3 (12-20 wt%), resulting in low $\text{K}_2\text{O}/\text{Al}_2\text{O}_3$ (generally < 0.5) in spite of their high K_2O contents. Leucite, plagioclase, sanidine, clinopyroxene, and olivine are

the main phenocryst phases, and nepheline is commonly present in the groundmass.

Group III rocks have fractionated LILE/HFSE ratios with pronounced depletions in Ba, Nb, and Ti, and are generally less enriched in incompatible elements compared to Group I (Foley et al., 1987). Trace element patterns for Group III plagioclinites are indistinguishable from Group II Italian kamafugites. Ultramafic nodules associated with Group III rocks are mainly clinopyroxenite, and have been documented only from the Roman Province (Giannetti, 1982).

1.6 Radiogenic isotope geochemistry of lamprophyres, potassic rocks, and ultrapotassic rocks

Lamprophyres generally have Sr, Nd, and Pb isotopic compositions that are more radiogenic than mid-ocean ridge basalts (MORB) and ocean island basalts (OIB).

$^{87}\text{Sr}/^{86}\text{Sr}$ ratios are typically close to or slightly greater than the value of Bulk Earth (0.7045), while $^{143}\text{Nd}/^{144}\text{Nd}$ ratios straddle the Chondritic Uniform Reservoir (CHUR) value of 0.51264 (DePaolo and Wasserburg, 1976). Higher $^{87}\text{Sr}/^{86}\text{Sr}$ ratios (> 0.7100) have been found in lamprophyres that are either transitional to (or perhaps better classified as) lamproites (Rock, 1991). The Sr and Nd isotopic compositions of lamprophyres from Central Europe and the U.S.A. (Navajo and Hopi Buttes) are plotted on Figure 1.2, and are similar to those of Group II and Group III ultrapotassic rocks.

Like MORB and OIB, the Pb isotopic ratios for most lamprophyres plot to the right of the geochron, a line that represents a primordial isochron along which all modern single-stage Pb should lie (Figure 1.3) (Faure, 1986). Lamprophyres generally plot above the Northern Hemisphere Reference Line (NHRL) defined by Pb-Pb values of MORB

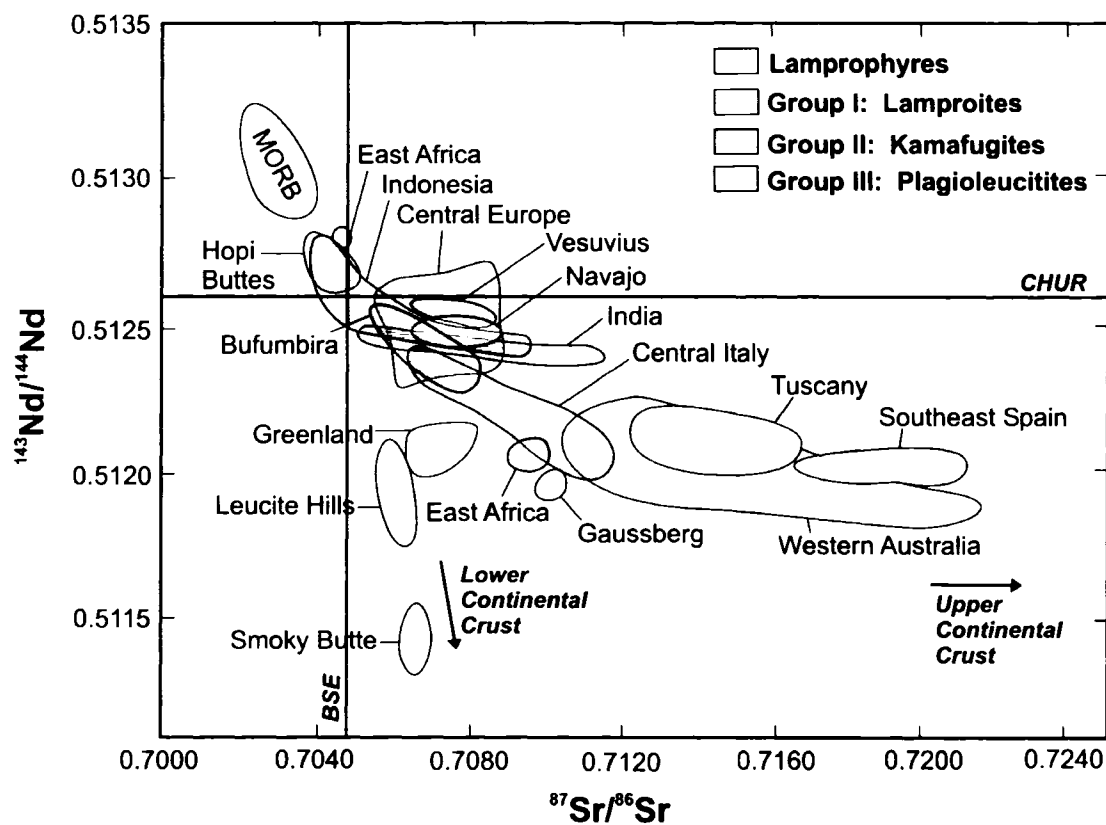


Figure 1.2. Published Sr-Nd isotopic compositions of selected lamprophyres and Group I, Group II, and Group III ultrapotassic rocks compared to the field of MORB. Note that some data from Italy and Indonesia are from potassic rocks, not ultrapotassic rocks. CHUR = Chondritic Uniform Reservoir; BSE = Bulk Silicate Earth. Data from Rock (1991), Nelson (1992), Peccerillo (1992) and references therein.

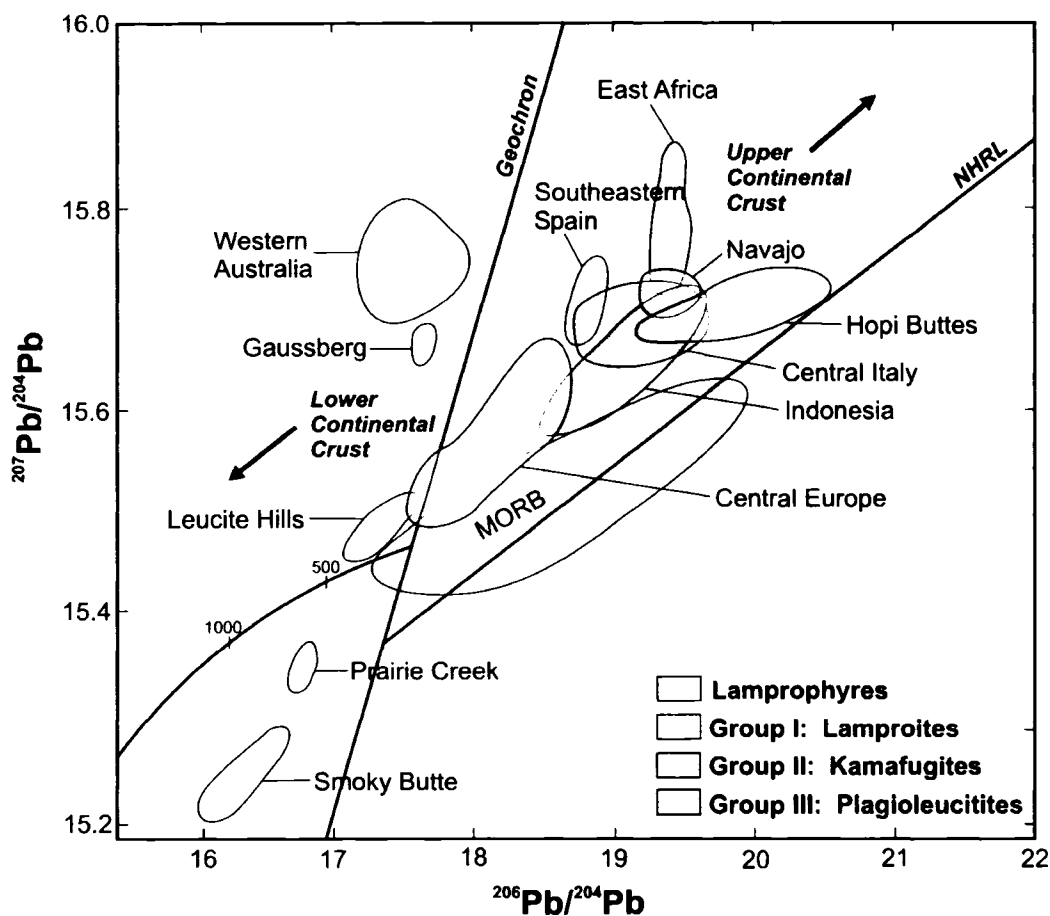


Figure 1.3. Published Pb isotopic compositions of selected lamprophyres and ultrapotassic rocks compared to the field of MORB. Note that some data from Italy and Indonesia are from potassic rocks, not ultrapotassic rocks. NHRL = Northern Hemisphere Reference Line. Data from Rock, (1991), Nelson (1992), Peccerillo (1992) and references therein.

and OIB from the Northern Hemisphere (Hart, 1984), indicating high $^{207}\text{Pb}/^{204}\text{Pb}$ and $^{208}\text{Pb}/^{204}\text{Pb}$ ratios relative to $^{206}\text{Pb}/^{204}\text{Pb}$. The high $^{87}\text{Sr}/^{86}\text{Sr}$, low $^{143}\text{Nd}/^{144}\text{Nd}$, and high Pb ratios of many mafic lamprophyres have been attributed to variable crustal contamination upon ascent, or metasomatism of the mantle by input of crustal material through subduction (Rock, 1991).

Potassic and ultrapotassic hypabyssal and volcanic rocks have more variable isotopic signatures than lamprophyres. Many potassic and ultrapotassic rocks have radiogenic isotopic signatures (i.e. high $^{87}\text{Sr}/^{86}\text{Sr}$ and low $^{143}\text{Nd}/^{144}\text{Nd}$ ratios) that trend toward the composition of either the upper or lower continental crust (Figure 1.2). Group I ultrapotassic rocks (lamproites) have the highest $^{87}\text{Sr}/^{86}\text{Sr}$ and lowest $^{143}\text{Nd}/^{144}\text{Nd}$ ratios of any mantle-derived igneous rock type, while Groups II and III have less extreme isotopic signatures. Relatively low $^{87}\text{Sr}/^{86}\text{Sr}$ (< 0.7080) and low $^{143}\text{Nd}/^{144}\text{Nd}$ ratios characterize Group I rocks from Smoky Butte, the Leucite Hills, and Greenland, while lamproites from Tuscany, southeast Spain, and Western Australia have high $^{87}\text{Sr}/^{86}\text{Sr}$ ratios (> 0.7100) that approach values typical of the upper continental crust. Most Group II and Group III ultrapotassic rocks have Sr and Nd isotopic ratios that are enriched relative to MORB and OIB. Pb isotopic ratios for Group I orogenic lamproites, Group II, and Group III rocks plot to the right of the geochron near the field of continental crust (Figure 1.3), while anorogenic lamproites (Smoky Butte, Prairie Creek, Leucite Hills, Gaussberg, Western Australia) plot to the left.

The Sr, Nd, and Pb isotopic characteristics of orogenic ultrapotassic rocks (e.g. Roman Province plagioclitites, Spanish lamproites, Sunda arc leucitites) as well as primitive lamprophyres suggest the possible involvement of upper continental crust in the

mantle. This topic has created much discussion (Peccerillo, 1985; Varne and Foden, 1986), as some authors have argued against the subduction of large amounts of buoyant, silica-rich continental crust. The enriched isotopic signatures of ultrapotassic rocks have also been attributed to mantle contamination by subducted marine sediments (Nelson, 1992), or derivation from ancient, highly-enriched subcontinental mantle, as proposed by Varne (1985) for the plagioclitites from the eastern Sunda arc.

1.7 Purpose of study

The main goals of this study are to:

- 1) Determine the mineralogy, chemistry, and isotopic signatures of magmatic rocks from the Western Alps and central-southern Italy (Roccamonfina and Ernici).
- 2) Integrate this data with previous work on Italian magmatic rocks in order to:
 - a) Examine the origin of the enriched isotopic signatures of Italian potassic and ultrapotassic rocks.
 - b) Evaluate the role of shallow (subduction-related) vs. deep (plume-related?) processes in the Italian mantle.
 - c) Examine the influence of the Alpine and Apennine orogenies on the Italian mantle.
- 3) Develop a model that relates the isotopic signatures of Italian magmatic rocks to the Cenozoic tectonic evolution of the Western Mediterranean.

CHAPTER 2

GEODYNAMIC EVOLUTION OF THE WESTERN MEDITERRANEAN

2.1 Introduction

The Cenozoic tectonic evolution of the Western Mediterranean reflects a complex interaction between the Alpine-Betic (Cretaceous-Miocene) and Apennine-Maghrebides (late Oligocene-Pleistocene) collision systems. Both are essentially the result of oblique convergence between Africa and Eurasia, resulting in consumption of Tethyan oceanic lithosphere followed by continental collision in the Tertiary. Areas affected by the Alpine-Betic and Apennine-Maghrebides orogenies can be viewed as internal and external units, respectively, where the internal units are locally metamorphosed to high temperatures and pressures, and the external units consist of weakly to non-metamorphosed basement overlain by Mesozoic to Cenozoic cover (Coward and Dietrich, 1989). As shown in Figure 2.1, internal units include the Kabylies, Calabria, parts of northeastern Sicily, Alpine Corsica, Liguria, the Betic-Rif cordillera, and the Pennine and Austroalpine nappes of the Alps *sensu stricto*. These are characterized by high-grade basement and associated sediments derived from both Africa and Eurasia, along with tectonically-emplaced slivers of oceanic crust. External fold and thrust belts include the Apennines, Maghrebides, Carpathians, central Sicily, most of the Dinarides and Hellenides, and external units of the Alpine and Betic-Rif belts.

Following the Alpine orogeny and partially overlapping in time with the Apennine orogeny, a series of E-W extensional basins began to form in the Western Mediterranean. Extension started with the formation of the late Oligocene Alboran,

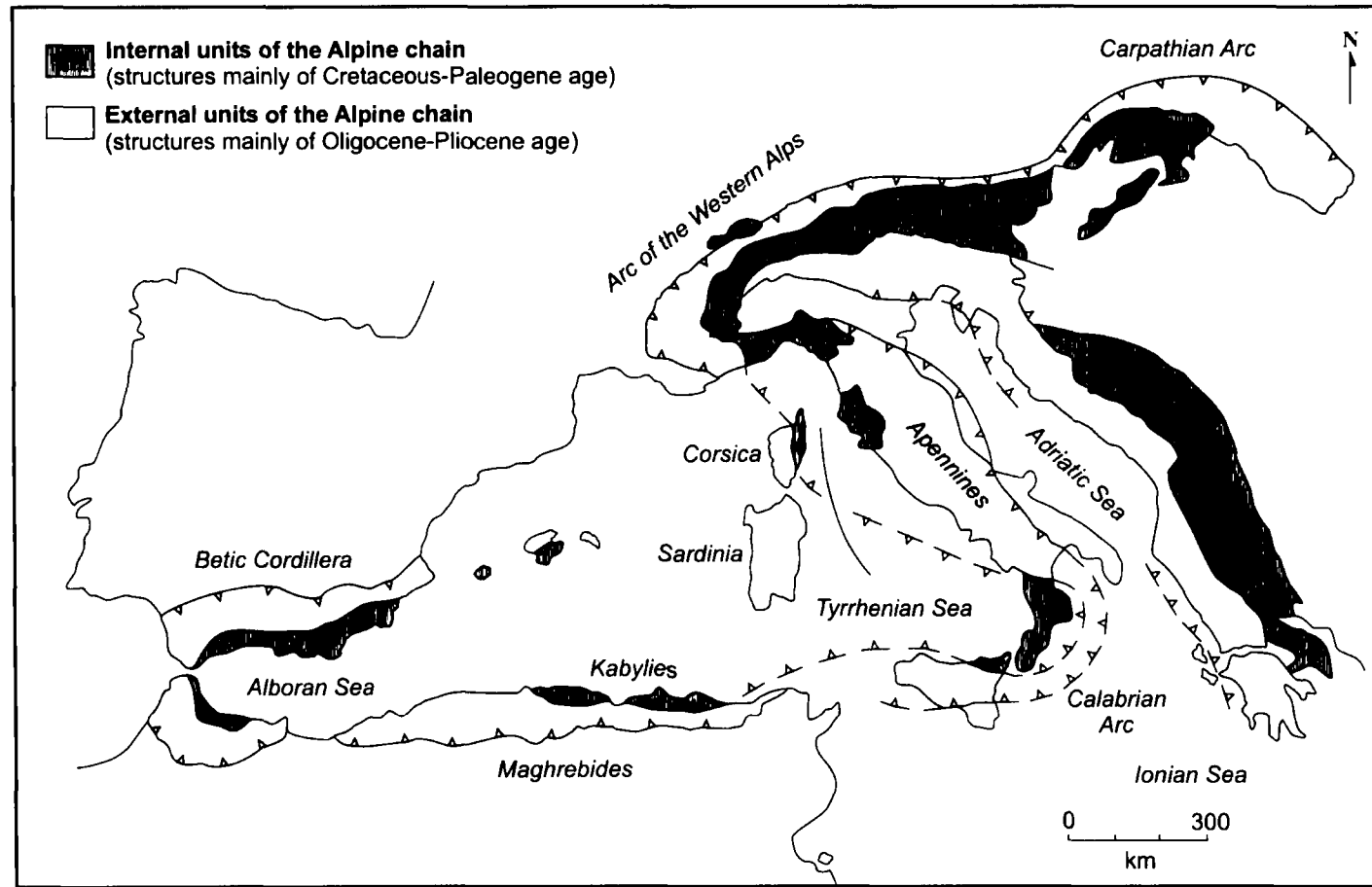


Figure 2.1. Simplified map of the internal and external units of the Alpine chain in Western Europe, showing the tight arcs and changes in vergence of thrusting. The internal units comprise slivers of oceanic crust and basement nappes with associated sediments from both continental margins and are affected by Alpine metamorphism. The external units consist of sedimentary décollement nappes and are generally only slightly affected by Alpine metamorphism (modified from Coward and Dietrich, 1989).

Valencia, and Liguro-Provençal basins in the west and was followed by the Miocene-Quaternary Tyrrhenian basin in the east. The force causing E-W extension in an overall compressional domain between Africa and Eurasia remains one of the major geodynamic problems in the evolution of the Western Mediterranean. Perhaps the most popular theory involves eastward roll-back of a westward-directed Apennine-Maghrebides subduction zone (e.g. Doglioni et al., 1997; Zeck, 1999). In this model, back-arc extension west of the subduction zone and mantle corner flow above the slab are the driving forces for rifting and basin formation in the Western Mediterranean.

This chapter deals with three main topics: 1) tectonic evolution of the Alpine belt with focus on the Western Alps, 2) formation of the major extensional basins, and 3) Apennine tectonics. Understanding the evolution of the western Mediterranean is critical to linking the chemistry of Italian magmatic rocks with the Alpine and Apennine orogenies. The important role of recent alkaline volcanism in determining the modern tectonic setting of Italy will be discussed at length in Chapter 3.

2.2 Alpine Tectonics

2.2a Mesozoic paleogeography

The Mesozoic paleogeography of the Western Mediterranean was controlled by the breakup of the supercontinent Pangaea, which started as early as the Triassic due to stress imposed by the initial opening of the present-day Atlantic. Rifting had separated West Africa from eastern North America in the early Jurassic (190 Ma), and by the early Cretaceous (120 Ma) Africa had separated from South America (Coward and Dietrich, 1989). This diachronous opening resulted in the formation of a large elongate pull-apart

basin of oceanic lithosphere between the northern Eurasian and southern African plates. This ocean, known as Tethys, was a global-scale feature that extended from the western Mediterranean to the eastern Himalayas. Dewey et al. (1989) estimated the maximum width of Tethys in the early Cretaceous to be slightly smaller than the width of the contemporaneous central Atlantic. In what is now the western Mediterranean, the Tethys Ocean was bounded by the European/Iberian margin to the west and the Adriatic promontory of Africa to the east (Coward and Dietrich, 1989). The northern and southern Tethyan margins, which formed the locations of the future Alpine and Calabrian Arcs, acted as principal transform fault boundaries. Throughout the late Mesozoic, large carbonate platforms accumulated within the Tethyan Ocean on what would eventually be the northern Alpine collision margin, while deep water basins dominated the future southern margin.

As pointed out by Coward and Dietrich (1989), the concept of Alpine continental collision as suggested by various authors depends entirely on their model of pre-Alpine Tethyan paleogeography. Collision is less clearly defined if the Tethys Ocean is considered a complex domain of small oceans and intervening stretched continental blocks (e.g. Lemoine and Trümpy, 1987) than if relatively distinct continental margins are assumed. The complexity of Alpine stratigraphy can best be explained by assuming that one large Tethyan ocean contained several Triassic to Cretaceous stretched basins on the continental margins (following Laubscher, 1970). Details of units found in the Western Alps derived from the southern continent, northern continent, and intervening ocean are provided in section 5.2b.

2.2b Eo-Alpine deformation (135 – 60 Ma)

In the mid-Cretaceous, the direction of plate motion in the Mediterranean changed from generally extensive to compressive, accompanied by the development of large strike-slip convergent zones. This change probably resulted from ocean floor spreading in the South Atlantic which caused Africa to move north and rotate in an anticlockwise direction (e.g. Lustrino, 2000). At this point, oceanic spreading in Tethys either stopped or was outpaced by the spreading of the Atlantic. Numerous Alpine units underwent high-pressure metamorphism at blueschist to eclogite facies conditions as the NW front of the Adriatic promontory converged with Eurasia during the late Cretaceous.

Blueschist-grade metabasic and ultrabasic rocks are exposed in the Tauern window in the Eastern Alps, and eclogitic micaschists and 'Gneiss Minuti' in the lower part of the Sesia-Lanzo Zone of the Western and Central Alps. Peak conditions in the Western Alps are recorded at >15 kb and 500-550°C, with the pressure maximum estimated at about 110 Ma (Hunziker et al., 1989).

This widespread tectonometamorphic event is related to subduction resulting from consumption of the Piemonte ocean basin (part of the Tethyan Ocean). Classical Alpine paleogeography assumes that high-pressure metamorphism affected *both* plate margins, necessitating two contemporaneous subduction processes on both the NW and SE margins (Hunziker and Martinotti, 1984). Due to the severe mechanical problems this scenario presents, most recent studies support one of two mutually exclusive possibilities: 1) NW-directed subduction, or 2) SE-directed subduction. Proponents of the NW-dipping model (i.e. subduction beneath Sardinia-Corsica and southern Europe) state that Alpine Corsica is linked to the northern Apennine system as an accretionary wedge

(Muttoni et al., 1998; Cello and Mazzoli, 1999). Carmignani et al. (1995) believe that this NW-directed subduction gave rise to the Oligo-Miocene magmatic arc of Sardinia. However, in the more popular model of SE-directed subduction, the Alpine nappes of Corsica are viewed as the southern continuation of the Western Alps, with European vergence and African backthrusts (Beccaluva et al., 1989; Doglioni et al., 1997). Subduction of the Piemonte basin under the Adriatic promontory is supported by ophiolites present in both the northern and southern Apennine chain, as well as Calabria (Di Girolamo et al., 1992).

As Lustrino (2000) noted, the lack of pre-Oligocene calc-alkaline magmatic activity in Sardinia and absence of a late Cretaceous – early Paleogene back-arc basin related to NW-directed subduction favors the SE-directed polarity of the downgoing slab. If this theory is correct, the abrupt change from SE-dipping Alpine subduction to NW-dipping Apennine subduction (see section 2.3e) is poorly understood. No direct evidence of subduction-related magmatism from this time period remains on either the European or Adriatic margin (von Blackenburg and Davies, 1995).

2.2c Meso-Alpine deformation (60 – 30 Ma)

The main phase of the Alpine orogeny is defined by Coward and Dietrich (1989) as the effect of continent-continent collision on the already deformed margins of the African Adriatic promontory and the Eurasian plate. A key to the understanding of this Meso-Alpine deformation is the continuous anticlockwise rotation of Africa relative to Eurasia from late-Cretaceous through mid-Tertiary time. This resulted in a diachronous

continental collision, with collision occurring earlier in the Eastern Alps and deformation progressing from east to west during the Tertiary (Coward and Dietrich, 1989).

Using Rb/Sr and K/Ar dates from mica combined with fission track data from apatite and zircon, Hunziker and Martinotti (1984) argued for a strong compressional phase in the Western Alps associated with actual continental collision in the early Eocene. This is supported by the Eocene age of the youngest sediments deposited in the Valais trough (a stretched basin on the European margin) (Trümpy, 1980). Meso-Alpine greenschist to amphibolite grade deformation pervasively overprinted most of the Eo-Alpine metamorphic domain, with the exception of the Sesia-Lanzo Zone in the Western Alps (Dal Piaz et al., 1972). Rb-Sr and K-Ar dates from mica, combined with stable isotope analyses (e.g. Hunziker, 1971), indicate that early Tertiary metamorphic events reached temperatures between 400°C and 600°C.

Ages of high-grade Alpine rocks suggest that subduction of thinned European continental crust occurred between 55 – 40 Ma, followed by uplift and cooling between 45 – 35 Ma (von Blanckenburg and Davies, 1995). During this time, the Austroalpine nappes (derived from the southern continent) along with remnants of intervening ocean were overthrust onto the nappes of the Eurasian plate in a WNW direction. Martinotti and Hunziker (1984) reported K-Ar phengite dates of ~38 Ma for the Dent Blanche nappe in the Western Alps, which has been interpreted as a complete resetting of isotope systematics under mid-Tertiary greenschist-facies conditions. Using apatite and zircon fission track analyses, Hurford et al. (1991) found that the Penninic Gran Paradiso massif, Dent Blanche nappe, Sesia-Lanzo Zone, and Ivrea Zone in the Western Alps had all cooled to ~225°C by 33 Ma.

The end of the Meso-Alpine phase in the Western Alps is marked by calc-alkaline to ultrapotassic magmatism around 32 – 30 Ma that is unaffected by greenschist-facies metamorphism. The reason for this widespread magmatism is not well understood, and Chapter 5 will discuss its location, chemistry, and significance. The onset of Oligocene molasse sedimentation in the Po basin is more or less contemporaneous with post-orogenic, magmatic activity across the Alps (Hunziker and Martinotti, 1984).

2.2d Neo-Alpine deformation (30 – 7 Ma)

The Neo-Alpine phase in the Western Alps from 27 – 18 Ma is restricted to local deformation effects linked to recrystallization of mica and amphibole (Hunziker and Martinotti, 1984). Later deformation in the Miocene/Pliocene (12 – 7 Ma) is mainly due to uplift and can only be recognized by fission track and mica-cooling ages. Hurford et al. (1991) found differential Neo-Alpine uplift in the major tectonic zones of the Western Alps, with rapid cooling and uplift of the Sesia-Lanzo Zone at ~25 Ma compared with slow cooling of the other units (Gran Paradiso massif, Dent Blanche nappe, Ivrea Zone) around 12 Ma. Thus, uplift does not follow a broad uniform regional pattern in the Western Alps but rather is episodic within specific areas. As Hurford et al. (1991) conclude, this argues strongly against simple isostatic uplift, and therefore a tectonically-induced uplift must be proposed.

Neo-Alpine deformation is synchronous with, and probably a mechanical consequence of, the main Apenninic phase plus the Neogene anticlockwise rotation of Sardinia-Corsica. According to Hunziker and Martinotti (1984), the most obvious expression of Apenninic movement in the Western Alps is the overthrust nappe structure

of the Monferrato region east of Torino, which shows no continuation into the oblique-trending Alpine units.

2.2e Summary of main Alpine tectonic features

- 1) Closure of the Mesozoic Tethyan basin(s) occurred at different times along the Alpine suture (generally proceeding from east to west) and involved different subduction kinematics and tectonic units. Most authors agree that the onset of compression between Africa and Eurasia was marked by the SE-directed subduction of oceanic lithosphere beneath the Adriatic promontory of Africa.
- 2) The Alpine chain is extremely arcuate with tight curvatures. Theories to explain strike direction changes of nearly 180° through the Western Alps and the Calabrian arc include: (a) complex paleogeographic outlines of the original Adriatic and Eurasian continental margins, and (b) rotational movements of the overthrusting margin relative to the underlying plate (Coward and Dietrich, 1989).
- 3) Strike-slip movement was very important in the formation of the Alpine chain. The general E-W trend of the Central and Eastern Alps can be considered a diffuse transpressive dextral shear belt along the northern transform boundary of Tethys, formed as a direct result of the anticlockwise rotation of the Adriatic promontory. Laubscher (1971) suggested 300 km of dextral strike-slip movement between the European foreland and the Adriatic hinterland.
- 4) The continent-continent collisional phase involved subduction of continental lithosphere, as evidenced by huge volumes of missing continental material in

reconstructed models and high-pressure/low-temperature metamorphism of continental crust in the Western Alps (Dal Piaz et al., 1972).

- 5) Extension of deep sub-vertical lithospheric roots about 200 km occur in the Central and Western Alps, and the Betic cordillera. Interpretations based on seismic reflection data include unidirectional SE-directed subduction of the European lithosphere (Marchant, 1993), bivergent subduction involving participation of lithosphere from both plates (Laubscher, 1974), and lithospheric thrusting of the southern plate over the northern plate with associated crustal thickening (Bayer et al., 1987).
- 6) Neither the Eurasian nor the Adriatic plates behaved as rigid bodies during the Alpine collision. Both deformed internally, reactivating Mesozoic faults and earlier Paleozoic steep strike-slip zones (Coward and Dietrich, 1989). Widespread tectonic basin inversion in NW Europe occurred from the middle Cretaceous to the Pliocene, accompanied by the development of a major rift system in the Oligocene to middle Miocene.
- 7) Opening of the various Tertiary extensional basins in the Western Mediterranean (discussed in section 2.3) resulted in fragmentation of the Alpine chain.

2.3 Extensional basin formation

2.3a Introduction

The opening of the Western Mediterranean can be considered in terms of two phases: I) late Oligocene to middle Miocene, and II) middle Miocene to Quaternary. Phase I rifting began in the western part near southern France/eastern Spain in the late

Oligocene, and was followed by Phase II in the eastern part as rifting migrated progressively towards Italy through the Miocene and into the Quaternary. Extension resulted in a series of basins, some containing thinned continental crust and some with newly-formed oceanic crust, that now separate the Eurasian plate from the African plate. Tectonic models for basin formation can be separated into two main groups: 1) asthenospheric upwelling in an intraplate environment, or 2) back-arc extension behind an active subduction zone. Sections 2.3b and 2.3c will describe Phase I and Phase II respectively, section 2.3d will summarize the main tectonic features, and 2.3e will review current theories regarding basin formation.

2.3b Phase I: late Oligocene – middle Miocene

The first phase of extension in the Western Mediterranean began with the eruption of calc-alkaline volcanic rocks in Sardinia (~32-13 Ma) and Provence (~34–20 Ma), followed by the opening of the Liguro-Provençal basin in the late Oligocene (Figure 2.2) (Beccaluva et al., 1994). A rift system ("Fossa Sarda") reflecting the continental stage of extension crosses the entire island of Sardinia from the Asinara Gulf to the Cagliari Gulf (~220 km). Syn-rift deposits along the western Sardinian and Provençal margins range from Oligocene to Aquitanian in age, and are unconformably overlain by late Aquitanian post-rift sequences (Faccenna et al., 1997). The Liguro-Provençal basin is characterized by oceanic crust within a central abyssal plain surrounded by narrow (except for the Gulf of Lyon) older sedimentary basins. Based on this geometry and the pattern of magnetic anomalies, the existence of a single rift (mid-ocean ridge style) has been proposed (Burrus, 1984) even if the characteristic ridge relief has not been observed on deep

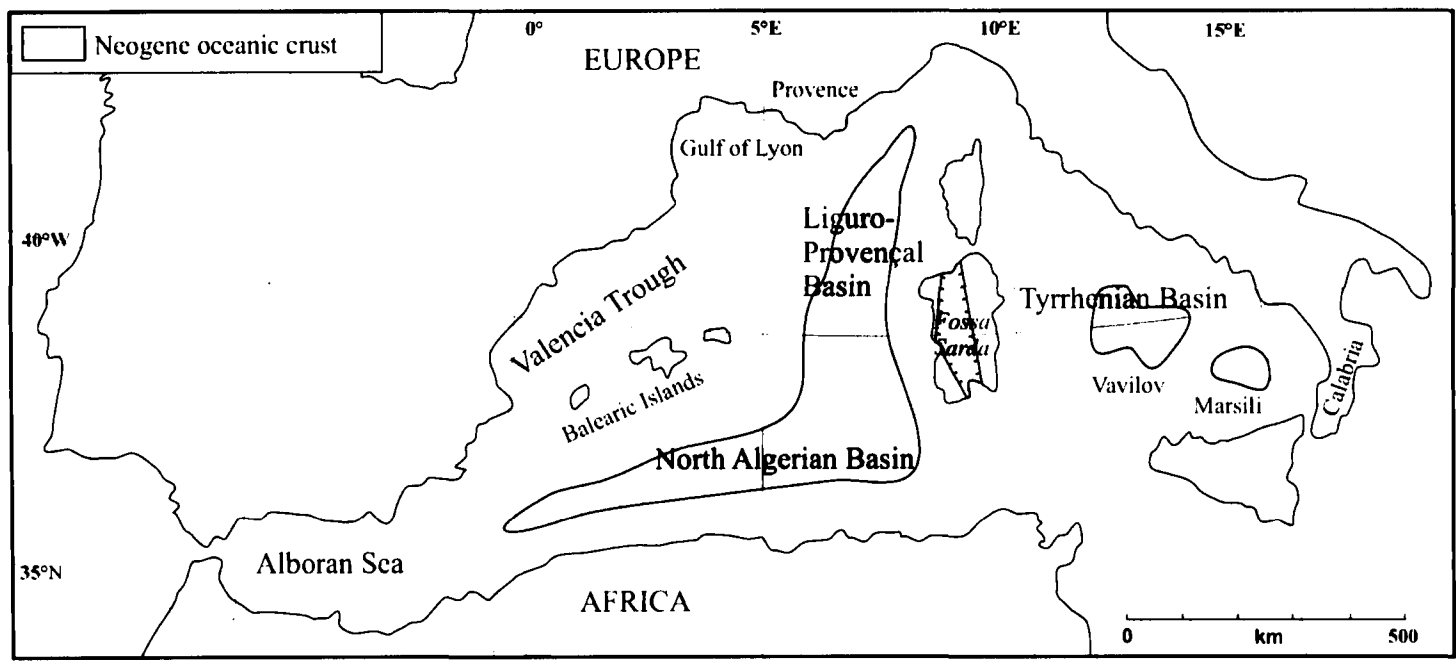


Figure 2.2. Extensional basins in the Western Mediterranean (modified from Gueguen et al., 1998).

seismic profiles.

A major consequence of sea-floor spreading in the Liguro-Provençal basin during the Miocene was the detachment of the Sardinia-Corsica continental block from its prior position adjacent to southern France. Paleomagnetic data indicate that the rigid block rotated anticlockwise $\sim 23^\circ - 30^\circ$ between 21 and 16 Ma (Van der Voo, 1993) at an estimated rate of about 4–5 cm/yr (Burrus, 1989). It is interesting that the Corsica-Sardinia block rotated rapidly in the "wrong" direction in the generally dextral transpressive environment that characterized the Africa-Eurasia plate boundary. Laubscher (1988) concluded that the only way to provide space for such a movement is vertical escape by means of sinking of large parts of the lithosphere to the east of the block. Geodetic data confirms that the Sardinia-Corsica block does not currently show any significant motion with respect to the Eurasian plate, and can thus be considered as part of a common lithospheric region (Devoti et al., 2002).

During this first phase of extension, the Alboran Sea opened (22-10 Ma) southeast of Spain and the continental crust of the Valencia trough thinned as the Balearic promontory shifted south (Comas et al., 1992). The Alboran, Valencia, and Liguro-Provençal basins can be considered a coherent system of inter-related troughs whose trend is oblique to that of the nearby Alpine-Betic front (Doglioni et al., 1997). Extension cross-cuts the Alpine belt and thus provides further evidence that the basins of the Western Mediterranean developed independently from the Alpine orogeny. All three basins contain normal faults that migrated progressively east toward the Miocene – Quaternary Algerian and Tyrrhenian basins.

2.3c Phase II: middle Miocene – Quaternary

During the middle Miocene, the Western Mediterranean underwent a major change in stress regime as the Corsica-Sardinia block collided with the continental margin of the Adriatic microplate. The lack of easily-subducted oceanic or thinned continental lithosphere may have effectively stalled the subduction process in the northern Apennines at ~13 Ma and led to the end of andesitic volcanism in Sardinia (Argnani and Savelli, 1999). Rifting and extension jumped from the Liguro-Provençal basin on the western side of Sardinia-Corsica to the Tyrrhenian basin on the eastern side. There is also a clear eastward migration of rifting within the Tyrrhenian basin itself, from Tortonian (~9 Ma) in the western part to Plio-Pleistocene in the east (Doglioni, 1991).

The Tyrrhenian basin is divided by the 41°N transform fault and associated magnetic anomaly into a northern and a southern part (see section 2.4c). Extension and crustal thinning in the northern Tyrrhenian is marked by a system of spaced crustal shear zones and sedimentary basins. Syn-rift deposits range from 15-20 Ma near Corsica to about 2 Ma along the Apennine watershed, where normal faults are still active (Faccenna et al., 1997). In the southern Tyrrhenian, syn-rift deposits are progressively younger from Sardinia (10-12 Ma) towards the Vavilov sub-basin (~5 Ma). The average velocity of extension in the southern Tyrrhenian (5-6 cm/yr) during the Pliocene was significantly higher than that of the northern Tyrrhenian (Patacca et al., 1990).

Formation of oceanic crust occurred in the southern Tyrrhenian after 5 Ma in two separate sub-basins, partially as a response to the southeastward drifting and arching of the Calabrian Alpine block. New ocean crust formed first in the Vavilov (4.0-3.5 Ma) and then in the Marsili (1.9-1.7 Ma) sub-basin, and became progressively younger

towards the ESE (Sartori, 1990). In contrast to Phase I rifting in the Liguro-Provençal basin, the style of extension in the Tyrrhenian as a whole is diffuse, with spreading centres distributed over a wide area. Faccenna et al. (1997) suggest that different styles of extension in the Western Mediterranean may be in part a function of pre-rift Moho temperature, where a relatively high temperature (600-800 °C) in the Tyrrhenian may have caused the wide rift region.

2.3d Summary of main tectonic features of basin formation

- 1) The Alpine orogeny preceded and partially overlapped with rifting and basin formation in the Western Mediterranean. The dominant N-S movement of the African continent is not considered by most authors to be a major factor in the creation of an E-W extensional regime.
- 2) There is a clear genetic link between both phases of rifting in the Western Mediterranean. Jumps in the thinning process and rejuvenation of extension towards the ESE has been shown in both the Liguro-Provençal and Tyrrhenian basins (Guegen et al., 1997). Asymmetric rifting with low angle, E-dipping normal faults is present in the western margin of the Liguro-Provençal basin and in the northern Apennines, as one might expect from an eastward-migrating zone of extension.
- 3) Up until the late Oligocene, the Alpine-Betic deformational front was likely continuous from the Western Alps through Corsica and into southern Spain (Doglioni et al., 1997). This SE-directed subduction system was subsequently

fragmented by the Miocene anticlockwise rotation of the Corsica-Sardinia continental block.

- 4) The Western Mediterranean is characterized by large variations in lithospheric and crustal thickness (e.g. Guegen et al., 1997). The lithosphere has been thinned to less than 60 km in the basins (50-60 km in the Valencia trough, 20-25 km in the Tyrrhenian) while it remains 65-80 km beneath Corsica-Sardinia and the Balearic Promontory. Typical crustal thicknesses are 8-15 km in the basins and 20-30 km beneath stretched continental blocks.

2.3e Geodynamics of basin formation

As mentioned earlier, the series of relatively young extensional basins located between Africa and Eurasia in the Western Mediterranean are considered the result of either: 1) asthenospheric upwelling in an intraplate environment, or 2) back-arc extension behind an active subduction zone. Although most authors consider the basins to have formed as a consequence of the latter, the debate is far from over. One of the often cited lines of evidence for back-arc extension is the eastward migration of basin formation over the past 30+ Ma, presumably as a response to the eastward migration of a W-dipping subduction zone. The subduction zone is thought to have migrated about 775 km across the western Mediterranean, consuming Adriatic oceanic or thinned continental lithosphere along the way and creating back-arc basins in its wake.

The subduction zone was oriented roughly parallel to the direction of Africa-Eurasia plate convergence during its whole lifetime, therefore the rate of accretion at the trench was likely low and subduction was probably driven by the slab's own negative

buoyancy (Malinverno and Ryan, 1986). Such slab rollback is a phenomenon amplified by the tectonic situation in the Western Mediterranean, but certainly not unknown in other regions. Figure 2.3 shows a simplified reconstruction of the geodynamic evolution of the Western Mediterranean based on a subduction system that initially developed at the present eastern Spanish coast and subsequently moved eastward by a series of slab rollback phases. The eastward-migrating subduction zone is commonly held responsible for the Phase I calc-alkaline magmatism in Sardinia as well as the structure of the modern Apennines (see section 2.4). However, the orientation and timing of the subduction system is poorly constrained. Faccenna et al. (2001) pointed out the slab must have reached a minimum depth of 100–150 km to produce melting in the mantle wedge and arc volcanism at the surface. These authors suggested that the subduction zone may have actually been initiated around 80 Ma during a large-scale rapid pulse of in-plane compressional stress in the circum-Mediterranean region.

An alternative tectonic scenario suggests that NW-directed subduction was initiated only after a polarity flip with an earlier Alpine SE-directed subduction zone. Estimates of the timing of this polarity flip include the Cretaceous-Tertiary boundary (65 Ma; Dercourt et al., 1986), the Paleocene (50 Ma; Boccaletti et al., 1971) or the Oligocene (30 Ma; Doglioni et al., 1997). The main objective of these alternative models is to explain the development of west-verging nappe structures in Alpine Corsica and east-verging Apenninic structures. However, a NW-dipping Apennine subduction zone and a SE-dipping Alpine subduction zone are not mutually exclusive, and Faccenna et al. (2001) support the model of a double-vergent Alpine-Apennine orogenic wedge in which NW-directed subduction started to the east of the pre-existing (inactive) front of the

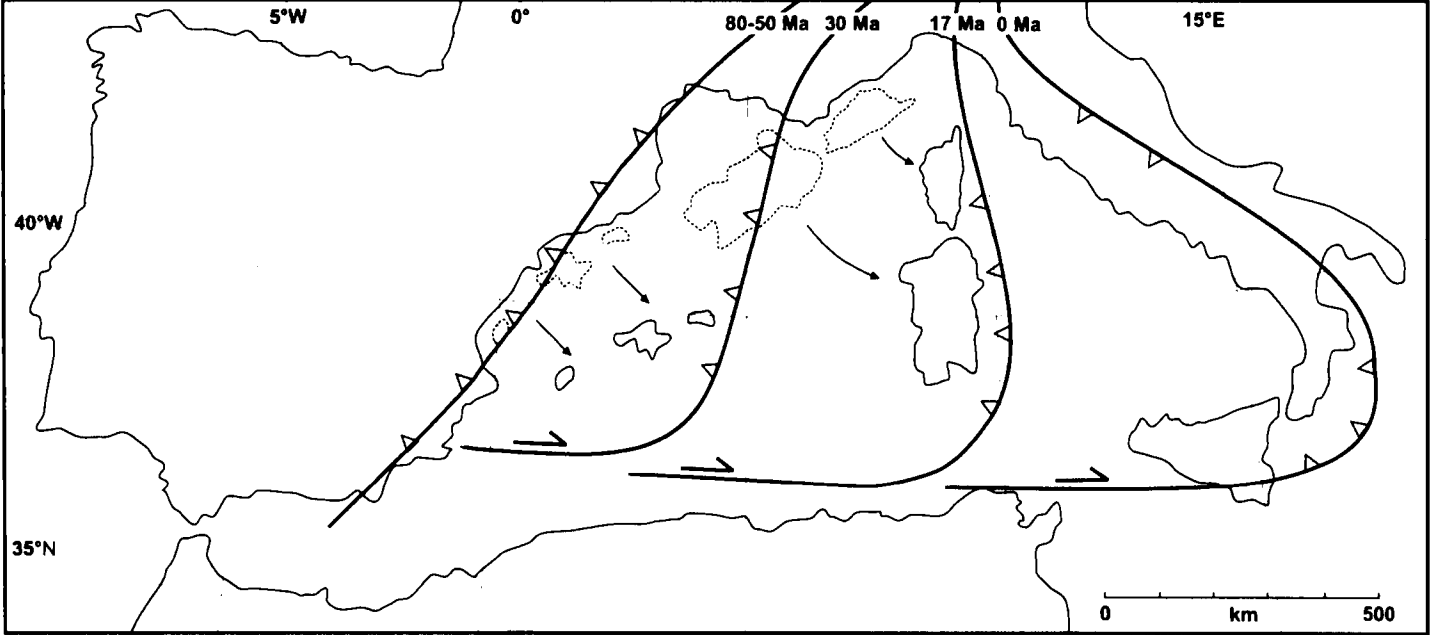


Figure 2.3 Paleogeographic reconstruction of eastward slab rollback and back-arc extension in the Western Mediterranean from the late Cretaceous to the present-day (after Wortel and Spakman, 1992).

Alpine-Betic chain.

While eastward rollback of a W-directed subduction zone explains some aspects of Western Mediterranean basin formation, it fails to account for others. For example, the scarcity of calc-alkaline rocks along peninsular Italy (considered the hallmark of subduction-related magmatism) raises some serious questions. Calc-alkaline volcanic rocks have thus far only been identified in Oligo-Miocene rifting in Sardinia and Provence, and in Pliocene rocks from deep boreholes in Campania, southern Italy (Di Girolamo, 1978). As discussed at length in Chapter 3, the vast majority of Neogene-Quaternary volcanic rocks in Italy are alkaline in character and quite similar in chemistry to those emplaced in intra-plate, rift-related settings (Stoppa and Cundari, 1995). If a subduction zone has indeed traversed the Western Mediterranean over the past 30 Ma, a more continuous spatial and temporal distribution of calc-alkaline volcanic rocks would be expected, but this is clearly not the case.

2.4 Apennine tectonics

2.4a Introduction

The Apennine fold and thrust belt is generally considered to represent an accretionary wedge that developed in response to the westward subduction of the Adriatic plate beneath the Tyrrhenian Sea. Active thrusting initiated in the early Miocene (~20 Ma) and has continued until the Quaternary in some areas, with total shortening estimated at several hundred kilometres (Bally et al., 1986). The aim of this section is to discuss the major structure of the Apennines and introduce some theories regarding its tectonic evolution. The Apennine chain *sensu stricto* runs along the length of Italy from the

western end of the Po Plain to central Sicily (excluding Calabria), while the continuation of the external fold and thrust belt in northern Africa is referred to as the Maghrebides.

2.4b Structure

The E- and NE-verging thrust sheets of the Apennine chain consist of allochthonous Meso-Cenozoic sedimentary rocks originally deposited on the continental and transitional crust of the Adriatic plate that were stripped from the basement during thrusting (Royden et al., 1987). Much of the belt is composed of carbonates from platform or back-reef facies intercalated with external basin sediments (Lucente et al., 1999). The Apennines have developed in the absence of major plate convergence, and as a result the entire chain is collapsing nearly as rapidly as it is rising (Cavinato and De Celles, 1999). The eastern (Adriatic) flank of the range is a narrow active compressional fold and thrust belt, while the larger western (Tyrrhenian) flank is dominated by ongoing Pliocene-Quaternary extension. Compression in the Apenninic foreland and extension in the hinterland has migrated across the Italian peninsula from west to east during the late Neogene.

Numerous Pleistocene to Recent NW-elongated extensional basins filled with alluvial, colluvial, lacustrine, and shallow-marine deposits are present along the western flank. Mature basins and major boundary faults are commonly associated with late Pleistocene mafic volcanic rocks (Cavinato and De Celles, 1999). The present-day stress field of much of western Italy is dominated by NE-SW extension, as determined by Montone et al. (1995) using breakout analysis and seismicity studies from the Quaternary volcanoes of Latium and Tuscany. As a result, there is widespread NW-SE normal

faulting as well as crosscutting of Plio-Pleistocene grabens across the whole of the Apennine thrust pile (Hippolyte et al., 1994).

Published models to explain the bimodal tectonic behavior of the Apennines include mantle upwelling in response to foundering of the thickened Alpine lithospheric root without any active subduction (Decandia et al., 1998), mantle upwelling above the subducting slab (Keller et al., 1994), and general eastward flow of the upper mantle beneath Italy (Doglioni, 1991). Gravitational collapse of overthickened crust is considered unlikely, as the crust is not particularly thick (25-30 km beneath the western flank) (Scarascia et al., 1994). Cavinato and De Celles (1999) proposed that corner flow in the mantle wedge beneath the crest of the range (crustal thickness 35-40 km) promotes contraction at the front of the orogenic belt while maintaining extension in the trailing part. Whether or not a compressional stress regime at the front of the belt could be maintained during slab rollback is a matter of debate.

2.4c Controls on tectonic evolution

The northwest-trending Apennine belt can be divided into three major segments: the northern Apennine, central-southern Apennine, and Calabrian arcs (Figure 2.4). The separation between the northern and central-southern Apennines is marked by a NE-SW trending lithological transition zone (Ancona-Anzio line), which corresponds with a major change in seismic tomography. Lucente et al. (1999) suggested that this deep discontinuity may represent a lateral structural margin within the subducting Adriatic lithosphere. The Ancona-Anzio line is spatially related to the 41°N offshore transform fault system, which likely resulted from differing rates of opening between the northern

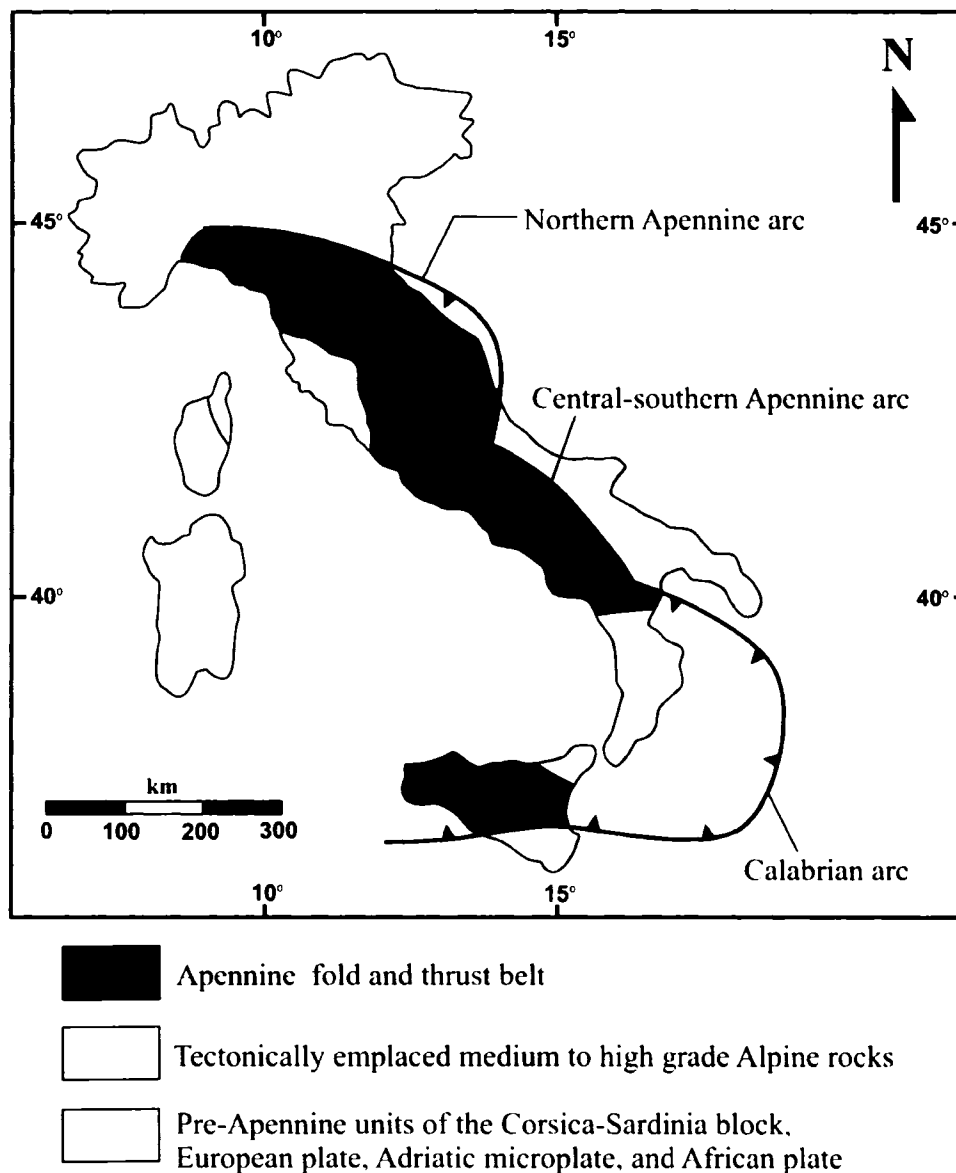


Figure 2.4. Simplified present-day distribution of arcs of peninsular Italy showing the northern Apennine, central-southern Apennine, and Calabrian arcs (modified from Lucente et al., 1999).

and southern Tyrrhenian sub-basins. The strike-slip movements along the 41°N fault and the normal movements along the older Ancona-Anzio line are consistent with an extensional stress field, although seismic data indicates that both fault systems are now largely inactive (Bruno et al., 2000). The limestone outcrops of the central-southern Apennines end abruptly in northern Calabria (Sanginetto line), where Paleozoic Alpine metamorphic rocks disrupt the continuity of the Apennine-Maghrebides chain.

The tectonic evolution of each segment of the Apennine chain is linked to the distribution of continental and oceanic lithosphere along the eastern margin of Italy. The Adriatic lithosphere is continental in origin (Suhadolc and Panza, 1989) while the adjacent Ionian lithosphere, which separates the Adriatic microplate from the African plate, is likely oceanic. Doglioni (1991) interpreted the northward-decreasing extension of the Tyrrhenian basin to be a function of the northward-decreasing capability of subducting the thick Adriatic continental lithosphere. Shortening in the northern Apennines shows a linear northward decrease from 170 to 35 km, confirming that extension and compression are genetically linked (Bally et al., 1986). In fact, the estimated contemporaneous amounts of extension in the Tyrrhenian and shortening in the Apennines appear to be very similar (Malinverno and Ryan, 1986). The pronounced curvature of the Calabrian Arc is likely controlled by the composition and thickness of the oceanic Ionian lithosphere, which is retreating southeastward (Doglioni, 1991).

2.4d The Adriatic microplate

The paleogeography of the Adriatic continental margin is just as important for the study of Apennine tectonics as it is for Alpine tectonics (see section 2.2). Because the

Apennines are considered the result of tectonic stacking of sedimentary rock units originally deposited on the thinned Adriatic margin, the distribution of embayments and promontories along the margin are important to understanding the development of the Northern and Central-southern Apennine arcs. Lucente et al. (1999) proposed that a thick promontory of the Adriatic plate reached the trench in the central-southern Apennines at about 6.5 Ma (Messinian), slowing slab roll-back in this region and leading the development of independent northern Apennine and Calabrian arcs where oceanic lithosphere was still subducting. Other authors (Doglioni et al., 1994) recognize two sub-domains in the Adriatic plate: a northern block (lithospheric thickness ~ 70 km) characterized by faster roll-back of the subduction hinge, and a southern block (lithospheric thickness ~ 100 km) also known as the Apulian carbonate platform. The sub-domains are separated by a seismically active E-W trending, second-order plate boundary called the Tremiti line (Console et al., 1993). Using GPS site velocities and seismicity, Oldow et al. (2002) also found a similar northern block within the Adriatic plate currently moving NE at ~3 mm/yr, and a southern block moving N to NW at velocities up to ~10 mm/yr. These velocity differentials have led to buckling of the thick lithosphere beneath the Apulian platform and active tensional and transtensional faulting in the Adriatic plate (Doglioni et al., 1994).

2.4e Summary of main Apennine tectonic features

- 1) The Apennines are composed of sedimentary rocks originally deposited on the western margin of the Adriatic microplate. These rocks are thought to have been

thrust eastward as a response to collision of a W-dipping subduction zone with the Adriatic microplate in the Miocene.

- 2) The Apennines are characterized by bimodal tectonics in which the western flank is currently undergoing extension, whereas the eastern flank is undergoing compression.
- 3) The continental crust in peninsular Italy is relatively thin, and ranges from 25-30 km thick on the western flank to 35-40 km thick beneath the axis of the Apennines.
- 4) Promontories and embayments on the Adriatic microplate may have been responsible for the formation of three tectonic segments within the Apennine chain; the northern Apennine, central-southern Apennine, and Calabrian arcs.
- 5) The lithosphere in the southern part of the Adriatic microplate is approximately 30 km thicker than in the northern part. This is due to the thick Apulian carbonate platform, which may have stalled subduction in central-southern Italy upon arrival at the Apenninic trench in the late Miocene (Lucente et al., 1999).

CHAPTER 3

CENOZOIC ITALIAN MAGMATIC PROVINCES

3.1 Introduction

The potassic alkaline Pliocene-Quaternary volcanism of central Italy has attracted interest ever since Washington (1906) first commented on the geochemical peculiarities of the "Roman Comagmatic Province". Classical studies have divided recent Italian magmatism into three main regions: the Tuscan Province, the Roman Comagmatic Province, and the Aeolian Arc in the southeastern Tyrrhenian Sea. However, during the past thirty years it has become increasingly apparent that the magmatism of peninsular Italy is much more complex than originally thought. Geochemical data now permits the recognition of at least ten major magmatic provinces (Figure 3.1), including several older (Paleocene-Miocene) provinces in northern Italy. The original area in central-southern Italy described by Washington (1906) is now subdivided into the Roman Province, the Southern Latium Transition Zone, and the Campanian Province (Peccerillo and Panza, 1999). The Southern Latium Transition Zone contains the study areas of Roccamonfina and Ernici, while samples from the Western Alps belong to the Tertiary Periadriatic Province in northern Italy.

In order to examine the relation between magmatism in the study areas and nearby magmatic provinces, a detailed description of the rock types, occurrences, geochemistry, and isotopic signatures of each of these provinces is given. The magmatism of the Western Alps, Roccamonfina, and Ernici can then be integrated into a regional framework by including data from northern and eastern Italy, Sicily, the Aeolian

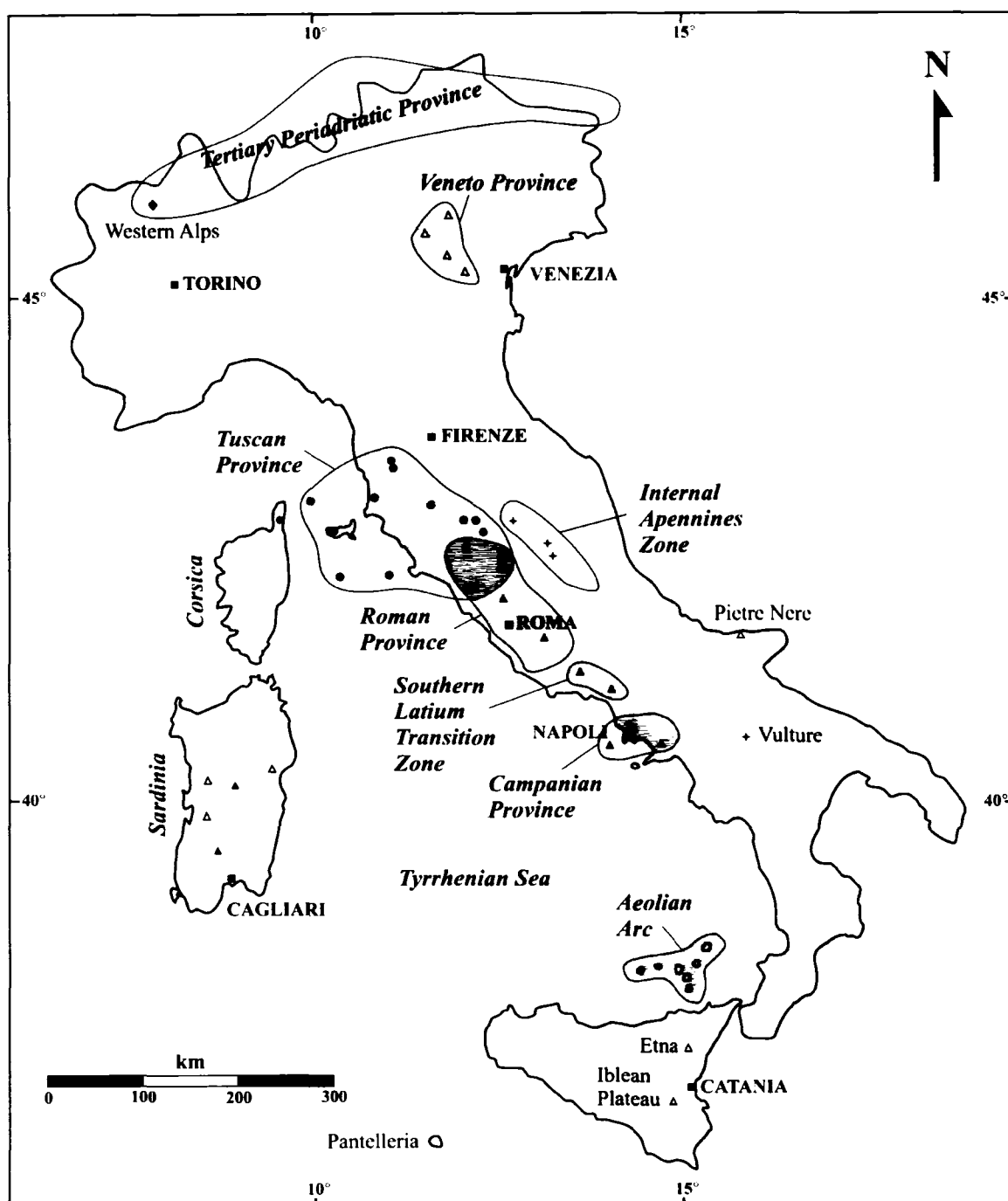


Figure 3.1. Cenozoic magmatic provinces of Italy. Symbols: filled black circles = lamproites; filled grey circles = anatectic centres; filled diamond = lamprophyres; crosses = kamafugite ± carbonatite; filled triangles = potassic volcanic centres; open triangles = sodic volcanic centres; filled squares = cities. Note that individual volcanic centres for the Tertiary Periadriatic Province are not shown (see Figure 3.2).

Islands, Sardinia, and the Tyrrhenian Sea floor. The purpose of this chapter is to demonstrate the wide variety of igneous rocks present in Italy and examine large-scale changes in isotope, major element, and trace element geochemistry.

3.2 Northern Italy

3.2a Tertiary Periadriatic Province

The Tertiary Periadriatic Province (TPP) is a linear magmatic zone that stretches from the Western Alps to the Eastern Alps (Figure 3.2). Magmatism in the TPP is confined to a narrow belt located immediately to the south and north of the Periadriatic Lineament, a major Alpine E-W dextral strike-slip feature thought to have accommodated the anti-clockwise Tertiary rotation of the Adriatic promontory against Europe (Coward and Dietrich, 1989). Beccaluva et al. (1983) suggested that the lineament is a site of deep discontinuity and crustal weakness that may have provided a preferential path for TPP magmatism. Intrusive ages for both mafic and felsic magmatism range from 42 to 24 Ma but display a pronounced maximum between 33 and 29 Ma (von Blanckenburg et al., 1995). Most TPP magmatic rocks intruded thrust nappe sheets and are considered to be syn- to post-collisional, associated in part with late thermal updoming related to Mesozoic Alpine metamorphism (Venturelli et al., 1984).

Almost all major intrusions of the TPP belong to the gabbro-tonalite-granodiorite-granite calc-alkaline suite, the largest of which are the Adamello, Bergell, and Rensson plutons. Variable assimilation of continental crustal material by mantle-derived magmas combined with fractional crystallization (AFC) is the main petrogenetic model for many of the granitoid intrusives (Cortecci et al., 1979; Taylor, 1980; Juteau et al., 1986). On

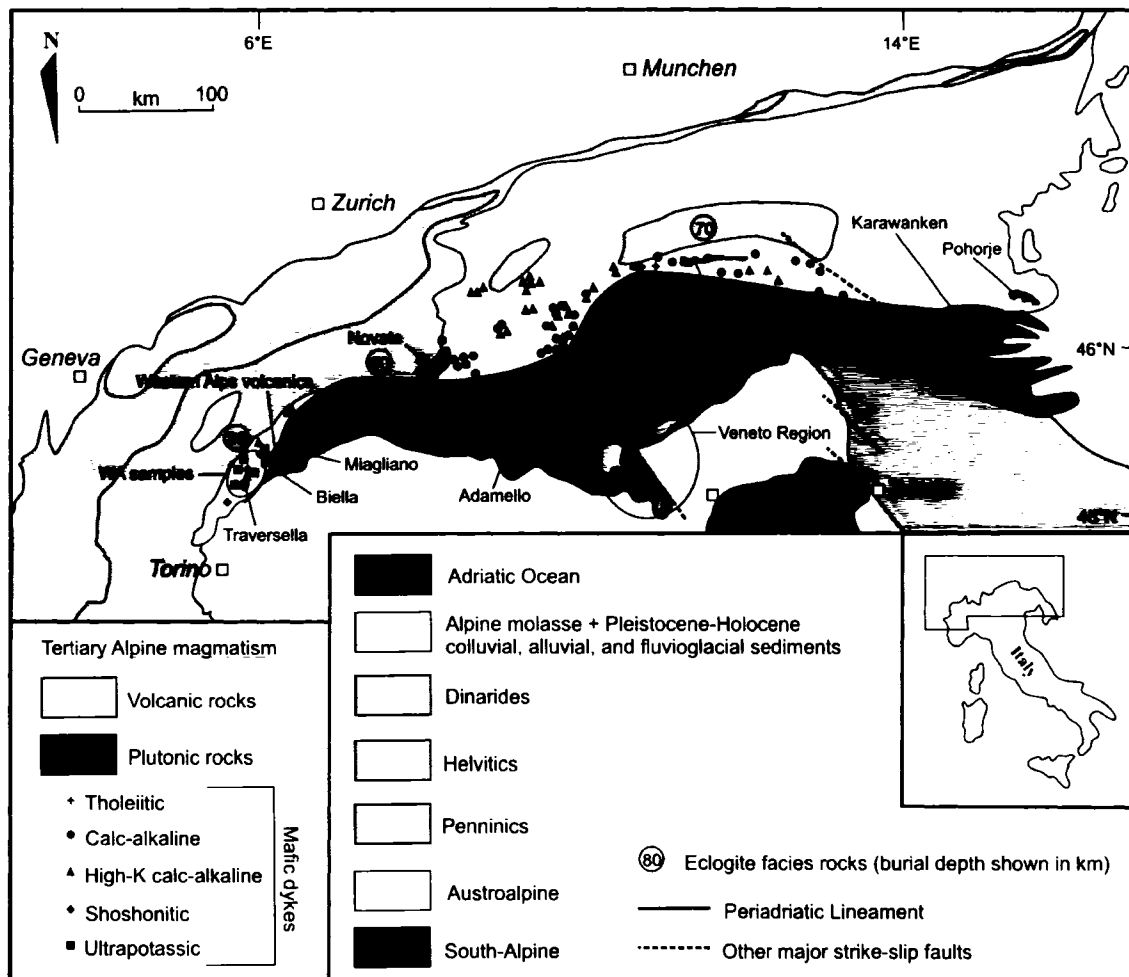


Figure 3.2. Simplified tectonic map of the Alps showing the distribution of Tertiary magmatic rocks along the Periadriatic Lineament (modified from Beccaluva et al., 1983; Dal Piaz, 1983; von Blanckenburg et al., 1998).

the basis of Sr-Nd isotopic ratios, Kagami et al. (1985) showed that intrusive rocks from the Eastern Alps have a weak crustal signature, while those from the Western Alps (Biella, Bergell, Traversella) have a stronger crustal signature with isotopic characteristics similar to basic granulites from the Southern Alps. Kagami et al. (1985) tentatively attributed the stronger crustal signatures to large-scale subduction of continental material during the Eocene with ensuing rapid uplift and anatexis melting.

Hypabyssal dykes of the TPP are widespread and more compositionally diverse than the granitoid intrusions. Beccaluva et al. (1983) observed that the dykes change gradually from tholeiitic/calc-alkaline in the Southeastern Alps and high-K calc-alkaline in the Central Alps, to shoshonitic and ultrapotassic in the Western Alps. All rock types exhibit negative Ti and Nb anomalies together with enrichment of LILE compared to HFSE; however, only the shoshonitic and ultrapotassic dykes show pronounced positive LREE and Th anomalies and a strong positive fractionation of Tb with respect to Yb (Beccaluva et al., 1983). The spatial changes in chemical composition have been related to: i) mantle melting at different depths, ii) different degrees of partial melting, iii) melting of a previously metasomatized mantle, and iv) crustal contamination of mantle-derived magmas (see von Blanckenburg et al., 1998).

3.2b Veneto Province

In the Veneto Region of the South-Eastern Alps, alkali, transitional, and tholeiitic basalts with an intra-plate geochemical signature erupted from four main volcanic centres during the late Paleocene to the late Oligocene (Figure 3.2) (Macera et al., 2003). The initiation of the mafic alkaline magmatic activity in the Veneto Region preceded the

widespread calc-alkaline magmatism of the TPP by only a few million years. Most basalts have Mg#s ≥ 50 , low SiO₂ (< 45 wt.%), low Al₂O₃ (<15 wt.%), and high Ni (160–270 ppm) and Cr (250–470 ppm) contents. According to some authors (Zampieri, 1995; De Vecchi and Seda, 1995; Milani et al., 1999), volcanism in the Veneto region is related to extensional tectonics that developed in the foreland of the Southern Alps in response to the WNW–SSE compression of the Adriatic and European plates during the Alpine orogeny. Alternatively, Macera et al. (2003) suggested that the Veneto volcanics may represent the shallow expression of mantle uprise following detachment of the subducted European lithosphere.

3.3 Central Italy

3.3a Tuscan Province

The Tuscan Province is a magmatically complex area that includes: 1) crustal anatectic rhyolites and granites, 2) ultrapotassic, mafic, high-silica lamproites, 3) hybrids between lamproitic magmas and ultrapotassic leucite-bearing magmas, and 4) hybrids between crustal melts and various types of mantle-derived potassic magmas.

Crustal anatectic rocks are represented by a number of scattered plutonic and volcanic centres in central and southern Tuscany (Table 3.1). Relatively small volcanic edifices at San Vincenzo, Roccastrada and Tolfa are composed primarily of rhyolitic lavas, whereas Amiata and Cimino are larger and more complex rhyodacitic volcanoes that also contain small volumes of latite. Detailed geochemical studies (Dupuy, 1970; Dupuy and Allègre, 1972) supplemented by isotopic evidence (Taylor and Turi, 1976; Hawkesworth and Vollmer, 1979) have shown that the rhyolites of San Vincenzo and

Name of Magmatic Province (age in Ma)	Names of Individual Magmatic Centres	Rock Types & Volcanic Landforms	Geochemical Highlights of Primitive Rock Types
Tuscan Province (14.2 – 0.2)	Sisco, Capanne, San Vincenzo, Roccastrada, Tolfa, Amiata, Cimino, Montecatini, Orciatice, Capraia, Torre Alfina, Radicofani, Vulsini	<i>Crustal anatectic rocks:</i> granitoid intrusions, aplites, pegmatites. Monogenic lava flows and domes, stratovolcanoes (Amiata, Cimino). <i>Mafic rocks (including lamproites):</i> small monogenic lava flows, plugs and necks.	Ultrapotassic ($K_2O = 7-14$ wt%) Silica-oversaturated Low Ca, Na, Al, Fe, moderate V, Sc High Mg# (75-80), Cr, Ni High LILE/HFSE ratio Negative anomalies of Ta, Nb, P, Ti, Ba, Ce, and Sr Contains mantle xenoliths (spinel harzburgite with minor phlogopite peridotite)
Roman Province (0.6 – 0.02)	Vulsini, Vico, Sabatini, Alban Hills	Large volcanoes formed by HKS (leucite-tephrite, leucitite, phonolite) and minor KS (trachybasalt, latite, trachyte) lavas and pyroclastics.	HKS: ultrapotassic, strongly silica-undersaturated, $K_2O/Na_2O = 0.9-2.4$ KS: potassic, silica-saturated, $K_2O/Na_2O = 2.4-5.6$ Both series have moderate Ca, Na, Al, V, and Sc and variable Mg#, Cr, and Ni. Higher LILE/HFSE than Tuscan lamproites. Large negative anomalies of Ta, Nb, and Ti, smaller troughs at Hf and Zr
Southern Latium Transition Zone (0.7 – 0.03)	Roccamonfina, Ernici	Monogenic cinder cones and minor lava flows (Ernici), stratovolcano (Roccamonfina) of KS and HKS rocks.	Moderate to high Ca, Na, and Al. Variable Mg#, Cr, Ni. Low TiO_2 Moderate-high LILE/HFSE.
Campanian Province (0.8 – present)	Somma-Vesuvius, Phlegrean Fields, Ischia, Procida, Ventotene	Stratovolcanoes with calderas formed by KS and minor HKS rocks.	Higher content of HFSE and lower LILE/HFSE ratios than KS of Roman Province and Southern Latium Transition Zone. No negative Nb-Ta anomalies Low B/Be (< 4)

Table 3.1. Summary of the rock types, volcanic landforms, and geochemistry of each central Italian magmatic province.

<i>Name of Magmatic Province (age in Ma)</i>	<i>Names of Individual Magmatic Centres</i>	<i>Rock Types & Volcanic Landforms</i>	<i>Geochemical Highlights of Primitive Rock Types</i>
Internal Apennines Zone (0.6 – 0.3)	San Venanzo, Polino, Colle Fabbri, Cupaello, Grotta del Cervo	Diatremes, maars, tuff-rings, lava flows and scattered pyroclastic deposits of ultrapotassic melilititic (kamafugitic) composition. Carbonate-rich (carbonatite?) pyroclastics.	Ultrapotassic Strongly silica-undersaturated $K_2O/Na_2O = 8-20$ Low Na and Al Kamafugites contain highest CaO (13.0-18.9 wt%) of all Italian ultrapotassic rocks Lower LREE/HREE than Roman Province
Vulture (0.7 – 0.1)		Stratovolcano with caldera formed by Na-K-rich tephrites, phonolites, nephelinites with abundant hauyne.	High K, Na, and S $K_2O \approx Na_2O$ Variable MgO, high Cr, Ni, Ba, Nb, Ta, Hf, and Zr Moderate to low LILE/HFSE Contains mantle xenoliths
Pietre Nere (56)		Mafic alkali syenite intrusion.	$Na_2O > K_2O$ Small negative anomalies of Th and K Positive anomalies of Ba, Ta, Nb, P, and Zr

Table 3.1. *Continued.*

Roccastrada are distinct from the rhyodacites of Amiata and Cimino. Neither of these groups can be related by any differentiation process, and the rhyolites and rhyodacites are considered to reflect compositional differences in crustal source rocks.

The anatectic origin of both groups is indicated by excess Al (Barberi et al., 1967), high $^{87}\text{Sr}/^{86}\text{Sr}$ ratios (0.711-0.726; Barberi et al., 1971), and extremely high $\delta^{18}\text{O}$ values (+11.2-16.4; Taylor and Turi, 1976). In contrast to the high and variable $^{87}\text{Sr}/^{86}\text{Sr}$ ratios, the Pb isotopic compositions of the Tuscan anatectic rocks are fairly uniform (Vollmer, 1977). Taylor and Turi (1976) suggested that Tuscan acid rocks have been derived from large-scale assimilation of argillaceous sediments or metasediments by calc-alkaline magmas, or by partial melting of sedimentary rocks.

Ultrapotassic, mafic, high-silica lamproites of the Tuscan Province are present at Montecatini, Orciatice and Torre Alfina. The lamproites are plagioclase-free, isolated hypabyssal dykes with Mg# (Mg/Mg+Fe) up to 75-80, high Ni (up to 350 ppm) and Cr (up to 800 ppm), and low Al, Ca, and Na. The high concentrations of compatible elements, as well as the presence of mantle-derived xenoliths (spinel harzburgite with minor phlogopite peridotite) at Torre Alfina, confirm that the lamproites are of mantle origin. LILE contents are high, and mantle-normalized incompatible element patterns closely resemble those of upper crustal rocks (Peccerillo et al., 1988).

Hybrid rocks intermediate in composition between Tuscan lamproites and Roman-type, ultrapotassic rocks are found at Radicofani (0.8-1.0 Ma), Cimino, and Latera (west Vulsinian district). The potassic rocks from Radicofani, a small volcanic neck (~100 m in elevation), have Mg#s between 67-74, and lower Ni (100-170 ppm) and Cr (400-590 ppm) contents than the lamproites. The LREE are enriched compared to the

HREE, and the $^{87}\text{Sr}/^{86}\text{Sr}$ ratios are high and variable (Poli et al., 1984).

Evidence for interaction between Tuscan magmas of anatectic origin and upper mantle-derived potassic magmas is seen in the form of “minette” inclusions enriched in incompatible elements found within the rhyodacitic lavas of Amiata and Cimino (Puxeddu, 1971; Van Bergen et al., 1983). The inclusions are petrographically similar to the late-stage mafic latitic flows and contain diopside, forsteritic olivine, and mica. Van Bergen et al. (1983) suggested that the inclusions represent a mafic end-member with geochemical affinities to potassic Roman magmas, and that both Roman-type and Tuscan anatectic magmas may have co-existed and produced hybrid rocks by mixing in a shallow crustal environment.

3.3b Roman Province

The Pleistocene Roman Province consists mainly of K-rich volcanic rocks with mafic to intermediate compositions that can be divided into two series: a potassic series (KS) and a highly potassic series (HKS) (Appleton, 1972; Peccerillo and Manetti, 1985). The two series can be classified on the basis of their $\text{K}_2\text{O}/\text{Na}_2\text{O}$ ratios and degree of silica saturation, Q , which equals the algebraic sum of normative quartz-(nepheline+leucite+kalsilite) (Conticelli and Peccerillo, 1992). The KS mafic rocks have $\text{K}_2\text{O}/\text{Na}_2\text{O}$ ratios of 0.9-2.4 and are slightly silica oversaturated ($Q = +3$ to -10), while the HKS rocks are strongly undersaturated ($Q = -36$ to -50) and have $\text{K}_2\text{O}/\text{Na}_2\text{O}$ ratios of 2.4-5.6. Figure 3.3 shows the fields for KS and HKS rocks on a diagram of $\text{K}_2\text{O}/\text{Na}_2\text{O}$ versus Q , as well as the fields for Italian kamafugites, lamproites, transitional KS-lamproites, and typical shoshonites and calc-alkaline arc volcanic rocks.

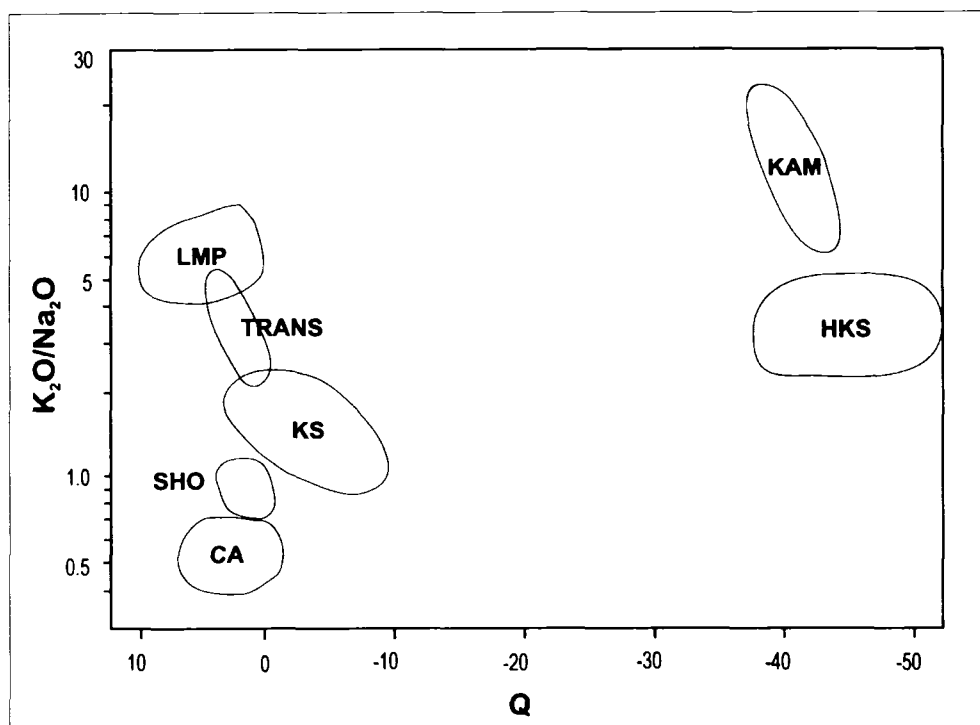


Figure 3.3. Geochemistry of the potassic series (KS), highly potassic series (HKS), Italian kamafugites, lamproites, transitional KS-lamproites, and typical shoshonites and calc-alkaline arc lavas ($Q = \text{algebraic sum of normative [quartz} - (\text{nepheline} + \text{leucite} + \text{kalsilite})]$). Modified from Conticelli and Peccerillo (1992).

The volcanic centres of Vulsini, Vico, Sabatini and the Alban Hills belong to the Roman Province (Table 3.1). These centres are dominated by HKS rocks, while the Southern Latium Transition Zone and Campanian Province to the south have a higher proportion of KS rocks. All KS and HKS rock types from the Roman Province are characterized by high CaO, Al₂O₃, and Na₂O combined with low TiO₂ contents. The HKS rocks contain leucite, clinopyroxene and plagioclase with minor olivine and subordinate magnetite and apatite, while the KS volcanic rocks are characterized by plagioclase and clinopyroxene with accessory olivine, apatite and magnetite. Although both the KS and the HKS rocks are enriched in incompatible trace elements, members of the HKS series have higher abundances of LILE and show a more marked negative Ba anomaly than those of the KS series (Conticelli and Peccerillo, 1992). The KS and HKS rocks are characterized by higher LILE/HFSE than Tuscan lamproites, and pronounced negative Ta, Nb, and Ti anomalies. The HKS rocks of the Roman Province exhibit a relatively restricted range of ¹⁴³Nd/¹⁴⁴Nd (0.51223-0.51218) and ⁸⁷Sr/⁸⁶Sr (0.7097-0.7108) ratios. These rocks have similar Nd isotopic ratios, but very different Sr isotopic compositions from the SiO₂-saturated, crustal-derived lavas of Tuscany.

3.3c Southern Latium Transition Zone

Roccamonfina and Ernici, located between Rome and Naples, make up the Southern Latium Transition Zone and can be considered geographically and geochemically transitional between the Roman and Campanian Provinces (Table 3.1). Roccamonfina (549-35 ka) is a partially dissected stratovolcano with a central caldera 6 km in diameter, while Ernici (700-100 ka) is represented by a series of about twenty

small volcanic edifices in the Media Valle Latina. Both volcanic centres produced silica-undersaturated HKS rocks that closely resemble the ultrapotassic rocks from the Roman Province, and silica-saturated KS rocks that are very similar to those from Campania. No intermediate series between the HKS and KS has been found. The HKS magmas have higher $^{87}\text{Sr}/^{86}\text{Sr}$ ratios, incompatible element abundances, and LILE/HFSE ratios, and lower $^{143}\text{Nd}/^{144}\text{Nd}$ ratios than the KS magmas.

3.3d Campanian Province

The Campanian Province includes the Somma-Vesuvius volcanic complex, the Phlegrean Fields, and the islands of Ischia, Procida, and Ventotene (Table 3.1). Somma-Vesuvius (25ka – present), located east of the Gulf of Naples, is one of the most intensively studied volcanoes in Italy. Sub-Plinian eruptions, strombolian-type activity, and effusive and explosive eruptions of tephritic leucitite to leucititic phonolite are characteristic of recent activity at Vesuvius (Civetta et al., 1991a). N-MORB normalized multi-element diagrams of rocks from Vesuvius exhibit selective enrichments of Sr, K, Rb, Th, and LREE, but the Nb and Ta negative anomalies commonly seen in rocks generated in subduction-related tectonic settings are absent (Ayuso et al., 1998).

The Phlegrean Fields (47 ka – present) is dominated by a large caldera about 12 km in diameter characterized by vertical deformation, intense fumarolic emission, and microseismic activity. Geophysical and petrological data suggest that a shallow magma chamber (located at a depth of about 5 km) is responsible for the seismicity and ground deformation (Armienti et al., 1983; Villemant, 1988). The nearby island of Ischia is also very active, with recent seismicity, ground deformation, and fumarolic emissions

characterized by anomalously high levels of Rn (Gasparini, 1963). The potassic volcanic rocks from Ischia (150-75 ka) have the least radiogenic Sr, the most radiogenic Nd and Pb, and the lowest $\delta^{18}\text{O}$ values of the Campanian potassic rocks, and also display an overall trend of decreasing $^{87}\text{Sr}/^{86}\text{Sr}$ and increasing $^{143}\text{Nd}/^{144}\text{Nd}$ with decreasing age.

3.3e Internal Apennines Zone

The Internal Apennines Zone, located east of the Tuscan and Roman Provinces along the axis of the main Apennine chain, includes the volcanic centres of San Venanzo, Polino, Colle Fabbri, Cupaello, and Grotta del Cervo. Magmatism (600-200 ka) is characterized by strongly undersaturated olivine melilitites, kalsilite melilitites and other foid-bearing rocks of kamafugitic affinity ($\text{K}_2\text{O}/\text{Na}_2\text{O} = 8\text{-}20$) associated with carbonate-rich pyroclastics (Laurenzi et al., 1994). Volcanic rocks form diatremes, maars, tuff-rings, lava flows, and scattered pyroclastic deposits that lie within a NNW-SSE trending band 200 km long and 50 km wide (Lavecchia and Boncio, 2000).

Although rocks from the Internal Apennines Zone have lower $\text{SiO}_2 + \text{Al}_2\text{O}_3$ and higher Mg#, $\text{K}/(\text{K} + \text{Na})$, $(\text{Cr} + \text{Ni})$ and LREE/HREE ratios than the KS and HKS volcanic rocks of the Roman Province, incompatible element patterns and radiogenic isotope signatures are similar (Castorini et al., 2000). The kamafugites contain small mantle xenoliths, xenocrysts and lapilli cored by olivine, pyroxene, and phlogopite with high Ni, Cr, and Mg#. The Polino and Cupaello rocks contain >50% carbonate and are compositionally comparable to carbonatites from Castignon Lake, Canada (Dimroth, 1970), Fort Portal, Uganda (Barker and Nixon, 1989), Tinderet, Kenya (Deans and Roberts, 1984) and Goudini, South Africa (Verwoerd, 1867). The carbonate-rich rocks

exhibit an exotic mineralogy typical of carbonatites, including monticellite, perovskite, baddeleyite, pyrochlore, and high contents of Sr, Ba and other incompatible trace elements in calcite (Stoppa and Woolley, 1997).

Peccerillo (1998), however, argued that the carbonate material that occurs in rocks of the Internal Apennines Zone may be of secondary origin, derived from the interaction between kamafugitic magmas and the >2000 m thick limestone sequences present in the area. High $\delta^{18}\text{O}$ (+21 to +26) in the carbonate-rich volcanics suggests a secondary origin, while $\delta^{13}\text{C}$ values (-4 to -14) are in the range of carbonatites (Stoppa and Woolley, 1997). The carbonate-rich rocks have the same radiogenic isotope ratios as the associated silicate lavas, which agrees with the hypothesis of a common origin, e.g. by liquid unmixing during magma ascent (Stoppa and Woolley, 1997). Because of the mixed carbonate-silicate nature of the Italian carbonatites, it is difficult to compare whole-rock geochemical data with published average carbonatite compositions.

3.3f Vulture

Vulture, a composite cone with a summit caldera situated approximately 100 km east of Vesuvius, is the only Italian volcano located on the eastern side of the Apennine chain. This relatively small complex consists of a 700 m thick lava and tuff sequence plus several parasitic vents, lava plugs, and domes composed of trachyte, phonolite, nephelinite and tephrite (La Volpe et al., 1984). Unlike many volcanic rocks from central Italy, the lavas from Vulture contain h a yne instead of leucite. The unusually high concentrations of Na_2O , CaO , Cl , and S in Vulture rocks compared to other Italian volcanics have been tentatively attributed to the interaction of magmas with CaSO_4 and

NaCl-rich aqueous solutions related to underlying Miocene or Triassic evaporites (De Fino et al., 1986). The K_2O/Na_2O ratios of basic lavas are similar to those of Roman-type KS magmas, but the enrichment of most incompatible elements and the high degree of silica undersaturation are closer to those of HKS series (De Fino et al., 1986).

In addition to silicate rocks, a carbonatite-melilitite tuff sequence referred to as the Monticchio Lakes Formation (MLF) has been recently identified at Vulture (Principe and Stoppa, 1994). The carbonatitic suite is compositionally similar to rocks of the Internal Apennines Zone and is the youngest example of this type of volcanism in Italy (ca. 0.13 Ma). Juvenile fragments in the MLF consist of melilite, phlogopite, Sr-Ba-REE-rich calcite, apatite, perovskite, and hauyne crystals set in a carbonatite or melilitite matrix. The MLF is the only carbonatite locality in Italy known to host peridotite xenoliths (Stoppa and Wooley, 1997).

3.3g Pietre Nere

Pietre Nere, a mafic alkali syenite of Paleocene-Eocene age (ca. 56 Ma), is located near Térmoli on the eastern side of the Apennine chain (Vollmer, 1976). Although much older than other volcanic centres in central Italy, the alkaline affinity of the Pietre Nere intrusion and its chemical similarity to mafic silicate rocks from Vulture have led some authors (Burri, 1961; Vollmer, 1976; Hawkesworth and Vollmer, 1979) to include it in discussions of Italian alkaline magmatism.

3.4 Southern Italy

3.4a Aeolian Islands

The Aeolian Arc in the southeastern Tyrrhenian Sea consists of several seamounts and seven volcanic islands, two of which (Stromboli and Vulcano) are presently active (Table 3.2). The Aeolian volcanoes lie on thinned continental crust (18-25 km), while seamounts in the Marsili basin to the north of the arc are emplaced on oceanic crust (Finetti and Morelli, 1973; Beccaluva et al., 1985). Volcanic rocks in the Aeolian arc range from calc-alkaline to high-K calc-alkaline to shoshonitic, and trend from basic to more evolved products within each suite (Keller, 1980; De Rosa, 1996). Major, trace element, and Sr-isotopic data suggest that crustal assimilation may have been the dominant process in the evolution of the potassic (KS) volcanics at Stromboli, which are chemically similar to KS volcanic rocks of the Campanian Province (Francalanci et al., 1989). The volcanoes of the Aeolian Islands are generally thought to be related to the NW-directed subduction of Ionian oceanic lithosphere (e.g. Francalanci and Manetti, 1994; De Astis' et al., 1997).

3.4b Tyrrhenian Sea

The southern Tyrrhenian Sea is dominated by large, N-S elongated seamounts that occupy the central region of both the Vavilov and Marsili basins (Table 3.2). The top of the Vavilov seamount is ~730 m below the ocean surface, while the younger Marsili seamount is ~500 m below the surface (Savelli, 1988). These volcanoes, along with the large Magnaghi seamount in the Vavilov basin, are located along deep N10-20°E trending crustal fractures. The deep to intermediate portions of the Marsili seamount are

<i>Name of Magmatic Province (age in Ma)</i>	<i>Names of Individual Magmatic Centres</i>	<i>Rock Types & Volcanic Landforms</i>	<i>Geochemical Highlights of Primitive Rock Types</i>
Aeolian Arc (1.0 – present)	Alicudi, Filicudi, Salina, Lipari, Vulcano, Panarea, Stromboli	Stratovolcanoes with dominant calc-alkaline (basalt-andesite-rhyolite) and shoshonitic compositions.	Relatively low-K Silica-saturated Moderate LILE/HFSE Stromboli is geochemically similar to KS of the Campanian Province.
Tyrrhenian Sea (7.0 – present)	Vavilov, Marsili	Co-existing intraplate (tholeiite, Na-transitional, and alkaline) and arc (calc-alkaline, shoshonitic) lavas. Several large seamounts.	Variable geochemistry Higher Mg#, Cr, Ni than Aeolian Arc volcanics Moderate LILE/HFSE Negative Sr anomalies
Etna (0.5 – present)		Large composite shield volcano of tholeiitic basalt and Na-alkaline trachybasalt.	Na ₂ O > K ₂ O Positive anomalies of P, Nb, and Ta Negative anomalies of K, Rb Geochemistry is transitional between the Iblean Plateau and the Aeolian Islands
Iblean Plateau (7.5 – 1.5)		Submarine and subaerial lava plateau of tholeiite, basanite, Na-alkali basalt, hawaiite, and minor nephelinite.	Na ₂ O > K ₂ O High Mg# (66-72), Ni, Cr, V Negative anomalies of Ba, Rb, K, Th, Pb, and Y Positive anomalies of P, Nb, and Ta Low LREE/HREE ratio Similar to oldest products of Etna Contains mantle xenoliths
Pantelleria (0.3 – 0.005)		Stratovolcano composed of Na-alkaline basalt, and peralkaline trachyte and rhyolite.	Silica-saturated Negative anomalies of K, Pb, Zr, and Hf Geochemistry is similar to the Iblean Plateau Most primitive fluid chemistry of Italian volcanic rocks

Table 3.2. Summary of the rock types, volcanic landforms, and geochemistry of each southern Italian magmatic province.

composed of calc-alkaline basalts, whereas the summit consists of high-K, calc-alkaline andesites. All samples from Marsili have an orogenic affinity except those from dredge station CT69/27, which are similar to OIB lavas (Selli et al., 1977; Serri, 1991). Savelli and Gasparotto (1994) proposed that the source of the Marsili seamount was modified by subduction-related fluids similar to those that affected the nearby Aeolian Arc.

3.4c Etna

Etna, the largest active volcano in Europe, is a stratovolcano about 40 km in diameter and 3300m in height located in eastern Sicily (Marty et al., 1994). The volcano lies on approximately 30 km of continental crust at the intersection of several major fault systems. Alkali trachybasalts (once known as "etnaites") are volumetrically dominant, and are similar in composition to the hawaiite-mugearite lavas found in the Hawaiian volcanoes (Marty et al., 1994). Unlike the nearby Aeolian Islands, Etna has produced no calc-alkaline lavas. The exceptionally high CO₂ plume flux of Etna has been attributed to a deep, volatile-rich source (Marty et al., 1994), and isotopic data indicates that lavas from Etna are among the least radiogenic in Italy (Carter and Civetta, 1977).

Geochemical data from Etna best fits a simple mixing model between a plume-enriched MORB mantle source and a subduction-related fluid with a ⁸⁷Sr/⁸⁶Sr ratio of about 0.708 (Tonarini et al., 2001). The lowest concentrations of fluid-mobile elements are found in the oldest lavas and higher amounts in the more recent lavas. The temporal variations in the trace element composition are considered to reflect a progressive transition from a predominantly mantle-plume source to an island-arc source over the past 500 ka (Schlano et al., 2001).

3.4d Iblean Plateau

The Iblean volcanic plateau (7.5 – 1.5 Ma), located in southeast Sicily, covers an area of about 350 km² and lies 30 km south of Etna (Tonarini et al., 1996). Volcanic activity was dominated by fissure eruptions and consisted of submarine lava flows with associated hyaloclastites and subordinate subaerial lavas (Romano and Villari, 1973). The Iblean lavas cover a wide compositional spectrum (tholeiitic to alkaline) and are poorly differentiated, without any definite spatial or temporal changes in magma chemistry. Beccaluva et al. (1998) estimated the volume of subaerial lava to be on the order of 10-15 km², in the following proportions: 62% tholeiite, 22% basanite, 8% alkali basalt, 4% hawaiiite, 3% transitional basalt, and 1% nephelinite.

3.4e Pantelleria

The island of Pantelleria (83 km², 836 m above sea level) is located about 100 km SW of Sicily and 70 km off the Tunisian coast on the axis of the Sicily Channel rift zone (Parello et al., 2000). Pantelleria has produced basaltic rocks as well as more evolved trachytes and quartz-saturated peralkaline rhyolites (pantellerites) (Table 3.2). Trace element patterns are similar to the tholeiitic and alkaline series of the Iblean Plateau, but are distinct from average OIB in that they show a relative depletion in K, Pb, Zr, and Hf (Esperança and Crisci, 1995). Measurements of hydrothermal fluids from Pantelleria indicate interaction between a CO₂-He-rich magmatic gas, and shallow aquifers of mixed marine-meteoric water (Parello et al., 2000). The hydrothermal fluids from Pantelleria are richer in ³He and have a lower (closer to MORB) δ¹³C than any fluid analyzed from volcanic regions in Italy and southern Europe, including Etna.

3.5 Sardinia

The Tertiary magmatic activity of Sardinia can be separated into two phases:

1) Oligo-Miocene (32-15 Ma) orogenic volcanism, and 2) Plio-Pleistocene (5.3-0.1 Ma) anorogenic volcanism (Lustrino et al., 2000). Oligocene calc-alkaline activity between 32 and 24 Ma is chemically similar to that of the Aeolian arc, and is represented by small lava domes of andesitic composition localized in southern Sardinia (Beccaluva et al., 1985). The climax of Oligo-Miocene volcanism was the eruption of high-K dacitic to rhyolitic ignimbrites and minor lavas between 21 and 18 Ma, coinciding with maximum extension and the opening of the Fossa Sarda rift system. The Sr-Nd isotopic field for the Oligo-Miocene rocks overlaps those of the younger HKS rocks of the Roman Province and Southern Latium Transition Zone (Downes et al., 2001). Downes et al. (2001) noted strong correlations between radiogenic isotopes and SiO₂, and weak correlations between isotopes and MgO, which are most easily explained by extensive (2-10%) mantle enrichment by subducted siliceous sediments.

The Plio-Pleistocene extensional volcanism of Sardinia is related to the opening of the Tyrrhenian Sea and is roughly contemporaneous with volcanic activity in central and southern Italy. Outcropping in the form of large volcanic complexes, basaltic plateaux, and lava flows associated with small volcanoes, rocks range from mafic to intermediate in composition and belong to the tholeiitic, transitional, and alkaline series (Lustrino et al., 2000). Isotopic data show that most Plio-Pleistocene Sardinian volcanics have slightly radiogenic ⁸⁷Sr/⁸⁶Sr, low ¹⁴³Nd/¹⁴⁴Nd, and very unradiogenic Pb compared to other Neogene-recent Italian anorogenic mafic volcanics (Lustrino et al., 2000). The isotopic signature of these volcanic rocks could reflect either mixing of depleted mantle

with 1-3% lower crustal material, or interaction with metasomatized lithospheric mantle (Lustrino et al., 2000). Recently, Gasperini et al. (2000) suggested that the geochemistry of Pleistocene basalts from Sardinia is compatible with the re-melting of ancient, plume-derived, ocean plateau material that has been recycled into the deep mantle.

3.6 Summary of main geochemical features of Cenozoic Italian magmatism

- 1) Italy is characterized by a wide range of mantle-derived rock types, including sub-alkaline, Na- and K-alkaline, and ultra-alkaline. The variable petrological and geochemical signatures of the mafic rocks require a heterogeneous Italian mantle.
- 2) Italian volcanic rocks are closely associated in space and time, and display variable degrees of evolution from primitive mafic compositions to highly evolved rhyolites, trachytes, and phonolites.
- 3) Lamproites, kamafugites, potassic (KS) and ultrapotassic (HKS) rocks in central Italy are characterized by high contents of incompatible trace elements and high LILE/HFSE ratios. Most KS and HKS rocks exhibit orogenic trace element patterns characterized by negative Nb and Ta anomalies and positive K, Rb, and Th anomalies. In contrast, the sodic alkaline rocks of Sicily (Etna and the Iblean Plateau) have anorogenic trace element patterns with positive Nb and Ta anomalies.
- 4) Magmatic rocks from the Tertiary Periadriatic Province, Tuscan Province, Roman Province, Southern Latium Transition Zone, Campanian Province, and Aeolian Islands show the strongest geochemical evidence for the involvement of a crustal component in their mantle source.

CHAPTER 4

PREVIOUS ISOTOPIC WORK

4.1 Introduction

Regional correlations in the isotopic ratios of Italian magmatic rocks were first noted in the mid-1960s, and by the late 1970s it became clear that the Italian upper mantle is chemically heterogeneous. Unusual enrichment in incompatible elements, possible input of foreign material into the mantle, isotopic mixing, and anomalous isotope geochemistry of mafic volcanic rocks became the topics of numerous papers over the past twenty years. A review of the history of isotopic work in Italy will prevent the reiteration of ideas that have already been proposed and serve to guide this study in new directions.

4.2 The early years (1966 – 1980): discovery of regional isotopic trends

Hurley et al. (1966) first noted the regional trend in Sr isotopic composition in the K-rich rocks of western Italy, a finding that was followed up by Vollmer, Hawkesworth, and co-workers in the mid-1970's. Vollmer (1976) observed that the Sr and Pb isotopic compositions of Italian alkaline rocks show a negative correlation combined with a regional trend, with $^{87}\text{Sr}/^{86}\text{Sr}$ ratios decreasing from 0.711 in northwest Italy (Tuscan Province) to 0.704 in southeast Italy (Vulture and Pietre Nere). $^{206}\text{Pb}/^{204}\text{Pb}$ ratios increase from 18.7 to 20.0 from north to south. This regional trend is depicted in Figure 4.1, which shows the average $^{87}\text{Sr}/^{86}\text{Sr}$ ratios from Italian magmatic provinces (note that data for Figure 4.1 are from numerous references; see Appendix A). Also, a positive correlation between $^{87}\text{Sr}/^{86}\text{Sr}$ and total Rb is present, but there is no correlation between

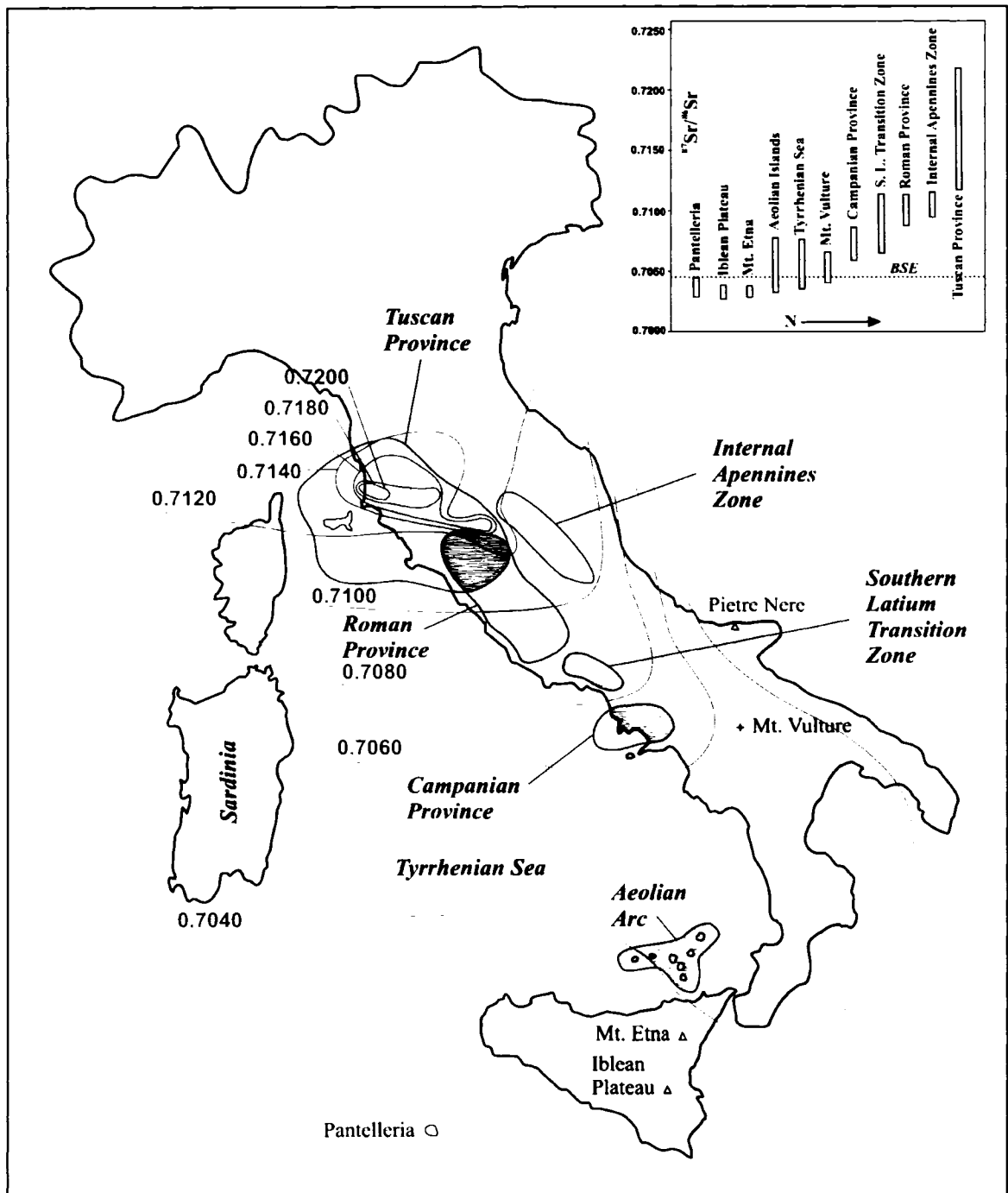


Figure 4.1. Regional trend in $^{87}\text{Sr}/^{86}\text{Sr}$, with the highest ratios in the Tuscan Province and the lowest in southern Italy (modified from Bell et al., 2003). BSE = Bulk Silicate Earth

the $^{87}\text{Sr}/^{86}\text{Sr}$ ratios and total Sr or the Rb/Sr ratio (Vollmer, 1976). Regarding Pb isotopes, no correlation between parent and daughter abundances was detected. Samples with $^{238}\text{U}/^{204}\text{Pb}$ ratios from 3 to 30 have similar $^{206}\text{Pb}/^{204}\text{Pb}$ ratios. Vollmer (1976) reasoned that two physical processes could be responsible for the observed isotopic variation: (i) time-dependent development in subsystems with different parent/daughter ratios (isochron model), or (ii) mixing of Sr (or Pb) with different isotopic compositions (mixing model). By combining both Sr and Pb isotopic measurements on a single diagram, Vollmer (1976) was able to show that magmas associated with each volcanic centre are formed by various degrees of mixing between two end-members. The isochron model was thus considered unlikely because of the strong correlation between the Sr and Pb isotopic systems, and because there is no relation between the measured isotopic ratios and their respective parent/daughter element ratios.

Vollmer (1976) suggested that the high $^{87}\text{Sr}/^{86}\text{Sr}$, low $^{206}\text{Pb}/^{204}\text{Pb}$ end-member is similar to the continental crust, whereas the low $^{87}\text{Sr}/^{86}\text{Sr}$, high $^{206}\text{Pb}/^{204}\text{Pb}$ end-member resembles a melt fraction derived from a small degree of partial fusion of an amphibole and phlogopite-bearing hydrous mantle. The possible occurrence of amphibole and phlogopite in the low $^{87}\text{Sr}/^{86}\text{Sr}$, high $^{206}\text{Pb}/^{204}\text{Pb}$ mantle source is based on the Sr concentration, low K/Rb ratio, and high TiO_2 of mafic rocks from Pietre Nere (Vollmer, 1976). This model, however, does not take into account the fact that partial melts from a phlogopite-bearing source should have high $^{87}\text{Sr}/^{86}\text{Sr}$ ratios, not low $^{87}\text{Sr}/^{86}\text{Sr}$ ratios. Two-component mixing is also supported by $\delta^{18}\text{O}$ variations (Turi and Taylor, 1976), which correlate on a regional scale with Sr and Pb isotopes. Vollmer (1976) suggested that a small mantle plume presently centered under Vulsini might be responsible for the

crustal isotopic signatures in the Tuscan Province and the increased contribution of original mantle material away from the plume to the southeast. Pietre Nere could be the scar of the plume 56 Ma ago, when the degree of interaction between the plume and the overlying crust was low. In Vollmer's (1976) geodynamic model, counterclockwise rotation of Italy during the Cenozoic resulted in northward movement of the zone of plume-crust interaction. Crustal isotopic signatures in the Tuscan Province are considered to be the result of increased crustal melting by hot plume material over time.

Cox et al. (1976) also concluded that a heterogeneous source was responsible for volcanic rocks with high $^{87}\text{Sr}/^{86}\text{Sr}$ co-existing with rocks with low $^{87}\text{Sr}/^{86}\text{Sr}$ rocks in the Southern Latium Transition Zone. Unlike Vollmer (1976), Cox et al (1976) found a positive correlation between $^{87}\text{Sr}/^{86}\text{Sr}$ and Sr abundance. Cox et al. (1976) proposed that the high and variable $^{87}\text{Sr}/^{86}\text{Sr}$ ratios and incompatible elements of primitive volcanics from central-southern Italy have been produced from a mantle source region that underwent variable degrees of enrichment. Assuming both a phlogopite-free source and limited low-pressure fractionation, Cox et al. (1976) estimated the age of the enrichment event to be 300 – 500 million years ago. Vollmer (1977) subsequently compared the Pb isotopic composition of Tuscan anatectic rocks with potassic alkaline rocks of the Roman and Campanian Provinces. Linear trends between the acid and alkaline rocks on Pb-Pb diagrams strongly favoured a two-component mixing between melts of mantle material and argillaceous sedimentary rocks. Vollmer (1977) recognized that hyperbolic mixing curves on $^{87}\text{Sr}/^{86}\text{Sr}$ versus $^{206}\text{Pb}/^{204}\text{Pb}$ diagrams of Italian magmatic rocks are the result of a time-integrated process that is dependent on the Pb and Sr concentrations of the two end-members.

By the late 1970s, it had become clear that, on a regional scale, two-component mixing was responsible for the geochemical and isotopic variations in Italian alkaline magmas. Discussion shifted to defining the location and nature of this mixing. Turi and Taylor (1976) and Taylor et al. (1979) preferred contamination of alkaline magmas by interaction with continental crust during ascent, while Vollmer (1976, 1977), Hawkesworth and Vollmer (1979), and Vollmer and Hawkesworth (1980) argued that only a deep-seated mixing process prior to magma ascent could account for the observed spatial variations in radiogenic Sr, Nd and Pb.

Variable and high $\delta^{18}\text{O}$ combined with high $^{87}\text{Sr}/^{86}\text{Sr}$ and low $^{143}\text{Nd}/^{144}\text{Nd}$ suggested to Taylor et al. (1979) that assimilation of country rocks (pelitic schist, flysch, and some carbonates) was an important petrologic process during fractional crystallization at Roccamonfina. Positive correlations between $\delta^{18}\text{O}$ and $^{87}\text{Sr}/^{86}\text{Sr}$ for volcanic rocks were taken as very strong evidence for major contamination and involvement with the continental crust. Taylor et al. (1979) emphasized that all of the ^{18}O enrichments exhibited by the potassic igneous rocks of Italy can be explained by various types of interactions between high ^{18}O crust and mantle-derived magmas. This interpretation is strongly at odds with the ideas of Hawkesworth and Vollmer (1979), who attributed all isotopic variations at Roccamonfina to upper mantle heterogeneities. Hawkesworth and Vollmer (1979) noted that many high $^{87}\text{Sr}/^{86}\text{Sr}$ lavas are SiO_2 -undersaturated, which suggests limited crustal involvement. Another argument against direct crustal contamination is the trend toward increasing Sr content with increasing $^{87}\text{Sr}/^{86}\text{Sr}$. This is inconsistent with the low average Sr content of the continental crust.

Hawkesworth and Vollmer (1979) argued that $^{87}\text{Sr}/^{86}\text{Sr}$ ratios up to 0.7095 and $\delta^{18}\text{O}$ values up to +7‰ or +8‰ may occur as primary features of magmas derived from metasomatized upper mantle. They envisaged a recent mixing event (< 90 Ma based on $^{206}\text{Pb}/^{204}\text{Pb}$ variations) between a broadly homogeneous upper mantle and a fluid characterized by high $^{87}\text{Sr}/^{86}\text{Sr}$, low $^{143}\text{Nd}/^{144}\text{Nd}$, high K, Rb, and LREE, and low Sr^{2+} and Eu^{2+} . Hawkesworth and Vollmer (1979) subsequently divided the volcanism of central-southern Italy into the Tuscan zone where magmas are believed to reflect crustal anatexis, a central crust/mantle hybrid zone, and a southern zone (south of Rome) where mantle-derived magmas may have had little interaction with the overlying continental crust. Hawkesworth and Vollmer (1979) suggested that the geochemistry of volcanic rocks from each zone is a result of mixing between LILE-enriched fluids and a range of initial mantle compositions. On the basis of isotope and trace element data, Vollmer and Hawkesworth (1980) proposed that the metasomatising fluid may be derived either from an old LILE-enriched mantle source, or from continental crust which has partially retained its chemical identity in the upper mantle.

4.3 The 1980s and 1990s: end-member signatures in a geodynamic context

As more isotopic data became available in the late 1970s, considerable debate began on the tectonic setting of the Italian magmatic rocks. Ninkovich and Hays (1972) related the potassic volcanoes south of Rome to subduction beneath the Calabrian Arc, an idea supported by Di Girolamo (1978) and Edgar (1980) but strongly contested by Cundari (1979, 1980). Thompson (1977) noted that the low TiO_2 contents of Italian alkaline lavas are similar to those of typical island arc rocks, and Ghiara and Lirer (1977)

observed that the KS series rocks possess marked calc-alkaline affinities on an AFM diagram. In contrast, Cundari (1979) demonstrated the rarity of leucite-bearing rocks in subduction-related environments and drew similarities between Italy and the Western Rift Valley of Uganda, a region well-known for its highly potassic volcanic rocks.

By the mid 1980s, trace element and isotopic data were being used in conjunction with major element data and other geologic evidence to evaluate the tectono-chemical signature of Italian volcanic rocks. Low Ti, Ta, and Nb concentrations in primitive Italian lavas, enrichment in Th and LILE, and position above the intra-plate field on Ta/Yb vs. Th/Yb diagrams all provided strong evidence in favour of a subduction-related origin for mantle source enrichment (Peccerillo, 1985; Rogers et al., 1985). However, the high $^{87}\text{Sr}/^{86}\text{Sr}$ and low $^{143}\text{Nd}/^{144}\text{Nd}$ of many Italian alkaline rocks are extreme for subduction-related magmas. To account for these unusual isotopic ratios, as well as the high $\delta^{18}\text{O}$ values, Holm et al. (1982) proposed the involvement of subducted sediments in the source of magmas from Vulcini. Calculations by Rogers et al. (1985) indicated that three components were involved in large-scale Italian mantle mixing: (1) E-type MORB, (2) a KS-component with $^{87}\text{Sr}/^{86}\text{Sr} \approx 0.7062$, $^{143}\text{Nd}/^{144}\text{Nd} \approx 0.5125$, high Sr/Nd, Th/Ta, Ba/Nb, and no Eu anomaly, and (3) a HKS-component with $^{87}\text{Sr}/^{86}\text{Sr} \approx 0.7105$, $^{143}\text{Nd}/^{144}\text{Nd} \approx 0.5120$, low Sr/Nd, very high Th/Ta, and a negative Eu anomaly.

Rogers et al. (1985) elaborated on the ideas of Holm et al. (1982), and suggested that the KS-component is consistent with H₂O-rich slab-derived fluids, while the HKS-component is derived largely from silicic melts rich in alkalis from subducted sediments. However, Rb/Ba ratios of the Italian lavas are too high to have been directly produced from the melting of sediments. Rogers et al. (1985) noted that a hydrous silicic melt can

interact with mantle peridotite to form a hybrid rock rich in pyroxenes and phlogopite, which could in turn provide a suitable source for the HKS magmas. In the context of subduction-related mantle metasomatism, Peccerillo (1985) suggested that the regional isotopic variations in Italian volcanics could be generated by several mechanisms, such as subduction of varying quantities of sediment along different sections of the Italian peninsula, differences in the isotopic signature of the subducted sediment, and/or differences in the type of crust being subducted along different sectors of the Apennine subduction zone.

Ellam et al. (1989) integrated data from the Aeolian Islands, and found that isotopic ratios of $^{87}\text{Sr}/^{86}\text{Sr} < 0.704$ and $^{143}\text{Nd}/^{144}\text{Nd} > 0.5128$ are required to characterize the KS-component of Rogers et al. (1985). Ellam et al. (1989) also proposed a model involving mixing among three isotopically distinct components: (1) OIB-type mantle, (2) low $^{87}\text{Sr}/^{86}\text{Sr}$, high $^{143}\text{Nd}/^{144}\text{Nd}$, high Sr/Nd, high Th/Ta basaltic ocean crust (MORB), and (3) high $^{87}\text{Sr}/^{86}\text{Sr}$, low $^{143}\text{Nd}/^{144}\text{Nd}$ low Sr/Nd, very high Th/Ta sediments. The identification of OIB-type mantle differs from the interpretation of E-type MORB of Rogers et al. (1985) and is characterized by highly radiogenic Pb. Instead of a mixing line between MORB and sediment on a Pb-Pb diagram, Ellam et al. (1989) noted that the Pb data trend from a sedimentary signature towards highly radiogenic values ($^{206}\text{Pb}/^{204}\text{Pb} > 19.5$) more typical of OIB. The OIB-type mantle signature is strongest in the lavas of Mt. Etna and at Pietre Nere. Ellam et al. (1989) found strong evidence for OIB mantle beneath much of southern Italy, and hypothesized that the high $^{206}\text{Pb}/^{204}\text{Pb}$ source may be relatively shallow (i.e. upper mantle).

Although it was generally accepted that the sources of Italian magmas were influenced by large-scale mixing involving isotopically distinct end-members, different authors continued to disagree about the cause of large radiogenic isotopic variations. Turi et al. (1986) stated that high and variable $^{87}\text{Sr}/^{86}\text{Sr}$ are primary magmatic values formed through mantle differentiation processes, while Holm and Munksgaard (1982) considered the radiogenic ^{87}Sr to be initially of crustal provenance and subsequently transported into the source region of the magmas. Holm and Munksgaard (1982) envisaged that fluids released from previously subducted sediments infiltrated and metasomatized normal mantle, thereby imprinting a crustal signature on the magma sources. It should be noted that by the mid-1980s Turi and co-authors no longer supported their earlier view (Turi and Taylor, 1976) that all radiogenic isotopic compositions exceeding typical mantle values are due to crustal assimilation. Disagreement persisted regarding the range of oxygen isotopic values which are considered to be primary magmatic values, and on the major and trace element composition of so-called primitive magmas in Italy. These topics will be discussed in subsequent sections on geochemistry and isotopes (Chapters 7 and 8).

Geochemical modeling of K, P, Ce, Sr, Rb, Ba, Sm, Eu, Gd, Y, Nb, and $^{87}\text{Sr}/^{86}\text{Sr}$ (Beccaluva et al., 1991) indicated that the addition of 3 to 20% of materials derived by partial melting of carbonaceous pelites to a Sr-enriched mantle wedge could explain the range of mantle sources in central-southern Italy. The production of the Sr-enriched mantle requires either the action of fluids related to dehydration of subducted ocean crust, or a small amount of carbonatitic metasomatism (Beccaluva et al., 1991). Conticelli and Peccerillo (1992) also noted that the hygromagmaphile patterns of many Italian volcanic

rocks are similar to those of upper crustal rocks. In particular, lamproites and lamproite-KS transitional rocks match very closely with pelitic sediments and their metamorphic equivalents from central Italy. Conticelli and Peccerillo (1992) concluded that the metasomatic agent responsible for the contamination of the KS, HKS, and kamafugite mantle source(s) consisted of fluids or melts released from subducted marly meta-sedimentary material.

Serri et al. (1993) considered the Italian rocks in terms of saturated (Qz-normative) and undersaturated compositions. The saturated rock series is thought to have been derived from low pressure (<50 km) partial melting of a phlogopite harzburgite source contaminated by a K-Si-rich, Ca-Sr-poor melt with $^{87}\text{Sr}/^{86}\text{Sr} > 0.717$ and $^{143}\text{Nd}/^{144}\text{Nd} < 0.5121$. According to Serri et al. (1993), trace element modeling of the undersaturated series involves three distinct source components: (a) a typical MORB-OIB mantle, (b) a high Sr, high Ca, low Si component carried by a carbonate-rich melt related to marine carbonates, and (c) a recently-added K-rich, Ca-Sr-poor crustal component with $^{87}\text{Sr}/^{86}\text{Sr} > 0.712$ and $^{143}\text{Nd}/^{144}\text{Nd} < 0.5120$. Most workers in the 1990s favoured subduction as the only mechanism available for bringing crustal material to mantle depths, yet a small group (Stoppa and Lavecchia, 1992; Cundari, 1994; Stoppa and Cundari, 1995; Stoppa and Woolley, 1997) favoured magma genesis in a rift environment based largely on the presence of kamafugites and newly-described carbonatites.

A key paper on the petrogenesis of Italian alkaline lavas based on Pb-Sr-Nd isotope relationships was published by D'Antonio et al. (1996). The authors presented new Pb isotope data for over thirty volcanic rocks from central-southern Italy, and

provided a comprehensive discussion on regional isotopic trends and source components in Italy. D'Antonio et al. (1996) recognized that, at first sight on a Sr-Nd diagram, Italian volcanics could be interpreted as binary mixing between a depleted MORB-type end-member and an enriched crust-type end-member. However, as also noted by Ellam et al. (1989), Sr-Nd diagrams by themselves cannot specify what type of mantle – MORB or OIB/HIMU – is involved. This question is better addressed with coupled Pb-Sr, Pb-Nd or Pb-Pb isotope data. Pb-Pb relationships showed that mafic KS and HKS volcanics lie in the field of Mediterranean sediments, not in the MORB or Calabrian crust fields, and that Pb isotopes are within the known range for island arc volcanics. D'Antonio et al. (1996) noted the significance of sodic volcanics from Mt. Etna, the Iblean Plateau and Pietre Nere, which have $^{206}\text{Pb}/^{204}\text{Pb}$ ratios as high as 20 and are typical of the high U/Pb (HIMU) sources of many ocean islands.

D'Antonio et al. (1996) compared Pb-Sr-Nd isotopic data from all Italian alkaline volcanics to globally-recognized oceanic mantle components DMM, EMI, EMII, and HIMU, as well as Mediterranean sediment and the Calabrian crust. They determined that the low $^{87}\text{Sr}/^{86}\text{Sr}$, high $^{143}\text{Nd}/^{144}\text{Nd}$ rocks from Mt. Etna, the Iblean Plateau and Pietre Nere can best be explained as a mixture of DMM and HIMU, and that this mixture in turn provides a good mantle end-member for the source of KS and HKS lavas. D'Antonio et al. (1996) noted that this mixture of DMM and HIMU appears to originate from a large-scale isotopic reservoir referred to as LVC (low velocity component) first characterized by Hoernle et al. (1995) that underlies the eastern Atlantic Ocean and Western Europe. Another important observation by D'Antonio et al. (1996) is that geochemical and isotopic evidence suggest little or no evidence for the presence of a sedimentary

component in igneous rocks from centres located outside the external limit of the Alpine-Apennine thrust belt, namely Pietre Nere, Pantelleria, and the Iblean Plateau.

Conversely, an enriched component isotopically similar to Mediterranean sediments is clearly involved in the petrogenesis of alkaline rocks located internally to the main compressional front.

4.4 Recent work (2000-2005): an additional end-member and a new geodynamic context

Prior to the year 2000, a number of authors had suggested and modeled three end-member isotopic mixing involving DMM, HIMU (or HIMU-like mantle), and continental crust for Italian magmatic rocks. In the year 2000, two different groups of workers found evidence for an additional mantle end-member in the Plio-Pleistocene volcanic rocks of Sardinia. Lustrino et al. (2000) recognized that the unradiogenic $^{206}\text{Pb}/^{204}\text{Pb}$ (17.55-18.01) and $^{143}\text{Nd}/^{144}\text{Nd}$ (0.5124-0.5126) and the mildly radiogenic $^{87}\text{Sr}/^{86}\text{Sr}$ (0.7043-0.7051) combined with relatively high Ba/Nb and La/Nb of the Sardinian volcanics closely resemble the EMI mantle component. Lustrino et al. (2000) proposed that the EMI signature, thought to represent ancient metasomatized lithospheric mantle or lower crustal material mixed with depleted mantle, may have been stabilized beneath Sardinia in the Precambrian during the Hercynian orogeny. This isotopic signature is not observed in any other Italian orogenic or anorogenic volcanic rocks, or in the Cenozoic European Volcanic Province. Gasperini et al. (2000) also interpreted the signature of Sardinian basalts as EMI, but suggested that the trace element and isotopic geochemistry of mafic

volcanic rocks from Sardinia reflect remelting of ancient oceanic plateau material that has been recycled in the mantle instead of contamination by lower continental crust.

Based on the work of D'Antonio et al. (1996), who first recognized that isotopic data from Mt. Etna, the Iblean Plateau, and Pietre Nere may be a mixture of DMM and HIMU, Gasperini et al. (2002) further characterized this component as $^{206}\text{Pb}/^{204}\text{Pb} = 19.8$, $^{87}\text{Sr}/^{86}\text{Sr} = 0.7025$, $\epsilon_{\text{Nd}} = +8$, and $\epsilon_{\text{Hf}} = +9$ using least squares regression. Gasperini et al. (2002) discounted the possibility that this mantle-derived component could be pure intermediate FOZO (Hart et al., 1992) or C (Hanan and Graham, 1996), despite the fact that the isotopic signatures of these components are nearly identical to those of Mt. Etna, the Iblean Plateau, and Pietre Nere. On the basis of an extensive compilation of almost 1000 isotopic analyses, Bell (2002) determined that FOZO is indeed a valid end-member for Italian isotopic mixing, and suggested that the FOZO component implies direct contribution from the lower mantle. Bell et al. (2003) recognized that Sr-Nd-Pb data form two mixing arrays that both converge towards FOZO. Isotopic mixing between FOZO and EMI occurs in Sardinia and the Tyrrhenian seafloor, while mixing between FOZO and ITEM (Italian Enriched Mantle; Bell et al., 2003) occurs in peninsular Italy and the Aeolian Arc. ITEM is characterized by very high $^{87}\text{Sr}/^{86}\text{Sr}$ ratios that are similar to those of Mediterranean sediment and the upper continental crust. Interestingly, EMI and ITEM do not show any mixing relationship.

The presence of a HIMU or FOZO-like mantle component, considered by many to be indicative of plume-related magmatism, in the source of apparently subduction-related Italian volcanics required major revisions to the geodynamic model. Gasperini et al. (2002) suggested that upwelling of deep mantle material through a so-called plate

window beneath Vesuvius formed by the differential subduction velocity between the fossil plate beneath Tuscany and the active plate beneath Sicily (Calabrian Arc) is responsible for the DMM-HIMU mixture. In this model, counterflow of mixed upper and lower mantle accounts for the low $^{87}\text{Sr}/^{86}\text{Sr}$, high $^{143}\text{Nd}/^{144}\text{Nd}$, and moderate $^{206}\text{Pb}/^{204}\text{Pb}$ of the DMM-HIMU end-member, while the crustal end-member may be acquired by interaction of the upwelling mantle material with the upper part of the subducted plate. Seismic tomography models of slab detachment in the Western Mediterranean (e.g. Wortel and Spakman, 1992) had not been previously integrated with petrologic and geochemical data. In contrast to the model of Gasperini et al. (2002), Bell et al. (2003) proposed large-scale mantle plume activity beneath the Tyrrhenian Sea and extending westwards under Sardinia and Corsica, northwards towards the Eastern Alps, and eastwards under the Italian peninsula. On the basis of FOZO-like isotopic signatures, deep-seated CO_2 emissions, geothermal activity in Tuscany, and a topographic bulge in the central Apennines, Bell et al. (2003) suggested that the low-volume, volatile-rich potassic melts of central and southern Italy are generated by low-degree partial melting associated with a relatively cool plume head.

After thirty years of intense geochemical and isotopic research, the overall picture of Italian volcanism is one of upwelling deep mantle material mixing with EMI in Sardinia and the Tyrrhenian Sea, mixing with enriched mantle (ITEM) along the Italian peninsula, and impinging on an ongoing subduction process near the Calabrian Arc. Important problems to address are those dealing with the timing of mantle contamination, and the geodynamic significance of the various isotopic end-members.

CHAPTER 5

GEOLOGY OF THE STUDY AREAS

5.1 Introduction

This chapter details the field work in the Western Alps and at Roccamonfina and Ernici, and provides an overview of the geological setting, morphology, and volcanic evolution of each study area. Previous work on the petrology and geochemistry of lamprophyres from the Western Alps, and KS and HKS volcanic rocks from Roccamonfina and Ernici, is also summarized.

5.2 Western Alps

5.2a Location and field work

Samples from the Western Alps were collected north of Torino in the Valle D'Aosta region of northern Italy. The closest large towns are Ivrea and Biella, located at the topographic transition between the Po Plain to the southeast and the Western Alps to the north and west. Field work in the Western Alps was carried out by K. Bell (Carleton University), G. Martinotti (Università di Torino), and A. Peccerillo (Università di Perugia) in August 2001. Samples were collected from eight undeformed, steeply-dipping, narrow (< 5 m width) dykes numbered WA 100 to WA 107 (locations provided in Appendix B). The dykes cross-cut the high-grade metamorphic country rocks of the Eclogitic Mica Schist complex (see section 5.2b).

Two samples were collected approximately 8 km west of Biella, while the remaining six sample sites are in the Val di Gressoney. The Val di Gressoney is a north-

trending valley that stretches from the town of Pont St. Martin (16 km north of Ivrea) towards the Swiss-Italian border. Paved roads connect Biella, Ivrea, Pont St. Martin, and a number of small villages in the area, while unpaved roads traverse the steeper slopes.

5.2b Geological setting

Tectonic units presently exposed in the Western Alps were once part of the Adriatic microplate, the European plate, and the intervening Tethyan oceanic crust (Figure 5.1). The lowermost unit consists of highly-deformed remnants of the European continental basement of Hercynian granitoids (Monté Rosa, Gran Paradiso and Dora Maira massifs) and polymetamorphic gneiss (Hurford et al., 1991). Quartzite and dolomitic limestone overlie the European continental basement, and both units have undergone Eo-Alpine blueschist and Meso-Alpine greenschist facies metamorphism. Jurassic and early Cretaceous clastic rocks, along with intercalated ocean floor mafic to ultramafic rocks, were thrust upon the northern units (Hurford et al., 1991). Collectively known as the *Piemont schistes lustrés*, the oceanic units probably mark the suture between the Adriatic and European plates. The uppermost tectonic unit in the Western Alps is represented by the Dent Blanche nappe system and Sesia-Lanzo Zone, both derived from the basement of the Adriatic promontory (Hurford et al., 1991).

All samples from the Western Alps were collected from dykes that outcrop within the Eclogitic Mica Schist Complex of the Sesia-Lanzo Zone. The latter stretches from Locarno to near Torino (about 150 km) and is bounded to the southeast by the Insubric Line, separating the Western Alps from the pre-Alpine high-grade Ivrea Zone of the Southern Alps. The Sesia-Lanzo Zone is characterized by pervasive Alpine deformation

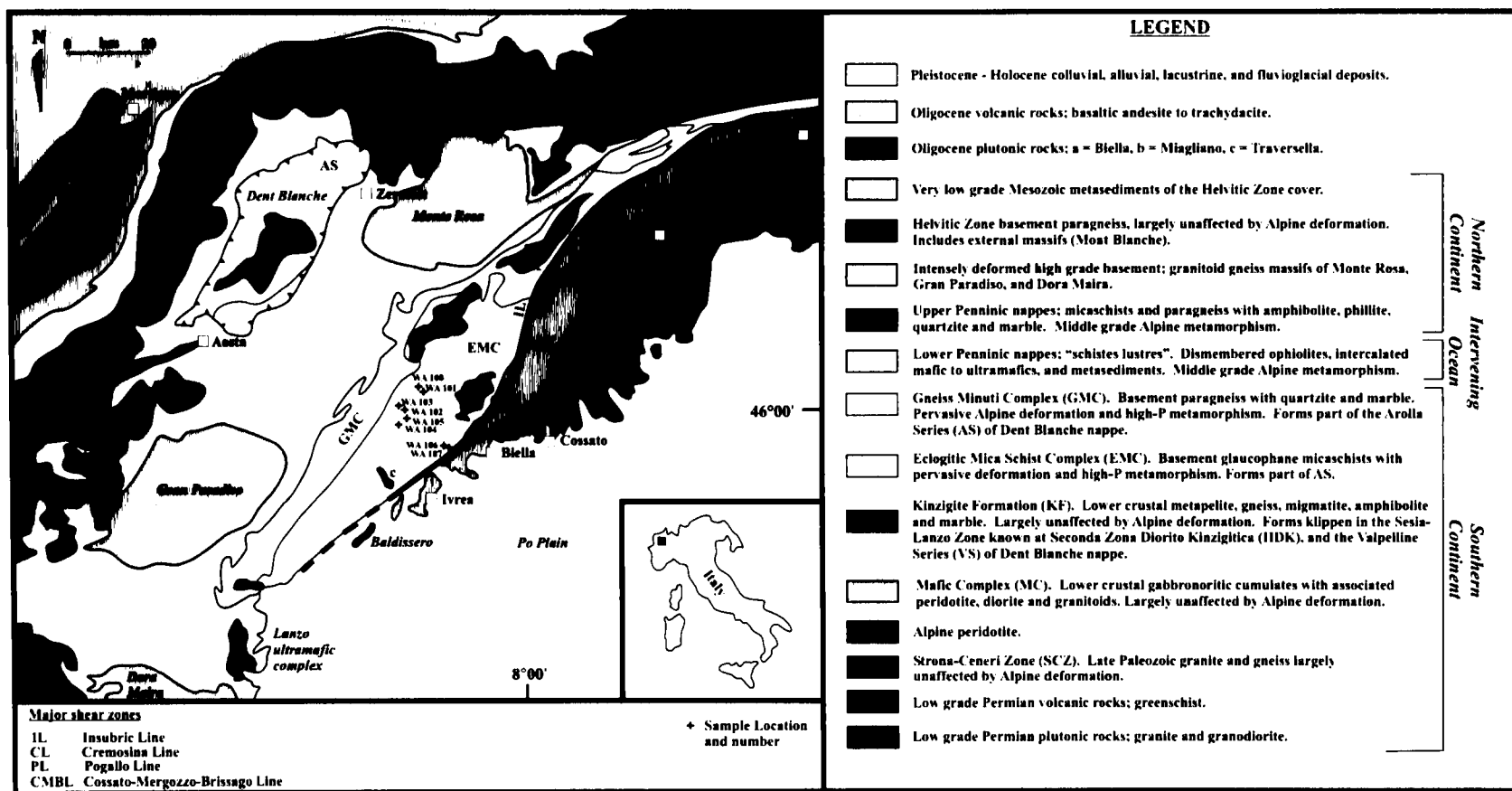


Figure 5.1. Simplified tectonic map of the Western Alps showing sample localities (after Carta Geologica D'Italia, Folgio 1 (1983), Hurford et al. (1991), and Snoke et al. (1999)). The highly deformed Sesia-Lanzo Zone is composed of the Eclogitic Mica Schist Complex (EMC), the Gneiss Minuti Complex (GMC), and the Seconda Zona Diorito Kinzigitica (IIDK). The Southern Alpine Ivrea Zone contains the Kinzigite Formation (KF) and the Mafic Complex (MC), and is separated from the Sesia-Lanzo Zone by the Insubric Line.

and high-pressure metamorphism. Compagnoni (1977) estimated that a minimum lithostatic load of 50-60 km was necessary to create the high pressures (15-17 kbar) and temperatures (500-600 °C) that characterize rocks from the Sesia-Lanzo Zone.

Three major sub-units in the Sesia-Lanzo Zone have been distinguished on the basis of lithological difference and metamorphic evolution; the Eclogitic Mica Schist complex, the Gneiss Minuti complex, and the Seconda Zona Diorite Kinzigitica (IIDK) complex (Dal Piaz et al., 1972). In classical Alpine models, these complexes are regarded as different tectonic elements stacked during plate convergence at depth and separated by thrust planes (Carraro et al., 1970). Unlike the high-grade Eclogitic Mica Schist and Gneiss Minuti complexes, the IIDK complex is composed of well-preserved pre-Alpine rocks with close affinity to the nearby Ivrea Zone. The IIDK unit has been interpreted either as a basal remnant of a thick, crustal cover derived from the overriding Adriatic promontory (Hurford et al., 1991), or as a consequence of differential strain partitioning within the Sesia-Lanzo Zone (Stünitz, 1989).

5.2c Previous work on the petrology and geochemistry of dykes from the Western Alps

The mafic dykes from the Western Alps can be separated into three main petrographic and geochemical groups: calc-alkaline, shoshonitic, and ultrapotassic (Venturelli et al., 1984). Calc-alkaline rock types include basalt, basaltic andesite, and andesite, characterized by abundant hornblende, clinopyroxene, plagioclase, and/or biotite phenocrysts in a groundmass of plagioclase, quartz, apatite, and Fe-Ti oxides. Shoshonitic basalts and latites contain biotite, zoned hornblende and/or clinopyroxene

phenocrysts contained in a groundmass of plagioclase, K-feldspar, and minor quartz.

Rocks of both the calc-alkaline and shoshonitic groups have experienced varying degrees of secondary alteration, and may contain chlorite, epidote, albite, and sericite. Venturelli et al. (1984) classified the ultrapotassic dykes as lamprophyres, made up of zoned biotite, clinopyroxene, K-feldspar, alkaline amphibole, carbonate, apatite, Fe-Ti oxides, and rare olivine.

The calc-alkaline and shoshonitic rocks have trace element contents comparable to similar rock types from active continental margins, and are characterized by high LILE/HFSE, Ce/Ta, Th/Nb, and Th/Ta ratios combined with negative Nb, Ta, and Ti anomalies and high MgO, Ni, and Cr contents (Venturelli et al., 1984). The ultrapotassic lamprophyres have low Al₂O₃, high K/Na ratios and high P₂O₅, Zr, Hf, Rb, K, LREE contents, unusually high Th (average 155 ppm) and U (average 33 ppm), strongly fractionated REE patterns (Ce/Yb_(N) = 32-40), and very high MgO, Ni, and Cr contents. Initial ⁸⁷Sr/⁸⁶Sr isotopic ratios for the lamprophyres range from 0.7165 to 0.7216, while the calc-alkaline and shoshonitic rock types have lower values between 0.7072 and 0.7123 (Venturelli et al., 1984).

Shallow-level fractional crystallization cannot account for trace element and isotopic variations within or between the magmatic groups (Venturelli et al., 1984). Plots of Zr/Y against Y and Ce/Yb_(N) against Yb_(N) indicate that chemical variations are inconsistent with fractional crystallization involving olivine ± plagioclase ± pyroxene ± amphibole. The wide variation in ⁸⁷Sr/⁸⁶Sr isotopic ratios also precludes a simple petrogenetic model based solely on fractional crystallization. Calculations by Venturelli et al. (1984) show that the Rb/K ratios of the mafic dykes from the Western Alps increase

significantly from the calc-alkaline to the ultrapotassic rocks, and are much higher than ratios expected from partial melting of "normal" primordial mantle. Since Rb and K are not significantly fractionated from one another during partial melting of peridotite, Venturelli et al. (1984) suggested that the variable Rb/K ratios indicate the presence of phases able to fractionate these elements (e.g. phlogopite) in the mantle source.

The calc-alkaline and shoshonitic melts are consistent with partial melting of metasomatized (phlogopite-bearing) mantle peridotite combined with subsequent fractional crystallization and crustal contamination. The ultrapotassic lamprophyres have extremely high $^{87}\text{Sr}/^{86}\text{Sr}$ ratios that are unusual for mantle-derived rocks with high Mg# (79-83), and require a metasomatized source with variable input from the continental crust (Venturelli et al., 1984). Direct crustal contamination by assimilation during ascent is unlikely for mafic lamprophyres with < 56 wt% SiO₂. Venturelli et al. (1984) suggested that subduction of European continental crust during the Alpine orogeny may have contributed to the incompatible trace element enrichment of the lamprophyres.

5.3 Roccamonfina

5.3a Location and field work

Roccamonfina volcano is located 140 km southeast of Rome and 50 km northwest of Naples at the intersection of two fault systems trending NW-SE and NE-SW (Di Brozolo et al., 1988). Accessibility to the volcano is facilitated by the nearby Rome-Naples autostrada that lies 6 km east of the town of Roccamonfina. The 1000m-high volcano is approximately 15 km in diameter at its base and covers an area of 115 km². Twenty-nine KS and HKS samples (RC 100 to RC 128) were collected from within the

central caldera and on the flanks of Roccamonfina by the author, K. Bell and V. Zanon (Università di Roma) in August, 2002 (see Appendix B for sample localities). No pyroclastic material was collected.

5.3b Geological setting

Roccamonfina is a Pleistocene to Recent partially dissected stratovolcano with a complex history of cone-building and summit collapse (Figures 5.2a and 5.2b). The volcano consists of a basal volcanic-fluvial succession overlain by a multi-stage stratocone with nested calderas, all of which rest on Mesozoic limestone units (Giannetti, 2001). Local Miocene flysch terrains, dominated by silts and sandy siltstones, unconformably overlie the surrounding carbonate units (Capuano et al., 1992).

Two main lava domes and the small town of Roccamonfina are contained within the well-developed, elliptical, 6 km wide, central caldera. The wall of the central caldera rises about 300 m above the caldera floor in its western half, but is poorly preserved in the east. Giannetti (1979) suggested that the two parts may be separated by a SW-NE fault that continues to the base of Mt. Cesima north of the volcano. The caldera walls are composed of interbedded lavas and tephra that slope radially away from center and are punctuated by parasitic domes of variable composition (Giannetti, 2001). A smaller horseshoe-shaped caldera about 3 km in diameter, known as the Gli Stagli, is located directly north of the central caldera. Walls of the Gli Stagli rise 250 m above the gently northward-sloping caldera floor and open to the north into a large diamond-shaped topographic low referred to as the northern depression (Giannetti, 2001). NNE (anti-Apenninic) and NW (Apenninic) trending normal faults separate the northern depression



Figure 5.2a. Geologic map of Roccamonfina volcano and surrounding area showing sample localities (modified from Giannetti, 2001).

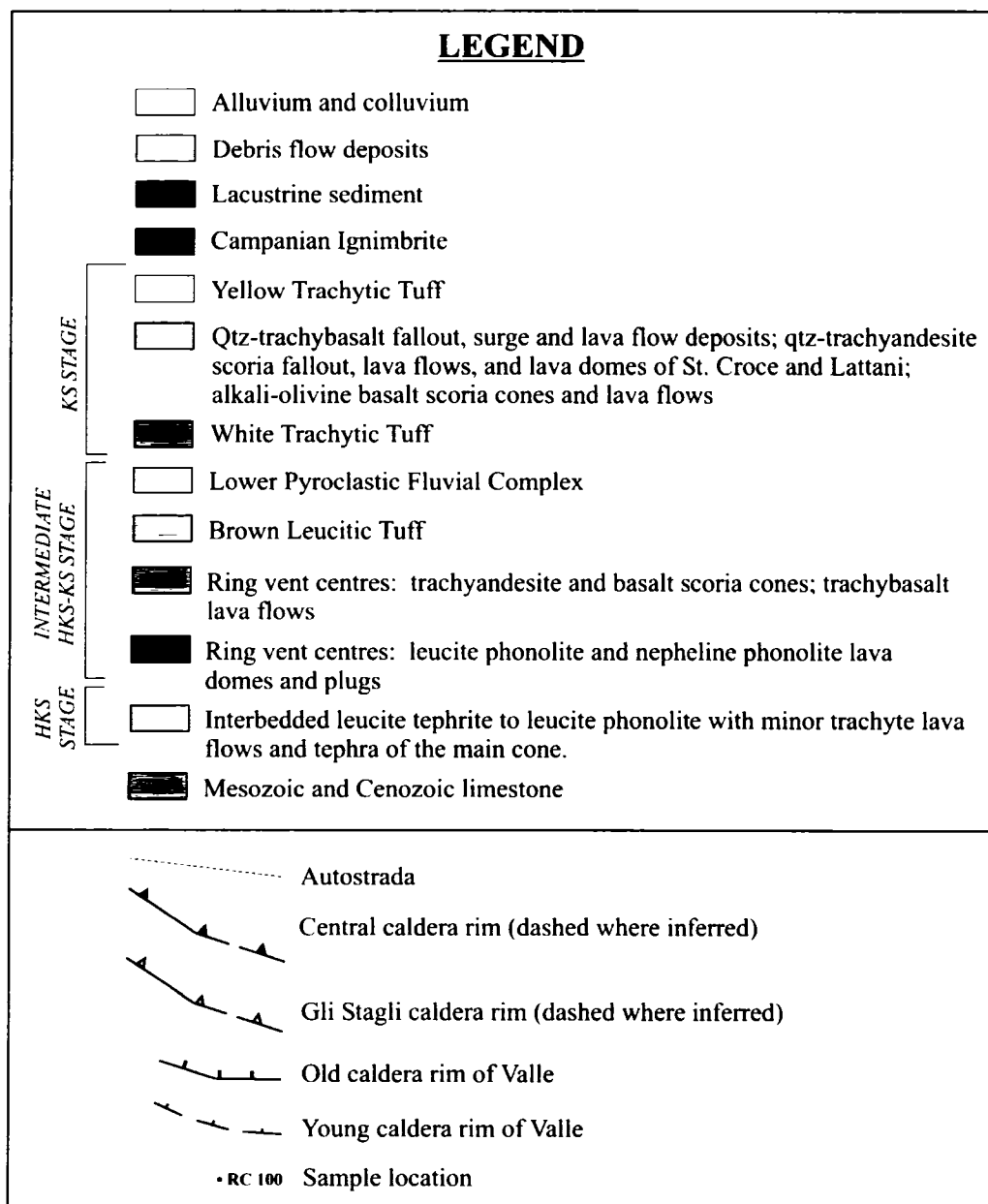


Figure 5.2b. Legend for the geologic map of Roccamonfina volcano (modified from Giannetti, 2001).

from Mt. Cesima and Mt. Camino.

Volcanic activity at Roccamonfina can be divided into a pre-caldera phase (Stage I) and a post-caldera phase (Stage II). Giannetti (2001) determined a K-Ar age of 549 ± 42 ka for the basal volcanic-fluvial succession of Stage I. The pre-caldera phase involved large, cone-building eruptions that account for more than 80% of the volume of the volcano. Detailed mapping, Landsat satellite imaging, and radiometric dating by Giannetti (2001) suggested that the Gli Stagli caldera subsided fairly early during Stage I, between 546 and 474 ka. The collapse of the central caldera marks the conclusion of Stage I. Field evidence, however, suggests that this event is not the result of a single eruption. Instead, Giannetti (2001) proposed that both the Gli Stagli and the central caldera formed incrementally through repeated draining of the magma chamber(s). Stage I is represented by interbedded HKS lavas and pyroclastic rocks, including leucite tephrite, tephritic leucitite, phonotephrite and leucite phonolite (Taylor et al., 1979). A major pyroclastic flow near the end of Stage I produced the 385-335 ka Brown Leucititic Tuff (Luhr and Giannetti, 1987), which ranges from leucite tephrite (HKS) to trachyte (KS).

The post-caldera phase (Stage II) started with the eruption of a large ash-pumice flow unit referred to as the White Trachytic Tuff (317-230 ka). Most of the subsequent volcanic activity was confined to the central caldera, giving rise to relatively minor KS lava domes (Santa Croce and Lattani), lava flows, and pyroclastic deposits (Plate 5.1). Stage II is characterized by KS trachyandesite, with subordinate potassic trachybasalt and basalt (Taylor et al., 1979). Despite the general dominance of HKS rocks in Stage I and KS rocks during Stage II, it should be noted that both series temporally overlap from 374-



Plate 5.1. The Santa Croce KS lava dome within the central caldera, looking north (width of dome is approximately 2.5 km).

323 ka, referred to by Giannetti (2001) as the Intermediate Concurrent HKS-KS Stage. The age of the last volcanic activity at Roccamonfina is uncertain. However, stratigraphic evidence indicates that activity ended before the eruption of the Campanian ignimbrite, a widespread event dated at 35-28 ka that originated near the Phlegrean Fields (Taylor et al., 1979).

5.3c Previous work on the petrology and geochemistry of KS and HKS volcanic rocks from Roccamonfina

Appleton (1972) subdivided the volcanic rocks of Roccamonfina into two series on the basis of age, petrography, and chemistry, and coined the terms High K Series (HKS) for ne- and lc-normative leucite-bearing lavas, and Low K Series (KS) for ne- to qz-normative olivine basalts, trachybasalts, and latites. The HKS lavas are enriched in K, P, Ba, Ce, Rb, Sr, Th, and Zr relative to the KS lavas, which Appleton (1972) attributed to two main differentiation processes. One process occurred at intermediate or high pressures and produced the HKS and KS parental magmas with specific levels of enrichment in K and associated elements, and another involved crystal fractionation processes at low pressures that controlled evolution towards felsic derivatives in each series. Subsequent work by Taylor et al. (1979) confirmed that low-pressure crystal fractionation is dominant in both the HKS and KS lavas, and supported Appleton's (1972) hypothesis that the HKS and KS series represent completely separate trends of magmatic differentiation involving different parent magmas.

Clinopyroxene is the dominant phenocryst phase in both the KS and the HKS volcanic rocks from Roccamonfina (Giannetti and Ellam, 1994). Clinopyroxene crystals

can reach up to 6 mm in length and are normally zoned with pale green cores and dark green (Fe-rich) rims. Rocks of the KS series are characterized by olivine ($Fe_{0.87-79}$) and plagioclase phenocrysts, and by the absence of leucite, sanidine, and nepheline. Rocks of the HKS series contain leucite both as a phenocryst and as a groundmass phase, but only rare olivine and plagioclase. Accessory minerals present in both the KS and the HKS rocks include biotite (altered to Fe-Ti oxides), Cr-spinel, magnetite, and apatite (Giannetti and Ellam, 1994).

Volcanic rocks from Roccamonfina are characterized by high Al_2O_3 (up to ~20 wt%), low TiO_2 (< 1.0 wt%), and a wide range of SiO_2 (~45 wt% to >56 wt%). The high Al_2O_3 contents of the HKS rocks, in particular, are considered to be one of the main geochemical features that distinguish Group III (plagiocleucitites) from Group I (lamproites) and Group II (kamafugites) (Foley et al., 1987). The incompatible trace element patterns of rocks from the KS series show enrichment of LILE with respect to HFSE, and have large negative anomalies at Ta, Nb, and Ti. Although the incompatible element patterns for the HKS series are similar to those from the KS series, the HKS rocks have higher absolute abundances of LILE and a more marked negative Ba anomaly (Conticelli and Peccerillo, 1992). The $^{87}Sr/^{86}Sr$ ratios of volcanic rocks from Roccamonfina show enriched isotopic signature, with values between 0.7064 and 0.7083 for the KS (olivine basalts, trachybasalts, trachytes) and from 0.7085 to 0.7100 in the HKS (tephritic phonolites, phonolitic leucite tephrite, leucitites) (Hawkesworth and Vollmer, 1979). Giannetti and Ellam (1994) confirmed that the HKS and KS lavas have distinct Sr isotopic compositions, and found that there is no progressive increase in $^{87}Sr/^{86}Sr$ from the primitive lavas to more evolved rock types.

Volcanic rocks from Roccamonfina, as well as from other centres in the Roman and Tuscan Provinces, shown positive correlations between $^{87}\text{Sr}/^{86}\text{Sr}$ ratios and $\delta^{18}\text{O}$ values. Measured $\delta^{18}\text{O}$ values range from +5.6 to +10.1 in the HKS and +6.6 to +8.8 in the KS (Taylor et al., 1979). The elevated $\delta^{18}\text{O}$ values (as well as $^{87}\text{Sr}/^{86}\text{Sr}$ ratios) are characteristic of the upper continental crust, but whether the isotopic variations are present in a heterogeneous, enriched upper mantle source (Hawkesworth and Vollmer, 1979) or are the result of crustal assimilation at some stage prior to eruption (Taylor et al., 1979) remains a matter of debate. Hawkesworth and Vollmer (1979) measured $^{143}\text{Nd}/^{144}\text{Nd}$ ratios that range from 0.51223 to 0.51231 in the HKS and from 0.51232 to 0.51245 in the KS, and noted that the lower HKS values are analytically indistinguishable from many of the Roman Province volcanic rocks to the north. Pb isotopic ratios are similar to those from the Roman and Campanian Provinces, with $^{206}\text{Pb}/^{204}\text{Pb}$ ratios that lie between 18.786 and 19.153 (Vollmer and Hawkesworth, 1980; D'Antonio et al., 1996).

5.4 Ernici

5.4a Location and field work

The Ernici volcanoes are located about 70 km southeast of Rome and 70 km northwest of Roccamonfina in the Media Valle Latina, a wide valley occupied by small villages (Arnara, Pofi, Ceccano, San Stefano, Giuliano di Roma, Patricia, Supino) and farmland. The Rome-Naples autostrada lies 4 km northeast of most of the Ernici volcanic rocks and 4 km southwest of Frosinone. Ernici consists of a series of about twenty small volcanic centres cropping out in a roughly WNW-ESE trend and covering



Plate 5.2. View of the Media Valle Latina looking east-northeast (+ = volcanic centre). The town of Frosinone overlies Neogene terrigenous sediments (Civetta et al., 1981), while the rest of the valley is composed of alluvial deposits, pyroclastic material, and minor lava flows.

an area of approximately 50 km² (Plate 5.2). Twenty-three KS and HKS samples (ER 100 to ER 122) were collected at Ernici by the author, K. Bell and V. Zanon in August, 2002 (see Appendix B for sample localities). Due to the relative scarcity of lava outcrops at Ernici, most samples are from bombs or scoria contained within pyroclastic deposits. One sample of pyroclastic material (ER 102) was collected east of Patricia.

5.4b Geological setting

The volcanic rocks of Ernici overlie Mesozoic carbonates and upper-middle Miocene calcareous and arenaceous sedimentary rocks (Figure 5.3) (Civetta et al., 1981). Elongated topographic highs to the south and west of the volcanic units are composed of Mesozoic limestone, which outcrops extensively in the Media Valle Latina. At the northern end of the volcanic field, much of the local bedrock is covered by Quaternary alluvial sediments deposited by the southeast-trending Sacco River. Regional compression in the late Miocene and Pliocene was followed by extension that caused subsidence along NW-SE and NE-SW lineaments. The alignment of the Ernici volcanic centres coincides with these large-scale fractures (Angelucci et al., 1974).

K-Ar dates indicate that volcanic activity at Ernici occurred between 700 and 100 ka (Basilone and Civetta, 1975). The HKS magmas erupted from about 700 to 200 ka, followed by KS magmas between 200 and 100 ka. Unlike Roccamonfina, there is no clear evidence for a temporal overlap between the HKS and KS series at Ernici. Volcanism during both the HKS and KS phases was mainly explosive, producing large volumes of pyroclastic material with subordinate lava flows (Civetta et al., 1981).

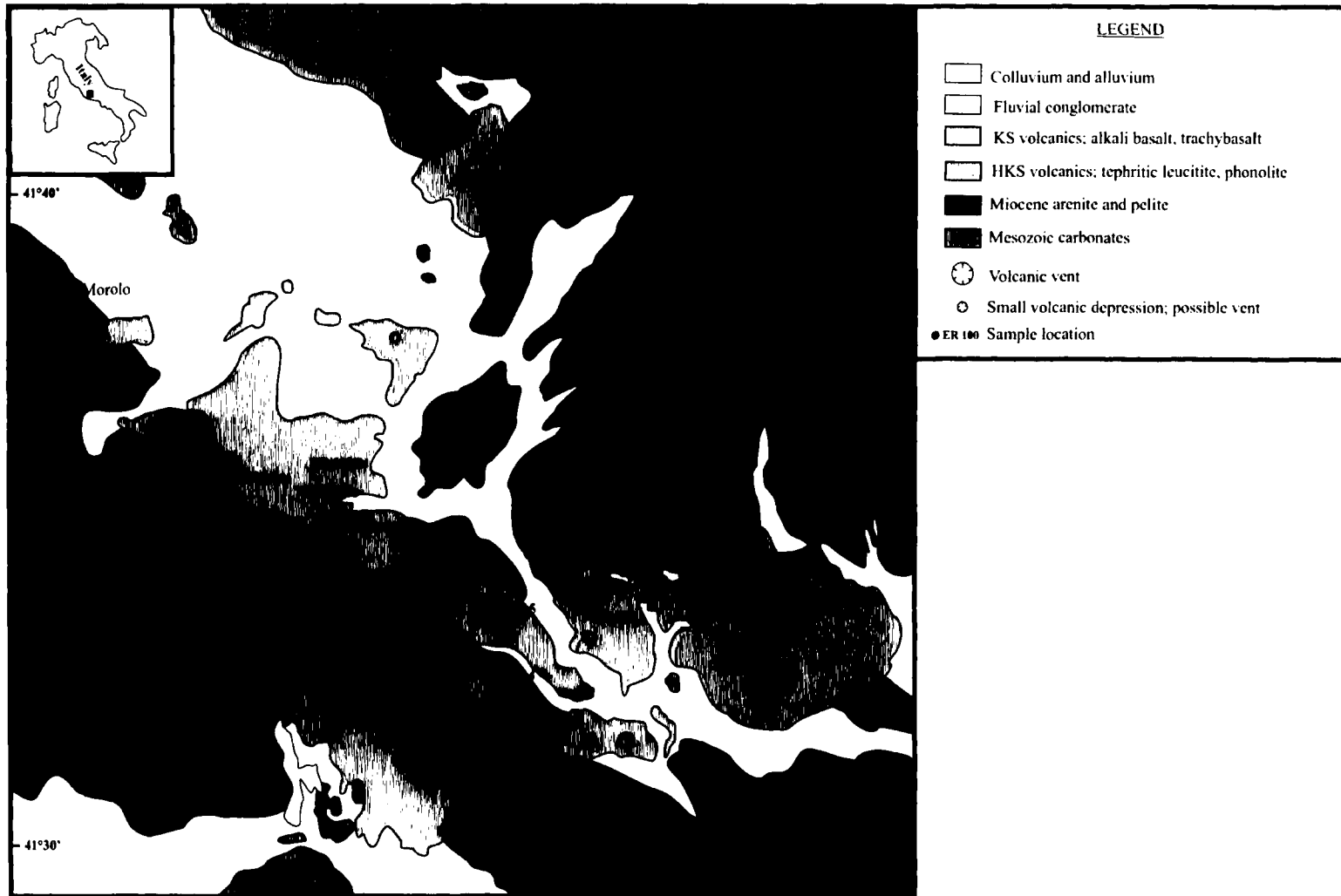


Figure 5.3. Geologic map of Ernici showing sample localities (modified from Civetta et al., 1981).

5.4c Previous work on the petrology and geochemistry of KS and HKS volcanic rocks from Ernici

Civetta et al. (1981) divided the volcanic rocks from Ernici into a potassic series (KS) and a highly potassic series (HKS). The KS volcanics include slightly undersaturated (normative ne 3-9%) alkali basalts and trachybasalts, while most of the HKS rocks are strongly undersaturated (normative $lc + ne = 27-50\%$) tephritic leucitites and phonotephrites (Civetta et al., 1981). The KS rocks display K_2O/Na_2O ratios close to unity and $Na_2O + K_2O$ between 5 and 6 wt%, while the HKS rocks are characterized by K_2O/Na_2O ratios of about 3 and $Na_2O + K_2O$ between 9 and 11 wt%. Rocks from both series have low SiO_2 (45-50 wt%), relatively high CaO contents (9.7-12.9 wt%) and high Mg#s (60-74). The KS and HKS series are characterized by high LILE concentrations (HKS rocks are enriched by a factor of 1.5 to 3 relative to KS) and high LREE and Y contents. The HKS samples display a significant negative Eu anomaly compared to the KS samples.

The KS volcanic rocks range from aphyric to porphyritic and consist of diopside phenocrysts with subordinate olivine (Fo_{85-90}) and rare microphenocrysts of plagioclase (Civetta et al., 1981). The groundmass is made up of strongly zoned plagioclase, zoned salite, olivine (Fo_{60-85}), magnetite, alkali feldspar, and rare nepheline (Civetta et al., 1979). Volcanic rocks of the HKS series are dominated by clinopyroxene and minor forsteritic olivine, while plagioclase is present only as sparse groundmass microlites. Two types of clinopyroxene are present in the HKS series, one with a green pleochroic ferrosalite core and a rim of colorless diopside, and the second with core of diopside and a rim of salite (Civetta et al., 1981). The groundmass of the HKS rocks contains leucite,

clinopyroxene, Fe-rich olivine, nepheline, alkali feldspar, and variable amounts of biotite and amphibole (Civetta et al., 1979). Some of the HKS rocks from Ernici contain abundant analcite, which has been interpreted as a pseudomorph after leucite (Civetta et al., 1981).

The trace element patterns for the KS and the HKS magma series cannot be accounted for simply by crystal fractionation from a single parent magma, and an unrealistically large quantity of any crustal contaminant would be required in order to produce the wide variations seen in some elements (K, Rb, Th). Extensive crustal contamination also conflicts with the moderate variations in the major element abundances as well as the high Mg#s (Civetta et al., 1981). The $^{87}\text{Sr}/^{86}\text{Sr}$ ratios measured by Civetta et al. (1981) range from 0.70622 to 0.70705 for rocks of the KS series and from 0.70953 to 0.71121 for those of the HKS series, clearly indicating two distinct groups based on Sr isotopic composition. As seen in the volcanic rocks from Roccamonfina, the $^{143}\text{Nd}/^{144}\text{Nd}$ ratios of the HKS lavas at Ernici are lower than the KS.

On the basis of REE and Sr isotopic data, Civetta et al. (1979) suggested that the HKS and KS rocks of Ernici could be generated by small degrees of partial melting (1% and 5% respectively) of a garnet peridotite heterogeneously enriched in LILE (at least 8-10x chondritic values) and radiogenic Sr. Disequilibrium melting of a source containing different amounts of apatite and perovskite could also be responsible for the generation of the HKS series (Civetta et al., 1979). This could explain the negative Eu anomaly as well as variably high Ba, Th and P. Based on the stronger degree of silica-undersaturation of the HKS series compared to the KS series, Civetta et al. (1981) suggested that the HKS source region is deeper than the KS source region at Ernici.

CHAPTER 6

PETROGRAPHY AND MINERAL CHEMISTRY

6.1 Introduction

Petrographic descriptions of all samples collected from the Western Alps, Roccamonfina, and Ernici are based on hand sample and thin section observation. Detailed petrography is presented prior to an analysis of the whole-rock chemistry (Chapter 7) due to the unusual nature of these rock types, particularly the lamprophyres. Silicate mineral chemistry for selected samples was determined by electron microprobe using a Camebax MBX at Carleton University (see Appendix G for analytical methods). The six main types of minerals analyzed are olivine, pyroxene, amphibole, mica, feldspar, and feldspathoid. The purpose of the microprobe work is to: 1) identify fine-grained or altered groundmass material, 2) determine the major oxide mineral chemistry of the rock-forming silicates, 3) use the mineral chemistry to constrain the physical and chemical conditions of crystallization, and 4) compare and contrast the mineral chemistry both within and between the three study areas.

6.2 Petrography

6.2a Western Alps

The eight samples from the Western Alps are hypabyssal (medium-grained equigranular) to porphyritic and contain at least one hydrous phenocryst phase (amphibole and/or mica). Feldspathoids, orthopyroxene, pigeonite, wollastonite, glass, and phenocrysts of quartz and feldspar are absent. Although no olivine is present, two

samples contain ovoid areas of talc that may represent olivine replacement. Several samples are pervasively altered, with the original minerals replaced by chlorite, talc, epidote, or serpentine. The samples from the Western Alps are classified as lamprophyres using the scheme and nomenclature of Le Maitre et al. (2002). The main characteristics of lamprophyres are (Le Maitre et al., 2002):

1. They normally occur as dykes and are not simply textural varieties of common plutonic or volcanic rocks.
2. They are porphyritic, mesocratic to melanocratic ($M' = 35-90$) but rarely holomelanocratic ($M' > 90$), where M' is the colour index.
3. Feldspars and/or feldspathoids, when present, are restricted to the groundmass.
4. They contain essential biotite and/or amphibole.
5. Hydrothermal alteration of olivine, pyroxene, biotite, and plagioclase, when present, is common.
6. Calcite, zeolites, and other hydrothermal minerals may appear as primary phases.
7. They tend to have high contents of K_2O and/or Na_2O , H_2O , CO_2 , S, P_2O_5 and Ba.

The lamprophyres from the Western Alps can be divided into minettes, spessartites, and kersantites (see Appendix C for lamprophyre classification) based on their predominant felsic and mafic silicate minerals. A minority of lamprophyres share the same mineralogy (plagioclase + hornblende + K-feldspar \pm clinopyroxene \pm biotite) as diorites, andesites, and shoshonites. Lamprophyres have the following features that set them apart: olivine pseudomorphs, primary carbonate and sulphate, kinked or bent mica, globular structures, castellated and panidiomorphic textures (Rock, 1991). Tables 6.1a and 6.1b list the mineralogy and a brief textural description of each lamprophyre.

Sample Number	Essential minerals	Accessory minerals	Texture
WA100 minette	diopside (15%) phlogopite (20%) orthoclase (35%) albite (20%)	calcite quartz pyrite ilmenite magnetite epidote chlorite allanite chalcopyrite	Relatively unaltered, glomeroporphyritic, with phenocrysts of phlogopite and diopside in a groundmass of diopside, phlogopite, orthoclase and albite. Sparse quartz xenocrysts rimmed by augite, epidote and albite. Augite-orthoclase-albite ocelli present.
WA101 spessartite	magnesiohornblende (25%) orthoclase (15%) albite (40%) epidote (10%)	chlorite titanite sericite pyrite rutile ilmenite magnetite quartz	Heavily altered, porphyritic with abundant sericite and chlorite. Phenocrysts of amphibole (magnesiohornblende) in a groundmass of orthoclase, albite, and epidote. Some quartz veining present.
WA102 minette	diopside (25%) phlogopite (25%) orthoclase (30%) albite (10%)	apatite titanite zircon chlorite talc quartz	Relatively unaltered, hypabyssal, with equigranular phlogopite, diopside, orthoclase, and albite. Possible replacement of olivine by talc.
WA103 spessartite	epidote (15%) magnesiohornblende (30%) albite (25%) orthoclase (5%) chlorite (10%) calcite (5%)	titanite muscovite quartz allanite magnetite pyrite apatite	Heavily altered, porphyritic with abundant chlorite and epidote. Relict phenocrysts of amphibole (magnesiohornblende) are largely replaced by epidote, calcite, and albite.

Table 6.1. Essential (≥ 5 vol.%) and accessory (< 5 vol.%) mineralogy of samples from the Western Alps. Estimates of modal percent given in brackets for essential minerals.

Sample Number	Essential minerals	Accessory minerals	Texture
WA104 minette	diopside (20%) phlogopite (20%) richterite (10%) orthoclase (40%)	zircon chlorite allanite apatite talc	Relatively unaltered, porphyritic, with phenocrysts of phlogopite, diopside, and apatite in a groundmass of orthoclase and richterite. Possible replacement of olivine by talc.
WA105 minette	diopside (20%) phlogopite (35%) orthoclase (30%) albite (5%)	magnetite titanomagnetite titanite ilmenite talc chlorite quartz apatite	Relatively unaltered, hypabyssal with equigranular phlogopite, diopside, orthoclase and minor albite. Minor chlorite and talc. Strong alignment of small biotite.
WA 106 kersantite	phlogopite (40%) albite (30%) dolomite (15%) quartz (5%)	talc serpentine apatite barite	Relatively unaltered, hypabyssal with phlogopite in a matrix of dolomite, albite and quartz. Minor serpentine and talc alteration. No pyroxene, amphibole or alkali feldspar.
WA107 spessartite	magnesiohastingsite (60%) albite (25%) chlorite (5%)	allanite muscovite pyrite magnetite chromite titanite apatite barite rutile quartz talc	Heavily altered, porphyritic with phenocrysts of amphibole (magnesiohastingsite) in a groundmass of albite and magnesiohastingsite. Replacement of magnesiohastingsite with chlorite and talc. Contains quartz xenocrysts with reaction rims.

Table 6.1. Continued.

6.2a.i Minettes

Samples WA 100, WA 102, WA 104 and WA 105 contain phlogopite > amphibole and alkali feldspar > plagioclase feldspar and are therefore classified as minettes. WA100 and WA104 are porphyritic with a fine-grained groundmass, while WA102 and WA105 are equigranular. Plates 6.1 and 6.2 show the difference between the porphyritic (WA100) and equigranular (WA102) textures. All studied minettes contain euhedral to subhedral crystals of zoned, kinked phlogopite, and euhedral to anhedral zoned clinopyroxene (diopside and augite). Kinked, strongly zoned mica are typical of lamprophyres (Rock, 1991). Several samples show a panidiomorphic texture common to lamprophyres, in which the pseudo-hexagonal crystals of phlogopite are readily distinguished from euhedral, pseudo-octagonal crystals of clinopyroxene.

Clinopyroxene commonly forms 15% to 25% of the rock, and phlogopite makes up 20% to 35%. Both minerals are present as phenocryst phases and in the groundmass. Clinopyroxene phenocrysts can be normally zoned (Mg-rich core and Fe-rich rim), reversely zoned (Fe-rich core and Mg-rich rim) (Plate 6.7), or oscillatory zoned (Plate 6.8). Inclusions of apatite are common in clinopyroxene. Phlogopite displays a disequilibrium texture in several samples (Plate 6.3) and is commonly present in multiple generations. Larger crystals may be partially resorbed while smaller crystals are unaltered (Plate 6.9), and resorption of phlogopite megacrysts is common (Plate 6.12). Phlogopite phenocrysts may be normally zoned (Plate 6.10) or reversely zoned (Plate 6.11), with both types of zoning commonly present in a single sample. Ovoid cores in some clinopyroxene and phlogopite phenocrysts suggest a complex history of growth followed by dissolution and reprecipitation.

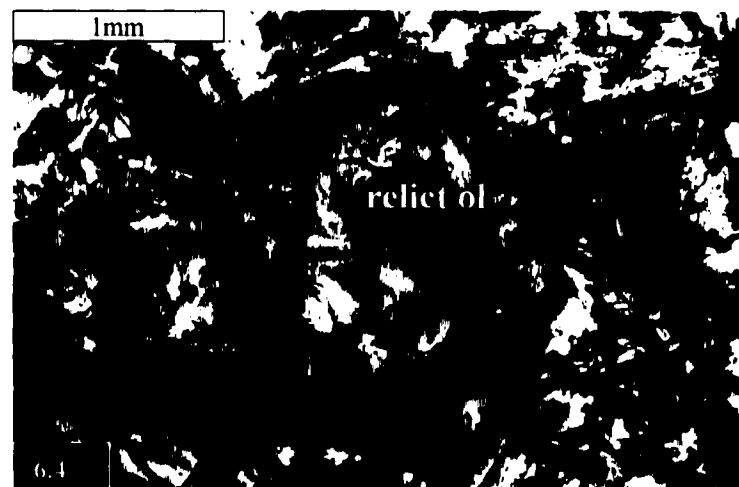
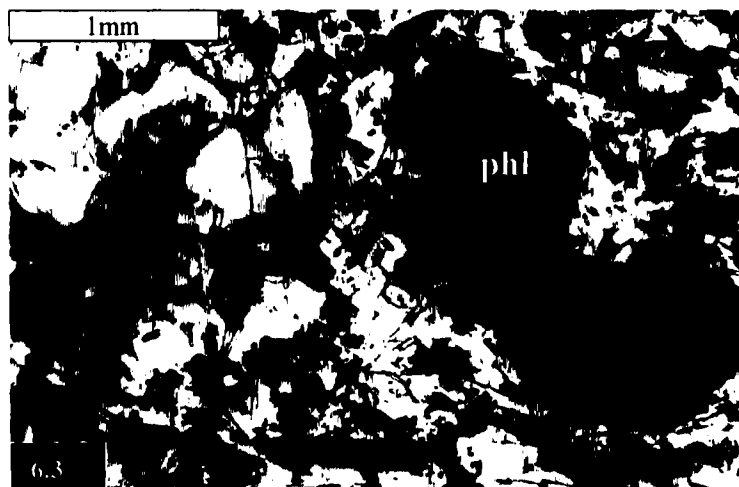
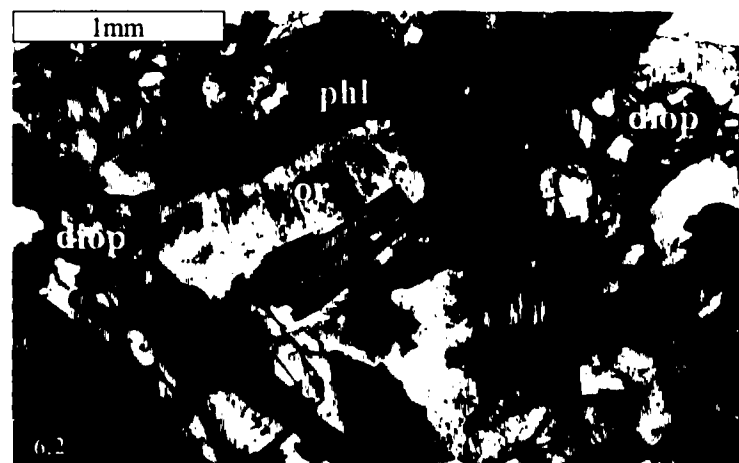
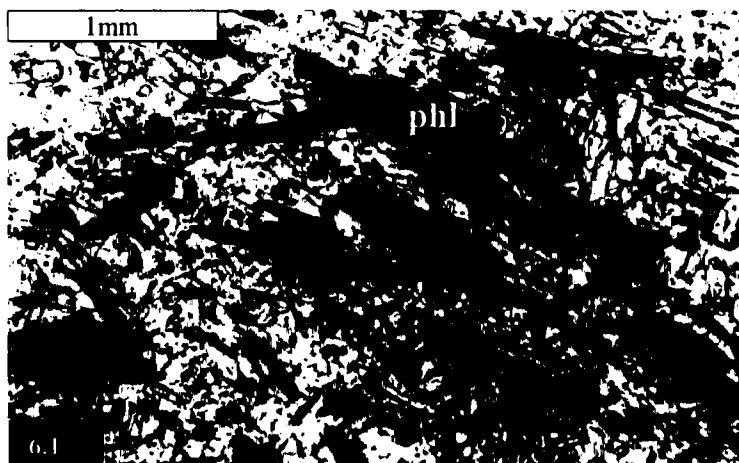


Plate 6.1. Porphyritic texture in sample WA 100 with phlogopite phenocrysts in a groundmass of phlogopite, diopside, orthoclase, albite, and accessory minerals as listed in Table 6.1.

Plate 6.2. Equigranular texture in sample WA 102 with medium-grained, equigranular phlogopite, diopside, and orthoclase.

Plate 6.3. Partially resorbed phlogopite phenocryst, sample WA104.

Plate 6.4. Complete replacement of possible olivine by talc, sample WA 104.

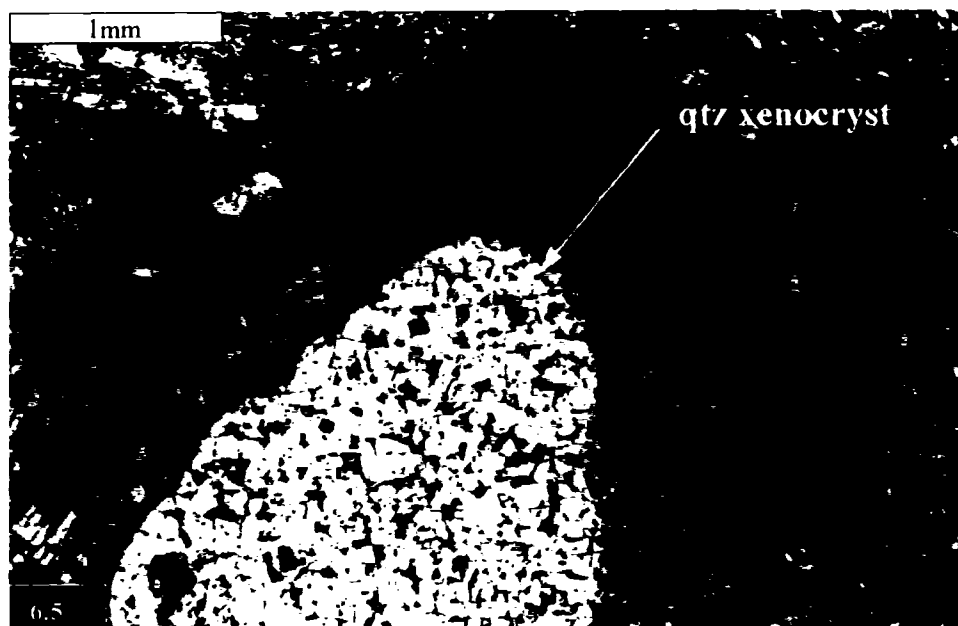
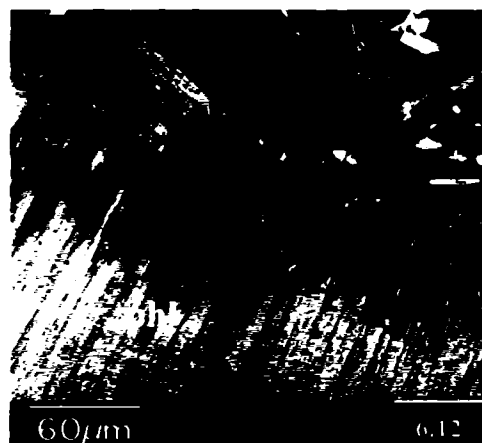
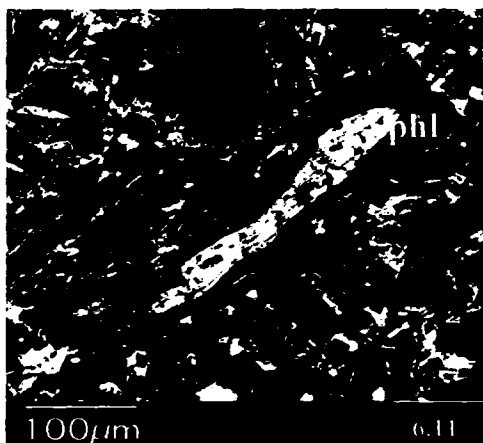
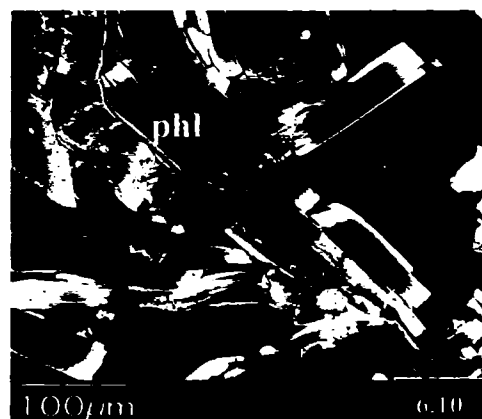
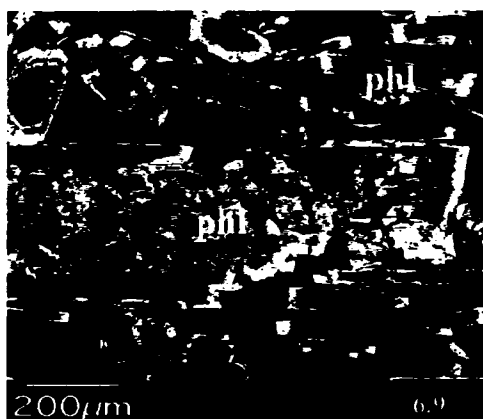
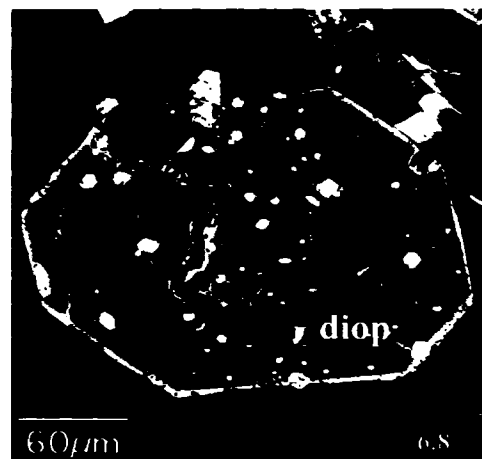
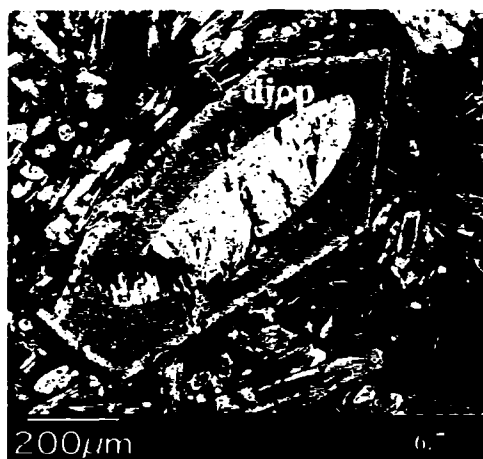


Plate 6.5. Quartz xenocryst rimmed by epidote, augite, and orthoclase, sample WA100. Disequilibrium between the quartz and the groundmass as shown by the reaction rim strongly suggests that the quartz is a xenocryst and may be the result of crustal contamination.



Plate 6.6. Globular structure composed of augite, orthoclase, and albite, sample WA100. Globular structures are typical of minettes and serve to distinguish them from more common rock types such as diorites, andesites, and shoshonites.



BSE images of diopside and phlogopite in minettes, Western Alps

Plate 6.7. Reversely zoned diopside phenocryst with ovoid core (100-17: core, 100-18: rim).

Plate 6.8. Concentrically zoned, euhedral diopside phenocryst with apatite inclusions (102-21: core, 102-22: rim).

Plate 6.9. Partially resorbed, zoned phlogopite phenocryst with 2nd generation of zoned unaltered phlogopite (102-12: large core, 102-11: large rim, 102-14: small core, 102-15: small rim).

Plate 6.10. Normally zoned, kinked phlogopite (102-7) in a groundmass of orthoclase.

Plate 6.11. Reversely zoned, partially resorbed phlogopite with ovoid core; sample WA 104.

Plate 6.12. Close-up of disequilibrium texture, phlogopite megacryst (104b-1: rim).

The groundmass of the minettes consists mainly of phlogopite, diopside, orthoclase, +/- albite, with accessory quartz, pyrite, chalcopyrite, ilmenite, magnetite, apatite, titanite, zircon and allanite present in the groundmass of at least one sample. Interstitial calcite is present in sample WA100. All minettes are relatively unaltered, but minor amounts of alteration minerals such as epidote, chlorite, and talc are present. Talc may have replaced olivine in at least one sample (Plate 6.4). Epidote only occurs in the minettes as acicular crystals that form rims around quartz xenocrysts in sample WA100. Quartz xenocrysts are present in several of the minettes and provide evidence of probable crustal contamination (Plate 6.5). Globular structures typical of lamprophyres occur in samples WA100 and WA104, and are composed mainly of augite with minor orthoclase and albite (Plate 6.6).

Sample WA 104 is the only minette that contains microscopic, anhedral amphibole. This amphibole-bearing sample differs from the other minettes in that it contains no plagioclase feldspar and no groundmass quartz. Although sample WA104 is mineralogically similar to lamproites, the absence of leucite, forsterite, and titanian phlogopite, combined with relatively low (K_2O+Na_2O/Al_2O_3), Sr (< 1000 ppm), and La (< 200 ppm) (see Chapter 7) is consistent with the classification of this sample as a minette, rather than a lamproite.

6.2a.ii Spessartites

Samples WA 101, WA 103 and WA 107 contain amphibole, have plagioclase in excess of potassium feldspar, and lack biotite and clinopyroxene. The spessartites are porphyritic with phenocrysts of euhedral to subhedral amphibole set in a groundmass of

fine-grained calcic amphibole, albite, +/- orthoclase. Sample WA107 is the only spessartite with no alkali feldspar present. Amphibole is the only phenocryst phase present in the spessartites and ranges in abundance from 25 vol.% in sample WA101 to 60 vol.% in sample WA107. Amphibole phenocrysts are commonly < 2 mm in diameter, but in sample WA107 amphibole macrocrysts are as large as ~8 mm. The spessartites show pervasive alteration of phenocryst and groundmass phases to sericite, epidote, and chlorite (Plates 6.13, 6.14). Sample WA103 contains approximately 5% interstitial calcite. Estimates of epidote abundance are as high as 15 vol.% in some spessartites; chlorite reaches 10 vol.%.

In some samples, epidote produces fan-shaped growths up to several mm in diameter composed of two distinct compositions. Plate 6.15 displays alteration of a magnesiohastingsite phenocryst to chlorite and epidote, and Plate 6.16 shows a magnified view of actinolite alteration of a tschermakite megacryst. The extreme alteration observed in the spessartites from the Western Alps is common in lamprophyres and is a result of their high volatile content. Minerals normally considered secondary (e.g. carbonates, chlorite, epidote, and serpentine) can also occur as primary magmatic phases in lamprophyres (Rock, 1991). These minerals may form well-crystallized grains or aggregates, and the textural distinction between primary and secondary phases may thus become blurred.

Accessory groundmass phases present in at least one spessartite sample include titanite, pyrite, rutile, ilmenite, magnetite, allanite, apatite, chromite, barite, and quartz. Globular structures rimmed by amphibole and filled with albite, quartz, amphibole, talc and chlorite are present in sample WA107 (Plate 6.17). Concentric structures of Fe-S-Si

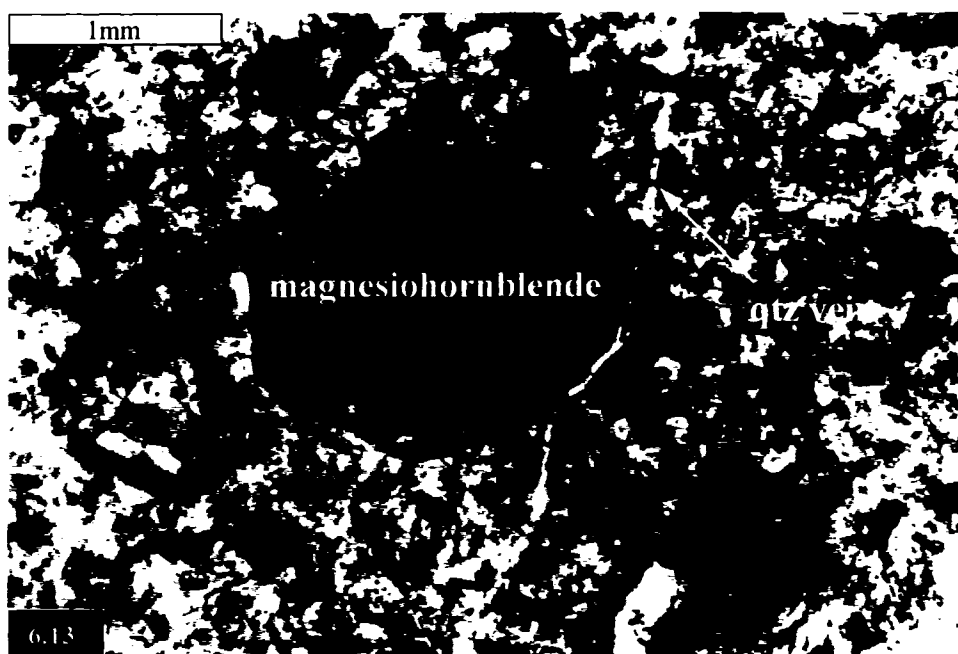
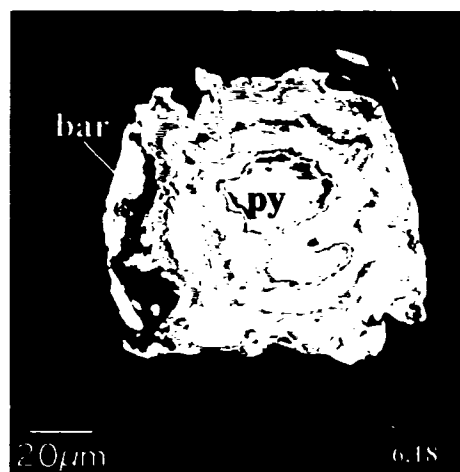
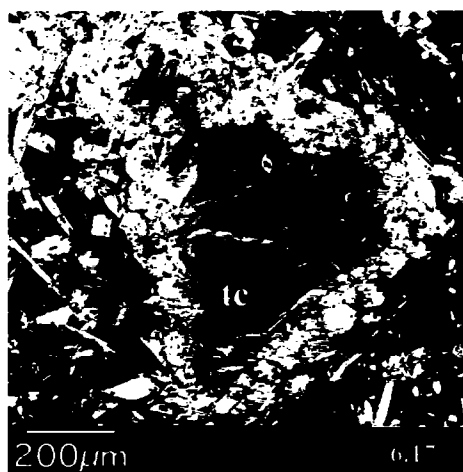
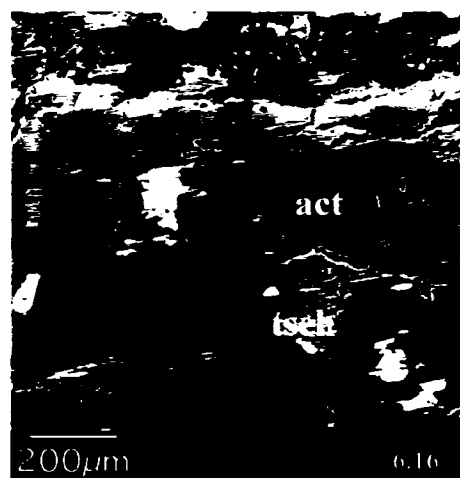
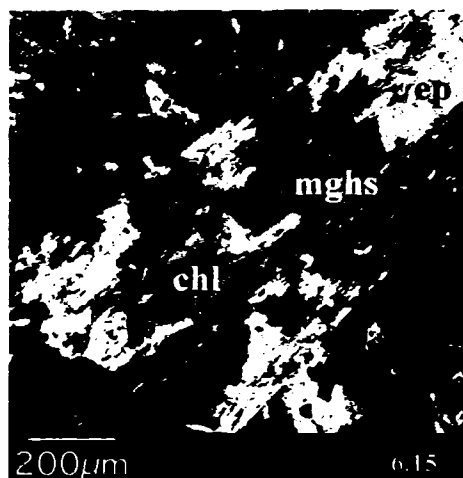


Plate 6.13. Heavily-altered euhedral magnesiohornblende phenocrysts in a groundmass of orthoclase, albite, chlorite, epidote, and sericite, sample WA101.



Plate 6.14. Highly chloritized magnesiohornblende phenocrysts and albite-rich groundmass, sample WA103.



BSE images of amphibole and alteration minerals in spessartites, Western Alps
Plate 6.15. Heavily altered magnesiohastingsite phenocryst (103-7) with chlorite and epidote.

Plate 6.16. Close-up of actinolite alteration of amphibole (tschermakite) megacryst (101-11 and 101-12).

Plate 6.17. Globular structure rimmed by amphibole filled by talc and small amount of quartz; WA 107.

Plate 6.18. Rings of Fe-S-Si alteration products with a core of pyrite and rim of barite; WA 107.

alteration minerals and barite (Plate 6.18) suggest complex oxidation-reduction histories. The oxidation of pyrite to goethite and H_2SO_4 likely precipitated barite from the melt.

6.2a.iii Kersantite

Sample WA 106 is a kersantite that contains phlogopite as the predominant mafic mineral and plagioclase in excess of potassium feldspar. Sample WA106 is a petrological oddity composed primarily of euhedral phlogopite, anhedral albite, anhedral dolomite, and quartz. No pyroxene, amphibole, potassium feldspar or other major silicate minerals are present in the kersantite. Plates 6.19 and 6.20 display the equigranular texture of sample WA 106, as well as its characteristic kinked phlogopite and fine-grained dolomite. A backscattered SEM image of the kersantite showing phlogopite, dolomite, albite, and quartz is given in Plate 6.21. The phlogopite is weakly normally zoned and can contain inclusions of apatite (Plate 6.22). Textural evidence suggests multiple stages of phlogopite growth. The patchy, anhedral nature of the dolomite suggests that it may be secondary, although its presence apparently within phlogopite phenocrysts indicates otherwise (Plate 6.23). Quartz is also commonly surrounded by phlogopite (Plate 6.24). Sample WA 106 is relatively unaltered, although some serpentine and talc are present. Accessory minerals include apatite and barite.

6.2b Roccamonfina

Volcanic rocks collected from Roccamonfina are porphyritic with a fine-grained to glassy groundmass. Unlike the lamprophyres from the Western Alps, volcanic rocks from Roccamonfina and Ernici cannot be properly named based on their mineralogy due

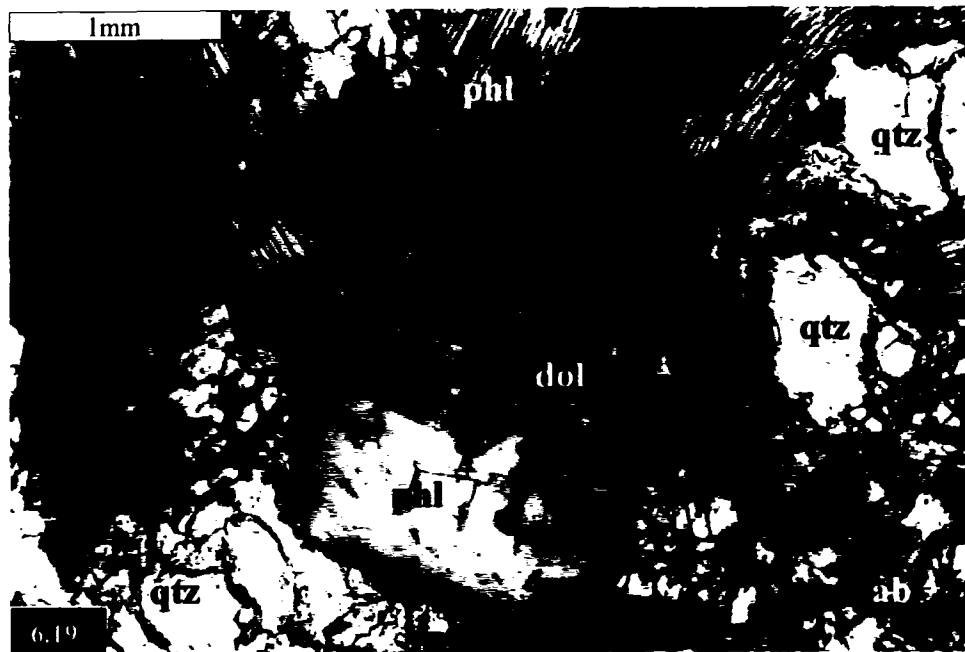


Plate 6.19. Phlogopite, quartz, dolomite and albite; sample WA106.

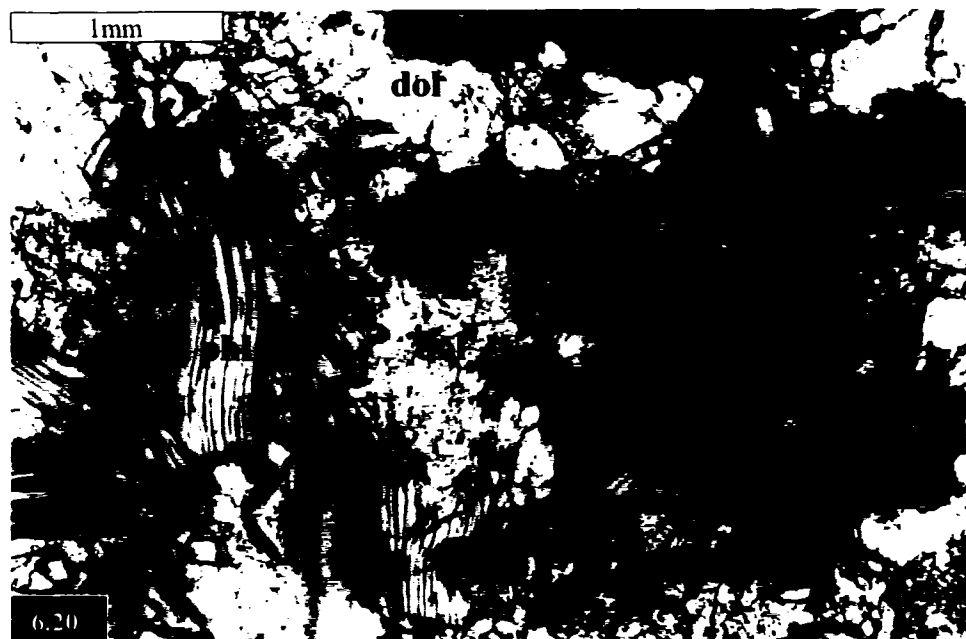
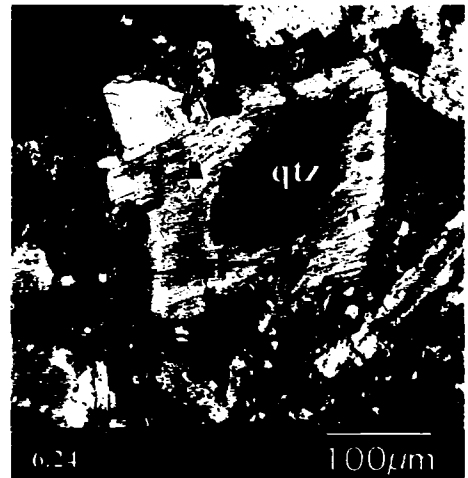
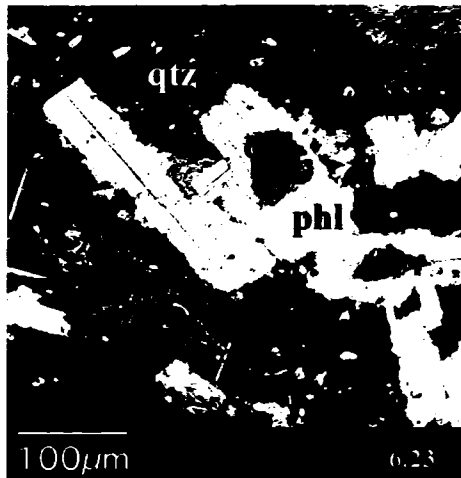
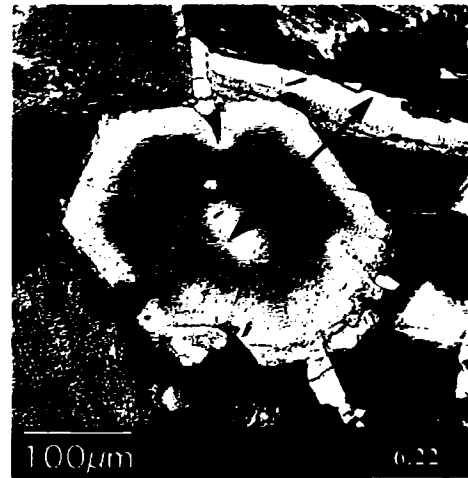
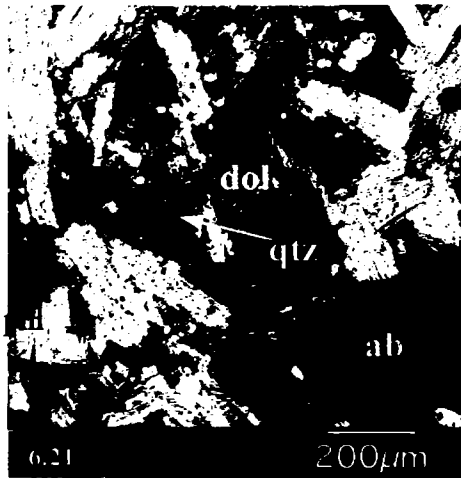


Plate 6.20. Kinked phlogopite surrounded by dolomite; sample WA106.



BSE images of dolomite, phlogopite, albite, quartz in kersantite, Western Alps
Plate 6.21. Phlogopite (106-7: core, 106-8: rim), albite (106-6), dolomite and quartz; WA 106.

Plate 6.22. Normally zoned euhedral phlogopite crystal with apatite inclusion; WA 106.

Plate 6.23. Dolomite surrounded by phlogopite in a quartz-dominated groundmass; WA 106.

Plate 6.24. Quartz surrounded by phlogopite, with abundant apatite in groundmass; WA 106.

to their fine-grained texture. Thus, naming of individual samples will be left until Chapter 7 following an examination of whole-rock geochemistry. As a general guide, KS rocks at Roccamonfina include potassic trachybasalt, basaltic andesite, shoshonite, and latite, while HKS rocks include phonotephrite and tephriphonolite (based on Total Alkalis-Silica classification). The samples from Roccamonfina can be separated into two distinct petrographic groups: a) leucite-absent and b) leucite-bearing (these groups are synonymous with the KS and HKS geochemical distinctions, respectively). Individual mineralogical and textural descriptions for each sample are given in Appendix D.

The grouping of all samples from Roccamonfina (and Ernici) into two series based primarily on K_2O content can result in broad generalizations. The aim of this study is to examine some of the mineralogical, geochemical, and isotopic differences *between* the KS and HKS rocks, not to focus on individual samples *within* the two series. The following section will compare and contrast the mineralogy of the leucite-absent (KS) and leucite-bearing (HKS) series. Table 6.2 is a summary of the essential minerals and accessory minerals present in the two series at Roccamonfina.

6.2b.i Potassic series (KS)

The KS rocks at Roccamonfina are dominated by clinopyroxene (diopside), plagioclase feldspar (labradorite-bytownite), and alkali feldspar (sanidine). Accessory groundmass apatite and magnetite are present in most samples. Although most are holocrystalline, glass makes up nearly 25-30% of some samples. Vesicles up to 2 mm in diameter are present in samples RC120, RC121, RC122, and are abundant in RC127.

Diopside occurs as both a phenocryst phase, where it is commonly euhedral, and

Series	Essential Minerals	Accessory Minerals
Potassic (KS)	clinopyroxene plagioclase alkali feldspar +/- olivine +/- phlogopite +/- orthopyroxene	apatite magnetite chlorite
Ultrapotassic (HKS)	leucite clinopyroxene plagioclase +/- olivine +/- phlogopite +/- nepheline	fluorite apatite magnetite chlorite

Table 6.2. Essential (≥ 5 vol.%) and accessory (< 5 vol.%) minerals of studied volcanic rocks from Roccamonfina.

as a subhedral groundmass phase. Phenocrystic diopside content ranges from 5 to 15 vol.%, and individual crystals reach up to 3 mm in diameter. Chemical zonation in diopside is common, with many crystals exhibiting light brown cores and dark brown rims in plane polarized light (Plate 6.25). Glomeroporphyritic texture, simple twinning, inclusions of opaque minerals, and/or corroded rims are characteristic of diopside. Groundmass orthopyroxene is present in sample RC106.

Plagioclase feldspar is ubiquitous as a groundmass phase and present as phenocrysts in many samples. Euhedral lath-shaped plagioclase microlites constitute most of the groundmass (up to 80 vol.%) and in many cases show a strong trachytic texture (Plate 6.25). "Swallow-tail" skeletal groundmass plagioclase is present in nearly all samples. Plagioclase phenocrysts commonly display strong sieve textures (Plate 6.26), and may be partially resorbed, broken, or show undulose extinction. Plagioclase phenocrysts are up to 3 mm in size and can be euhedral, subhedral and/or anhedral. Phenocrysts are commonly concentrically zoned, and can contain apatite and magnetite.

Alkali feldspar is present only as a groundmass phase in rocks of the KS series. Sample RC119 has a very fine network of microscopic alkali feldspar that makes up approximately 65% of the groundmass. Phlogopite, with light brown cores and dark brown rims, occurs in some samples as sparse phenocrysts up to 3 mm in size and as small elongate groundmass crystals. Resorption of phlogopite, as well as bent or broken phenocrysts, is common. Subhedral to anhedral olivine (forsterite) occurs as a phenocryst and/or groundmass phase in some KS samples. Phenocrystic olivine is characterized by reddish-brown reaction rims of "iddingsite" (smectite + chlorite + iron oxide) (Plate 6.27).

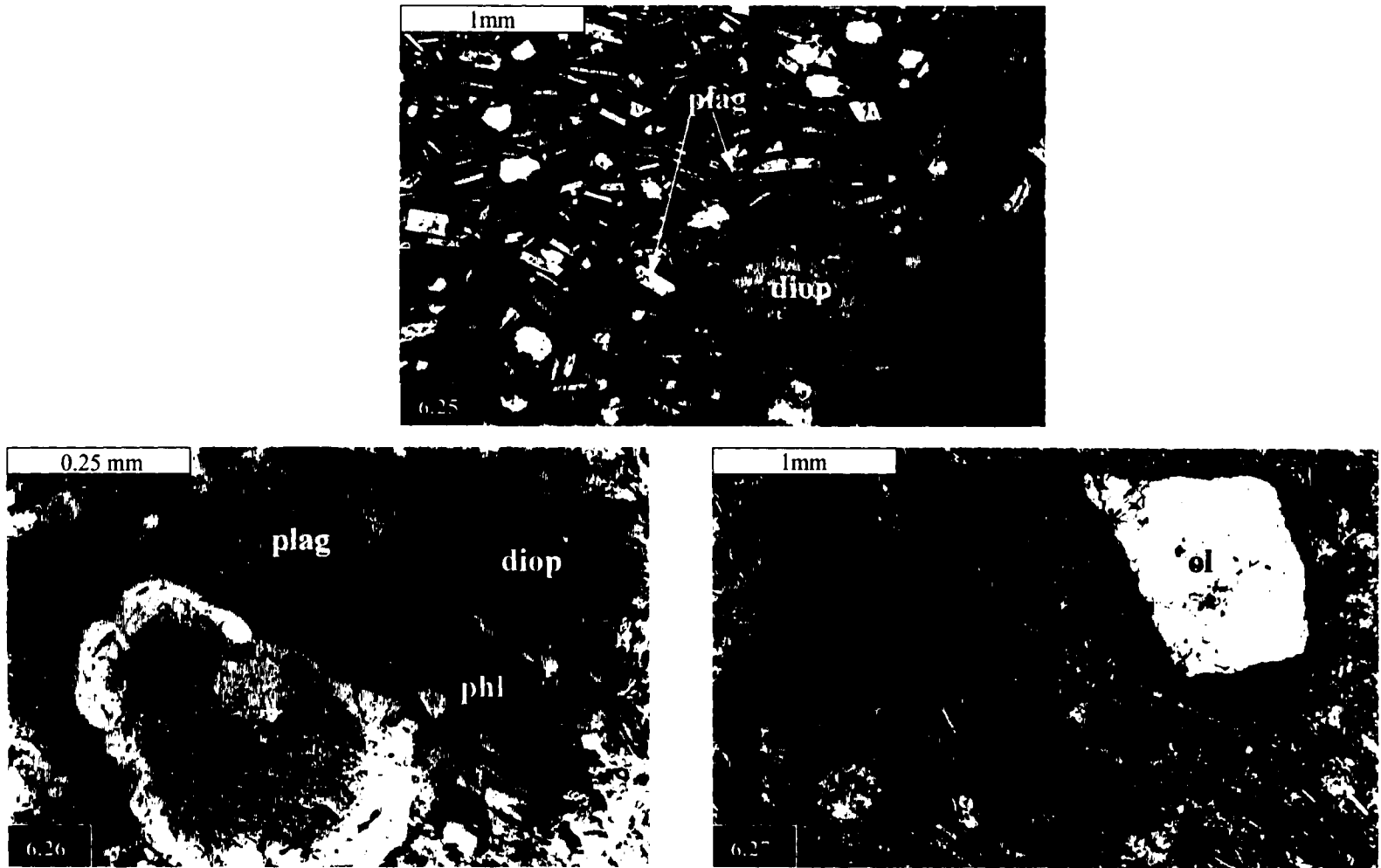


Plate 6.25. Trachytic texture of plagioclase phenocrysts with zoned euhedral diopside phenocryst; KS sample RC107.

Plate 6.26. Sieve-textured plagioclase phenocryst (bytownite), phlogopite, and diopside in a groundmass of aligned plagioclase microlites; KS sample RC106.

Plate 6.27. Anhedral olivine phenocryst with reddish-brown reaction rim; KS sample RC110.

6.2b.ii Ultrapotassic series (HKS)

Most HKS samples at Roccamonfina are composed primarily of leucite, diopside, and calcic plagioclase. Leucite occurs both as phenocryst and groundmass phases, and is commonly the most abundant mineral. Phenocrysts are euhedral to anhedral and can contain acicular inclusions of apatite. The average diameter of leucite phenocrysts is approximately 1-2 mm; however, in some samples leucite can reach up to 1 cm (Plate 6.28). Leucite phenocrysts commonly show zones of microporosity and are variably fractured. Groundmass leucite is subhedral to anhedral in most samples (Plate 6.29), but occurs as rounded, cross-shaped, or star-shaped skeletal crystals (penetration twins?) in glassy samples (Plate 6.30). Both groundmass and phenocryst leucite are commonly rimmed by groundmass apatite.

Clinopyroxene (diopside), ubiquitous in HKS samples, occurs as both a phenocryst and groundmass phases. Most diopside phenocrysts are euhedral, concentrically zoned, and green-brown in plane-polarized light, but a few samples also contain anhedral, highly fractured diopside. Phenocrysts are up to 3 mm in diameter, and are usually second to leucite in abundance.

Plagioclase is the only feldspar present in the HKS series. Phenocryst and groundmass plagioclase commonly show sieve textures and concentric zoning. Groundmass plagioclase is generally euhedral and may be weakly aligned in a trachytic texture (Plate 6.31). Several samples are cryptocrystalline and contain microscopic, skeletal plagioclase.

Phlogopite, olivine, and nepheline are less common in the HKS series of Roccamonfina, and were only observed in some samples. Phlogopite is usually present

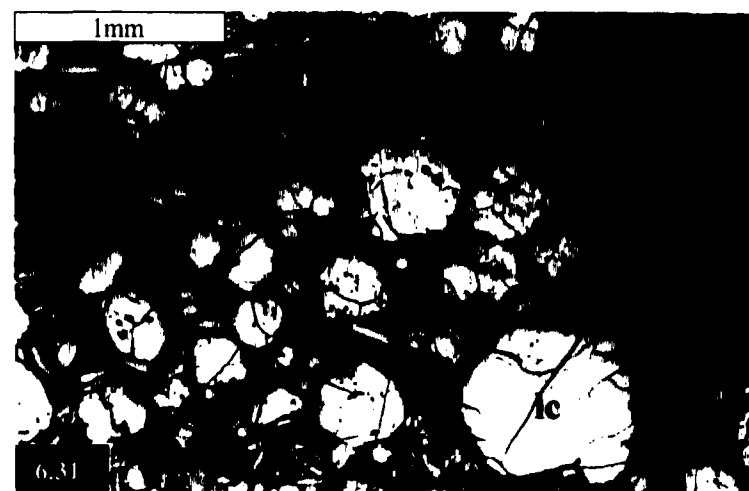
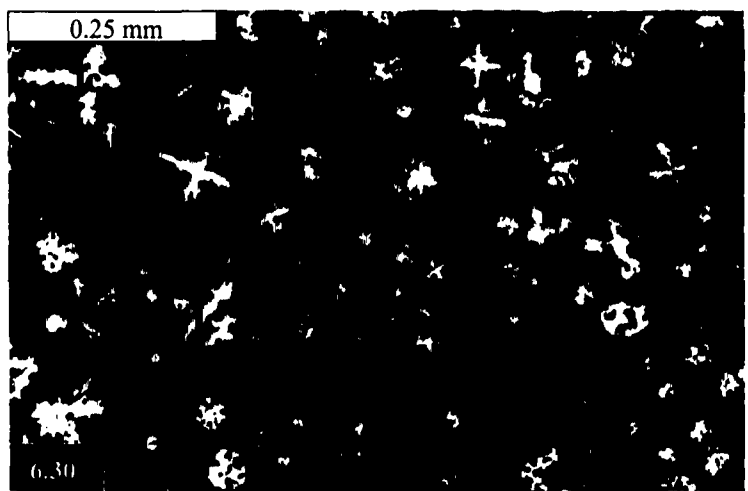
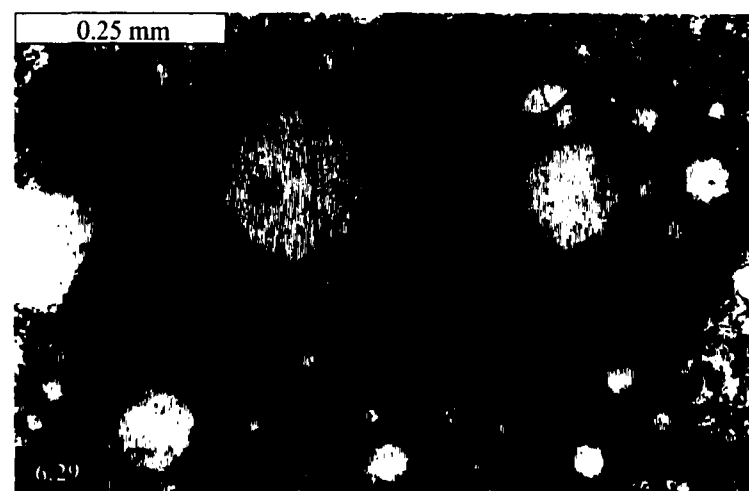


Plate 6.28. Euhedral-subhedral leucite and zoned clinopyroxene phenocrysts in a leucite-dominated groundmass; HKS sample RC100.
Plate 6.29. Leucite and plagioclase groundmass of HKS sample RC 113.
Plate 6.30. Cross-shaped and star-shaped leucite crystals in a glassy groundmass; HKS sample RC 117.
Plate 6.31. Weak alignment of small euhedral plagioclase; HKS sample RC123.

as small (<0.5 mm), euhedral to subhedral crystals with black rims. Olivine is also present as euhedral to subhedral groundmass crystals and as anhedral zoned phenocrysts. Rare groundmass nepheline was identified using the electron microprobe.

6.2c Ernici

Volcanic rocks collected from Ernici contain minerals similar to those from Roccamonfina, but are generally finer-grained (see Appendix D for individual mineralogical and textural descriptions). Similar to Roccamonfina, the samples from Ernici can be separated into two main petrographic groups: a) leucite-absent and b) leucite-bearing (also synonymous with the KS and HKS geochemical distinctions). The KS rocks at Ernici include basalt and potassic trachybasalt, while HKS rocks include tephrite and phonotephrite (based on the TAS classification). Many samples collected from Ernici have a high glass content (> 50 vol.%) and are highly vesicular. Vesicles are variable in shape (irregular to rounded), and reach up to 3-4 mm in diameter (Plate 6.32). Most of the glass is fresh, although some samples contain small amounts of devitrified glass. Table 6.3 is a summary of the minerals present in the two series at Ernici.

6.2c.i Potassic series (KS)

The KS series rocks at Ernici are dominated by clinopyroxene (diopside), olivine (forsterite), and calcic plagioclase feldspar (bytownite), all of which occur both as phenocrysts and groundmass phases. Although no alkali feldspar was found in the KS samples, it should be noted that Civetta et al. (1979) observed rare interstitial alkali feldspar in rocks of the KS series at Ernici. Diopside phenocrysts are commonly light

Series	Essential minerals	Accessory minerals
Potassic (KS)	clinopyroxene olivine plagioclase	+/- analcime +/- biotite apatite iron oxides
Ultrapotassic (HKS)	leucite clinopyroxene +/- olivine +/- nepheline +/- biotite	+/- amphibole +/- plagioclase +/- spinel apatite iron oxides

Table 6.3. Essential (≥ 5 vol.%) and accessory (< 5 vol.%) minerals of studied volcanic rocks from Ernici.

greenish- brown, euhedral to subhedral, and slightly zoned. Both reversely zoned crystals (Plate 6.34) and normally zoned crystals (Plate 6.35) are present. The co-existence of both types of zoned clinopyroxene has been found in other potassic rocks of central Italy, and has been explained as due to either variation in P, T and P_{H_2O} in the same magma (Dolfi and Triglia, 1978), or to magma mixing (Thompson, 1977; Brooks and Printzlau, 1978). Most diopside crystals are < 1.5 mm in size, but some reach 3-4 mm in several samples. Many diopside phenocrysts are fractured, and glomeroporphyritic textures are common. Groundmass diopside is generally light green, subhedral to anhedral, and abundant (up to 25 vol.% of the groundmass).

Olivine is euhedral to anhedral, can reach up to 3-4 mm in size (Plate 6.36), and commonly has red, oxidized rims. Olivine is present in all samples of the KS series, although it is always subordinate to clinopyroxene.

Plagioclase feldspar is abundant in the groundmass as euhedral laths, some of which show skeletal, swallow-tail textures. In some samples they form a slight trachytic texture, while in others are randomly orientated. Plagioclase is relatively uncommon as a phenocryst phase, but does occur as sparse euhedral to subhedral crystals (Plate 6.37).

Besides clinopyroxene, olivine, and plagioclase, several of the KS samples from Ernici contain a significant amount (up to 40 vol.%) of groundmass analcime. Samples ER 109 and ER 117, in particular, are analcime-rich. The analcime has the same shape and distribution as leucite in the HKS series, suggesting that the analcime may be pseudomorphed after leucite (Plate 6.38). Samples with abundant analcime also contain other hydrous minerals including micas (Plate 6.39). Phlogopite is present almost exclusively in these analcime-rich samples, where it forms both large, euhedral crystals

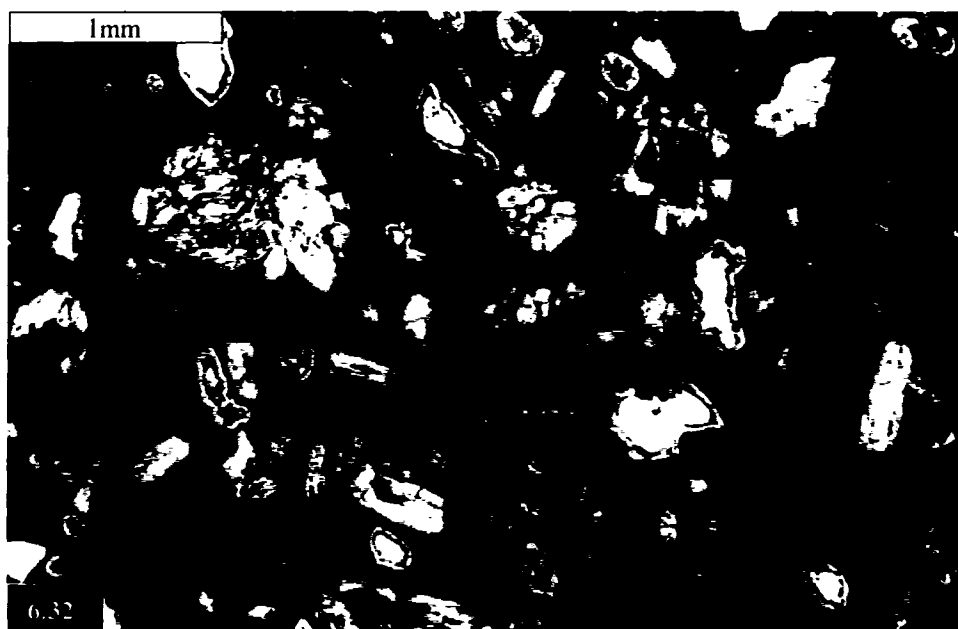


Plate 6.32. Glassy groundmass with irregular amygdules and euhedral to subhedral phenocrysts of diopside; KS sample ER 113.

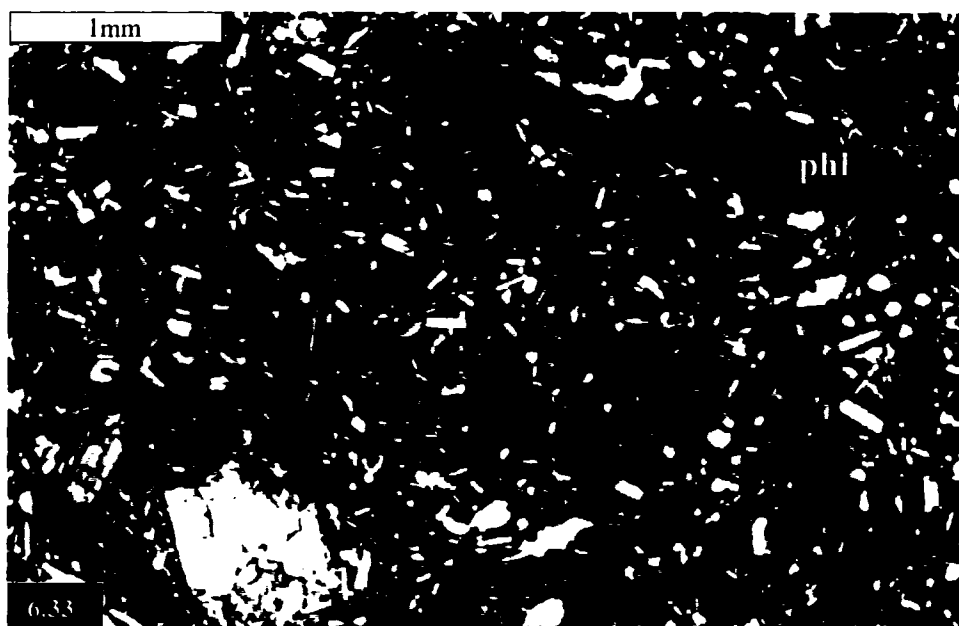
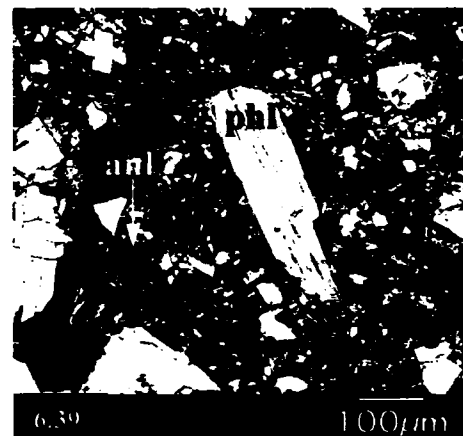
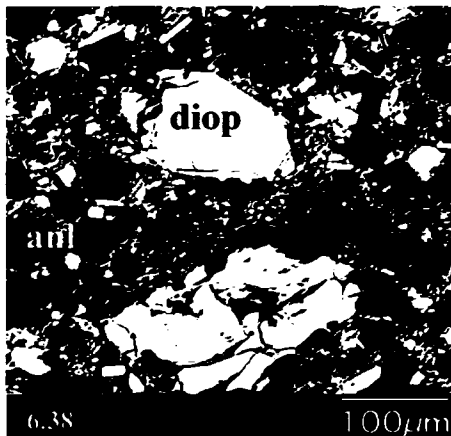
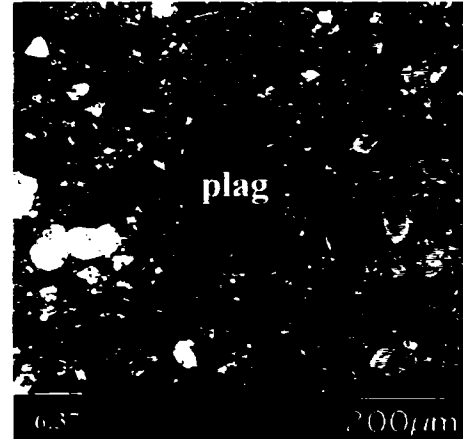
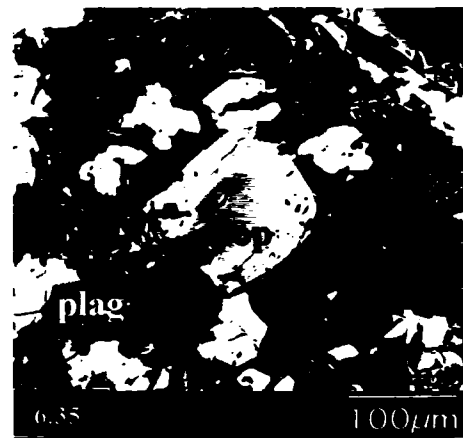
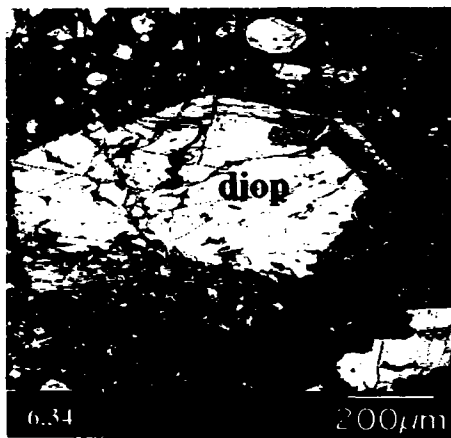


Plate 6.33. Analcime-rich KS sample ER 109 with phenocrysts of biotite and clinopyroxene in a groundmass of diopside, plagioclase feldspar, olivine, analcime and apatite.



BSE images of diopside, plagioclase, olivine, phlogopite, analcime in KS rocks, Ernici

Plate 6.34. Reversely zoned euhedral diopside phenocryst (109-9: core, 109-10: rim).

Plate 6.35. Normally zoned diopside (121-12: core, 121-13: rim) in a groundmass of plagioclase (121-15) and analcime (121-14).

Plate 6.36. Olivine phenocryst with Fe-rich rim (121-9: core, 121-10: rim).

Plate 6.37. Euhedral plagioclase (bytownite) phenocrysts (109-15).

Plate 6.38. Analcime-rich sample ER 117 with reversely zoned diopside (117-5: core, 117-6: rim), unzoned diopside, and groundmass plagioclase.

Plate 6.39. Analcime-rich sample ER 117 showing phlogopite phenocryst (117-8).

(0.5-1.1 cm in length) and, to a lesser extent, a groundmass phase (Plate 6.33). Although Civetta et al. (1979) observed rare nepheline in the groundmass of the Ernici KS series, no nepheline was found in these samples. Tabular groundmass apatite is very common in all members of the KS series.

6.2c.ii Ultrapotassic series (HKS)

Rocks from the HKS series at Ernici contain essential leucite and clinopyroxene (diopside), and variable amounts of amphibole, olivine, nepheline, phlogopite, and plagioclase feldspar. Unlike the HKS rocks of Roccamonfina, leucite from Ernici rarely forms large euhedral phenocrysts. Many samples from Ernici show a fine-grained, equigranular texture (< 0.1 mm) (Plate 6.40). Subhedral to anhedral leucite is commonly the most abundant groundmass mineral (25-60 vol.%), and is too small to be recognized in hand sample.

In most samples, clinopyroxene is the most abundant phenocryst phase. Diopside phenocrysts are commonly zoned with dark green pleochroic cores and pale green to light brown rims. Rounded cores and euhedral rims are typical. Civetta et al. (1981) noted large clinopyroxene up to 3-5 cm in diameter in HKS series rocks from Ernici, but none were found in this study. Plates 6.44 and 6.45 show diopside phenocrysts from sample ER 118. The diopside in Plate 6.44 has simple concentric zoning, while complex zoning is shown in Plate 6.45. Glomeroporphyritic clinopyroxene is characteristic of many samples, as are crystals with resorbed cores and intact rims.

Amphibole is present in some of the HKS samples, and occurs both in the groundmass and as a phenocryst phase. Amphibole makes up < 15 vol.% of the rock in

all samples, and is commonly strongly zoned with green-brown pleochroism. Both phenocryst and groundmass amphibole are anhedral and/or resorbed.

Olivine occurs in most HKS samples as phenocrysts and/or as a groundmass phase. Olivine phenocrysts constitute a very small per cent of the samples (up to 5 vol.%), and can reach up to 1 mm in diameter. Most are slightly fractured and variably resorbed with red reaction rims (Plate 6.41). Phenocrystic olivine is generally Mg-rich forsterite (Plate 6.46), while groundmass olivine is more Fe-rich (Plate 6.47).

Nepheline can occur as a groundmass phase and is generally sub-microscopic and anhedral. Phlogopite is found in only two samples from the HKS (ER 110 and ER 111). Rare altered phlogopite phenocrysts up to 3 mm in length are present only in sample ER 110 (Plate 6.42), while small (< 0.1 mm), fresh, anhedral groundmass crystals are found in small amounts (about 2-3 vol.%) in both ER 110 and ER 111.

Plagioclase feldspar is present as both microscopic groundmass laths and as extremely resorbed phenocrysts in a number of HKS samples from Ernici. Fresh plagioclase phenocrysts and potassium feldspar were not found. Interstitial alkali feldspar was observed in the HKS series by Civetta et al. (1979), but not in the present study. Several samples contain spinel (< 2 vol.%) that forms black groundmass crystals with red rims. In a similar fashion to the KS series, groundmass apatite and oxides are very common in the HKS series. Apatite is abundant as inclusions in leucite (Plate 6.43).

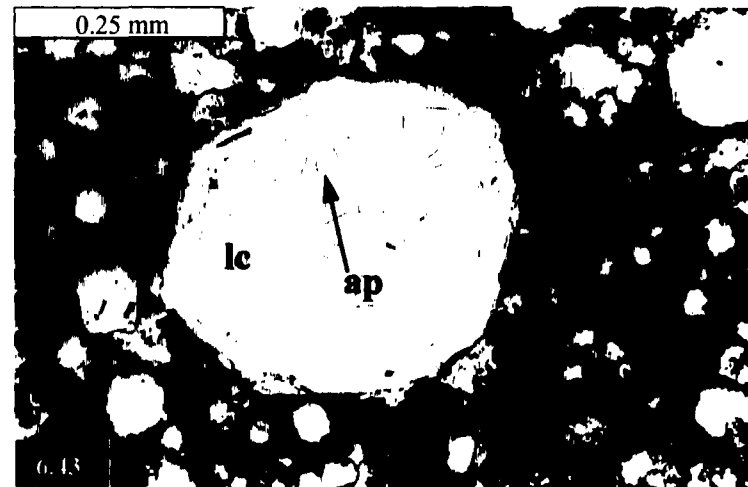
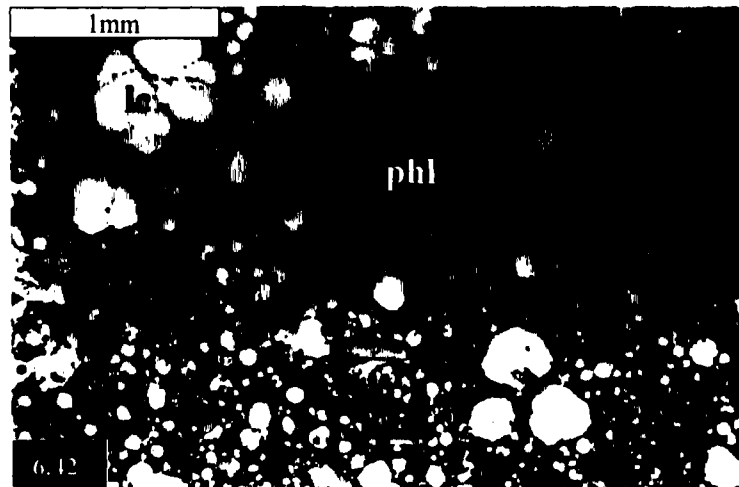
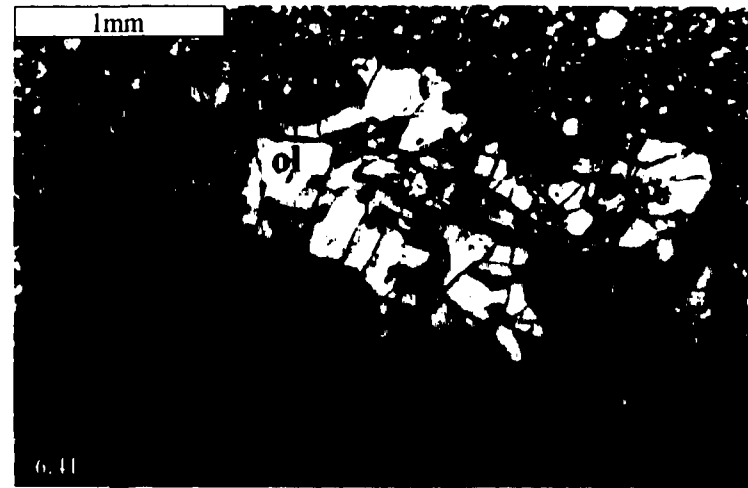
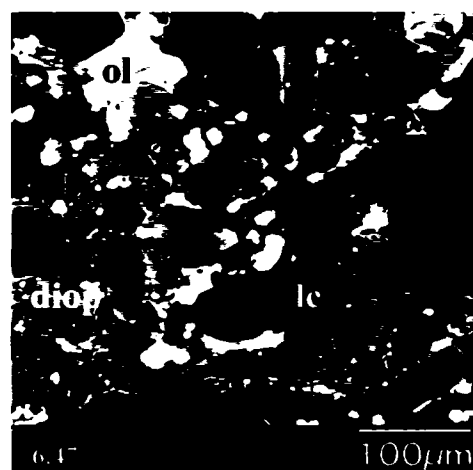
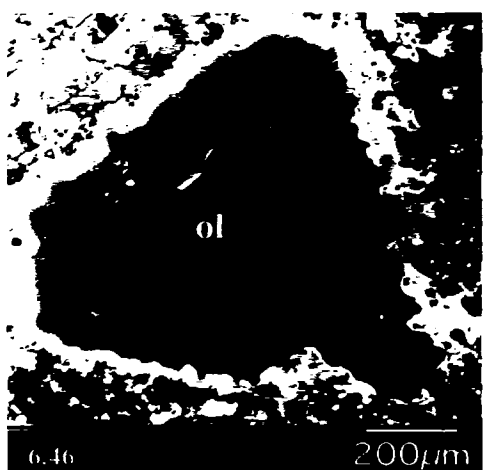
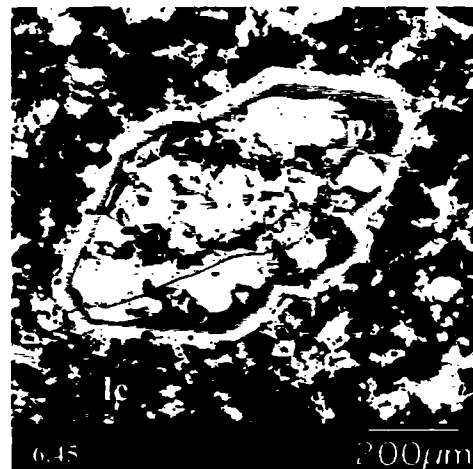
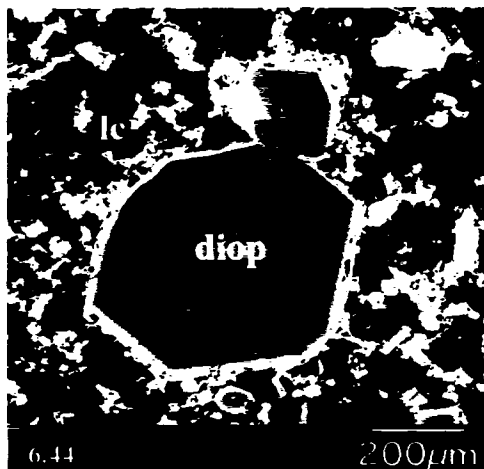


Plate 6.40. Equigranular texture of leucite and diopside typical of leucite-bearing samples from Ernici; HKS sample ER 105.

Plate 6.41. Partially resorbed olivine phenocryst with red reaction rim. Glassy groundmass with abundant small leucite crystals; HKS sample ER 118.

Plate 6.42. Large phlogopite and abundant euhedral to subhedral leucite phenocrysts; HKS sample ER 110.

Plate 6.43. Close-up view of HKS sample ER 110 showing leucite phenocryst with acicular inclusions of apatite.



BSE images of diopside, leucite, olivine in HKS rocks, Ernici

Plate 6.44. Euhedral, normally zoned diopside phenocryst (118-12: core, 118-13: rim) in a groundmass of leucite and diopside.

Plate 6.45. Complex irregular zoning in diopside phenocryst (118-14: core, 118-15: dark zone, 118-16: rim).

Plate 6.46. Partially resorbed olivine (forsterite) phenocryst (104-12).

Plate 6.47. Groundmass olivine (fayalite) (118-6: core, 118-7: rim), diopside (118-4: core, 118-5: rim), leucite (118-8), and Fe-oxides.

6.3 Mineral chemistry

6.3a Calculation of mineral formulae

The major element chemistry of silicate phases including olivine, pyroxene, amphibole, mica, feldspar, and feldspathoid (nepheline and leucite), were determined for selected samples from the Western Alps, Roccamonfina, and Ernici. Data for microprobe analyses can be found in Appendix E, where b.d. = below detection limit. The general chemical formula and naming procedure for each type of mineral are as follows:

6.3a.i Olivine

Olivine formulae are calculated on the basis of 4 oxygen anions and are expressed in terms of the end member compositions Mg_2SiO_4 (forsterite; Fo) and Fe_2SiO_4 (fayalite; Fa). All olivine analyses are given in terms of magnesium number, where $\text{Mg\#} = 100\text{Mg}/(\text{Mg}+\text{Fe}^{2+})$, and the notation $\text{Fo}_{\text{Mg\#}}$ will be used.

6.3a.ii Pyroxene

The general chemical formula for all pyroxenes is $\text{M}_2\text{M}_1\text{T}_2\text{O}_6$, where M2 refers to cations in a generally distorted cubic coordination (Mg^{2+} , Fe^{2+} , Mn^{2+} , Li^+ , Ca^{2+} , Na^+), M1 to cations in a regular octahedral coordination (Al^{3+} , Fe^{3+} , Ti^{4+} , Cr^{3+} , V^{3+} , Ti^{3+} , Zr^{4+} , Sc^{3+} , Zn^{2+} , Mg^{2+} , Fe^{2+} , Mn^{2+}), and T to tetrahedrally coordinated cations (Si^{4+} , Al^{3+} , Fe^{3+}). Pyroxene formulas in the present study were calculated from major element chemical compositions using the program FORMULA by T.S. Ercit, and valence states for Fe were determined by normalizing the anion sum to 6 and the cation sum to 4. FeO^* and Fe_2O_3^* in Appendix E indicate calculated values.

Naming of the pyroxenes follows the International Mineralogical Association (IMA) classification scheme of Morimoto et al. (1989), who recommend division into four chemical groups: Ca-Mg-Fe pyroxenes, Na-Ca pyroxenes, Na pyroxenes, and Other pyroxenes. In this procedure, the pyroxenes are classified using the total number of specified cations at the M (M1 and M2) sites on the basis of 6 oxygen atoms. The M1 and M2 sites are considered together as M sites, without considering the preference of atoms between the two sites. In order to determine the chemical group of a pyroxene, the numbers of Ca, Mg, Fe²⁺ and Na cations in the M sites are plotted on a Q-J diagram where $Q = \text{Ca} + \text{Mg} + \text{Fe}^{2+}$ and $J = 2\text{Na}$.

All pyroxenes from the Western Alps, Roccamonfina, and Ernici are Ca-Mg-Fe pyroxenes, which form a wide range of solid solutions in the quadrilateral system $\text{Mg}_2\text{Si}_2\text{O}_6$ (enstatite) – $\text{Fe}_2^{2+}\text{Si}_2\text{O}_6$ (ferrosilite) – $\text{CaMgSi}_2\text{O}_6$ (diopside) – $\text{CaFe}^{2+}\text{Si}_2\text{O}_6$ (hedenbergite). The Ca-Mg-Fe pyroxenes are defined on the basis of symmetry and relative amounts of $\text{Ca}_2\text{Si}_2\text{O}_6$ (wollastonite), enstatite, and ferrosilite end members, where the composition is normalized to $\text{Ca} + \text{Mg} + \sum\text{Fe} = 100$ with $\sum\text{Fe} = \text{Fe}^{2+} + \text{Fe}^{3+} + \text{Mn}^{2+}$. Mg#s for pyroxenes in this study are calculated as $100\text{Mg}/(\text{Mg} + \text{Fe}^{2+} + \text{Fe}^{3+} + \text{Mn})$ (Deer et al., 1992). Chemical substitutions in the analyzed pyroxenes will be discussed on an individual basis in the following sections, and adjectival modifiers used for pyroxene names follow recommendations by the IMA (Morimoto et al., 1989).

6.3a.iii Amphibole

The standard amphibole formula is $\text{AB}_2^{\text{vi}}\text{C}_5^{\text{iv}}\text{T}_8\text{O}_{22}(\text{OH})_2$, where A is usually a monovalent cation (Na, K, or a vacancy□), B contains two octahedral cations (Na, Ca,

Mg, Fe²⁺, Mn²⁺, Li, Zn, Ni, Co), C is a composite of five octahedral cation sites (Mg, Fe²⁺, Mn²⁺, Li, Zn, Ni, Co, Al, Fe³⁺, Mn³⁺, Cr³⁺, Ti⁴⁺, Zr⁴⁺), T corresponds to eight tetrahedrally coordinated sites (Si, Al, Ti⁴⁺), and the anion sites can include F, Cl, OH, and/or O (Leake et al., 1997). The amphibole formulae in this study are calculated on the basis of 24(O, OH, F, Cl) as recommended by Leake et al. (1997). H₂O* concentrations calculated by stoichiometry assuming 2(OH, F, Cl). The procedure adopted to divide the Fe into Fe³⁺ and Fe²⁺ can influence the resulting name, especially if a composition is near Mg/(Mg + Fe²⁺) = 0.50 or Fe³⁺/(Fe³⁺ + ^{vi}Al) = 0.50. The IMA recommends adjusting the sum (Si + Al + Cr + Ti + Fe + Mg + Mn) to 13 by varying the Fe³⁺ and Fe²⁺ appropriately (Leake et al., 1997). The program FORMULA by T.S. Ercit was used in this study to calculate Fe³⁺/Fe²⁺ ratios, although it is noted that any calculation of Fe³⁺ and Fe²⁺ is subject to considerable uncertainty.

Following Leake et al. (1997), amphiboles are classified into four groups on the basis of B site occupancy: 1) magnesium-iron-manganese-lithium amphiboles, 2) calcic amphiboles, 3) sodic-calcic amphiboles, and 4) sodic amphiboles. The Mg-Fe-Mn-Li amphiboles possess (Ca + Na)_B < 1.00 atoms per formula unit and (Mg,Fe,Mn,Li)_B ≥ 1.00 in the standard formula. The calcic amphiboles are defined as those in which (Ca + Na)_B ≥ 1.00, and Na_B < 0.50; usually Ca_B ≥ 1.50. Sodic-calcic amphiboles have (Ca + Na)_B ≥ 1.00 and 0.50 < Na_B < 1.50, and sodic amphiboles have Na_B ≥ 1.50.

Within these groups, the amphiboles are divided into individually named species based on heterovalent substitutions: Si⁴⁺ = ^{iv}Al³⁺, □ = (Na,K)⁺_A, Ca²⁺_B = Na⁺_B, O²⁻ = (OH,F,Cl)⁻, etc. Homovalent substitutions also occur within the species, most commonly Mg²⁺ = Fe²⁺, ^{vi}Al³⁺ = Fe³⁺, and OH⁻ = F⁻. In amphibole nomenclature, prefixes are an

essential part of the mineral name, whereas modifiers indicate a compositional variant, and are optional in naming. Modifiers generally represent subsidiary substitutions, and prefixes denote major substitutions (see IMA nomenclature; Leake et al., 1997).

6.3a.iv Mica

Micas are phyllosilicates with the general formula $IM_{2-3}\square_{1-0}T_4O_{10}A_2$, where I is an interlayer cation in 12-fold coordination (Cs, K, Na, NH₄, Rb, Ba, Ca), M are octahedral cations (Li, Fe, Mg, Mn, Zn, Al, Cr, V, Ti), \square represents a vacancy, T are tetrahedral cations (Be, Al, B, Fe³⁺, Si), and A are anions (Cl, F, OH, O, S) (Rieder et al., 1998). Most mica compositions in this study fall between the biotite end-members $KFe^{2+}_3AlSi_3O_{10}(OH)_2$ (annite) and $KMg_3AlSi_3O_{10}(OH)_2$ (phlogopite). In members of this series, the octahedral (M) sites are ideally completely filled, but many analyses show that some vacancies occur and that M can range from 3 down to about 2.65 (Deer et al., 1992). The IMA states that optional modifying terms may be used to express chemical deviation from end member compositions if the element in question exceeds 10%, but not 50%, of the real occupancy of the position (Rieder et al., 1998).

6.3a.v Feldspar

Feldspar analyses in this study are recalculated on the basis of 16 oxygen atoms (equivalent to one half of the unit cell). Analyses are stated in terms of the molecular percentage of $NaAlSi_3O_8$ (albite; Ab), $KAlSi_3O_8$ (K-feldspar; Or), and $CaAl_2Si_2O_8$ (anorthite; An). No data on Al-Si site ordering in feldspars was collected in this study; classification will therefore be made on the basis of morphology and mineral chemistry.

6.3a.vi Feldspathoids

The formula of most nepheline is close to $\text{Na}_3(\text{K},\text{Na})\text{Al}_4\text{Si}_4\text{O}_{16}$, a composition regarded as a distinct ordered intermediate compound in the binary $\text{NaAlSiO}_4 - \text{KAlSiO}_4$ system, where KAlSiO_4 is kalsilite. Rossi et al. (1989) noted that the 'ideal' nepheline composition with $\text{K}:\text{Na} = 1:3$ is not found in nature, and substitution of Ca^{2+} for K^+ (or Na^+) can lead to vacancies at the (K,Na) site to maintain charge balance. Almost all natural nepheline contains more Si and less Al than is represented by the ideal formula; however, the sum of the Si and Al atoms is usually still close to the ideal cell content of 16 (Deer et al., 2004). The excess SiO_2 is shown in nepheline analyses by calculating the normative percentages of the sodium molecule (NaAlSiO_4 , Ne), the potassium molecule (KAlSiO_4 , Ks) and SiO_2 (Q).

Leucite has the chemical formula KAlSi_2O_6 and a crystal structure based on an (Si,Al)-O framework similar to that of analcime, $\text{NaAlSi}_2\text{O}_6 \cdot \text{H}_2\text{O}$. In fact, leucite readily converts to analcime at low temperatures in hydrous systems by the reaction $\text{KAlSi}_2\text{O}_6 + \text{Na}^+_{\text{aq}} + \text{H}_2\text{O} \leftrightarrow \text{NaAlSi}_2\text{O}_6 \cdot \text{H}_2\text{O} + \text{K}^+_{\text{aq}}$. At high temperature ($> 625^\circ\text{C}$), leucite has a cubic structure with large rings of (Si,Al) O_4 tetrahedra filled by K ions (H_2O molecules fill similar cavities in analcime). At low temperature, the K ions are probably too small to fill the tetrahedral rings, and the resultant collapse of the (Si,Al)-O framework can be correlated with a change to tetragonal symmetry. The compositions of pure leucite do not differ significantly from the ideal formula. The Si:Al ratio is approximately 2:1 and the replacement of K by Na rarely exceeds 10 wt% (Deer et al., 2004). Small amounts of ferric iron are present in most leucite, commonly <1.0 wt% Fe_2O_3 .

6.3b Western Alps

6.3b.i Olivine

No olivine was found in any sample from the Western Alps. Samples WA107 (spessartite) and WA 104 (minette) contain ovoid areas of talc that may represent olivine replacement. Talc can form through the low-grade metamorphism and hydrothermal alteration of mafic rocks, and is favoured by high $a\text{SiO}_2$ and relatively low Al and Ca. There are no remnants of original olivine phenocrysts in samples from the Western Alps.

6.3b.ii Pyroxene

None of the samples from the Western Alps contain orthopyroxene, and only the minettes contain clinopyroxene. All analyzed clinopyroxene plot in the ternary system $\text{Ca}_2\text{Si}_2\text{O}_6$ (Wo) – $\text{Mg}_2\text{Si}_2\text{O}_6$ (En) – $\text{Fe}_2\text{Si}_2\text{O}_6$ (Fs) (Figure 6.1). All of the clinopyroxene contain atomic Mg > atomic Fe^{2+} , and most contain 45 - 50 per cent of the $\text{Ca}_2\text{Si}_2\text{O}_6$ (Wo) component. The clinopyroxene cover a fairly small range of compositions from augite to diopside. Almost all of the clinopyroxene is low Al-Ti diopside, typical of minettes (Rock, 1991). Although several samples contain diopside that is ferrian ($\text{Fe}^{3+} > 0.10$ apfu) and/or aluminian ($\text{Al}^{3+} > 0.10$ apfu), some clinopyroxene have insufficient Si + Al to fill the tetrahedral sites. These clinopyroxene must contain small amounts of ${}^{\text{iv}}\text{Fe}^{3+}$, similar to clinopyroxene from lamproites (Mitchell and Bergman, 1991).

Clinopyroxene phenocrysts can be unzoned and zoned within the same sample, and most zoning is normal with Mg-rich cores and Mg-poor rims. The decrease in Mg content towards the crystal rim is balanced by an increase in Fe content, and accompanied by a decrease in SiO_2 and increase in Al_2O_3 . In normally zoned

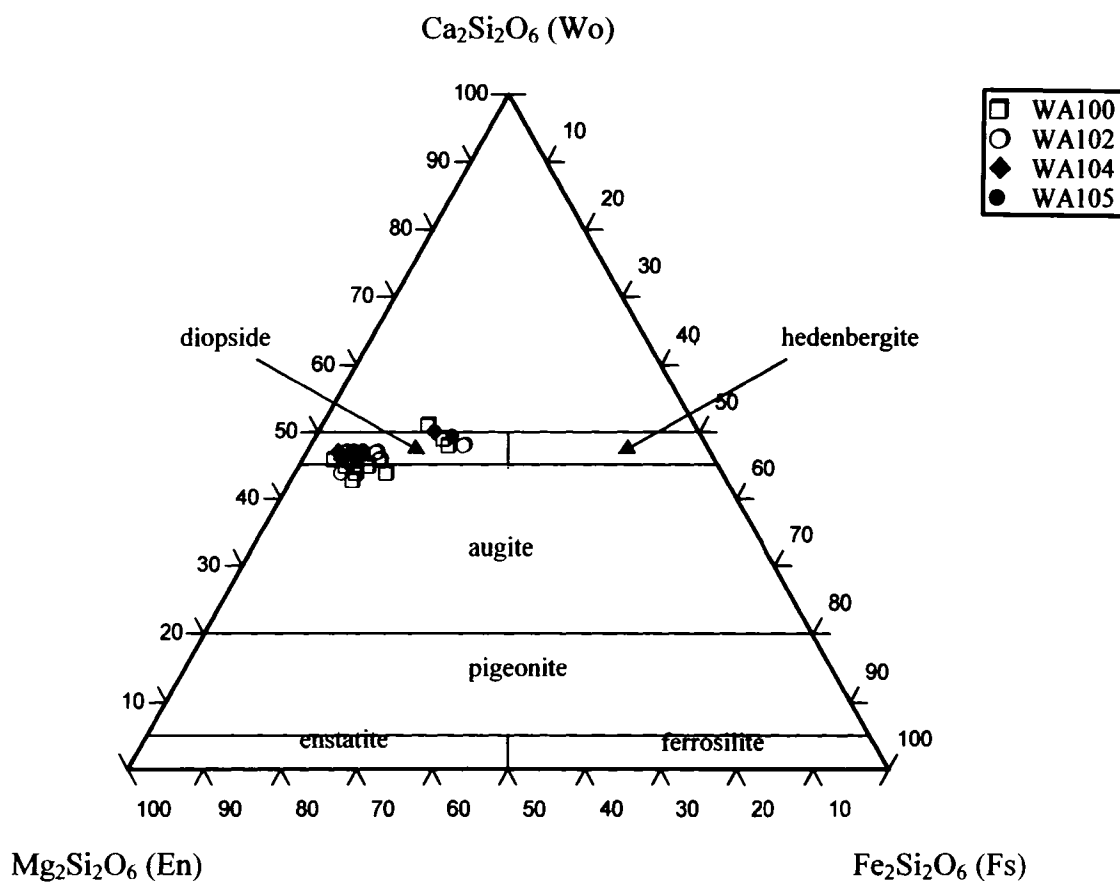


Figure 6.1. Ternary Ca₂Si₂O₆ (Wo) – Mg₂Si₂O₆ (En) – Fe₂Si₂O₆ (Fs) diagram for clinopyroxene from Western Alpine minettes.

phenocrysts, MnO, Na₂O, and TiO₂ increase towards the rim, while CaO and Cr₂O₃ show no change. The presence of reversely zoned clinopyroxene could be explained by the concomitant crystallization of magnetite under oxidizing conditions, which would lower the melt content of both Fe³⁺ and Fe²⁺ and allow Mg-rich compositions to crystallize after Fe-rich compositions. Alternatively, reversely zoned clinopyroxene may be a result of magma mixing, whereby chemical disequilibrium promotes partial resorption of Fe-rich phenocrysts and new growth of Mg-rich rims. Experimental studies have also demonstrated that changing P_{H₂O} also affects clinopyroxene composition (Dolfi and Trigila, 1983). A decrease in P_{H₂O} results in a decrease of Fe³⁺ and Al in the tetrahedral site and a correspondent increase of Mg and Si. Clinopyroxene from the samples from the Western Alps display weakly negative correlations between Mg and ^{iv}Al, suggesting that P_{H₂O}-related compositional variation may account for some of the reverse zoning.

6.3b.iii Amphibole

Amphibole is present in all the studied spessartites from the Western Alps, as well as minette WA 104. Amphibole from the spessartites fall into the calcic amphibole group, where $(Ca+Na)_B \geq 1.00$ and $Na_B < 0.50$. Calcic amphiboles are by far the most common type present in world-wide spessartites, and can be classified using two diagrams (Figures 6.2 and 6.3). Figure 6.2 refers to calcic amphiboles with $(Na+K)_A \geq 0.50$ and $Ti < 0.50$, whereas Figure 6.3 refers to those with $(Na+K)_A < 0.50$ and $Ca_A < 0.50$. Most analyses fall into the magnesiohastingsite (^{vi}Al < Fe³⁺) field in Figure 6.2 and into the actinolite and magnesiohornblende – tschermakite fields in Figure 6.3. Two data points on Figure 6.2 have higher Si than magnesiohastingsite and are classified edenite.

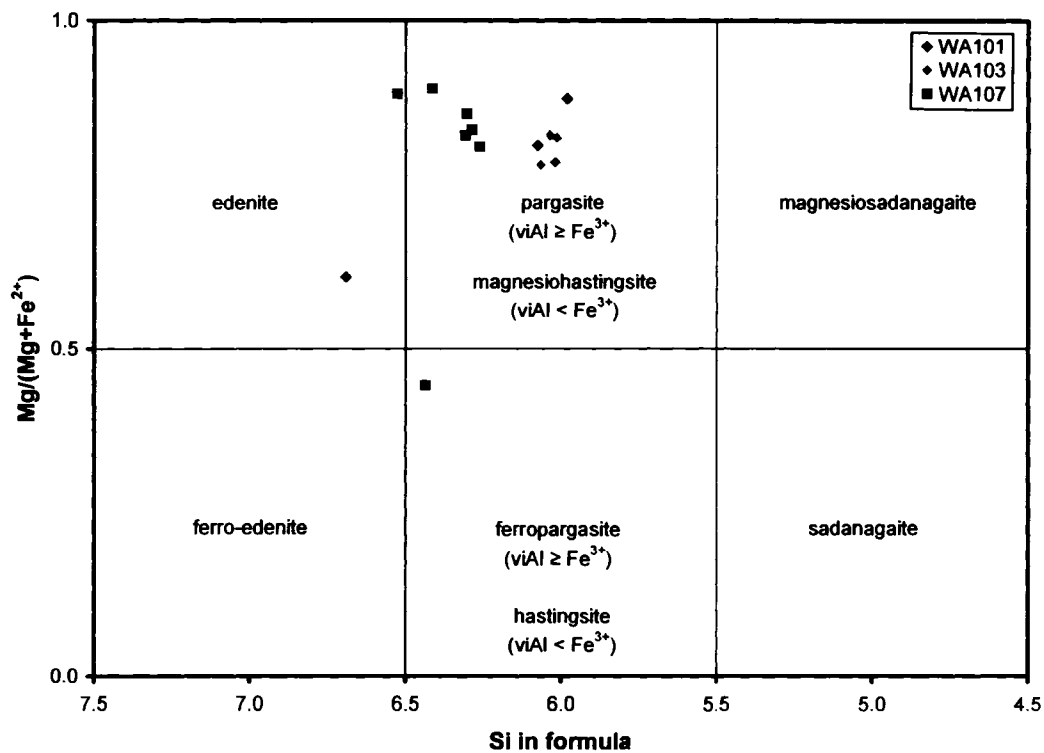


Figure 6.2. Calcic amphibole classification for parameters $Ca_B \geq 1.50$; $(Na+K)_A \geq 0.50$; $Ti < 0.50$. Data from spessartites WA 101, WA 103, and WA 107.

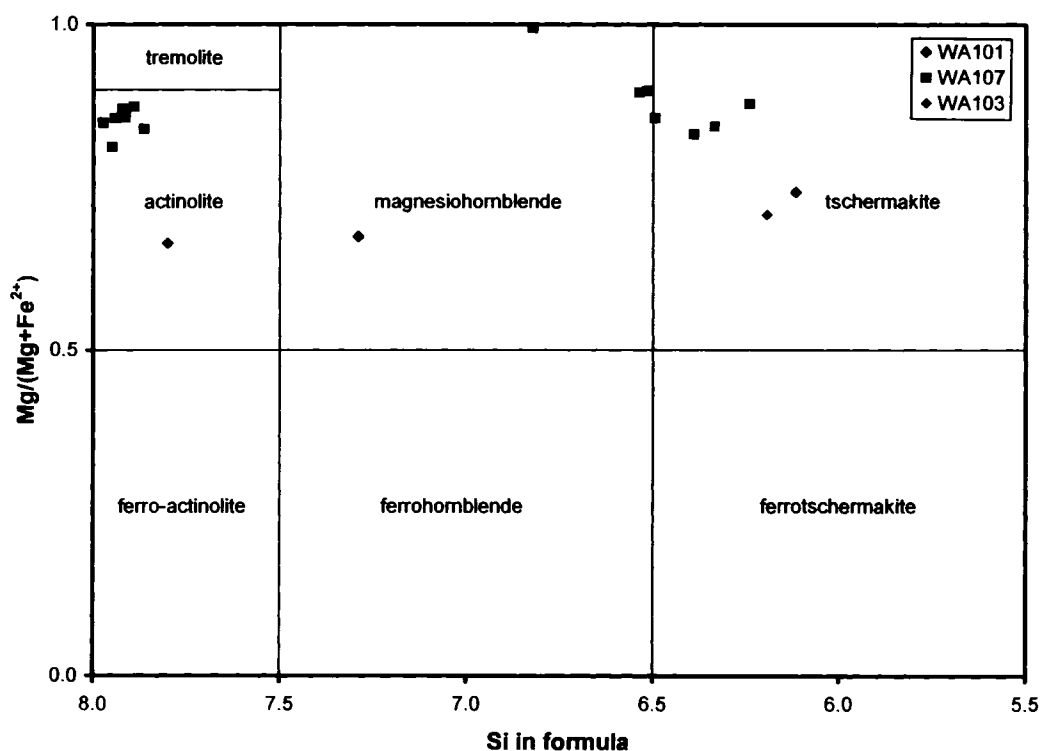


Figure 6.3. Calcic amphibole classification for parameters $Ca_B \geq 1.50$; $(Na+K)_A < 0.50$; $Ca_A < 0.50$. Data from spessartites WA 101, WA 103, and WA 107.

Almost all the actinolite analyses on Figure 6.3 are from sample WA 107.

The actinolite in sample WA 107 is probably an alteration mineral derived from the interaction of water with earlier-formed pyroxene or less silicic amphibole such as magnesiohornblende or tschermakite. All of the spessartites contain amphibole of tschermakite composition, in which Al^{3+} substitutes for Si^{4+} in the T site coupled with Al^{3+} for Mg^{2+} and Fe^{2+} in the C or B sites. A compilation of lamprophyre amphibole analyses by Rock (1991) shows that tschermakitic amphibole is virtually confined to minettes and spessartites, and is absent in other alkaline rock types such as kimberlite and lamproite. Many of the magnesiohastingsites are titanian (up to 2.76 wt%) and several of the tschermakites are titanian and/or ferrian. The one ferropargasite analysis from sample WA 107 contains 1.68 wt% K_2O (0.33 apfu) and therefore qualifies as potassian.

The chemistry of amphibole from minette WA 104 is very different from those of the spessartites. Amphibole from sample WA 104 fall into the sodic-calcic group, where $(\text{Ca}+\text{Na})_{\text{B}} \geq 1.00$ and $0.50 \leq \text{Na}_{\text{B}} < 1.50$. These amphibole have $(\text{Na}+\text{K})_{\text{A}} \geq 0.50$ and are high in silica (> 7.5 apfu). On Figure 6.4, amphibole from sample WA 104 plot as richterite and ferrichterite. These amphiboles are potassian or potassic (K_2O ranges from 1.92 wt% to 2.52 wt%) and most are titanian (TiO_2 ranges from 2.12 wt% to 3.33 wt%). Titanian potassian richterite is considered diagnostic of lamproites (Rock, 1991). The richterite and ferrichterite are relatively rich in F (up to 0.34 apfu), while the calcic amphiboles generally contain < 0.10 apfu. Substitution on F for (OH) in sodic-calcic amphiboles is not uncommon (Deer et al., 1997).

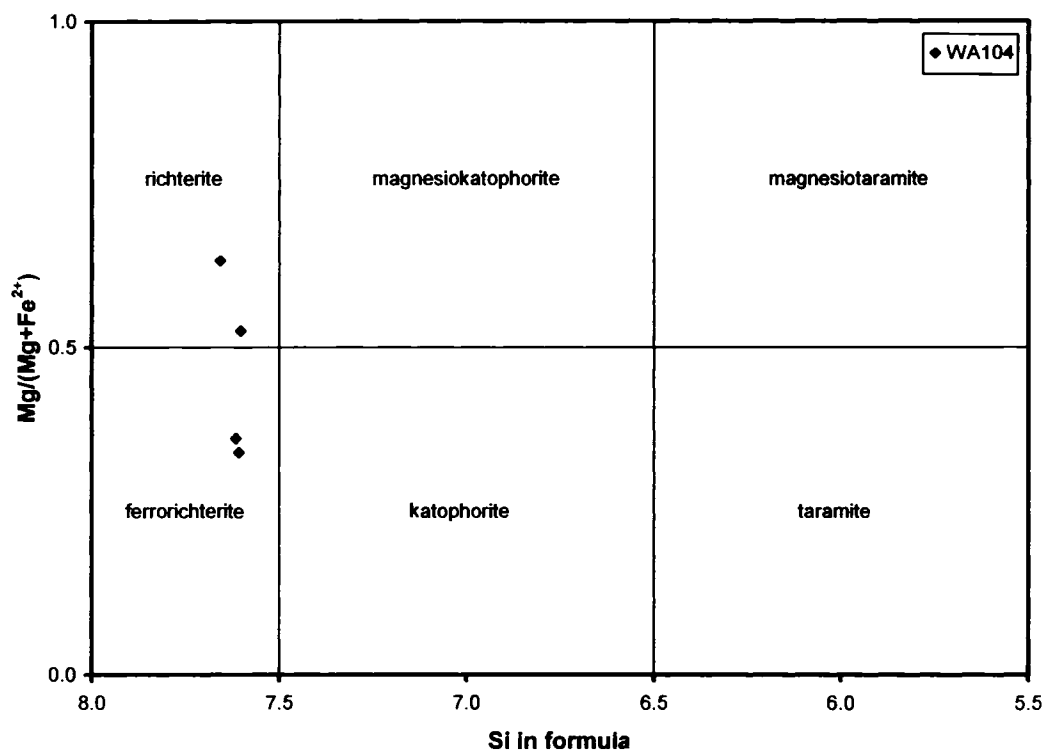


Figure 6.4. Sodic-calcic amphibole classification for parameters $(\text{Na}+\text{K})_{\text{A}} \geq 0.50$; $(\text{Ca}+\text{Na})_{\text{B}} \geq 1.00$; $0.50 < \text{Na}_{\text{B}} < 1.50$. Data from minette WA 104.

6.3b.iv Mica

Mica is present in all of the minette samples from the Western Alps as well as in the kersantite and two of the spessartites. The dominant mica in the minettes is phlogopite, where the distinction between phlogopite and annite is at the 50:50 Fe:Mg division ($\text{Fe} = \text{Fe}^{2+} + \text{Fe}^{3+}$) (Rieder et al., 1998). The phlogopite shows appreciable substitution of Al for (Mg,Fe) balanced by Al for Si in the tetrahedral site (Tschermak's substitution), leading towards $\text{KFe}^{2+}_2\text{AlAl}_2\text{Si}_2\text{O}_{10}(\text{OH})_2$ (siderophyllite) if Fe-rich and $\text{KMg}_2\text{AlAl}_2\text{Si}_2\text{O}_{10}(\text{OH})_2$ (eastonite) if Mg-rich. The majority of the phlogopite analyses contain $\text{Al}_2\text{O}_3 \approx 13\text{-}16$ wt%, typical for lamprophyres (Rock, 1991). Although experimental work has shown that substitution of Al in the T site is favoured by high temperature crystallization conditions (Deer et al., 1992), other factors such as $a\text{SiO}_2$ and oxidation conditions also influence Al site distribution. Phlogopite from the Western Alps minettes is commonly Ti-rich, and the average value for all analyses is 3.73 wt% TiO_2 (0.42 apfu Ti). Titanium occurs in octahedral sites, usually in place of Al, and is balanced by either Al for Si in the T site or M site vacancies. Several phlogopite analyses from minettes of the Western Alps contain moderately high F (> 0.50 apfu).

The phlogopite phenocrysts in the minettes are commonly zoned with Mg-rich, Si-rich cores and Fe-rich, Al-rich rims. Zoning is also found for Ti, Cr, F, and Ba, but is variable between minette samples. In general, phenocryst cores and megacrysts contain more Ba and more F than rim and groundmass phlogopite. Manganese does not exceed 0.10 apfu. One minette (WA 104) contains megacrysts of annite that are strongly zoned with respect to Ba (core = 1.86 wt%; rim = 0.37 wt%). The annite from sample WA 104 is the only mica of this composition to be analyzed in samples from the Western Alps.

The occurrence of annite adjacent to very Mg-rich phlogopite in sample WA 104 suggests that the annite could be xenocrystic.

The kersantite sample (WA 106) contains phlogopite which is similar in composition to that from the minettes. Average TiO_2 contents are high (average 2.22 wt%; 0.24 apfu), but not as high as seen in phlogopite from the minettes. Al_2O_3 contents are also slightly lower in the phlogopite from the kersantite. Most of the phlogopite in the kersantite is zoned with cores rich in Mg, Cr, K, Na, and F, and rims rich in Ti and Ba. F contents range between 0.15 and 0.36 apfu.

Phlogopite is absent in the spessartites. Small amounts of muscovite, however, are located in heavily altered areas in association with chlorite, epidote and albite. The muscovite probably crystallized by the leaching of K, Al, and Si from feldspars at sub-liquidus temperatures (Deer et al., 1992). Muscovite is absent in the minettes and kersantite.

6.3b.v Feldspar

Minettes from the Western Alps contain both potassic and sodic feldspar (Figure 6.5). The K-feldspar is likely orthoclase, and ranges from Or_{89} to Or_{98} . The Na-feldspar in the minettes ranges from Ab_{89} to Ab_{98} , and can be considered nearly pure albite. No plagioclase more calcic than oligoclase is present in the minettes. BaO contents in several orthoclase analyses exceed 1.00 wt%. Fe_{total} is commonly < 0.30 wt%, but can reach as high as 1.39 wt% in sample WA 104. The feldspars from minettes appear to be alkali feldspars that are completely unmixed at a sub-microscopic scale (no perthitic texture noted with SEM). Alternatively, the Na-rich feldspars were originally Ca-rich

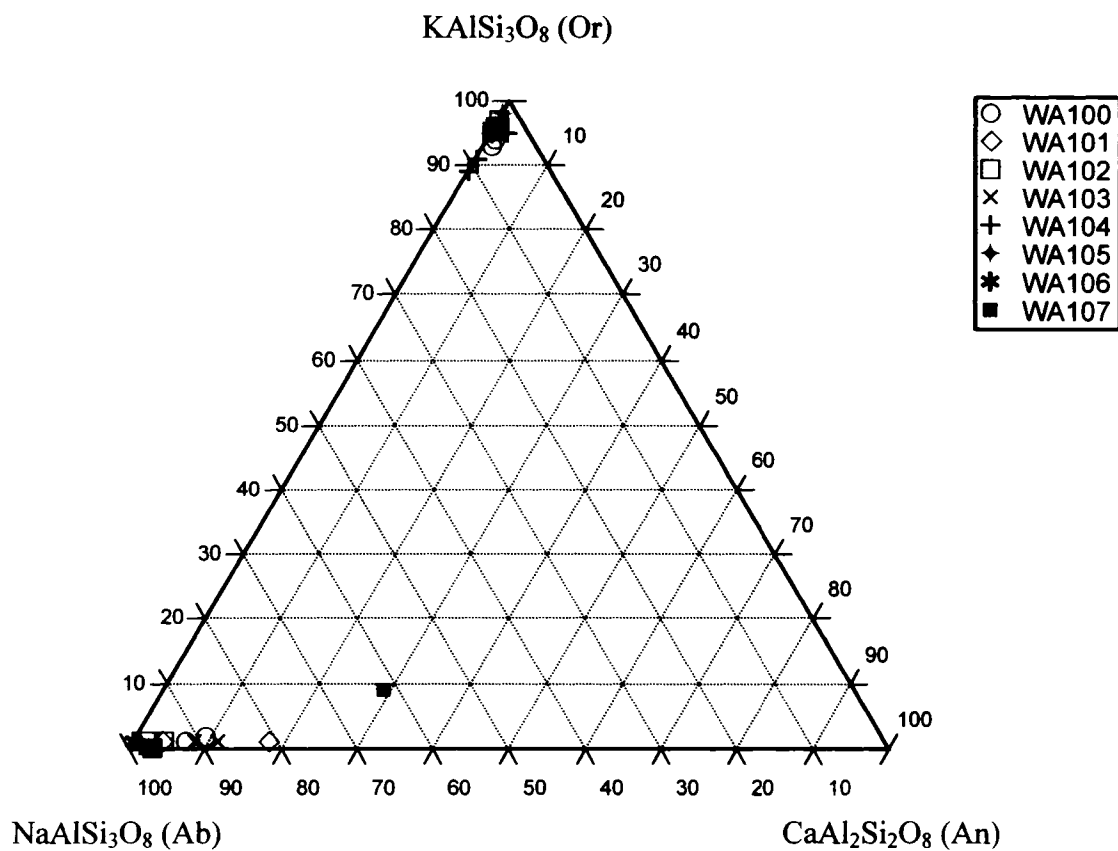


Figure 6.5. Ternary KAlSi_3O_8 (Or) – $\text{NaAlSi}_3\text{O}_8$ (Ab) – $\text{CaAl}_2\text{Si}_2\text{O}_8$ (An) diagram for feldspars from lamprophyres from the Western Alps.

feldspars that become albitized in the presence of a Na-rich fluid phase.

The spessartites from the Western Alps also contain both K- and Na-rich feldspars. The K-rich feldspar averages Or₉₅, while plagioclase ranges from Ab₈₂ to Ab₉₈. Oligoclase in the spessartites extends to slightly more calcic compositions compared to those from the minettes. BaO and Fe_{total} concentrations are similar to those of the minettes. One spessartite, WA 107, contains andesine. The kersantite contains only pure Na-rich feldspar with a composition of Or₁An₀Ab₉₉. This extremely sodic albite contains an average of 0.16 wt% K₂O, 0.02 wt% CaO, and 11.82 wt% Na₂O.

6.3b.vi Feldspathoid

No feldspathoids were found in any of the samples from the Western Alps.

6.3b.vii Summary of mineral chemistry

The main chemical features of major silicate minerals from the lamprophyres from the Western Alps are summarized in Table 6.4. The three types of lamprophyres are characterized by distinct mineral assemblages and mineral chemistry. Olivine and feldspathoid minerals were not found in any of the lamprophyres, and low Al-Ti clinopyroxene is only present in the minettes. Amphiboles are absent in the kersantite, and are very different chemically in the minettes (potassic richterite and ferrichterite; sample WA 104) and the spessartites (calcic amphiboles). Mica was found in all samples, although the minettes and kersantite contain Al- and Ti-rich phlogopite while the spessartites contain secondary muscovite. Nearly pure albite is present in all of the lamprophyres, but only the minettes and spessartites contain alkali feldspar. Complex

Mineral	Main chemical features
Olivine	N/A
Pyroxene	Minette: only lamprophyre group to contain cpx, no opx. Most cpx is low Al-Ti diopside. Mg-rich cores and Mg-poor rims.
Amphibole	Minette: only sample WA 104 contains amphibole. Sodic-calcic potassic richterite and ferrichterite, Ti- and F-rich. Spessartite: Ti-rich calcic amphiboles, most are magnesiohastingsite, magnesiohornblende, tschermakite, and actinolite. Kersantite: no amphibole.
Mica	Minette: Al- and Ti-rich phlogopite, some have high F. Mg-rich cores and Mg-poor rims. Sample WA 104 contains megacrysts of zoned annite. Spessartite: muscovite associated with alteration. Kersantite: phlogopite, zoned with rims rich in Ti and Ba.
Feldspar	Minette: Ba-rich orthoclase, nearly pure albite. Sample WA 104 has Fe-rich orthoclase. Spessartite: orthoclase, albite and oligoclase. Sample WA 107 contains andesine. Kersantite: essentially pure albite (Or ₁ An ₀ Ab ₉₉).
Feldspathoid	N/A

Table 6.4. Summary of main chemical features of silicate minerals from Western Alps lamprophyres.

zoning, including normal and reverse in clinopyroxene and phlogopite, indicates changing chemical or physical conditions, and may be linked to variable P_{H_2O} . The dissimilar mineral chemistry of the minettes, spessartites, and kersantite is consistent with different melt chemistry, and suggests different melt evolution or derivation from separate source regions.

6.3c Roccamonfina and Ernici

Mineral chemical data for Roccamonfina and Ernici will be presented together in order to facilitate direct comparison between the KS and HKS rocks at each centre.

6.3c.i Olivine

Groundmass olivine in the KS series of Roccamonfina ranges from Fo₅₅ to Fo₆₅, while phenocryst olivine has values of Fo₈₁ to Fo₈₈. Mg#s >80 in olivine are high for mafic rocks. Most gabbroic rocks, for example, have olivine in the compositional range Fo₅₀ to Fo₈₀ (Deer et al., 1992). At Ernici, KS groundmass olivines range from Fo₆₂ to Fo₇₆, while phenocrysts are richer in Mg, with cores of Fo₈₆ to Fo₉₀ and rims of Fo₆₇ to Fo₈₀. The olivines from the KS series of Ernici are slightly more Mg-rich on average than those from Roccamonfina. Al₂O₃ substitution for SiO₂ in KS olivine from both centres is minimal, with < 0.13 wt% Al₂O₃ in all analyzed olivine. MnO and CaO are < 1.00 wt% in all KS olivine, and NiO reaches a maximum of 0.25 wt% in the most magnesian olivine analyzed (Fo₉₀).

Groundmass olivine from the HKS series of Roccamonfina have relatively low Mg contents ranging from Fo₄₄ to Fo₇₀, with most compositions < Fo₆₅. Ernici HKS

groundmass olivines have an even wider range of Mg/Fe ratios (Fe_{34} to Fe_{80}), suggesting olivine crystallization throughout melt evolution. Olivine crystallization over an extended interval is favoured by hydrous conditions before plagioclase becomes a liquidus phase, and produces derivative liquids low in MgO and high in Al_2O_3 (Lima, 2000). Several HKS samples from Ernici contain groundmass olivine with fayalitic composition ($Fe < 50$). Olivine phenocrysts from the HKS series of both volcanic centres are forsteritic, and typically zoned with Mg-rich, Mn-poor cores and Mg-poor, Mn-rich rims. Al_2O_3 contents in HKS olivine from both Roccamonfina and Ernici are comparable to the KS olivine (up to 0.13 wt%), while MnO and CaO contents are generally higher (up to 1.74 and 2.20 wt% respectively). Both MnO and CaO are higher in the groundmass olivines compared to phenocrysts from the same sample. NiO contents in olivine from the HKS series reach up to 0.31 wt%, although most analyses show NiO contents < 0.10 wt%.

Overall, there is very little difference in olivine composition between the HKS rocks from Roccamonfina and the HKS rocks from Ernici, and between the KS from Roccamonfina and the KS from Ernici. The biggest chemical difference between the two HKS series is the average value of 1.36 wt% for MnO at Ernici compared to 0.86 wt% at Roccamonfina. However, there are marked differences between the HKS and the KS series at both centres. The average atomic Fe/Mg ratio for olivine from the HKS series at Ernici is 0.98, while for the KS it is 0.28. The Fe/Mg difference is also seen in the samples from Roccamonfina as well, but it not as pronounced. Many olivine from the HKS series at Ernici contain appreciable Fe, as shown by the presence of groundmass fayalite.

MnO and CaO also display a systematic difference between the HKS and KS olivines. Figure 6.6 shows that the absolute abundances of both MnO and CaO (wt%) are greater in the HKS rocks from Roccamonfina and Ernici compared to the KS rocks. Al₂O₃ and NiO show essentially no difference between the two series.

6.3c.ii Pyroxene

All the analyzed clinopyroxene plot in the ternary system Ca₂Si₂O₆ (Wo) – Mg₂Si₂O₆ (En) – Fe₂Si₂O₆ (Fs), and most contain atomic Mg > atomic Fe (Figures 6.7 and 6.8). The most common type of pyroxene found in the KS rocks of Roccamonfina and Ernici is aluminian diopside (Al³⁺ > 0.10 apfu). Al₂O₃ shows extreme variability in abundance, and can display a wide range of values in a single zoned crystal. The largest variation found in this study is from a KS phenocryst from Ernici, with 0.09 apfu (2.04 wt% Al₂O₃) in the core and 0.39 apfu (9.07 wt% Al₂O₃) in the rim. Al₂O₃ contents greater than 3 wt% are considered high for natural Ca-Mg-Fe clinopyroxenes (Klein and Hurlbut, 1993). In most cases, aluminum increases from core to rim at the expense of silica, resulting in rims which can be classified as subsilicic (Si⁴⁺ < 1.75 apfu). The Al₂O₃ contents of clinopyroxene from Roccamonfina and Ernici are within the range typically found in potassic and ultrapotassic rocks from the Roman Province (e.g. Aurisicchio et al., 1988; Cellai et al., 1994; Bindi et al., 1999).

Both the KS and HKS clinopyroxene from both Roccamonfina and Ernici are characterized by low Ti contents, typical of lavas of the Roman Province (Lima, 2000). Low values of Ti in clinopyroxene can be caused by early crystallization of titanian magnetite (high *f*O₂), which depletes the melt in Ti and in turn leads to lower Ti in

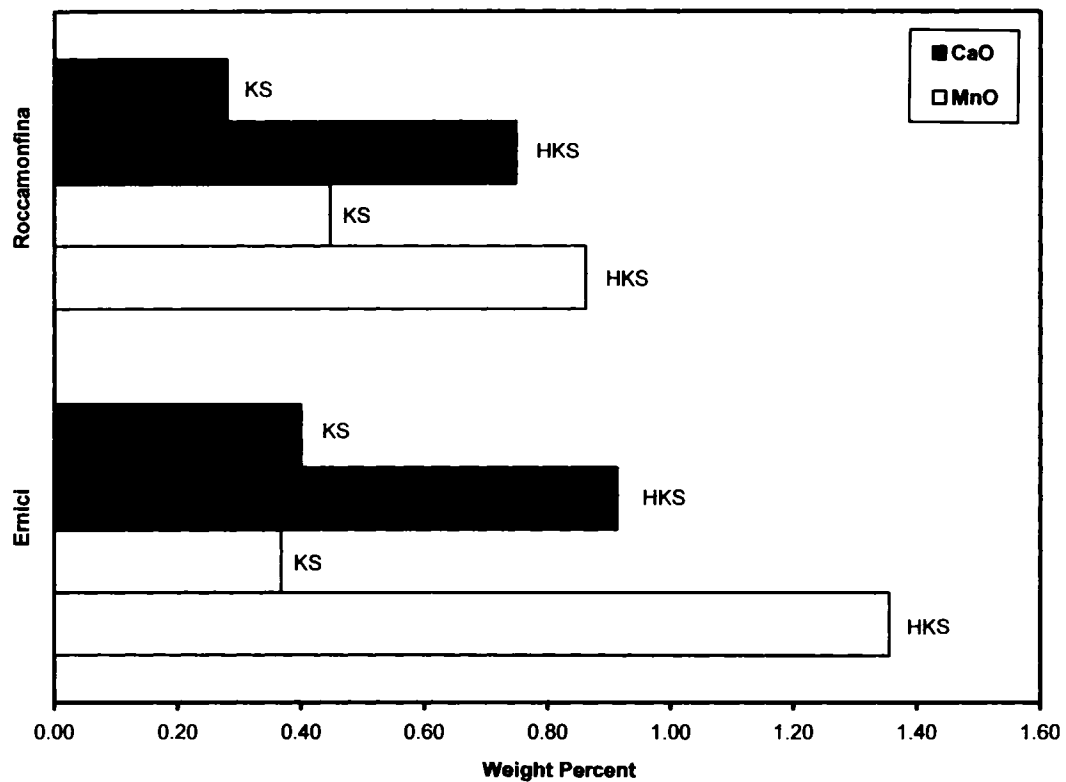


Figure 6.6. Comparison of MnO and CaO abundance (wt%) in olivine from the HKS and KS rocks of Roccamonfina and Ernici.

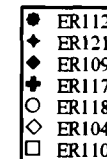
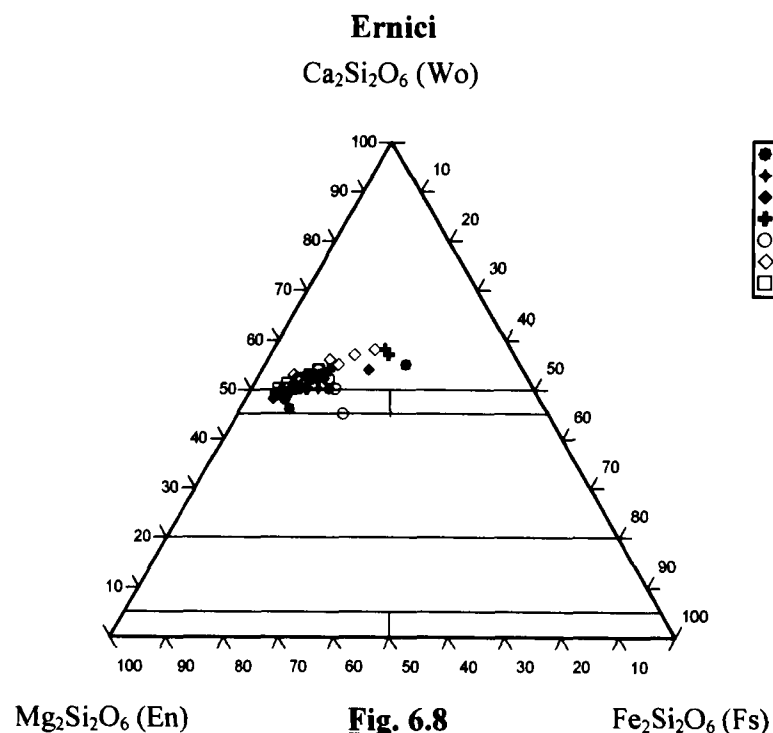
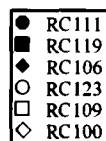
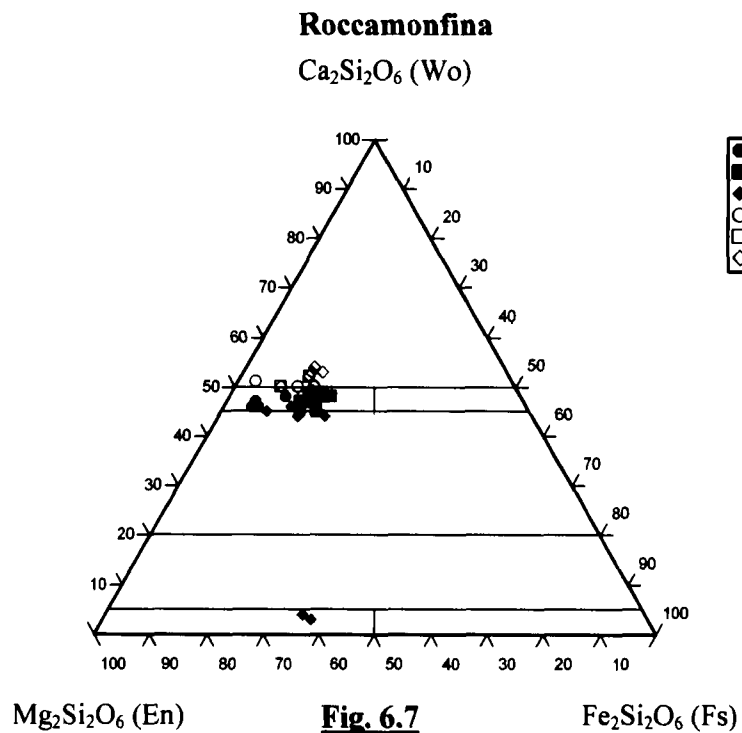


Figure 6.7. Ternary Ca₂Si₂O₆ (Wo) – Mg₂Si₂O₆ (En) – Fe₂Si₂O₆ (Fs) diagram for pyroxene from the Roccamonfina KS and HKS rocks. Note the excess of the Ca₂Si₂O₆ (Wo) component in the HKS clinopyroxene and the presence of orthopyroxene in KS sample RC 106. KS series samples are filled symbols; HKS series samples are open symbols.

Figure 6.8. Ternary Ca₂Si₂O₆ (Wo) – Mg₂Si₂O₆ (En) – Fe₂Si₂O₆ (Fs) diagram for pyroxene from the Ernici KS and HKS rocks. Note the excess of the Ca₂Si₂O₆ (Wo) component in the HKS clinopyroxene, as well as samples ER 109 and ER 117. KS series samples are filled symbols; HKS series samples are open symbols.

clinopyroxene. Early crystallization of Fe-Ti oxides and consequent suppression of Fe-enrichment is a defining characteristic of rocks from the calc-alkaline magma series.

Rare chromian diopside was found as an apparent phenocryst phase in KS samples from both Roccamonfina and Ernici, and subsilicic ferrian aluminian diopside is present both as groundmass crystals and as rims on phenocrysts at Ernici. The presence of chromian diopside (Cr_2O_3 up to 0.65 wt%), commonly found as xenocrysts in kimberlite (Mitchell, 1986), suggests high-pressure crystallization conditions for some clinopyroxene in the KS rocks. Aluminian augite as well as non-aluminian diopside were also found in the KS samples at Roccamonfina.

The KS series clinopyroxene phenocrysts at Ernici commonly show normal zonation with Mg-rich cores (average Mg# = 87) and Mg-poor rims (average Mg# = 75), suggesting crystallization from a relatively primitive melt. The KS clinopyroxene phenocrysts from Roccamonfina are slightly less Mg-rich, but show the same type of normal zonation. Groundmass clinopyroxene are more Fe-rich, with an average Mg# of 69 at Ernici and 67 at Roccamonfina. Rare hedenbergite is present as a groundmass phase in some KS samples at Ernici, but not at Roccamonfina. Orthopyroxene (enstatite) is located in the groundmass of some KS samples at Roccamonfina. Deer et al. (1992) stated that the maximum amount of CaO in typical orthopyroxene does not exceed 1.5 wt%. However, the KS enstatite analyses contain up to 2.04 wt% CaO, which reflects the high αCaO of these rocks (see Chapter 7).

All of the clinopyroxene analyzed from the HKS series at Roccamonfina are aluminian diopside. The HKS clinopyroxene from Ernici also contain very high amounts of aluminum, and many data points plot above the 50 % $\text{Ca}_2\text{Si}_2\text{O}_6$ (Wo) line on the

$\text{Ca}_2\text{Si}_2\text{O}_6$ (Wo) – $\text{Mg}_2\text{Si}_2\text{O}_6$ (En) – $\text{Fe}_2\text{Si}_2\text{O}_6$ (Fs) ternary diagram (Figure 6.8). Al_2O_3 averages 6.04 wt% for HKS clinopyroxene from Ernici, and reaches a maximum of 13.01 wt% (0.58 apfu Al^{3+}). The most strongly aluminian crystals are subsilicic and can usually be classified as ferrian as well, as Fe^{3+} increases to maintain charge balance and substitutes with Al^{3+} into the T and M1 sites (Figure 6.9). It should be stressed that Fe^{3+} is a calculated, not a measured value, and no petrogenetic interpretations will be made on the basis of Fe^{3+} content in the clinopyroxenes.

The large excess of Al_2O_3 at the expense of SiO_2 found in many HKS clinopyroxenes results from a chemical substitution involving the calcium Tschermak's component (CaAlAlSiO_6). This molecule is created from an excess of aluminum whereby Al^{3+} substitutes into both the T site and the M1 site. The Al-Al coupled substitution produces the high-Al clinopyroxene formerly known as fassaite (now referred to as ferrian aluminian diopside or augite), which is present in many members of the HKS series. The replacement of Mg^{2+} and Fe^{2+} by Al^{3+} in the M1 site of these clinopyroxene leads to data that plots above the 50 % $\text{Ca}_2\text{Si}_2\text{O}_6$ (Wo) line on the standard pyroxene ternary diagrams shown in Figures 6.7 and 6.8.

The excess Al in clinopyroxene from Roccamonfina and Ernici can be demonstrated on the Q-J diagram of Morimoto et al. (1989), in which $Q = \text{Ca} + \text{Mg} + \text{Fe}^{2+}$ and $J = 2\text{Na}$ (Figure 6.10). All analyzed clinopyroxenes contain low concentrations of Na and thus plot in the "Quad" area near the Q-axis, with Q values between 1.5 and 2.0. Pyroxenes that plot within this area have components other than Q and J at less than 25% of the M sites. Q values approaching 1.5 are a result of Tschermak's substitution, whereby the total Q is lowered by replacement of Mg and Fe^{2+} in the M1 site by Al^{3+} .

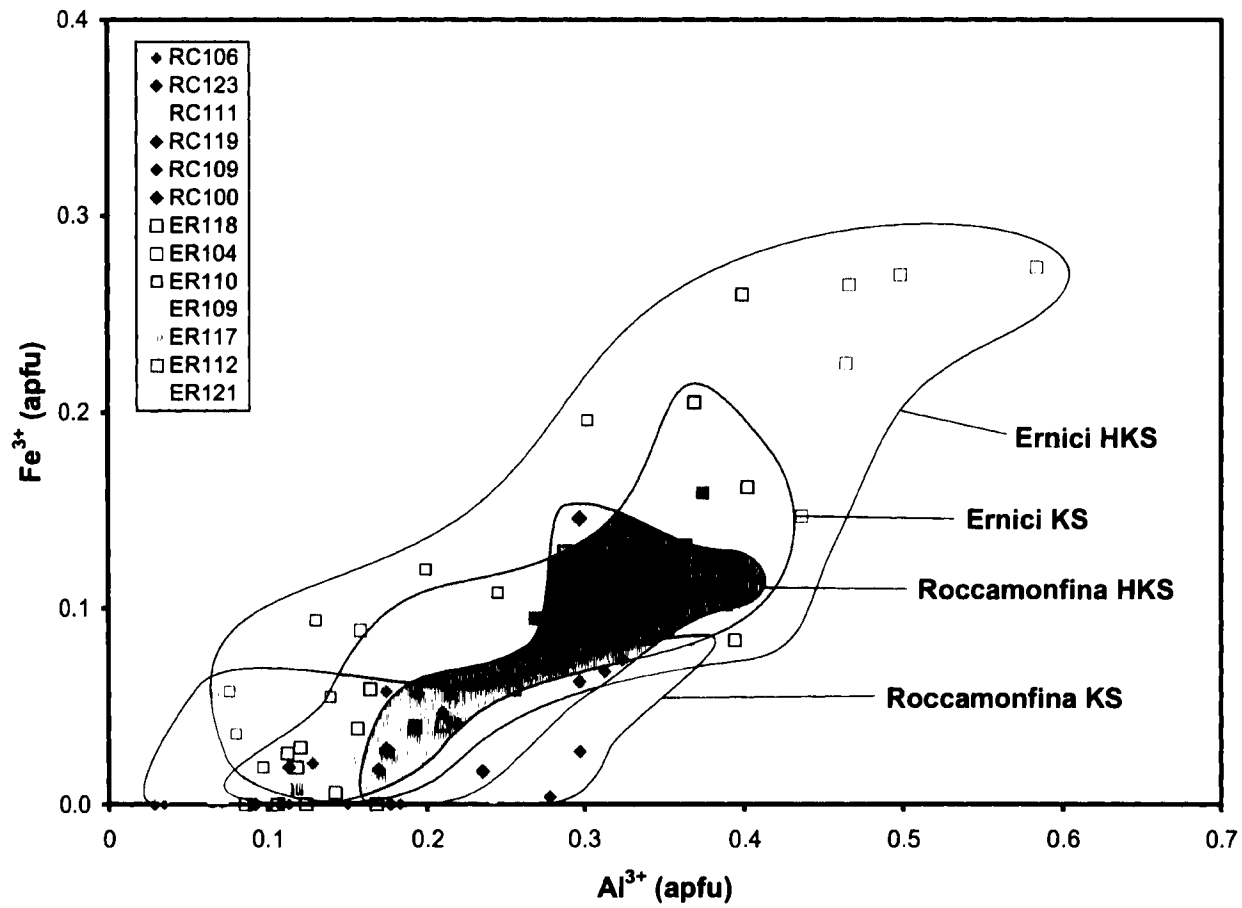


Figure 6.9. Fe³⁺ vs. Al³⁺ for Roccamonfina and Ernici clinopyroxene. Note the high Fe³⁺ and Al³⁺ in the HKS series of Ernici, and the low Fe³⁺ and Al³⁺ in the KS series clinopyroxene from Roccamonfina.

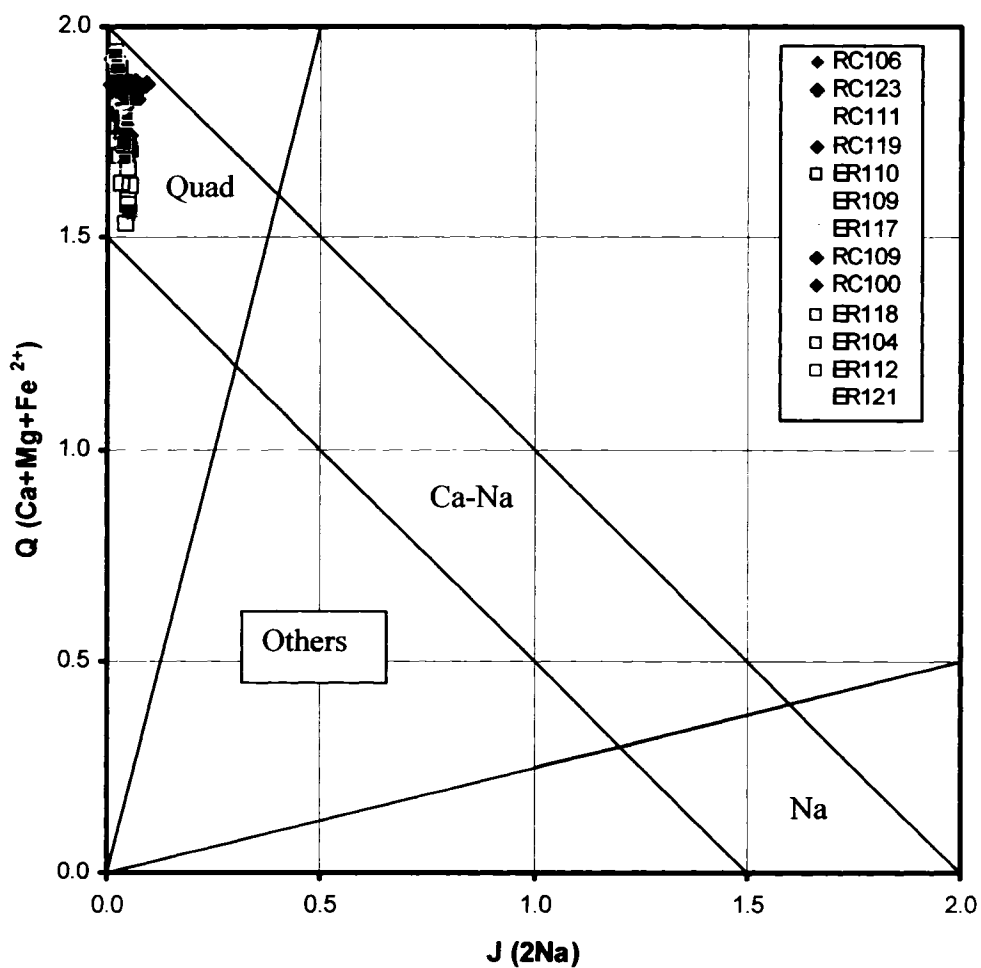


Figure 6.10. Q-J diagram for clinopyroxene from Roccamonfina and Ernici. Note the low Q values for HKS clinopyroxene from Ernici. Squares are for data from Ernici, diamonds for Roccamonfina. Yellow-red symbols are KS series, blue-green symbols are HKS series, grey symbols are for samples ER 109 and ER 117.

Figure 6.10 shows that this substitution is most extreme for members of the Ernici HKS series, and least extreme for members of the Roccamonfina KS series. A plot of Al^{3+} vs. Si^{4+} (apfu) also demonstrates the Si-poor, Al-rich nature of the Ernici HKS clinopyroxene, and the Si-rich, Al-poor nature of the Roccamonfina KS clinopyroxene (Figure 6.11). Data from all samples plot on the upper side of the 1:1 Si:Al line, indicating an excess of aluminum.

Many clinopyroxene phenocrysts from the HKS samples at Roccamonfina are unzoned, and those that are display less variation than those from the KS series. The average Mg#s for phenocryst cores and rims are about 72, while the average Mg# for groundmass clinopyroxene is 68. The phenocryst cores in the HKS clinopyroxene have lower Mg# than those of the KS clinopyroxene. At Ernici, average Mg contents are very similar in both the phenocryst cores and groundmass clinopyroxene (Mg# = 76-77), but lower for phenocryst rims (Mg# = 70). It should be noted that the Mg# for extremely aluminian analyses is greatly decreased using the calculation scheme of $\text{Mg\#} = \text{Mg}/(\text{Mg} + \text{Fe}^{2+} + \text{Fe}^{3+} + \text{Mn})$. For example, the most aluminian clinopyroxene analyzed ($\text{Al}_2\text{O}_3 = 13.01$ wt%) has a recalculated Fe_2O_3 of 9.56 wt% (0.27 apfu) while MgO is 6.98 wt% (0.40 apfu). The high value of Fe^{3+} (a result of the Tschermak's substitution of trivalent elements into the M1 site) leads to a Mg# of 47 for this sample.

Samples ER 109 and ER 117 from Ernici contain abundant analcime in the groundmass, and are grouped with the KS series on the basis of their relatively low K_2O content. Analysis of clinopyroxene chemistry for ER 109 and ER 117 confirms that these two samples were probably members of the HKS series, and the analcime likely formed through a secondary process. The clinopyroxene from ER 109 and ER 117 has extreme

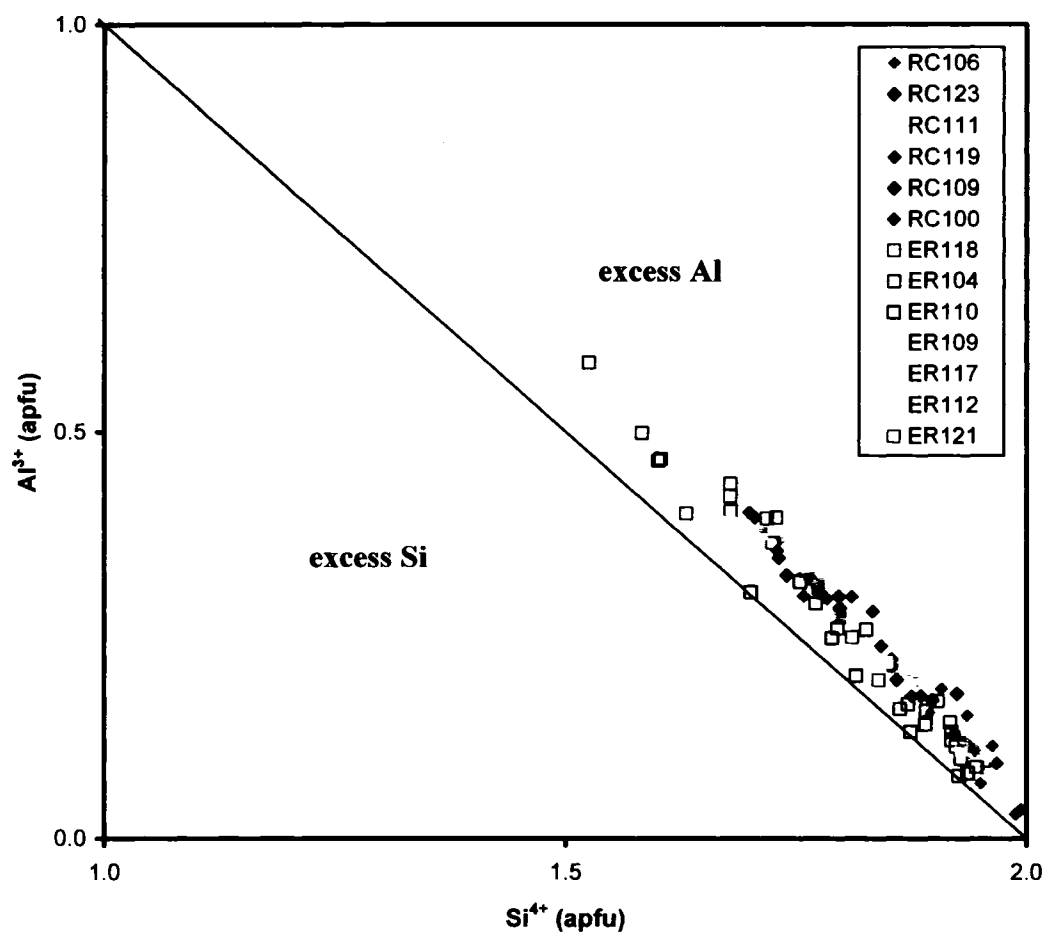


Figure 6.11. Al^{3+} vs. Si^{4+} for clinopyroxene from Roccamonfina and Ernici. Note the excess Al in all samples.

excesses of aluminum (up to 57-58 % $\text{Ca}_2\text{Si}_2\text{O}_6$ on Figure 6.8, which is equivalent to ~12 wt% Al_2O_3) that are in the same range as those from the HKS series. Most of the clinopyroxene analyses from these samples plot above the 50 % $\text{Ca}_2\text{Si}_2\text{O}_6$ (Wo) line, and many are both ferrian and/or subsilicic.

6.3c.iii Crystal structure simulation of clinopyroxene from Ernici

One of the main reasons for determining the mineral chemistry of silicate phases from the KS and HKS rocks of Roccamonfina and Ernici is to constrain the physical and chemical conditions of crystallization. Previous workers have suggested that the HKS magma source is deeper than the KS source, based on the stronger degree of silica-undersaturation of the HKS rocks (Civetta et al., 1981; Peccerillo and Panza, 1999). The chemistry of clinopyroxene phenocrysts may be able to provide evidence for or against this hypothesis.

Microprobe analyses have shown that clinopyroxene from the HKS series at both volcanic centres have higher contents of Al^{3+} than those from the KS series. The replacement of Mg and Fe^{2+} by Al^{3+} is considered typical of clinopyroxene crystallized under high-pressure conditions (Thompson., 1974), and seems to support a deeper source for the HKS magmas. However, a more quantitative estimate of clinopyroxene crystallization pressure is desirable. Few geobarometric methods are available for determining the pressures of crystallization of igneous minerals, and those that are usually require specific mineral assemblages or knowledge of the equilibrium liquid (e.g. Ghiorso and Sack, 1995; Yang et al., 1996; Putirka et al., 1996).

In order to circumvent these restrictions, Nimis (1995) measured the crystal chemical response of magmatic clinopyroxenes to variations in pressure and magma composition using experimentally synthesized clinopyroxene. Nimis (1995) found a linear relation between pressure and the unit cell parameters of the clinopyroxene, and refined a technique known as crystal-structure simulation. Specifically, the volumes of both the unit cell (V_{cell}) and the M1 site (V_{M1}) decrease with increasing pressure. Crystal-structure simulation is applicable to a wide range of igneous rock types, and enables the structural parameters and crystallization pressure of clinopyroxene to be calculated using only an electron microprobe analysis.

The anhydrous structural geobarometer of Nimis and Ulmer (1998) was used to determine the crystallization pressure of clinopyroxene phenocrysts from the KS and HKS series of Ernici (Owen et al., 2005). Pressures are underestimated by ~ 1 kbar per 1 wt% H_2O in the melt. The geobarometer was not applied to samples from Roccamonfina, because many of these rocks have very high contents of Al_2O_3 (see Chapter 7). Nimis (1995) found that the accuracy of the geobarometer is significantly reduced in igneous rocks with $\text{Al}_2\text{O}_3 > 18$ wt.%. Microprobe analyses of clinopyroxene from Ernici that did not have $\Sigma\text{T} = 2.000 \pm 0.002$, $\Sigma(\text{M1}+\text{M2}) = 2.000 \pm 0.005$, $(\text{Ca}+\text{Na}) > 0.5$ apfu, and $\text{Mg}/(\text{Mg}+\text{Fe}^{2+}) > 0.7$ were not used. The estimated standard error on the $P_{\text{crystallization}}$ calculations is 1.7 kbar (1σ) (Nimis, 1999).

The $P(\text{kbar})$ of clinopyroxene crystallization was calculated as a function of atomic fraction using the formula: $P(\text{kbar}) = 771.48 + 4.956 \cdot \text{Al}_{\text{T}} - 28.756 \cdot \text{Fe}^{2+}_{\text{M1}} - 5.345 \cdot \text{Fe}^{3+} + 56.904 \cdot \text{Al}_{\text{M1}} + 1.848 \cdot \text{Ti} + 14.827 \cdot \text{Cr} - 773.74 \cdot \text{Ca} - 736.57 \cdot \text{Na} - 754.81 \cdot \text{Mg}_{\text{M2}} - 763.20 \cdot \text{Fe}^{2+}_{\text{M2}} - 759.66 \cdot \text{Mn} - 1.185 \cdot (\text{Mg}_{\text{M2}})^2 - 1.876 \cdot (\text{Fe}^{2+}_{\text{M2}})^2$. The

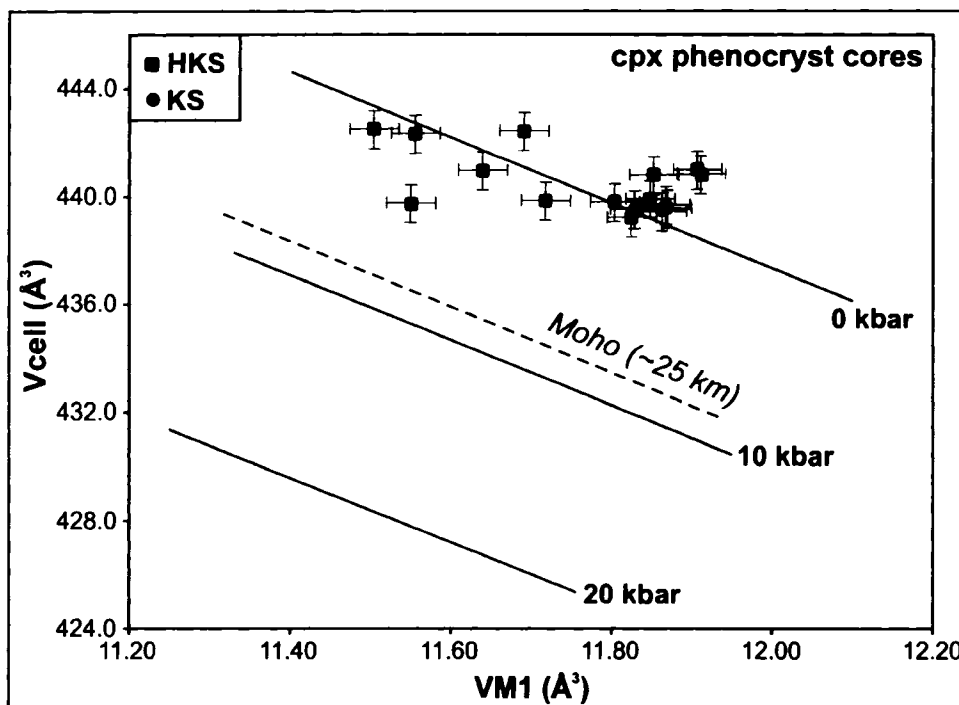


Figure 6.12. Calculated Vcell and VM1 for clinopyroxene phenocryst cores from the HKS (n = 12) and KS (n = 7) series of Ernici. Isobars from Nimis and Ulmer (1998).

calculations were performed using the Excel program Cpxbar (Nimis and Ulmer, 1998; Nimis, 1999), which can be downloaded at <http://dmp.unipd.it>. The estimated V_{cell} and V_{M1} are also included in the program output.

Results from the crystal structure simulation of clinopyroxene from Ernici are shown in Figure 6.12. Data from clinopyroxene from both the KS and HKS series lie close to the 0 kbar isobar, indicating low-pressure crystallization in shallow-level magma chambers. Data from the KS series forms a tight cluster at approximately $V_{\text{cell}} = 440 \text{ \AA}^3$ and $V_{\text{M1}} = 11.85 \text{ \AA}^3$, while data from the HKS series is more widespread and extends to higher values of V_{cell} and lower values of V_{M1} . The relatively low V_{M1} of clinopyroxene from the HKS series is due to the higher amount of Al^{3+} in the M1 site, where it has replaced Fe^{2+} and Mg (Figure 6.13). However, the higher levels of Al^{3+} in the M1 site do not result in a linear decrease in V_{cell} (Figure 6.14). The volume of the clinopyroxene unit cell is a complex function of changes in the M2, M1, and T sites due to a combination of chemical substitutions: $\text{Ca}_{\text{M2}}\text{Mg}_{\text{M1}} \rightarrow \text{Na}_{\text{M2}}\text{Al}_{\text{M1}}$ (jadeite), $\text{Mg}_{\text{M1}}\text{Si}_{\text{T}} \rightarrow \text{Al}_{\text{M1}}\text{Al}_{\text{T}}$ (fassaite), and $\text{Ca}_{\text{M2}} \rightarrow \text{Mg}_{\text{M2}}$ (clinoenstatite) (Nimis and Ulmer, 1998). Figure 6.15 highlights the effects of various substitutions on clinopyroxene V_{cell} and V_{M1} .

The clinopyroxene from the HKS series of Ernici have higher levels of Al^{3+} in the M1 site because of the low a_{SiO_2} and the high a_{CaO} in the HKS magma (Nimis, 1995). The low a_{SiO_2} results in high Al_{T} and an increase in the volume of the T site. Undercharging of the coordinated O atoms caused by the $\text{Si}^{4+} \rightarrow \text{Al}^{3+}$ substitution are counterbalanced by relatively high contents of small Al^{3+} cations in the M1 site and consequent V_{M1} contraction. The results of these changes are an increase in V_{cell} and a decrease in V_{M1} , which together displace the clinopyroxene structural data parallel to the

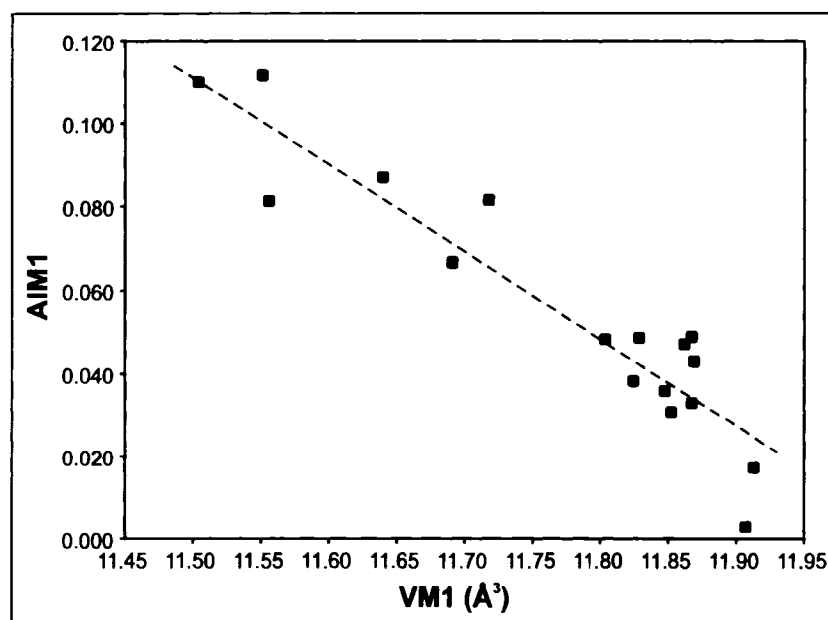


Figure 6.13. Relation between AIM1 and VM1 for clinopyroxene from Ernici.

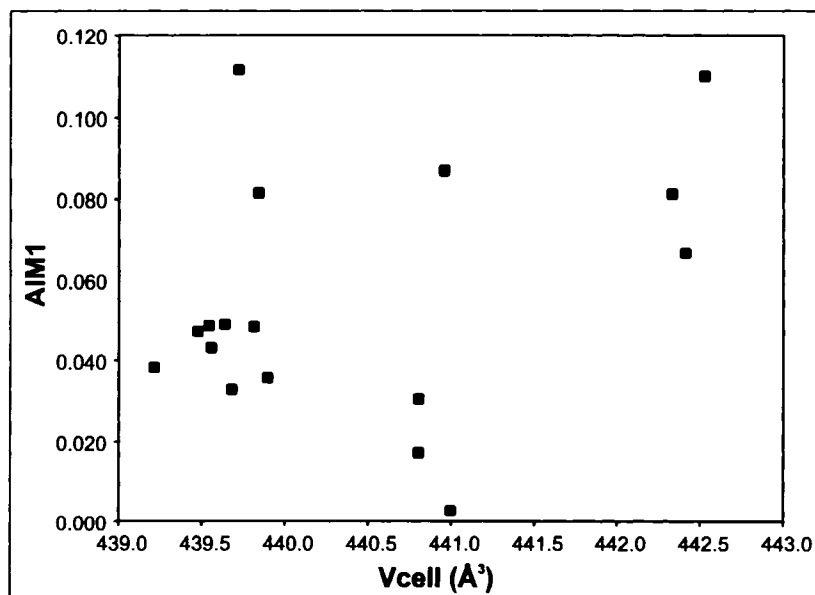


Figure 6.14. Lack of relation between AIM1 and Vcell for clinopyroxene from Ernici.

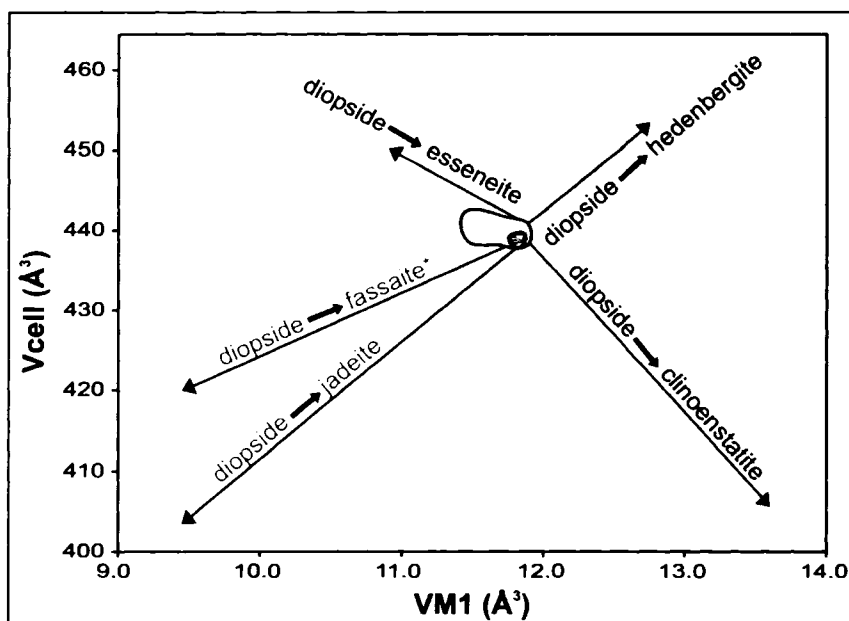


Figure 6.15. The crystal chemical effects of common substitutions on the V_{cell} and V_{M1} parameters of clinopyroxene (Nimis, 1999). Substitutions that result in a decrease in V_{cell} and V_{M1} are highlighted in red. Data from clinopyroxene of the HKS series are shown in blue; data for the KS series shown in red. *Fassaite is not a valid mineral name, however, the term is used here to denote the CaAlAlSiO_6 component.

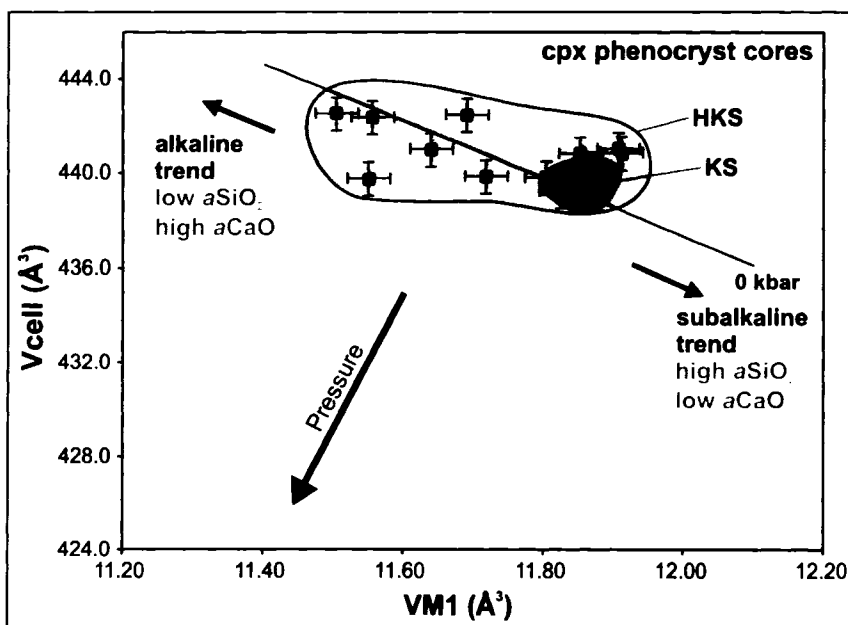


Figure 6.16. Crystal structure effects of alkaline (low $a\text{SiO}_2$, high $a\text{CaO}$) and subalkaline (high $a\text{SiO}_2$, low $a\text{CaO}$) melts on clinopyroxene.

isobars (Figure 6.16). Therefore, high Al^{3+} in the M1 site of cpx from strongly silica-undersaturated magmas does not necessarily imply cpx crystallization at high pressure.

The main conclusions from the crystal structure simulation of clinopyroxene from Ernici are: 1) clinopyroxene phenocrysts from both the HKS and the KS magmas crystallized at low pressure, 2) clinopyroxene from the HKS series have lower V_{M1} (and higher V_{cell}) than those from the KS series, 3) the high Al^{3+} in the M1 site of the HKS clinopyroxene reflects the low $a\text{SiO}_2$ of the melt, and 4) the clinopyroxene crystal chemistry does not provide evidence that the HKS magmas are derived from a deeper source than the KS magmas.

6.3c.iv Amphibole

No amphibole was found in any sample from Roccamonfina. Calcic amphibole was observed in thin section in the groundmass of samples from the HKS series at Ernici, and is characterized by relatively low SiO_2 , high Al_2O_3 , $\text{Ca}_B \geq 1.50$ apfu, $(\text{Na}+\text{K})_A \geq 0.50$ apfu, $\text{Ti} < 0.50$ apfu, and $\text{Mg}/(\text{Mg}+\text{Fe}^{2+}) < 0.50$. The amphiboles are classified as potassian fluoro-ferropargasite and potassian fluorohastingsite. The only difference between the two types of amphibole is ${}^{\text{vi}}\text{Al} > \text{Fe}^{3+}$ in ferropargasite, and ${}^{\text{vi}}\text{Al} < \text{Fe}^{3+}$ in hastingsite. The amphiboles are extremely rich in F, with values that range from 2.66 to 2.69 wt% (1.316-1.336 apfu). F contents in this range indicate a major substitution of F for OH^- , typically the dominant anion in the OH site. The high K contents (1.84-1.97 wt%) are similar to those of amphibole found in other ultrapotassic rocks from the Roman Province (e.g. Alban Hills; Federico and Peccerillo, 2002), but the F contents of amphibole from Ernici are higher than those from the Alban Hills.

6.3c.v Mica

All analyzed mica from Roccamonfina and Ernici is phlogopite. Phlogopite typically occurs as a primary mineral in leucite-rich rocks such as those from West Kimberly (Australia), Wyoming (USA), and southeast Spain (Foley et al., 1987). The KS phlogopite from Roccamonfina is low in F, Cl, and Ba (maximums of 1.37 wt%, 0.12 wt%, and 0.34 wt% respectively). TiO₂ is higher in the KS phlogopite from Roccamonfina (average 3.69 wt%) compared to the HKS phlogopite (average 2.76 wt%), and zoning is uncommon in phlogopite from both the KS and the HKS series. At Ernici, phlogopite phenocrysts and megacrysts are present in the analcime-rich KS samples ER 109 and ER 117 that may have originally been members of the HKS series. The phlogopite from these two samples is typically unzoned, and also has low contents of F, Cl, and Ba (maximums of 0.61 wt%, 0.02 wt%, and 0.48 wt% respectively). Groundmass phlogopite was not observed in samples ER 109 or ER 117.

The HKS phlogopite from Roccamonfina also has low concentrations of Cl and Ba but is strongly enriched in F, with typical values of 5-6 wt%. High Mg/Fe ratios and high temperature favour increased substitution of F for (OH) (Deer et al., 1992), which suggests that magmas of the HKS series may have crystallized at higher temperatures than those of the KS series. The HKS phlogopite is more Mg-rich than phlogopite from the KS rocks, with average atomic Mg:Fe ratios of 4:1 compared to 2:1 for the KS (where Fe = Fe²⁺+Fe³⁺). The high F content of mica (and amphibole) from the HKS series, as well as the presence of fluorite in some samples from Roccamonfina, indicates low $a_{\text{H}_2\text{O}}$ and the prevalence of F in the magmatic fluid phase. This agrees with experimental work

suggesting that generation of strongly silica-undersaturated, K-rich magmas is favoured by the presence of dissolved F (Conceição and Green, 2000).

Phlogopite from HKS sample ER 110 from Ernici occurs as an anhedral groundmass phase and has very different chemistry from the other Ernici micas. The main differences are extremely high concentrations of BaO (9.31 – 9.76 wt%) and F (5.20 – 5.27 wt%). The K₂O concentration of phlogopite in sample ER 110 (average K₂O = 6.43 wt%) is lower than that of phlogopite from the analcime-rich samples (average K₂O = 9.52 wt%). The average K:Ba ratio in apfu for sample ER 110 is about 2:1, while in other samples from Ernici the ratio is about 88:1.

There is a strong inverse correlation between Ba and K in mica, and it has been hypothesized that the $K^+ \leftrightarrow Ba^{2+}$ exchange also involves a substitution in the tetrahedral site such that charge neutrality is maintained in the following manner: $^{[12]}Ba^{2+} + ^{[4]}Al^{3+} \leftrightarrow ^{[12]}K^+ + ^{[4]}Si^{4+}$ (Brigatti et al., 1998). However, this cannot be the only mechanism that permits the entrance of Ba into the phlogopite in sample ER 110, as the sum of Si⁴⁺ and Al³⁺ is not enough to fill the tetrahedral sites (Si + Al < 8). Fe³⁺ probably fills the remainder of the tetrahedral sites, suggesting that the *f*O₂ of the ER 110 magma at the time of phlogopite crystallization was relatively high.

Phlogopite from sample ER 110 is similar to that found in HKS lavas from the Alban Hills, Roman Province (Gaeta et al., 2000). These phlogopite have very high BaO (up to 9.70 wt%) and F (up to 7.50 wt%) contents that are among the highest reported from ultrapotassic rocks (Foley, 1989). Gaeta et al. (2000) suggested that the very high BaO content of phlogopite from the Alban Hills is due to passive enrichment of Ba in the melt, reflecting the absence of sanidine and mica during earlier phases of crystallization.

The extremely high F contents reflect the low $a_{\text{H}_2\text{O}}$ of the magma, and may also help to increase BaO in the phlogopite. Increased F content should decrease the inter-layer distance and favour the entrance of Ba, whose ionic radius in 12-fold co-ordination is slightly less than that of K (Shannon, 1976).

6.3c.vi Feldspar

The KS rocks at Roccamonfina contain both potassic and sodic feldspars (Figure 6.17). Unlike the K-rich alkali feldspar in the Western Alps samples, the alkali feldspar from the KS rocks at Roccamonfina is intermediate between KAlSi_3O_8 (Or) and $\text{NaAlSi}_3\text{O}_8$ (Ab) and has an average composition of $\text{Or}_{58}\text{An}_{07}\text{Ab}_{35}$ (sanidine). Alkali feldspars normally contain less than 5 % $\text{CaAl}_2\text{Si}_2\text{O}_8$ for compositions between $\text{Or}_{100}\text{Ab}_0$ and $\text{Or}_{60}\text{Ab}_{40}$ (Deer et al., 2001). However, the Ca-rich sanidine from the KS series of Roccamonfina contain between 5 and 9 % $\text{CaAl}_2\text{Si}_2\text{O}_8$. Limited amounts of Fe^{2+} , Fe^{3+} , and more rarely Ba, are also present. Compared to other potassic and ultrapotassic rocks, sanidine from the KS rocks of Roccamonfina is relatively poor in BaO (below detection limit). Plagioclase compositions for the KS series at Roccamonfina vary between andesine and anorthite, with a maximum value of An_{92} and a minimum of An_{42} . Almost all of the analyzed KS plagioclase feldspars from Roccamonfina fall within the range of labradorite-bytownite ($\text{An}_{50} - \text{An}_{90}$) and contain < 5 mol.% KAlSi_3O_8 .

High-temperature, quenched, ternary feldspars form a fine-grained, groundmass mesh in KS sample RC 119. These feldspars have Na-K-Ca compositions that plot in the middle of the standard ternary diagram due to the increased solid solution between the albite, anorthite, and orthoclase end-members at high temperatures. Homogeneous, high-

Roccamonfina

$KAlSi_3O_8$ (Or)

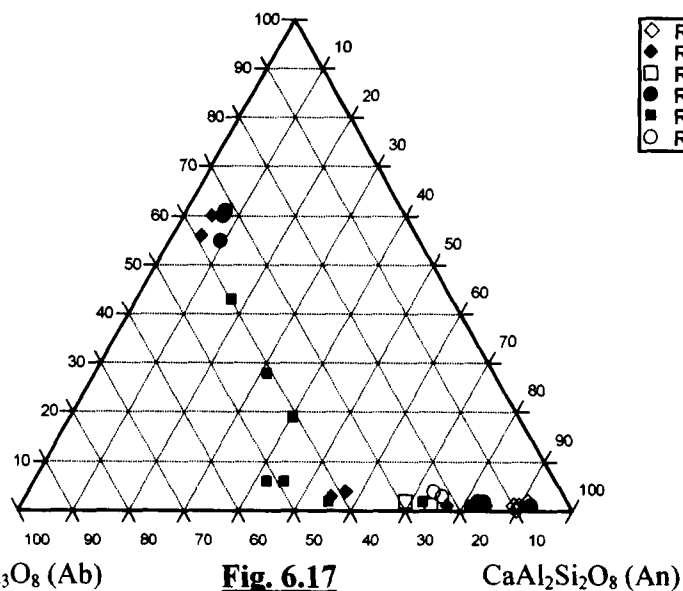


Fig. 6.17

Ernici

$KAlSi_3O_8$ (Or)

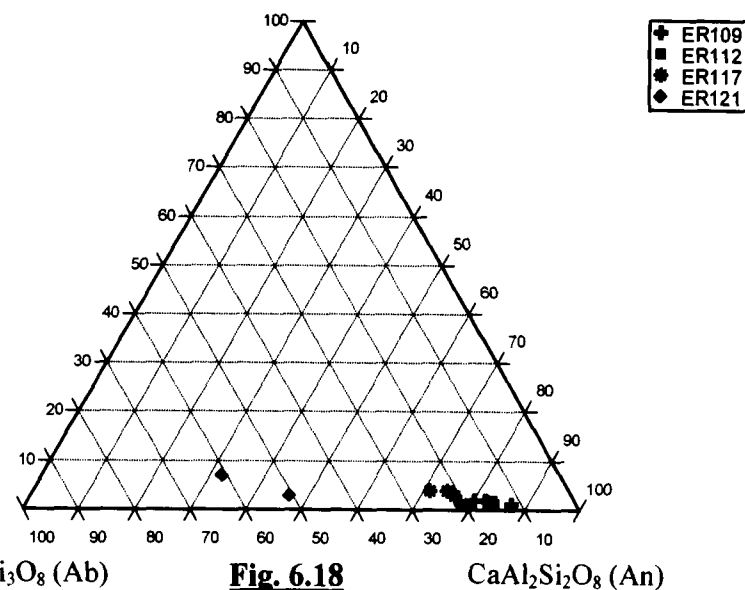


Fig. 6.18

Figure 6.17. Ternary $KAlSi_3O_8$ (Or) – $NaAlSi_3O_8$ (Ab) – $CaAl_2Si_2O_8$ (An) diagram for HKS and KS feldspars from Roccamonfina. Filled symbols represent analyses from the KS series, while open symbols are from the HKS series.

Figure 6.18. Ternary $KAlSi_3O_8$ (Or) – $NaAlSi_3O_8$ (Ab) – $CaAl_2Si_2O_8$ (An) diagram for HKS and KS feldspars from Ernici. Filled symbols represent analyses from the KS series.

temperature, disordered feldspars such as these are typical of volcanic rocks. The ternary feldspars in KS sample RC 119 have a constant Ab content of about 40 mol.% and a variable K:Ca ratio.

The KS samples from Ernici lack alkali feldspar and contain plagioclase in the compositional range An₇₈ – An₈₄ (bytownite) (Figure 6.18). Andesine (An₃₂) and labradorite (An₄₆) are also present in sample ER 121. Most plagioclase have < 4 mol.% Or, except the andesine analysis which contains 7 mol.%. Samples ER 109 and ER 117 contain only plagioclase of bytownite composition (An₇₁ – An₈₇). No feldspars were observed in the analyzed HKS samples from Ernici.

The HKS samples from Roccamonfina contain no alkali feldspar, but do contain plagioclase. The plagioclase is generally more calcic than that of the KS series, with a range of An₆₉ (labradorite) to An₉₁ (anorthite). Most analyses fall within the range An₇₀ – An₉₀ (bytownite), and are more restricted in composition compared to those from the KS series.

6.3c.vii Feldspathoids

Leucite is lacking in the KS series, but is present in all members of the HKS series at Roccamonfina and Ernici. The leucite analyses do not deviate appreciably from the ideal formula, KAlSi₂O₆. Although the solid solution of NaAlSi₂O₆ in leucite has been shown experimentally to be extensive in hydrous systems (up to 28% at P_{H₂O} = 1 kbar) (Deer et al., 1992), the average Na₂O content of leucite from Roccamonfina is quite low (0.29 wt%; 0.02 apfu). The leucite in the HKS rocks of Ernici contain even less Na₂O (average = 0.11 wt%; 0.01 apfu), suggesting a relatively anhydrous system. Small

amounts of excess SiO₂ are a common feature of leucite at Roccamonfina, an observation also noted by Giannetti and Ellam (1994). In general, little chemical difference exists between phenocryst and groundmass leucite. Some samples show an increase in Fe₂O₃ (= FeO + Fe₂O₃) in groundmass leucite compared to phenocrysts (1.82 wt% compared to 0.43 wt%), while other samples show the opposite effect. CaO content is negligible.

Nepheline is common in the HKS samples from Ernici, but absent in the KS samples. All HKS nepheline show excess Si (>1:1 stoichiometric Si:Al ratio) and are relatively Na-rich (77-81 normative molecular % Ne). High SiO₂ (or Si oversaturation) is typical of Na-rich nepheline, and may be due to greater solubility of SiO₂ in NaAlSiO₄ than in KAlSiO₄. The average K₂O content in the HKS nepheline from Ernici (excluding sample ER 110) is 3.63 wt% (0.87 apfu), while the average Na₂O is 15.65 wt% (5.66 apfu). CaO ranges from 1.23 wt% to 2.70 wt%, and Fe₂O₃ (= Fe_{total}) contents are < 1.00 wt%. The incorporation of Ca in the nepheline structure is charge-balanced by the substitution (Na,K) = ½Ca, or by a combination of Si-Al exchange and site vacancies (Rossi et al., 1989). Nepheline also is present in the HKS rocks at Roccamonfina, but analyses are poor due to small crystal size.

The nepheline from sample ER 110 is chemically different than that of the other HKS samples at Ernici. The K₂O content is higher (average 8.64 wt%; 2.15 apfu) at the expense of both Na₂O and CaO. The average composition of this nepheline is Ne₆₉K_{S28}Q₃, compared to Ne₇₉K_{S12}Q₉ for other HKS samples. The chemical formula for sample ER 110 nepheline approximates Na₃K(AlSiO₄)₄, while the other HKS samples are much closer to Na₃Na(AlSiO₄)₄. BaO contents remain negligible; however Fe₂O₃ reaches a maximum of 3.27 wt% in one analysis.

6.3c.viii Summary of mineral chemistry

A summary of the silicate mineral chemistry and petrogenetic implications from the KS and HKS samples from Roccamonfina and Ernici is provided in Table 6.5. The main differences between the HKS and the KS series are: 1) higher CaO and MnO in olivine from the HKS series, 2) higher Al₂O₃ and Fe₂O₃, lower SiO₂ in clinopyroxene from the HKS series, 3) higher Mg# in olivine and clinopyroxene from the KS series, 4) higher Mg# and F, lower TiO₂ in phlogopite from the HKS series, and 5) lack of nepheline and leucite in the KS series.

The Mg-rich olivine and clinopyroxene of the KS rocks support mafic magma generation from a mantle source similar to a four-phase lherzolite. In contrast, the more Fe-rich fayalite and clinopyroxene of the HKS rocks indicate that the HKS source has been significantly modified. Olivine and clinopyroxene zoning from Mg-rich cores to Fe-rich rims in samples from both the HKS and KS series are consistent with melt evolution by fractional crystallization. This agrees with previous work by Appleton (1972) and Taylor et al. (1979). The strong silica-undersaturation of the HKS series is evident in the high Al³⁺ contents of clinopyroxene, and in the presence of nepheline and leucite. Because the high Al³⁺ in the M1 site of HKS clinopyroxene reflects the low a_{SiO_2} of the melt, no inference on source depth can be made. However, the high Mg/Fe and F of the HKS phlogopite suggest high temperature crystallization conditions that may be related to a deeper source region. High F contents in phlogopite and amphibole from the HKS rocks indicate low $a_{\text{H}_2\text{O}}$ in the HKS magmas, and point to a magmatic fluid rich in F relative to H₂O.

Mineral	Main chemical features	Differences between KS and HKS	Petrogenetic implications
Olivine	<p>KS: phenocrysts Mg-rich (Fo₈₁-Fo₉₀), groundmass less Mg-rich (Fo₅₅-Fo₇₆) at both RC and ER.</p> <p>HKS: groundmass is Fe-rich (Fo₃₄-Fo₈₀) and highly variable at ER.</p>	Higher Fe/Mg, CaO, and MnO in olivines from the HKS series.	Mg-rich olivine phenocryst crystallization from a mafic melt. Melt changed to a more Fe-rich composition for groundmass olivine crystallization.
Pyroxene	<p>KS: aluminian diopside is dominant. Rare chromian diopside. Strongly zoned with Mg-rich cores and Al-rich rims. Opx in groundmass of RC.</p> <p>HKS: aluminian diopside, very high Al₂O₃ up to 13.01 wt.% at ER. High Fe³⁺ to maintain charge balance.</p>	Higher Al ₂ O ₃ and Fe ₂ O ₃ , lower SiO ₂ in HKS series. Cpx from the KS series is more Mg-rich.	Crystal structure simulation shows that the high Al ³⁺ in the M1 site of cpx from the HKS series is due to low aSiO ₂ of the magma. No inferences on source depth can be made.
Amphibole	Calcic amphibole only found in HKS series at ER. Potassian and F-rich (~2.7 wt%).	N/A	High F indicates low aH ₂ O of melt.
Mica	<p>KS: phlogopite, low F, Cl, and BaO. Unzoned to weakly zoned.</p> <p>HKS: phlogopite, enriched in F (5-6 wt.%). Very high BaO (9.76 wt.%) and F (5.27 wt.%) in HKS from ER.</p>	Higher TiO ₂ in KS series phlogopite. Higher Mg# in HKS phlogopite.	High Mg/Fe ratios and F contents of HKS phlogopite suggest high temperature crystallization conditions and low aH ₂ O.
Feldspar	<p>KS: no alkali feldspar at ER, sanidine present at RC (high An content). Plagioclase is An₄₂-An₉₂ at RC, An₇₈-An₈₄ at ER. Quenched feldspars.</p> <p>HKS: no feldspars at ER. Plagioclase at RC ranges from An₆₉-An₉₁.</p>	<p>Roccamonfina: KS has alkali + plagioclase HKS has only plagioclase</p> <p>Ernici: KS has only plagioclase HKS has no feldspar</p>	Quenched feldspars indicate rapid cooling. Lack of alkali feldspar in the HKS rocks likely due to preferential leucite crystallization.
Feldspathoid	<p>KS: leucite and nepheline absent</p> <p>HKS: leucite has very little Na₂O, small amount of Fe. Nepheline has excess Si and high Na₂O. Nepheline from sample ER 110 has high K₂O.</p>	KS rocks lack feldspathoids. Nepheline is more abundant in HKS rocks from ER than RC.	Presence of feldspathoids indicates silica-undersaturation of the HKS series. Leucite suggests relatively anhydrous melt.

Table 6.5. Summary of the main chemical features and petrogenetic indicators from silicate minerals from Roccamonfina and Ernici.

CHAPTER 7

WHOLE-ROCK GEOCHEMISTRY

7.1 Introduction

In this chapter, the major element geochemistry of lamprophyres from the Western Alps and potassic and ultrapotassic volcanic rocks from Roccamonfina and Ernici is discussed first, followed by trace element geochemistry. Samples selected for whole-rock geochemistry include all of the lamprophyres collected from the Western Alps, fourteen volcanic rocks from Roccamonfina (8 KS, 6 HKS), and fourteen volcanic rocks from Ernici (7 KS, 7 HKS). Sample selection for Roccamonfina and Ernici was based on freshness, variety, and geographic location. Major and trace element analyses of whole rock powders were conducted by Activation Laboratories Ltd. in Ancaster, Ontario using ICP, ICP-MS, INAA, PGNA, and ISE techniques (see Appendix F for sample preparation methods). A summary of analytical methods and detection limits for each element can be found in Appendix G.

7.2 Major element geochemistry

7.2a Western Alps

Lamprophyres from the Western Alps are extremely variable in major element geochemistry. The samples are ultrabasic to intermediate in composition, with SiO₂ contents that vary from 43.69 to 54.30 wt% (Table 7.1). Most of the lamprophyres have SiO₂ contents that are close to that of an "average lamprophyre", based on 1590 analyses from world-wide minettes, spessartites, kersantites, and vogesites (Rock, 1991). The

Sample	Minette WA 100	Spessartite WA 101	Minette WA 102	Spessartite WA 103	Minette WA 104	Minette WA 105	Kersantite WA 106	Spessartite WA 107	Average lamprophyre¹
SiO₂	54.01	54.30	50.21	51.02	52.30	50.38	43.69	50.22	51.0
TiO₂	0.997	0.988	1.180	0.962	1.250	1.122	1.036	0.637	1.1
Al₂O₃	13.35	16.15	11.45	16.17	11.12	11.74	8.56	10.26	14.0
Fe₂O₃*	7.41	8.12	6.79	7.71	6.04	6.77	7.50	7.95	8.2
MnO	0.131	0.127	0.119	0.120	0.117	0.108	0.125	0.138	0.13
MgO	6.98	5.43	11.88	4.69	8.77	10.87	13.11	16.19	7.0
CaO	6.55	6.78	7.18	7.28	5.29	7.45	7.57	7.52	7.0
Na₂O	1.81	2.95	0.70	3.79	1.13	1.40	0.92	2.23	2.7
K₂O	5.65	2.58	7.18	1.50	9.21	6.58	5.35	0.37	3.1
P₂O₅	1.00	0.40	1.29	0.31	1.43	1.10	1.56	0.14	0.6
LOI	1.64	2.27	2.10	5.21	1.59	1.90	9.46	3.02	2.0
Total	99.53	100.10	100.08	98.76	98.25	99.42	98.88	98.68	99.3
Mg#	74.2	67.1	84.2	65.0	81.6	83.0	84.2	86.1	75.0

Table 7.1. Major element geochemistry of the Western Alps lamprophyres. *Fe₂O₃ is total Fe. ¹Average lamprophyre is from a compilation of 1590 minettes, spessartites, kersantites, and vogesites by Rock (1991).

spessartites have slightly higher average SiO_2 and Al_2O_3 contents than the minettes, perhaps as a result of the alteration of calcic amphiboles to silica-rich varieties such as actinolite. The kersantite (sample WA 106), which contains no pyroxene, amphibole, or alkali feldspar, has the lowest SiO_2 and Al_2O_3 contents. Loss on ignition (LOI) for all the samples shows a large variation from 1.59 to 9.46 wt%, typical of volatile-rich lamprophyres. The highest LOI value is from the kersantite (WA 106), which contains a high percentage of dolomite in the groundmass (~15-20 vol.%). The high LOI of many of the samples, as well as their variable degrees of alteration, precludes the use of the standard total alkalis-silica (TAS) diagram, which should only be used for fresh rocks with $\text{H}_2\text{O}^+ < 2\%$ and $\text{CO}_2 < 0.5\%$ (Le Maitre et al., 2002).

The high and variable MgO concentrations in the lamprophyres range from 16.19 wt% in spessartite sample WA 107 to 4.69 wt% in spessartite sample WA 103. The high MgO content of spessartite WA 107 is typical of olivine-rich picrites, although there is no fresh olivine in the sample. The abundant MgO must therefore be contained in the magnesiohastingsite phenocrysts and alteration minerals such as chlorite and talc. The Mg#'s for the lamprophyres range from 65 to 86, and are calculated as $\text{Mg}/(\text{Mg}+\text{Fe}^{2+})$ where $\text{Fe}^{3+}/\text{Fe}_{\text{total}}$ is estimated at 0.35 based on typical values for lamprophyres (Rock, 1991). Most of the lamprophyres from the Western Alps have higher MgO contents and Mg#'s than those of average lamprophyres (Rock, 1991). No correlation is seen for MgO vs. SiO_2 , or Fe_{total} vs. SiO_2 , which suggests that the lamprophyres as a group are not related by simple crystal fractionation.

The spessartites are sodic in composition ($\text{K}_2\text{O}/\text{Na}_2\text{O} < 1$), while the minettes and kersantite are ultrapotassic using the criteria $\text{K}_2\text{O} > 3$ wt.%, molar $\text{K}_2\text{O}/\text{Na}_2\text{O} > 2$, and

MgO > 3 wt.% (Foley et al. 1987). The spessartites contain more than twice the Na₂O of the minettes (average values are 2.99 wt% and 1.26 wt% respectively), which is reflected in the high albite content of the spessartites. Conversely, K₂O is much more abundant in the minettes (average 7.16 wt%) than the spessartites (1.48 wt%). The kersantite also contains high K₂O, most of which is likely contained within phlogopite phenocrysts. The K₂O contents of the minettes (5.65 – 9.21 wt%) and kersantite (5.35 wt%) from the Western Alps are much higher than the amount of K₂O in an average lamprophyre (3.1 wt%). The ultrapotassic composition of these samples set them apart from world-wide lamprophyres, which are closer in composition to more common calc-alkaline or shoshonitic rock types.

Compared to other mafic dykes of the Tertiary Periadriatic Province, the lamprophyres from the Western Alps have a much wider range of major element compositions. Figure 7.1 shows a plot of K₂O vs. SiO₂ for dykes from both the present study and from von Blanckenburg and Davies (1995). Data from the Western Alps spessartites plot within the calc-alkaline and tholeiitic fields (K₂O < 3 wt.%), and are similar to many of the Periadriatic dykes. Minette samples from the Western Alps have higher K₂O contents than most other mafic dykes, and plot in the shoshonitic to ultrapotassic fields. Minette WA 104, in particular, has one of the highest K₂O contents found in any of the Alpine dykes (9.21 wt%). Potassium contents in this range are more typical of lamproites than lamprophyres (Rock, 1991). The kersantite WA 106 has the highest K₂O content of any Alpine dyke with < 45 wt% SiO₂. The ultrapotassic nature of the minette and kersantite samples agrees with previous work by Beccaluva et al. (1983), who observed that dykes of the Tertiary Periadriatic Province change gradually from

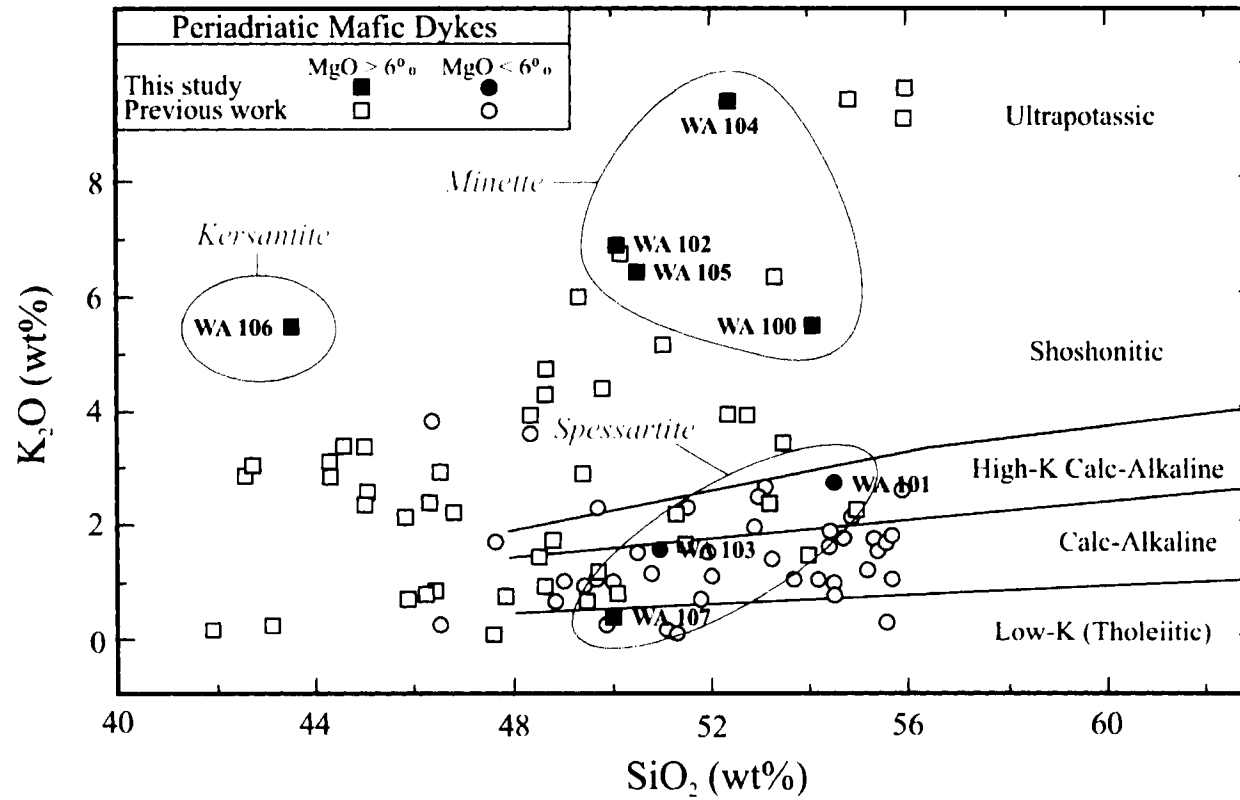


Figure 7.1. K_2O vs. SiO_2 (wt %) for mafic dykes along the Periadriatic Line in the Alps (modified from von Blanckenburg and Davies, 1995). Data fields for the minettes, spessartites, and kersantite from the Western Alps are highlighted. The spessartites are the most altered, and have the lowest K_2O contents.

tholeiitic/calc-alkaline in the Southeastern Alps, through high-K calc-alkaline in the Central Alps, to shoshonitic and ultrapotassic in the Western Alps.

7.2b Roccamonfina

Volcanic rocks from the KS series at Roccamonfina contain < 5 wt% K_2O , while rocks from the HKS series contain > 5 wt% K_2O (Table 7.2a). The HKS rocks have an average value of 8.02 wt% K_2O , while KS rocks contain an average of 3.57 wt%. This difference is reflected in the presence of leucite phenocrysts in rocks of the HKS series. The average K_2O content of the HKS rocks at Roccamonfina is much higher than similar leucite-bearing volcanic rocks from the alkaline series in the Sunda arc, Indonesia (Edwards et al., 1993). The HKS rocks from Roccamonfina have K_2O contents that are among the highest recorded for world-wide volcanic rocks, and reach a maximum of 10.67 wt% in this study (sample RC 100). K_2O and Na_2O show very different behavior, given that Na_2O contents from the KS and HKS series are nearly identical (1.85 – 3.18 wt%). All analyzed samples from the KS series have K_2O/Na_2O between 1 and 2, while all samples from the HKS series have $K_2O/Na_2O > 2$.

Samples from Roccamonfina range from basic to intermediate in silica content (49 – 57 wt% SiO_2), and there is little difference in SiO_2 between rocks of the KS and HKS series. The volcanic rocks from Roccamonfina can be classified based on their SiO_2 and total alkali contents using the TAS diagram (Figure 7.2). Rocks of the KS series include high-K basaltic andesite, potassic trachybasalt, shoshonite, and latite (all samples have $Na_2O - 2.0 < K_2O$). The HKS rocks include phonotephrite and tephriphonolite (see Appendix I for further subdivisions of areas A, B, and C based on

Table 7.2a Roccamonfina

Sample	RC 100	RC 103	RC 104	RC 106	RC 107	RC 109	RC 110	RC 111	RC 113	RC 118	RC 119	RC 121	RC 123	RC 127
SiO ₂	51.67	49.10	51.01	57.22	53.30	50.02	54.72	50.41	55.44	49.82	51.47	52.73	50.18	52.94
Al ₂ O ₃	20.71	19.30	16.04	18.12	18.40	18.01	16.92	16.94	19.55	19.43	17.86	18.36	18.78	16.59
Fe ₂ O ₃ *	5.90	8.45	7.87	6.45	8.56	8.60	6.50	9.08	5.24	8.05	7.66	7.73	7.81	8.39
MnO	0.120	0.163	0.151	0.135	0.149	0.157	0.143	0.144	0.119	0.152	0.147	0.151	0.142	0.144
MgO	1.82	2.62	6.95	2.72	4.36	4.00	4.89	6.42	1.40	2.90	3.80	3.82	3.64	5.94
CaO	5.26	7.70	9.92	6.58	8.65	9.33	8.56	10.06	4.88	7.44	6.33	7.61	7.97	9.88
Na ₂ O	2.28	2.47	1.95	3.18	2.15	2.38	2.84	1.85	3.20	2.51	2.64	2.78	2.08	1.92
K ₂ O	10.67	8.14	3.12	4.53	3.05	5.76	4.28	3.20	8.98	7.63	3.86	3.75	6.94	2.73
TiO ₂	0.605	0.816	0.778	0.684	0.812	0.896	0.679	0.958	0.561	0.795	0.789	0.797	0.775	0.762
P ₂ O ₅	0.39	0.52	0.25	0.26	0.26	0.41	0.20	0.30	0.25	0.47	0.30	0.31	0.45	0.23
LOI	0.61	0.63	1.16	0.33	0.10	0.24	0.27	0.50	0.31	0.72	3.98	2.03	1.51	0.20
Total	100.03	99.91	99.19	100.21	99.78	99.79	100.01	99.86	99.92	99.92	98.84	100.05	100.27	99.72
Mg #	50.4	48.6	72.9	58.2	59.0	58.7	69.7	66.7	47.0	52.4	60.2	60.1	58.7	66.7

Table 7.2b Ernici

Sample	ER 101	ER 104	ER 105	ER 107	ER 109	ER 110	ER 112	ER 114	ER 115	ER 116	ER 117	ER 118	ER 121	ER 122
SiO ₂	48.81	47.30	47.08	46.87	49.05	46.51	47.37	48.56	46.49	48.41	46.95	47.87	48.94	47.07
Al ₂ O ₃	17.18	16.23	15.68	15.50	17.88	15.14	14.53	14.30	16.01	14.35	15.52	15.96	13.01	15.22
Fe ₂ O ₃ *	7.59	7.76	8.20	8.38	8.54	8.74	9.45	8.37	8.26	9.61	7.82	8.17	8.53	10.28
MnO	0.146	0.146	0.150	0.152	0.148	0.154	0.163	0.149	0.144	0.160	0.139	0.147	0.153	0.172
MgO	4.63	5.62	6.35	6.65	5.60	4.80	8.34	8.24	6.13	7.83	5.76	5.93	9.60	8.34
CaO	10.50	11.84	11.95	12.26	10.90	9.97	14.48	13.48	12.34	14.40	12.56	11.61	14.26	14.02
Na ₂ O	2.45	1.91	1.97	1.86	3.99	1.68	1.72	2.27	1.37	2.49	3.76	2.01	3.03	1.55
K ₂ O	6.65	7.04	6.45	6.59	1.22	8.82	0.68	2.73	6.71	0.36	1.05	6.51	0.49	0.45
TiO ₂	0.864	0.852	0.860	0.870	1.120	1.067	0.875	0.828	0.971	0.909	0.858	0.843	0.805	0.970
P ₂ O ₅	0.38	0.44	0.41	0.43	0.35	1.00	0.21	0.25	0.49	0.22	0.41	0.45	0.23	0.22
LOI	0.90	0.89	1.08	0.67	1.58	1.77	1.92	0.80	1.10	1.55	4.83	0.49	0.70	1.61
Total	100.10	100.02	100.17	100.23	100.38	99.64	99.73	99.97	100.01	100.29	99.64	100.00	99.74	99.92
Mg #	65.0	68.8	70.2	70.8	65.0	62.6	68.6	73.6	67.8	66.8	67.6	68.9	73.6	66.8

Tables 7.2.a and 7.2.b Major element geochemistry for samples from Roccamonfina and Ernici. *Fe₂O₃ is total Fe.

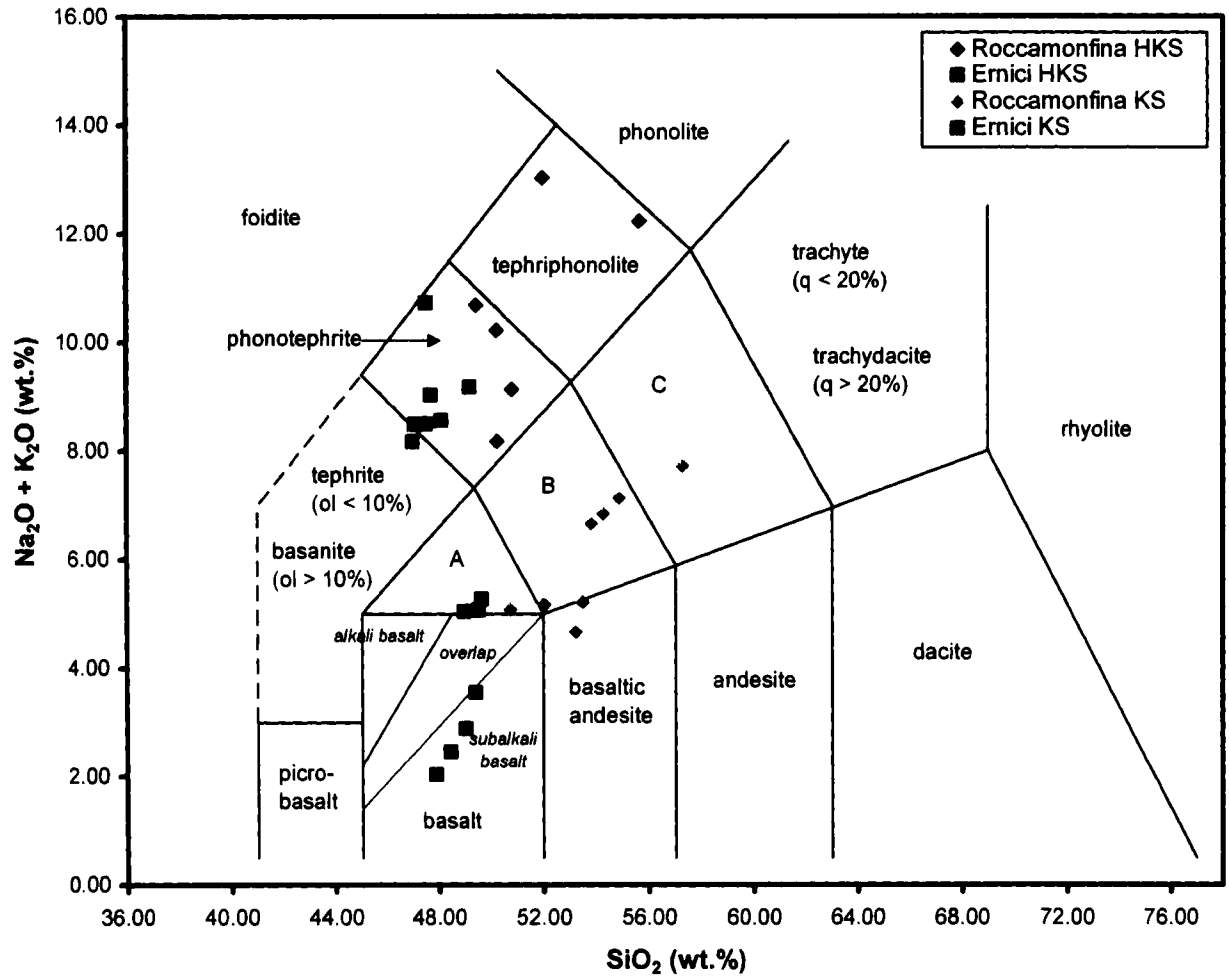


Figure 7.2. Total alkalis-silica (TAS) diagram for analyzed KS and HKS samples from Roccamonfina and Ernici (see Appendix H for subdivisions of fields A, B, and C). All analyses were recalculated to 100% on an H_2O - and CO_2 -free basis. See section 7.2c for discussion of alkali basalt, subalkali basalt, and overlap fields.

Na₂O and K₂O content). Because the Na₂O contents of rocks from the KS and HKS series are similar, the total alkali content in Figure 7.2 primarily reflects the difference in K₂O between the two series.

In addition to K₂O, the major oxides CaO, MgO, and Al₂O₃ show systematic differences between the KS and HKS series. The KS rocks from Roccamonfina have slightly higher CaO and MgO contents compared to the HKS rocks. CaO ranges from about 6 to 10 wt% (average = 8.45 wt%) in the KS rocks and from 5 to 9 wt% (average = 7.10 wt%) in the HKS rocks, while MgO averages 4.86 wt% in the KS and 2.73 wt% in the HKS rocks. Several samples from the HKS series at Roccamonfina have MgO contents < 3 wt%, which excludes them from being classified as ultrapotassic according to the criteria of Foley et al. (1987). The Mg#s of volcanic rocks from Roccamonfina range from 47 to 73, and are higher in the KS series (average = 64) than the HKS series (average = 53). Al₂O₃ ranges from about 16 to 18 wt% (average = 17.40 wt%) in rocks of the KS series and from 18 to 21 wt% (average 19.30 wt%) in those from the HKS series. These values are high for volcanic rocks and are similar to high-alumina calc-alkaline basalts and andesites. There is little difference between the average TiO₂, MnO, P₂O₅ and total Fe contents of the KS and HKS series at Roccamonfina.

7.2c Ernici

Volcanic rocks from the KS series at Ernici contain < 5 wt% K₂O, while those from the HKS series contain > 5 wt% K₂O (Table 7.2b). The average K₂O value for the HKS rocks at Ernici is 6.97 wt%, while the KS rocks average 1.00 wt% K₂O. The low K₂O of many of the KS samples is less than most world-wide, potassic volcanic rocks,

that are typically in the range of 2-3 wt% K_2O (Peccerillo, 1992). In fact, almost all of the KS samples from Ernici have $Na_2O > K_2O$, which makes them sodic rather than potassic. The relatively high Na_2O and low K_2O contents of the KS rocks are reflected in the presence of Na-rich plagioclase feldspar and absence of leucite. The HKS samples have $K_2O/Na_2O > 2$, consistent with the definition of ultrapotassic volcanic rocks (Foley et al., 1987).

The KS and HKS samples from Ernici all have low silica contents (46 – 49 wt% SiO_2) and can be described as basic. The SiO_2 (wt%) and alkali (K_2O+Na_2O wt%) contents of volcanic rocks from Ernici are shown in Figure 7.2. The HKS rocks are classified as phonotephrite and tephrite, while the KS rocks include potassic trachybasalt, hawaiite, and basalt. Potassic trachybasalt refers to rocks that have $Na_2O - 2.0 \leq K_2O$ in field A on Figure 7.2, while hawaiite is the name used for rocks in the same field that have $Na_2O - 2.0 \geq K_2O$. The KS samples ER 109 and ER 117, which contain abundant analcime and have high Na_2O contents (average 4.00 wt%), are tentatively classified as hawaiite in this study.

The KS basalts can be further divided into alkali basalt or subalkali basalt according to their degree of silica saturation. An alkali basalt is silica-undersaturated and contains nepheline in the CIPW norm, while a subalkali basalt does not (Le Maitre et al., 2002). Sample ER 121 contains a small percentage of nepheline in the CIPW norm (see section 7.2e), and lies on the dividing line between the subalkali basalt field and the overlap field (see Figure 7.2). The overlap field is necessary because the undersaturation plane in the basalt tetrahedron of Yoder and Tilley (1962) consists of various planar surfaces (one for each normative type), none of which is perpendicular to the TAS

surface. Therefore, an exact correlation between the TAS diagram and the degree of silica saturation can never be achieved (Le Maitre et al., 2002). The presence of nepheline in the CIPW norm of sample ER 121, and its position on the subalkali-overlap dividing line, defines this sample as an alkali basalt.

The remaining three basalt samples are classified as subalkali basalts, a group that contains a number of varieties of basalt including calc-alkali basalt, mid-ocean ridge basalt, tholeiitic basalt, and transitional basalt. Although none of these varieties have been chemically defined by the IUGS Subcommittee on the Systematics of Igneous Rocks, members of the tholeiitic and calc-alkaline series can be differentiated by their Al_2O_3 content (Wilson, 1989). Calc-alkaline basalts contain 16 – 20 wt% Al_2O_3 , whereas their tholeiitic counterparts typically contain 12 – 16 wt%. A plot of Alkali Index (A.I. = $(\text{Na}_2\text{O} + \text{K}_2\text{O}) / (\text{SiO}_2 - 43) * 0.17$) versus Al_2O_3 wt% can be used to distinguish between tholeiitic and calc-alkaline basalts (Middlemost, 1975) (Figure 7.3). All subalkali basalts from Ernici plot within the tholeiitic field. The subalkali basalts can be further subdivided into low-K, medium-K, and high-K fields (Peccerillo and Taylor, 1976; Le Maitre et al., 2002). It should be noted that high-K is not synonymous with potassic, as high-K rocks can have more Na_2O than K_2O . All subalkali basalt samples from Ernici are classified as medium-K, tholeiitic basalts (Figure 7.4).

Small differences in the CaO, MgO, and Al_2O_3 contents of samples from the KS and HKS series are present at Ernici. The CaO and MgO contents of rocks from the KS series are higher than those of the HKS series. CaO ranges from about 11 to 14 wt% in the KS rocks (average = 13.44 wt%) and from 10 to 12 wt% (average = 11.50 wt%) in the HKS rocks. These values are very high for mafic volcanic rocks, and are similar to

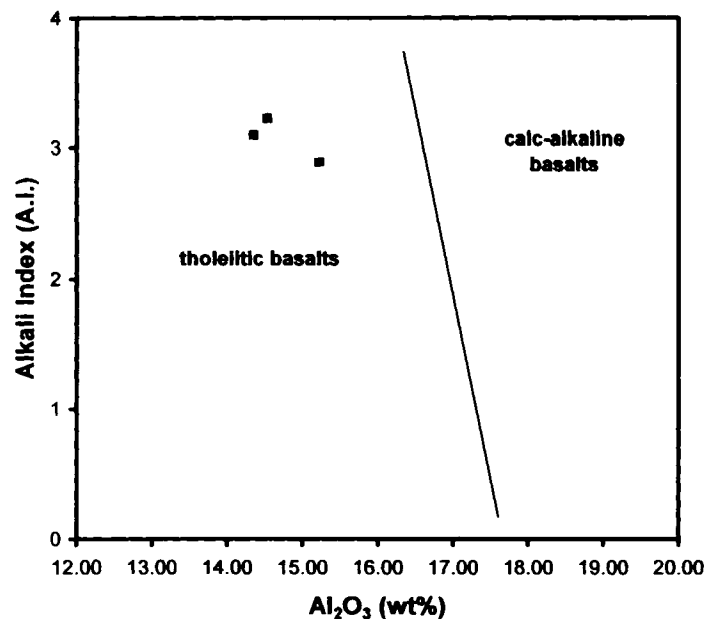


Figure 7.3. Plot of Alkali Index (A.I.) versus Al₂O₃ (wt%) for subalkali basalt samples ER 112, ER 116, and ER 122 from Ernici (Middlemost, 1975).
 $A.I. = (Na_2O + K_2O) / (SiO_2 - 43) * 0.17$

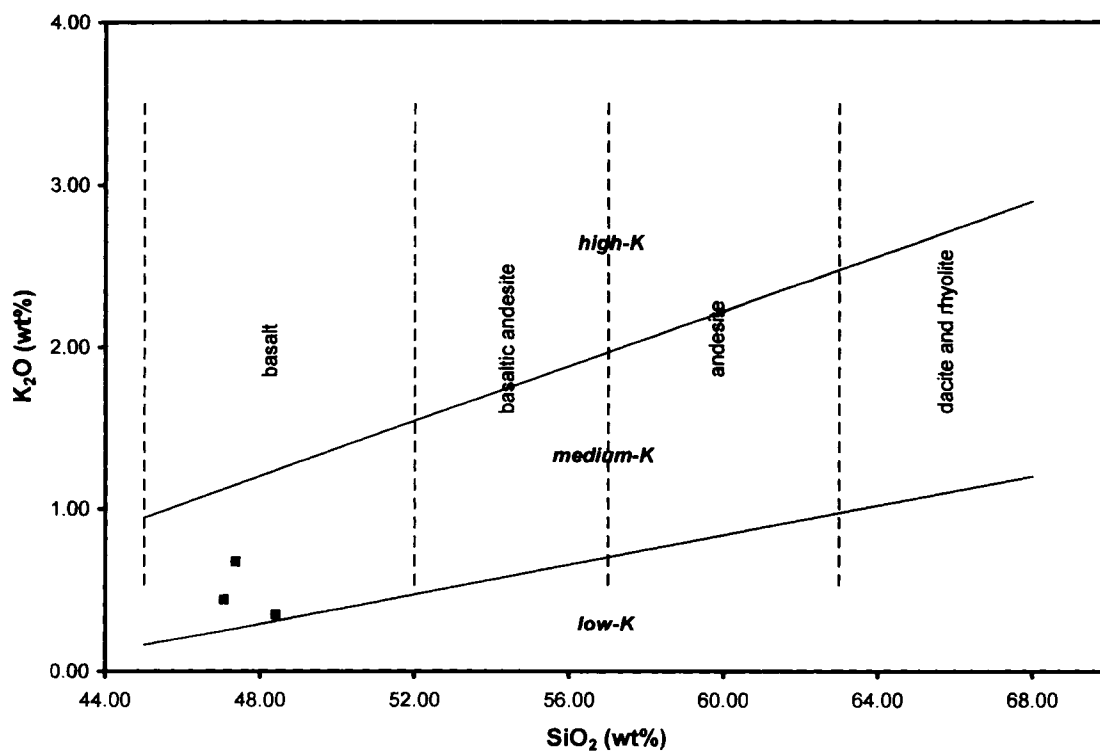


Figure 7.4. Division of the basalt-rhyolite series into low-K, medium-K, and high-K types (Le Maitre et al., 2002; simplified and modified after Peccerillo and Taylor, 1976).

alkaline rocks from the East African Rift (Davies and Lloyd, 1988) and Tristan da Cunha (Baker et al., 1984). MgO averages 7.67 wt% in the KS series at Ernici, and 5.73 wt% in the HKS series. All samples from Ernici have MgO > 3 wt%, and therefore all samples from the HKS series can be considered ultrapotassic rocks (Foley et al., 1987). Mg#s range from 62 to 73, and are nearly identical in rocks of the KS series (average = 69) and HKS series (average = 68). Al₂O₃ is slightly higher on average in rocks of the HKS series, ranging from 13 to 18 wt% in the KS (average = 14.97 wt%), and from 15 to 17 wt% in the HKS (average = 15.96 wt%). The average TiO₂, MnO, P₂O₅ and total Fe contents of both the KS and HKS series at Ernici are similar.

7.2d Comparison between Roccamonfina and Ernici

The most significant differences in major element geochemistry between the volcanic rocks of Roccamonfina and Ernici are: 1) higher SiO₂ and Al₂O₃ at Roccamonfina, 2) higher MgO and CaO at Ernici, and 3) higher K₂O in both the KS and HKS series at Roccamonfina. These differences are highlighted in a series of Harker diagrams (Figures 7.5a – 7.5d). Separation between the KS and HKS at both volcanic centres is clearly seen on a plot of K₂O vs. SiO₂ (Fig. 7.5a). This figure shows the higher and somewhat more variable SiO₂ contents of samples from Roccamonfina, and the large differences in K₂O between the KS and HKS series at both Ernici and Roccamonfina. The K₂O contents of rocks from the HKS series are similar at both Roccamonfina and Ernici, but the K₂O content of most KS samples from Ernici are notably lower than the KS samples from Roccamonfina. Most of the KS rocks from Ernici have K₂O < 1.5 wt%, while the lowest K₂O value in a KS rock from Roccamonfina is 2.73 wt%.

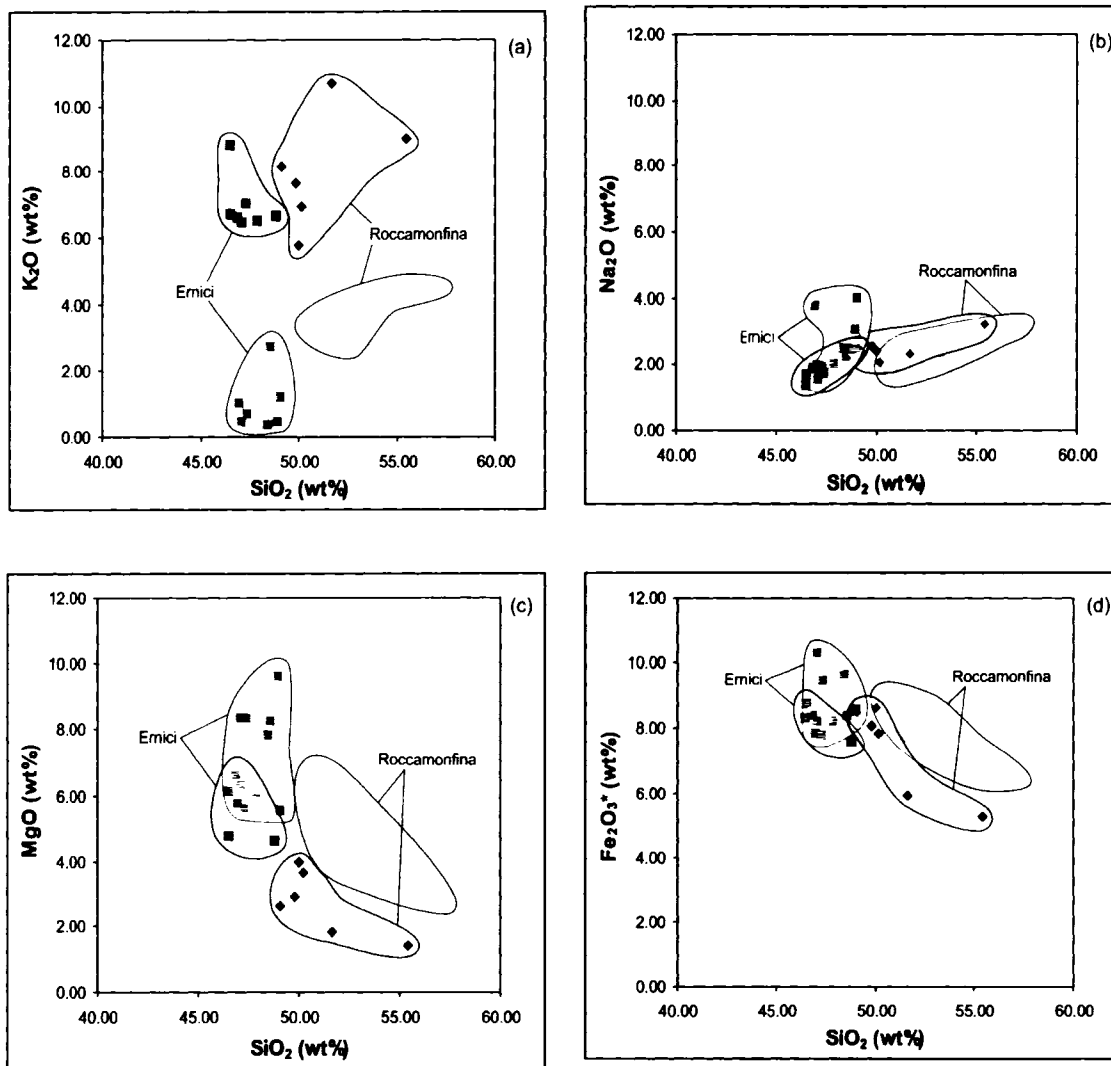


Figure 7.5.a. K₂O vs. SiO₂ Harker diagram for samples from Roccamonfina and Ernici.
Figure 7.5.b. Na₂O vs. SiO₂ Harker diagram for samples from Roccamonfina and Ernici.
Figure 7.5.c. MgO vs. SiO₂ Harker diagram for samples from Roccamonfina and Ernici.
Figure 7.5.d. Fe_{total} (FeO+Fe₂O₃) vs. SiO₂ Harker diagram for samples from Roccamonfina and Ernici.

□ = KS volcanics □ = HKS volcanics

Symbols are the same as those used in Figure 7.2.

Figure 7.5b demonstrates that the Na_2O contents of the KS and HKS rocks at Roccamonfina and Ernici are similar, with most values between about 1.5 and 3.0 wt%. Although there are no sodic rocks at Roccamonfina (all samples have $\text{K}_2\text{O}/\text{Na}_2\text{O} > 1$), most members of the KS series at Ernici have $\text{K}_2\text{O}/\text{Na}_2\text{O} < 1$. The low $\text{K}_2\text{O}/\text{Na}_2\text{O}$ ratios of the Ernici KS series reflect the low K_2O contents of the samples, rather than high Na_2O contents.

Figures 7.5c and 7.5d show that the MgO and Fe_{total} ($\text{FeO} + \text{Fe}_2\text{O}_3$) are highest in the KS series of Ernici, and lowest in the HKS series of Roccamonfina. Rocks of the HKS series at both Ernici and Roccamonfina contain lower MgO and lower Fe_{total} than the KS series at each centre. The negative correlation between MgO (and Fe_{total}) and SiO_2 for samples from Roccamonfina suggests that crystal fractionation of olivine and/or pyroxene may have played a role in the evolution of more silica-rich samples. This agrees with previous work by Appleton (1972) and Giannetti and Ellam (1994) (see Chapter 5). Similar fractionation trends are not observed in the data from Ernici.

One of the principal major element characteristics of volcanic rocks from central-southern Italy is the high Al_2O_3 content of rocks from both the KS and HKS series. Figure 7.6 shows a plot of SiO_2 vs. $(\text{Na}_2\text{O} + \text{K}_2\text{O})/\text{Al}_2\text{O}_3$ for the samples from Roccamonfina and Ernici, as well as Tuscan lamproites, the Sisco lamproite, and Italian kamafugites (Conticelli and Peccerillo, 1992). The $(\text{Na}_2\text{O} + \text{K}_2\text{O})/\text{Al}_2\text{O}_3$ ratio is a measure of the peralkalinity of a rock, whereby an excess of alkalis ($\text{Na}_2\text{O} + \text{K}_2\text{O} > \text{Al}_2\text{O}_3$) will lead to the formation of alkali-bearing minerals such as feldspar, nepheline, leucite, melilite, or kalsilite. The Sisco lamproite and the kamafugites have $\text{Na}_2\text{O} + \text{K}_2\text{O} > \text{Al}_2\text{O}_3$, indicating that these rocks are peralkaline, while the Tuscan lamproites have

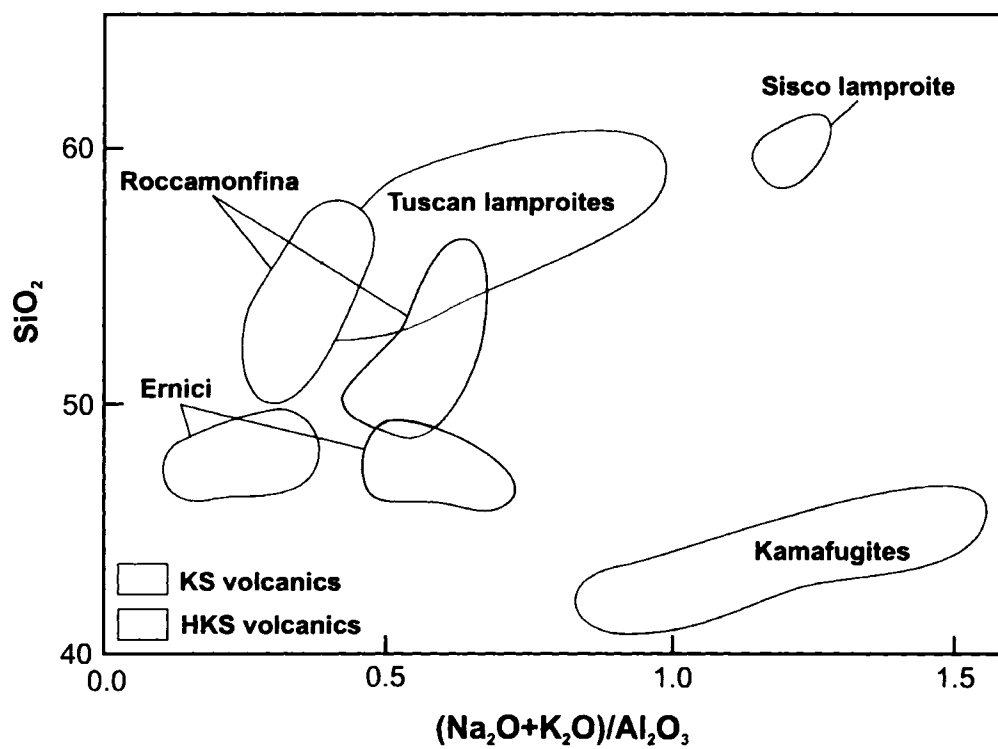


Figure 7.6. Comparison of data from KS and HKS volcanic rocks from Roccamonfina and Ernici with Tuscan lamproites, the Sisco lamproite, and Italian kamafugites (modified from Conticelli and Peccerillo, 1992).

$\text{Na}_2\text{O} + \text{K}_2\text{O} < \text{Al}_2\text{O}_3$. The Tuscan lamproites are unusually rich in Al_2O_3 compared to world-wide lamproites (Foley, 1992), and overlap with data from Roccamonfina on Figure 7.6. This reflects both the relatively high SiO_2 contents (>53 wt%) of the Tuscan lamproites and rocks from Roccamonfina, and the Al_2O_3 -rich nature (up to 21 wt%) of the KS and HKS rock series.

Figure 7.6 also shows that samples from Ernici have lower SiO_2 contents than those from Roccamonfina, but similar degrees of peralkalinity. The range of SiO_2 in volcanic rocks from Ernici is less than that from Roccamonfina, although this could simply be a result of sampling bias. As expected, rocks from the HKS series from both centres have higher $\text{Na}_2\text{O} + \text{K}_2\text{O} / \text{Al}_2\text{O}_3$ ratios than rocks from the KS series. The higher peralkalinity of the HKS series results from the large increase in K_2O between the KS and HKS series.

7.2e CIPW normative compositions of samples from Roccamonfina and Ernici

Normative calculations are used to help determine the degree of silica- or aluminum-saturation of a fine-grained or glassy volcanic rock. The reasons for calculating the CIPW norms for samples from Ernici and Roccamonfina are to:

1) classify basalts as alkali or subalkali (see section 7.2c), 2) compare the KS and HKS rocks from Ernici and Roccamonfina to Italian kamafugites, lamproites, and transitional KS-lamproites as in Figure 3.2, and 3) examine differences in silica saturation between the KS and HKS series.

CIPW norms were calculated using the Excel program written by Kurt Hollocher (Union College, Schenectady, NY), based on the work of Johannsen (1931). It is

important to note that CIPW norm calculations assume that the magma is anhydrous, thus minerals such as mica or amphibole are not permitted. Therefore, the results of the CIPW norm calculation provide only a hypothetical mineral assemblage based on weight percents of idealized end-members. Estimated oxidation ratios used in the norm calculations were based on rock type using $\text{Fe}_2\text{O}_3/\text{FeO}$ ratios recommended by Middlemost (1989). CIPW norms were not calculated for the volatile-rich lamprophyres from the Western Alps, as amphibole and/or mica make up a major component of these rocks.

Results of the CIPW norm calculations show that rocks of the HKS series at Ernici are more silica-undersaturated than those of the HKS series at Roccamonfina (see Appendix I). Rocks from the Ernici HKS series contain up to 70% normative feldspathoids (nepheline and/or leucite), while rocks from the Roccamonfina HKS series contain < 35% feldspathoids. In fact, the HKS of Roccamonfina and the KS of Ernici have similar degrees of silica-undersaturation, and are distinguished from one another mainly by the high normative plagioclase/alkali feldspar ratio of the Ernici KS rocks. In addition, the CIPW norms show that the KS rocks from both volcanic centres contain more normative plagioclase than the HKS rocks, and the KS of Roccamonfina is the only series that is slightly silica-oversaturated. Several KS samples from Roccamonfina and Ernici are hypersthene-normative. Besides the main silicate rock-forming minerals (quartz, feldspars, feldspathoids, pyroxene, and olivine), ilmenite, magnetite, apatite, and calcite are present in the norms of most samples. Overall, the CIPW norm calculations indicate that volcanic rocks from Ernici are more silica-undersaturated than those from Roccamonfina.

7.3 Degree of mantle fertility in the Western Alps and central-southern Italy based on major element geochemistry

Magmatic rocks with K_2O contents similar to those of samples from the Western Alps, Roccamonfina, and Ernici, are found in both convergent margin and rift-related environments (see Chapter 1). However, rocks associated with these two distinct tectonic settings are characterized by different abundances of Fe_2O_3 , TiO_2 , CaO , Na_2O and Al_2O_3 , elements that can be used to indicate the degree of fertility of a mantle source. Fertile mantle (lherzolite) has the capacity to generate basaltic magmas, whereas depleted mantle (harzburgite, dunite) has undergone previous partial melting of garnet or spinel and clinopyroxene, leaving a residuum depleted in Fe, Ti, Ca, Na and Al. The asthenospheric upper mantle source of MORB has been depleted by continuous extraction of basaltic magma throughout geologic time, while the Fe_2O_3 , TiO_2 , CaO , Na_2O , and Al_2O_3 contents of intraplate magmas are commonly enriched relative to MORB (Wilson, 1989).

Figure 7.7 shows the Fe_2O_3 and TiO_2 contents of lamprophyres from the Western Alps and volcanic rocks from Roccamonfina and Ernici compared to Tuscan lamproites, kamafugites, MORB, continental intraplate rocks from the East African Rift (Rogers et al. 1992), and oceanic intraplate rocks from Tristan da Cunha (le Roex et al., 1990). The Fe_2O_3 and TiO_2 contents of all the Italian magmatic rocks, including lamproites and kamafugites, are depleted relative to intraplate rocks from the East African Rift and Tristan da Cunha. The TiO_2 contents of Italian rocks range from about 0.5 to 1.8 wt%, while those of continental and oceanic intraplate potassic rocks range from 1.9 to 4.5 wt%. In addition, Fe_2O_3 is < 10 wt% in Italian rocks, and > 10 wt% in rocks from the

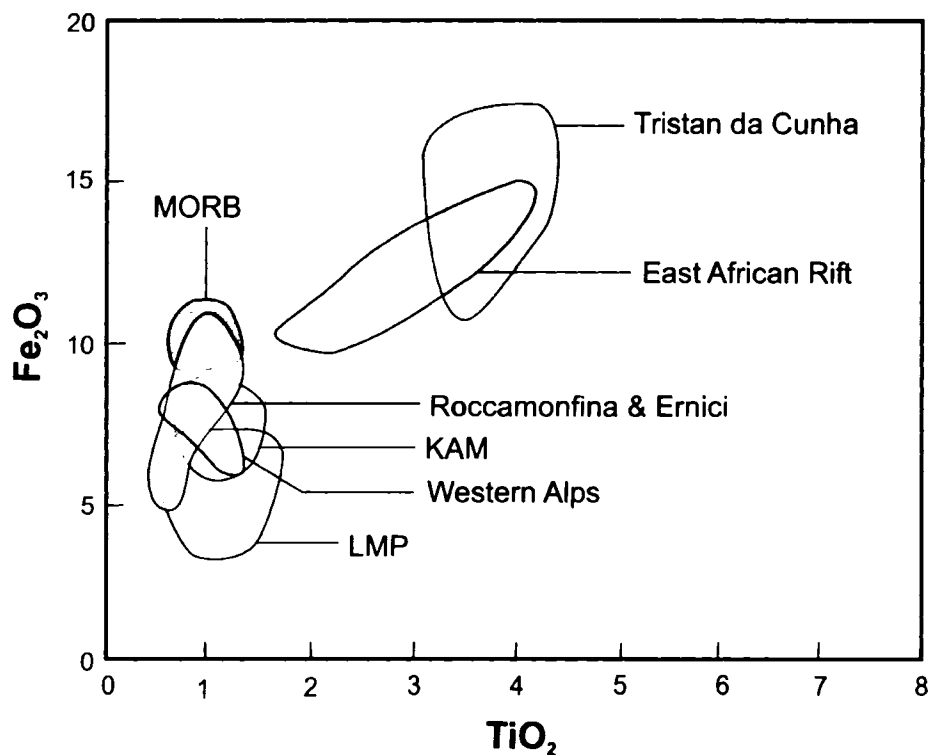
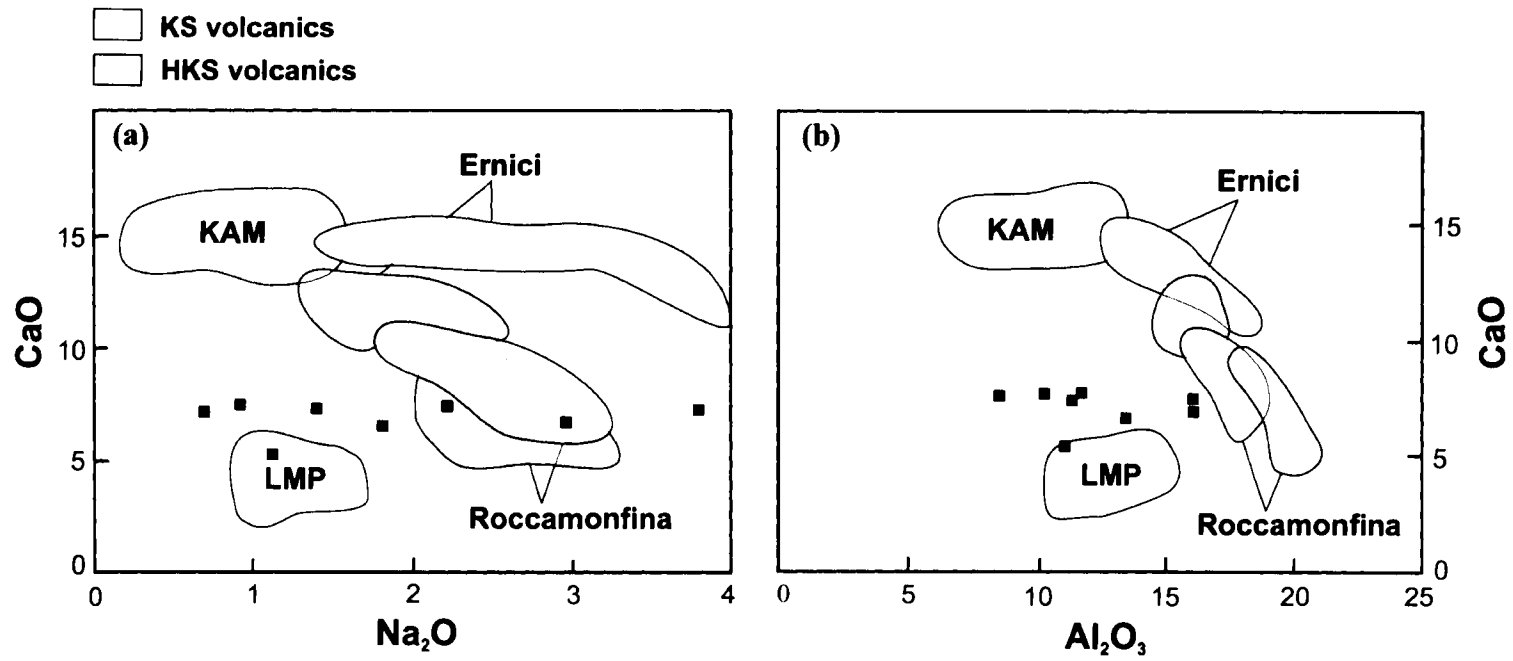


Figure 7.7. Comparison of data from rocks of Roccamonfina, Ernici, and the Western Alps with Tuscan lamproites (LMP), Italian kamafugites (KAM), MORB glasses, and intraplate mafic potassic/ultrapotassic rocks from Tristan da Cunha (le Roex et al., 1990) and the East African Rift (Rogers et al. 1992). Note that $\text{Fe}_2\text{O}_3 = \text{Fe}_{\text{total}}$. Modified from Conticelli et al. (2004).

East African Rift and Tristan da Cunha. The low Fe_2O_3 and TiO_2 contents of the Italian rocks suggest a depleted mantle similar to the source of MORB, i.e. less fertile than the source of typical intraplate magmas.

Compared to other Italian ultrapotassic rock types (lamproites and kamafugites), the KS and HKS rocks from Roccamonfina and Ernici have high Na_2O (1.5-4.0 wt%), high Al_2O_3 (12-21 wt%), and a wide range of CaO (5-15 wt%) contents (Figures 7.8a and 7.8b). The lamproites and kamafugites both contain low abundances of Na_2O and Al_2O_3 characteristic of magmas derived from an upper mantle depleted by previous partial melting (Peccerillo et al., 1988; Conticelli and Peccerillo, 1992). The unusually high CaO contents (13-17 wt%) of the kamafugites have been attributed to assimilation of sedimentary carbonates (Peccerillo, 1998) or interaction with a carbonatitic melt (Stoppa and Cundari, 1995). In contrast to the volcanic rocks from Roccamonfina and Ernici, the lamprophyres from the Western Alps have variable Na_2O , low Al_2O_3 , and a remarkably constant, low CaO value of ~ 7.5 wt%.

The relatively high CaO , Na_2O , and Al_2O_3 contents of samples from Roccamonfina and Ernici provide evidence for magma generation in a mantle more fertile than the source of Italian lamproites or kamafugites. However, the low Fe_2O_3 and TiO_2 contents of all Italian magmatic rocks compared to typical intraplate rocks suggest derivation from a depleted mantle. Overall, the major element chemistry suggests that the Italian mantle has undergone variable degrees of depletion, with the sources of the lamproites and kamafugites the most depleted, and the source of the KS and HKS rocks in central-southern Italy somewhat less depleted. The low Fe_2O_3 , TiO_2 , Al_2O_3 , CaO , and



Figures 7.8a and 7.8.b. Comparison of data from KS and HKS volcanic rocks of Roccamonfina and Ernici with that of Tuscan lamproites (LMP) and Italian kamafugites (KAM) (modified from Peccerillo and Panza, 1999). Data from the Western Alps lamprophyres are plotted as solid squares.

variable Na₂O contents of the lamprophyres from the Western Alps are consistent with partial melting of a depleted mantle source.

7.4 Trace element geochemistry

7.4a Introduction

The trace element geochemistry of samples from the Western Alps, Roccamonfina, and Ernici will be discussed in terms of compatible elements (preferentially retained in residual solids during partial melting) and incompatible elements (concentrated in the liquid phase during partial melting). Incompatible elements can be further sub-divided into the large ion lithophile elements (LILE), which have an ionic potential less than 2.0, and the high field strength elements (HFSE), which are small, highly charged cations with ionic potential greater than 2.0 (Rollinson, 1993). LILE include Rb, Ba, Sr, and Eu, while HFSE include Th, Zr, Hf, Nb, Ta, and the REE.

REE data are normalized to average chondritic values, using data from Nakamura (1974) and values for Pr, Tb, Ho, and Tm from Haskin et al. (1968). Chondrite normalizing values are also used in extended incompatible element (spider) diagrams in order to maintain consistency with REE diagrams and to avoid the subjectivity inherent in models of the primitive mantle. Chondritic values are preferred because they are directly measured rather than estimated. Spider diagrams for samples from the Western Alps, Roccamonfina, and Ernici use the element order and chondritic normalizing values of Thompson (1982), who uses the REE data of Nakamura (1974) and Rb, K, and P from the primitive mantle values of Sun (1980).

Europium anomalies (Eu/Eu^*) are calculated by dividing the normalized measured concentration (Eu) by the expected concentration obtained by interpolating between the normalized values of Sm and Gd (Eu^*). The formula is $\text{Eu}/\text{Eu}^* = \text{Eu}_N / \sqrt{[(\text{Sm}_N)^*(\text{Gd}_N)]}$ (Taylor and McLennan, 1985).

7.4b Western Alps

7.4b.i Compatible elements

Compatible elements (Ni, Cr, Co) correlate positively with MgO and are highly variable. Ni ranges from 3 to 449 ppm, Cr from 36.5 to 1030 ppm, and Co from 21.4 to 55.6 ppm (Table 7.3). Primary magmas in equilibrium with a typical four-phase lherzolite should have Ni concentrations >400-500 ppm, and Cr >1000 ppm (Wilson, 1989). Of the samples from the Western Alps, only spessartite WA 107 fits these criteria with 449 ppm Ni and 1030 ppm Cr. Several samples contain Ni > 240 ppm and Cr > 450 ppm, which are very high compared to common tholeiitic, calc-alkaline, and alkaline rock types, but not high enough to be considered primary. Spessartite samples WA 103 and WA 101 have particularly low Ni (3 – 17 ppm) and Cr (36.5 – 149 ppm) contents.

7.4b.ii Incompatible elements

The chondrite-normalized REE patterns for all of the lamprophyres from the Western Alps are broadly similar (Fig. 7.9). The LREE are enriched relative to HREE, and $\text{Ce}/\text{Yb}_{(N)}$ ratios range from 7 to 32. Compared to world-wide ultrapotassic rock types, the highly fractionated $\text{Ce}/\text{Yb}_{(N)}$ ratios of the lamprophyres are similar to those of kamafugites and plagiolecitites, but lower than those of lamproites (Foley et al., 1987).

Sample	Minette WA 100	Spessartite WA 101	Minette WA 102	Spessartite WA 103	Minette WA 104	Minette WA 105	Kersantite WA 106	Spessartite WA 107
Be	11	3	7	2	15	11	7	1
F (%)	0.21	0.13	0.34	0.08	0.46	0.35	0.34	0.12
Cl (%)	0.04	0.02	0.04	0.04	0.03	0.07	0.03	0.02
Sc	30.1	27.2	24.1	25.7	17.1	28.9	33.2	25.9
V	175	185	143	188	112	159	163	135
Cr	309	149	656	36.5	455	594	665	1030
Co	28.1	25.8	40.1	21.4	28.6	36.4	44.8	55.6
Ni	93	17	309	3	290	246	326	449
Cu	32	21	10	16	28	12	39	50
Zn	54	68	77	69	72	52	57	67
Rb	296	96	430	43	506	328	292	5
Sr	830	480	530	551	870	910	680	510
Y	28	24	30	23	40	29	24	15
Zr	378	165	371	144	681	451	236	90
Nb	29.0	12.6	27.8	11.8	42.8	31.0	16.2	5.8
Cs	11.0	1.5	12.4	1.5	8.6	8.4	22.1	0.0
Ba	3740	1200	3470	1110	4740	4240	3250	1750
La	60.2	38.4	70.2	43.0	127	114	53.9	21.7
Ce	140	77.0	159	78.9	298	264	121	41.4
Pr	19.7	9.23	21.5	8.80	39.3	35.4	16.0	4.81
Nd	90.0	37.8	95.8	33.7	172	155	70.7	18.9
Sm	20.6	8.09	22.8	7.10	39.4	32.8	16.0	4.11
Eu	3.85	1.98	4.25	1.79	7.14	5.68	3.43	1.20
Gd	13.3	6.89	15.8	6.28	26.9	20.7	12.5	3.82
Tb	1.36	0.99	1.66	0.92	2.52	1.75	1.30	0.57
Dy	5.77	4.94	6.73	4.60	9.68	6.78	5.31	2.86
Ho	0.92	0.93	1.00	0.88	1.31	0.95	0.82	0.54
Er	2.65	2.78	2.66	2.62	3.56	2.66	2.20	1.62
Tm	0.370	0.390	0.354	0.371	0.458	0.344	0.284	0.225
Yb	2.29	2.55	2.15	2.37	2.70	2.10	1.71	1.45
Lu	0.304	0.364	0.270	0.344	0.321	0.245	0.212	0.202
Hf	11.1	4.6	9.2	3.8	5.0	11.6	6.6	2.4
Ta	1.74	0.74	1.75	0.74	2.35	1.69	0.83	0.36
Pb	41	20	94	15	79	54	40	21
Th	108	24.4	81.9	21.1	189	150	45.8	6.71
U	25.3	3.87	15.2	4.25	23.4	20.7	10.4	3.22

Table 7.3. Trace element concentrations (in ppm except where noted) of lamprophyres from the Western Alps.

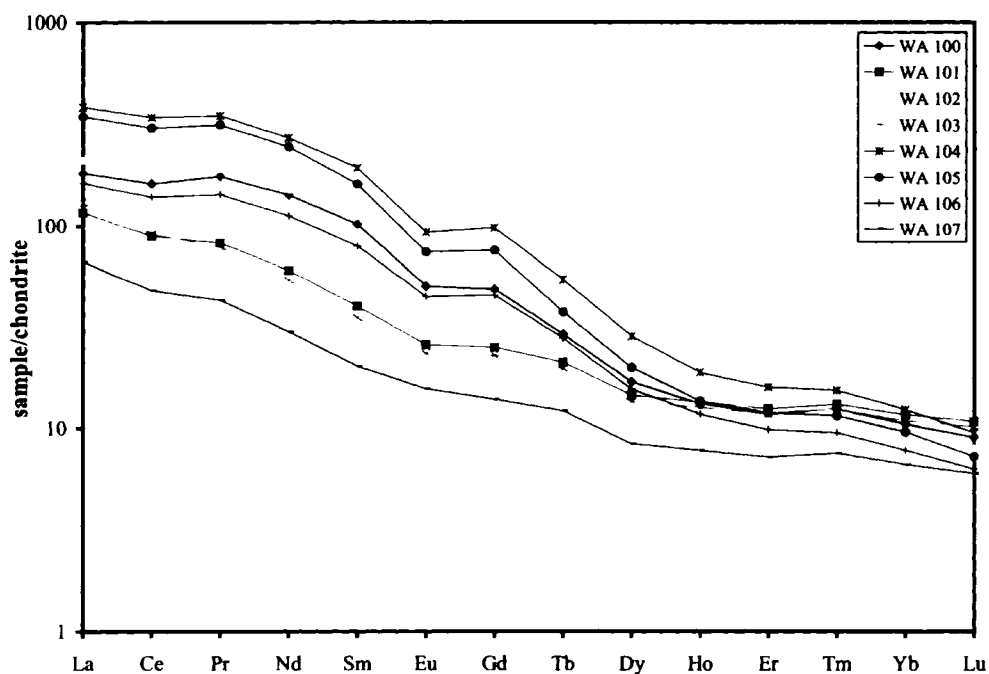


Figure 7.9. Chondrite-normalized REE diagram for lamprophyres from the Western Alps. Normalizing values from Nakamura (1974) and Haskin et al. (1968).

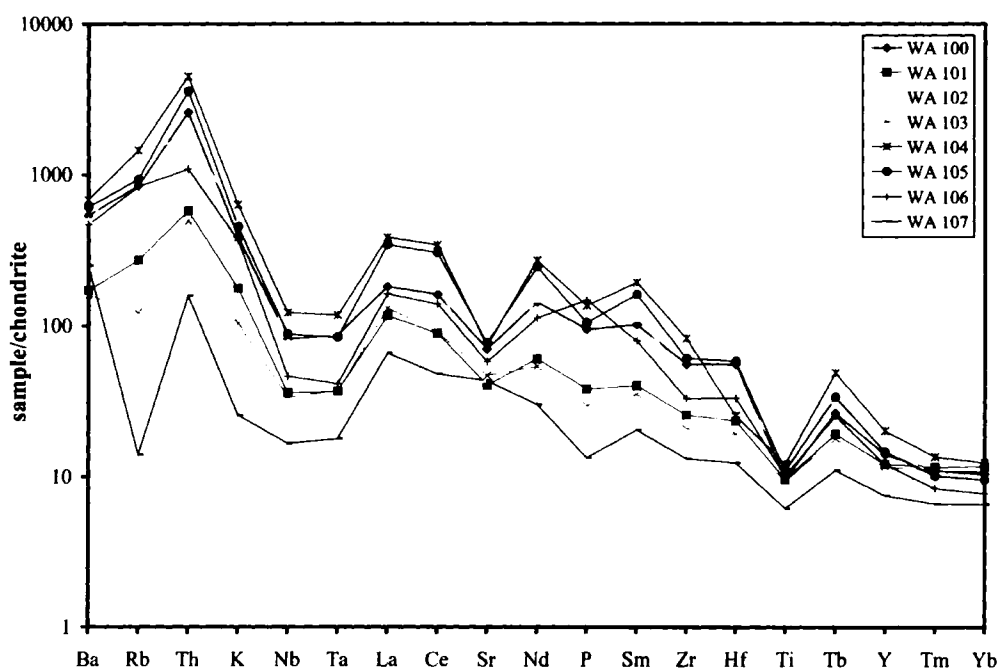


Figure 7.10. Chondrite-normalized extended multi-element (spider) diagram for lamprophyres from the Western Alps. Normalizing values from Thompson (1982).

The sodic lamprophyres (spessartites) contain the lowest concentrations of LREE (~100x chondrite), while the ultrapotassic minettes WA 104 and WA 105 contain the highest values (~400x chondrite). The HREE slopes are nearly flat (~10x chondrite), although the minettes and kersantite show a slight decrease in element abundance from Dy to Lu.

Most samples from the Western Alps appear to have a negative Eu anomaly, which is greater in the minettes (average $\text{Eu}/\text{Eu}^* = 0.69$) than in the spessartites (average $\text{Eu}/\text{Eu}^* = 0.86$). Samples with high LREE/HREE ratios have greater Eu anomalies than those with low LREE/HREE ratios, and the negative Eu anomaly is absent in sample WA 107. The negative Eu anomalies present in most samples from the Western Alps indicate plagioclase feldspar removal from the melt by crystal fractionation, or residual feldspar in the source (Rollinson, 1993).

Chondrite-normalized spider diagrams of incompatible element data from the Western Alps lamprophyres (Fig. 7.10) also show broadly similar features, particularly the extreme enrichment in Th (> 4000x chondrite) and relatively low values of Nb, Ta, and Ti in all samples. The high LILE (Ba, Rb, Th, K) and low HFSE (Nb, Ta, Ti) contents of the lamprophyres from the Western Alps are considered typical of igneous rocks generated at convergent margins. The high LILE/HFSE ratios of arc-related rocks are thought to reflect the strong mobility of LILE, and weak mobility of HFSE, in a fluid phase formed during slab dehydration.

Most samples from the Western Alps have a strong negative Sr anomaly, which may be a consequence of low-pressure fractionation of plagioclase. Alternatively, the Sr depletion may be a source characteristic, as was proposed for the low Sr values in Group I lamproites from southeast Spain (Nixon et al., 1984). Small negative P anomalies are

present in all of the samples other than the kersantite (WA 106), which has a small positive anomaly. The main differences on incompatible trace element diagrams between the various types of lamprophyres are the high values of Rb and K (> 500x chondrite) in the minettes and kersantite, and the negative anomalies of Rb and lower K contents in the spessartites.

7.4c Roccamonfina

7.4c.i Compatible elements

Volcanic rocks from Roccamonfina have fairly low concentrations of compatible trace elements. Although three samples from the KS series contain over 200 ppm Cr, most contain Cr < 100 ppm, Co < 30 ppm, and Ni < 50 ppm (Table 7.4). In general, rocks from the KS series have higher abundances of compatible elements than those from the HKS series. The average compatible element contents of the KS samples are Cr = 136 ppm, Co = 25 ppm, and Ni = 36 ppm, while the average HKS values are Cr = 18 ppm, Co = 21 ppm, and Ni = 15 ppm. The low contents of compatible elements in the volcanic rocks from Roccamonfina suggest either derivation from an atypical mantle source, significant modification by crustal contamination, or crystal fractionation of olivine and clinopyroxene.

7.4c.ii Incompatible elements

The REE patterns of both the KS and HKS rocks from Roccamonfina show enrichment of the LREE, but the two series are characterized by different LREE/HREE ratios (Fig 7.11). Although rocks from both series have similar HREE abundances

Sample	HKS	HKS	KS	KS	KS	HKS	KS	KS	HKS	HKS	KS	KS	HKS	KS
	RC 100	RC 103	RC 104	RC 106	RC 107	RC 109	RC 110	RC 111	RC 113	RC 118	RC 119	RC 121	RC 123	RC 127
B	48	53	13	41	39	62	18	20	71	44	27	17	26	34
Be	7	9	2	5	3	7	3	3	8	8	4	4	6	3
Sc	4.6	5.9	32.6	13.3	20.8	17.0	22.2	25.6	4.1	8.1	18.8	17.9	9.5	28.2
V	142	227	219	159	198	250	179	219	137	210	178	140	209	199
Cr	0.0	14.9	328.0	43.4	23.2	21.6	205.0	178.0	26.3	27.5	46.0	47.1	19.4	219.0
Co	16.0	24.3	31.0	16.3	25.0	28.1	21.8	32.2	11.0	24.3	23.8	23.1	24.5	28.3
Ni	8	7	74	10	14	25	47	60	10	15	22	23	23	37
Cu	35	43	56	14	25	48	40	30	15	42	46	41	52	39
Zn	78	89	63	69	89	79	74	83	78	93	75	71	84	76
Rb	597	379	125	201	131	362	113	150	391	720	157	148	977	130
Sr	1950	2410	770	910	1000	1590	940	810	1960	2150	710	930	1890	890
Y	25	33	30	29	24	29	29	266	31	31	29	29	27	22
Zr	200	262	119	202	130	207	175	134	259	232	178	179	206	115
Nb	15.5	19.2	10.5	19.5	12.1	13.6	15.4	12.2	21.8	19.9	16.6	16.7	17.1	10.9
Cs	56.7	27.9	3.3	9.3	8.3	25.5	2.0	4.4	35.0	40.9	8.9	10.3	57.5	10.1
Ba	1280	1410	580	570	570	1030	710	620	1130	1320	580	610	1080	480
La	104.0	131.0	46.2	63.4	41.5	90.9	65.6	49.6	124.0	126.0	54.9	59.6	99.5	36.4
Ce	186.0	240.0	82.8	111.0	79.1	171.0	122.0	91.4	221.0	222.0	97.5	104.0	183.0	70.3
Pr	20.6	27.6	10.2	12.7	9.53	20.2	14.3	11.8	24.4	25.5	12.2	12.3	20.7	8.59
Nd	66.5	89.7	35.8	41.8	33.3	70.2	48.5	41.7	76.3	81.8	41.7	41.4	67.9	30.2
Sm	11.7	16.7	8.08	8.62	7.01	13.9	10.1	9.13	13.8	15.1	9.03	8.81	12.6	6.55
Eu	2.53	3.51	2.09	2.04	1.76	3.13	2.42	2.14	2.92	3.24	2.18	2.12	2.77	1.61
Gd	7.22	10.40	6.39	6.28	5.39	9.62	7.47	6.93	8.64	9.71	6.67	6.81	8.21	5.16
Tb	1.03	1.44	1.01	1.06	0.88	1.34	1.15	1.04	1.26	1.33	1.07	1.04	1.15	0.80
Dy	5.00	7.18	5.32	5.64	4.83	6.43	5.94	5.68	6.32	6.61	5.77	5.66	5.73	4.47
Ho	0.87	1.21	0.98	1.06	0.91	1.12	1.08	1.06	1.10	1.15	1.09	1.06	0.98	0.86
Er	2.29	3.21	2.59	2.92	2.51	2.88	2.88	2.74	3.01	3.04	2.97	2.89	2.68	2.36
Tm	0.346	0.457	0.389	0.469	0.398	0.411	0.423	0.426	0.441	0.435	0.483	0.455	0.384	0.367
Yb	2.17	2.97	2.35	2.95	2.45	2.53	2.57	2.63	2.70	2.74	2.96	2.86	2.42	2.28
Lu	0.305	0.396	0.329	0.442	0.368	0.360	0.376	0.373	0.373	0.378	0.439	0.412	0.335	0.332
Hf	4.3	6.1	3.3	5.5	3.8	5.8	4.6	4.3	6.1	5.4	5.0	4.9	4.8	3.5
Ta	0.91	1.02	0.52	1.09	0.70	0.64	0.84	0.70	1.27	0.98	0.84	0.86	0.79	0.58
Pb	55	58	7	16	5	15	25	11	79	51	21	16	27	15
Th	39.6	47.1	8.88	21.5	8.7	25.2	15.3	10.1	46.2	42.9	17.2	16.9	32.2	8.31
U	8.84	9.70	1.60	6.62	1.99	6.25	3.28	2.24	10.50	8.89	4.80	4.55	7.30	1.97

Table 7.4. Trace element concentrations of KS and HKS volcanic rocks from Roccamonfina (values in ppm).

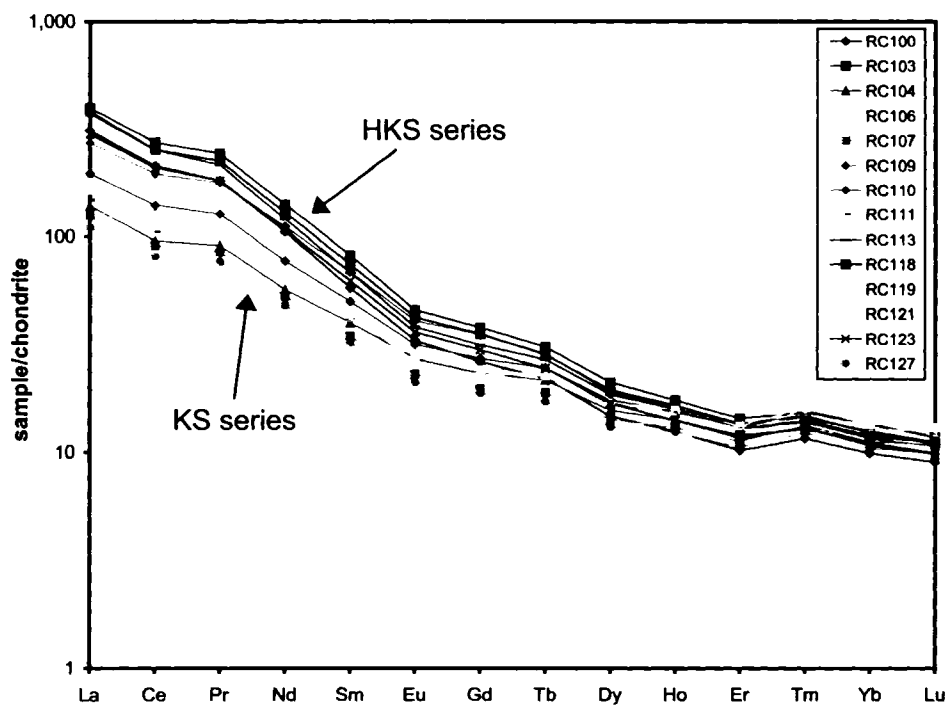


Figure 7.11. REE diagram for KS and HKS samples from Roccamonfina. Normalizing values are from Nakamura (1974) with Pr, Tb, Ho, and Tm from Haskin et al. (1968). The KS series is in red/orange, HKS in blue/green.

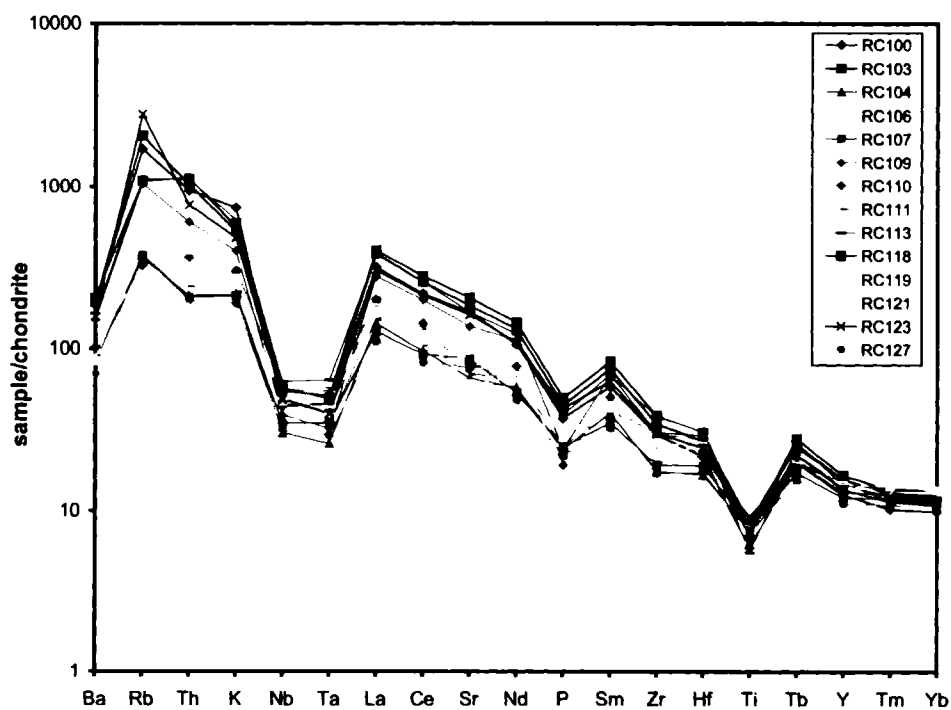


Figure 7.12. Chondrite-normalized extended multi-element (spider) diagram. Normalizing values from Thompson (1982). The KS series is in red/orange, HKS in blue/green.

(~10x chondrite), rocks from the HKS are more enriched in the LREE than those from the KS. This results in higher LREE/HREE ratios for the HKS series than the KS series. The La concentration in samples from the HKS series reaches ~400x chondrite, while in the KS series the maximum is ~200x chondrite. Therefore, the Ce/Yb_(N) for the HKS is more than twice that of the KS (20.0 compared to 9.2). Despite the difference in abundance of LREE, the patterns for the two series are remarkably similar. Small negative Eu anomalies are present in all samples and range from about 0.82 to 0.89.

Spider diagrams for Roccamonfina also show similar patterns for the KS and HKS rocks, but the concentration of incompatible elements in the HKS samples, as expected, is higher than that of the KS samples (Fig. 7.12). Samples from Roccamonfina are characterized by selective enrichment of LILE such as Rb and K, and low abundances of HFSE such as Nb, Ta, Ti, and P, a signature typical of volcanic rocks from convergent margins. However, the strong negative anomaly of Ba seen in rocks of both the KS and the HKS series is unusual for subduction-related rocks. The element order of the spider diagram is one of increasing incompatibility from right to left, such that Ba, which is a LILE, should have a similar value to Rb. The strong depletion of Ba in all samples suggests crystal fractionation of a Ba-rich phase, or the presence of Ba-rich residual minerals in the source.

7.4d Ernici

7.4d.i Compatible elements

The volcanic rocks from Ernici have compatible trace element contents that are more than twice as high as those from Roccamonfina, but are still much lower than those

expected in a primary melt (Table 7.5). The concentrations of compatible elements in samples from Ernici are higher in the KS series than the HKS series, similar to the samples from Roccamonfina. The average compatible element contents of the KS samples are Cr = 297 ppm, Co = 36 ppm, and Ni = 63 ppm, while the average HKS values are Cr = 111 ppm, Co = 29 ppm, and Ni = 47 ppm.

7.4d.ii Incompatible elements

The REE patterns of rocks from Ernici are broadly similar to those from Roccamonfina, but there are also some notable differences (Fig. 7.13). For example, although samples from both Ernici and Roccamonfina show strongly fractionated REE patterns with LREE >100x chondrite, the HREE abundances of rocks from Ernici are slightly lower for the KS series than the HKS series. At Ernici, the chondrite-normalized HREE contents of the KS rocks do not overlap with those of the HKS rocks. The LREE abundances of samples from the KS series at Ernici fall in the range of alkalic basalts (Sun and Hanson, 1975), whereas values for the HKS series are much higher (~300x chondrite). The high LREE abundances and strong LREE/HREE fractionation of rocks from the HKS series are reflected in their high average Ce/Yb_(N) ratio of 24.2, which is more than twice that of the KS series (Ce/Yb_(N) = 11.2). These values are comparable to the LREE/HREE ratios observed in rocks from Roccamonfina. Most samples from Ernici show a slight negative Eu anomaly, and have Eu/Eu* ratios similar to those from Roccamonfina (0.78 – 0.89). Data from the analcime-rich samples ER 109 and ER 117 plot between the members of the KS and HKS series on the REE diagram.

Sample	HKS	HKS	HKS	HKS	KS	HKS	KS	KS	HKS	KS	KS	HKS	KS	KS
	ER 101	ER 104	ER 105	ER 107	ER 109	ER 110	ER 112	ER 114	ER 115	ER 116	ER 117	ER 118	ER 121	ER 122
B	40	50	77	46	32	54	7.6	31	45	13	15	58	19	11
Be	7	7	7	7	3	10	2	3	6	2	4	7	2	2
Sc	18.5	21.0	26.0	28.4	21.2	24.8	38.5	38.7	26.4	25.3	34.4	28.0	40.7	41.8
V	230	239	235	253	233	241	255	216	268	264	255	249	222	275
Cr	42.2	124	176	212	90.5	16.2	316	251	124	146	400	80.2	611	266
Co	26.2	26.3	30.6	32.2	27.8	31.4	38.9	40.2	27.2	28.1	33.9	29.1	38.5	43.6
Ni	41	49	62	62	33	28	68	55	45	46	79	45	97	64
Cu	75	71	83	74	33	114	71	75	71	90	69	60	81	107
Zn	69	67	61	62	76	70	58	59	60	64	55	61	55	64
Rb	437	346	357	399	276	465	192	128	433	451	249	340	173	11
Sr	1860	2060	1760	1710	1270	1410	1090	980	1300	860	1830	1630	870	1030
Y	30	33	31	31	29	44	21	21	32	22	31	32	20	24
Zr	250	254	247	243	174	499	92	103	245	88	209	244	101	94
Nb	15.4	14.3	14.0	13.7	13.5	37.8	9.8	9.9	13.4	8.4	8.5	12.8	9.1	7.6
Cs	36.5	35.6	28.8	30.2	14.2	54.8	29.6	8.8	31.3	18.6	30.0	29.4	9.7	3.0
Ba	1280	1580	1140	1110	820	4160	480	530	1300	420	1120	820	470	520
La	105	116	105	101	65.8	261	35.6	43.9	104	32.8	90.6	99.2	37.1	36.4
Ce	193	214	199	197	127	473	67	82.6	202	62.4	170	198	71.6	65
Pr	22.6	24.9	23.3	23.0	15.2	51.8	8.06	9.4	23.7	7.8	20.3	23.2	8.34	8.59
Nd	74.2	85.3	78.6	77.7	51.7	169	29.0	32.5	81.3	28.0	68.9	78.9	29.5	31.1
Sm	14.6	17.0	17.0	16.8	11.2	33.3	6.72	7.52	17.6	6.84	14.9	16.9	7.04	7.45
Eu	3.10	3.59	3.53	3.41	2.61	6.62	1.67	1.84	3.62	1.72	3.07	3.38	1.75	1.91
Gd	9.74	11.3	10.9	10.7	7.76	19.2	5.15	5.34	11.3	5.21	9.59	10.6	5.23	5.87
Tb	1.33	1.56	1.53	1.48	1.16	2.44	0.83	0.83	1.54	0.82	1.32	1.50	0.81	0.94
Dy	6.44	7.29	7.26	6.90	6.02	10.70	4.30	4.52	7.33	4.49	6.27	7.24	4.37	4.91
Ho	1.08	1.19	1.17	1.15	1.06	1.60	0.78	0.82	1.19	0.83	1.04	1.19	0.79	0.88
Er	2.71	2.997	2.9	2.87	2.88	3.81	2.09	2.14	2.97	2.16	2.61	3.04	2.04	2.32
Tm	0.378	0.415	0.405	0.396	0.424	0.452	0.316	0.328	0.420	0.323	0.356	0.425	0.303	0.349
Yb	2.35	2.52	2.43	2.35	2.54	2.79	1.87	1.98	2.42	1.96	2.16	2.50	1.83	2.02
Lu	0.322	0.332	0.328	0.309	0.350	0.353	0.264	0.266	0.332	0.270	0.300	0.340	0.257	0.290
Hf	6.6	6.6	6.8	6.7	4.9	13.3	3.1	3.3	7.1	3.1	5.4	7.2	3.1	2.9
Ta	0.71	0.59	0.54	0.51	0.69	2.01	0.38	0.48	0.53	0.37	0.38	0.50	0.44	0.37
Pb	52	52	38	38	5	93	12	0	39	14	48	34	20	9
Th	35.3	38.5	29.6	29.5	14.6	91.2	8.16	10.0	30.4	7.52	25.9	28.1	9.23	8.00
U	8.59	8.55	6.94	7.16	3.27	5.61	1.50	3.11	7.80	1.79	6.01	6.66	2.48	1.49

Table 7.5. Trace element concentrations of KS and HKS volcanic rocks from Ernici (values in ppm).

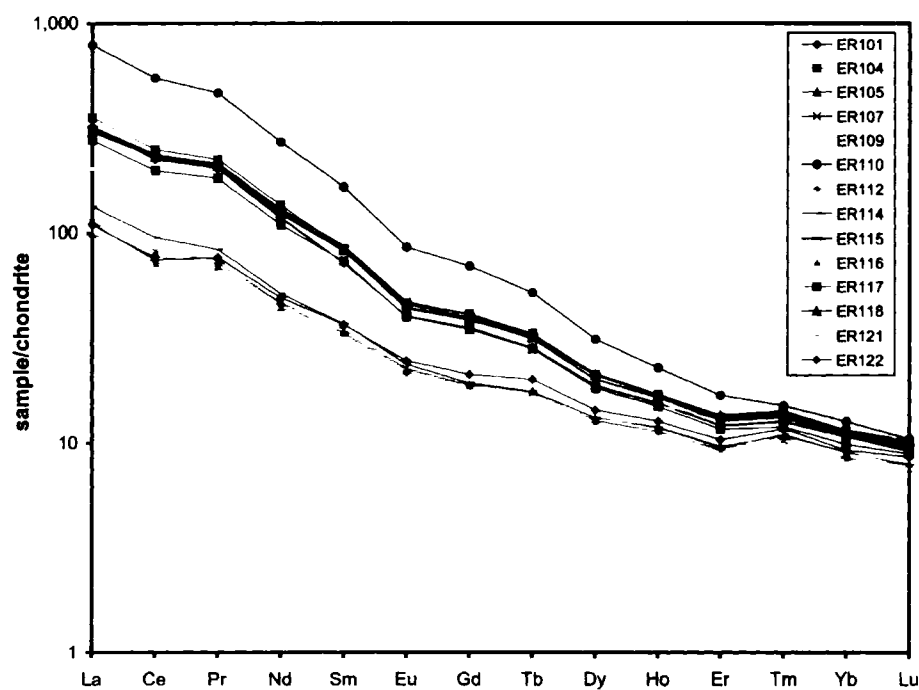


Figure 7.13. REE diagram for KS and HKS samples from Ernici. Normalizing values are from Nakamura (1974) with Pr, Tb, Ho, and Tm from Haskin et al. (1968). The KS series is in red/orange, HKS in blue/green.

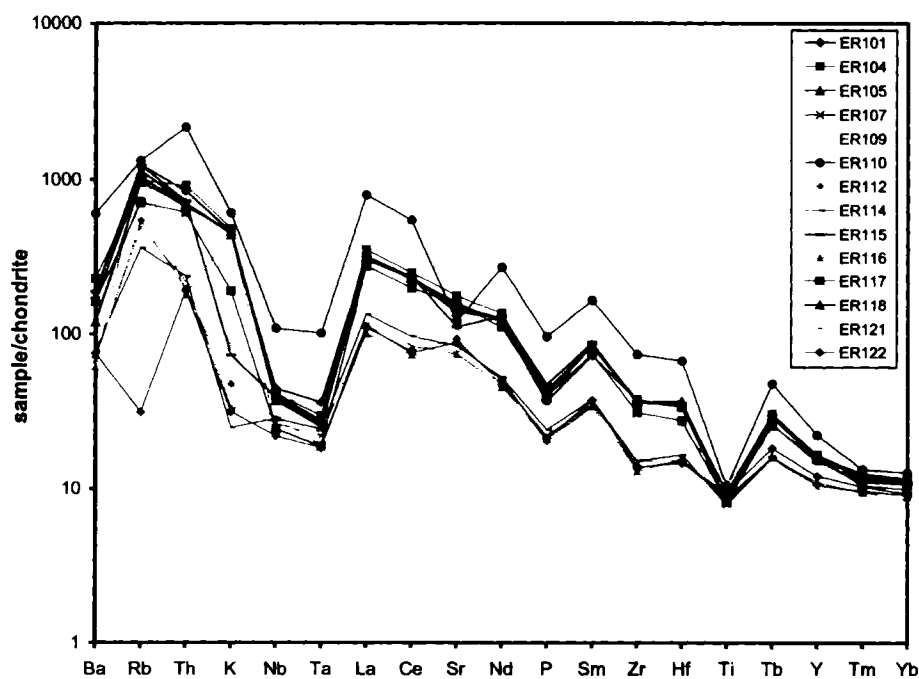


Figure 7.14. Chondrite-normalized extended multi-element (spider) diagram. Normalizing values from Thompson (1982). The KS series is in red/orange, HKS in blue/green.

One sample, HKS phonotephrite ER 110, is much more highly enriched in LREE than any of the other samples from Ernici ($Ce/Yb_{(N)} = 43.1$). The high $Ce/Yb_{(N)}$ ratio of this sample influences the average calculated HREE/LREE ratio of the entire HKS series (average $Ce/Yb_{(N)}$ of the HKS rocks without sample ER 110 is 21.05). Sample ER 110 has LREE and MREE contents that are approximately twice those of other members of the HKS series (normalized La content $\sim 800x$ chondrite). This sample has a very similar REE distribution to sample M1 of Civetta et al. (1981), a strongly silica undersaturated phonolitic leucitite dated at 0.7 Ma (Basilone and Civetta, 1975). Sample ER 110 also has the highest K_2O , lowest Mg# and SiO_2 , and lowest Ni and Cr contents of any sample from Ernici in this study.

Spider diagrams for volcanic rocks from Ernici are characterized by enrichment of LILE and relative depletion of HFSE, similar to patterns from world-wide subduction-related rocks (Fig. 7.14). The HKS samples from Ernici are enriched by a factor of 1.5 to 3 relative to the KS samples, and rocks from both series show strong negative Ba and P anomalies. Data from analcime-rich samples ER 109 and ER 117 plot between the members of the KS and HKS series on the spider diagram. The HFSE Ti, Ta, and Nb show different behavior in the HKS and KS series, whereby the concentration of Ti is constant in all samples (8-10x chondrite) while Nb and Ta are higher in the HKS series than the KS. Sample ER 110 is highly enriched ($> 2.5x$ the incompatible element content of other HKS rocks) and has a distinct trace element pattern characterized by a peak at Th, high values of Nb and Ta, and a strong negative Sr anomaly. KS sample ER 122 is the only sample from Ernici to show a strong negative Rb anomaly.

7.4e Comparison of trace element data from Roccamonfina and Ernici

Although volcanic rocks from Ernici contain higher amounts of compatible elements than Roccamonfina, the KS rocks from Roccamonfina have similar incompatible trace element abundances to those from Ernici, and the HKS rocks from Roccamonfina are similar to those from Ernici (Figure 7.15). All samples show similar patterns on spider diagrams, except HKS sample ER 110, which is anomalously enriched in most incompatible elements, and KS sample ER 122, which has very low Rb. Differences in the incompatible element contents of rocks from Roccamonfina and Ernici include: 1) higher Rb, Th, and K in the HKS series of Roccamonfina, and 2) lower K in the KS series of Ernici.

7.4f Can the samples from Roccamonfina and Ernici be considered primitive?

Primitive magmas derived from a four-phase lherzolite generally have $Mg\# > 65$, $SiO_2 < 50$ wt%, and high values of Ni, Cr, and Co. Several samples from Roccamonfina and Ernici do not fit these criteria, suggesting that some magmas may have undergone variable degrees of crustal contamination or crystal fractionation upon ascent, or were generated from an atypical mantle. Although $Mg\#$, SiO_2 , and compatible trace element contents can be applied to common basaltic rocks, they may not be as useful for primitive potassic and ultrapotassic magmas derived from metasomatized source regions. Mantle xenoliths found in pyroclastic deposits at Roccamonfina are dominated by phlogopite-clinopyroxenite (Giannetti and Luhr, 1990), which suggests that the mantle in central-southern Italy has been affected by a volatile-bearing metasomatic agent. Rogers et al. (1985) recognized that a phlogopite-rich, olivine-free pyroxenite source could explain the

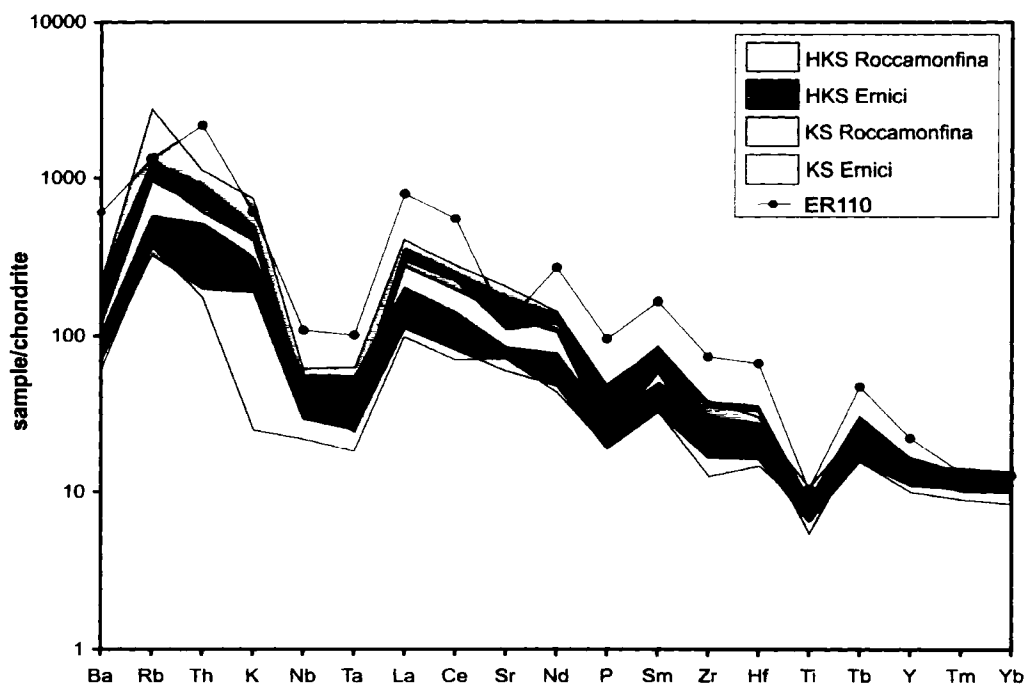


Figure 7.15. Comparison of the incompatible trace element patterns of samples from the HKS and KS series at Roccamonfina and Ernici (excluding ER122).

relatively low Mg#, Ni, and Cr of the Italian volcanic rocks. The stabilization of phlogopite in the central-southern Italian upper mantle could have resulted from the introduction of hydrous silicic melts rich in alkalis derived from subducted sedimentary material (Rogers et al., 1985). The migration of silica from subducted sediments into the overlying mantle wedge may also be responsible for generating primitive, silica-rich ($\text{SiO}_2 > 50 \text{ wt}\%$) liquids (Peccerillo, 1990).

Mineralogical and geochemical evidence in favour of mantle metasomatism makes it difficult to establish whether the potassic and ultrapotassic magmas of Roccamonfina and Ernici are primitive or evolved (Vollmer, 1990). Peccerillo (1990) stated that the best criteria for recognizing primitive potassic melts still remains the Mg# and MgO content, and many authors consider only those rocks with $\text{Mg}\# > 65$ and $\text{MgO} > \sim 4.0 \text{ wt}\%$ to be primitive. The KS and HKS rocks from Roccamonfina and Ernici have MgO contents that range from $\sim 1.5 \text{ wt}\%$ to $\sim 10.0 \text{ wt}\%$, and Mg#s between 47 and 73. Most samples from Roccamonfina have $\text{Mg}\# < 65$, while most from Ernici have $\text{Mg}\# > 65$, suggesting that volcanic rocks from Ernici are more primitive than those from Roccamonfina. This is consistent with previous work that supports crystal fractionation as a dominant process at Roccamonfina (Appleton, 1972; Giannetti and Ellam, 1994). In spite of the differences in Mg#, the similarity in incompatible element diagrams for rocks from Ernici and Roccamonfina (see Figure 7.15) indicates that trace element patterns can still be used effectively to evaluate processes that have affected the mantle source regions of the KS and HKS rocks.

7.4g Incompatible trace element data from the Western Alps, Roccamonfina and Ernici compared to other Italian magmatic rocks

The incompatible trace element patterns of the lamprophyres from the Western Alps are broadly similar to those of calc-alkaline volcanic rocks from the Eastern Alps, as well as lamproites from Tuscany (Figure 7.16). The rocks from the Eastern Alps belong to the same magmatic province as the lamprophyres (Tertiary Periadriatic Province), while lamproites from the Tuscan Province are younger (late Miocene – Pleistocene) and show transitional features to ultrapotassic rocks from the Roman Province. The Alpine and Tuscan magmatic rocks are closest in geography and age to samples from the Western Alps.

Early Miocene, calc-alkaline volcanic rocks from the easternmost segment of the Periadriatic Line range from low-K and medium-K andesites to medium-K dacites, and outcrop near the Pohorje tonalite. The chemical signatures of these rocks have been attributed to plagioclase, clinopyroxene, olivine, and titanomagnetite fractionation during melt evolution (Altherr et al., 1995). However, relative abundances of incompatible elements such as K, Ba, and U are more consistent with derivation from different mantle sources rather than with different degrees of partial melting or fractionation (Altherr et al., 1995). The calc-alkaline rocks from the Eastern Alps have similar trace element patterns to lamprophyres from the Western Alps (high Rb and Th, low Ba, Nb-Ta, Sr, P, and Ti), but the calc-alkaline rocks have much lower concentrations of both LILE and HFSE compared to the lamprophyres.

Magmatic rocks from the entire Tertiary Periadriatic Province have been ascribed to subduction-related melting following the Alpine orogeny (Venturelli et al., 1984; von

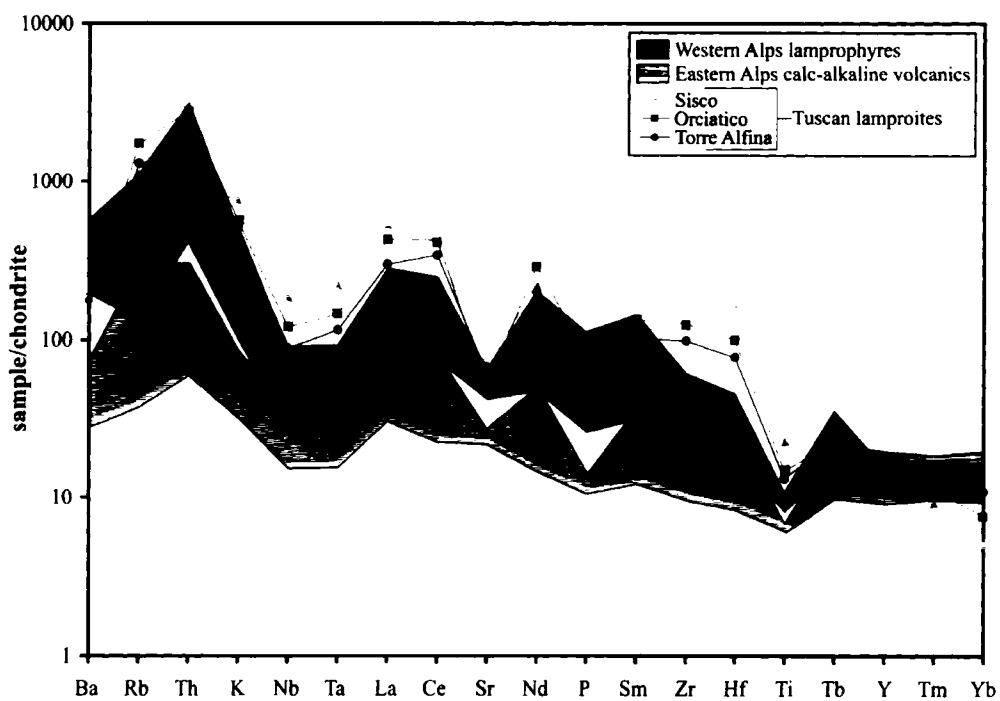


Figure 7.16. Average chondrite-normalized incompatible element concentrations for lamprophyres from the Western Alps, calc-alkaline volcanic rocks from the Eastern Alps (Altherr et al., 1995), Sisco (Peccerillo et al., 1988), Orciatico (Conticelli et al., 1992), and Torre Alfina (Conticelli and Peccerillo, 1990).

Blanckenburg et al., 1998). The similar incompatible element patterns of rocks from the Eastern Alps and the Western Alps are consistent with widespread modification of the Alpine mantle by subduction-related fluids. The higher levels of incompatible elements in the lamprophyres may be due to either lower degrees of partial melting, or interaction with a more enriched metasomatic fluid (see section 5.2).

The lamprophyres from the Western Alps generally have lower abundances of incompatible trace elements than the Tuscan lamproites (represented on Figure 7.16 by Sisco, Orciatico, and Torre Alfina). The minettes (samples WA 100, WA 102, WA, 104, and WA 105) have the highest incompatible element concentrations of samples from the Western Alps, and are most similar to the lamproites. Although both the lamprophyres and lamproites have fractionated LILE/HFSE ratios, the Tuscan lamproites have notably higher concentrations of HFSE (Nb, Ta, and Ti), La, Ce, Nd, Zr, and Hf than the lamprophyres. The Tuscan lamproites have similar trace element patterns to lamproites from southeast Spain, which are located in the Betic Cordillera and are thought to derive their incompatible element characteristics from subduction-related metasomatism during the Alpine orogeny (Nixon et al., 1984). Therefore, it appears that the mantle in southeast Spain, Tuscany, and the Alps was variably affected by trace element enrichment as a result of the Alpine orogeny.

The samples from Roccamonfina and Ernici have incompatible trace element compositions that overlap with data from rocks of the nearby Roman and Campanian Provinces. Figure 7.17 shows trace element patterns for Roccamonfina and Ernici, Vulsini and Sabatini in the Roman Province (Conticelli and Peccerillo, 1992), Procida and Ventotene in the Campanian Province (D'Antonio et al., 1999), Vesuvius (Somma et

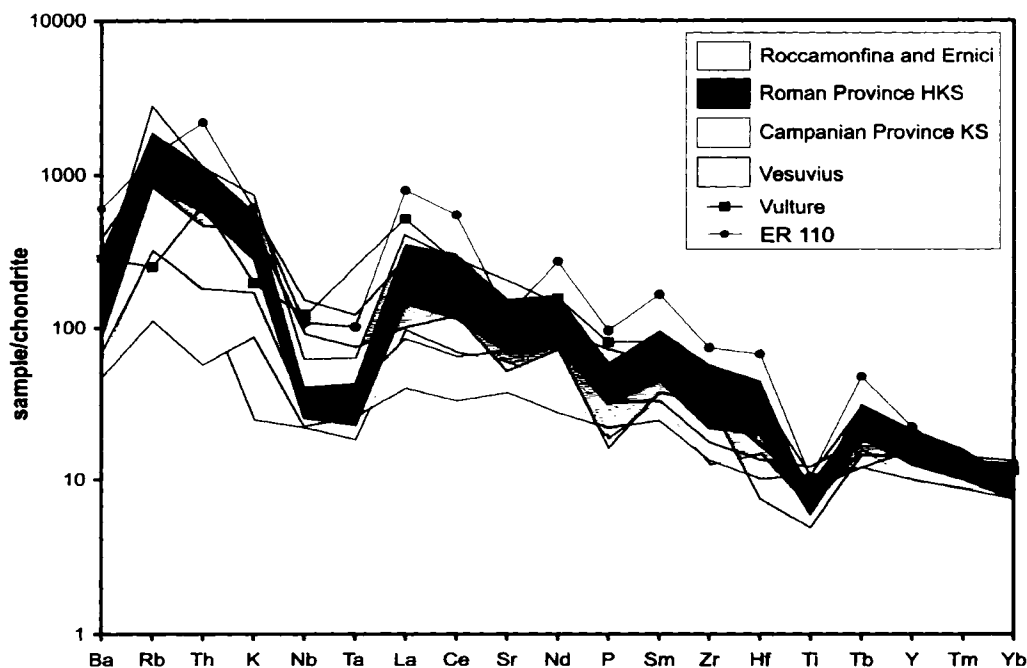


Figure 7.17. Incompatible trace element data of samples from Roccamonfina and Ernici, HKS rocks from the Roman Province (Vulsini and Sabatini; Conticelli and Peccerillo, 1992), KS rocks from the Campanian Province (Procida and Ventotene (D'Antonio et al., 1999), HKS rocks from Vesuvius (Somma et al., 2001), and a basanite from Vulture (Beccaluva et al., 2002).

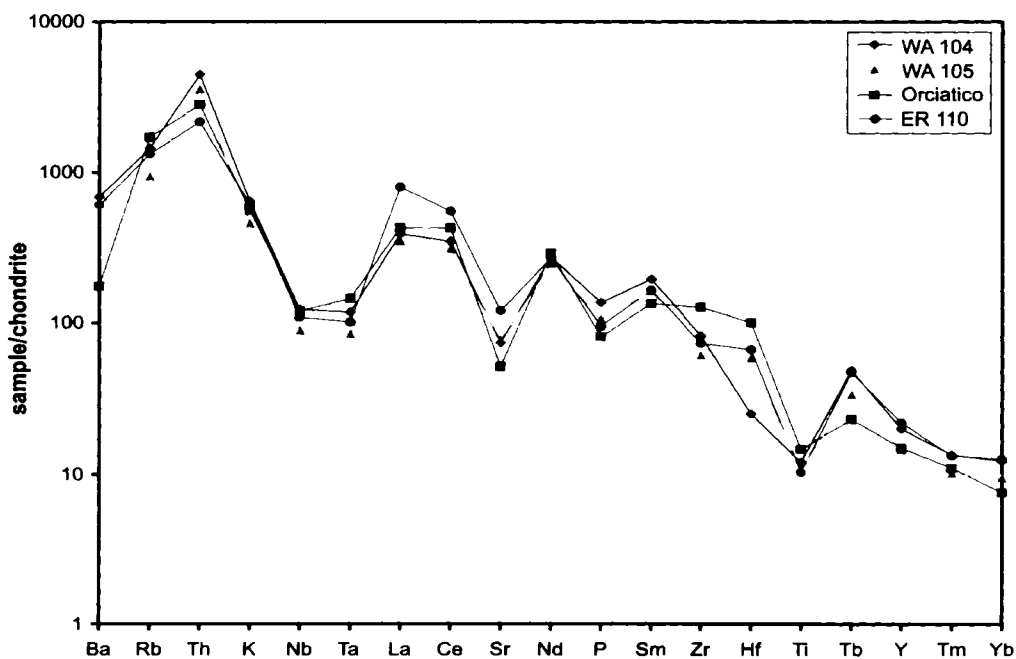


Figure 7.18. Incompatible trace element data of samples WA 104 and WA 105 from the Western Alps (minettes), sample ER 110 (phonotephrite), and the Orciatico lamproite (Conticelli and Peccerillo, 1992).

al., 2001), and Vulture (Beccaluva et al., 2002). In general, most of the KS and HKS rocks from central Italy have similar abundances of HFSE, but the HKS rocks are more strongly enriched in LREE and LILE than the KS rocks. An important feature to note from Figure 7.17 is the absence of a negative Ti anomaly in volcanic rocks from Procida and Ventotene in the Campanian Province (see discussion in section 7.5a.i).

Spider patterns for Vesuvius and Vulture also show fractionated LILE/HFSE ratios that are similar to those of the KS and HKS rocks from Roccamonfina, Ernici, the Roman Province, and the Campanian Province. However, volcanic rocks from Vesuvius and Vulture have Nb and Ta contents that are 3-4x higher than those of other KS and HKS rocks located in central Italy. Rocks from Vesuvius and Vulture share trace element characteristics with basanites and nephelinites from the Iblean Plateau that are typical of alkaline anorogenic magmas from within-plate or rift settings (Beccaluva et al., 2002). Most volcanic rocks from Vesuvius have Nb/Ta ratios that range from 13 to 25 and overlap with the ratios of OIB (Nb/Ta ~12-22) (Civetta et al., 1991a), and low B/Be ratios (< 4) that are significantly less than those of typical arc volcanics (Morris et al., 1993; Ayuso et al., 1998). The OIB-like trace element characteristics of volcanic rocks from Vesuvius led Gasperini et al. (2002) to suggest the upwelling of deep mantle material through a slab window (see Chapter 9).

HKS sample ER 110 has a distinct trace element pattern that is very similar to those of Tuscan lamproites and minettes from the Western Alps. Figure 7.18 shows the incompatible trace element patterns for samples WA 104 and WA 105 from the Western Alps (minettes), sample ER 110, and the Orciatico lamproite (Conticelli and Peccerillo, 1992). All patterns are characterized by extremely high LILE contents, Nb and Ta

contents that are ~100x chondrite, strong negative Sr and P anomalies, and fractionated LILE/HFSE ratios. The only differences between the trace element patterns of samples ER 110, WA 104, WA 105, and Orciatice are the relatively low Ba content of the Orciatice lamproite (~175x chondrite) and the fractionated Zr/Hf ratio in minette WA 104. The similar trace element patterns in magmatic rocks with very different major element compositions suggests that the mantle in the Western Alps, Tuscany, and central-southern Italy may have undergone metasomatism by an agent that had a constant chemical composition over a large area. This has important implications not only for the origin of the metasomatic agent, but for the chemical evolution of the Italian mantle (Chapter 9).

7.5 Evidence for a crustal component in the mantle of the Western Alps and central-southern Italy

7.5a Introduction

Early petrogenetic models for potassic and ultrapotassic rocks commonly involved variable degrees of assimilation of continental crust by mantle-derived magmas, which seemed to explain contradictory geochemical features including high Mg#, Ni, and Cr (mantle characteristics) and high Rb, K, Zr, and Ba (crustal characteristics). Crustal assimilation hypotheses were widely accepted until the 1960s, when various authors demonstrated that potassic and ultrapotassic magmas have much higher incompatible element abundances than crustal rocks (e.g. Savelli, 1967). In addition, many ultrapotassic rocks are strongly silica-undersaturated, which precludes a general origin by assimilation of silica-rich crustal material.

Potassic and ultrapotassic rocks are now believed to acquire their crustal trace element characteristics through metasomatism, whereby an incompatible element-enriched fluid or melt interacts with the mantle and results in crystallization of amphibole above depths of ~100 km (Green, 1973) and mica at greater depths (Kushiro et al., 1967). Mantle metasomatism is supported by the presence of mantle xenoliths with primary hydrous mineral phases, such as amphibole or mica, in many ultrapotassic rocks. The presence of a metasomatic crustal component in the source of rocks from the Western Alps, Roccamonfina, and Ernici is provided by: 1) incompatible trace element patterns, 2) tectonic discrimination diagrams using HFSE, 3) Ce/Pb and Nb/U ratios, and 4) B and Be systematics. These are discussed in turn below.

7.5b Incompatible trace element patterns

The average chondrite-normalized REE concentrations for minettes, spessartites, and the kersantite from the Western Alps, along with the REE distribution of the average upper continental crust (UCC), are shown in Figure 7.19 (Taylor and McLennan, 1981). The average spessartite has REE concentrations that are similar to that of the UCC, while the minettes and kersantite have LREE concentrations about twice as high. Therefore, it seems unlikely that bulk crustal contamination can be responsible for the high LREE/HREE ratios or fractionated LILE/HFSE patterns of the lamprophyres from the Western Alps. Metasomatism involving the introduction of an enriched crustal component into the Alpine mantle, coupled with selective enrichment of LILE and LREE derived from a fluid/melt phase, better explains the trace element signatures of the lamprophyres.

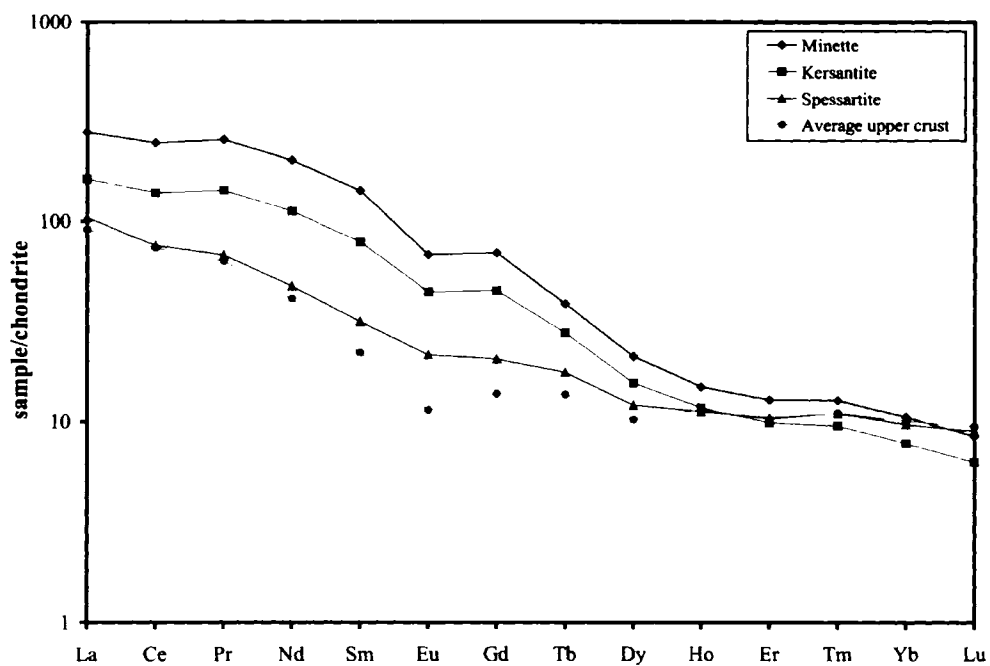


Figure 7.19. Average chondrite-normalized REE concentrations for minette ($n = 4$), kersantite ($n = 1$), and spessartite ($n = 3$) samples from the Western Alps. Average upper continental crust from Taylor and McLennan (1981).

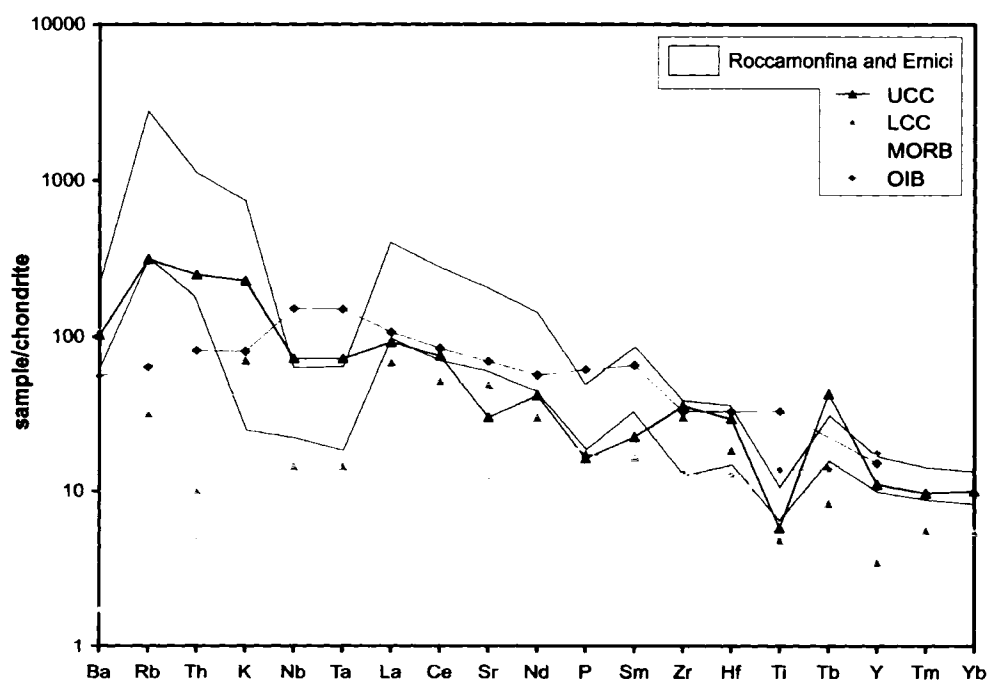


Figure 7.20. Incompatible trace element data from rocks from Roccamonfina and Ernici (excluding ER 110) compared with the upper continental crust (UCC) (Taylor and McLennan, 1981), the lower continental crust (LCC) (Weaver and Tarney, 1984), average n-MORB (Sun, 1980; Saunders and Tarney, 1984), and average OIB (Sun, 1980).

The incompatible trace element patterns of samples from Roccamonfina and Ernici are also broadly similar to that of upper continental crust (UCC) (Figure 7.20). In fact, volcanic rocks from Roccamonfina and Ernici have higher LILE contents, lower HFSE contents, and therefore more fractionated LILE/HFSE ratios than the UCC. The similarity between the incompatible trace element patterns of potassic and ultrapotassic rocks from central-southern Italy and the UCC has been previously noted by a number of authors, including Rogers et al. (1985), Peccerillo (1985), Conticelli (1989), Beccaluva et al. (1991), Conticelli and Peccerillo (1992), and Serri et al. (1993). For comparison, the trace element pattern of the lower continental crust (LCC) is also shown on Figure 7.20. The LCC is characterized by depletions in HFSE, Rb, Th, Tb, Y, Tm, and Yb relative to the UCC.

The incompatible element patterns of leucite-bearing volcanic rocks from oceanic islands (e.g. Tristan da Cunha) and continental rift systems (e.g. East African Rift) are very different from those of the UCC and LCC, and are marked by high HFSE (Nb, Ta, and Ti) contents and relatively unfractionated LILE/HFSE ratios (Baker et al., 1977; Thompson et al., 1984). The KS and HKS rocks from Roccamonfina and Ernici have chondrite-normalized Nb and Ta contents between those of OIB and MORB, but their Ti contents are much lower than either OIB or MORB (Figure 7.20). Negative Nb, Ta and Ti anomalies are typical of subduction-related magmatic rocks; however, the reason for these features remains unclear (see section 7.5b.i).

7.5b.i Significance of negative Nb, Ta and Ti anomalies in incompatible trace element diagrams

Negative Nb, Ta and Ti anomalies are perhaps the most striking characteristics of incompatible trace element patterns for magmatic rocks of the Western Alps, Roccamonfina, and Ernici. Although it is generally accepted that the enrichment of LILE in magmas generated at convergent margins reflects contributions from fluids related to slab dehydration, the depletion of Nb, Ta, and Ti still remains a contentious issue (e.g. McCulloch and Gamble, 1991). In Italy, the fractionated LILE/HFSE ratios of Plio-Quaternary lamproites, kamafugites, ultrapotassic rocks, and potassic rocks, have been taken as evidence of subduction-related magmatism by numerous authors (e.g. Peccerillo, 1985; Beccaluva et al., 1991; Conticelli and Peccerillo, 1992; Ayuso et al., 1998). However, the occurrence of mafic potassic rocks in the Asuncion-Sapucaí graben of Paraguay that are remarkably similar in mineralogy and petrology to KS and HKS rocks from central-southern Italy raises concerns about the use of negative Nb, Ta, and Ti anomalies as a "subduction signature" (Cundari, 1994).

The Asuncion-Sapucaí graben contains a suite of potassic and ultrapotassic lavas, dykes, carbonatites, and tholeiitic flood basalts associated with crustal extension (Comin-Chiaromonte et al., 1992). Ultrapotassic rocks from the Asuncion-Sapucaí graben have high LILE/HFSE ratios with negative Ta, Nb, P, Zr, and Ti anomalies that are virtually identical to those from the HKS lavas of Italy (Lavecchia and Stoppa, 1996). The presence of negative HFSE anomalies in magmatic rocks that appear to be unrelated to recent subduction prompts a discussion about the significance and origin of Nb, Ta, and Ti anomalies in mantle-derived lavas.

There are two main hypotheses for the depletion of Nb, Ta, and Ti in mafic orogenic rocks: 1) partitioning of HFSE into residual titanate phases such as rutile (TiO_2), titanite ($\text{CaTiO}(\text{SiO}_4)$), ilmenite (FeTiO_3), or perovskite (CaTiO_3) in order to retain Nb, Ta, and Ti in the source regions during partial melting (Foley and Wheller, 1990), and 2) low abundances of Nb, Ta, and Ti in the mantle wedge due to depletion by previous melting events (McCulloch and Gamble, 1991).

In order for Nb, Ta, and Ti to partition into titanate phases, the TiO_2 content of the melt, which is P-T dependent, must be in equilibrium with titanate minerals in the mantle source. Experimental studies indicate that melt compositions with > 60 wt% SiO_2 are saturated with respect to titanite at 0.5-1.0 wt% TiO_2 , whereas compositions with ≤ 52 wt% SiO_2 are saturated at 1.5-8.0 wt% TiO_2 (Green and Pearson, 1986). Basalts from arc-related tectonic settings typically contain low SiO_2 and low TiO_2 (< 1.0 wt%), which seem to preclude the presence of titanate minerals in the sub-arc mantle (Wilson, 1989). However, Green and Pearson (1986) also found that increased stability of residual titanate minerals (i.e. low TiO_2 saturation levels) are favoured by high pressure, low temperature, high H_2O content, high content of alkali elements (LILE) and REE, and high $f\text{O}_2$. Such conditions are to be expected in a mantle wedge modified by the addition of H_2O - and LILE-rich fluids derived from slab dehydration (Foley and Wheller, 1990). It should also be noted, with regard to the presence of carbonatites in both Italy and the Asuncion-Sapucaí graben, that high CO_2 contents in the mantle can promote crystallization of titanate minerals from melts with only 1.0-1.5 wt% TiO_2 at high pressures (Meen et al., 1989).

The Nb and Ta partition coefficients are much larger for rutile than for titanite, ilmenite or magnetite at pressures of 4-16 kbar (Green and Pearson, 1987). As such, Foley and Wheller (1990) suggested that rutile is the most likely residual titanate mineral present in the source of arc-related magmas with stronger depletions in Nb and Ta relative to Ti.

McCulloch and Gamble (1991) argued against rutile in either the mantle wedge or the subducting slab because of systematic correlations amongst HFSE ratios (Zr/Nb , Sm/Nb , and TiO_2/Zr) relative to Nb abundances. As an alternative to a residual titanate in the source, McCulloch and Gamble (1991) proposed that low Nb and Ta concentrations in arc volcanics could reflect the relative immobility of these elements during slab dehydration processes, while low TiO_2 may be due to previous depletion of the mantle wedge at a divergent margin such as a mid-ocean ridge or back-arc basin spreading centre.

McCulloch and Gamble (1991) suggested a revision of the order of elements on incompatible element diagrams in order to enable the recognition of "slab-derived" (LILE) components based on the variable mobility of different elements in a subduction environment. Figure 7.21 shows the recommended incompatible element order of McCulloch and Gamble (1991), in which Nb and Th are moved to the right (less mobile) and Pb and Sr are moved to the left (more mobile) with respect to the usual element order. The addition of Ta and Hf to Figure 7.21, as well as normalization to chondrite instead of N-MORB, are minor changes to the work of McCulloch and Gamble (1991) made by this author. Based purely on the mobility of each trace element in a slab-derived hydrous fluid, the data should form a smooth curve that increases from right to left.

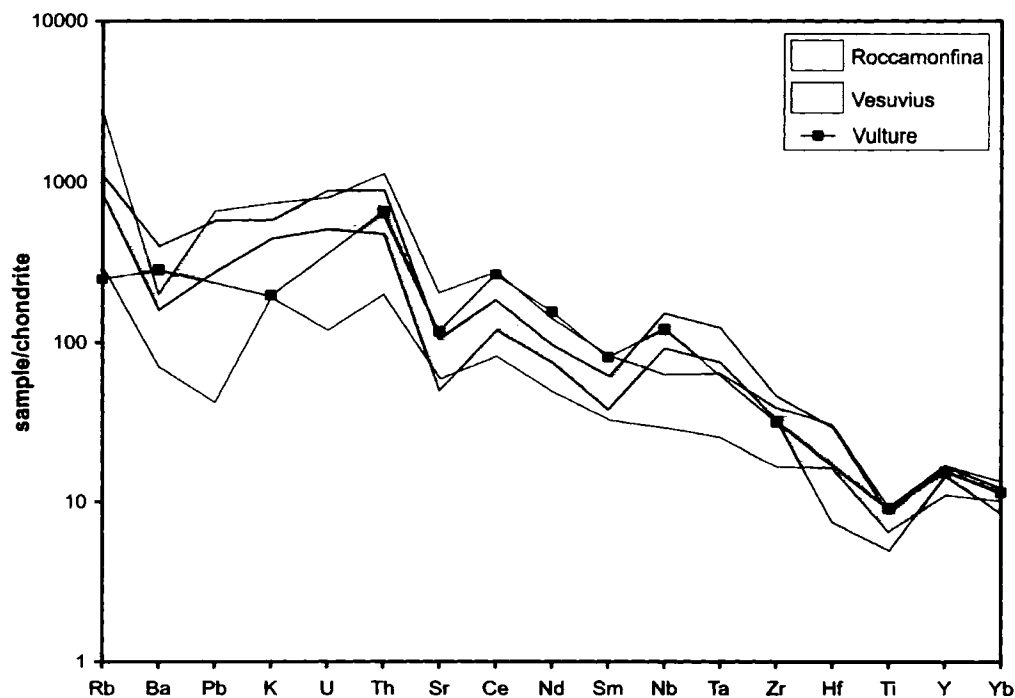


Figure 7.21. Incompatible trace element patterns of KS and HKS rocks from Roccamonfina, HKS rocks from Vesuvius (Somma et al., 2001), and a basanite from Vulture (Beccaluva et al., 2002), using the element order of McCulloch and Gamble (1991) with the addition of Ta and Hf. Note that lack of a Nb-Ta anomaly in rocks from Roccamonfina, and the positive Nb-Ta anomaly in rocks from Vesuvius and Vulture.

Incompatible trace element data from the volcanic rocks of Roccamonfina, Vesuvius (Somma et al., 2001), and Vulture (Beccaluva et al., 2002) are shown in Figure 7.21 (samples from Ernici and the Western Alps have been omitted for clarity, but show trends similar to those from Roccamonfina). The most important features of the incompatible element pattern for Roccamonfina are the negative Ba, Pb and Ti anomalies, and the lack of a Nb-Ta anomaly. Although Ba and Ti anomalies are present in trace element diagrams using the unmodified element order (see Figure 7.12), by simply changing the order of the elements based on fluid-mobility, the negative Nb-Ta anomaly disappears. In contrast, the trace element patterns for Vesuvius and Vulture (Figure 7.21) have positive Nb-Ta anomalies, implying that they have Nb and Ta abundances that are higher than expected from slab-dehydration processes that introduced fluids into the mantle wedge.

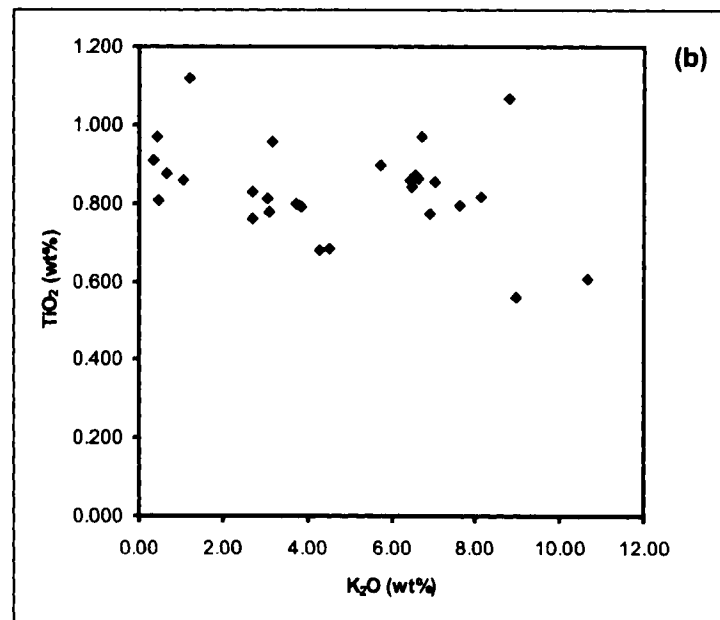
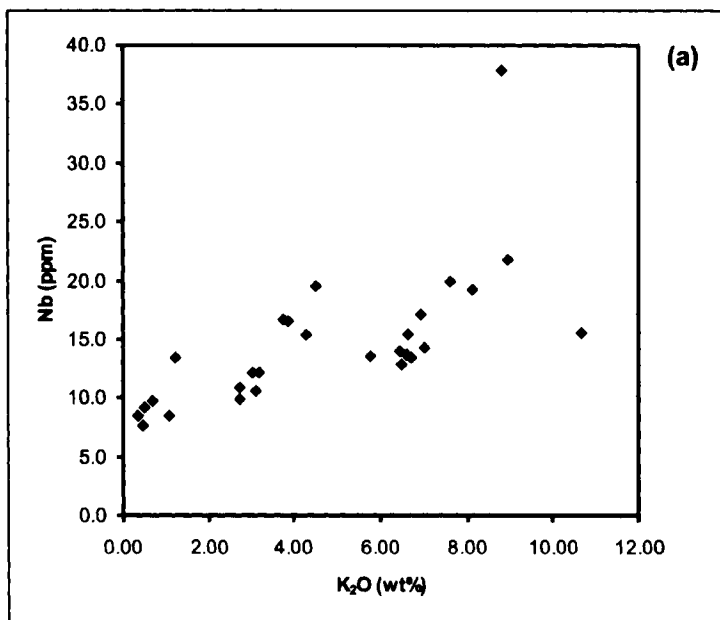
The positive Nb-Ta anomalies for Vesuvius and Vulture support previous geochemical work that suggests that the mantle beneath these volcanoes has OIB-like trace element characteristics (Civetta et al., 1991a; Morris et al., 1993; Ayuso et al., 1998). Although the KS and HKS rocks of Roccamonfina do not show positive or negative Nb-Ta anomalies on Figure 7.21, they do show a strong negative Ti anomaly. This suggests that the HFSE were decoupled either during source metasomatism or crystal fractionation, a situation similar to that observed in potassic and ultrapotassic volcanic rocks from the Sunda arc (Wheller et al., 1987).

One of the most interesting geochemical features of rocks from the Sunda arc is a positive correlation between Nb and K_2O , but no correlation between TiO_2 and K_2O , suggesting that a K-rich metasomatic agent introduced Nb, but not Ti, into the source of

the Sunda magmas (Foley and Wheller, 1990). The KS and HKS rocks of Roccamonfina and Ernici also show positive correlations between Nb and K₂O, but not between TiO₂ and K₂O (Figures 7.22a and 7.22b). The positive correlation between Nb and K₂O (as well as the lack of a Nb-Ta anomaly on Figure 7.21) provides evidence against the total control of HFSE by residual titanates in the source. The negative Nb-Ta anomalies are consistent with the relative immobility of these elements in a slab-derived fluid, and therefore there is no need to invoke Nb and Ta partitioning into a residual titanate such as rutile in the mantle of central-southern Italy.

Further evidence against residual rutile in the mantle beneath Roccamonfina and Ernici is provided by the high Nb/Ta ratios of the KS and HKS rocks. The Nb/Ta ratios of samples from Roccamonfina and Ernici average 20.9 and reach a maximum of 26.7, significantly higher than the primitive mantle ratio of 17.5 ± 2.0 (Sun and McDonough, 1989). Magmas influenced by a fluid in equilibrium with residual rutile should have Nb/Ta values that are lower than mantle values, given that the $D_{\text{Nb}}/D_{\text{Ta}}$ for rutile/fluid is ~ 1.25 (Green, 1995).

Although the negative Nb-Ta anomalies may be due to the low mobility of these elements, the negative Ti anomaly of rocks from Roccamonfina and Ernici is much more pronounced than would be expected simply from the low fluid-mobility of Ti. The low TiO₂ contents of samples from Roccamonfina and Ernici could be a result of either a residual titanate that retains more Ti than Nb or Ta (e.g. ilmenite), or "pre-arc" partial melting processes that produced a depleted mantle wedge similar to the source of MORB. Another possibility for the low TiO₂ contents and decoupling of Nb-Ta and Ti could be the interaction of a carbonate-rich fluid or melt with the mantle source (Rudnick et al.,



Figures 7.22a. and 7.22b. Nb (ppm) vs. K₂O (wt%) (7.29a) and TiO₂ (wt%) vs. K₂O (wt%) (7.29b) for KS and HKS rocks of Roccamonfina and Ernici. Note the positive correlation between Nb and K₂O, and the weakly negative correlation between TiO₂ and K₂O.

1993; Ionov et al., 1993; Laurora et al., 2001; Ionov et al., 2002). Rudnick et al. (1993) found that the carbonatites responsible for metasomatizing parts of the Tanzanian mantle were depleted in Ti, but were not depleted in Nb or Ta relative to La. Metasomatism of a depleted mantle wedge by carbonatitic melts similar to those proposed for Tanzania would result in Nb-Ta enrichment, in contrast to the Nb-Ta depletion that is typical of arc-related magmas (Rudnick et al., 1993). This has important implications for the mantle sources of Vesuvius and Vulture, which show anomalous Nb-Ta enrichment that is greater than expected in a subduction-related environment.

In summary, the differing behavior of Nb, Ta, and Ti in the presence of a fluid phase indicates that the HFSE are decoupled in magmatic rocks from Roccamonfina, Ernici, and the Western Alps. The apparent negative anomalies of Nb and Ta on incompatible trace element diagrams can be explained by the relative immobility of these elements in a subduction environment, while the strong negative Ti anomalies can be attributed to: 1) a residual titanate that retains more Ti than Nb or Ta (e.g. ilmenite), 2) "pre-arc" partial melting processes that produced a depleted mantle wedge, or 3) metasomatism by a Ti-poor, Nb-Ta-rich carbonatite.

7.5c Tectonic discrimination diagrams using HFSE

The magmatic rocks from the Western Alps, Roccamonfina, and Ernici can be separated into orogenic and anorogenic environments, i.e. convergent versus intraplate tectonic settings, using plots of Th/Yb vs. Ta/Yb (Figure 7.23) and Th^*100/Zr vs. Nb^*100/Zr (Figure 7.24). These plots are based on the observation that island arc and active continental margin basaltic and andesitic rocks are significantly more enriched in

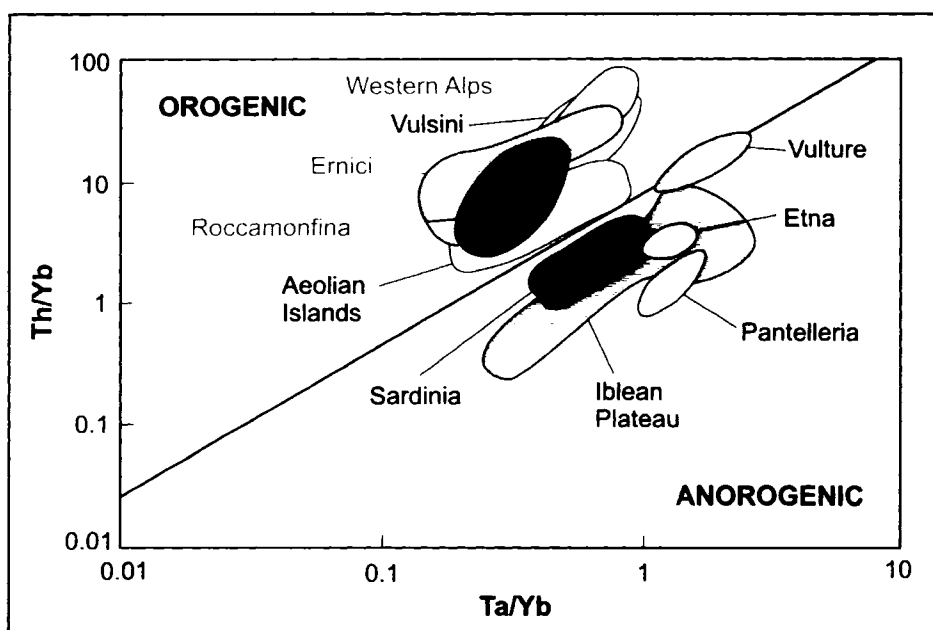


Figure 7.23. Tectonic discrimination diagram for data from Roccamonfina, Ernici, and the Western Alps, along with assorted magmatic rocks from Italy (modified from Wilson and Bianchini (1999), after Pearce (1982)).

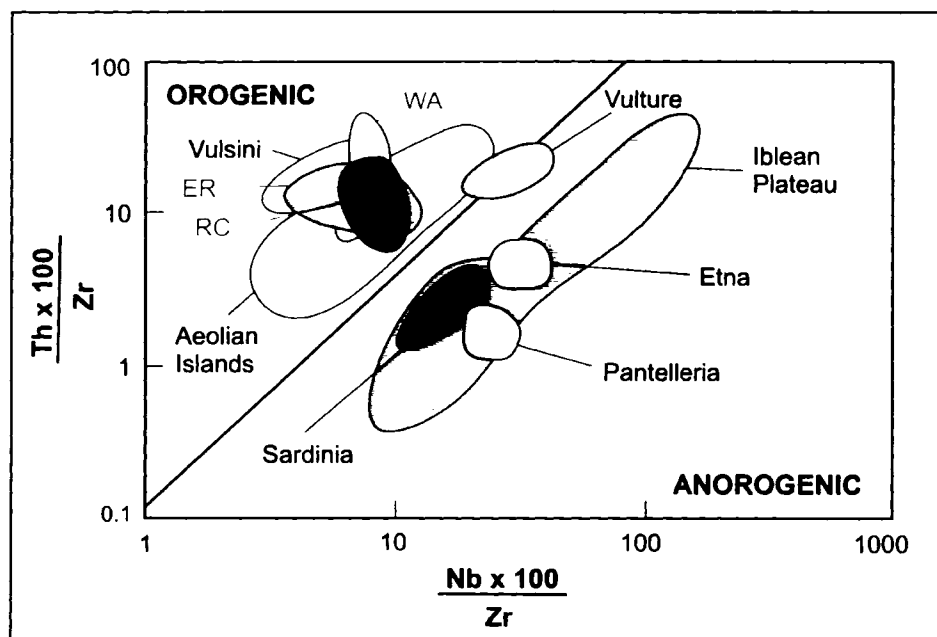


Figure 7.24. Tectonic discrimination diagram for data from Roccamonfina (RC), Ernici (ER), and the Western Alps (WA), along with assorted magmatic rocks from Italy (modified from Wilson and Bianchini (1999)).

Th than either Ta or Nb (Gill, 1981). Normalization to Yb (or Zr) reduces the effects of fractional crystallization of common minerals such as pyroxene, feldspar, amphibole and mica. As such, Th/Yb and Th/Zr ratios are thought to reflect source variations instead of melt evolution processes. Tectonic discrimination diagrams using HFSE have been useful in determining the tectonic settings of world-wide potassic and ultrapotassic rocks from known convergent or intraplate environments. Data from potassic and ultrapotassic volcanic rocks of the Sunda arc plot in the orogenic field, while data from alkaline rocks of Tristan da Cunha (oceanic intraplate) and the East African Rift (continental intraplate) plot in the anorogenic field (Thompson et al., 1984).

Data from the Western Alps, Roccamonfina, and Ernici plot in the orogenic field on Figures 7.23 and 7.24, along with data from the HKS and KS rocks of the Roman Province and calc-alkaline basalts from the Aeolian Islands. In contrast, data from sodic basalts of Sicily, Pantelleria, and the Plio-Pleistocene series of Sardinia plot in the anorogenic field. Data from Mt. Vulture, whose tectonic setting remains enigmatic, lies on the dividing line in both figures. The high Th/Yb and high Th/Zr ratios of rocks from Roccamonfina, Ernici, and the Western Alps are consistent with magma generation at a convergent plate margin.

7.5d Ce/Pb and Nb/U ratios as sediment tracers

The incompatible element ratios Ce/Pb and Nb/U are also useful in assessing potential crustal/sediment input into the mantle (Hofmann et al., 1986). Although the Ce/Pb and Nb/U ratios of mantle-derived mafic rocks cannot be expected to accurately reflect source values, these ratios are still useful because they are significantly different in

MORB and OIB compared to carbonaceous chondrites, the primitive mantle, and the continental crust (Figures 7.25 and 7.26). Hofmann et al. (1986) showed that Ce/Pb ratios average 25 ± 5 and Nb/U ratios average 47 ± 10 in both MORB and OIB. In contrast, the continental crust has much lower Ce/Pb (~ 4) and Nb/U (~ 10) ratios, which may be due in part to the migration of Pb from the mantle to the crust, and the retention of Nb in the mantle during partial melting processes (Hofmann et al., 1986).

The Ce/Pb ratios of the HKS and KS volcanic rocks of Roccamonfina and Ernici range from 2.8 to 15.5 (excluding two samples from Ernici with very low Pb contents). The HKS and KS samples have similar Ce/Pb ratios, but the HKS rocks have higher concentrations of Ce (and Pb) than the KS. Lamprophyres from the Western Alps also have very low Ce/Pb ratios (1.7 to 5.2) that overlap with fields for average continental crust and pelagic sediments. The Nb/U ratios of samples from Roccamonfina and Ernici (1.4 – 6.7) and the Western Alps (1.1 – 3.3) are extremely low. These Nb/U ratios are significantly lower than those of pelagic sediments, and may reflect Nb depletion (or U gain) related to fluid-mobility in a subduction environment (see section 7.5b.i).

The Nb/U and Ce/Pb ratios of rocks from the Western Alps, Roccamonfina, and Ernici are much lower than those of the continental lithospheric mantle, MORB, and OIB, and are consistent with crust/sediment input into the Italian mantle.

7.5e Boron and beryllium systematics

One of the most clear-cut indicators of recycled pelagic sediment and altered oceanic crust in the source of arc magmas is the presence of the short-lived ($t_{1/2} = 1.5$ Ma) cosmogenic isotope ^{10}Be in many lavas from convergent margins (Morris et al., 1990).

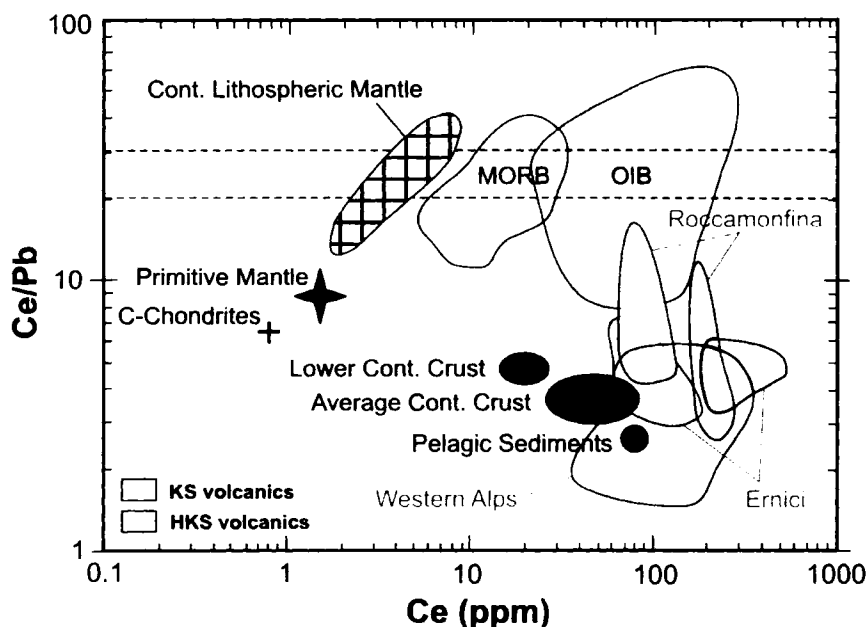


Figure 7.25. Ce/Pb vs. Ce plotted on a log-log scale. MORB and OIB data are plotted relative to the mantle Ce/Pb ratio of 25 ± 5 (Hofmann et al., 1986). Dashed lines indicate range of mantle values. References for carbonaceous chondrites, primitive mantle, continental lithospheric mantle, lower continental crust, average continental crust, and pelagic sediments given in Sims and De Paolo (1997).

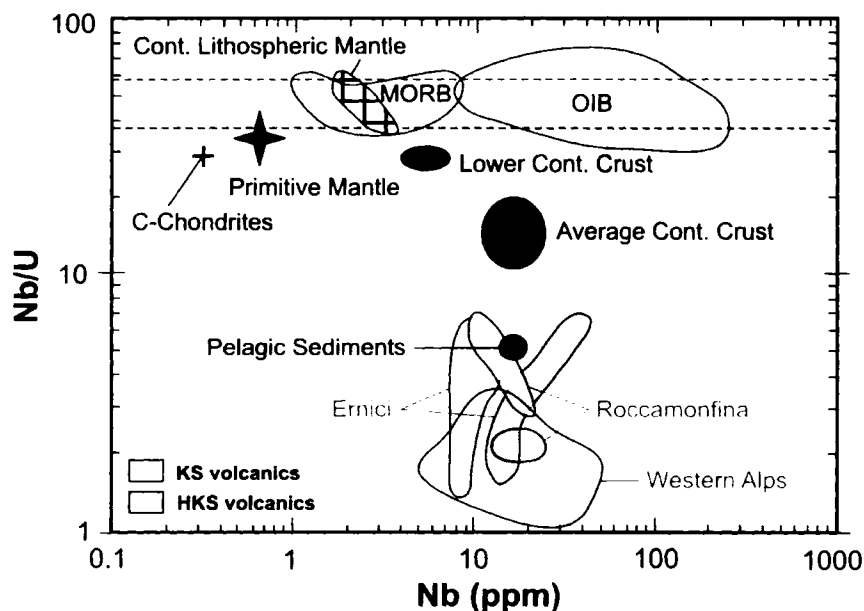


Figure 7.26. Nb/U vs. Nb plotted on a log-log scale. MORB and OIB data are plotted relative to the mantle Nb/U ratio of 47 ± 10 (Hofmann et al., 1986). Dashed lines indicate range of mantle values. References for carbonaceous chondrites, primitive mantle, continental lithospheric mantle, lower continental crust, average continental crust, and pelagic sediments given in Sims and De Paolo (1997).

^{10}Be is highly enriched in the uppermost several metres of ocean floor sediment, and can become incorporated into the source of arc magmas through subduction (Ryan, 2002). Positive correlations between $^{10}\text{Be}/\text{Be}$ and B/Be ratios in arc-related magmas indicate that the B/Be ratios of volcanic rocks can be used as a proxy to evaluate the contribution of sediment and altered oceanic crust to the mantle (Morris et al., 1990).

7.5e.i Geochemical behavior of B and Be

Boron is a highly incompatible trace element that is strongly enriched in ocean sediments due to its high concentration in sea water (average 4.3 ppm) and adsorption onto illite and mica (Ryan and Langmuir, 1993) (Table 7.6). Boron is highly soluble and is quickly partitioned into a fluid phase at temperatures above 375°C, resulting in very high concentrations (10-300 ppm) in hydrothermally-altered oceanic crust (Donnelly et al., 1980). Boron shows strong affinities for fluids liberated from the slab during dehydration, and is rapidly recycled at convergent margins before returning to surface reservoirs. Arc lavas generally have higher and more variable B contents than magmas with comparable silica content from intraplate or divergent tectonic settings (Morris et al., 1990). Boron contents in most arc lavas typically range from 10-90 ppm, while B contents in MORB and OIB are quite low (<3 ppm and <5 ppm respectively). Shale and pelagic sediments average about 100 ppm B, while marine carbonates have concentrations that range from 2-60 ppm (Harder, 1970).

Beryllium is also an incompatible trace element enriched in pelagic sediments, although it is substantially less soluble than B or other alkaline elements (Morris et al., 2002). The Be content of volcanic arc rocks ranges from <0.1 ppm in tholeiitic basalts to

Rock Type	Average B (ppm)	Average Be (ppm)	B/Be
Pelagic sediments	100	1-2	50-100
Shale	100	1-2	50-100
Marine carbonate	2-60	<1	2-60
Altered oceanic crust	10-300	<5	30-170
Average lower crust	<1-2	~1	1-2
Average upper crust	~15	~3	~5
MORB	<3	<2.5	3-5
OIB	<5	<1-10	3-5
Arc volcanic	1-90	<0.1-10	1-100

Table 7.6. B and Be contents and B/Be ratios of sedimentary and igneous rock types. Note the very high B concentration in altered oceanic crust, and the high B/Be in arc volcanics. References: Taylor and McLennan (1985), Shaw et al. (1988), Morris et al. (1990), Ryan and Langmuir (1993), Edwards et al. (1993), Ryan (2002).

over 10 ppm in alkalic arc lavas from the Mexican Volcanic Belt and the Sunda Arc (Table 7.6). MORB typically contain low Be (<2.5 ppm), while alkaline intraplate basalts have higher and more variable contents of 1-10 ppm (Ryan, 2002). Shale and marine sediments range from 1-2 ppm Be (Mn nodules can concentrate Be up to ~ 15 ppm), and marine carbonates normally contain <1 ppm Be (Graham et al., 1998).

The difference in mobility between B and Be in a fluid phase results in the preferential transport of B from the slab to the mantle wedge, which can create a source region for arc volcanic rocks with a high B/Be ratio (Morris et al., 1990). Since B and Be have similar bulk distribution coefficients, the B/Be ratio is largely unaffected by subsequent partial melting and crystal fractionation. Therefore, the B/Be ratios of primitive volcanic rocks are thought to directly reflect the B/Be ratios of the source (Edwards et al., 1993). Elevated B/Be ratios (>10) have been found in Quaternary lavas from the Aleutian, Central America, Southern Chile, Hokkaido, and Bismarck arcs (Morris et al., 1990; Edwards et al., 1993; Tera et al., 1986), while the B/Be ratios of MORB and OIB are much lower (3-5). The high mobility of B precludes long-term B enrichment of the sub-arc mantle. Based on correlations between B/Be ratios and ^{10}Be abundances, Morris et al. (1990) suggested that mantle modified by subduction processes older than about 5 Ma is too depleted in B to produce typical arc signatures.

7.5e.ii B and Be data from Roccamonfina and Ernici

The KS and HKS volcanic rocks from Roccamonfina and Ernici have high and variable B contents that range from 13.4 to 71.1 ppm, and 7.6 to 76.6 ppm, respectively (Table 7.7) (Owen and Bell, 2004). The B concentrations of samples from both volcanic

Sample ID	B (ppm)	Be (ppm)	B/Be
RC 100	48.1	7	6.9
RC 103	52.5	9	5.8
RC 104	13.4	2	6.7
RC 106	40.5	5	8.1
RC 107	39	3	13.0
RC 109	61.9	7	8.8
RC 110	17.6	3	5.9
RC 111	20	3	6.7
RC 113	71.1	8	8.9
RC 118	43.9	8	5.5
RC 119	26.8	4	6.7
RC 121	17.4	4	4.4
RC 123	25.6	6	4.3
RC 127	33.6	3	11.2
RC 129	20	3	6.7
ER 101	40	7	5.7
ER 104	50.2	7	7.2
ER 105	76.6	7	10.9
ER 107	45.9	7	6.6
ER 109	31.7	3	10.6
ER 110	54.3	10	5.4
ER 112	7.6	2	3.8
ER 114	30.9	3	10.3
ER 115	45.1	6	7.5
ER 116	13.4	2	6.7
ER 117	14.6	4	3.7
ER 118	57.8	7	8.3
ER 121	19.3	2	9.7
ER 122	10.9	2	5.5
ER 123	48.7	6	8.1

Table 7.7. B and Be concentrations and B/Be ratios of KS and HKS volcanic rocks from Roccamonfina and Ernici.

centres clearly exceed the values of MORB and OIB, and are more compatible with rocks from subduction-related environments (Figure 7.27). The enrichment in B indicates the involvement of a hydrous fluid phase in the mantle beneath Roccamonfina and Ernici, and imposes severe constraints on the timing of mantle metasomatism. The short residence time of B in the sub-arc mantle (< 5 Ma) suggests that both the KS and HKS source regions have been recently enriched in B. The B contents of samples from Roccamonfina and Ernici correlate positively with K_2O (Figure 7.28), which implies that the metasomatic agent that introduced B into the sub-arc mantle was also responsible for the enrichment in K (Owen et al., 2004).

The Be content of the KS and HKS volcanic rocks ranges from 3 to 9 ppm at Roccamonfina and from 2 to 10 ppm at Ernici. These values are significantly greater than the Be content of mid-ocean ridge tholeiites and are similar to the Be contents of both alkaline intraplate basalts (OIB) and alkaline arc volcanics from the Mexican Volcanic Belt and the Sunda arc (Morris et al., 1990). There is a positive correlation between Be and K_2O (Figure 7.29) in samples from Roccamonfina and Ernici, which suggests that the metasomatic agent that introduced K (and B) into the Italian upper mantle also carried HFSE such as Be (Owen et al., 2004). Since Be is relatively immobile in a fluid phase, the high Be concentrations in samples from Roccamonfina and Ernici provide evidence for the involvement of a metasomatic *melt* in the mantle source regions.

The B/Be ratios of KS and HKS rocks from Roccamonfina and Ernici range from 3.7 to 13.0, and are generally higher than those of MORB and OIB (Morris et al., 1990). The samples from Roccamonfina and Ernici also have higher B/Be ratios than those of potassic and ultrapotassic rocks from Vesuvius (< 5), which overlap with the values of

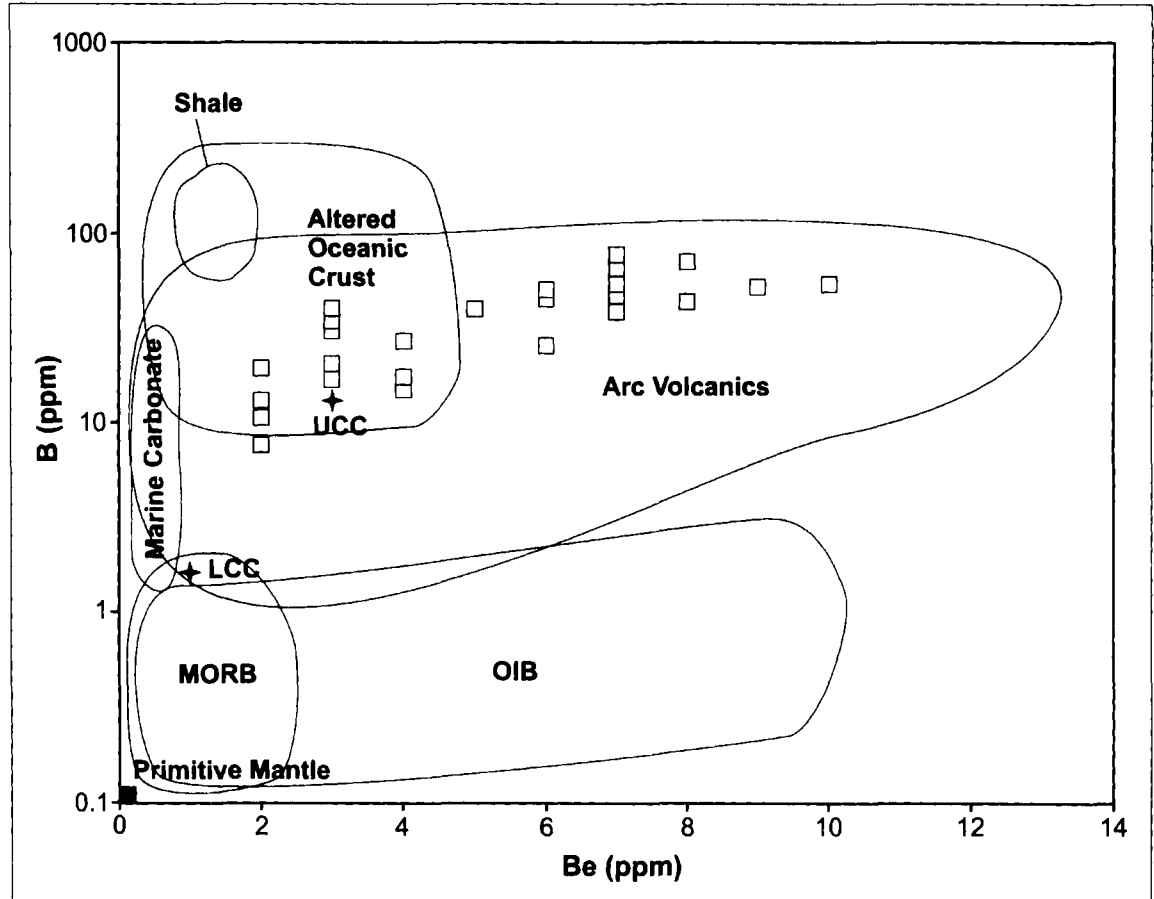


Figure 7.27. B and Be data from Roccamonfina and Ernici (filled squares) as well as the range of values for various sedimentary and igneous rock types. Data from Roccamonfina and Ernici fall entirely within the arc volcanics field. UCC = upper continental crust; LCC = lower continental crust. References are the same as in Table 7.6.

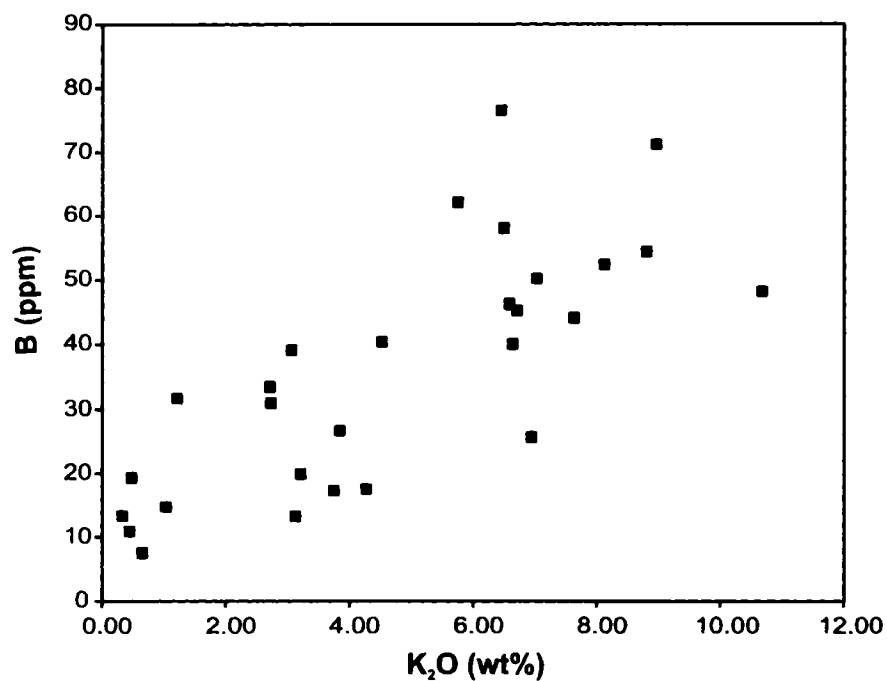


Figure 7.28. B (ppm) vs. K₂O (wt%) for KS and HKS samples from Roccamonfina and Ernici. Note the higher B content for members of the HKS series (K₂O > 5 wt%) at both volcanic centres.

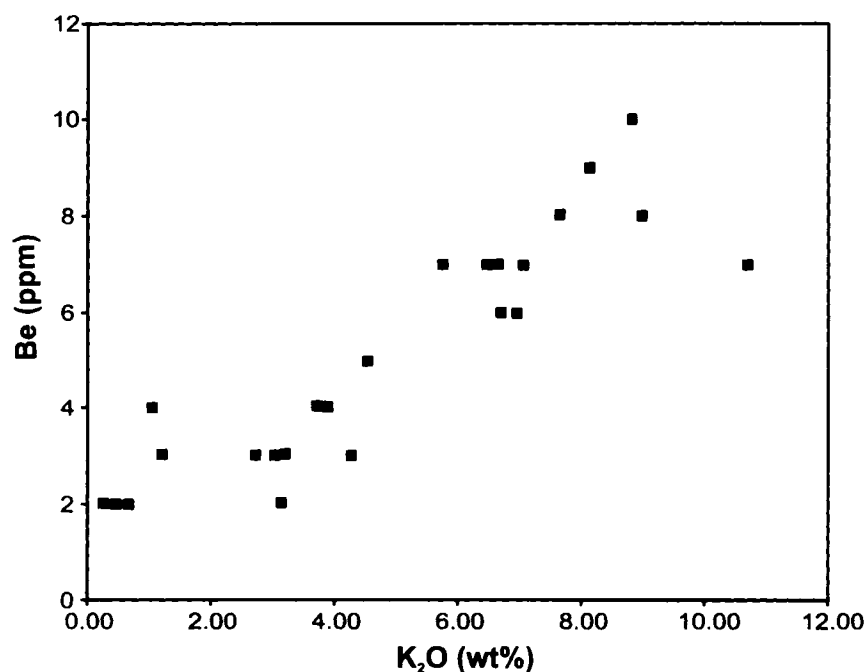


Figure 7.29. Be (ppm) vs. K₂O (wt%) for KS and HKS samples from Roccamonfina and Ernici. Note the higher Be content for members of the HKS series (K₂O > 5 wt%) at both volcanic centres.

MORB and OIB (Morris et al., 1993). However, Morris et al. (1993) noted that the low B/Be ratios of rocks from Vesuvius cannot be used unequivocally to argue against recent subduction in the Campanian region because other explanations such as crustal contamination, insufficient sediment subduction, loss of B from an unusually hot slab through prograde metamorphic reactions, or ineffective element transfer from the slab to the mantle wedge can also explain the low B/Be values.

7.5e.iii Comparison of B-Be data from Roccamonfina and Ernici with the Sunda arc

The Sunda arc displays a wide variety of rock series including tholeiite, calc-alkaline, high-K calc-alkaline, and potassic alkaline (leucitite and shoshonite). The leucitites and shoshonites are commonly compared to the HKS and KS rocks, respectively, of central Italy due to their similar major and trace element abundances (Foley et al., 1987). Figure 7.30 shows that the B and Be contents of volcanic rocks from Roccamonfina and Ernici are similar to those of potassic alkaline rocks from the Sunda arc (Edwards et al., 1993). Rocks of the Sunda potassic alkaline series are higher in Be, and generally lower in B, than those of the calc-alkaline and high-K calc-alkaline series. Volcanic rocks from the Sunda arc also show a positive correlation between Be and K_2O , but no correlation between B and K_2O . As a result, rocks with high K_2O contents have relatively low B/Be ratios due to both low B and high Be (Figure 7.31). The B/Be ratios of the Sunda arc calc-alkaline series range from about 8 to 109, while those from the potassic alkaline series range from about 1 to 7 (Edwards et al., 1993). Samples from Roccamonfina and Ernici have similarly low B/Be ratios, but extend to even higher

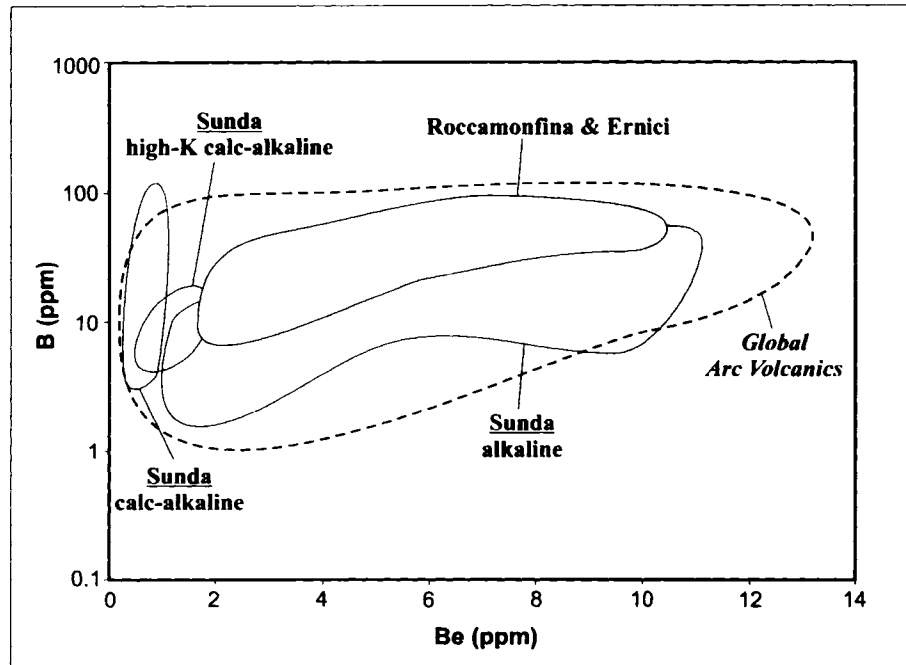


Figure 7.30. B-Be data from Roccamonfina and Ernici compared to rocks from the Sunda arc, Indonesia. Data for the Sunda arc from Edwards et al. (1993).

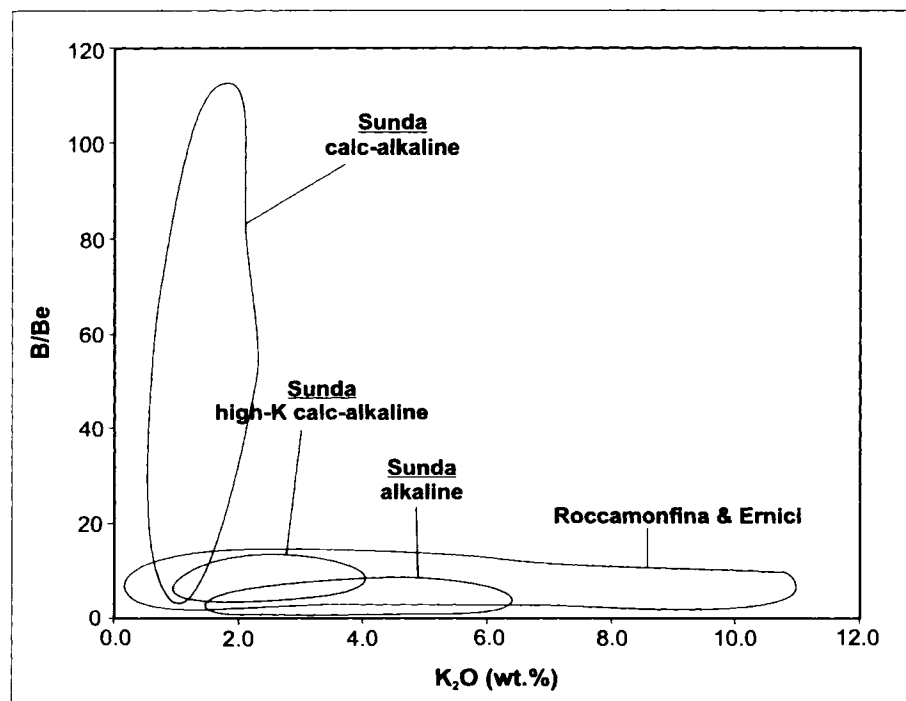


Figure 7.31. B-Be and K₂O contents of samples from Roccamonfina and Ernici compared to rocks from the Sunda arc, Indonesia. Data for the Sunda arc from Edwards et al. (1993).

values of K_2O than the Sunda alkaline rocks.

Edwards et al. (1993) argued that because the Sunda alkaline rocks always have low B/Be ratios, they must be derived from localized, non-metasomatized portions of the mantle not affected by recent subduction processes. The B and Be data from the KS and HKS rocks of Roccamonfina and Ernici suggest an alternative model. The Be concentrations of the Sunda calc-alkaline series are low (< 1.5 ppm) and constant, while the Be concentrations of Sunda alkaline rocks (and KS and HKS rocks from Roccamonfina and Ernici) are high and variable (~ 1.5 -11 ppm). The positive correlation between Be and K_2O in samples from both the Sunda arc and Roccamonfina and Ernici suggests that Be may be stored in a K-rich metasomatic phase (e.g. phlogopite or amphibole) that is preferentially melted during formation of the potassic and ultrapotassic magmas. The presence of phlogopite in the mantle beneath Roccamonfina is supported by phlogopite clinopyroxenite xenoliths found in pyroclastic deposits (Giannetti and Luhr, 1990). The low Be contents of calc-alkaline rocks from the Sunda arc may simply reflect the absence of this K-bearing metasomatic mineral in their source.

Thus, instead of concluding that the Sunda alkaline rocks have been derived from portions of the mantle which have not been modified by subduction, it is possible that the low B/Be ratios of these rocks (and KS and HKS rocks of Roccamonfina and Ernici) reflect source metasomatism by a slab-derived melt that was rich in Be and K_2O relative to B. The melt interacted with the resident lherzolite to form a mantle rich in pyroxene and phlogopite, as proposed by Rogers et al. (1985) for central-southern Italy.

The most important findings from the B and Be data of Roccamonfina and Ernici are: 1) the use of B/Be ratios as tracers of a "subduction signature" may not be valid for

potassic and ultrapotassic rocks derived from metasomatized source regions, 2) the positive correlations between B, Be, and K_2O suggest the presence of a metasomatic mineral in the central-southern Italian mantle that contains these elements, such as phlogopite, and 3) the difference between the generation of typical calc-alkaline magmas and highly-enriched potassic and ultrapotassic magmas at a convergent margin may be linked to the type of metasomatizing agent that influenced each source. The source region of calc-alkaline magmas may be produced by the interaction of a hydrous, slab-derived, LILE-enriched *fluid* with the mantle wedge, whereas the source region of potassic and ultrapotassic magmas could be the result of the modification of "normal" peridotitic mantle by silicic or carbonatitic *melts* that contain both LILE and HFSE.

7.5f Nature of the metasomatising agent: hydrous fluid or silicate melt?

The B and Be data from Roccamonfina and Ernici have shown that the metasomatizing agent in central-southern Italy must have been capable of transporting both fluid-mobile (LILE) and fluid-immobile (HFSE) trace elements. The chemical composition of the metasomatizing agent(s) currently remains one of the main questions in Plio-Quaternary Italian magmatism. Hawkesworth and Vollmer (1979) suggested that the geochemistry of Italian volcanic rocks resulted from mixing between an LILE-enriched fluid and a range of initial mantle compositions, and proposed that the metasomatising fluid may be derived either from an old LILE-enriched mantle source, or from subducted continental crust that partially retained its chemical identity in the upper mantle. Rogers et al. (1985) envisioned two distinct LILE-enriched metasomatizing agents; a KS-component with high Sr/Nd, Th/Ta, Ba/Nb, and no Eu anomaly, and a

HKS-component with low Sr/Nd, very high Th/Ta, and a negative Eu anomaly. Subsequently, Ellam et al. (1989) recognized that the KS component of Rogers et al. (1985) had chemical characteristics similar to basaltic ocean crust (MORB), and that the HKS component had affinities with pelagic sediments. Conticelli and Peccerillo (1992), on the other hand, concluded that fluids or melts from subducted marly, metasedimentary material were responsible for metasomatism of both the KS and HKS source regions.

The contrasting geochemical behavior of LILE and HFSE in samples from the Western Alps, Roccamonfina, and Ernici can provide some constraints on the nature of the metasomatizing agents. The concentrations of LILE in melts derived from metasomatized source regions reflect the contribution of a hydrous fluid, while the HFSE are more strongly controlled by crystal/melt processes that have taken place during melt evolution. LILE/HFSE ratios such as Ba/Nb are typically high in subduction-related volcanic rocks, while HFSE/HFSE ratios such as Zr/Nb are largely unaffected by the addition of mobile slab-derived components (Abratis and Wörner, 2001; Gertisser and Keller, 2003). Figure 7.32 shows a plot of Ba/Nb versus Zr/Nb for samples from the Western Alps, Roccamonfina, and Ernici, as well as for the average continental crust, N-MORB, and the mantle reservoirs EMI, EMII, HIMU. Enriched mantle reservoirs, such as EMI, EMII, and HIMU, have low Zr/Nb (< 15), while N-MORB, which originates from the depleted reservoir DMM, has a high Zr/Nb ratio of ~ 30 (Saunders et al., 1988; Weaver, 1991). All mantle reservoirs have low Ba/Nb (< 20), while average continental crust has a Ba/Nb ratio of about 54 (Saunders et al., 1988; Weaver, 1991).

The KS and HKS volcanic rocks of Roccamonfina and Ernici have higher Ba/Nb ratios than typical mantle values, and in fact the data from many samples lie well above

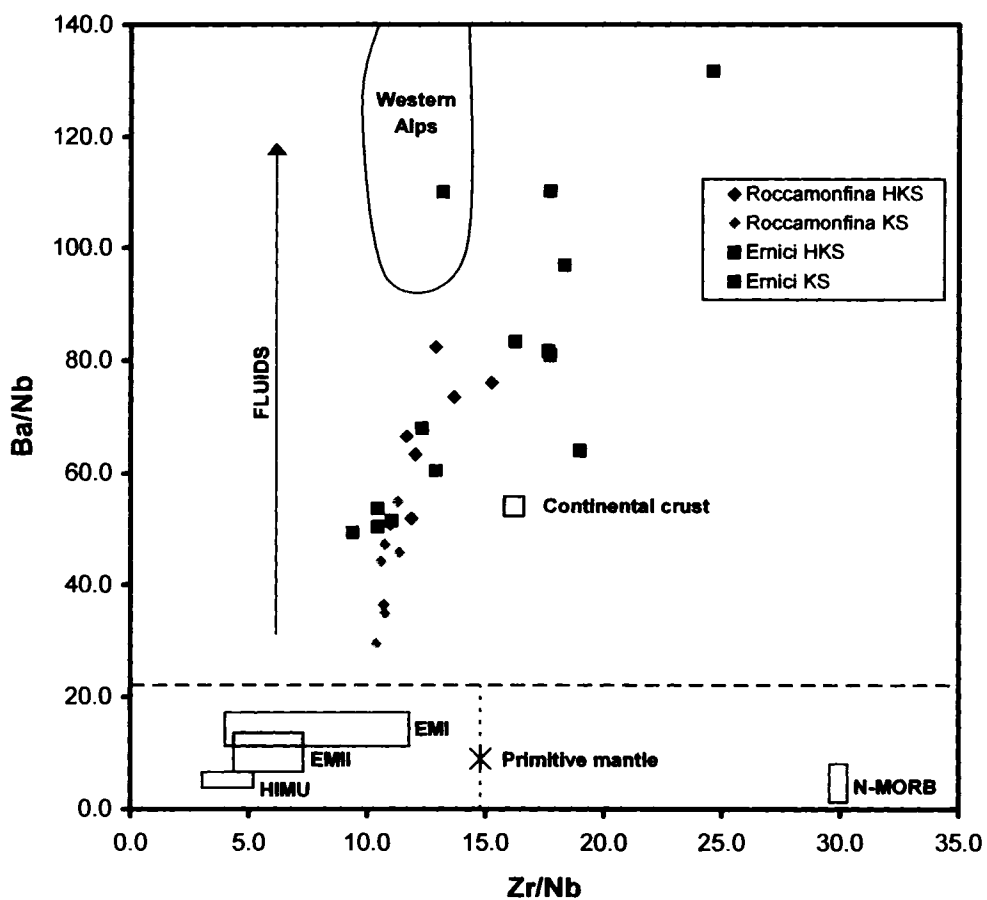


Figure 7.32. Ba/Nb vs. Zr/Nb diagram for samples from the Western Alps, Roccamonfina and Ernici, showing enriched mantle reservoirs EMI, EMII and HIMU, as well as the average continental crust, primitive mantle and N-MORB. Note the higher Ba/Nb in HKS samples compared to KS samples from Roccamonfina and Ernici. Crust and mantle data from compilations given in Saunders et al. (1988) and Weaver (1991).

that of average continental crust. The Ba/Nb ratios are higher in rocks of the HKS series than in those of the KS series (with the exception of sample ER 117). Lamprophyres from the Western Alps also have very high and variable Ba/Nb ratios (95 – 300), while the Zr/Nb ratios are fairly constant (11-15). The high Ba/Nb ratios of all the samples from Roccamonfina, Ernici and the Western Alps provide evidence for the involvement of a metasomatic agent that preferentially enriched the mantle in northern and central-southern Italy with LILE compared to HFSE.

Although samples from all three study areas are less enriched in HFSE than LILE, they still have higher concentrations of HFSE than MORB (except for Ti). The HFSE Th, La, and Ce are trace elements whose compounds are generally insoluble in water (Faure and Mensing, 2005). However, these elements are strongly enriched ($\geq 100x$ chondrite) in most samples from the Western Alps, Roccamonfina, and Ernici, suggesting the influence of a metasomatizing agent that may be CO₂-rich rather than H₂O-rich. Rogers et al. (1985) suggested that silicic, alkaline melts from subducted sediments may be responsible for the high HFSE contents of volcanic rocks from central-southern Italy, while Serri et al. (1993) proposed a high-Sr, high Ca, low Si component carried by a carbonatitic melt generated from marine carbonates.

Significant differences in the Th/Ta ratios of KS and HKS rocks from Roccamonfina and Ernici suggest that there may be different HFSE-mobilizing melts responsible for metasomatizing the KS and HKS source regions. Figure 7.33 shows a clear gap between the Th/Ta ratios of samples from the KS and HKS series at Roccamonfina and Ernici. Rocks of the KS series have relatively low Th/Ta ratios (< 25), while rocks of the HKS series have high Th/Ta ratios (> 35) that overlap with

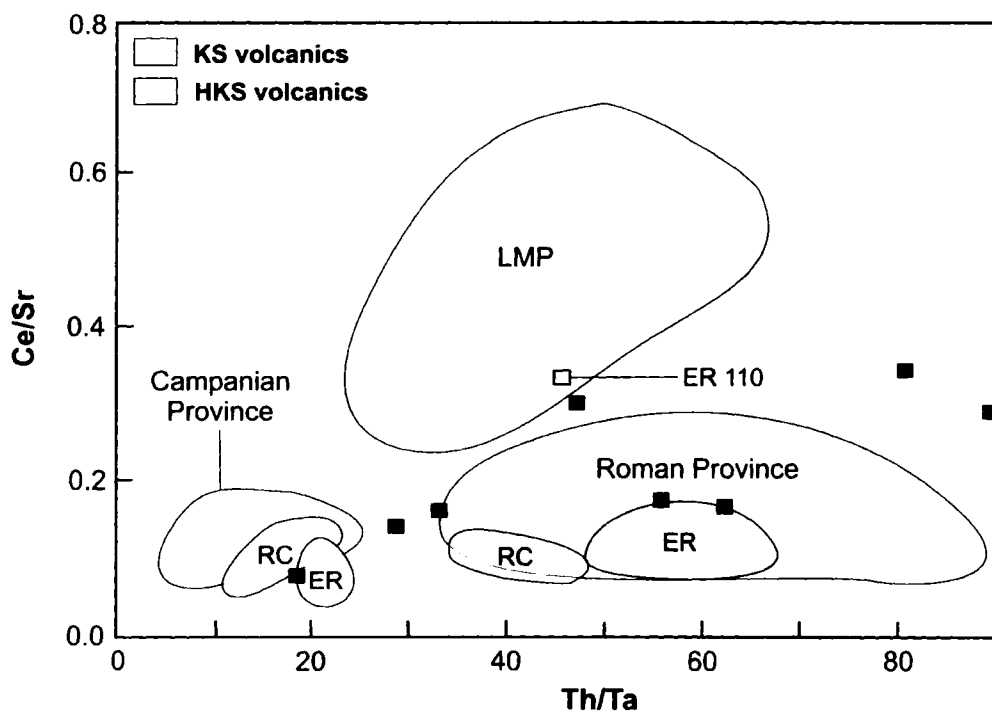


Figure 7.33. Comparison of KS and HKS volcanic rocks from Roccamonfina and Ernici with Tuscan lamproites (LMP) and potassic and ultrapotassic rocks from the Roman and Campanian Provinces. Modified from Peccerillo and Turco (2004). Data from the Western Alps are plotted as solid squares. Note the high Th/Ta of the HKS series at Roccamonfina and Ernici compared to the low Th/Ta of the KS series. Also note the high Ce/Sr of HKS sample ER 110.

values from the HKS rocks of the Roman Province. The different Th/Ta ratios of rocks from the Roman and Campanian Provinces (Figure 7.33) support the hypothesis that the KS and HKS source regions may have been affected by separate metasomatic events. Peccerillo (2001) and Peccerillo and Turco (2004) suggested that the high Th, La, and Ce contents of the HKS rocks in the Roman Province may be due to melts derived from the subduction of marly material from the Adriatic plate, while the KS rocks of the Campanian Province and Stromboli in the Aeolian Islands may be a result of fluids derived from the Ionian plate. According to this model, the co-existence of HKS and KS rocks at Roccamonfina and Ernici is due to mantle contamination by both the Adriatic and the Ionian plates. However, this hypothesis is difficult to reconcile with the positive correlations between Nb, Ti, B, Be, and K₂O (see Figures 7.22a, 7.22b, 7.28, 7.29) that appear to be continuous from the KS to the HKS series.

The lamprophyres from the Western Alps have a wide range of Th/Ta ratios, and several samples have high Ce/Sr ratios similar to those of Tuscan lamproites. Although the high Ce/Sr ratios of the Tuscan (and Spanish) lamproites are considered to be a source characteristic (Nixon et al., 1984), the high Ce/Sr ratios of lamprophyres from the Western Alps may reflect low-pressure plagioclase fractionation. One sample from Ernici (ER 110) has a Ce/Sr ratio that plots within the field of the Tuscan lamproites, consistent with the similar trace element signature of this sample to both Tuscan lamproites and lamprophyres from the Western Alps. Sample ER 110 contains no plagioclase feldspar, suggesting that the high Ce/Sr ratio of this sample is likely a source characteristic, and thus providing another geochemical link between the Tuscan mantle and parts of the central-southern Italian mantle.

Overall, LILE and HFSE evidence from the KS and HKS volcanic rocks of Roccamonfina and Ernici indicates magma generation from a variably metasomatized mantle. Although the metasomatic melt was capable of transporting both LILE and HFSE, the strong enrichment of LILE compared to HFSE suggests an associated fluid component similar to that typical of subduction zones. Major and trace element evidence such as high CaO, low SiO₂, high Th, La, and Ce, and lack of a negative Sr anomaly in most samples from Roccamonfina and Ernici favors metasomatism by a carbonate-rich melt rather than a silicic melt, as proposed by Serri et al. (1993). A carbonate-rich melt could be provided by either recent (Peccerillo and Turco, 2004) or ancient subduction of marine carbonates beneath the Italian peninsula or by anorogenic processes similar to those that have produced carbonatite magmas in the East African Rift (Stoppa and Wooley, 1997). The lamprophyres from the Western Alps also have high LILE/HFSE ratios that are typical of magmas generated in convergent tectonic settings. The trace element data from the lamprophyres is consistent with subduction-related metasomatism of the sub-Alpine mantle, as suggested by Venturelli et al. (1984).

7.6 Summary of whole-rock geochemistry

7.6a Western Alps

Although the lamprophyres from the Western Alps are extremely variable in both major and trace element geochemistry, they are all characterized by high Mg#s (>65) and relatively low SiO₂ contents (< 54 wt%). The lamprophyres have low CaO, Al₂O₃, Fe₂O₃, and TiO₂ combined with variable Na₂O, suggesting that the mantle beneath the Western Alps underwent partial melting *prior* to generation of the lamprophyres.

Subsequently, the depleted mantle underwent subduction-related metasomatism during the Alpine orogeny, as shown by the very high concentrations of LREE (> average continental crust) and strongly fractionated LREE/HREE and LILE/HFSE ratios of the lamprophyres. Bulk crustal contamination is considered unlikely because of high Mg#s and relatively high contents of compatible trace elements. A convergent margin tectonic setting is supported by high Th/Yb and Th/Zr ratios that are comparable to arc-related magmatic rocks (Wilson and Bianchini, 1999), and very low Ce/Pb and Nb/U ratios similar to those of pelagic sediments (Sims and De Paolo, 1997). Overall, the geochemistry of the lamprophyres is consistent with low-degree partial melting of a depleted mantle that was variably metasomatized by subduction-related fluids.

7.6b Roccamonfina and Ernici

Rocks of the KS series at both Roccamonfina and Ernici are characterized by higher CaO and MgO, lower K₂O and Al₂O₃, and lower abundance of incompatible trace elements than those of the HKS series. Volcanic rocks from both series have relatively low Fe₂O₃ and TiO₂ contents, indicating a mantle source more depleted than that of typical intraplate rocks. However, rocks from Roccamonfina and Ernici contain higher levels of CaO, Na₂O and Al₂O₃ than the Tuscan lamproites and kamafugites, suggesting that the mantle in central-southern Italy is less depleted than beneath Tuscany or the central Apennines. The MORB-like major element chemistry (except for K₂O) of the primitive KS and HKS rocks is consistent with previous partial melting of the mantle source, a signature observed in many subduction-related magmatic rocks.

Rocks from both the KS and HKS series are characterized by high LREE contents coupled with enrichment of LILE and relative depletion of Ba, P, and HFSE. The incompatible trace element patterns of samples from Roccamonfina and Ernici have negative anomalies of Nb, Ta, and Ti typical of arc-related rocks, and are broadly similar to the upper continental crust. Evidence for a crustal component in the mantle of central-southern Italy is provided by high Th/Yb and Th/Zr ratios, and low Ce/Pb and Nb/U ratios, of rocks from both volcanic centres. Very high B concentrations (up to 76 ppm) strongly suggest subduction of altered oceanic crust and pelagic sediment, and constrain metasomatism of the Italian mantle to the past 5 Ma. K₂O correlates positively with both LILE (Cs, Rb, Ba, Pb) and HFSE (La, Ce, Th, Nb, Ta, U) in all samples, indicating that the metasomatic agent was able to transport both fluid-mobile (LILE) and fluid-immobile (HFSE) trace elements. This suggests that the dominant metasomatic agent was a melt, rather than a fluid. The continuity of K₂O enrichment trends from the KS to the HKS series argues strongly against two different metasomatic melts, and instead supports varying degrees of source enrichment resulting from a single metasomatic event. Major and trace element evidence such as the high CaO, low SiO₂, high Th, La, and Ce, and lack of a negative Sr anomaly in most samples from Roccamonfina and Ernici favors a metasomatic component carried by a carbonate-rich melt, rather than a silicic melt.

CHAPTER 8

ISOTOPE GEOCHEMISTRY

8.1 Introduction

The most important recent development in the study of Italian magmatism is the suggestion of a HIMU or FOZO-like isotopic component, considered by many to be indicative of plume-related magmatism (see Chapter 4). Major revisions to the geodynamic model of the Western Mediterranean resulted in new models involving the upwelling of deep mantle material through a slab window (Gasperini et al., 2002), or mantle upwelling in the absence of a slab component (Bell et al., 2003). While previous work has indicated large-scale mixing between several distinct isotopic components (DMM, EMI, HIMU, and ITEM), the geodynamic significance of the isotopic end-members and the timing of mantle contamination remains unresolved. The mantle source regions of magmas from the Western Alps, Roccamonfina, and Ernici are located in areas that have been strongly influenced by the Alpine and Apennine orogenies. Detailed Rb-Sr, Sm-Nd, and U-Pb isotopic work on these volcanic rocks may help to clarify the nature and timing of mantle metasomatism in northern and central-southern Italy.

All isotopic analyses were conducted on whole-rock powders for the same samples as those analyzed for major and trace element geochemistry. Isotope ratios were measured on a multi-collector Finnigan-MAT 261 thermal-ionization mass spectrometer at Carleton University (sample loading procedures and filament types are given in Appendix G). Sample preparation and clean lab procedures for ion exchange columns are described in Appendix F.

8.2 Radiogenic isotope systems

8.2a Rb-Sr

Rubidium has two naturally occurring isotopes, ^{85}Rb and ^{87}Rb , of which ^{87}Rb is radioactive and decays to stable ^{87}Sr by emission of a negative β particle. Strontium has four naturally occurring isotopes, ^{88}Sr , ^{87}Sr , ^{86}Sr , and ^{84}Sr , all of which are non-radioactive. Rb is an alkali metal with an ionic radius similar to K, which allows Rb to substitute for K in K-bearing minerals such as mica and alkali feldspar (Faure and Mensing, 2005). Sr is a member of the alkaline earth group and has an ionic radius very similar to Ca. During fractional crystallization, Sr tends to be concentrated in plagioclase feldspar, whereas Rb remains in the melt. Consequently, the Rb/Sr ratio of the magma increases gradually during the course of progressive fractional crystallization. Crustal rocks generally have high Rb/Sr ratios (Rb/Sr \sim 0.32; Taylor and McLennan, 1981), whereas the primordial mantle is estimated to have an Rb/Sr ratio of approximately 0.03 (McDonough et al., 1991). As a result, the upper crust has developed much higher present-day $^{87}\text{Sr}/^{86}\text{Sr}$ ratios than the upper mantle.

8.2b Sm-Nd

Samarium has a large number of naturally occurring isotopes, of which ^{147}Sm undergoes α -emission to ^{143}Nd . In contrast to the Rb-Sr parent-daughter pair, Sm and Nd are both incompatible light REE whose concentrations increase in igneous rocks with increasing degree of differentiation (Faure and Mensing, 2005). The ionic radius of Nd (1.08 Å) is slightly larger than that of Sm (1.04 Å), and as a result Nd is slightly more incompatible and becomes concentrated in the melt relative to Sm during the course of

crystal fractionation. Therefore, typical crustal rocks have lower Sm/Nd ratios than rocks derived from the upper mantle, and will evolve lower time-integrated $^{143}\text{Nd}/^{144}\text{Nd}$ ratios compared to the upper mantle. Sm and Nd, along with other LREE, tend to concentrate in major rock-forming minerals such as feldspar, biotite, and apatite (Faure and Mensing, 2005). The REE may also occur in high concentrations in zircon, allanite, monazite, and other accessory minerals. The REE are less mobile than the alkali metals and alkaline earths during regional metamorphism, hydrothermal alteration, and chemical weathering, making the Sm-Nd system more robust than the Rb-Sr system.

$^{143}\text{Nd}/^{144}\text{Nd}$ isotope ratios are commonly expressed as epsilon (ϵ) values, which are a measure of the difference between the initial $^{143}\text{Nd}/^{144}\text{Nd}$ ratio of the sample and the corresponding ratio of CHUR at the same time. DePaulo and Wasserburg (1976) introduced the ϵ notation in order to resolve the problem of inter-laboratory differences in normalization procedures. A positive ϵ value implies that the magmas were formed from depleted mantle, whereas a negative value indicates that they were derived from enriched mantle sources that had a lower Sm/Nd than CHUR. Present-day ϵ values were calculated using $(^{143}\text{Nd}/^{144}\text{Nd})_{\text{present}} = 0.512638$, and ϵ values at $t = 30$ Ma for the Western Alps samples were calculated using $(^{143}\text{Nd}/^{144}\text{Nd})_{30\text{Ma}} = 0.512599$.

8.2c U-Th-Pb

Uranium has three naturally occurring isotopes, ^{238}U , ^{235}U , and ^{234}U , all of which are radioactive. Thorium is essentially monoisotopic with one long-lived radioactive isotope, ^{232}Th , and a number of short-lived decay products of ^{238}U , ^{235}U , and ^{232}Th . These three isotopes are each the parent of a chain of intermediate radioactive daughters

ending with a stable isotope of Pb, whereby $^{238}\text{U} \rightarrow ^{206}\text{Pb}$, $^{235}\text{U} \rightarrow ^{207}\text{Pb}$, and $^{232}\text{Th} \rightarrow ^{208}\text{Pb}$. The only isotope of Pb that is non-radiogenic is ^{204}Pb , which is used as a stable reference isotope. The two isotopes of Pb produced by the decay of U show contrasting behavior due to the differing decay rates of ^{235}U and ^{238}U . ^{207}Pb evolved rapidly in the early history of the Earth due to the rapid decay of ^{235}U , which is now essentially extinct. In contrast, the decay of ^{238}U is presently more prominent and as a consequence modern $^{206}\text{Pb}/^{204}\text{Pb}$ ratios show a greater spread than $^{207}\text{Pb}/^{204}\text{Pb}$ ratios.

U and Th are both members of the actinide series and substitute extensively for each other in nature because they have similar ionic radii in the tetravalent state (1.05 Å and 1.10 Å, respectively). However, under oxidizing conditions U can become mobile due to the formation of the water-soluble uranyl (UO_2^{2+}) ion, while Th exists only in the tetravalent state and is insoluble in water (Faure and Mensing, 2005). U and Th are both incompatible and become enriched in the melt relative to the residuum. As a result, the abundance of U and Th in more differentiated rocks is generally higher than in mafic or ultramafic rocks. Common rock-forming minerals typically contain U and Th on the order of a few parts per million or less, while accessory minerals such as zircon, allanite, uraninite, thorianite, monazite, apatite, and titanite can contain substantial amounts.

8.3 Isotopic data

8.3a Western Alps

The lamprophyres from the Western Alps are considered to be approximately 30 Ma, based on previous work from magmatic rocks of the Western Alps (Venturelli et al., 1984). This age is in agreement with the intrusion of numerous dykes and plutons along

the Periadriatic Lineament in the early Oligocene (von Blanckenburg et al., 1995). Due to the age and high parent/daughter ratios of some samples, measured isotopic ratios needed to be corrected to account for post-crystallization radiogenic growth. Both measured and initial isotopic ratios are given in Table 8.1. All isotopic data discussed regarding the Western Alps lamprophyres will refer to initial ratios at $t = 30$ Ma.

Initial $^{87}\text{Sr}/^{86}\text{Sr}$ ratios of the lamprophyres from the Western Alps are extremely heterogeneous, and range from 0.70590 to 0.71884 (Table 8.1). Most of the ratios are higher than the mantle components EMI and EMII, and indicate a mantle source that is anomalously enriched. The minettes (average $^{87}\text{Sr}/^{86}\text{Sr} = 0.71586$) are more radiogenic than the spessartites (average $^{87}\text{Sr}/^{86}\text{Sr} = 0.70916$), and the kersantite has an initial $^{87}\text{Sr}/^{86}\text{Sr}$ ratio of 0.71280. Initial $^{143}\text{Nd}/^{144}\text{Nd}$ ratios are quite low and range from 0.51203 to 0.51242, which also suggests an enriched source. Sr-Nd isotopic data from the lamprophyres of the Western Alps are significantly more enriched than "average" world-wide lamprophyres, which generally have $^{87}\text{Sr}/^{86}\text{Sr} < 0.7090$ and $^{143}\text{Nd}/^{144}\text{Nd} > 0.5123$ (see Figure 1.2) (Rock, 1991). This reflects the fact that the studied lamprophyres have much higher Rb/Sr ratios (avg. 0.35) than world-wide lamprophyres (avg. 0.09) (Rock, 1991). The lamprophyres have values of ϵ_{Nd} at $t = 30$ Ma that range from -3.6 to -11.1.

The Pb isotopic ratios of most samples from the Western Alps are very similar, with $^{206}\text{Pb}/^{204}\text{Pb} \sim 18.65$, $^{207}\text{Pb}/^{204}\text{Pb} \sim 15.67$, and $^{208}\text{Pb}/^{204}\text{Pb} \sim 38.78$. One exception is sample WA 107, which has a slightly higher $^{206}\text{Pb}/^{204}\text{Pb}$ ratio (18.84) than the other lamprophyres, and lower $^{207}\text{Pb}/^{204}\text{Pb}$ (15.60) and $^{208}\text{Pb}/^{204}\text{Pb}$ (38.19) ratios. The U/Pb and Th/Pb ratios of samples from the Western Alps range from 0.16 to 0.62 and from 0.32 to 2.79, respectively. These values overlap with the average ratios for world-wide

Sample	Rb/Sr	$^{87}\text{Sr}/^{86}\text{Sr}_m$	$^{87}\text{Sr}/^{86}\text{Sr}_0$	Sm/Nd	$^{143}\text{Nd}/^{144}\text{Nd}_m$	$^{143}\text{Nd}/^{144}\text{Nd}_0$
WA 100	0.36	0.71281	0.71237	0.23	0.51212	0.51209
WA 101	0.20	0.71111	0.71086	0.21	0.51230	0.51227
WA 102	0.81	0.71669	0.71569	0.24	0.51210	0.51207
WA 103	0.08	0.71082	0.71072	0.21	0.51232	0.51229
WA 104	0.58	0.71955	0.71884	0.23	0.51212	0.51209
WA 105	0.36	0.71701	0.71657	0.21	0.51205	0.51203
WA 106	0.43	0.71333	0.71280	0.23	0.51222	0.51219
WA 107	0.01	0.70592	0.70590	0.22	0.51244	0.51242

Sample	U/Pb	Th/Pb	$^{206}\text{Pb}/^{204}\text{Pb}_m$	$^{207}\text{Pb}/^{204}\text{Pb}_m$	$^{208}\text{Pb}/^{204}\text{Pb}_m$	$^{206}\text{Pb}/^{204}\text{Pb}_0$	$^{207}\text{Pb}/^{204}\text{Pb}_0$	$^{208}\text{Pb}/^{204}\text{Pb}_0$
WA 100	0.62	2.63	18.854	15.689	39.051	18.641	15.679	38.759
WA 101	0.19	1.23	18.692	15.654	38.882	18.625	15.651	38.747
WA 102	0.16	0.87	18.669	15.677	38.910	18.614	15.674	38.814
WA 103	0.28	1.38	18.773	15.669	38.906	18.677	15.665	38.753
WA 104	0.29	2.38	18.712	15.677	39.095	18.610	15.672	38.832
WA 105	0.38	2.79	18.716	15.681	39.134	18.583	15.674	38.825
WA 106	0.26	1.14	18.799	15.676	38.910	18.710	15.672	38.784
WA 107	0.16	0.32	18.895	15.605	38.224	18.842	15.603	38.188

Table 8.1. Measured (m) and age-corrected ($t = 30$ Ma) isotopic data for Western Alps lamprophyres.

lamprophyres ($U/Pb = 0.23$; $Th/Pb = 0.69$) (Rock, 1991). Similar to most other world-wide lamprophyres, the samples from the Western Alps plot above the NHRL (see Chapter 1) and contain higher ratios of $^{207}Pb/^{204}Pb$ and $^{208}Pb/^{204}Pb$ than MORB and OIB (Rock, 1991).

Considering the major and trace element evidence for the rather primitive nature of the lamprophyres from the Western Alps, their enriched isotopic signature appears to be a geochemical feature of the mantle in northern Italy. The only known reservoirs of highly radiogenic ($^{87}Sr/^{86}Sr > 0.7200$) material are the continental crust and pelagic or terrigenous sediments (Rollinson, 1993). Therefore, the isotopic data from lamprophyres in the Western Alps provide strong evidence for variable contamination of the sub-Alpine mantle by the subduction of continental crust or sediments during the Alpine orogeny.

The subduction-related tectonic setting is supported by the enriched incompatible element signatures and high LILE/HFSE ratios of the lamprophyres from the Western Alps (see Chapter 7). Bulk assimilation of significant amounts of crustal material is considered unlikely due to the very high Mg#s, relatively low SiO_2 , and high Cr, Ni, and Co contents of the lamprophyres. The extreme isotopic heterogeneity (especially for Sr and Nd) in samples from the Western Alps cannot be explained by crystal fractionation processes or by bulk crustal contamination upon ascent, as most lamprophyres show little or no petrological evidence for direct interaction with the continental crust. The isotopic heterogeneity provides evidence that each lamprophyre was derived from a different source region characterized by a distinct isotopic composition. This may reflect variable metasomatism of the Alpine mantle, or may be a result of isotopic mixing between mantle reservoirs with different isotopic signatures. The isotopic data from this study

supports the work of Kagami et al. (1985), who suggested that the strong crustal signature of magmatic rocks in the Western Alps may be a result of large-scale subduction of continental material during the Eocene.

The Sr-Nd isotopic data from lamprophyres from the Western Alps are similar to that of magmatic rocks from the Tuscan Province (Conticelli, 1998), and overlap with data from Hercynian lamprophyres in central Europe (Turpin et al., 1988) and calc-alkaline plutons of the Tertiary Periadriatic Province in the Central and Eastern Alps (Juteau et al., 1986; Kagami et al., 1991; von Blanckenburg et al., 1992) (Figure 8.1). Highly variable $^{87}\text{Sr}/^{86}\text{Sr}$ isotopic ratios, even for different phases of the same intrusion, characterize rocks from the Tuscan Province and the Tertiary Periadriatic Province (von Blanckenburg et al., 1992). The Sr and Nd isotopic ratios of Tertiary-Quaternary alkaline volcanic rocks in central Europe are very different from those of the older Hercynian lamprophyres, and form a comparatively tight cluster characterized by relatively low $^{87}\text{Sr}/^{86}\text{Sr}$ (< 0.7045) and high $^{143}\text{Nd}/^{144}\text{Nd}$ ratios (> 0.51260) (Wörner et al., 1986; Wilson et al., 1995). The isotopic signatures of the Tertiary-Quaternary European volcanic rocks are much more depleted than those of the lamprophyres from the Western Alps.

Overall, the data on Figure 8.1 suggest mixing between a depleted mantle component (best represented by the Tertiary-Quaternary European volcanic rocks) and an enriched source best represented by the Western Alps lamprophyres and Tuscan magmatic rocks. The depleted mantle component has been interpreted as a mixture of HIMU and DMM (Wilson and Downes, 1992), while the enriched component has a higher $^{87}\text{Sr}/^{86}\text{Sr}$ ratio than either EMI or EMII, and has affinities with the upper continental crust. The proposed mantle reservoirs known as LVC (Low Velocity

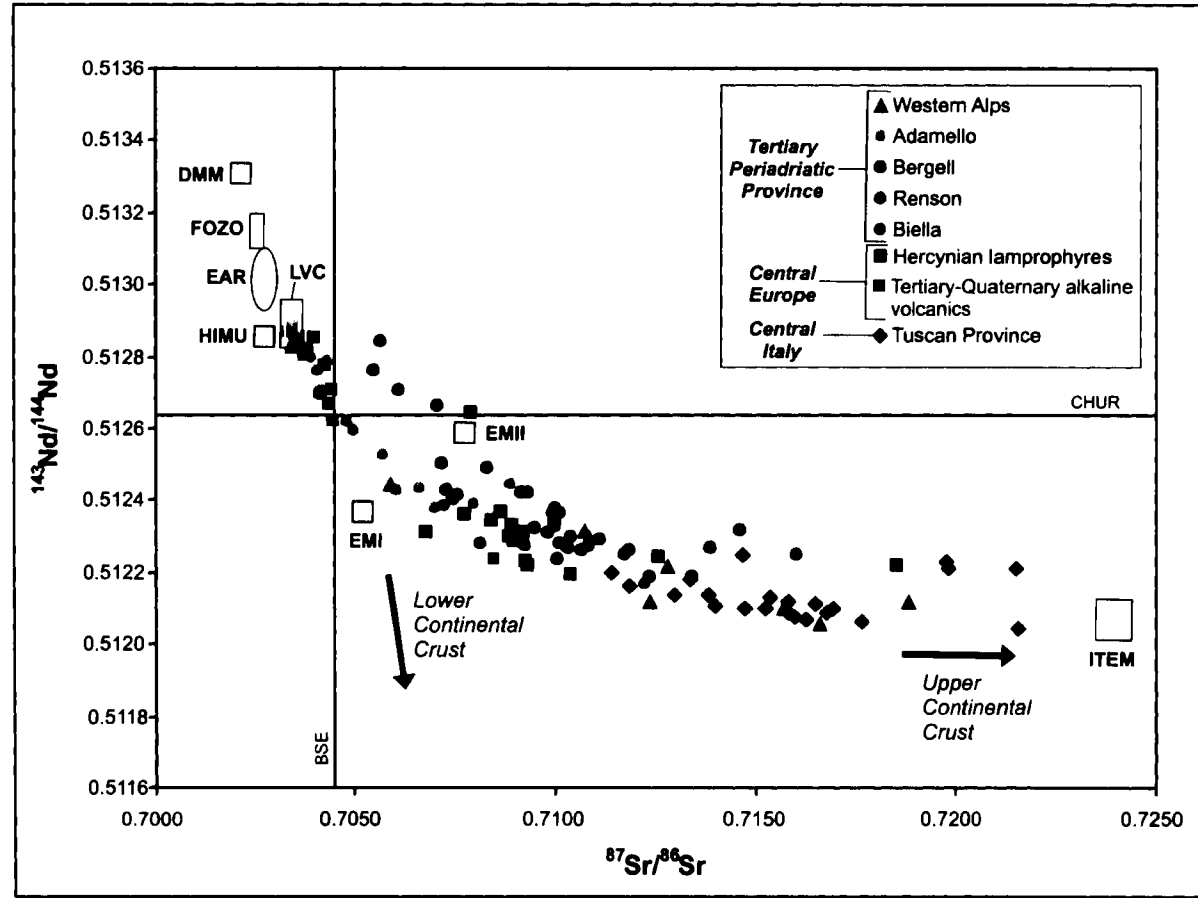


Figure 8.1. Nd-Sr anti-correlation diagram for lamprophyre samples from the Western Alps, as well as calc-alkaline plutons from the Tertiary Periadriatic Province (Adamello, Bergell, Renson and Biella), Hercynian lamprophyres and Tertiary-Quaternary melilitites, basanites, leucitites, and nephelinites from central Europe, and magmatic rocks of the Tuscan Province in central Italy. References: Juteau et al. (1986), Wörner et al. (1986), Turpin et al. (1988), Kagami et al. (1991), Oschidari and Ziegler (1992), von Blanckenburg et al. (1992), and Wilson et al. (1995). BSE = Bulk Silicate Earth, CHUR = CHondritic Uniform Reservoir.

Component; Hoernle et al., 1995), EAR (European Asthenospheric Reservoir; Cebriá and Wilson, 1995), and FOZO (Focus Zone; Hart et al., 1992) are also shown on Figure 8.1, and will be discussed in detail following presentation of isotopic data for Roccamonfina and Ernici. The enriched, crustal-like end-member is referred to as ITEM (Italian Enriched Mantle) (Bell et al., 2003), and is characterized by a $^{87}\text{Sr}/^{86}\text{Sr}$ ratio > 0.7220 and a $^{143}\text{Nd}/^{144}\text{Nd}$ ratio ≤ 0.51200 .

Most samples from the Western Alps, along with calc-alkaline plutons of the Tertiary Periadriatic Province and the Tuscan magmatic rocks, have a very narrow range of $^{206}\text{Pb}/^{204}\text{Pb}$ ratios (18.60-18.75), but a relatively wide range of $^{207}\text{Pb}/^{204}\text{Pb}$ (15.60-15.73) and $^{208}\text{Pb}/^{204}\text{Pb}$ (38.75-39.30) ratios. Figure 8.2 ($^{207}\text{Pb}/^{204}\text{Pb}$ vs. $^{206}\text{Pb}/^{204}\text{Pb}$) shows that data from the Alpine and Tuscan magmatic rocks plots to the right of the geochron and lies above the depleted mantle trend that runs between DMM and HIMU. Data from these rocks plots in the field of overlap between the upper continental crust, lower continental crust, and oceanic sediments, which are all characterized by high $^{207}\text{Pb}/^{204}\text{Pb}$ (and $^{208}\text{Pb}/^{204}\text{Pb}$) ratios at a given $^{206}\text{Pb}/^{204}\text{Pb}$ ratio relative to MORB (Wilson, 1989). The enriched mantle component EMII, originally described as a common component in Dupal OIB (Dupré and Allègre, 1983), also has a Pb isotopic composition similar to that of lamprophyres from the Western Alps. In contrast, Pb isotopic data from the European Hercynian lamprophyres and Tertiary-Quaternary alkaline volcanic rocks show a wide range of $^{206}\text{Pb}/^{204}\text{Pb}$ ratios that plot closer to the NHRL than the lamprophyre data from the Western Alps.

The different Pb isotopic signatures of the Alpine and Tuscan rocks compared to the European rocks are important for determining the origin of the ITEM component. The

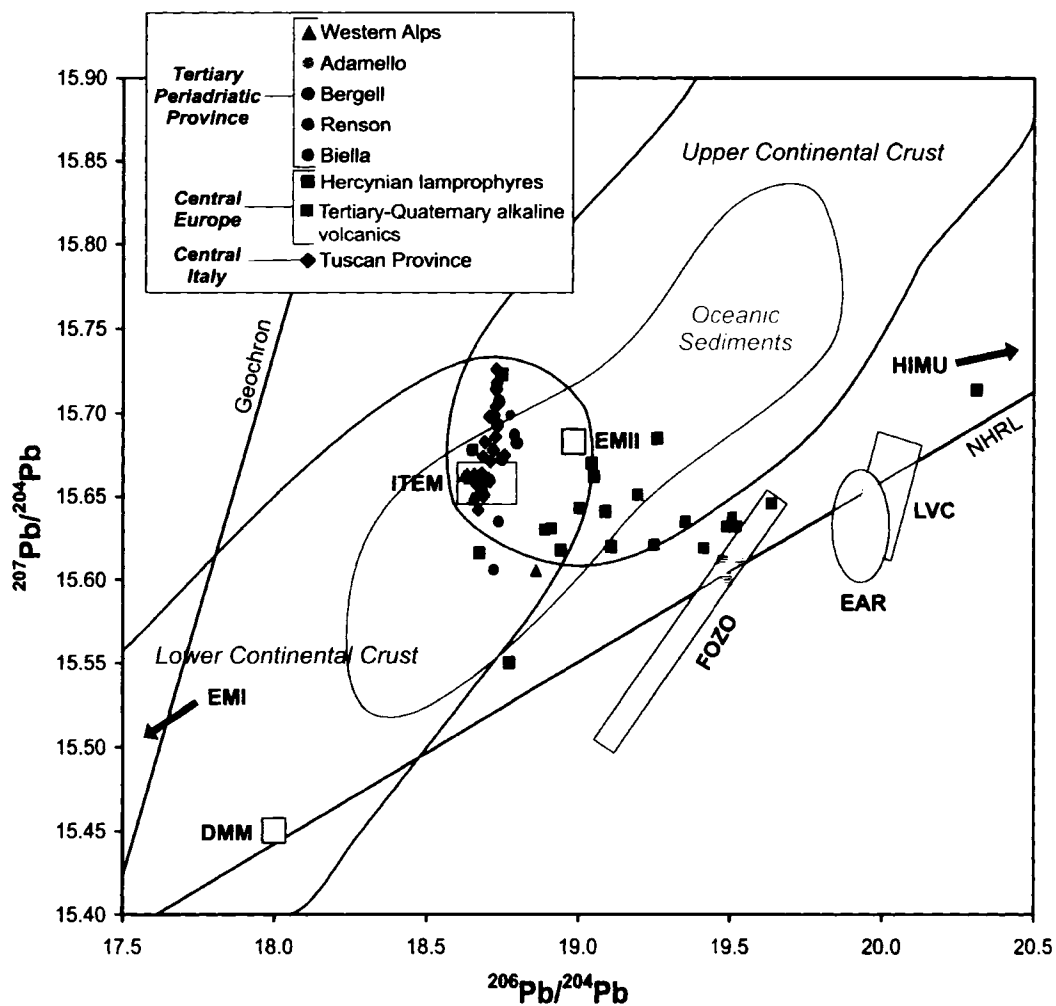


Figure 8.2. Pb-Pb diagram for lamprophyre samples from the Western Alps, as well as calc-alkaline plutons from the Tertiary Periadriatic Province (Adamello, Bergell, Renson and Biella), Hercynian lamprophyres and Tertiary-Quaternary melilitites, basanites, leucitites, and nephelinites from central Europe, and magmatic rocks of the Tuscan Province in central Italy. References: Juteau et al. (1986), Wörner et al. (1986), Turpin et al. (1988), Kagami et al. (1991), Oschidari and Ziegler (1992), von Blanckenburg et al. (1992), and Wilson et al. (1995). The fields for the upper and lower continental crust from Wilson (1989), and the field for oceanic sediments is from Zartman and Doe (1981).

highly enriched signatures of magmatic rocks from Tuscany and the Western Alps are not found in either older European rocks (the Hercynian lamprophyres) or younger European rocks (the Tertiary-Quaternary alkaline volcanics). This suggests that the ITEM component, which is "strongest" in northern and central Italy, did not contribute to the metasomatism of the European sub-continental mantle. However, there is strong evidence that ITEM did influence the isotopic compositions of Plio-Quaternary volcanic rocks from Italy (Bell et al., 2003). This topic will be discussed following an examination of the regional isotopic mixing trends in Italy (including Roccamonfina and Ernici) in the next section.

8.3b Roccamonfina and Ernici

Unlike the Oligocene lamprophyres from the Western Alps, the Pleistocene volcanic rocks from Roccamonfina and Ernici do not require any age correction to their measured isotopic ratios. The isotopic signatures of KS and HKS volcanic rocks from Roccamonfina and Ernici are significantly more radiogenic than those of MORB, with $^{87}\text{Sr}/^{86}\text{Sr}$ ratios that range from 0.7065 to 0.7110, and $^{143}\text{Nd}/^{144}\text{Nd}$ ratios between 0.51245 and 0.51210. There are also important differences between the Sr, Nd, and Pb isotopic compositions of the KS and the HKS series at both volcanic centres. The HKS rocks have higher $^{87}\text{Sr}/^{86}\text{Sr}$ ratios than the KS rocks, while the KS rocks have higher $^{143}\text{Nd}/^{144}\text{Nd}$ ratios than the HKS (Table 8.2). The average $^{87}\text{Sr}/^{86}\text{Sr}$ ratio of the HKS series at Roccamonfina and Ernici is ~ 0.7095 , and the average of the KS series is ~ 0.7070 . These values are similar to those published by Hawkesworth and Vollmer (1979), who found that the $^{87}\text{Sr}/^{86}\text{Sr}$ ratios for the HKS series at Roccamonfina range

Series	Sample	$^{87}\text{Sr}/^{86}\text{Sr}$	$^{143}\text{Nd}/^{144}\text{Nd}$	$^{206}\text{Pb}/^{204}\text{Pb}$	$^{207}\text{Pb}/^{204}\text{Pb}$	$^{208}\text{Pb}/^{204}\text{Pb}$
HKS	RC 100	0.70954	0.512187	18.799	15.671	39.006
HKS	RC 103	0.70955	0.512188	18.797	15.670	39.004
KS	RC 104	0.70691	0.512423	19.089	15.680	39.193
KS	RC 106	0.70703	0.512408	19.009	15.673	39.127
KS	RC 107	0.70755	0.512317	18.902	15.683	39.073
HKS	RC 109	0.70878	0.512237	18.852	15.681	39.059
KS	RC 110	0.70713	0.512406	19.053	15.686	39.189
KS	RC 111	0.70836	0.512252	18.843	15.669	39.013
HKS	RC 113	0.70948	0.512187	18.808	15.667	39.000
HKS	RC 118	0.70944	0.512203	18.813	15.683	39.046
KS	RC 119	0.70689	0.512390	19.014	15.697	39.177
KS	RC 121	0.70693	0.512398	19.008	15.689	39.159
HKS	RC 123	0.70927	0.512183	18.808	15.675	39.015
KS	RC 127	0.70748	0.512300	18.893	15.690	39.113
HKS	ER 101	0.70947	0.512185	18.814	15.690	39.055
HKS	ER 104	0.70990	0.512138	18.817	15.701	39.090
HKS	ER 105	0.70975	0.512178	18.808	15.681	39.033
HKS	ER 107	0.70983	0.512165	18.808	15.682	39.039
KS	ER 109	0.70834	0.512290	18.849	15.680	39.031
KS	ER 109*	0.70832	0.512290			
HKS	ER 110	0.71120	0.512150	18.732	15.676	38.999
KS	ER 112	0.70671	0.512414	18.910	15.679	39.050
KS	ER 114	0.70682	0.512377	18.954	15.684	39.073
HKS	ER 115	0.70992	0.512175	18.812	15.683	39.036
KS	ER 116	0.70654	0.512413	18.919	15.697	39.095
KS	ER 117	0.70977	0.512184	18.814	15.681	39.037
KS	ER 117*	0.70976	0.512165			
HKS	ER 118	0.70975	0.512195	18.820	15.673	39.016
KS	ER 121	0.70670	0.512377	18.936	15.674	39.035
KS	ER 122	0.70659	0.512433	18.898	15.673	39.025

Table 8.2. Measured isotopic compositions of KS and HKS samples from Roccamonfina and Ernici. * = duplicate analysis.

from 0.7085-0.7100, and the $^{87}\text{Sr}/^{86}\text{Sr}$ ratios for the KS series range from 0.7064-0.7083. The $^{143}\text{Nd}/^{144}\text{Nd}$ ratios of samples from Roccamonfina and Ernici range from 0.5123-0.5124 in the KS series and from 0.5121-0.5122 in the HKS series.

The Sr and Nd isotopic data from the KS and HKS volcanic rocks of Roccamonfina and Ernici plot on a mixing trend between a component with low $^{87}\text{Sr}/^{86}\text{Sr}$ (< 0.7060) and a component with high $^{87}\text{Sr}/^{86}\text{Sr}$ (> 0.7120) (Figure 8.3). The Sr and Nd isotopic compositions for KS and HKS samples from Ernici are more extreme than those of Roccamonfina, i.e. data from the KS series extend to lower $^{87}\text{Sr}/^{86}\text{Sr}$ ratios while HKS data extend to higher $^{87}\text{Sr}/^{86}\text{Sr}$ ratios. While previous studies have suggested that the KS and HKS magma series are isotopically distinct (Giannetti and Ellam, 1994), the data from Roccamonfina show that the highest $^{87}\text{Sr}/^{86}\text{Sr}$ ratio of rocks from the KS series is very close to the lowest $^{87}\text{Sr}/^{86}\text{Sr}$ ratio of rocks from the HKS series.

Two samples from the KS series of Ernici, ER 109 and ER 117, have significantly higher $^{87}\text{Sr}/^{86}\text{Sr}$ (> 0.7080) and lower $^{143}\text{Nd}/^{144}\text{Nd}$ (< 0.5123) ratios compared to other members of the KS series. Sample ER 117 plots in the field of the HKS rocks, while sample ER 109 plots between the KS and HKS series on the isotopic mixing trend (see Figure 8.3). No samples with $^{87}\text{Sr}/^{86}\text{Sr}$ and $^{143}\text{Nd}/^{144}\text{Nd}$ ratios similar to those of ER 109 and ER 117 have previously been reported from Ernici (Civetta et al., 1981). Duplicate Sr and Nd isotopic analyses for ER 109 and ER 117 agreed with the initial data (see Table 8.2). Samples ER 109 and ER 117 contain abundant analcime, which can form either as a primary magmatic phase or through the secondary alteration of leucite by hydrous fluids (Deer et al., 1992). However, the formation of analcime through secondary processes is unlikely to change the isotopic ratios present in a rock, especially

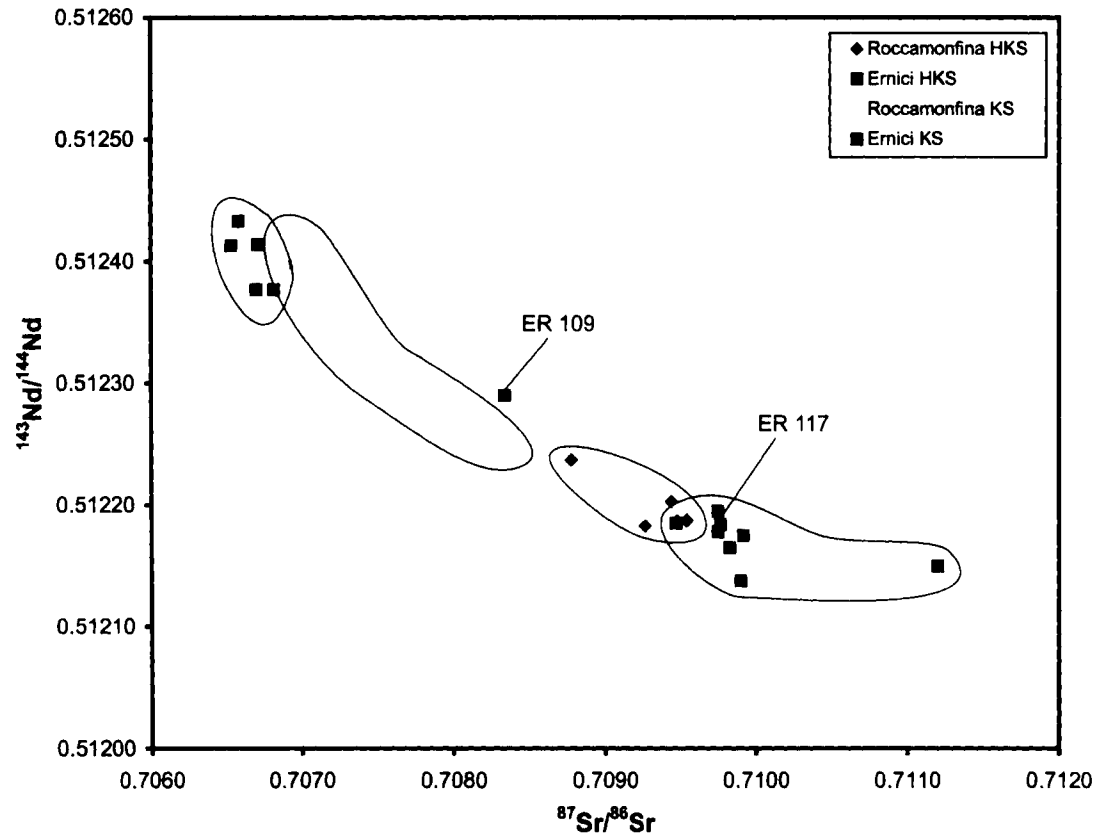


Figure 8.3. Nd-Sr isotope ratio diagram for KS and HKS rocks from Roccamonfina and Ernici. Note the position of data from samples ER 109 and ER 117 from Ernici.

for the Sm-Nd isotopic system (Rollinson, 1993). This raises the possibility of mixing between the KS and HKS source reservoirs, which have generally been thought to be isolated from one another.

The Sr and Nd isotopic data from Roccamonfina and Ernici correlate well with $^{206}\text{Pb}/^{204}\text{Pb}$ ratios, but not with $^{207}\text{Pb}/^{204}\text{Pb}$ and $^{208}\text{Pb}/^{204}\text{Pb}$ ratios. The $^{206}\text{Pb}/^{204}\text{Pb}$ ratios decrease with increasing $^{87}\text{Sr}/^{86}\text{Sr}$ (Figure 8.4), while the $^{207}\text{Pb}/^{204}\text{Pb}$ and $^{208}\text{Pb}/^{204}\text{Pb}$ ratios show little or no change (Figure 8.5). Figure 8.4 also suggests that the $^{206}\text{Pb}/^{204}\text{Pb}$ ratios may be slightly higher in the KS samples (avg. = 18.97) from Roccamonfina than the KS samples from Ernici (avg. = 18.90), although more analyses are required for confirmation. The $^{207}\text{Pb}/^{204}\text{Pb}$ and $^{208}\text{Pb}/^{204}\text{Pb}$ ratios show no significant difference between the KS and HKS series.

The KS rocks from Roccamonfina and Ernici are isotopically similar to rocks from the Campanian Province, while the HKS rocks are similar to those from the Roman Province (Figure 8.6). Sample ER 110, which has anomalously high concentrations of incompatible elements, has a higher $^{87}\text{Sr}/^{86}\text{Sr}$ ratio than any rock measured from the Roman Province. Although the volcanic rocks of the Roman Province are isotopically distinct from those of the Campanian Province, the Southern Latium Transition Zone (Roccamonfina and Ernici) appears to contain rock types that are isotopically transitional between the Roman and Campanian rocks (Hawkesworth and Vollmer, 1979; D'Antonio et al., 1996). However, most authors maintain that the KS and the HKS series are isotopically distinct and are related to two separate metasomatic events (e.g. Peccerillo, 2001). Figure 8.6 suggests that the apparent lack of rock types with $^{87}\text{Sr}/^{86}\text{Sr}$ and $^{143}\text{Nd}/^{144}\text{Nd}$ ratios between those of the Roman and Campanian Provinces may have been

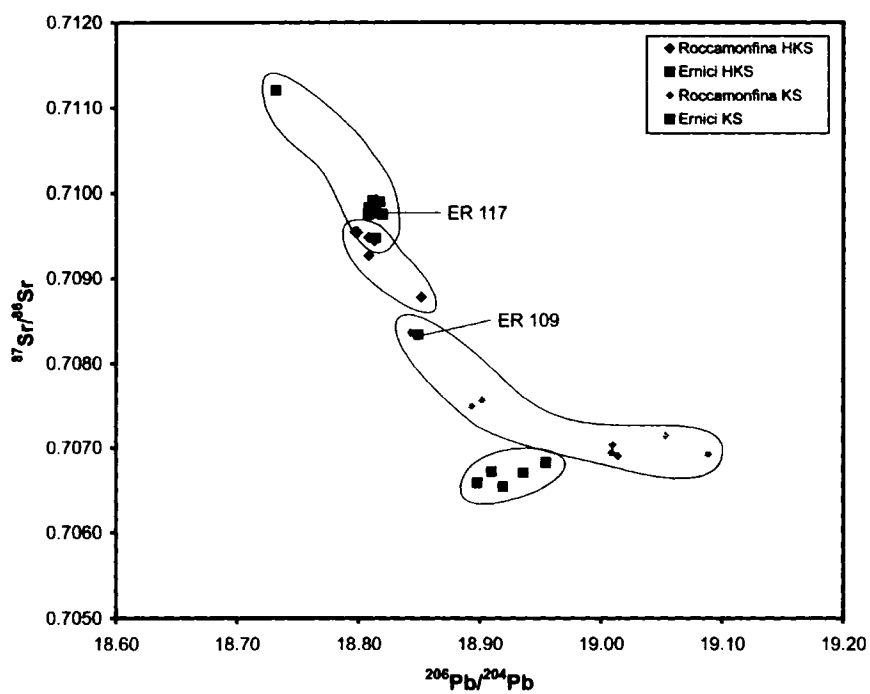


Figure 8.4. $^{87}\text{Sr}/^{86}\text{Sr}$ vs. $^{206}\text{Pb}/^{204}\text{Pb}$ ratios for HKS and KS rocks from Roccamonfina and Ernici.

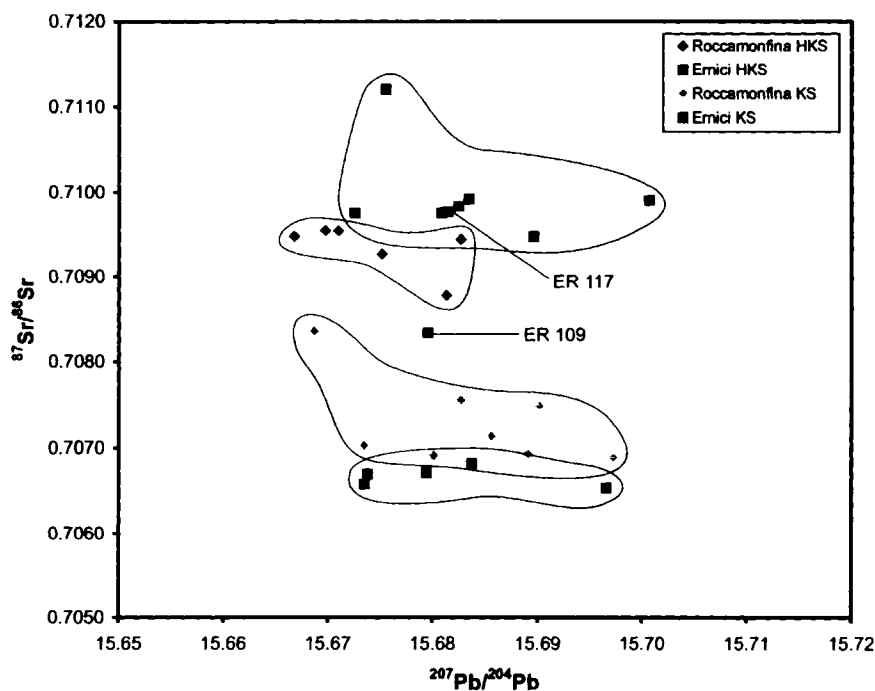


Figure 8.5. $^{87}\text{Sr}/^{86}\text{Sr}$ vs. $^{207}\text{Pb}/^{204}\text{Pb}$ ratios for HKS and KS rocks from Roccamonfina and Ernici.

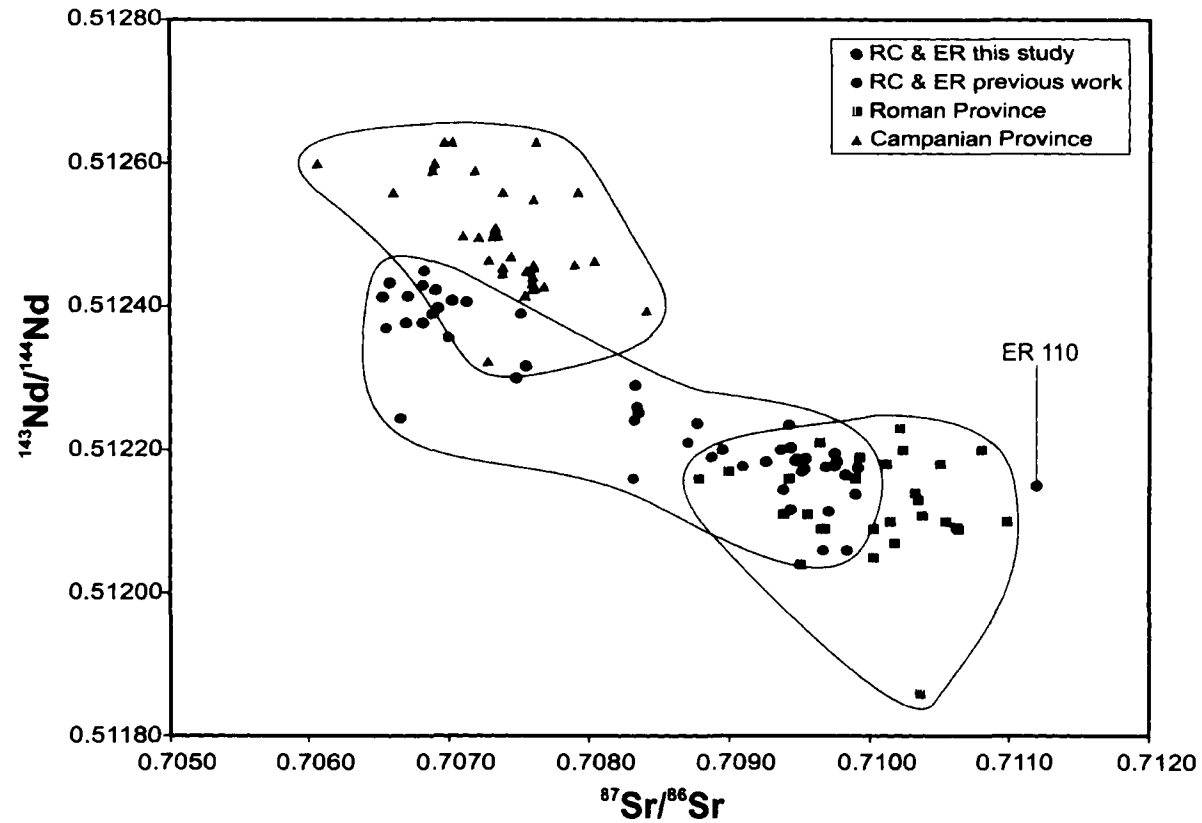


Figure 8.6. Sr-Nd anti-correlation diagram for volcanic rocks from Roccamonfina and Ernici, the Roman Province, and the Campanian Province. Previous work for Roccamonfina and Ernici is from Hawkesworth and Vollmer (1979), Gianetti and Luhr (1990), and D'Antonio et al. (1996). Data for the Campanian Province is from Hawkesworth and Vollmer (1979), Civetta et al. (1991b), D'Antonio et al. (1996), and Ayuso et al. (1998). Data for the Roman Province is from Hawkesworth and Vollmer (1979), Rogers et al. (1985), Federico et al. (1994), D'Antonio et al. (1996), Battistini et al. (2001), and Conticelli et al. (2002).

due to insufficient sampling at Roccamonfina and Ernici. It is important to note that petrological differences between the potassic (KS) and the ultrapotassic (HKS) rock types, as well as differences in major and trace element geochemistry, still support the division of the rocks from Roccamonfina and Ernici into two magma series. However, data from this study suggests that the KS and the HKS series may be *isotopically* continuous. This has important implications for the metasomatic history of the Italian mantle, and the origin of the potassium-bearing metasomatic agents (see Chapter 9).

8.4 Regional isotopic trends and end-member reservoirs

8.4a Introduction

Regional correlations in the Sr, Nd, Pb, and O isotopic ratios of Plio-Quaternary Italian magmatic rocks were first recognized in the 1960s and 1970s (Hurley et al., 1966; Vollmer, 1976). Early work focused on two-component mixing between a depleted mantle end-member and a crust-like end-member characterized by high $^{87}\text{Sr}/^{86}\text{Sr}$ and low $^{143}\text{Nd}/^{144}\text{Nd}$ ratios (Figure 8.7) (Vollmer, 1976, Turi and Taylor, 1976; Vollmer, 1977). The depleted end-member is best represented by magmatic rocks from Mt. Etna, the Iblean Plateau, Pantelleria, and Pietre Nere, and has been described as E-MORB (Rogers et al., 1985), OIB + MORB (Ellam et al., 1989), a mixture of DMM and HIMU (D'Antonio et al., 1996; Gasperini et al., 2002), LVC (Hoernle et al., 1995), EAR (Cebriá and Wilson, 1995) and FOZO (Bell, 2002) (see Chapter 4). The enriched, crust-like end-member is referred to as ITEM (Bell et al., 2003), and is strongest in rocks from Tuscany and the Western Alps. The origin of the ITEM signature has been ascribed to ancient, sub-continental lithosphere (Vollmer and Hawkesworth, 1980; Varne, 1985), subducted

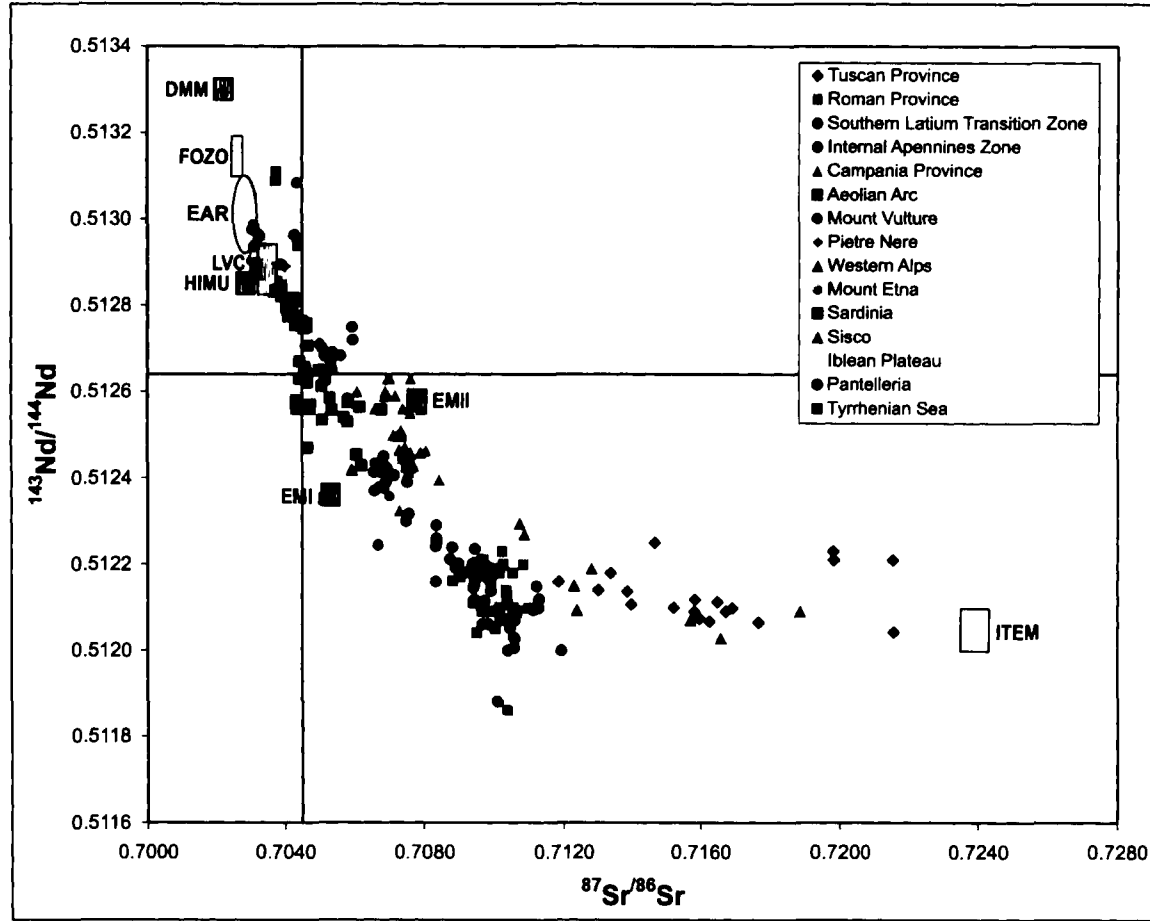


Figure 8.7. Nd-Sr anti-correlation diagram for Italian magmatic rocks showing the mantle end-members DMM, EMI, EMII, and HIMU, as well as FOZO, EAR, LVC, and the crustal end-member ITEM. References can be found in Appendix A.

sediments (Holm et al., 1982; Ellam et al., 1989; D'Anontio et al., 1996; Bell et al., 2004), slab-derived hydrous silicic melts (Rogers et al., 1985), subducted carbonaceous pelites (Beccaluva et al., 1991; Conticelli and Peccerillo, 1992), and a deep, isolated mantle reservoir (Bell et al., 2004). The depleted and enriched end-members will be examined using a compilation of Sr, Nd, and Pb isotopic data from Italian magmatic rocks as well as new data from Roccamonfina, Ernici, and the Western Alps.

8.4b The depleted end-member

The depleted end-member in Italian magmatic rocks is characterized by low $^{87}\text{Sr}/^{86}\text{Sr}$ (< 0.7040) and high $^{143}\text{Nd}/^{144}\text{Nd}$ (> 0.5130) ratios similar to those of both MORB and OIB (Wilson, 1989). Data from the most isotopically depleted Italian rocks plots near the mantle reservoirs DMM, HIMU, LVC, EAR, and FOZO on Figure 8.7. Pb isotopic data can help to determine which of these reservoirs best fits the depleted end-member involved in Italian isotopic mixing. A plot of $^{206}\text{Pb}/^{204}\text{Pb}$ vs. $^{87}\text{Sr}/^{86}\text{Sr}$ (Figure 8.8) shows that although DMM, HIMU, FOZO, EAR and LVC all have low ratios of $^{87}\text{Sr}/^{86}\text{Sr}$, they have very different values of $^{206}\text{Pb}/^{204}\text{Pb}$. HIMU is characterized by high ratios of $^{206}\text{Pb}/^{204}\text{Pb}$ (> 21.5), DMM has low ratios of $^{206}\text{Pb}/^{204}\text{Pb}$ (< 18.5), and FOZO, EAR and LVC have intermediate values that lie between those of HIMU and DMM. The depleted end-member has $^{206}\text{Pb}/^{204}\text{Pb}$ ratios that are close to those of FOZO, EAR, and LVC, but do not extend to either HIMU or DMM. This provides evidence that the depleted end-member is either a very homogeneous mixture of HIMU and DMM (D'Antonio et al., 1996; Gasperini et al., 2002), or that it is composed of "pure" FOZO (Bell, 2002), EAR (Cebriá and Wilson, 1995), or LVC (Hoernle et al., 1995).

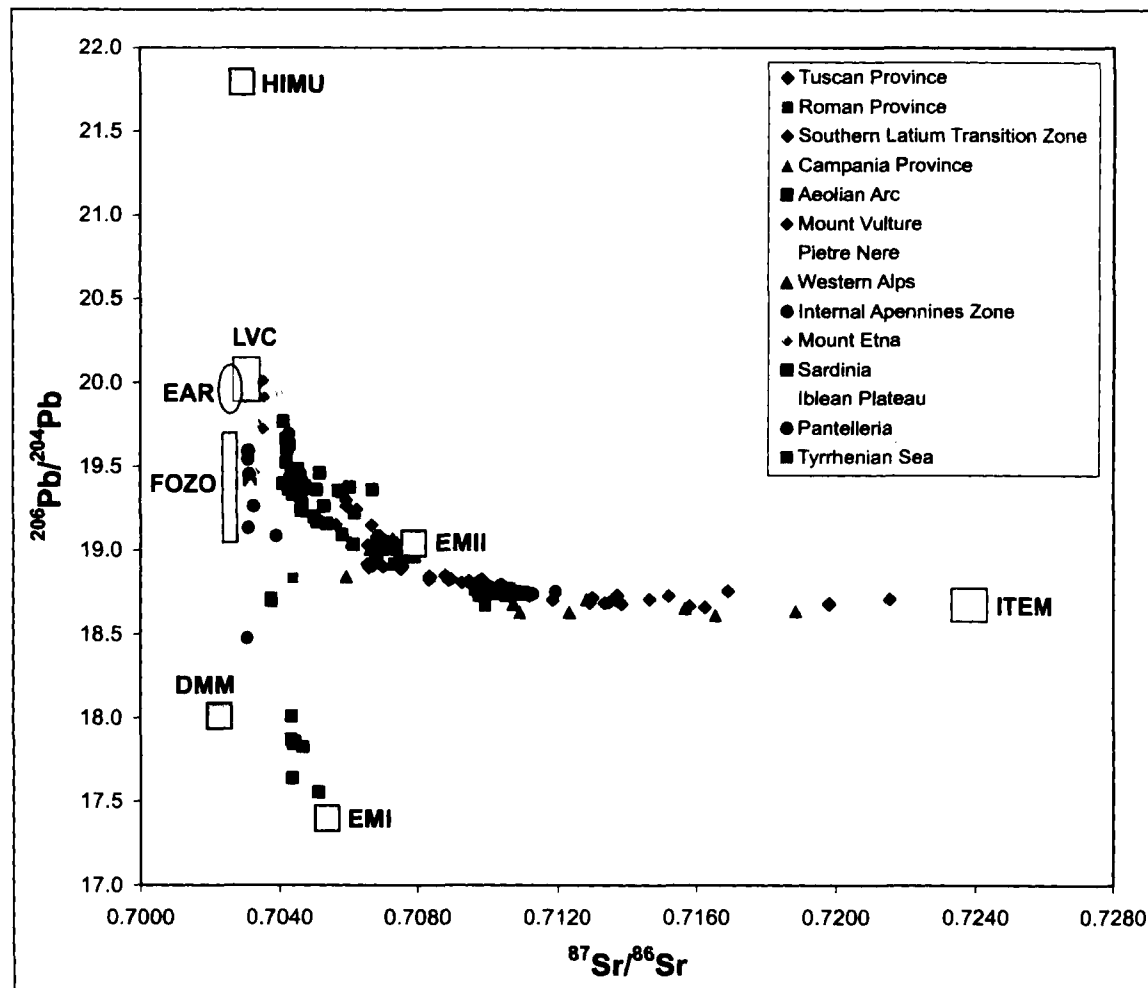


Figure 8.8. Pb-Sr diagram for Italian magmatic rocks showing the mantle end-members DMM, EMI, EMII, and HIMU, as well as FOZO, LVC, and the crustal end-member ITEM. References can be found in Appendix A.

Similar diagrams using $^{208}\text{Pb}/^{204}\text{Pb}$ and $^{207}\text{Pb}/^{204}\text{Pb}$ ratios show the same result, except that there is more scatter in the $^{208}\text{Pb}/^{204}\text{Pb}$ and $^{207}\text{Pb}/^{204}\text{Pb}$ isotopic ratios than in the $^{206}\text{Pb}/^{204}\text{Pb}$ ratio. The depleted end-member shows a mixing relation with EMI in Sardinia and the Tyrrhenian seafloor, and with high $^{87}\text{Sr}/^{86}\text{Sr}$ mantle (ITEM) in peninsular Italy and the Aeolian Arc. Interestingly, EMI and ITEM do not show any mixing relationship, as first noted by Bell et al. (2003). This lack of "communication" between EMI and ITEM is important in reconstructing the contamination history of the Italian mantle, and the origin of the depleted and enriched end-members.

8.4b.i What are FOZO, LVC and EAR?

Sr, Nd, and Pb isotopic data have shown that the depleted end-member in Italian magmatic rocks is similar to the proposed mantle reservoirs FOZO, LVC, and EAR. The concept of FOZO was developed by Hart et al. (1992), who found that data from world-wide OIBs, when plotted in Sr-Nd-Pb isotope space, lie largely within a tetrahedron delineated by four mantle end-members (DMM, HIMU, EMI, and EMII). The focusing of data into the corners of the tetrahedron suggested that the end-members are fairly restricted in composition (particularly for DMM and HIMU). However, data from individual islands and island groups shows sub-linear, elongated arrays that may indicate mixing between various mantle reservoirs. Hart et al. (1992) noted that the arrays are fan-shaped and appear to diverge from a 'Focus Zone' at the base of the mantle tetrahedron (between DMM and HIMU) towards a variety of enriched mantle end-members. This common component is referred to as FOZO, and is thought to be the signature of lower mantle material entrained into plumes originating from the core-

mantle boundary layer. The main lines of evidence against an upper mantle origin for FOZO include the high $^3\text{He}/^4\text{He}$ ratios of many OIBs, which are believed to originate from a primordial, unmixed, deep-seated reservoir (Wilson, 1989), and the lack of a DMM signature in the OIB mixing arrays.

Subsequent work showed that the location of FOZO in the mantle tetrahedron as originally proposed by Hart et al. (1992) may not be satisfactory, since some oceanic island arrays (e.g. the Macdonald Seamounts) trend from HIMU or DMM towards the middle of the tetrahedron. Therefore, Hauri et al. (1994) revised the concept of FOZO to a somewhat less depleted signature bearing a strong resemblance to PREMA (PREvalent MAntle). Again, this component was also identified with elevated levels of ^3He . In addition, Hauri et al. (1994) suggested that the entrainment of uppermost mantle into plumes is insignificant, while the extent of lower mantle entrainment is quite variable (between 5% and 90%). The positive fluid dynamic evidence for the preferential entrainment of lower mantle material into upwelling plumes also supports a lower mantle origin for the FOZO reservoir.

On the basis of MORB Sr-Nd-Pb isotopic data, Hanan and Graham (1996) defined a common component that is nearly identical to FOZO and is referred to simply as C. The similar isotopic characteristics of FOZO, C, and PHEM (Primitive Helium Mantle; a high $^3\text{He}/^4\text{He}$ component in many plumes named by Farley et al. (1992)) suggest that these all may represent the same mantle reservoir. However, Hanan and Graham (1996) argued against a lower mantle origin for C, and proposed that this component is located in the transition zone (410 – 670 km) based on $^{206}\text{Pb}/^{204}\text{Pb}$ and Ce/Pb ratios. In this model, C material with low $^3\text{He}/^4\text{He}$ ratios may originate from

regions of the transition zone where recycled or altered oceanic crust has been stored, while C with high $^3\text{He}/^4\text{He}$ ratios may be due to a relatively larger amount of mass transfer from the lower mantle (Hanan and Graham, 1996).

In contrast to the deep-seated origin proposed by Hart et al. (1992) and Hauri et al. (1994) for FOZO, LVC and EAR are generally considered to be relatively shallow, asthenospheric mantle reservoirs located within the upper mantle. The LVC can be described as a large region of mantle upwelling that resembles an inclined sheet and extends from the eastern Atlantic Ocean to Central Europe and the Western Mediterranean (Hoernle et al., 1995). This region is estimated to have a width of approximately 2,500 km in the NNE direction, and is characterized by low S-wave velocities and a narrow range of depleted Sr-Nd-Pb isotopic values defined by primitive magmatic rocks from the Canary Islands to the western Pannonian basin. The oldest volcanism that displays an LVC signature has been dated at ~65 Ma. Tomographic models (Zhang and Tanimoto, 1992) are consistent with a low-velocity, W-dipping sheet that underlies the lithosphere (~100 km depth) in the Italian region and extends to depths greater than 500 km beneath the eastern Atlantic. An important feature noted by Hoernle et al. (1995) is that there appears to be no tomographic evidence for deep roots of the LVC beneath central Europe or the western Mediterranean. Volcanic rocks located within the LVC region have relatively low $^3\text{He}/^4\text{He}$ ratios that are similar to MORB, which suggests that either the LVC is exclusively an upper mantle feature, or it has been disconnected from a deep source for a sufficiently long time that the $^3\text{He}/^4\text{He}$ ratio has been lowered by radiogenic ^4He production.

The EAR is defined by primitive mafic volcanic rocks from the Tertiary Central European Volcanic Province that have distinct Sr-Nd-Pb isotopic trends that converge on a common depleted source composition (Cebriá and Wilson, 1995). The volcanism within western and central Europe is spatially and temporally related to the development of a major intra-continental rift system and to domal uplift of Variscan basement massifs on a scale of 100s of km (Wilson and Downes, 1991; Wilson and Patterson, 2001). These features, along with Paleocene-Recent mantle melting in central Europe, have been attributed to the diapiric upwelling of small-scale, finger-like convective instabilities originating from the EAR reservoir, which is thought to be located in the asthenospheric mantle above the transition zone (Cebriá and Wilson, 1995).

Asthenospheric upwellings have been identified on the basis of local seismic tomography studies in the Massif Central (France) and Eifel (Germany) volcanic districts, and are estimated to be about 100-300 km across and up to 100-200°C hotter than ambient mantle (Granet et al., 1995; Ritter et al., 2001; Keyser et al., 2002). The so-called "hot fingers" of asthenospheric material are much smaller in diameter than the plumes of Hawaii or Iceland, and are thought to originate from the parent EAR layer located at a depth of 200-400 km. Granet et al. (1995) proposed that this layer may be a "fossil" plume head that has spread out above the transition zone but is not thermally equilibrated with the surrounding mantle.

An alternative hypothesis for the origin of the EAR reservoir involves 500-400 Ma oceanic lithosphere subducted during the Hercynian orogeny and subsequently incompletely mixed into the convecting asthenospheric upper mantle (Wilson and Downes, 1991). This type of source could provide the trace element characteristics and

moderate $^{206}\text{Pb}/^{204}\text{Pb}$ ratios of the EAR, which are not as extreme as the $^{206}\text{Pb}/^{204}\text{Pb}$ ratios developed by HIMU-dominated centres such as St. Helena (Chaffey et al., 1989).

Some authors (Goes et al., 1999; Ritter et al., 2001) have proposed that the low-velocity material in the European asthenosphere is fed by a large lower mantle upwelling located between 660 and 2000 km depth. Goes et al. (1999) attributed the large-scale rifting and widespread volcanism of central Europe to the interaction of a deep-seated plume with subducted material in the transition zone; however, the ability of a plume to provide a thermal anomaly *above* the large amount of subducted lithosphere in southern Europe and the western Mediterranean is a contentious issue. It should be noted that the EAR and the LVC reservoirs may well be essentially one and the same.

Geodynamic interpretation of the FOZO, LVC and EAR mantle reservoirs in the context of Italian magmatism will be discussed in detail in Chapter 9, following an examination of tomographic models for the Western Mediterranean and central Europe.

8.4c The enriched end-member

The enriched end-member ITEM is characterized by very high $^{87}\text{Sr}/^{86}\text{Sr}$ (> 0.7220) and low $^{143}\text{Nd}/^{144}\text{Nd}$ (< 0.51220) ratios that are more extreme than those of the enriched mantle reservoirs EMI and EMII (Rollinson, 1993). ITEM has a much higher value of $^{87}\text{Sr}/^{86}\text{Sr}$ than is typically observed in subduction-related volcanic rocks, even the potassic and ultrapotassic rocks from the Sunda arc (Foley and Wheller, 1990; Nelson, 1992). The ITEM end-member has a very distinct, well-defined $^{206}\text{Pb}/^{204}\text{Pb}$ isotopic ratio between 18.60-18.75 (see Figure 8.8). The high $^{87}\text{Sr}/^{86}\text{Sr}$ ratio and distinct $^{206}\text{Pb}/^{204}\text{Pb}$ ratio provide an isotopic "fingerprint" for the ITEM end-member that is

remarkably constant. In contrast, the $^{207}\text{Pb}/^{204}\text{Pb}$ and $^{208}\text{Pb}/^{204}\text{Pb}$ ratios show more variability, and range from 15.65-15.70 and 38.85-39.15, respectively.

The origin of the ITEM end-member is controversial. Although most authors believe that ITEM reflects the contribution of continental crust or oceanic sediment to the Italian mantle (Holm et al., 1982; Ellam et al., 1989; Beccaluva et al., 1991; Conticelli and Peccerillo, 1992; D'Anontio et al., 1996), other models include ancient, enriched sub-continental lithosphere (Vollmer and Hawkesworth, 1980; Varne, 1985; Bell et al., 2004) or even deep-seated material originating from the core-mantle boundary (Bell et al., 2004). Figure 8.2 showed that magmatic rocks from Tuscany and the Western Alps have a Pb isotopic composition that falls in the field of overlap between the upper continental crust, the lower continental crust, and oceanic sediments (Wilson, 1989).

The possibility of a crustal or sedimentary source for the ITEM end-member is also indicated in Figure 8.9, which displays the Pb isotopic ratios for the Calabrian continental crust (D'Antonio et al., 1996), the Tuscan continental crust (Conticelli et al., 2004), deeply subducted crustal rocks from the Dora Maira Massif in the Western Alps (Tilton et al., 1989), and oceanic sediments (Wilson, 1989). The ITEM end-member does not overlap with the fields for the Calabrian continental crust or the Dora Maira Massif, but does have Pb isotopic ratios that are similar to the Tuscan continental crust and oceanic sediments. Therefore, if the enriched signature of the ITEM end-member is due to crustal contamination of the Italian mantle through subduction, the most likely sources are the Tuscan continental crust or oceanic sediment. This topic will be discussed in a geodynamic framework in Chapter 9.

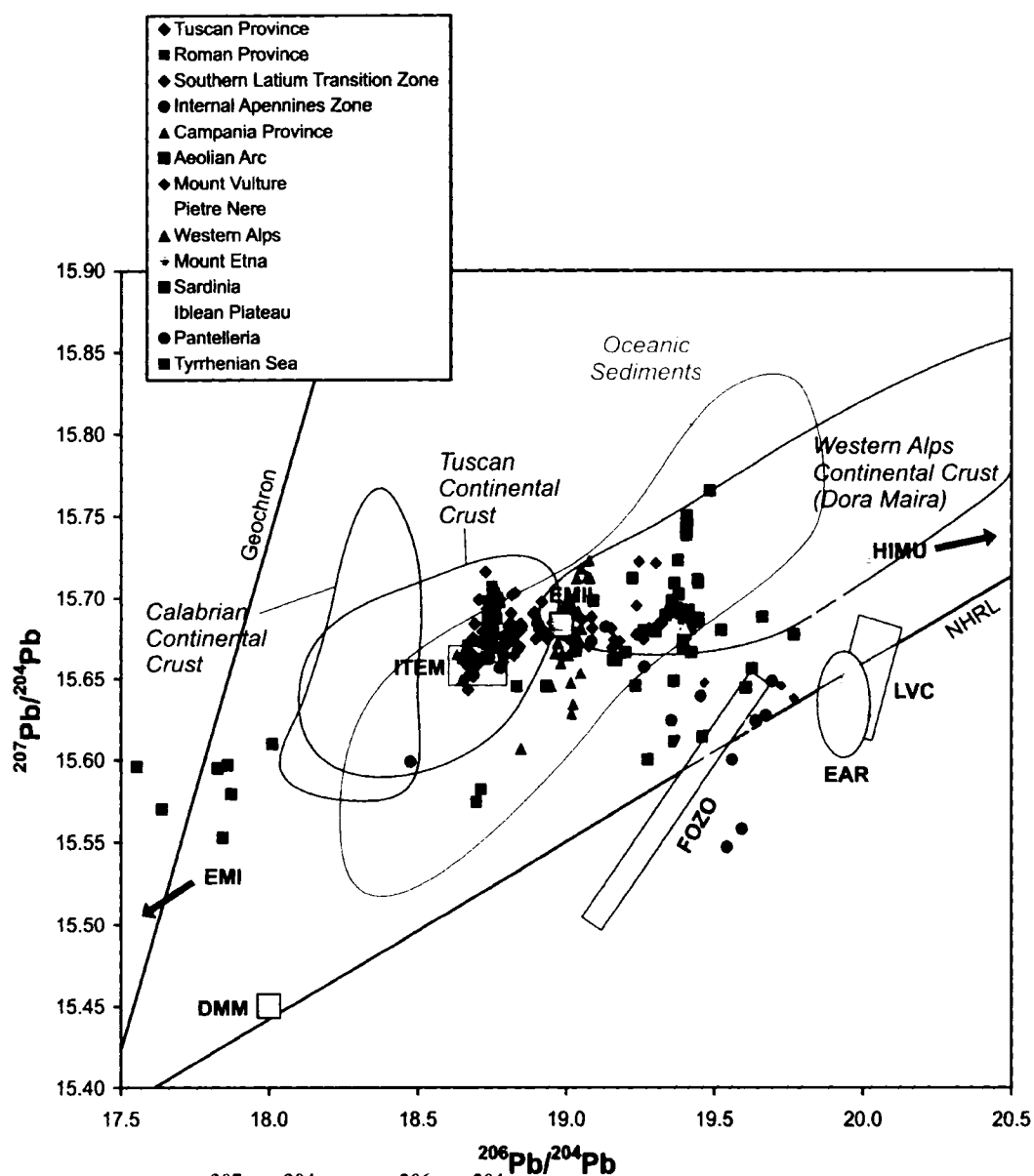


Figure 8.9. $^{207}\text{Pb}/^{204}\text{Pb}$ vs. $^{206}\text{Pb}/^{204}\text{Pb}$ diagram for Italian magmatic rocks showing the mantle end-members DMM, EMI, EMII, and HIMU, as well as FOZO, LVC, and the crustal end-member ITEM. Data for Tuscan Continental Crust, Calabrian Continental Crust, and oceanic sediment from Wilson (1989), D'Antonio et al. (1996), Conticelli et al. (2004) and references therein. References for Pb-Pb data of Italian magmatic rocks can be found in Appendix A.

8.5 Geochemical signature of ITEM

The metasomatic agent that imparted the ITEM signature into the Italian mantle also affected the major and trace element chemistry of the mantle. Trace elements were more strongly influenced than major elements, and in fact the $^{87}\text{Sr}/^{86}\text{Sr}$ ratios of samples from Roccamonfina, Ernici, and the Western Alps do not correlate well with Mg and most other major elements, except for K. The correlation of K_2O with $^{87}\text{Sr}/^{86}\text{Sr}$ is a general feature of Italian magmatism (Conticelli et al., 2002; Conticelli et al., 2004), as the ultrapotassic rocks of the Western Alps, Tuscany, the Roman Province, and the Internal Apennines Zone have the highest K_2O contents and the highest $^{87}\text{Sr}/^{86}\text{Sr}$ ratios, and the sodic rocks of Mt. Etna, the Iblean Plateau, Pantelleria, and Pietre Nere have the lowest $^{87}\text{Sr}/^{86}\text{Sr}$ ratios.

Figure 8.10 is a plot of K_2O (wt%) vs. $^{87}\text{Sr}/^{86}\text{Sr}$ for samples from the Western Alps as well as lamprophyres from Venturelli et al. (1984). Both data sets show the same positive linear relation between K_2O and $^{87}\text{Sr}/^{86}\text{Sr}$. At Roccamonfina and Ernici, the HKS rocks have higher $^{87}\text{Sr}/^{86}\text{Sr}$ ratios than those of the KS series (Figure 8.11). However, when the $^{87}\text{Sr}/^{86}\text{Sr}$ vs. K_2O trend for samples from Roccamonfina and Ernici is compared to the trend from the Western Alps (Figure 8.12), it is clear that there is a major difference in slope between $^{87}\text{Sr}/^{86}\text{Sr}$ and K_2O in northern and central-southern Italy. Magmatic rocks from the Western Alps with $\text{K}_2\text{O} = 10.0$ wt% are characterized by $^{87}\text{Sr}/^{86}\text{Sr}$ ratios of ~ 0.7220 , while samples from Roccamonfina and Ernici with the same amount of K_2O have $^{87}\text{Sr}/^{86}\text{Sr}$ ratios of ~ 0.7100 . This provides evidence that K_2O and $^{87}\text{Sr}/^{86}\text{Sr}$ ratios for individual volcanic centres or nearby groups of volcanic rocks show correlations that are not present on a regional scale. The lack of regional correlation

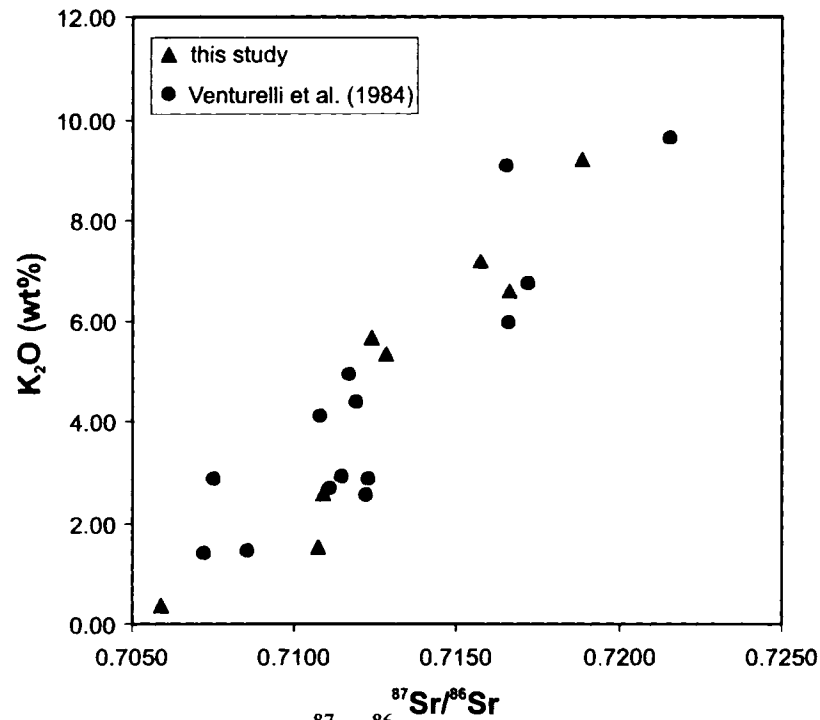


Figure 8.10. K_2O (wt%) vs. $^{87}Sr/^{86}Sr$ ratios for studied lamprophyres from the Western Alps, as well as samples from Venturelli et al. (1984).

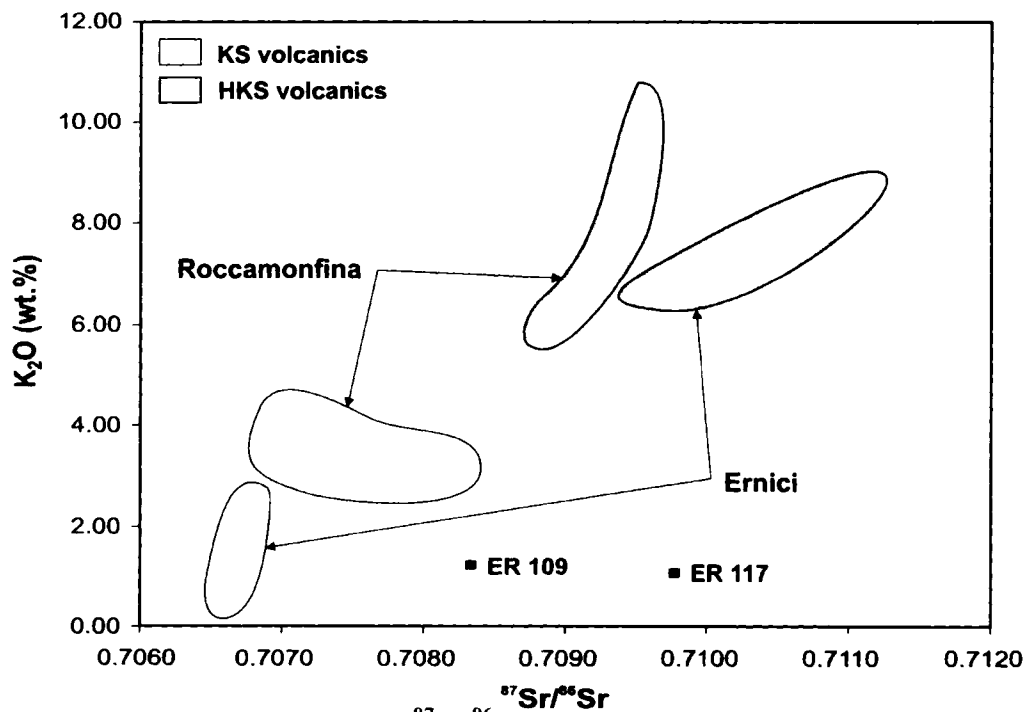


Figure 8.11. K_2O (wt.%) vs. $^{87}Sr/^{86}Sr$ ratios for KS and HKS samples from Roccamonfina and Ernici.

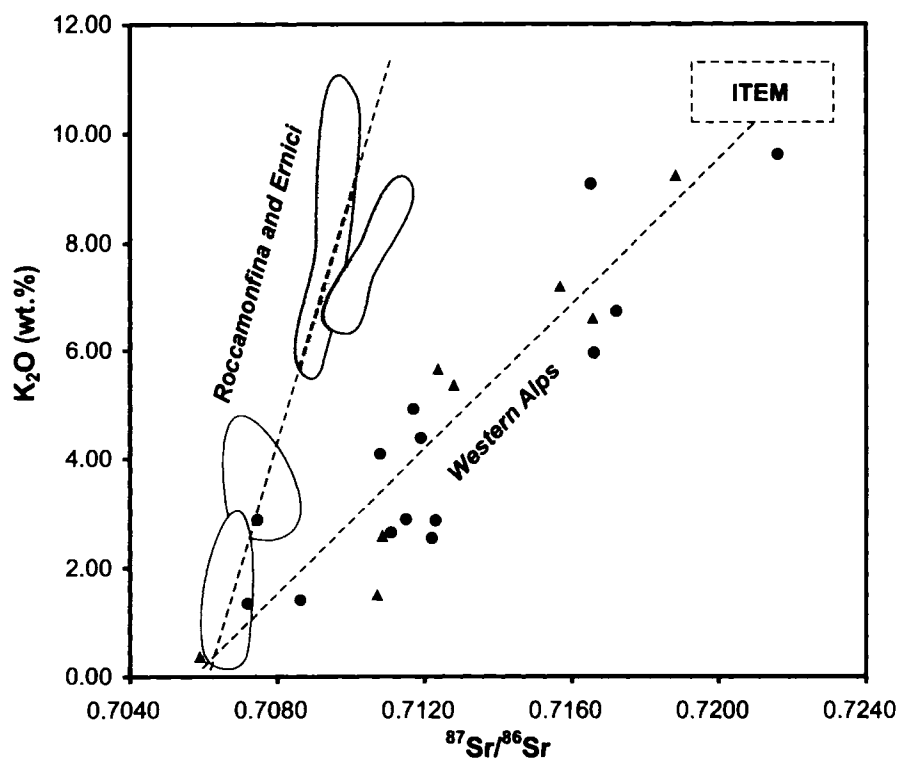


Figure 8.12. K_2O (wt%) vs. $^{87}Sr/^{86}Sr$ ratios for samples from Roccamonfina, Ernici, and the Western Alps, along with additional data from the Western Alps (Venturelli et al., 1984). Note the different trends defined by samples from the Western Alps, and those from central-southern Italy.

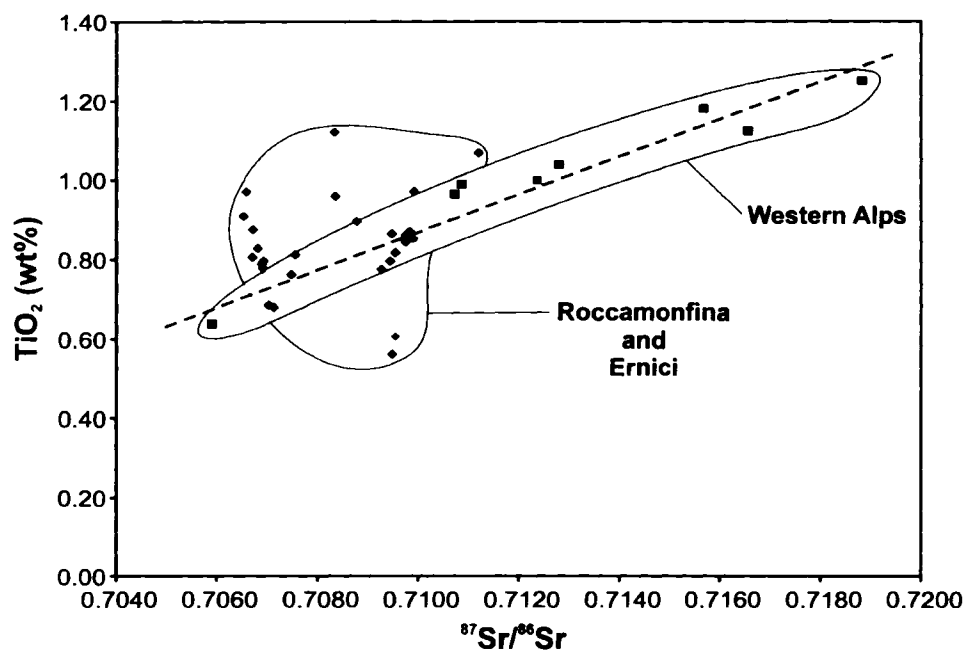


Figure 8.13. TiO_2 (wt%) vs. $^{87}Sr/^{86}Sr$ ratios for lamprophyres from the Western Alps and KS and HKS volcanic rocks from Roccamonfina and Ernici.

between K_2O and $^{87}Sr/^{86}Sr$ shows that the isotopic signatures of Italian magmatic rocks are not directly related to their major element geochemistry. Widely variable rock types (e.g. lamproites, kamafugites, ultrapotassic rocks, potassic rocks, sodic rocks) all plot on the same mixing line between the two distinct isotopic end-members.

Ti also shows differences between samples from the Western Alps and those from Roccamonfina and Ernici. TiO_2 (wt%) correlates strongly with $^{87}Sr/^{86}Sr$ ratios in the lamprophyres from the Western Alps, but shows no relation to $^{87}Sr/^{86}Sr$ in samples from Roccamonfina and Ernici (Figure 8.13). The incompatible trace elements Nb and Ta also show similar behavior to Ti. Unlike K_2O , which is strongly enriched in many Italian magmatic rocks, the TiO_2 contents of samples from the Western Alps are typical of depleted mantle values and are similar to those of MORB (Conticelli et al., 2004).

However, the positive correlation between TiO_2 and $^{87}Sr/^{86}Sr$ in samples from the Western Alps suggests that the metasomatic agent responsible for the ITEM signature may have also introduced Ti into the Alpine mantle. The low TiO_2 (and Nb and Ta) contents of samples from the Western Alps with low $^{87}Sr/^{86}Sr$ ratios indicates that the pre-metasomatic Alpine mantle wedge may have been previously depleted by partial melting events, as is typical in subduction-related tectonic settings (McCulloch and Gamble, 1991) (see Chapter 7). The lack of a positive correlation between TiO_2 and $^{87}Sr/^{86}Sr$ in samples from Roccamonfina and Ernici provides evidence that the ITEM isotopic end-member may be decoupled from the major element composition of rocks in central-southern Italy. The only other major element to show a correlation with the isotopic data in all three study areas is P, which shows a weak positive correlation with $^{87}Sr/^{86}Sr$ ratios.

The incompatible trace elements, including both LILE and HFSE, also show correlations with isotopic data from the Western Alps, Roccamonfina, and Ernici. In Chapter 7, the high concentrations of HFSE such as Th and La were used as evidence for the possible involvement of a melt phase in the source regions of the KS and HKS volcanic rocks from Roccamonfina and Ernici. Th and La also show positive correlations with $^{87}\text{Sr}/^{86}\text{Sr}$ in samples from the Western Alps, Roccamonfina, and Ernici (Figures 8.14 and 8.15). This suggests that the metasomatic agent that introduced HFSE such as Th and La into the Italian upper mantle may also be responsible for the enriched $^{87}\text{Sr}/^{86}\text{Sr}$ isotopic signatures. However, Th is much more strongly enriched in lamprophyres from the Western Alps compared to the volcanic rocks of Roccamonfina and Ernici. The highly enriched Th contents and $^{87}\text{Sr}/^{86}\text{Sr}$ ratios of lamprophyres from the Western Alps are similar to magmatic rocks of the Tuscan Province (Poli et al., 1984; Conticelli and Peccerillo, 1992), and may be partly related to low degrees of partial melting.

Figure 8.15 also indicates that there may be two distinct trends of LREE enrichment for magmatic rocks from central-southern Italy and from the Western Alps and Tuscany. The Western Alps lamprophyres have much higher $^{87}\text{Sr}/^{86}\text{Sr}$ ratios for a given La concentration than the data from Roccamonfina and Ernici. Note that the highly-enriched sample ER 110 (La = 261 ppm, $^{87}\text{Sr}/^{86}\text{Sr} = 0.71120$) has been omitted from Figure 8.15 for clarity, but still lies on the Roccamonfina-Ernici trend. The different LREE enrichment trends support the hypothesis that the mantle beneath the Western Alps and Tuscany may have been metasomatized by a different fluid or melt than the mantle beneath central-southern Italy (Peccerillo and Turco, 2004).

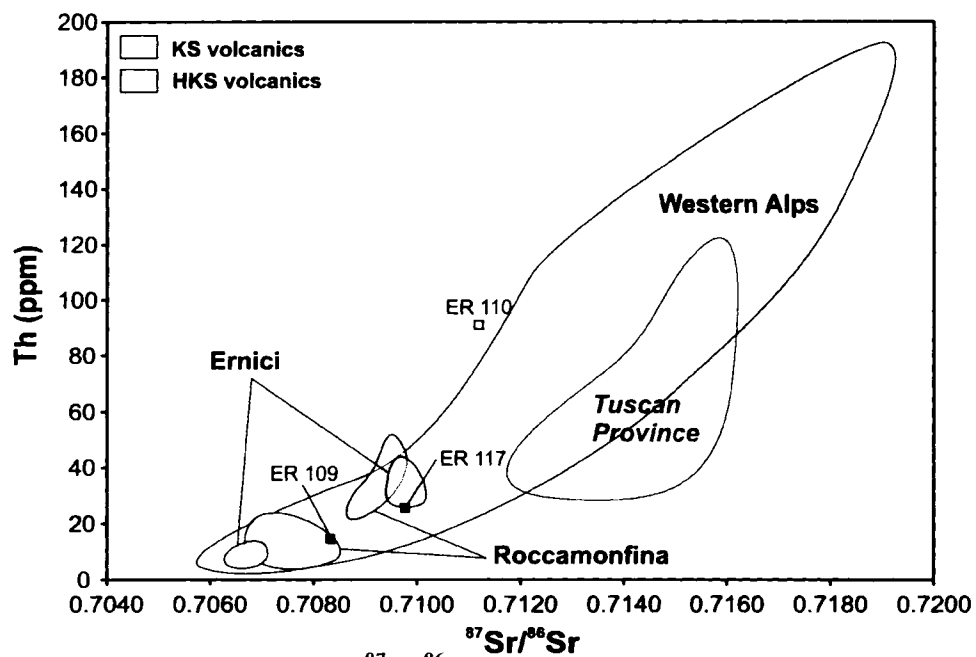


Figure 8.14. Th (ppm) vs. $^{87}\text{Sr}/^{86}\text{Sr}$ for lamprophyres from the Western Alps as well as KS and HKS volcanic rocks from Roccamonfina and Ernici.

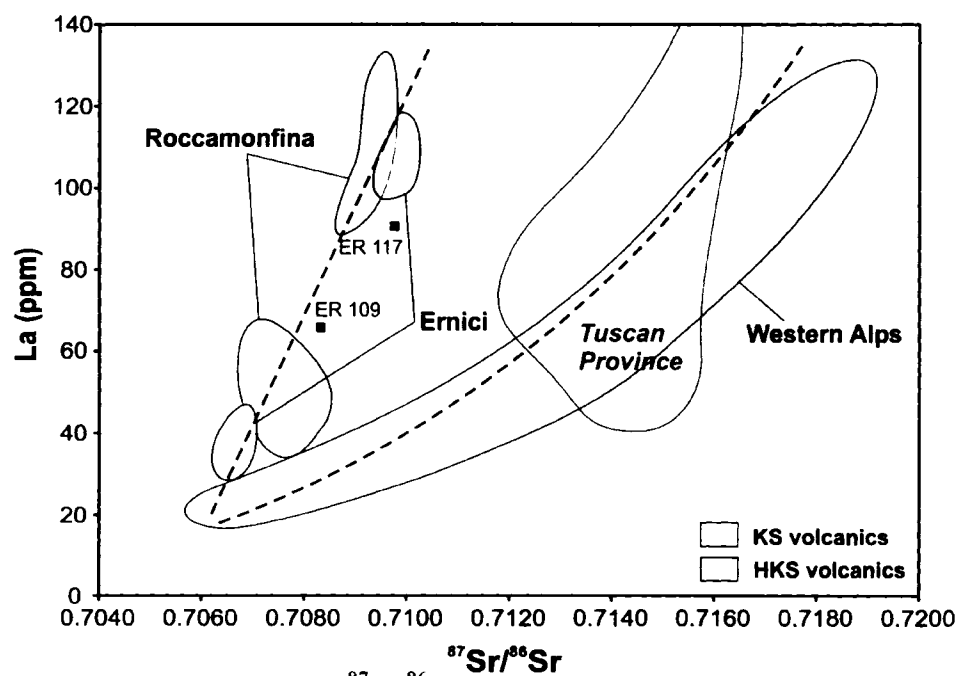


Figure 8.15. La (ppm) vs. $^{87}\text{Sr}/^{86}\text{Sr}$ for lamprophyres from the Western Alps as well as KS and HKS volcanic rocks from Roccamonfina and Ernici.

In terms of LILE, Ba has the strongest positive correlation with $^{87}\text{Sr}/^{86}\text{Sr}$, even though it is relatively depleted (60-680x chondrite) compared to other LILE such as Rb and K (see Chapter 7). Figure 8.16 highlights the correlation between Ba and $^{87}\text{Sr}/^{86}\text{Sr}$ for the studied samples, and the extreme enrichment in Ba (and $^{87}\text{Sr}/^{86}\text{Sr}$) in the lamprophyres from the Western Alps. Despite the fact that Th and Ba have different ionic charge, ionic radius, and behavior in the presence of a fluid phase, they both show strong positive correlations with $^{87}\text{Sr}/^{86}\text{Sr}$ (c.f. Figure 8.14 compared to Figure 8.16).

There is general consensus that HFSE, REE, Be and Th are not efficiently transferred from the subducting slab to the overlying mantle wedge by fluids, due to their extremely low fluid/slab partition coefficients (Brenan et al., 1995; Keppler, 1996; Stadler et al., 1998). However, these elements may be transferred by a melt originating from the sediment cover of the subducting oceanic lithosphere (Plank and Langmuir, 1998; Johnson and Plank, 1999). The enrichment trends of both HFSE and LILE in samples from the Western Alps, Roccamonfina, and Ernici suggest that a silicate (or carbonate) melt phase may have been involved in metasomatizing the mantle in both northern and central-southern Italy. The positive correlation of Th, La, Ba, and other incompatible trace elements with $^{87}\text{Sr}/^{86}\text{Sr}$ ratios in all of the study areas indicates that the isotopic enrichment was accompanied by trace element enrichment.

The LILE/HFSE ratios of Italian rocks from different magmatic provinces show important variations in relation to $^{87}\text{Sr}/^{86}\text{Sr}$ ratios. The Ba/La ratio can be used as a measure of LILE/HFSE fractionation, whereby high ratios ($> \sim 17$) suggest preferential transport of LILE by a fluid phase, and low Ba/La ratios suggest the transport of both LILE and HFSE by a melt (McCulloch and Gamble, 1991). Figure 8.17 shows a plot of

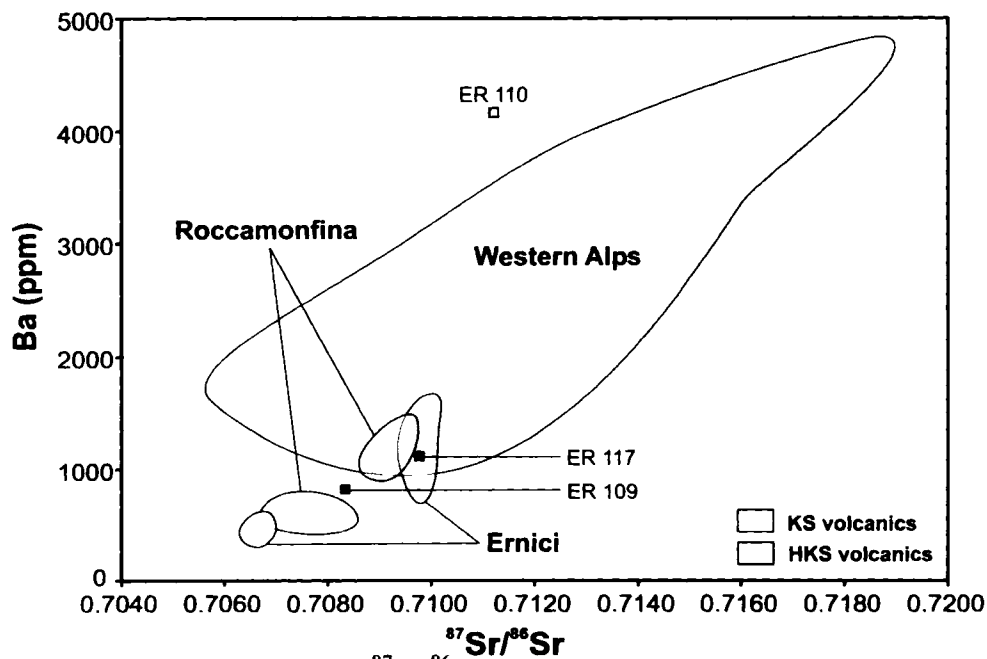


Figure 8.16. Ba (ppm) vs. $^{87}\text{Sr}/^{86}\text{Sr}$ for lamprophyres from the Western Alps and KS and HKS volcanic rocks from Roccamonfina and Ernici.

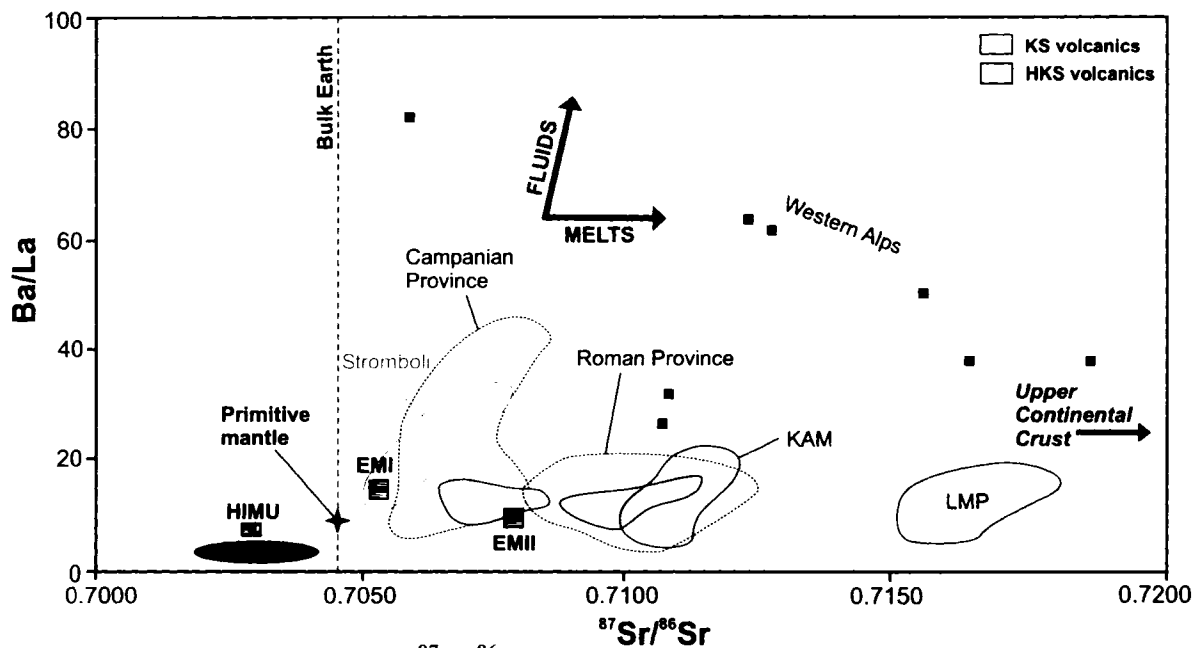


Figure 8.17. Ba/La vs. $^{87}\text{Sr}/^{86}\text{Sr}$ for lamprophyres from the Western Alps as well as KS and HKS volcanic rocks from Roccamonfina and Ernici, Tuscan lamproites (LMP), Italian kamafugites (KAM), and volcanic rocks from the Roman and Campanian Provinces. Data for the Western Alps lamprophyres plotted as solid squares. Modified from Peccerillo and Panza (1999).

Ba/La vs. $^{87}\text{Sr}/^{86}\text{Sr}$ ratios for samples from the Western Alps, Roccamonfina, and Ernici. The Ba/La ratios of volcanic rocks from Roccamonfina and Ernici range from 8-16, and are similar to rocks from the Roman Province, kamafugites from the Internal Apennines Zone, and Tuscan lamproites (Peccerillo and Panza, 1999). These ratios are less than the Ba/La ratio of the upper continental crust (~25) (Saunders et al., 1988; Weaver, 1991) and less than the Ba/La ratio of typical island-arc calc-alkaline basalts (~30) (Sun, 1980). In fact, the Ba/La ratios of many Italian magmatic rocks, including those from Roccamonfina and Ernici, are more similar to those of intraplate alkalic rock types (Ba/La ~11) than arc-related rock types (Sun, 1980).

Figure 8.17 also shows that the potassic and ultrapotassic rocks of the Campanian Province have a wider range of Ba/La ratios than other magmatic rocks of peninsular Italy. The Ba/La ratios of some rocks from the Campanian Province are > 40, which is high compared to calc-alkaline rocks from convergent margins (Wilson, 1989). The Ba/La ratios of rocks from the Campanian Province overlap with the field of potassic, shoshonitic, and high-K calc-alkaline volcanic rocks from Stromboli, the easternmost of the Aeolian Islands (Francalanci et al., 1989). This supports the hypothesis of Peccerillo (2001) and Peccerillo and Turco (2004) that the mantle beneath the Campanian Province in central-southern Italy and the mantle beneath the Aeolian arc have been metasomatized by fluids or melts derived from the same source.

The Ba/La ratios of samples from the Western Alps are high and variable. The Ba/La ratios (26 – 80) are consistent with the extremely high LILE contents of the lamprophyres. The high Ba/La ratios of the Western Alps lamprophyres suggest that a metasomatic *fluid* was dominant in the Alpine mantle, whereas the relatively low Ba/La

ratios of samples from Roccamonfina and Ernici provide further evidence that a metasomatic *melt* may have been dominant in the central-southern Italian mantle.

In summary, there are significant differences in the correlations between isotopic ratios, major elements, and trace elements for magmatic rocks from the Western Alps, Roccamonfina, and Ernici. While isotopic ratios correlate well with K_2O , HFSE, and LILE at each individual magmatic centre, they do not appear to correlate on a regional scale. This suggests that although ITEM is responsible for the enriched isotopic signature of the Italian magmatic rocks, it is not directly responsible for the major and trace element signatures of the rocks. One of the most important inferences from the isotopic mixing curves on Figures 8.7 and 8.8 is that the magmatic rocks of the Aeolian Islands, the Tyrrhenian Sea, Vulture, the Campanian Province, the Southern Latium Transition Zone, the Internal Apennines Zone, and the Roman Province are all characterized by varying amounts of *both* ITEM and the depleted end-member. This means that both end-members must be present in the mantle of peninsular Italy, the Tyrrhenian Sea, and the Aeolian Islands, but in different proportions. Any geodynamic model for the geographic origin of the depleted and enriched isotopic end-members and the events that resulted in large-scale mixing must take into account that there is a small proportion of ITEM present in the mantle of southern Italy, and a small proportion of isotopically depleted mantle in northern Italy.

CHAPTER 9

GEODYNAMIC INTERPRETATION OF ITALIAN ISOTOPIC MIXING

9.1 Introduction

The isotopic signatures of Cenozoic magmatic rocks from Italy (excluding those from Sardinia) reflect large-scale binary mixing between an enriched end-member (ITEM) and a depleted end-member. Sodic rocks from Mt. Etna, Pantelleria, Pietre Nere, and the Iblean Plateau best reflect the depleted end-member, while ultrapotassic lamproites from Tuscany and lamprophyres from the Western Alps best reflect ITEM. The isotopically-depleted rocks are derived from partial melting of either African (Mt. Etna, Pantelleria, Iblean Plateau) or Adriatic (Pietre Nere) mantle, and are separated from the Tyrrhenian basin by the NW-directed Apennine-Maghrebides subduction system (Figure 9.1). Magmatic rocks located west of the Apennine-Maghrebides thrust front show the influence of the ITEM component in their source, and have fractionated LILE/HFSE trace element signatures that are typical of subduction-related tectonic settings (Rogers et al., 1985; Beccaluva et al., 1991; Peccerillo, 1992). However, a number of authors have ascribed the geochemistry of these rocks to asthenospheric upwelling in an intraplate tectonic setting (Cundari, 1980; Vollmer et al., 1981; Stoppa and Lavecchia, 1992; Lavecchia and Stoppa, 1996).

Models for asthenospheric (mantle upwelling-related) versus lithospheric (subduction-related) mantle processes are constrained by the present-day arrangement of major tectonic boundaries, subducted slabs, and zones of asthenospheric upwelling in the Italian region. The first section of this chapter will examine recent seismic tomographic

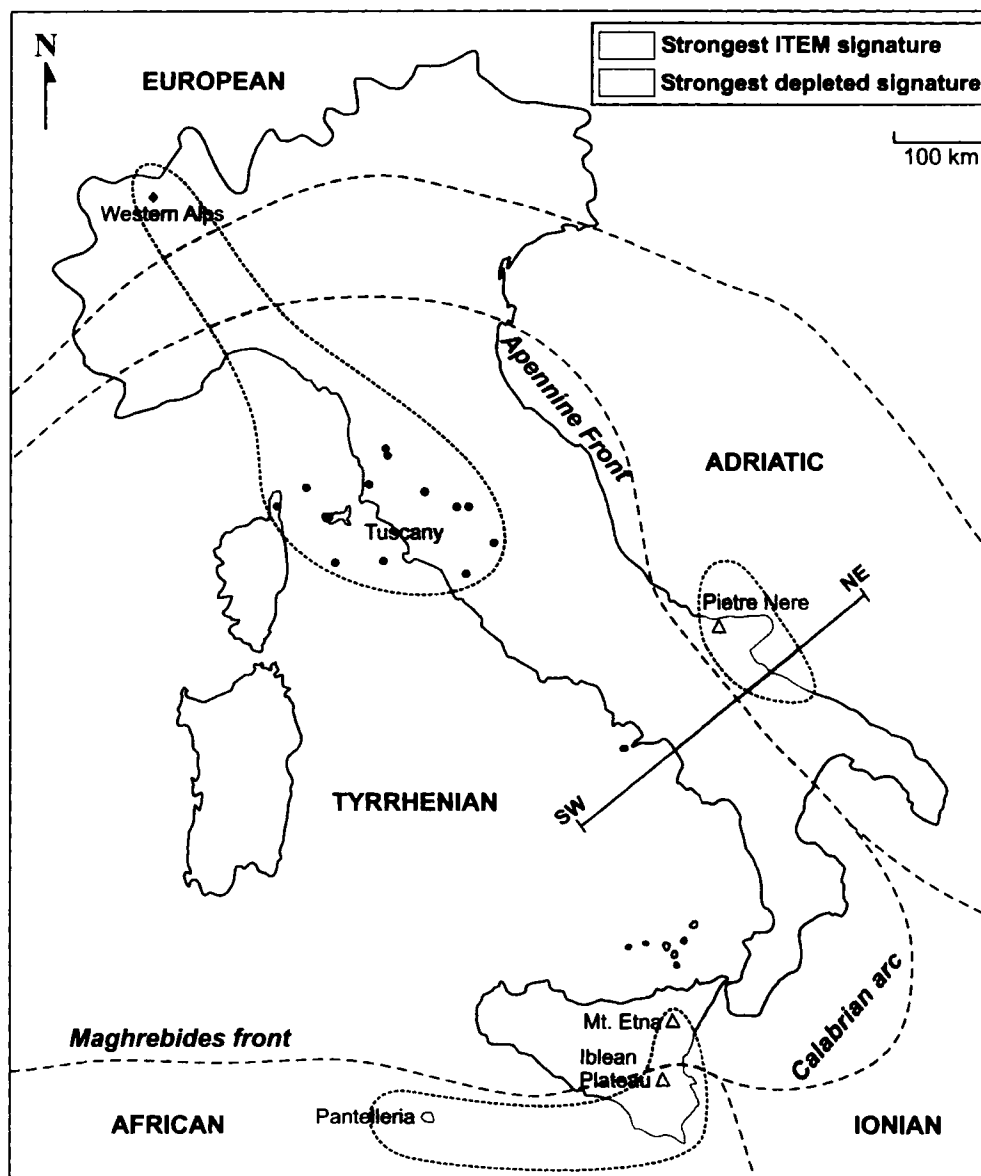


Figure 9.1. Simplified tectonic plate boundaries in the Italian region and locations of magmatic rocks with the strongest depleted and enriched isotopic signatures. Note that most plate boundaries are debatable (modified from Gvirtzman and Nur, 2001).

studies of the Western Mediterranean, and highlight properties of the mantle beneath the Western Alps and central-southern Italy. Different models for the origin of the depleted and enriched isotopic end-members will then be discussed, and an integrated model relating the isotopic signatures of Italian magmatic rocks to the Cenozoic tectonic evolution of the Western Mediterranean will be presented.

9.2 Seismic tomography

9.2a Introduction

The upper mantle extends from the base of the crust down to about 670 km depth, and includes the lower part of the lithosphere, the asthenosphere, and part of the mesosphere. The lithosphere (50-200 km thick) is characterized by high seismic velocity, while the asthenosphere, which extends from the base of the lithosphere to about 250 km, has relatively low seismic velocities. The attenuation of shear waves in the asthenosphere is thought to indicate the presence of a partial melt phase (Wilson, 1989). Beneath the asthenosphere lies the mesosphere, in which major structural changes occur in silicate minerals at 410 km (olivine → spinel) and 670 km (spinel → perovskite). The phase change at 670 km separates the upper mantle from the lower mantle, and the region between 410 and 670 km depth is referred to as the transition zone.

The high seismic velocity of the lithosphere is primarily due to temperature differences between the "cold" lithosphere and "hot" asthenosphere. Although seismic velocities are sensitive to a number of parameters such as chemical composition, anisotropy, anelasticity, phase transitions, presence of partial melt, and water content (Karato, 1993; Goes et al., 2000), studies have shown that most mantle velocity variation

can be attributed to changes in temperature (Ranalli, 1996), while the effects of mantle composition likely contribute < 1% of the total variation (Sobolev et al., 1997; Goes et al., 2000). A temperature difference of only 100°C results in a velocity anomaly of about 50 m/s, which amounts to about 0.5 % V_p velocity perturbation (Wortel and Spakman, 1992). Positive velocity anomalies are equated with subducted lithosphere in the Western Mediterranean based on the following evidence: 1) elongate, planar shape of the anomalies, 2) dip of anomalies comparable to those of world-wide subduction zones, 3) thickness (70–100 km) and velocity contrasts (2–4% V_p) in agreement with values predicted from thermal modeling (Lay, 1994), and 4) correspondence between the high-velocity anomalies and areas of intermediate to deep seismicity.

9.2b Tomographic images of the Alpine mantle

The tomographic model of Piromallo and Morelli (2003) shows cross-sections through the Western, Central, and Eastern Alps (Figure 9.2). The Alpine belt is underlain by continuous high-velocity material at 100 km depth (Fig. 9.2a), while at 200 km depth the high-velocity signature is weaker and present only in the Western and Central Alps (Fig. 9.2b). Cross-sections perpendicular to the Alpine belt show a strong, steeply southward-dipping, continuous high-velocity anomaly extending from the surface down to 300 km in the Western Alps (Fig. 9.2c), a similar anomaly extending to ~200 km in the Central Alps (Fig. 9.2d), and a shallow, discontinuous high-velocity anomaly extending to 50 km in the Eastern Alps (Fig. 9.2e).

Figure 9.2c also shows a shallow, horizontal, high-velocity anomaly located to the east of the steeply-dipping anomaly ~50 km beneath the Po Plain (northeast Italy). This

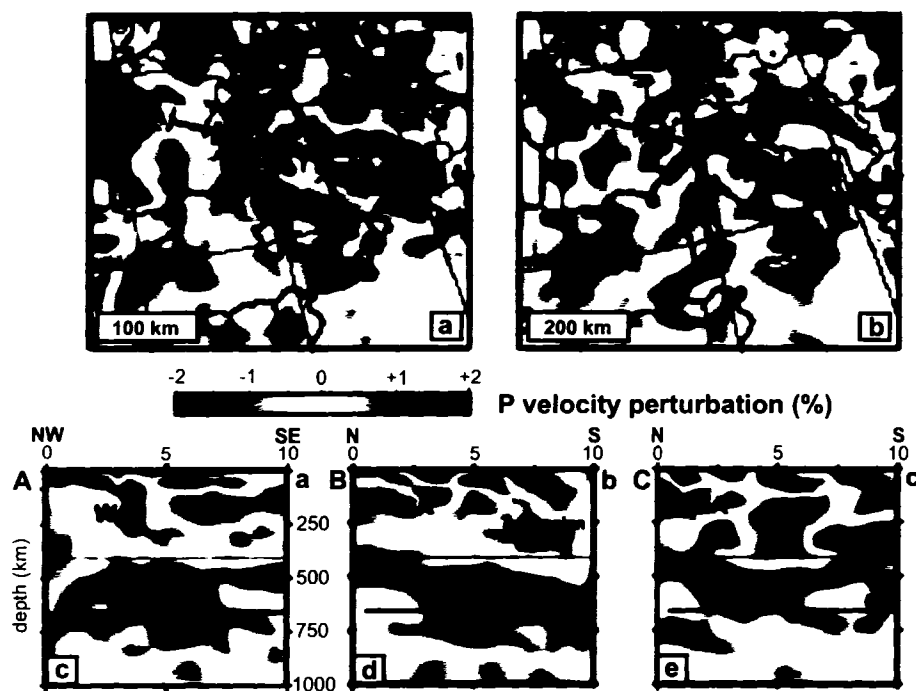


Figure 9.2. Maps (a) and (b) show horizontal layers in the upper mantle at 100 and 200 km, respectively, from the PM0.5 tomographic model of Piromallo and Morelli (2003). Vertical profiles of model PM0.5 through the Western (A-a), Central (B-b), and Eastern (C-c) Alps are shown in figures (c), (d), and (e). Horizontal scale is in degrees from the section margin. Modified from Piromallo and Faccenna (2004).

zone is underlain by a low-velocity anomaly that characterizes the eastern Po Plain and northern Adriatic Sea from ~100 to 250 km depth (also seen on Figs. 9.2d and 9.2e). High-velocity material is present in the transition zone in all three cross-sections, and appears to penetrate the 670 km discontinuity and extend into the lower mantle. While a number of studies have imaged the high-velocity lithospheric root of the Alps to ~200 km depth (Babuska et al., 1990; Spakman et al., 1993; Piromallo and Morelli, 1997; Lucente et al., 1999), there appears to be no robust physical connection between the steeply-dipping, high-velocity anomalies beneath the Alpine belt and the high-velocity material in the transition zone, especially in the Eastern Alps.

9.2c Evidence for slab break-off beneath the Alpine orogen

The tomographic images of the Alpine orogenic belt are consistent with the southward subduction of European lithosphere beneath the Adriatic plate (Spakman et al., 1993; Lucente et al., 1999; Piromallo and Morelli, 2003; Piromallo and Faccenna, 2004). The shallow (~50 km) high-velocity anomaly located in the eastern Po Plain and northern Adriatic Sea is generally interpreted as the Adriatic continental lithosphere that has overthrust the European lithosphere. Subducted European lithosphere reaches depths of 300 km in the Western Alps, but estimates of the amount of convergence between Africa and the Adriatic plate during the Tertiary range from ~500 km (Schmid et al., 1996) to ~540 km (Piromallo and Faccenna, 2004). Taking into account the mid-Cretaceous (ca. 90 Ma) change in plate motion in the Mediterranean from generally extensive to compressive and assuming that subduction of oceanic lithosphere began soon after,

Piomallo and Faccenna (2004) estimated that more than 700 km of lithosphere should have been consumed at the Alpine trench.

The significant discrepancy between the estimated (~700 km) and observed (~300 km) amounts of subducted material, combined with the large amount of high-velocity material in the transition zone beneath northern Italy, led Piomallo and Faccenna (2004) to propose that the material in the transition zone is part of the subducted European lithosphere that has broken off beneath the Alps. By subtracting the observed slab length as deduced from tomography from the amount of predicted subduction, Piomallo and Faccenna (2004) estimated that slab break-off occurred at approximately 30-35 Ma, which agrees with observations from Alpine magmatism and foredeep basin evolution. Von Blanckenburg and Davies (1995) suggested slab break-off as a mechanism to explain the widespread magmatism along the Periadriatic line in the Alps which peaked at 30-32 Ma. Sinclair (1997) interpreted the molasse-flysch transition as a signal of uplift and basin shallowing related to slab break-off and the loss of slab pull at about 30-33 Ma.

Slab break-off beneath the Alpine orogen may have been caused by the locking of the subduction zone due to the arrival of buoyant continental material at the trench at 45-50 Ma (von Blanckenburg and Davies, 1995; Wong et al., 1997; Regard et al., 2003). Plate reconstructions by Piomallo and Faccenna (2004) indicate that more than 200 km of continental material subducted before the trench became totally locked, a value in good agreement with theoretical estimates based on buoyancy analysis (Ranalli, 2000; Regard et al., 2003) and with the occurrence of ultra-high pressure (UHP) minerals in continental crustal units of the Western Alps (Chopin, 1984).

9.2d Tomographic images of the Apennine mantle

The tomographic model of the Western Mediterranean proposed by Bijwaard and Spakman (2000) shows many features that were also detected in earlier studies (Wortel and Spakman, 1992; Amato et al., 1993; Spakman et al., 1993; Selvaggi and Chiarabba, 1995; Piromallo and Morelli, 1997). At a depth of 200 km (Figure 9.3a), high-velocity anomalies are found below the Betic-Alboran region, the Calabrian arc, the northern Apennines, the Aegean region, and the east Carpathians. Strong, low-velocity anomalies at 200 km depth occur in the southern Tyrrhenian basin and outboard of the Apenninic front on the Adriatic and African plates. At 600 km depth, a broad high-velocity anomaly is located beneath nearly the entire Western Mediterranean, as well as the Alpine chain and the Carpathian arc. Below Calabria, the Apennine slab broadens with depth (Fig. 9.4a-d), particularly below 200 km, where it starts to underlie the central and southern Apennines and the east Tyrrhenian basin (Fig. 9.3d).

Vertical slices through the Calabrian arc (Fig. 9.3e) and the central-southern Apennines (Fig. 9.3f) show subducted lithosphere in the transition zone beneath the Tyrrhenian basin. Directly below the Calabrian arc, the slab is imaged as a nearly continuous 80 km thick high-velocity anomaly that extends from the surface into the transition zone, dipping toward the NW with a subvertical dip and becoming almost horizontal in the transition zone (Lucente et al., 1999). The tomographic model of Bijwaard and Spakman (2000) shows no deep discontinuity of the Calabrian slab, but Lucente et al. (1999) found a section of low-velocity material at ~500 km depth that appears to separate the steep, upper portion from the deeper sub-horizontal portion. Most studies suggest a continuous Calabrian slab in the upper 200 km of the mantle (as shown

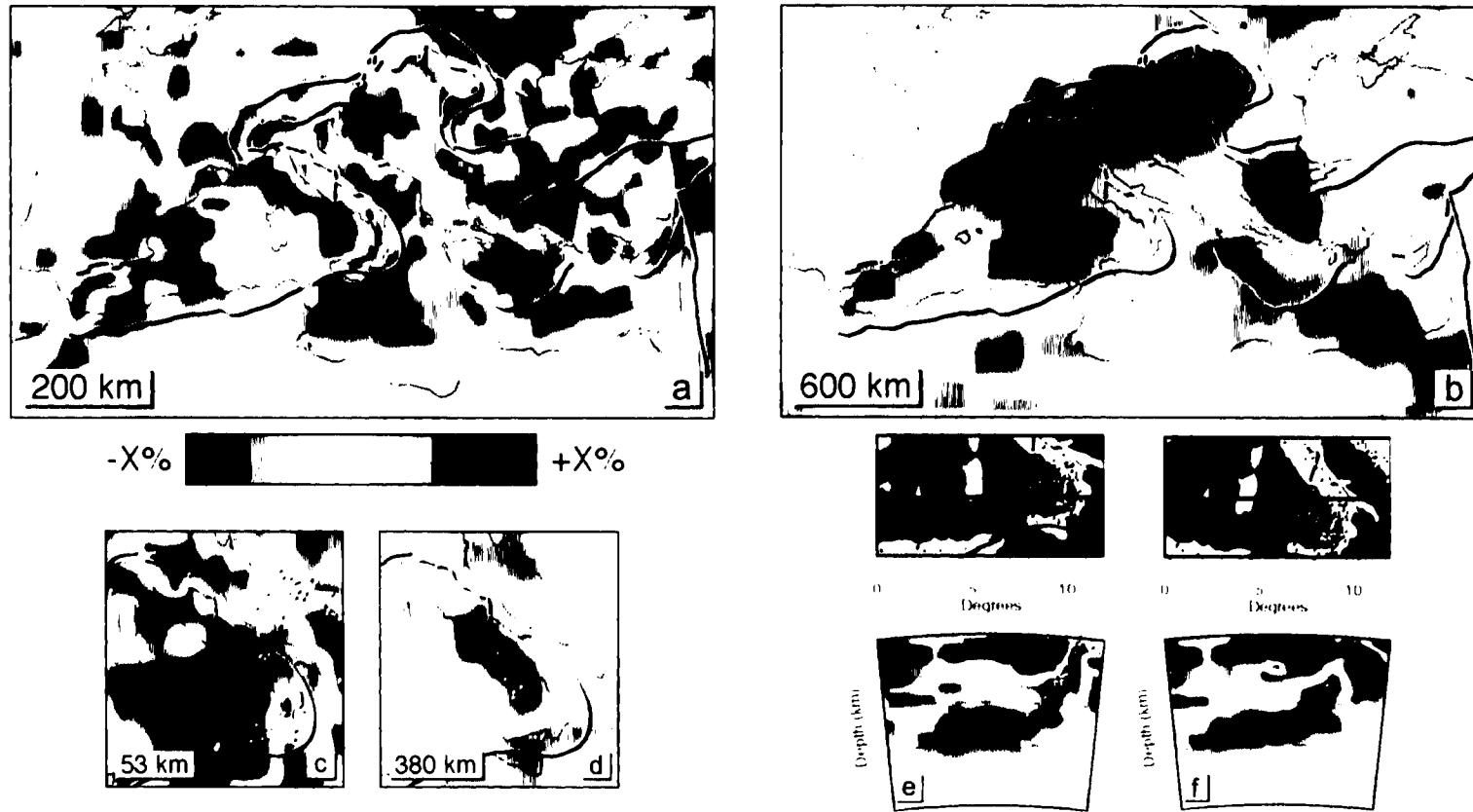


Figure 9.3. Tomographic images of P-wave velocity anomalies for the Mediterranean/Carpathian region (tomographic model of Bijwaard and Spakman, 2000, shown in Wortel and Spakman, 2000). Colours indicate seismic wave speed anomalies as percentage deviations from average mantle velocities. (a) and (b) show map view images at 200 and 600 km depth, respectively. (c) and (d) are views of the Apennine-Calabrian region at 53 and 380 km depth, and (e) and (f) are vertical slices computed along great circle segments through the Calabrian arc and the central-southern Apennines. White dots indicate earthquakes, and dashed lines in (e) and (f) indicate the 410 and 660 km mantle discontinuities.

in Fig. 9.3e), but the possibility of small gaps in the slab (< 25 km) cannot be excluded (Selvaggi and Chiarabba, 1995).

The slab below the central-southern Apennines has no high-velocity connection to crustal levels and is entirely overlain with low-velocity material (Figs. 9.3a, c, f). The central-southern Apennine mantle has low-velocity material in the upper 250 km, but below 250 km the high-velocity anomaly becomes stronger and dips steeply down to 600 km, where it joins the wide high-velocity anomaly that marks the bottom of the Tyrrhenian upper mantle (Lucente et al., 1999). Below the northern Apennines, all regional tomographic models image a 70-100 km thick slab-like anomaly across the upper mantle. Some models, however, image a continuous anomaly (Amato et al., 1993; Piromallo and Morelli, 1997; Lucente et al., 1999) while others detect a low-velocity interruption between 150 and 200 km (Spakman et al., 1993).

In summary, the main findings of numerous tomographic studies of the Apennine mantle are: 1) the Apennine slab is laterally complex and shows heterogeneities on a scale of only a few hundred kilometers, 2) there is evidence for a shallow slab in both the northern Apennines and in the Calabrian arc, and 3) there appears to be no shallow slab in the central-southern Apennines. The tomographic data supports previous work based on foredeep basin evolution that suggests that the subducted lithosphere beneath the Italian peninsula is segmented (e.g. Royden et al., 1987).

9.3 Origin of the depleted isotopic end-member in Italian magmatic rocks

9.3a Introduction

The depleted end-member has isotopic characteristics that are similar to FOZO

(Hart et al., 1992), LVC (Hoernle et al., 1995), and EAR (Cebriá and Wilson, 1995). Each of these isotopic "reservoirs" have been interpreted in different ways (see Chapter 8), but all are characterized by relatively low $^{87}\text{Sr}/^{86}\text{Sr}$, high $^{143}\text{Nd}/^{144}\text{Nd}$, and $^{206}\text{Pb}/^{204}\text{Pb}$ ratios intermediate between those of DMM and HIMU. Models that could explain the incorporation of FOZO into the Tyrrhenian mantle can be separated into those which propose lower mantle upwelling within the Tyrrhenian domain (e.g. Bell et al., 2004), and those which invoke upwelling within the Adriatic domain (e.g. Doglioni, 1991; Wortel and Spakman, 1992; Gvirtzman and Nur, 1999; Gasperini et al., 2002). In the latter case, upwelling deep-mantle material located in the Adriatic domain east of the Apenninic subduction zone must pass "through" the slab by means of slab tearing, slab detachment, or a slab window, into the Tyrrhenian mantle where it mixes with the enriched end-member ITEM. If the isotopic end-member is considered to be LVC or EAR, then there is no need to invoke a deep-seated plume-type source. In this case, the depleted end-member may simply represent the asthenospheric mantle underlying the Tyrrhenian and African-Adriatic domains.

9.3b Geodynamic models for the origin of FOZO in the Adriatic mantle

Model I. Lithospheric stretching and boudinage of the Apennine slab in the Calabrian arc (Doglioni, 1991)

Doglioni (1991) noted that bending of a lithospheric plate during subduction can result in horizontal shear, boudinage, and stretching of the downgoing slab. The Calabrian arc is currently the narrowest arc on Earth (300 km wide) and has an extremely arcuate shape (Figure 9.4). The arc is laterally restricted between the continental Adriatic

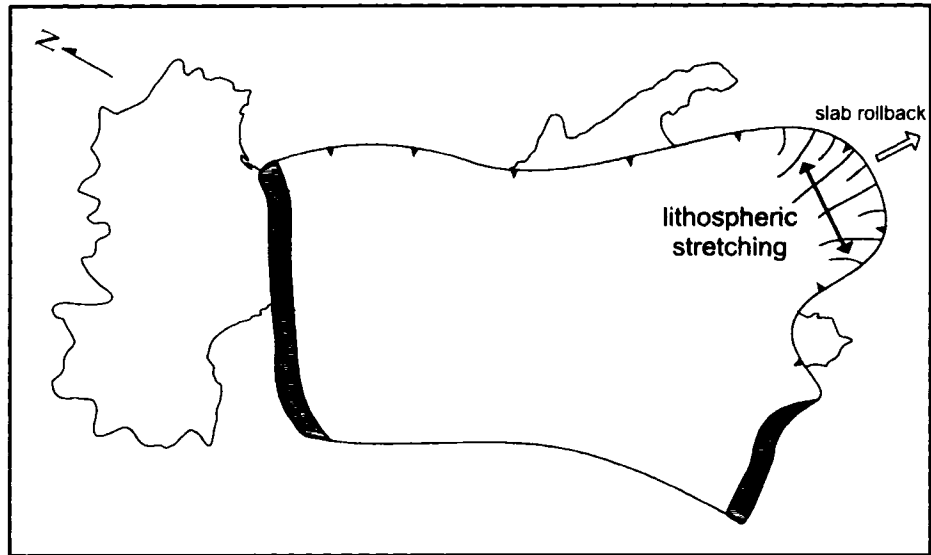


Figure 9.4. Model I: schematic of horizontal stretching of the downgoing Apennine slab in the Calabrian arc as a response to bending and rollback (based on work by Doglioni, 1991). Dark grey areas represent sides of slab.

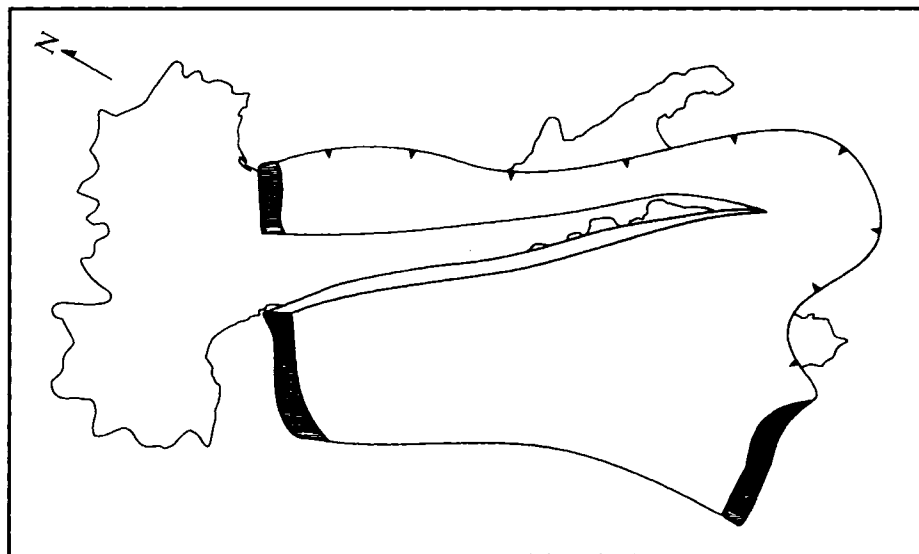


Figure 9.5. Model II: schematic of lateral slab detachment beneath the Italian peninsula (Wortel and Spakman, 1992).

microplate and the African plate (see Figure 9.1), and is thought to have subducted Mesozoic Ionian oceanic lithosphere throughout most of the Tertiary (Selvaggi and Chiarabba, 1995). The Ionian lithosphere is thinner than that of the Adriatic and African foreland, and consists of about 6 km of sediments and an oceanic crust 8-10 km thick (Catalano et al., 2001). In contrast, the Adriatic and African crusts are composed primarily of thick carbonate shelves and siliciclastic sedimentary rocks.

Compared to similar deep Benioff zones world-wide, the Calabrian arc shows a high concentration of seismic events in the 150-250 km range, only a few sparse events below 400 km, and none below 500 km (Lucente et al., 1999). This atypical earthquake distribution suggests that the slab may have attained its maximum curvature and rollback position, despite the continued availability of Ionian lithosphere in front (southeast) of the arc. Doglioni (1991) stated that horizontal extension in the subducted slab should increase downward. Stretching and/or fragmentation of the slab at depths greater than ~400 km may explain the lack of deep earthquakes in the Calabrian arc. Tomographic images by Lucente et al. (1999) of the lateral view of the Apennine slab under Calabria show a discontinuous high-velocity body at depths greater than 400 km. Fragmentation of the deep Apennine slab beneath Calabria due to horizontal extension could allow material with a FOZO-like isotopic signature from the forearc (Adriatic) to pass through gaps in the slab into the back-arc (Tyrrhenian).

Model II. Lateral slab detachment beneath the Italian peninsula (Wortel and Spakman, 1992)

Wortel and Spakman (1992) interpreted the velocity heterogeneities beneath the

Italian peninsula as the result of a process referred to as slab detachment. The authors noted the absence of shallow (< 200 km) high-velocity material along the length of Italy (excluding the Calabrian arc), and the reappearance of high-velocity material at depths greater than 200 km. The absence of a shallow slab in the northern Apennines is in contrast to the continuous slab imaged by Amato et al. (1993), Piromallo and Morelli (1997), and Lucente et al. (1999). According to Wortel and Spakman (1992), slab detachment started at the northernmost end of the Apennine subduction zone (northern Italy) and progressed by lateral migration along strike towards present-day Calabria (Figure 9.5). The detachment process is self-propagating, as the weight of the detached slab is partially transferred to the adjacent continuous part of the slab, leading to a concentration of slab pull forces at the point of detachment. Wortel and Spakman (1992) estimated a horizontal migration velocity of 15 cm/year for the detachment tear.

It is possible that the interaction of transform faults with the trench system, or a significant change in the type of subducting lithosphere (e.g. from oceanic to continental) may initiate the process of slab detachment. Upwelling low-velocity material from the Adriatic plate would presumably fill the gap created by the detached Apennine slab. The major problem with the slab detachment model of Wortel and Spakman (1992) is that it is inconsistent with the geochemical and isotopic evidence. If the detachment occurred first in northern Italy and subsequently migrated south, the strongest FOZO-like isotopic signature should be seen in northern Italy, where more material from the Adriatic plate was able to interact with the supra-slab mantle. In fact, the opposite is true and the Italian magmatic rocks with the strongest FOZO component are located in southern Italy in the Aeolian arc and the Campanian Province.

Model III. Lateral asthenospheric flow due to differential slab rollback (Gvirtzman and Nur, 1999)

The highly arcuate shape of the Calabrian arc is thought to be due to the preferential subduction of oceanic Ionian lithosphere, located between the continental Adriatic and African plates. Gvirtzman and Nur (1999) calculated the thickness of mantle lithosphere beneath Calabria by matching the total buoyancy of the lithosphere to the observed surface elevation. Results indicated negligible mantle lithosphere and suggested that the asthenosphere has reached the base of the crust under Calabria. Gvirtzman and Nur (1999) proposed that the top of the Apennine slab under Calabria is deep enough to create a lateral window that allows material to flow from beneath the African plate into the wedge between the base of the Tyrrhenian plate and the top of the subducting slab (Figure 9.6). The direction of the asthenospheric flow is governed by the SE-directed rollback of the Ionian lithosphere, which creates low pressure under Calabria. Asthenospheric upwelling from the base of the African lithosphere (~100 km deep) to the base of the crust under Calabria (~20 km deep) results in decompression and partial melting. The melt then migrates to the surface through the faulted crust of Sicily to feed Mt. Etna, which is located at the junction of the African plate with the Tyrrhenian and Ionian plates.

Gvirtzman and Nur (1999) also suggested that the uplift of Calabria and increased magmatism in the Aeolian arc about 700 kyr ago are due to the decoupling of the slab from the Calabrian crust. The gap between the slab and Calabria was then filled by asthenospheric material from beneath the neighboring African plate. The vertical sinking of the Apennine slab, without a significant change in dip, following decoupling from the

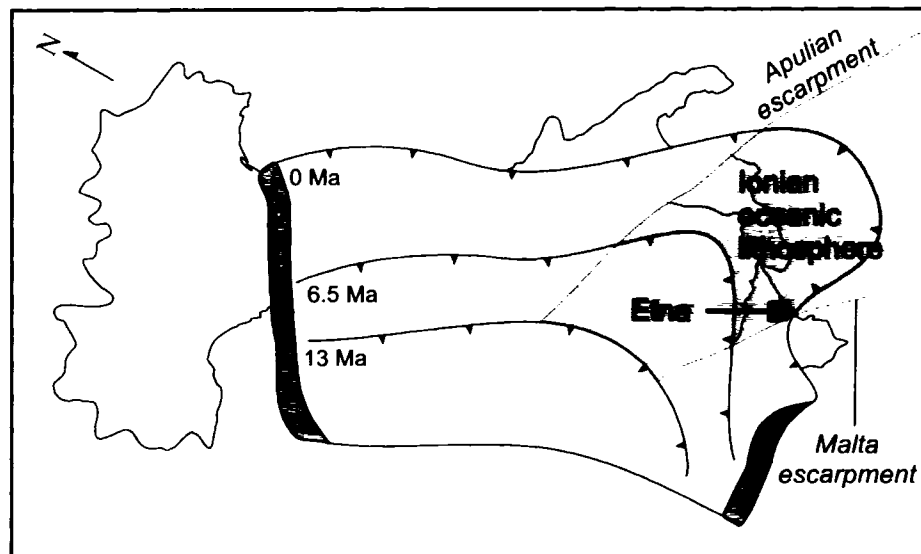


Figure 9.6. Model III: schematic of SE-directed rollback of the Ionian oceanic lithosphere, which is laterally constrained between the African and Adriatic continental lithospheres. Mt. Etna is located at the Ionian-African plate boundary (based on work by Gvirtzman and Nur, 1999). Brown colour represents the Ionian oceanic lithosphere.

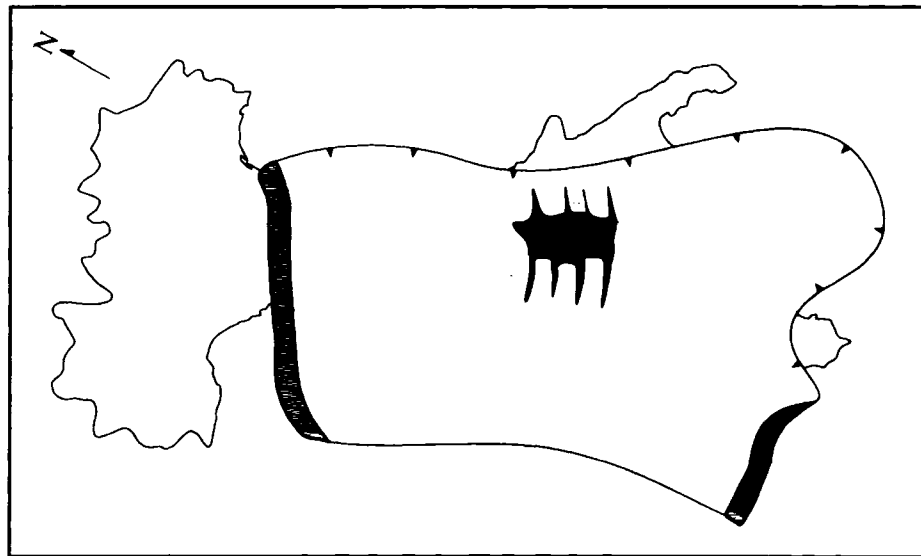


Figure 9.7. Model IV: schematic of a window in the Adriatic slab below central-southern Italy through which the counterflow of mixed upper and lower mantle is channeled to the upper part of the subducted slab (Gasperini et al., 2002).

Calabrian crust may also explain why the top of the slab under the Aeolian Islands is presently much deeper (200-250 km) than in most island arcs (~150 km).

The boundary between the Ionian and the African plates is thought to be represented by the Malta escarpment, while the boundary between the Ionian and the Adriatic plates may be the Apulian escarpment (Gvirtzman and Nur, 1999). If asthenospheric mantle is upwelling along the African-Ionian boundary beneath Etna, there may also be upwelling along the Adriatic-Ionian boundary in southern peninsular Italy. Local asthenospheric flow at the Adriatic-Ionian plate boundary may be responsible for the Quaternary volcanism of the Campanian Province (Gvirtzman and Nur, 1999), and may have introduced Adriatic mantle material with a FOZO isotopic signature into the Tyrrhenian mantle.

Model IV. Slab window beneath central-southern Italy due to differential slab rollback (Gasperini et al., 2002)

The collision of the eastward-migrating Apennine subduction zone with the Adriatic microplate in the mid-Miocene resulted in a dramatic reorganization of the stress regime in the Western Mediterranean (Devoti et al., 2002). Arrival of thick continental Adriatic lithosphere at the trench may have stalled the subduction process in northern Italy, while the easily-subducted thin Ionian lithosphere continued to be consumed in southern Italy. Current rates of passive subduction (i.e. gravitational sinking) beneath Tuscany are on the order of 1 cm/yr, while active subduction beneath Calabria is estimated at 5 cm/yr (Gasperini et al., 2002). The velocity differential between subduction in northern and southern Italy, along with the sharp change in azimuth from

W-directed to NW-directed subduction, may have caused a rupture of the Adriatic plate. In contrast to the hypothesis that asthenospheric upwelling is restricted to the boundary between the Ionian and Adriatic plates (see Model III), Gasperini et al. (2002) proposed a 400 km-wide NW-SE gap in the subducting plate beneath central-southern Italy (Figure 9.7). This geodynamic model differs from that of slab detachment (Wortel and Spakman, 1992) by the active role played by the change in the direction of subduction.

The existence of a slab window is supported by geophysical evidence that indicates that the slab below the central-southern Apennines has no physical connection to crustal levels (Wortel and Spakman, 1992; Amato et al., 1993; Piromallo and Morelli, 1997; Lucente et al., 1999; Bijwaard and Spakman, 2000). At depths above 250 km, the upper mantle beneath the Campanian Province instead shows anomalously low-velocity material (Fig. 9.3c). Tomographic work by Doglioni et al. (1999) and Bijwaard and Spakman (2000) suggests that the low-velocity region may be continuous from just below the surface to the transition zone east of the subducting slab. Below 250 km depth, the high-velocity anomaly joins the widespread high-velocity anomaly marking the bottom of the Tyrrhenian upper mantle (Fig. 9.3f).

Gasperini et al. (2002) argued that the presence of a strong HIMU component in magmatic rocks from southern Italy indicates that material from the deep mantle is channeled toward the surface through this slab window. The authors suggested that the trailing edge of the Adriatic plate torn off below central-southern Italy induces a counterflow of mixed upper and lower mantle, which then spreads laterally in the mantle wedge above the Apennine subduction zone. The restricted isotopic composition of the depleted mantle end-member over the entire length of Italy indicates that the vertical

mixing between the upper mantle (DMM) and the lower mantle (HIMU) components in the counterflow is efficient and steady. Gasperini et al. (2002) envisioned thorough mixing between the DMM and HIMU components prior to incorporation of the crustal isotopic end-member, which they believe is derived from the upper surface of the subducting Apenninic slab. The weaker influence of the HIMU mantle component towards northern Italy is considered to be due to smaller inputs of HIMU mantle melt from a more distant source, and the interaction of these melts with a thick and ubiquitous continental crust.

One problem with the slab window model of Gasperini et al. (2002) is the lack of a mechanism by which lower mantle material (> 670 km depth) moves upwards and through the gap in the slab, which only extends to ~250 km depth. The presence of a deep-seated mantle plume beneath central-southern Italy could provide an active mode of transport for lower mantle material through the slab window into the uppermost mantle.

Model V. Slab window beneath central-southern Italy due to collision of the Apulian platform with the Apennine subduction zone

While Gasperini et al. (2002) recognized the lithological differences between the continental Adriatic plate and the oceanic Ionian plate, their model fails to account for the paleogeography of the Adriatic plate. Promontories and embayments of the Adriatic plate had a profound effect on the present structure of the Apennine chain, which is considered to be a result of tectonic stacking of sedimentary rock units originally deposited on the thinned Adriatic margin (Royden et al., 1987). The largest promontory of the Adriatic plate was the Apulian platform, a thick carbonate shelf located in central-

southern Italy. Collision of the Apulian platform with the Apennine subduction zone in the late Miocene may have created a slab window beneath central-southern Italy that allowed for the migration of Adriatic FOZO mantle into the Tyrrhenian domain.

Figure 9.8 outlines a hypothetical model for the Apennine chain and Tyrrhenian basin from the Burdigalian (early Miocene) to the present. Extension in the Tyrrhenian started at approximately 17 Ma, following the first phase of rifting in the Western Mediterranean and the anticlockwise rotation of the Corsica-Sardinia block (see Chapter 2). At this time, fragments of the Alpine chain (Calabria, NE Sicily, and Alpine Corsica) lay to the west of the W-dipping subduction zone, and a small accretionary wedge had begun to develop (Fig. 9.8a). Eastward trench migration and contemporaneous back-arc extension throughout the early and middle Miocene (Fig. 9.8b) were driven by slab pull of the passively subducting Ionian oceanic lithosphere (Faccenna et al., 1996). Progressive thinning of the Tyrrhenian lithosphere was accompanied by growth of the accretionary wedge of sedimentary material scraped off the subducting Adriatic plate.

Lucente et al. (1999) estimated that the continental promontory of the Adriatic plate (Apulian platform) reached the trench at about 6.5 Ma (Messinian). The thick Apulian carbonate platform stalled subduction in central-southern Italy, and led to the development of arcs in the northern Apennines and Calabria (Figs. 9.8c and 9.8d). Evidence that the Apulian lithosphere was unable to effectively subduct is provided by seismic profiles and deep boreholes, which have revealed the presence of the Apulian carbonate platform at a depth of ~10 km beneath the Tyrrhenian margin in central-southern Italy (Mostardini and Merlini, 1986). The effects of slab pull from previously subducted oceanic lithosphere below the Apulian platform and the traction of the

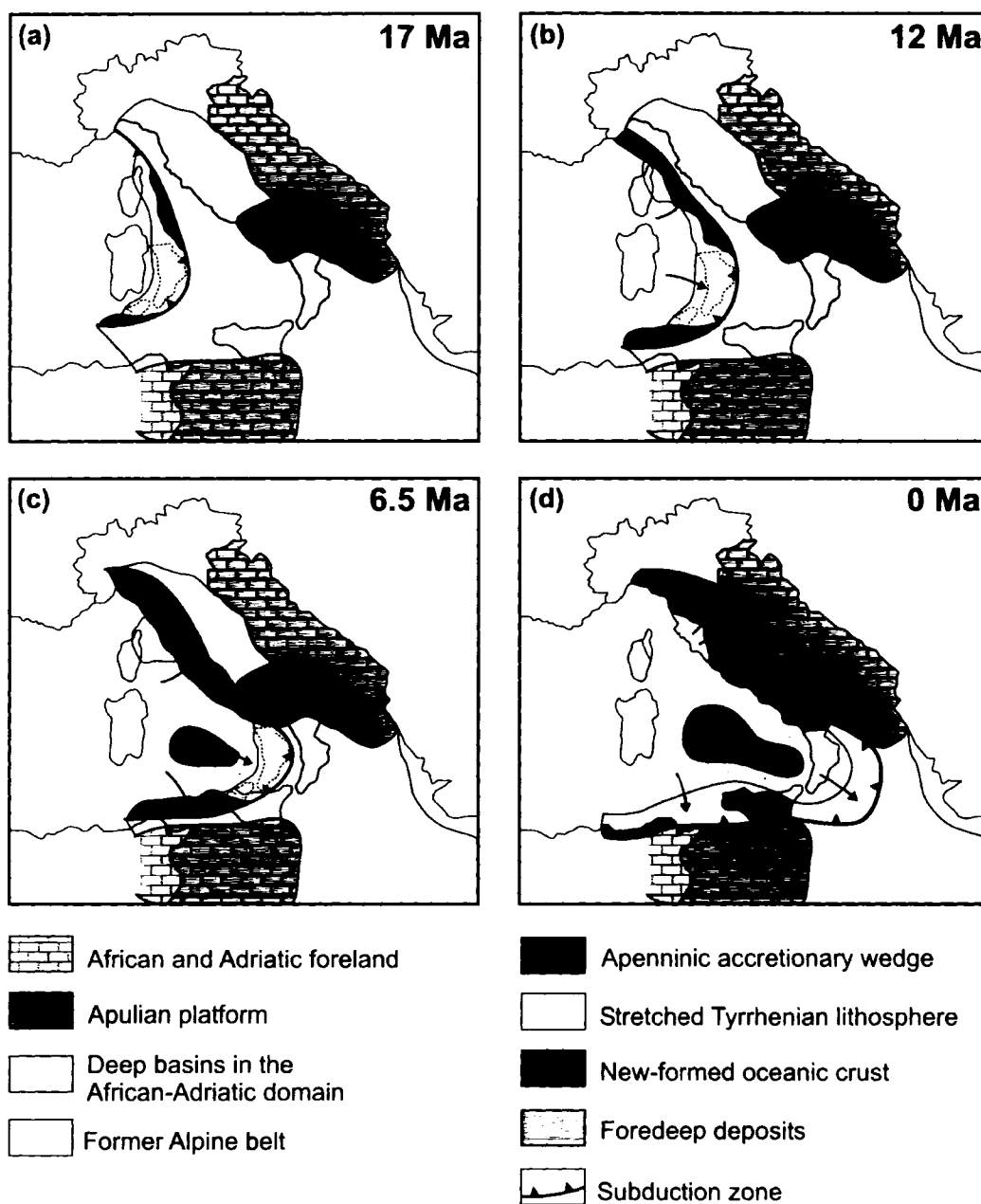


Figure 9.8. Hypothetical evolution of the Apennine chain and Tyrrhenian basin from 17 Ma to the present day (modified from Lucente et al., 1999). Arrows represent direction of slab rollback. (Note that the low number of present-day deep earthquakes at the Calabrian trench strongly suggests that slab rollback in this area may have ceased)

neighboring active subductions in the northern Apennines and Calabria created a tear in the slab at the oceanic-continental lithosphere transition (Figures 9.9a and 9.9b). The previously subducted oceanic lithosphere then continued to passively sink towards the transition zone, still attached at depth to the slab segments to the north and south. Outcrops of Cretaceous to late Miocene platform carbonates in central-southern Italy suggest that these rocks were once part of the Apulian platform (Lucente et al., 1999), and support the hypothesis that the Apulian lithosphere was incorporated into the Italian peninsula instead of subducted.

The main problem with this model involves timing of magmatism. Lucente et al. (1999) estimated that the Apulian platform reached the Apenninic trench at about 6.5 Ma, but data from rocks of the Tuscan Province that are as old as 14.2 Ma fall on the mixing curve between the depleted end-member and ITEM (e.g. the Sisco lamproite). Assuming a period of several million years between the arrival of the Apulian platform at the trench and the initiation of slab break-off, material from the Adriatic mantle cannot have passed through the slab window before about 5 Ma. Therefore, this model cannot explain the presence of a FOZO isotopic component in Italian magmatic rocks older than Pliocene.

9.3c Geodynamic model for the origin of FOZO in the Tyrrhenian mantle

Bell et al. (2003, 2004) proposed that Italian magmatism is related to a large-scale, asymmetric plume located beneath the Western Mediterranean region that has been in existence for at least 30-35 Ma (Figure 9.10). In this model, the depleted isotopic signatures of Italian volcanic rocks, occurrence of ultra-alkaline rock types in the Internal Apennines Zone, and intensive thinning of the Tyrrhenian lithosphere are attributed to an

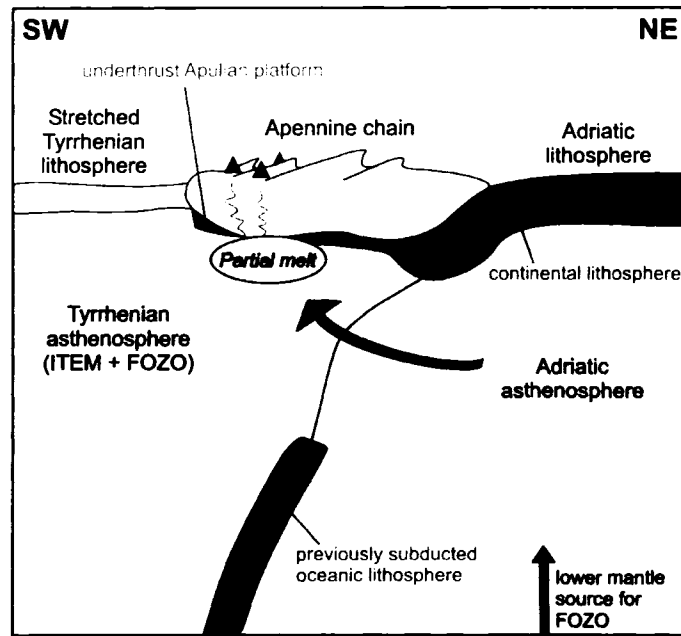


Figure 9.9a. SW-NE schematic cross-section of a slab window beneath central-southern Italy (not to scale). The Apulian platform of the continental Adriatic plate has underthrust the Apennine chain but did not subduct, leading to breakoff and passive sinking of previously-subducted oceanic lithosphere.

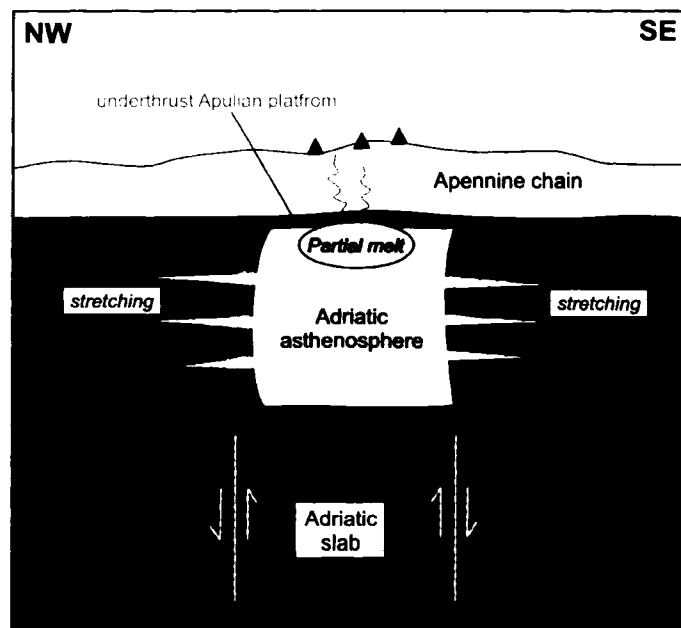


Figure 9.9b. NW-SE schematic cross-section of a slab window beneath central-southern Italy (not to scale). The previously subducted oceanic lithosphere is attached at depth to the slab segments to the north and south. Horizontal stretching and vertical shearing probably accompanied rollback of the northern Apennine and Calabrian arcs.

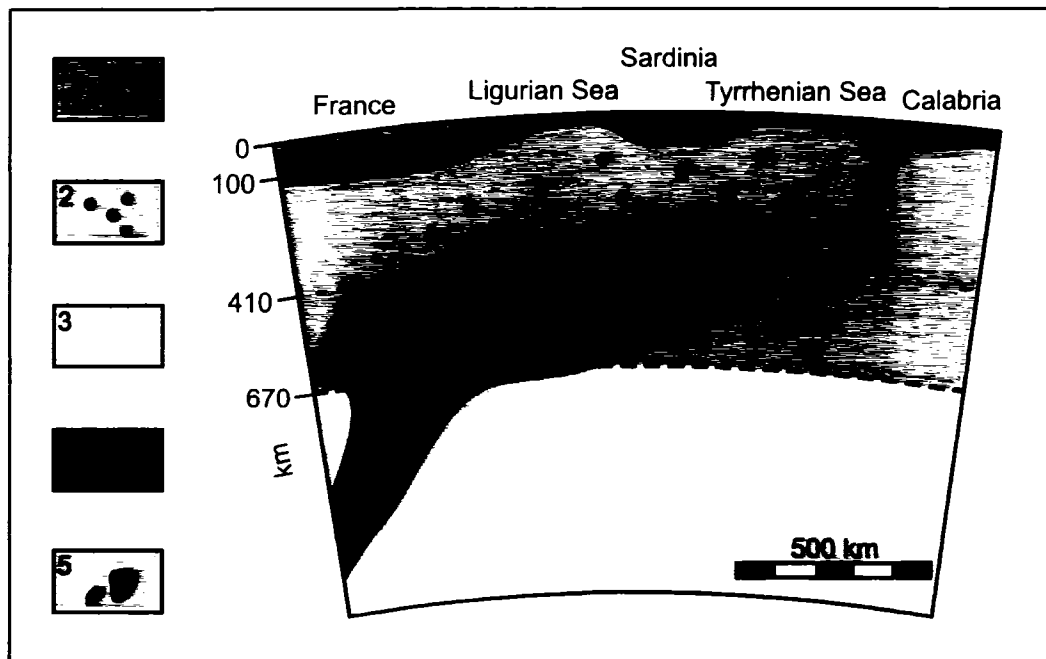


Figure 9.10. Interpretive transect showing a degassed mantle plume trapped in the Mediterranean transition zone (Bell et al., 2004). The geometry of the plume is largely hypothetical and derived from Brunet and Yuen (2000); the size of the plume is predicted by Lavecchia and Creati (in press) based on an areal-balance technique. Key: (1) lithosphere, (2) asthenosphere invaded by metasomatic fluids, (3) mesosphere, (4) degassed heterogeneous plume (colours mark the decrease in density moving from the outer to the innermost parts of the plume), (5) remnants of the Tethyan lithosphere that was subducted to the SE beneath the Adriatic foreland during the Cretaceous-Paleocene.

eastward-growing plume head trapped within the transition zone between the 410 and 670 km discontinuities. The lack of flood basalts in the Tyrrhenian basin can be explained by a plume head that has not yet reached a sufficiently high level to produce basaltic liquids (Bell et al., 2004). A similar model was previously proposed by Griffiths and Campbell (1991) to explain the lack of flood basalts in East Africa.

In opposition to a plume-related model, Lucente et al. (1999) pointed out that the sub-horizontal geometry of cold lithosphere resident in the transition zone beneath the Tyrrhenian basin probably precludes a lower mantle origin for material in the Tyrrhenian upper mantle (see Figs. 9.3e and f). It seems unlikely that a mantle plume could burn through subducted lithosphere and produce volcanic chains parallel to a subduction boundary (Morris and Hart, 1983). However, Bell et al. (2004) argued that some of the velocity patterns seen in tomographic studies may reflect chemical rather than thermal variations. The high-velocity anomaly in the transition zone could represent a highly depleted plume head which has lost volatiles and fluids during upward migration, while overlying low-velocity material might represent a plume-modified region enriched by H₂O- and CO₂-rich fluids released from the plume.

Unlike the previous models discussed for the origin of FOZO, the model of Bell et al. (2004) does not involve any W-directed subduction of Adriatic lithosphere beneath the Italian peninsula. This is contrary to the theory of subduction and slab rollback as a major geodynamic factor in the evolution of the Western Mediterranean (Malinverno and Ryan, 1986; Wortel and Spakman, 1992; Guegen et al., 1997; Lucente et al., 1999). In addition, the presence of a well-defined high-velocity zone beneath the Calabrian arc, most commonly explained as NW-directed subduction of Ionian oceanic lithosphere

beneath the Tyrrhenian basin, is modeled as SE-directed subduction by Bell et al. (2004). These authors suggested that the lithosphere beneath the Calabrian arc may be a remnant of Tethyan lithosphere subducted during the Cretaceous-Paleocene Alpine orogeny.

9.3d Geodynamic model for the origin of LVC-EAR in the Western Mediterranean mantle

If the depleted end-member is not sourced in the lower mantle (FOZO), then the end-member may be referred to as either LVC (Hoernle et al., 1995) or EAR (Cebriá and Wilson, 1995). The LVC and EAR are both considered to originate from an isotopically depleted layer located in the upper mantle above the transition zone (see Chapter 8). The oldest volcanic rocks that display an LVC-EAR isotopic signature are from the Eastern Atlantic (Canary and Madeira islands; 60 Ma), the Massif Central in France (65 Ma), Pietre Nere (56 Ma), and the Veneto region (56 Ma) (Vollmer, 1976; Holik and Rabinowitz, 1991; Wilson and Downes, 1991; Macera et al., 2003).

The presence of the widespread LVC-EAR isotopic end-member in the Eastern Atlantic – Central European – Western Mediterranean upper mantle therefore predates the first phase of extension in the Western Mediterranean, which began with the eruption of calc-alkaline volcanics in Sardinia (~32-13 Ma) and Provence (~34–20 Ma) and was followed by the opening of the Liguro-Provençal basin in the late Oligocene (Beccaluva et al., 1994). This volcanism and associated back-arc extension is generally explained by a NW-directed Apenninic subduction zone. As discussed in Chapter 2, Faccenna et al. (2001) have modeled the initiation of subduction in the Western Mediterranean in the late Cretaceous (80 Ma), while other authors have suggested the Cretaceous-Tertiary

boundary (65 Ma; Dercourt et al., 1986), the Paleocene (50 Ma; Boccaletti et al., 1971) or the Oligocene (30 Ma; Doglioni et al., 1997).

If the initiation of subduction is older than ~65 Ma, the LVC-EAR isotopic reservoir may have been able to spread laterally across the Western Mediterranean unobstructed by the Apenninic slab. This could explain how LVC-EAR signatures are seen in magmatic rocks located in both the Apenninic fore-arc (Pietre Nere, Mt. Etna, Pantelleria, the Iblean Plateau) and in the back-arc (Tuscan Province, Roman Province, Southern Latium Transition Zone, Campanian Province, Aeolian arc, Tyrrhenian Sea). In the models of Hoernle et al. (1995) and Cebriá and Wilson (1995), the entire Western Mediterranean and Central European lithosphere has been underlain by an asthenospheric layer with a LVC-EAR isotopic signature since the late Cretaceous.

The westward dip of the LVC layer noted by Hoernle et al. (1995) may be an important clue to the origin of the depleted isotopic signature. While the low $^3\text{He}/^4\text{He}$ ratios of volcanic rocks in the Western Mediterranean suggest that LVC-EAR may be exclusively an upper mantle feature, global seismic tomographic studies also reveal the existence of a zone of low seismic velocities at depths of 900 to 1400 km in the lower mantle, extending from Iceland to the Eifel volcanic province of northern Germany, the Massif Central of France, the Hoggar massif in northern Africa and the Canary Islands (Spakman et al., 1993). An isotopic component geochemically similar to EAR is known to exist within the Icelandic plume system, preferentially sampled by relatively rare, low-degree, partial melts such as nephelinites and alkali basalts (Breddam and Kurz, 2001). Some authors have proposed that the diapiric upper mantle upwellings thought to have triggered Tertiary-Quaternary volcanic activity within Europe could be dynamically

linked to the upwelling and lateral spreading of the Iceland mantle plume (Wilson and Patterson, 2001). Hoernle et al. (1995) also suggested that the LVC may reflect a combination of eastward asthenospheric flow and lithospheric drag. In contrast, Goes et al. (1999) suggested a local lower mantle source directly beneath Central Europe

The question of whether the LVC-EAR isotopic component in Central Europe and the Western Mediterranean has (or had) a lower mantle source continues to be a matter of debate. While tomographic evidence suggests a possible connection between the Iceland plume and the low-velocity anomalies underlying areas of Cenozoic volcanism in the Western Mediterranean (Spakman et al., 1993), Foulger et al. (2000) pointed out that the Iceland plume itself may be an upper mantle phenomenon. If the LVC-EAR component originated from the lower mantle, then LVC, EAR, and FOZO can be considered broadly similar and may represent essentially the same isotopic reservoir. On the other hand, if LVC-EAR is strictly an upper mantle feature, as suggested by Wilson and Downes (1991), Hoernle et al. (1995), and Granet et al. (1995), then there is no need to invoke lower mantle upwelling.

9.3e Evaluation of geodynamic models for the depleted end-member in Italian magmatic rocks

The geodynamic models for the origin of the depleted end-member in the *Adriatic* lower mantle (Model I – Model V) all involve upwelling through a tectonically-induced gap in the Apenninic slab. The major problem with most of these models is that the inflow of Adriatic mantle into the Tyrrhenian asthenosphere is geographically restricted to an area of central-southern Italy or the Calabrian arc. The isotopic mixing curves

shown in Chapter 8 imply that the source regions of magmatic rocks from as far away as the Tuscan Province and Sardinia have been influenced by the depleted end-member. The mechanism of transport of isotopically and geochemically distinct material with a depleted isotopic signature to distal source regions is unknown, and is a weakness of these models.

The model of Bell et al. (2004) involves lower mantle upwelling beneath the *Tyrrhenian* basin, and infiltration of the Western Mediterranean asthenosphere by metasomatic fluids derived from a degassed, heterogeneous plume head. This model is difficult to reconcile with the presence of large amounts of cold, lithospheric material in the transition zone as deduced from seismic tomography, and is weakened by the lack of evidence to support SE-directed subduction beneath the Calabrian arc. However, there are similarities between the plume model of Bell et al. (2004) and models for the origin of the LVC-EAR signature. Bell et al. (2004) envision a large plume with a source region in the lower mantle of the eastern Atlantic, which is similar to the concept of a W-dipping sheet developed by Hoernle et al. (1995) for the LVC, and also to the idea of Wilson and Patterson (2001) that the EAR reservoir may be linked to eastward asthenospheric spreading of the Iceland plume. The main difference in these models is that Bell et al. (2004) have the plume head (i.e. FOZO reservoir) trapped in the transition zone, while the LVC and EAR reservoirs are considered to be located above the transition zone in the asthenosphere.

The preferred model in this study for the origin of the depleted end-member, whether it is referred to as FOZO, LVC, or EAR, is one in which the asthenosphere beneath Central Europe and the Western Mediterranean has been contaminated by the

isotopic signature of a "fossil" plume head (Figures 9.11a and b) (Granet et al., 1995). This implies that the plume was once, but is no longer, sourced by material from the lower mantle. The original source of the plume may have been located in the lower mantle of Central Europe, the Western Mediterranean, or the Eastern Atlantic, but it cannot still be feeding the plume due to the abundance of subducted lithosphere now present in the transition zone (see Figure 9.3b).

In order to account for the depleted isotopic signatures of late Cretaceous volcanic rocks in Central Europe and the Western Mediterranean, the age of the plume must be ≥ 65 Ma. This indicates that plume material with a FOZO-LVC-EAR isotopic signature was present in the Italian upper mantle prior to either the Alpine or Apennine orogenies. The plume head was cut off from its lower mantle source during the Tertiary by the accumulation of lithospheric slabs at the base of the upper mantle as a result of Alpine and Apennine subduction events. This process resulted in the isolation of a widespread, homogeneous, isotopically depleted layer in the asthenosphere above the subducted slabs.

One consequence of severing the deep mantle "root" of the plume may be the absence of a strong thermal anomaly and associated flood basalts in the Western Mediterranean. The plume material located above the transition zone may be relatively cool, and unable to provide the heat necessary for large-scale, voluminous partial melting. The model of a fossil plume head is in accordance with evidence presented by Hart et al. (1992) in support of a lower mantle origin for FOZO, and is consistent with the observation that all Pliocene-Recent Italian magmatic rocks sample variable amounts of the depleted end-member. However, it should be noted that the thermal and rheological constraints on plume-lithosphere interaction in this scenario are unknown.

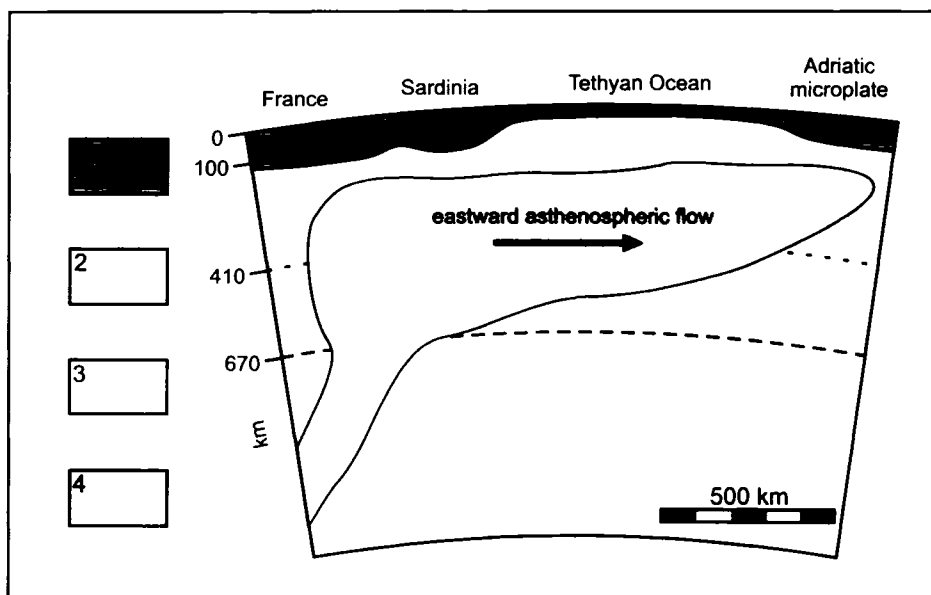


Figure 9.11a. Late Cretaceous position of the proposed mantle plume beneath the Western Mediterranean. Key: (1) lithosphere, (2) asthenospheric and mesospheric upper mantle (3) lower mantle, and (4) mantle plume.

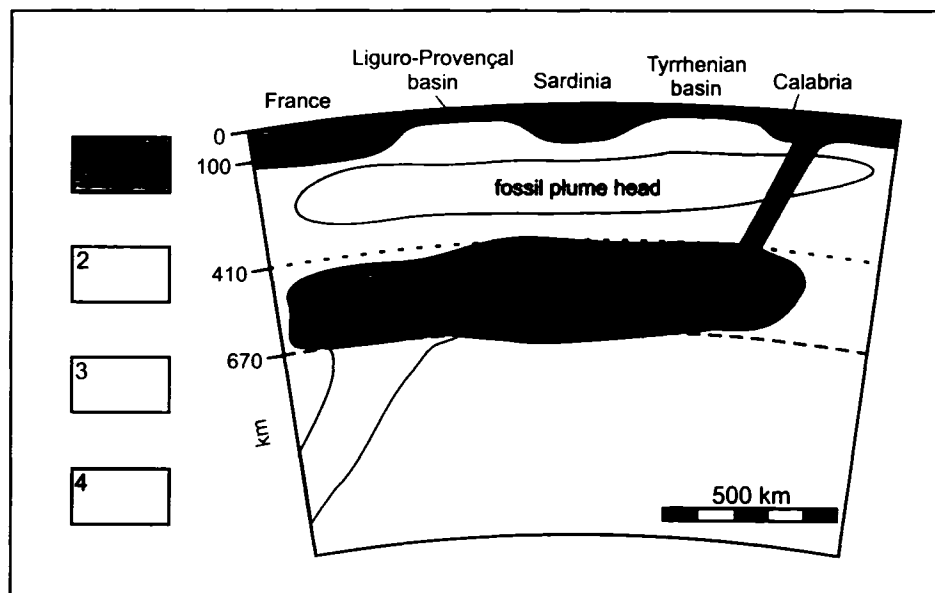


Figure 9.11b. Mid-Late Tertiary position of the mantle plume head beneath the Western Mediterranean. The lower mantle "root" of the plume has been disconnected from the head due to the accumulation of lithosphere in the transition zone. Note that the lithosphere in the transition zone is probably a result of both the Alpine and the Apennine orogenies. Compare this figure to the tomographic model of Bijwaard and Spakman (2000) in Figure 9.3e. Key: (1) lithosphere, (2) asthenospheric and mesospheric upper mantle (3) lower mantle, and (4) mantle plume.

This preliminary model, involving a fossil plume head in the Western Mediterranean, can be tested by evaluating such features as noble gas signatures (Xe, Ar, He, Kr, etc), mineralogy and geochemistry of mantle xenoliths, and daughter products of extinct radionuclides in primitive, mantle-derived Italian rocks. Similarities between Italian rocks and world-wide plume-related rocks could provide support for a deep-seated origin of the isotopically depleted Sr, Nd, Pb signatures in the Western Mediterranean.

9.4 Origin of the ITEM isotopic component in Italian magmatic rocks

Potential sources for the enriched ITEM signature of Italian magmatic rocks include: 1) ancient asthenospheric metasomatism of the Italian upper mantle, 2) recent asthenospheric metasomatism of the Italian upper mantle, 3) pelagic sediments and/or continental crust subducted during the Apennine orogeny, and 4) pelagic sediments and/or continental crust subducted during the Alpine orogeny.

Ancient metasomatism can produce high $^{87}\text{Sr}/^{86}\text{Sr}$ and low $^{143}\text{Nd}/^{144}\text{Nd}$ ratios after a period of isolation allowing for the long-term decay of ^{87}Rb and ^{147}Sm , a process suggested for the source of kimberlites in stable cratonic regions (Nelson et al., 1986). It seems unlikely, however, that the upper mantle beneath Italy has been chemically isolated for hundreds of millions of years, given the active plate movements in the Western Mediterranean at least since the Paleozoic. Therefore, models involving ancient metasomatism will not be considered here. Geodynamic models involving recent asthenospheric metasomatism and the introduction of subducted material during the Alpine and Apennine orogenies will be discussed below.

Model I: Recent asthenospheric metasomatism of the Italian upper mantle

Recent (Cenozoic) asthenospheric metasomatism may be correlated with present-day, low-velocity anomalies (i.e. zones of "hot" mantle upwelling) that can be detected using seismic tomography. The tomographic model of Piromallo and Morelli (2003) indicates a shallow (<50 km) high-velocity zone beneath northeastern Italy and northern Adriatic Sea underlain by a low-velocity anomaly from ~100 to 250 km depth (Fig. 9.2). The low-velocity anomaly has a temperature excess of about 220–280 K, which is in agreement with estimates for mantle plumes (McKenzie, 1984; Sleep, 1990; Shen et al., 1996). Primitive Tertiary lavas from the Veneto region of northeastern Italy (South-Eastern Alps) overlie this low-velocity anomaly and display geochemical features consistent with plume-related volcanism (Beccaluva et al, 2000; Macera et al., 2003). Alkaline basalts from Veneto have unradiogenic Sr and Nd isotopic signatures ($^{87}\text{Sr}/^{86}\text{Sr} = 0.70306\text{--}0.70378$; $\epsilon\text{Nd} = +3.9$ to $+6.8$), and $^{206}\text{Pb}/^{204}\text{Pb}$ ratios (18.786–19.574) that are intermediate between those of HIMU and DMM. Macera et al. (2003) proposed that plume-related upwelling of asthenospheric mantle through a gap in the Alpine slab may have been the cause of the alkaline basaltic volcanism in the Veneto region.

The isotopic compositions of plume-related volcanic rocks from the Veneto region are identical to the FOZO-LVC-EAR depleted end-member. Therefore, it seems that Tertiary Central European and Western Mediterranean volcanic rocks attributed to recent asthenospheric metasomatism are characterized by a depleted, not an enriched, isotopic signature. One of Bell et al. (2004)'s suggestions was that the ITEM reservoir may be situated at the D" core-mantle boundary, and may represent a highly-enriched layer that has been isolated from mantle convection. Although deep-seated mantle

plumes originating from the D" layer could provide a mechanism for the transport of this highly-enriched material into the source of Italian volcanic rocks, ITEM has not been found in world-wide OIBs, many of which are thought to be plume-related. While it is possible that the ITEM reservoir is located in the deep mantle, geochemical and isotopic evidence strongly supports the involvement of crustal material.

Model II: Pelagic sediments and/or continental crust subducted during the Apennine orogeny

The Apennine fold and thrust belt is composed of E and NE-verging thrust sheets of allochthonous Meso-Cenozoic sedimentary rocks originally deposited on the continental and transitional crust of the Adriatic plate (Royden et al., 1987). Although the structural and tectonic evolution of the Apennines is complex, the belt is generally considered to represent an accretionary wedge that developed in response to the west-directed subduction of the Adriatic plate beneath the Tyrrhenian basin.

There is geological and geophysical evidence to support the subduction of both pelagic sediments and limited amounts of continental crust during the Apennine orogeny. The Ionian oceanic lithosphere, considered by some to represent a fragment of Tethyan lithosphere that survived after the Alpine orogeny (Suhadolc and Panza, 1989), is probably representative of the type of lithosphere subducted during most of the Apennine orogeny. Currently, the Ionian lithosphere is characterized by a thick accumulation of sediments (~6 km) overlying oceanic crust. The thick sedimentary package is thought to obscure the trench in the Calabrian arc, which is weak to non-existent on bathymetry maps of the Western Mediterranean (Compagnoni and Galluzzo, 2004).

Evidence for the subduction of Tuscan continental crust is provided by the continued eastward migration of active tectonic fronts and foredeep deposits in the northern Apennines following collision of the Corsica-Sardinia block with the Adriatic microplate. Several authors have proposed that the subducted slab continued to roll back throughout the Pliocene and Pleistocene in northern-central Italy (Keller et al., 1994; Pialli and Alvarez, 1997). In this scenario, the continental lithosphere of the Adriatic plate was either obducted and incorporated into the accretionary wedge, or subducted. Balanced cross-sections across the outer part of the Northern Apennine fold and thrust belt show a minimum crustal shortening of 60 km, whereas areal balancing of the crust in the same sector indicates that 35 km of crust is lacking (Barchi et al., 1998). Alvarez and Pialli (1989) suggested that the missing continental crust was subducted during the Apennine orogeny and subsequently changed to eclogite. The granulite-eclogite phase change and associated density increase facilitates passive subduction, and may have allowed continued eastward rollback of the trench (Gualteri and Zappone, 1998).

There is less evidence for subduction of crustal rocks beneath the central-southern Apennines. The presence of Apulian platform carbonates at a depth of ~10 km beneath the Tyrrhenian margin in central-southern Italy (Mostardini and Merlini, 1986) suggests that the thick Apulian lithosphere was unable to effectively subduct and instead underplated the Italian lithosphere (see section 9.3b, Model V). There is no evidence for subduction of continental crust beneath the Calabrian arc.

The isotopic data presented in Chapter 8 show that the ITEM end-member has a composition similar to both pelagic sediments and Tuscan continental crust. However, the major problem with attributing the ITEM isotopic signature to subduction of crust or

sediments during the Apennine orogeny is the age and location of magmatic rocks from the Alps. The lamprophyres from the Western Alps, along with many other Eocene-Oligocene (42 – 24 Ma) rocks from the Tertiary Periadriatic Province, have Pb isotopic signatures characteristic of ITEM, but are older than the Apennine orogeny. In addition, there is little evidence that the Apennine orogeny affected the sub-Alpine mantle.

It is important to note that metasomatism of the Italian mantle may well have occurred during the Apennine orogeny, but it cannot be considered the "dominant" isotopic imprint in the mantle source of Italian magmatic rocks. The smooth isotopic mixing curves between ITEM and the depleted end-member strongly suggest a single, homogeneous, widespread origin for the ITEM end-member. This conclusion contrasts with the model of Peccerillo and Turco (2004), who suggested two-stage metasomatism, first involving Alpine subduction processes and then followed by Apenninic subduction. In their model, Alpine subduction introduced upper crustal material into the mantle beneath the Western Alps and Tuscany, and then subduction of a new type of crustal material derived from the Adriatic plate occurred beneath the Italian peninsula during the Apennine orogeny. While certainly there is geological and geophysical evidence to support subduction during both the Alpine and Apennine orogenies, isotopic evidence strongly indicates that only one of these events is responsible for the ITEM end-member.

Model III: Pelagic sediments and/or continental crust subducted during the
Alpine orogeny

The entire length of the Piemont (Tethyan) Ocean, along with associated pelagic sediments, was consumed during Alpine subduction (Figure 9.12). It is this oceanic

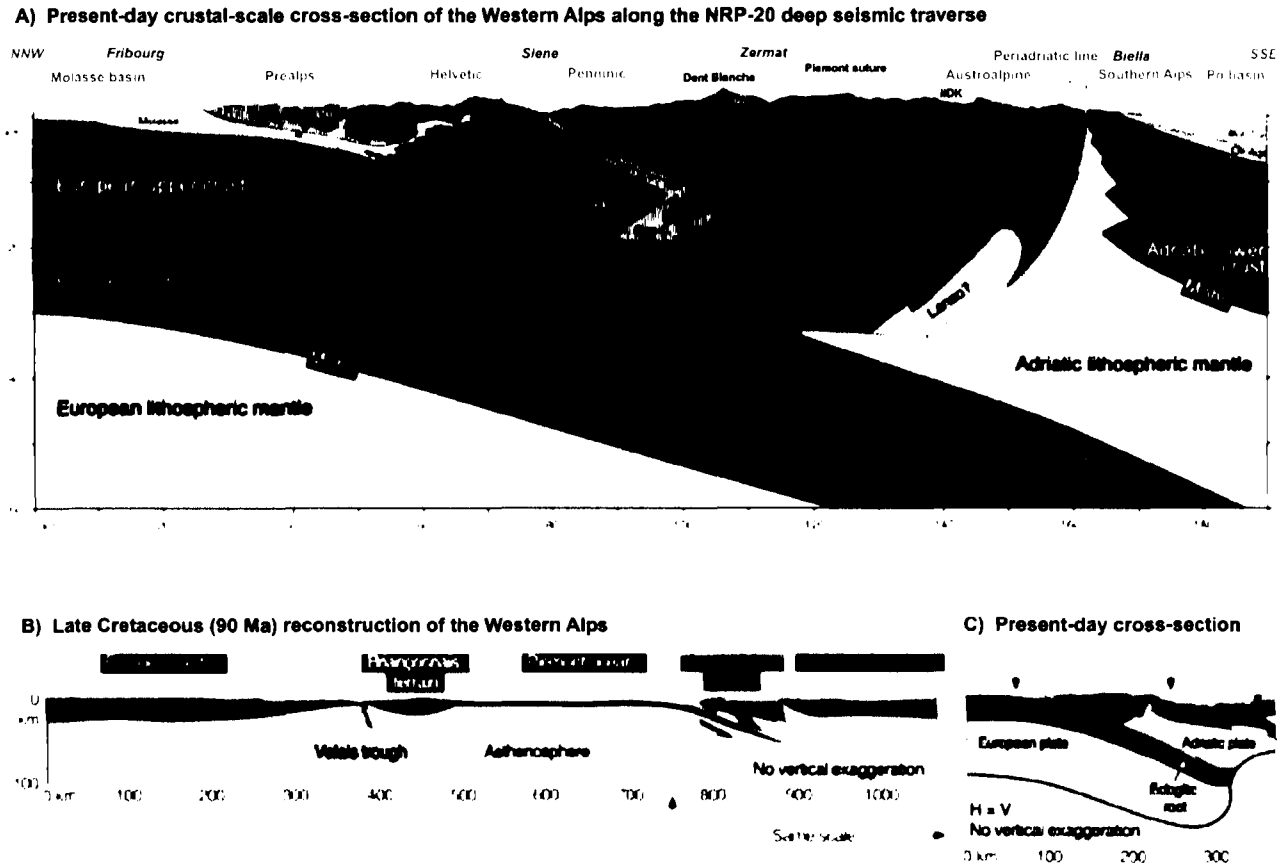


Figure 9.12. Present-day crustal-scale cross-section of the Western Alps (A), late Cretaceous (90 Ma) reconstruction of the Western Alps (B), and present-day simplified lithospheric cross-section (C) showing SE-directed subduction of the European plate beneath the Adriatic plate (modified from Marchant, 1993; Marchant and Stampfli, 1997).

lithosphere that Piromallo and Faccenna (2004) believe now resides in the transition zone beneath the Alpine belt in northern Italy (see section 9.2c). Along with the subducted oceanic lithosphere, mineralogical evidence strongly suggests that continental lithosphere, derived mostly from the European plate (and Briançonnais terrain), was subducted to a depth of at least 100 km and exhumed. Chopin (1984) first described the co-existence of coesite and pure Mg-Al garnet pyrope in high-grade blueschists of the Dora Maira Massif in the Western Alps. Metamorphic conditions are estimated to be 28-33 kilobars and 700-800°C, corresponding to a geothermal gradient of 6-7°C/km, typical of subduction zones (Chopin, 1984). This ultra-high pressure metamorphism is attributed to subduction of parts of the European continent during the peak of continental collision in the Eocene (Goffé and Chopin, 1986; Chopin, 1987). Subducted continental lithosphere may be partly responsible for the present-day continuous high-velocity signature located at a depth of 100 km beneath the Alpine chain (see section 9.2b).

The subduction of metasedimentary material, such as that from Dora Maira, provides a possible mechanism for creating isotopically enriched mantle (Tilton et al., 1989). However, there are several problems with this model. Firstly, the Pb isotopic ratios of mineral separates from the high-pressure rocks of Dora Maira are quite radiogenic, and do not overlap with the Pb isotopic signature of ITEM (see Figure 8.9). Secondly, the geographic extent of subducted European continental crust was likely very limited, and was probably restricted to the area directly beneath the Alps. This is difficult to reconcile with the fact that magmatic rocks as far south as the Aeolian Arc lie on a mixing curve between ITEM and the depleted end-member. The origin of the ITEM component must be geographically widespread.

9.4a Evaluation of geodynamic models for the ITEM end-member in Italian magmatic rocks

Pelagic sediment and continental lithosphere subducted during the Apennine orogeny is too young to account for the ITEM signature in Oligocene magmatic rocks from the Alps, and continental lithosphere subducted during the Alpine orogeny is too radiogenic and geographically restricted. Therefore, the most likely source for the ITEM end-member is pelagic sediment associated with the subduction of Tethyan oceanic lithosphere. During the closure of the Tethyan Ocean, an estimated 700 km of oceanic and thinned continental lithosphere was consumed in the Western Mediterranean (Piromallo and Faccenna, 2004). The widespread high-velocity anomaly between 410 and 670 km depth beneath the Tyrrhenian basin, and the discrepancy between the estimated amount of subduction and the depth of the Alpine orogenic root, suggests that much of the subducted Tethyan oceanic lithosphere may currently reside in the transition zone (Piromallo and Faccenna, 2004). Figure 9.3b shows that this high-velocity anomaly is widespread and extends from the Betic Cordillera to the Pannonian basin. Pelagic sediments associated with the subduction of Tethyan oceanic lithosphere during the Alpine orogeny are of the appropriate age, geographic distribution, and isotopic signature to account for the enriched ITEM end-member involved in Italian isotopic mixing.

9.5 An integrated model for the origin of the enriched and depleted end-members involved in Italian isotopic mixing

Isotopic data from the lamprophyres from the Western Alps, and KS and HKS volcanic rocks from Roccamonfina and Ernici, combined with data from other Tertiary

Italian magmatic rocks, support a geodynamic model in which a widespread, isotopically depleted asthenospheric layer with a FOZO-LVC-EAR signature was variably contaminated by pelagic sediments subducted during the Alpine orogeny. The depleted asthenospheric layer is interpreted as a fossil plume head cut off from its original lower mantle source by oceanic lithosphere subducted during the Alpine and Apennine orogenies. This model can explain some of the unusual geochemical features of Italian magmatic rocks, including 1) the north-south gradation of radiogenic isotopic ratios along the length of the Italian peninsula, 2) the lack of isotopic mixing between ITEM and EMI in Sardinia, 3) the fractionated LILE/HFSE ratios and high B contents of Italian potassic and ultra-potassic rocks, and 4) the different isotopic ratios of rocks from the KS and the HKS series at Roccamonfina and Ernici.

1) Magmatic rocks from northern Italy (Western Alps, Tuscany) show the strongest ITEM isotopic signature, whereas rocks from southern Italy (Aeolian arc, Campanian Province) have the weakest ITEM signature. Paleogeographic reconstructions of the Western Mediterranean in the late Oligocene show that the Alpine-Betic trench and deformational front were located along the southern edge of modern-day Europe (Figure 9.13) (Doglioni et al., 1997). Magmatic rocks that have the strongest ITEM signature are located close to the Alpine subduction front, and include Spanish lamproites, the Sisco lamproite in Corsica, Tuscan lamproites, and the Western Alps lamprophyres. The mantle beneath these areas formed a coherent NE-SE trending region in the late Oligocene, which was later fragmented by the rotation of Corsica-Sardinia and the southeastward movement of Calabria in the Miocene (Doglioni et al., 1997).

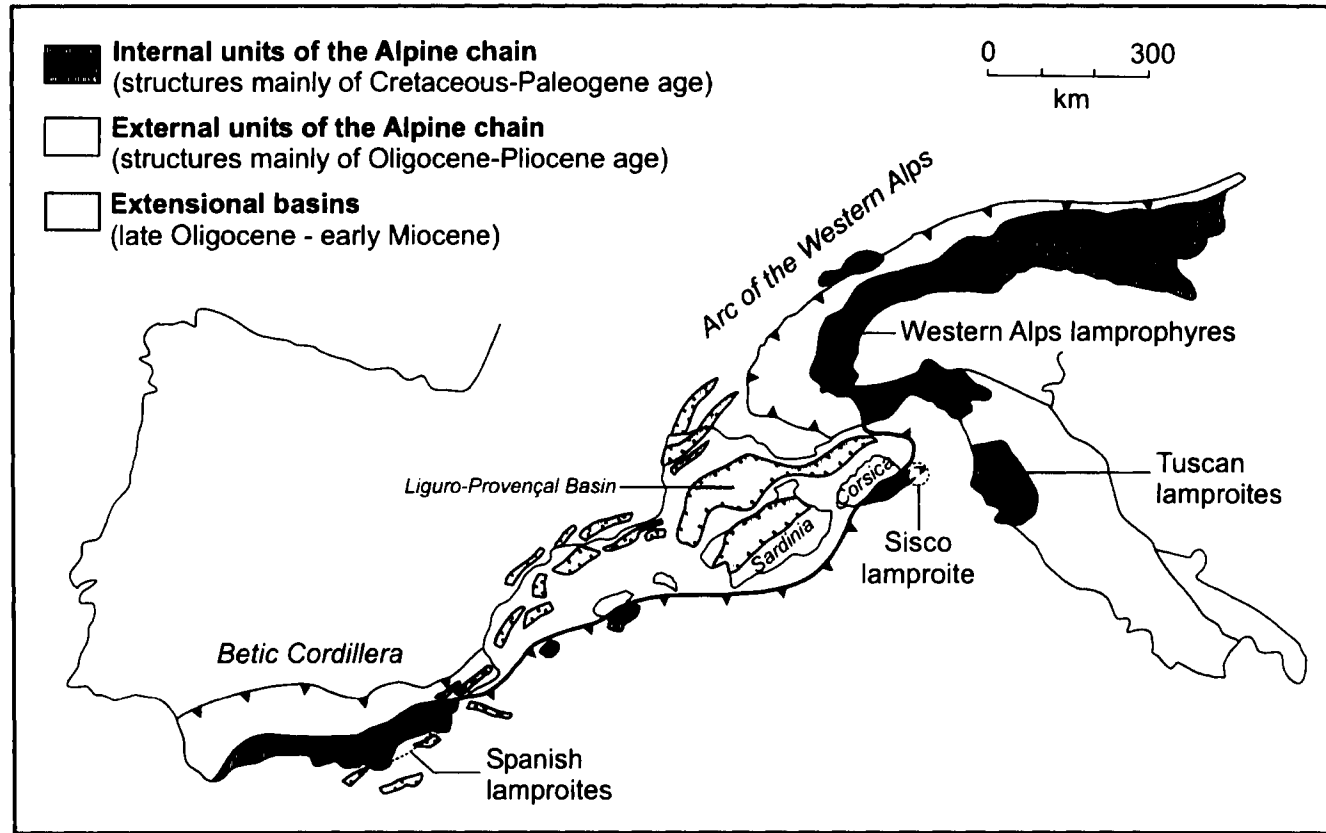


Figure 9.13. Paleogeographic reconstruction of the European margin of the Western Mediterranean in the late Oligocene (modified from Doglioni et al., 1997). The main late Oligocene – early Miocene extensional basins and the position of the Alpine-Betic front are shown, as well as the locations of the Spanish, Tuscan, and Sisco lamproites and the Western Alps lamprophyres. Note the absence of Calabria in southern Italy, which was moved into its present position during the Neogene.

The similar trace element and isotopic geochemistry of the lamproites and lamprophyres suggest derivation from a common source region (Peccerillo, 2001). Tilton et al. (1989) suggested that the isotopic signatures and high K contents of Spanish lamproites may have been supplied by deeply-subducted continental crust with a composition similar to that of the Dora Maira Massif in the Western Alps. However, Pb isotopic ratios from the Spanish magmatic rocks do not overlap with data from the Dora Maira Massif. It is more likely that the magmatic rocks from Spain, Tuscany, Corsica, and the Alps simply have a higher proportion of oceanic sediment in their source compared those from southern Italy. The "strength" of the ITEM signature in Italian magmatic rocks may be directly related to their distance from the Alpine trench.

2) Plio-Pleistocene magmatic rocks with an EMI isotopic signature from Sardinia show no influence of the ITEM end-member (see Figure 8.8), suggesting that sediment subduction during the Alpine orogeny did not affect their source. This fits well with the paleogeographic reconstruction provided in Figure 9.13, which shows that Sardinia was located on the European (fore-arc) side of the Alpine-Betic subduction zone.

3) The fractionated LILE/HFSE ratios and high B contents of Italian potassic and ultrapotassic rocks are typical of volcanic rocks from subduction-related tectonic settings. However, previous work has shown that mantle modified by subduction processes older than about 5 Ma is too depleted in B to produce the high concentrations (> 10 ppm) seen in KS and HKS rocks from Roccamonfina and Ernici (Morris et al., 1990). This puts serious constraints on the time at which B was introduced into the central-southern Italian mantle. Alpine subduction cannot be responsible for the B-enrichment of the Italian mantle, because B would have returned to the surface hydrosphere long before the

eruption of Pliocene-Recent volcanic rocks in Italy. Therefore, more recent (Apenninic) subduction is likely responsible for the B-enrichment.

The positive correlations between B and LILE (including K) shown in Figure 7.28 indicate that Apenninic subduction is also responsible for the high LILE contents and fractionated LILE/HFSE ratios of Italian potassic and ultrapotassic rocks. Therefore, it must be concluded that Apennine subduction resulted in the trace element (and K₂O) signatures of Italian magmatic rocks, but Alpine subduction provided the dominant enriched isotopic signature (ITEM). This statement is supported by the lack of regional correlations between Sr-Nd-Pb isotopic ratios and incompatible trace elements (see Chapter 8). The decoupling of isotopic signatures and trace element signatures in Italian magmatic rocks may be a result of the complex interaction of the Alpine and Apennine orogenic systems in the Western Mediterranean during the past 65 Ma.

One of the most important points to consider in the above model is the “preservation” of the highly enriched ITEM isotopic signature in the Italian mantle during later Apennine subduction. The type of material subducted during the Apennine orogeny, as well as the nature of the metasomatic agent in central-southern Italy, may have played a significant role. Geochemical evidence for source enrichment at Roccamonfina and Ernici supports a carbonate-rich, metasomatic melt (see Chapter 7) consistent with subduction of marine carbonates and pelagic sediment beneath the Italian peninsula during the Apennine orogeny. The low Rb/Sr ratio of the carbonate (~ 0.005; Faure and Mensing, 2005) may have diluted the high Rb/Sr ratio of the pelagic sediment (up to 0.85; Plank and Langmuir, 1998), resulting in an isotopic component with an ⁸⁷Sr/⁸⁶Sr ratio intermediate between that of pelagic sediment (up to 0.7350; Plank and

Langmuir, 1998) and Mesozoic marine carbonate (< 0.7080 ; Faure and Mensing, 2005).

In contrast, the extremely high $^{87}\text{Sr}/^{86}\text{Sr}$ ratio of the ITEM end-member is attributed solely to pelagic sediment subducted during the closure of the Tethyan Ocean. The retention of the ITEM signature in the Italian mantle can be explained by the inability of the mixed, intermediate isotopic signature of the carbonate-rich, metasomatic melt to significantly modify the more enriched ITEM end-member.

4) The KS rocks from Roccamonfina and Ernici are characterized by lower $^{87}\text{Sr}/^{86}\text{Sr}$, higher $^{143}\text{Nd}/^{144}\text{Nd}$, and lower $^{206}\text{Pb}/^{204}\text{Pb}$ ratios compared to the HKS rocks. The presence of two petrographically and geochemically distinct rock series with different isotopic signatures at a single volcanic centre presents problems for any geodynamic model. It is generally agreed that the KS and HKS magmas have separate source regions, and previous authors have suggested that the HKS source is deeper than the KS source based experimental evidence that supports stronger silica-undersaturation of potassic magmas at greater depths (Civetta et al., 1981; Conceição and Green, 2000).

One possible explanation is a vertically stratified mantle with different mineralogy and isotopic compositions, in which the HKS source layer contains a higher proportion of isotopically-enriched material than the KS source. This isotopically-enriched material can be envisioned as "pods" of mantle strongly influenced by fluids or melts derived from sediments subducted during the Alpine orogeny. Partial melting of a mantle source with a higher proportion of these enriched pods could result in magmas with more enriched isotopic signatures. Further work is necessary to determine the relative and absolute depths of the KS and HKS source regions.

An alternative to a vertically stratified mantle is different degrees of partial melting of the same source region, whereby the HKS magmas are generated from relatively low degrees of partial melting and the KS magmas by higher degrees. In this model, isotopically-enriched mica- or amphibole-bearing veins melt first due to their low solidus temperature, followed by wall-rock melting (and subsequent isotopic dilution) at higher degrees of partial melting (Foley, 1992b). The relative degrees of source melting for the KS and HKS magmas at Roccamonfina and Ernici are currently unknown, and may help explain the differing isotopic signatures.

9.6 Summary of major geodynamic events that influenced the geochemistry of Italian magmatic rocks in chronological order

- 1) A mantle plume with a FOZO-LVC-EAR depleted isotopic signature invaded the upper mantle in the Eastern Atlantic, Central Europe, and the Western Mediterranean prior to the late Cretaceous.
- 2) Large-scale subduction of Tethyan oceanic lithosphere during the Cretaceous-Miocene Alpine orogeny introduced pelagic sediments with a highly radiogenic isotopic signature into the Mediterranean asthenosphere.
- 3) Mixing between plume-derived, isotopically-depleted mantle and enriched, subducted sediments occurred during the Tertiary along the length of the Italian peninsula.
- 4) At the same time, the late Oligocene-Pleistocene Apennine subduction zone was moving eastwards across the Western Mediterranean and introducing incompatible elements, including K and B, into the upper mantle.

5) Collision of the Apenninic trench with the Adriatic microplate in the mid-Miocene slowed or stopped subduction, and left the Italian upper mantle with high LILE and LILE/HFSE ratios in the absence of active subduction.

In summary, the isotopic compositions of Pliocene-Recent ultrapotassic, potassic, and sodic rocks in Italy reflect older metasomatic events (mixing between a depleted plume head and Tethyan oceanic sediments), while their trace element characteristics reflect younger metasomatic events (Apennine subduction-related metasomatism).

CHAPTER 10

CONCLUSIONS

The main conclusions drawn from the study of lamprophyres from the Western Alps and potassic and ultrapotassic volcanic rocks from Roccamonfina and Ernici are:

10.1 Western Alps

1. Oligocene, hypabyssal, mafic dykes from the Western Alps, northern Italy, are classified as lamprophyres based on their mineralogy, texture, and mode of occurrence. All samples contain essential amphibole and/or mica, and lack olivine, feldspathoids, orthopyroxene, and phenocrysts of quartz and feldspar. The lamprophyres commonly show a panidiomorphic texture in which many of the amphibole, mica, or pyroxene phenocrysts are completely euhedral. Hydrothermal alteration, typical of volatile-rich lamprophyres, is pervasive in some samples.
2. Three types of lamprophyres were identified in this study: minettes, spessartites, and kersantites. The minettes are characterized by euhedral phenocrysts of zoned low Al-Ti diopside and high Al-Ti phlogopite set in a groundmass of albite and Ba-rich orthoclase. The spessartites contain abundant phenocrysts of Ti-rich calcic amphibole variably altered to chlorite, talc, epidote, and muscovite. The kersantite mineralogy is dominated by euhedral zoned Ti- and Ba-rich phlogopite, albite, dolomite, and groundmass quartz.

3. The lamprophyres from the Western Alps are characterized by high Mg#s (>65) and relatively low SiO₂ (< 54 wt%), CaO, Al₂O₃, Fe₂O₃, and TiO₂ contents consistent with melt generation in a previously depleted mantle. The lamprophyres have very high concentrations of LREE (> average continental crust) and strongly fractionated LREE/HREE and LILE/HFSE ratios. High Th/Yb and Th/Zr ratios are comparable to those of arc-related magmatic rocks (Wilson and Bianchini, 1999), and very low Ce/Pb and Nb/U ratios are similar to those of pelagic sediments (Sims and De Paolo, 1997). Trace element geochemistry supports low-degree partial melting of an upper mantle variably metasomatized by subduction-related fluids.

4. The Sr, Nd, and Pb isotopic ratios of the lamprophyres from the Western Alps are extremely heterogeneous and highly radiogenic. ⁸⁷Sr/⁸⁶Sr ratios range from 0.70590 to 0.71884, and ¹⁴³Nd/¹⁴⁴Nd ratios range from 0.51203 to 0.51242. The Pb isotopic ratios of most samples from the Western Alps are very similar, with ²⁰⁶Pb/²⁰⁴Pb ~18.74, ²⁰⁷Pb/²⁰⁴Pb ~15.67, and ²⁰⁸Pb/²⁰⁴Pb ~38.98. Data from the samples from the Western Alps plot above the NHRL and contain higher ratios of ²⁰⁷Pb/²⁰⁴Pb and ²⁰⁸Pb/²⁰⁴Pb than even the most enriched MORB or OIB. The enriched isotopic signature of the lamprophyres from the Western Alps is a geochemical feature of the mantle in northern Italy, and is consistent with metasomatism of the Alpine mantle by the subduction of pelagic sediments during the Alpine orogeny. The lamprophyres from the Western Alps best represent the enriched end-member (ITEM) involved in large scale Italian isotopic mixing (see section 10.3).

5. Sr-Nd isotopic data from the lamprophyres from the Western Alps are similar to those from magmatic rocks of the Tuscan Province, and overlap with data from Hercynian lamprophyres in central Europe and calc-alkaline plutons of the Tertiary Periadriatic Province in the Central and Eastern Alps. However, the Pb isotopic signatures of the Alpine and Tuscan rocks are different from those of the European alkaline rocks. This suggests that the ITEM component, which is "strongest" in northern and central Italy, did not contribute to the metasomatism of the European sub-continental mantle.

10.2 Roccamonfina and Ernici

1. Potassic (KS) volcanic rock types from Roccamonfina include high-K basaltic andesite, potassic trachybasalt, shoshonite, and latite, while ultrapotassic (HKS) rock types include phonotephrite and tephriphonolite. At Ernici, KS rocks include potassic trachybasalt, hawaiite, alkali basalt, and medium-K tholeiitic basalt, while HKS rock types include phonotephrite and tephrite.

2. The KS rocks at Roccamonfina and Ernici are composed of zoned aluminian diopside and calcic plagioclase phenocrysts set in a groundmass of diopside, plagioclase, olivine, mica, apatite, and iron oxides. Groundmass alkali feldspar and orthopyroxene are also present in KS samples from Roccamonfina. The HKS rocks at Roccamonfina and Ernici contain abundant leucite and aluminian diopside phenocrysts, and variable amounts of zoned groundmass olivine, calcic plagioclase, mica, nepheline, apatite, and iron oxides.

3. The main differences in mineral chemistry between the KS and HKS rocks at both Ernici and Roccamonfina are: a) olivine in rocks of the HKS series have higher Fe/Mg, CaO, and MnO contents than those from the KS series, b) diopside in the HKS rocks have higher Al₂O₃ and Fe₂O₃ contents than those in the KS rocks, and c) phlogopite in the HKS rocks have lower TiO₂ contents and higher Mg# than those in the KS rocks.

4. The most important petrogenetic indicators for the KS and HKS rocks, as reflected in their mineral chemistry, are: a) high Mg/Fe ratios (> 4) and F contents (up to 5.27 wt%) in mica from the HKS rocks suggest high temperatures of crystallization and relatively low *a*H₂O, b) high Al₂O₃ contents (up to 13.01 wt%) of diopside from the HKS rocks result from the low *a*SiO₂ of the melt and cannot be used to determine relative source depth, c) zoning from Mg-rich cores to Fe-rich rims in olivine and diopside from both series indicates changing melt chemistry, perhaps through crystal fractionation, d) quenched feldspars in some samples indicate rapid cooling, typical of high-temperature volcanic rocks, and e) the presence of feldspathoids (nepheline + leucite) in rocks of the HKS series again reflects the low *a*SiO₂ of the HKS magmas.

5. Volcanic rocks from Roccamonfina and Ernici are characterized by high CaO and Al₂O₃ coupled with relatively low Fe₂O₃ and TiO₂ contents compared to world-wide potassic rock types. The major element chemistry (except for K₂O) of the KS and HKS rocks is consistent with previous partial melting of the upper mantle source. Rocks from both series are enriched in LREE and LILE, depleted in Ba, P, and HFSE (Nb, Ta, and Ti), and have trace element patterns similar to that of the upper continental crust.

6. Mantle metasomatism at Roccamonfina and Ernici is indicated by the high Th/Yb and Th/Zr ratios and low Ce/Pb and Nb/U ratios of the KS and HKS rocks. Very high B concentrations (up to 76 ppm) strongly suggest subduction of altered oceanic crust and pelagic sediment, and constrain metasomatism of the Italian mantle to the past 5 Ma. The metasomatic agent was able to transport both fluid-mobile LILE (Cs, Rb, Ba, Pb, K) and fluid-immobile HFSE (La, Ce, Th, Nb, Ta, U), suggesting the involvement of a metasomatic melt, rather than a fluid. Continuous K₂O enrichment trends from the KS rocks to those of the HKS series argue against two different metasomatic melts in central-southern Italy, and instead support varying degrees of source enrichment resulting from a single metasomatic event. Major and trace element evidence such as the high CaO, low SiO₂, high Th, La, and Ce, and lack of a negative Sr anomaly in most samples favors a metasomatic component carried by a carbonate-rich melt, rather than a silicic melt.

7. The isotopic signatures of KS and HKS volcanic rocks from Roccamonfina and Ernici are significantly enriched relative to MORB, with ⁸⁷Sr/⁸⁶Sr ratios that range from 0.7065 to 0.7110, and ¹⁴³Nd/¹⁴⁴Nd ratios between 0.51245 and 0.51210. The HKS rocks have higher ⁸⁷Sr/⁸⁶Sr ratios than the KS rocks, while the KS rocks have higher ¹⁴³Nd/¹⁴⁴Nd ratios than the HKS. The Sr and Nd isotopic data from Roccamonfina and Ernici correlate well with ²⁰⁶Pb/²⁰⁴Pb ratios (18.73 – 19.09), but not with ²⁰⁷Pb/²⁰⁴Pb and ²⁰⁸Pb/²⁰⁴Pb ratios. Mixing between the KS and HKS source reservoirs, generally thought to be isolated from one another, is suggested by the intermediate isotopic signatures of two KS samples from Ernici (ER 109 and ER 117). No rocks with ⁸⁷Sr/⁸⁶Sr and ¹⁴³Nd/¹⁴⁴Nd ratios similar to these samples had previously been reported from Ernici.

8. The KS rocks from Roccamonfina and Ernici are isotopically similar to rocks from the Campanian Province, while the HKS rocks are similar to those from the Roman Province. The Southern Latium Transition Zone (Roccamonfina and Ernici) also appears to contain rock types that are isotopically transitional between the Roman and Campanian rocks, suggesting that the KS and the HKS series may be isotopically continuous. The lack of previous isotopic data in this range may simply reflect insufficient sampling at Roccamonfina and Ernici.

9. Volcanic rocks from Roccamonfina and Ernici show different trends of LREE, LILE, and HFSE enrichment with increasing $^{87}\text{Sr}/^{86}\text{Sr}$ isotopic ratios than lamprophyres from the Western Alps. This suggests that the mantle beneath northern Italy may have been metasomatized by a different fluid or melt than the mantle beneath central-southern Italy.

10.3 Geodynamic implications of Italian isotopic mixing

Isotopic data from the Western Alps, Roccamonfina, Ernici, and numerous other Italian volcanic rocks fall on a previously-defined (Vollmer, 1976; D'antonio et al., 1996; Gasperini et al., 2002; Bell et al., 2003), two-component mixing line between a depleted, mantle end-member and an enriched, crust-like end-member (ITEM). The depleted end-member is best represented by magmatic rocks from Mt. Etna, the Iblean Plateau, Pantelleria, and Pietre Nere, while the crust-like signature is strongest in rocks from Tuscany and the Western Alps (see Bell et al., 2004). The smooth mixing curve strongly suggests that the isotopic end-members are homogeneous and geographically widespread.

The depleted end-member is characterized by low $^{87}\text{Sr}/^{86}\text{Sr}$ (< 0.7040) ratios, high $^{143}\text{Nd}/^{144}\text{Nd}$ (> 0.5130) ratios, and $^{206}\text{Pb}/^{204}\text{Pb}$ ratios that are close to those of proposed mantle components FOZO, EAR, and LVC (Ellam et al., 1989; Bell, 2002). The enriched end-member ITEM is characterized by very high $^{87}\text{Sr}/^{86}\text{Sr}$ (> 0.7220) and low $^{143}\text{Nd}/^{144}\text{Nd}$ (< 0.51220) ratios more extreme than those of the enriched mantle reservoirs EMI and EMII, and a very distinct, well-defined $^{206}\text{Pb}/^{204}\text{Pb}$ isotopic ratio of 18.60-18.75.

The origin of the depleted isotopic end-member best fits a geodynamic model involving a "fossil" plume head with a FOZO-LVC-EAR isotopic signature. The age of the plume must be ≥ 65 Ma in order to account for the depleted isotopic signatures of late Cretaceous volcanic rocks in Central Europe and the Western Mediterranean. During the Tertiary, the plume head may have been cut off from its lower mantle source by the accumulation of lithospheric slabs at the base of the upper mantle as a result of Alpine and Apennine subduction events. This resulted in the isolation of a widespread, homogeneous, isotopically depleted layer in the asthenosphere above the subducted slabs.

The enriched isotopic end-member best fits a geodynamic model involving widespread subduction of pelagic sediments and Tethyan oceanic lithosphere during the closure of the Tethyan Ocean. Although ITEM has a similar Pb isotopic composition to both pelagic sediments and the Tuscan continental crust, subduction of Tuscan crust during the Apennine orogeny is too young to explain the enriched signatures of Oligocene magmatic rocks from the Western Alps. There is little evidence that the Apennine orogeny had any effect on the sub-Alpine mantle. Magmatic rocks that have the strongest ITEM signature are located relatively close to the Alpine subduction front, and include Spanish lamproites, the Sisco lamproite in Corsica, Tuscan lamproites, and

the Western Alps lamprophyres. The mantle beneath these areas formed a coherent NE-SE trending region in the late Oligocene, and may have contained a higher proportion of subducted pelagic sediment compared to the mantle beneath southern Italy. Sardinia was located on the European (i.e. fore-arc) side of the Alpine-Betic subduction zone, and therefore Sardinian Plio-Pleistocene magmatic rocks show no influence of subducted sediment and the ITEM isotopic end-member.

Although Alpine subduction is thought to have provided the dominant enriched isotopic signature (ITEM) of Italian magmatic rocks, it cannot be responsible for the B-enrichment of the central-southern Italian mantle as B has a relatively short mantle residence time (< 5 Ma). Therefore, more recent (Apenninic) subduction is likely responsible for the B-enrichment. The positive correlations between B and LILE (including K) also suggest that Apenninic subduction is responsible for the high LILE contents and fractionated LILE/HFSE ratios of Italian potassic and ultrapotassic rocks. Therefore, it must be concluded that Apennine subduction resulted in the trace element (and K_2O) signatures of magmatic rocks from peninsular Italy.

In summary, the isotopic compositions of Pliocene-Recent ultrapotassic, potassic, and sodic rocks in Italy reflect older metasomatic events (mixing between a depleted plume head and Tethyan oceanic sediments), while their trace element (and K_2O) signatures reflect much younger metasomatic events (Apennine, subduction-related metasomatism).

REFERENCES

- Abratis, M. and Wörner, G. (2001) Ridge collision, slab-window formation, and the flux of Pacific asthenosphere into the Caribbean realm. *Geology* **29**, 127-130.
- Altherr, R., Lugovic, B., Meyer, H.-P. and Majer, V. (1995) Early Miocene post-collisional calc-alkaline magmatism along the easternmost segment of the Periadriatic fault system (Slovenia and Croatia). *Mineralogy and Petrology* **54**, 225-247.
- Alvarez, W. and Piali, G. (1989) Driving of thrust belts by sinking of densified (eclogitic) lower continental crust; the Apennine-Tyrrhenian system. *GSA Abstracts with Programs* **21**, 318.
- Amato, A., Alessandrini, B. and Cimini, G.B. (1993) Teleseismic wave tomography of Italy. In: Iyer, H.M. and Hirahara, K. (eds) *Seismic Tomography: Theory and Practice*. Chapman and Hall, New York, pp. 361-396.
- Amato, A. and Chiarabba, C. (1995) Recent uplift of the Alban Hills Volcano (Italy); evidence for magmatic inflation? *Geophysical Research Letters* **22**, 1985-1988.
- Angelucci, A., Brotzu, P., Civitelli, G., Morbidelli, T. and Traversa, G. (1974) Il vulcanismo pleistocenico della Media Valle Latina (Lazio). Caratteristiche petrografiche e geologiche dei principali affioramenti lavici. *Geol. Romana* **13**, 83-123.
- Appleton, J.D. (1972) Petrogenesis of potassium-rich lavas from the Roccamonfina volcano, Roman Region, Italy. *Journal of Petrology* **13**, 425-456.
- Argnani, A. and Savelli, C. (1999) Cenozoic volcanism and tectonics in the southern Tyrrhenian sea: space-time distribution and geodynamic significance. *Journal of Geodynamics* **27**, 409-432.
- Armienti, P., Barberi, F., Bizouard, H., Clocchiatti, R., Innocenti, F., Metrich, N., Rosi, M. and Sbrana, A. (1983) The Phlegraean Fields: magma evolution within a shallow chamber. *Journal of Volcanology and Geothermal Research* **17**, 289-311.
- Armienti, P., D'Orazio, M., Innocenti, F., Tonarini, S. and Villari, L. (1996) October 1995 – February 1996 Mt. Etna explosive activity: Trace element and isotopic constraints on the feeding system. *Acta Vulcanologica* **8**, 1-6.
- Aurischio, C., Federico, M. and Gianfagna, A. (1988) Clinopyroxene chemistry of the high-potassium suite from the Alban Hills, Italy. *Mineralogy and Petrology* **39**, 1-19.

Ayuso, R.A., De Vivo, B., Rolandi, G., Seal, R.S. and Paone, A. (1998) Geochemical and isotopic (Nd-Pb-Sr-O) variations bearing on the genesis of volcanic rocks from Vesuvius, Italy. *Journal of Volcanology and Geothermal Research* **82**, 53-78.

Babuska, V., Plomerova, J. and Granet, M. (1990) The deep lithosphere in the Alps: A model inferred from P residuals. *Tectonophysics* **176**, 137-165.

Bailey, D.K. and Collier, J.D. (2000) Carbonatite-melilitite association in the Italian collision zone and the Ugandan rifted craton: significant common factors. *Mineralogical Magazine* **64**, 675-682.

Baker, B.H., Goles, G.G., Leeman, W.P. and Lindstrom, M.M. (1977) Geochemistry and petrogenesis of a basalt-benmoreite-trachyte suite from the southern part of the Gregory Rift, Kenya. *Contributions to Mineralogy and Petrology* **64**, 303-332.

Baker, P.E., Gass, I.G., Harriss, P.G. and Le Maitre, R.W. (1984) The Volcanological report of the Royal Society Expedition to Tristan da Cunha. *Philosophical Transactions of the Royal Society of London* **A256**, 439-578.

Bally, A.W., Cooper, J.C., Burbi, L. and Ghelardoni, R. (1986) Thrust geometry of the central Apennines, Italy. *Abstracts with Programs, Geological Society of America* **18**, 533.

Barberi, F., Innocenti, F. and Mazzuoli, R. (1967) Contributo alla conoscenza chimica, petrografica e magmatologica delle rocce intrusive, vulcaniche e filoniane del Campigliese (Toscana). *Memorie della Societe Geologica Italiana* **6**, 643-681.

Barberi, F., Innocenti, F. and Ricci, C.A. (1971) Il magmatismo nell'Appennino Centro Settentrionale ('La Toscana Meridionale'). *Special Issue, Rendiconti della Societe Italiana di Mineralogia e Petrologie* **27**, 1-45.

Barberi, F., Santacroce, R. and Varet, J. (1982) Chemical aspects of rift magmatism. In: Palmason, G. (ed.) *Continental and oceanic rifts*. American Geophysical Union, Washington, DC., pp. 223-258.

Barchi, M.R., Minelli, G. and Pialli, G. (1998) The CROP 03 profile; a synthesis of results on deep structures of the Northern Apennines. *Memorie della Società Geologica Italiana* **52**, 383-400.

Barker, D.S. and Nixon, P.H. (1989) High-Ca, low alkali carbonatite volcanism at Fort Portal, Uganda. *Contributions to Mineralogy and Petrology* **103**, 166-177.

Basilone, P. and Civetta, L. (1975) Datazione K/Ar dell'attività vulcanica dei Monti Ernici (Latina). *Rendiconti della Societe Italiana di Mineralogia e Petrologie* **31**, 175-179.

Bayer, R., Cazes, M., Dal Piaz, G.V., Damotte, B., Elter, G., Hirn, A., Lanza, R., Lombardo, B., Mugnier, J.L., Nicolas, A., Nicolich, R., Polino, R., Roure, F., Sacchi, R., Scarascia, S., Tabacco, I., Tapponnier, P., Tardy, M., Taylor, M., Thouvenot, F., Torrelles, G. and Villien, A. (1987) Premiers résultats de la traversée des Alpes occidentales par sismique réflexion verticale (Programme ECORS-CROP). *Comptes-Rendus de l'Académie des Sciences de Paris* **305**, 1461-1470.

Beccaluva, L., Bigioggero, B., Chiesa, S., Colombo, A., Fanti, G., Gatto, G.O., Gregnanin, A., Montrasio, A., Piccirillo, E.M. and Tunesi, A. (1983) Post collisional orogenic dyke magmatism in the Alps. *Memorie della Società Geologica Italiana* **26**, 341-359.

Beccaluva, L., Gabbianelli, G., Lucchini, F., Rossi, P.L. and Savelli, C. (1985) Petrology and K/Ar ages of volcanics dredged from the Eolian seamounts: implications for geodynamic evolution of the southern Tyrrhenian basin. *Earth and Planetary Science Letters* **74**, 187-208.

Beccaluva, L., Macciotta, G., Morbidelli, L., Serri, G. and Traversa, G. (1989) Cainozoic tectono-magmatic evolution and inferred mantle sources in the Sardo-Tyrrhenian area. In: Boriani, A., Bonafede, M., Piccardo, G.B. and Vai, G.B. (eds). *The lithosphere in Italy. Atti Convegni Lincei* **80**, 229-248.

Beccaluva, L., Di Girolamo, P. and Serri, G. (1991) Petrogenesis and tectonic setting of the Roman Volcanic Province, Italy. *Lithos* **26**, 191-221.

Beccaluva, L., Coltorti, M., Galassi, B., Macciotta, G. and Siena, F. (1994) The Cainozoic calc-alkaline magmatism of the Western Mediterranean and its geodynamic significance. *Bollettino di Geofisica Teoretica ed Applicata* **36**, 293-308.

Beccaluva, L., Siena, F., Coltorti, M., Di Grande, A., Lo Giudice, A., Macciotta, G., Tassinari, R. and Vaccaro, C. (1998) Nephelinitic to tholeiitic magma generation in a transtensional tectonic setting: an integrated model for the Iblean volcanism, Sicily. *Journal of Petrology* **39**, 1547-1576.

Beccaluva, L., Coltorti, M., Milani, L., Salvini, L., Siena, F. and Tassinari, R. (2000) Tertiary nephelinitic to tholeiitic magma generation in the Veneto Volcanic Province, Southern Alps. *Goldschmidt Conference Abstracts* **5(2)**, 204.

Beccaluva, L., Coltorti, M., Di Girolamo, P., Melluso, L., Milani, L., Morra, V. and Siena, F. (2002) Petrogenesis and evolution of Mt. Vulture alkaline volcanism (southern Italy) *Mineralogy and Petrology* **74**, 277-297.

Bell, K. (2002) The isotope geochemistry of the mantle below Italy. *Eurocarb Workshop*, abstract volume, pp. 16-18.

- Bell, K., Castorina, F., Rosatelli, G. and Stoppa, F. (2003) Large scale, mantle plume activity below Italy: Isotopic evidence and volcanic consequences. *Geophysical Research Abstracts* **5**, 14217.
- Bell, K., Castorina, F., Lavecchia, G., Rosatelli, G. and Stoppa, F. (2004) Is there a mantle plume below Italy? *EOS* **85-50**, 541-547.
- Bigazzi, G., Bonadonna, F.P., Ghezzi, C., Giuliani, O., Radicati, F., di Brozolo, F. and Rita, F. (1981) Geochronological study of the Monte Amiata lavas (central Italy). *Bulletin Volcanologique* **44**, 455-465.
- Bijwaard, H. and Spakman, W. (2000) Non-linear global P-wave tomography by iterated linearized inversion. *Geophysical Journal International* **141**, 71-82.
- Bindi, L., Cellai, D., Mulluso, L., Conticelli, S., Morra, V. and Menchetti, S. (1999) Crystal chemistry of clinopyroxene from alkaline undersaturated rocks of the Monte Vulture volcano, Italy. *Lithos* **46**, 259-274.
- Boccaletti, M., Elter, P. and Guazzone, G. (1971) Polarità strutturali delle Alpi e dell'Appennino Settentrionale in rapporto all'inversione di una zona di subduzione nord-tirrenica. *Memorie della Società Geologica Italiana* **10**, 371-378.
- Borsi, S., Ferrara, G. and Tongiorgi, E. (1964) Determinazione con il metodo K/Ar delle età delle rocce magmatiche della Toscana. *Bolletino della Società Geologica Italiana* **86**, 403-410.
- Breddam, K. and Kurz, M.D. (2001) Helium isotopic signatures of Icelandic alkaline lavas. AGU Fall Meeting, abstract #V22B-1025.
- Brigatti, M.F., Lugli, C., Poppi, L. and Elburg, M. (1998) Crystal chemistry of biotites from mafic enclaves in the Warburton granodiorite, Lachlan Fold Belt (Australia). *European Journal of Mineralogy* **10**, 855-864.
- Brooks, C.K. and Printzlau, I. (1978) Magma mixing in mafic alkaline volcanic rocks: the evidence from relict phenocryst phases and other inclusions. *Journal of Volcanology and Geothermal Research* **4**, 315-331.
- Brunet, D. and Yuen, D. (2000) Mantle plumes pinched in the transition zone. *Earth and Planetary Science Letters* **178**, 13-27.
- Bruno, P.P., Di Fiore, V. and Ventura, G. (2000) Seismic study of the "41st Parallel" Fault System offshore the Campanian-Latinal continental margin, Italy. *Tectonophysics* **324**, 37-55.
- Burrus, J. (1984) Contribution to a geodynamic synthesis of the Provençal basin (north-western Mediterranean). *Marine Geology* **55**, 247-269.

- Burrus, J. (1989) Review of geodynamic models for extensional basins; the paradox of stretching in the Gulf of Lions (Northwest Mediterranean). *Bulletin of the Geological Society of France* **8**, 377-393.
- Callegari, E. (1983) Geological and petrological aspects of the magmatic activity at Adamello (northern Italy). *Memorie della Società Geologica Italiana* **26**, 83-103.
- Capuano, P., Continisio, R. and Gasparini, P. (1992) Structural setting of a typical alkali-potassic volcano: Roccamonfina, southern Italy. *Journal of Volcanology and Geothermal Research* **53**, 355-369.
- Carmignani, L., Decandia, F.A., Disperati, L., Fantozzi, P.L., Lazzarotto, A., Liotta, D. and Oggiano, G. (1995) Relationships between the Tertiary structural evolution of the Sardinia-Corsica-Provençal Domain and the Northern Apennines. *Terra Nova* **7**, 128-137.
- Carraro, F., Dal Piaz, G.V. and Sacchi, R. (1970) Serie di Valpelline e Il Zona Diorito-Kizigitica sono i relitti di un recoprimento proveniente dalla zona Ivrea-Verbano. *Memorie della Società Geologica Italiana* **9**, 197-224.
- Carta Geologica D'Italia, Folgio 1 (1983) In: Ogniben, L. (ed.) *Structural Model of Italy, 1:1,000,000 scale*. Centro Nazionale di Researche.
- Carter, S.R. and Civetta, L. (1977) Genetic implications of the isotope and trace element variations in the Eastern Sicilian Volcanics. *Earth and Planetary Science Letters* **36**, 168-180.
- Carter, S.R., Evensen, N.M., Hamilton, P.J. and O'Nions, R.K. (1978) Continental volcanics derived from enriched and depleted source regions: Nd and Sr isotope evidence. *Earth and Planetary Science Letters* **37**, 401-408.
- Cassignol, C. and Gillot, P.Y. (1982) Range and effectiveness of unspiked potassium argon dating: experimental ground work and application. In: Odin, G.S. (ed) *Numerical dating in stratigraphy*, pp. 160.
- Castorina, F., Stoppa, F., Cundari, A. and Barbieri, M. (2000) An enriched mantle source for Italy's melilitite-carbonatite association as inferred by its Nd-Sr isotope signature. *Mineralogical Magazine* **64**, 625-639.
- Catalano, R., Dogioni, C. and Merlini, S. (2001) On the Mesozoic Ionian Basin. *Geophysical Journal International* **144**, 49-64.
- Cavinato, G.P. and De Celles, P.G. (1999) Extensional basins in the tectonically bimodal central Apennines for-thrust belt, Italy: Response to corner flow above a subducting slab in retrograde motion. *Geology* **27**, 955-958.

- Cebriá, J.M. and Wilson, M. (1995) Cenozoic mafic magmatism in Western/Central Europe: a common European asthenospheric reservoir, *Terra Nova Abstract Supplement* **7**, 162.
- Cellai, D., Conticelli, S. and Menchetti, S. (1994) Crystal-chemistry of clinopyroxenes in Italian lamproites and kamafugite: implication on their genesis. *Contributions to Mineralogy and Petrology* **116**, 301-315.
- Cello, G. and Mazzoli, S. (1999) Apennine tectonics in southern Italy; a review. *Journal of Geodynamics* **27**, 191-211.
- Chaffey, D.J., Cliff, R.A. and Wilson, B.M. (1989) Characteristics of the St. Helena magma source. In: Saunders, A.D. and Norry, M.J. (eds) *Magmatism in the Ocean Basins. Geological Society of London Special Publication* **42**, 257-276.
- Chopin, C. (1984) Coesite and pure pyrope in high-grade blueschists of the western Alps: A first record and some consequences. *Contributions to Mineralogy and Petrology* **86**, 107-118.
- Chopin, C. (1987) Very high pressure metamorphism in the Western Alps: Implications for subduction of continental crust. *Philosophical Transactions of the Royal Society of London* **A321**, 183-197.
- Cimini, G.B. and De Gori, P. (2001) Nonlinear P-wave tomography of subducted lithosphere beneath central-southern Apennines (Italy). *Geophysical Research Letters* **28**, 4387-4390.
- Civetta, L., Innocenti, F., Lirer, L., Manetti, P., Munno, R., Peccerillo, A., Poli, G. and Serri, G. (1979) Serie potassica ed alta in potassio dei Monti Ernici (Lazio Meridionale): Considerazioni petrologiche e geochemiche. *Rendiconti della Società Italiana di Mineralogia e Petrologia* **35**, 227-249.
- Civetta, L., Innocenti, F., Manetti, P., Peccerillo, A. and Poli, G. (1981) Geochemical characteristics of potassic volcanics from Mts. Ernici (Southern Latium, Italy). *Contributions to Mineralogy and Petrology* **78**, 37-47.
- Civetta, L., Galati, R. and Santacroce, R. (1991a) Magma mixing and convective compositional layering within the Vesuvius magma chamber. *Bulletin of Volcanology* **53**, 287-300.
- Civetta, L., Gallo, G. and Orsi, G. (1991b) Sr- and Nd-isotope and trace-element constraints on the chemical evolution of the magmatic system of Ischia (Italy) in the last 55 ka. *Journal of Volcanology and Geothermal Research* **46**, 213-230.

- Civetta, L., Carluccio, E., Innocenti, F., Sbrana, A. and Taddeucci, G. (1991c) Magma chamber evolution under the Phlegraean Fields during the last 10 ka: trace element and isotope data. *European Journal of Mineralogy* **3**, 415-428.
- Civetta, L., D'Antonio, M., Orsi, G. and Tilton, G.R. (1998) The geochemistry of volcanic rocks from Pantelleria Island, Sicily Channel: petrogenesis and characteristics of the mantle source region. *Journal of Petrology* **39**, 1453-1491.
- Comas, M.C., Garcia Duenas, V. and Jurado, M.J. (1992) The Alboran Basin; Neogene structure and evolution. *Actas del Congreso Latinoamericano de Geologia* **8**, 496-505.
- Condomines, M., Tanguy, J.C., Kieffer, G. and Allègre, C.J. (1982) Magmatic evolution of a volcano studied by ^{230}Th - ^{238}U disequilibrium and trace elements systematics: the Etna case. *Geochimica et Cosmochimica Acta* **46**, 1397-1416.
- Comin-Chiaramonti, P., Cundari, A., Gomes, G.B., Piccirillo, E.M., Censi, P., De Min, A., Bellieni, G., Velasquez, V.F. and Orue, D. (1992) Potassic dyke swarm in the Sapucaí graben, eastern Paraguay: Petrographical, mineralogical and geochemical outlines. *Lithos* **28**, 283-301.
- Compagnoni, R. (1977) The Sesia-Lanzo Zone: High-pressure – low-temperature metamorphism in the Austroalpine continental margin. *Rendiconti della Società Italiana di Mineralogia e Petrologia* **33**, 335-374.
- Compagnoni, B. and Galluzzo, F. (2004) *Geological Map of Italy. 1:1 250 000 Scale*. Dipartimento Difesa del Suolo, Servizio Geologico d'Italia.
- Conceição, R.V. and Green, D.H. (2000) Behavior of the cotectic curve En-Ol in the system leucite-olivine-quartz under dry conditions to 2.0 GPa. *Geochemistry, Geophysics, Geosystems* **1**, 2000GC000071.
- Console, R., Di Giovambattista, R., Favali, P., Presgrave, B.W. and Smriglio, G. (1993) Seismicity of the Adriatic Microplate. *Tectonophysics* **218**, 343-354.
- Conticelli, S. (1989) Genesi del magmatismo alcalino-potassico dell'Italia centrale: evidenze petrologiche, geochimiche e petrologico Sperimentali. *Ph.D. thesis*, University of Florence, Italy, pp. 404.
- Conticelli, S. (1998) The effect of crustal contamination on ultrapotassic magmas with lamproitic affinity: mineralogical, petrological and isotope data from the Torre Alfina lavas and xenoliths, Central Italy. *Chemical Geology* **149**, 51-81.
- Conticelli, S. and Peccerillo, A. (1990) Petrological significance of high pressure ultramafic xenoliths from ultrapotassic rocks of Central Italy. *Lithos* **24**, 305-322.

Conticelli, S. and Peccerillo, A. (1992) Petrology of potassic and ultrapotassic volcanism in central Italy: petrogenesis and inference on the evolution of the mantle sources. *Lithos* **28**, 221-240.

Conticelli, S., Manetti, P. and Menichetti, S. (1992) Mineralogy, geochemistry and Sr-isotopes in orendites from South Tuscany, Italy; constraints on their genesis and evolution. *European Journal of Mineralogy* **4**, 1359-1375.

Conticelli, S., D'Antonio, M., Pinarelli, L. and Civetta, L. (2002) Source contamination and mantle heterogeneity in the genesis of Italian potassic and ultrapotassic rocks: Sr-Nd-Pb isotope data from Roman Province and Southern Tuscany. *Mineralogy and Petrology* **74**, 189-222.

Conticelli, S., Melluso, L., Perini, G., Avanzinelli, R. and Boari, E. (2004) Petrologic, geochemical and isotopic characteristics of potassic and ultrapotassic magmatism in central-southern Italy: inference on its genesis and on the nature of mantle sources. *Periodico di Mineralogia* **73**, 135-164.

Cortecchi, G., Del Moro, A., Leone, G. and Pardini, G.C. (1979) Correlation between strontium and oxygen isotopic compositions of rocks from the Adamello Massif (Northern Italy). *Contributions to Mineralogy and Petrology* **68**, 421-427.

Coward, M. and Dietrich, D. (1989) Alpine tectonics – an overview. In: Coward, M.P., Dietrich, D. and Park, R.G. (eds) *Alpine Tectonics. Geological Society of London Special Publication* **45**, 1-29.

Cox, K.G., Hawkesworth, C.J., O'Nions, R.K. and Appleton, J.D. (1976) Isotopic evidence for the derivation of some Roman Region volcanics from anomalously enriched mantle. *Contributions to Mineralogy and Petrology* **56**, 173-180.

Cundari, A. (1979) Petrogenesis of the leucite-bearing lavas in the Roman volcanic region, Italy. The Sabatini Lavas. *Contributions to Mineralogy and Petrology* **70**, 9-21.

Cundari, A. (1980) Role of subduction in the genesis of leucite-bearing rocks: fact or fashion? *Contributions to Mineralogy and Petrology* **73**, 432-434.

Cundari, A. (1994) Role of subduction in the genesis of potassic basaltic rocks: A discussion paper on the unfashionable side of the role. *Mineralogica et Petrographica Acta* **37**, 81-90.

Dal Piaz, G.V., Hunziker, J.C. and Martinotti, G. (1972) La zona Sesia-Lanzo e l'evoluzione tettonico-metamorfica delle Alpi nordocci-dentali interne. *Memoire della Società Geologica Italiana* **11**, 433-466.

Dal Piaz, G.V. and Venturelli, G. (1983) Brevi riflessioni sul magmatismo post-ofiolitico nel quadro dell'evoluzione spazio-temporale delle alpi. *Memoire della Società Geologica Italiana* **26**, 5-19.

D'Antonio, M., Tilton, G.R. and Civetta, L. (1996) Petrogenesis of Italian alkaline lavas deduced from Pb-Sr-Nd isotope relationships. In: *Earth Processes: Reading the Isotopic Code. Geophysical Monograph* **95**, 253-267.

D'Antonio, M., Civetta, L. and Di Girolamo, P. (1999) Mantle source heterogeneity in the Campanian Region (South Italy) as inferred from geochemical and isotopic features of mafic volcanic rocks with shoshonitic affinity. *Mineralogy and Petrology* **67**, 163-192.

Davies, G.R. and Lloyd, F.E. (1988) Pb-Sr-Nd isotope and trace element data bearing on the origin of the potassic subcontinental lithosphere beneath south west Uganda. In: *Proceedings of the 4th International Kimberlite Conference*. Perth, Western Australia. Blackwell Scientific, Oxford.

Deans, T. and Roberts, B. (1984) Carbonatite tuffs and lava clasts of the Tinderet foothills, western Kenya: a study of calcified natrocarbonatites. *Journal of the Geological Society of London* **141**, 563-580.

De Astis, G., La Volpe, L., Peccerillo, A. and Civetta, L. (1997) Volcanological and petrological evolution of Vulcano Island (Aeolian Arc, southern Tyrrhenian Sea). *Journal of Geophysical Research* **102**(B4), 8021-8050.

De Astis, G., Peccerillo, A., Kempton, P.D., La Volpe, L. and Wu, T.W. (2000) Transition from calc-alkaline to potassium-rich magmatism in subduction environments: geochemical and Sr, Nd, Pb isotopic constraints from the island of Vulcano (Aeolian arc). *Contributions to Mineralogy and Petrology* **139**, 684-703.

Decandia, A.F., Lazzarotto, A., Liotta, D., Cernobori, L. and Nicolich, R. (1998) The CROP 03 traverse; insights on post-collisional evolution of Northern Apennines. *Memorie della Società Geologica Italiana* **52**, 427-439.

Deer, W.A., Howie, R.A. and Zussman, J. (1992) *An introduction to the rock-forming minerals*. Pearson Education Limited, England, pp. 696.

Deer, W.A., Howie, R.A. and Zussman, J. (1997) *Rock-Forming Minerals. Volume 2B. Double-Chain Silicates*. Geological Society of London, pp. 764.

Deer, W.A., Howie, R.A. and Zussman, J. (2001) *Rock-Forming Minerals. Volume 4A. Framework Silicates: Feldspars*. Geological Society of London, pp. 984.

Deer, W.A., Howie, R.A. and Zussman, J. (2004) *Rock-Forming Minerals. Volume 4B. Framework Silicates, Silica Minerals, Feldspathoids and Zeolites*. Geological Society of London, pp. 958.

De Fino, M., La Volpe, L., Peccerillo, A., Piccarreta, G. and Poli, G. (1986) Petrogenesis of Monte Vulture volcano (Italy): inferences from mineral chemistry, major and trace element data. *Contributions to Mineralogy and Petrology* **92**, 135-145.

Del Moro, A., Gioncada, A., Pinarelli, L., Sbrana, A. and Joron, J.-L. (1998) Sr, Nd, and Pb isotope evidence for open system evolution at Vulcano, Aeolian Arc, Italy. *Lithos* **43**, 81-106.

DePaolo, D.J. and Wasserburg, G.J. (1976) Nd isotopic variations and petrogenetic models. *Geophysical Research Letters* **3**, 249-252.

De Rosa, R., Mazzuoli, R. and Ventura, G. (1996) Relationships between deformation and mixing processes in lava flows: a case study from Salina (Aeolian Islands, Tyrrhenian Sea). *Bulletin of Volcanology* **58**, 286-297.

De Vecchi, G. and Sedeà, R. (1995) The Paleogene basalts of the Veneto Region (NE Italy). *Memorie della Società Geologica Italiana* **47**, 253-274.

Dercourt, J., Zonenshain, L.P., Ricou, L.E., Kazmin, V.G., Le Pichon, X., Knipper, A.L., Grandjacquet, C., Sbertshikov, I.M., Geysant, J., Lepvrier, C., Perchersky, D.H., Boulin, J., Sibuet, J.C., Savostin, L.A., Sorokhtin, O., Westphal, M., Bazhenov, M.L., Laur, J.P. and Biju-Duval, B. (1986) Geological evolution of the Alpine Tethys belt from the Atlantic to the Pamir since Lias. *Tectonophysics* **123**, 241-315.

Devoti, R., Ferraro, C., Gueguen, E., Lanotte, R., Luceri, V., Nardi, A., Pacione, R., Rutigliano, P., Sciarretta, C. and Vespe, F. (2002) Geodetic control on recent tectonic movements in the central Mediterranean area. *Tectonophysics* **346**, 151-167.

Dewey, J.F., Helman, M.L., Turco, E., Hutton, D.H.W. and Knott, S.D. (1989) Kinematics of the western Mediterranean. In: Coward, M.P., Dietrich, D. and Park, R.G. (eds) *Alpine Tectonics. Geological Society of London Special Publication* **45**, 1-29.

Di Battistini, G., Montanini, A., Vernia, L., Venturelli, G. and Tonarini, S. (2001) Petrology of melilite-bearing rocks from the Montefiascone Volcanic Complex (Roman Magmatic Province): new insights into the ultrapotassic volcanism of central Italy. *Lithos* **59**, 1-24.

Di Brozolo, F.R., Di Girolamo, P., Turi, B. and Oddone, M. (1988) ^{40}Ar - ^{39}Ar and K-Ar dating of K-rich rocks from the Roccomonfina Volcano, Roman Co-magmatic Region, Italy. *Geochimica et Cosmochimica Acta* **52**, 1435-1441.

Di Girolamo, P. (1978) Geotectonic settings of Miocene-Quaternary volcanism in and around the Eastern Tyrrhenian Sea Border (Italy) as deduced from major element geochemistry. *Bulletin Volcanologique* **41**, 229-250.

- Di Girolamo, P., Morra, V. and Perrone, V. (1992) Ophiolitic olistoliths in middle Miocene turbidites (Cilento Group) at Mt. Centaurino (Southern Apennines, Italy). *Ophioliti* **17**, 199-217.
- Dimroth, E. (1970) Meimechites and carbonatites of the Castignon Lake complex, New Quebec. *N. Jahrb Min Abh* **112**, 239-278.
- Dogliani, C. (1991) A proposal for the kinematic modeling of W-dipping subductions – possible applications to the Tyrrhenian-Apennines system. *Terra Nova* **3**, 423-434.
- Dogliani, C., Mongelli, F. and Pieri, P. (1994) The Puglia uplift (SE Italy): an anomaly in the foreland of the Apenninic subduction due to buckling of a thick continental lithosphere. *Tectonics* **13**, 1309-1321.
- Dogliani, C., Gueguen, E., Sabat, F. and Fernandez, M. (1997) The Western Mediterranean extensional basins and the Alpine orogen. *Terra Nova* **9**, 109-112.
- Dogliani, C., Harabaglia, P., Merlini, S., Mongelli, F., Peccerillo, A. and Piromallo, C. (1999) Orogens and slabs vs. their direction of subduction. *Earth Science Reviews* **45**, 167-208.
- Dolfi, D. and Triglia, R. (1978) Clinopyroxenes from potassic lavas of Central Italy Quaternary volcanism. *Progress in Exploration and Petrology* **D11**, 18-22.
- Dolfi, D. and Triglia, R. (1983) Clinopyroxene solid solutions and water in magmas: results in the system phonolitic tephrite-H₂O. *Mineralogical Magazine* **47**, 347-351.
- Donnelly, T.W., Thompson, G. and Salisbury, M.H. (1980) The chemistry of altered basalts at site 417, Deep Sea Drilling Project Leg 51. *Initial Reports DSDP* **51-53**, 1319-1330.
- Downes, H., Thirlwall, M.F. and Trayhorn, S.C. (2001) Miocene subduction-related magmatism in southern Sardinia: Sr-Nd- and oxygen isotopic evidence for mantle source enrichment. *Journal of Volcanology and Geothermal Research* **106**, 1-21.
- Downes, H., Kostoula, T., Jones, A.P., Beard, A.D., Thirlwall, M.F. and Bodinier, J.-L. (2002) Geochemistry and Sr-Nd isotopic compositions of mantle xenoliths from the Monte Vulture carbonatite-melilitites volcano, central southern Italy. *Contributions to Mineralogy and Petrology* **144**, 78-92.
- Dupré, B. and Allègre, C.J. (1983) Pb-Sr isotopic variations in Indian Ocean basalts and mixing phenomena. *Nature* **303**, 142-146.
- Dupuy, C. (1970) Contribution a l'etude des fractionnements Geochimiques des Alcalins, des Alcalino-Terreux et du Gallium au cours des processus magmatiques. *D.Sc. thesis*. Univ. Montpellier.

- Dupuy, C. and Allègre, C.J. (1972) Fractionment K/Rb dans les suits ignimbriques de Toscane. Un exemple de rejuvenation crustale. *Geochimica et Cosmochimica Acta* **36**, 437-458.
- Edgar, A.D. (1980) Role of subduction in the genesis of leucite-bearing rocks; discussion. *Contributions to Mineralogy and Petrology* **73**, 429-431.
- Edwards, C.M.H., Morris, J.D. and Thirlwall, M.F. (1993) Separating mantle from slab signatures in arc lavas using B/Be and radiogenic isotope systematics. *Nature* **362**, 530-533.
- Ellam, R.M., Menzies, M.A., Hawkesworth, C.J., Leeman, W.P., Rosi, M. and Serri, G. (1988) The transition from calc-alkaline to potassic orogenic magmatism in the Aeolian Islands, Southern Italy. *Bulletin of Volcanology* **50**, 386-398.
- Ellam, R.M., Hawkesworth, C.J., Menzies, M.A. and Rogers, N.W. (1989) The volcanism of southern Italy: role of subduction and the relationship between potassic and sodic alkaline magmatism. *Journal of Geophysical Research* **94**(B4), 4589-4601.
- Esperança, S., Crisci, G.M., De Rosa, R. and Mazzuoli, R. (1992) The role of the crust in the magmatic evolution of the island of Lipari (Aeolian Islands, Italy). *Contributions to Mineralogy and Petrology* **112**, 450-462.
- Esperança, S. and Crisci, G.M. (1995) The island of Pantelleria: A case for the development of DMM-HIMU isotopic compositions in a long-lived extensional setting. *Earth and Planetary Science Letters* **136**, 167-182.
- Faccenna, C., Davy, P., Brun, J.P., Funicello, R., Giardini, D., Mattei, M. and Nalpas, T. (1996) The dynamics of back-arc extension: an experimental approach to the opening of the Tyrrhenian Sea. *Geophysical Journal International* **126**, 781-795.
- Faccenna, C., Mattei, M., Funicello, R. and Jolivet, L. (1997) Styles of back-arc extension in the Central Mediterranean. *Terra Nova* **9**, 126-130.
- Faccenna, C., Becker, T.W., Lucente, F.P., Jolivet, L. and Rossetti, F. (2001) History of subduction and back-arc extension in the Central Mediterranean. *Geophysical Journal International* **145**, 809-820.
- Farley, K.A., Natland, J.H. and Craig, H. (1992) Binary mixing of enriched and undegassed (primitive?) mantle components (He, Sr, Nd and Pb) in Samoan lavas. *Earth and Planetary Science Letters* **111**, 183-99
- Faure, G. (1986) *Principles of Isotope Geology*. John Wiley & Sons, New York, pp. 589.
- Faure, G. and Mensing, T.M. (2005) *Isotopes*. John Wiley & Sons, New Jersey, pp. 897.

- Federico, M. and Peccerillo, A. (2002) Mineral chemistry and petrogenesis of granular ejecta from the Alban Hills volcano (Central Italy). *Mineralogy and Petrology* **74**, 223-252.
- Federico, M., Peccerillo, A., Barbieri, M. and Wu, T.W. (1994) Mineralogical and geochemical study of granular xenoliths from the Alban Hills Volcano, central Italy; bearing on evolutionary processes in potassic magma chambers. *Contributions to Mineralogy and Petrology* **115**, 384-401.
- Finetti, I. and Morelli, C. (1973) Geophysical exploration of the Mediterranean Sea. *Bollettino di Geofisica Teoretica ed Applicata* **15**, 263-341.
- Foley, S.F. (1992a) Petrological characterization of the source components of potassic magmas: geochemical and experimental constraints. *Lithos* **28**, 187-204.
- Foley, S.F. (1992b) Vein-plus-wall-rock melting mechanisms in the lithosphere and the origin of potassic alkaline magmas. *Lithos* **28**, 435-453.
- Foley, S.F., Venturelli, G., Green, D.H. and Toscani, L. (1987) The ultrapotassic rocks: characteristics, classification, and constraints for petrogenetic models. *Earth-Science Reviews* **24**, 81-134.
- Foley, S.F. and Wheller, G.E. (1990) Parallels in the origin of the geochemical signatures of island arc volcanics and continental potassic igneous rocks: The role of residual titanites. *Chemical Geology* **85**, 1-18.
- Foucher, J.P., Mauffret, A., Steckler, M.S., Brunet, M.F., Maillard, A., Rehault, J.P., Alonso, B., Desegaulx, P., Murillas, J. and Ouillon, G. (1992) Heat flow in the Valencia Trough; geodynamic implications. *Tectonophysics* **203**, 77-97.
- Foulger, G.R., Pritchard, M.J., Julian, B.R., Evans, J.R., Allen, R.M., Nolet, G., Morgan, W.J., Bergsson, B.H., Erlendsson, P., Jakobsdottir, S., Ragnarsson, S., Stefansson, R. and Vogfjord, K. (2000) The seismic anomaly beneath Iceland extends down to the mantle transition zone and no deeper. *Geophysical Journal International* **142**, F2-F5.
- Francalanci, L., Manetti, P. and Peccerillo, A. (1989) Volcanological and magmatological evolution of Stromboli volcano (Aeolian Islands): the roles of fractional crystallization, magma mixing, crustal contamination and source heterogeneity. *Bulletin of Volcanology* **51**, 355-378.
- Francalanci, L., Taylor, S.R., McCulloch, M.T. and Woodhead, J.D. (1993) Geochemical and isotopic variations in the calc-alkaline rocks of Aeolian Arc, Southern Tyrrhenian Sea, Italy: Constraints on magma genesis. *Contributions to Mineralogy and Petrology* **113**, 300-313.

- Francalanci, L. and Manetti, P. (1994) Geodynamic models of the Southern Tyrrhenian region: constraints from the petrology and geochemistry of the Aeolian volcanic rocks. *Bollettino di Geofisica Teoretica ed Applicata* **36**, 283-292.
- Gaeta, M., Fabrizio, G. and Cavarretta, G. (2000) F-phlogopites in the Alban Hills Volcanic District (Central Italy): indications regarding the role of volatiles in magmatic crystallization. *Journal of Volcanology and Geothermal Research* **99**, 179-193.
- Gasparini, P. (1963) Radioactivity of the lavas of the island of Ischia. *Annales Ossica del Vesuviano* **5**, 33-50.
- Gasperini, C., Iannaccone, G., Scandone, P. and Scarpa, R. (1982) Seismotectonics of the Calabrian Arc. *Tectonophysics* **82**, 267-286.
- Gasperini, D., Blichert-Toft, J., Bosch, D., Del Moro, A., Macera, P., Telouk, P. and Albarede, F. (2000) Evidence from Sardinian basalt geochemistry for recycling of plume heads into the Earth's mantle. *Nature* **408**, 701-704.
- Gasperini, D., Blichert-Toft, J., Bosch, D., Del Moro, A., Macera, P. and Albarede, F. (2002) Upwelling of deep mantle material through a plate window: Evidence from the geochemistry of Italian basaltic volcanics. *Journal of Geophysical Research* **107**(B12), 2367.
- Gertisser, R. and Keller, J. (2000) From basalt to dacite: origin and evolution of the calc-alkaline series of Salina, Aeolian Arc, Italy. *Contributions to Mineralogy and Petrology* **139**, 607-626.
- Gertisser, R. and Keller, J. (2003) Trace element and Sr, Nd, Pb and O isotope variations in medium-K and high-K volcanic rocks from Merapi volcano, central Java, Indonesia: evidence for the involvement of subducted sediments in Sunda Arc magma genesis. *Journal of Petrology* **44**, 457-489.
- Ghiara, M.R. and Lirer, L. (1977) Mineralogy and geochemistry of the 'low potassium' series of the Roccamonfina Volcanic Suite (Campania, South Italy). *Bulletin Volcanologique* **40**, 39-56.
- Ghiorso, M.S. and Sack, R.O. (1995) Chemical mass transfer in magmatic processes. IV. A revised and internally consistent thermodynamic model for the interpolation and extrapolation of liquid-solid equilibria in magmatic systems at elevated temperatures and pressures. *Contributions to Mineralogy and Petrology* **119**, 197-212.
- Giannetti, B. (1979) The geology of the Roccamonfina caldera (Campanian Province, Italy). *G. Geol.* **43**, 187-206.
- Giannetti, B. (1982) Cumulate inclusions from K-rich magmas, Roccamonfina volcano, Italy. *Earth and Planetary Science Letters* **57**, 313-335.

- Giannetti, B. (2001) Origin of the calderas and evolution of Roccamonfina volcano (Roman Region, Italy). *Journal of Volcanology and Geothermal Research* **106**, 301-319.
- Giannetti, B. and Luhr, J.F. (1990) Phlogopite-clinopyroxenite nodules from high-K magmas, Roccamonfina Volcano, Italy: evidence for a low-pressure metasomatic origin. *Earth and Planetary Science Letters* **101**, 404-424.
- Giannetti, B. and Ellam, R. (1994) The primitive lavas of Roccamonfina volcano, Roman region, Italy: new constraints on melting processes and source mineralogy. *Contributions to Mineralogy and Petrology* **116**, 21-31.
- Goes, S., Spakman, W. and Bijwaard, H. (1999) A lower mantle source for Central European volcanism. *Science* **286**, 1928-1931.
- Goes, S., Govers, R. and Vacher, P. (2000) Shallow mantle temperatures under Europe from P and S wave tomography. *Journal of Geophysical Research* **105**(B5), 11153-11169.
- Goffé, B. and Chopin, C. (1986) High-pressure metamorphism in the Western Alps: Zoneography of metapelites, chronology and consequences. *Schweiz. Mineral. Petrogr. Mitt.* **66**, 41-52.
- Graham, I.J., Dichtburn, R.G. and Whitehear, M.E. (1998) ^{10}Be spikes in Plio-Pleistocene cyclothem, Wanganui Basin, New Zealand: identification of the local flooding surface (LFS). *Sedimentary Geology* **122**, 193-215.
- Granet, M., Wilson, M. and Achauer, U. (1995) Imaging a mantle plume beneath the French Massif Central. *Earth and Planetary Science Letters* **136**, 281-296
- Green, T.H. (1973) Experimental melting studies on a model upper mantle composition at high pressure under water-saturated and water under-saturated conditions. *Earth and Planetary Science Letters* **19**, 37-53.
- Green, T.H. (1995) Significance of Nb/Ta as an indicator of geochemical processes in the crust-mantle system. *Chemical Geology* **120**, 347-359.
- Green, T.H. and Pearson, N.J. (1986) Ti-rich accessory phase saturation in hydrous mafic-felsic compositions at high P,T. *Chemical Geology* **54**, 185-201.
- Green, T.H. and Pearson, N.J. (1987) An experimental study of Nb and Ta partitioning between Ti-rich minerals and silicate liquids at high pressure and temperature. *Geochimica et Cosmochimica Acta* **51**, 55-62.
- Griffiths, R.W. and Campbell, I.H. (1991) Interaction of mantle plume heads with the Earth's surface and onset of small-scale convection. *Journal of Geophysical Research* **96**, 18295-18310.

- Gualteri, L. and Zappone, A. (1998) Hypothesis of ensialic subduction in the northern Apennines: a petrophysical contribution. *Memorie della Società Geologica Italiana* **52**, 205-214.
- Gueguen, E., Doglioni, C. and Fernandez, M. (1997) Lithospheric boudinage in the Western Mediterranean back-arc basin. *Terra Nova* **9**, 184-187.
- Gümbel, C.W. (1874) *Die Paleolithischen Eruptivgesteine des Fichtelgebirges*. Franz, Munich, Germany.
- Gvirtzman, Z. and Nur, A. (1999) The formation of Mount Etna as the consequence of slab rollback. *Nature* **401**, 782-785.
- Gvirtzman, A. and Nur, A. (2001) Residual topography, lithospheric structure and sunken slabs in the central Mediterranean. *Earth and Planetary Science Letters* **187**, 117-130.
- Hamilton, W.B. (1988) Plate tectonics and island arcs. *Geological Society of America Bulletin* **100**, 1503-1527.
- Hanan, B.B. and Graham, D.W. (1996) Lead and helium isotope evidence from oceanic basalts for a common deep source of mantle plumes. *Science* **272**, 991-995.
- Harder, H. (1970) Boron content of sediments as a tool in facies analysis. *Sedimentary Geology* **4**, 153-175.
- Hart, S.R. (1984) The DUPAL anomaly: a large-scale isotopic anomaly in the southern hemisphere. *Nature* **309**, 753-756.
- Hart, S.R., Hauri, E.H., Oschmann, L.A. and Whitehead, J.A. (1992) Mantle plumes and entrainment: isotopic evidence. *Science* **256**, 517-520.
- Haskin, L.A., Haskin, M.A., Frey, F.A. and Wildman, T.R. (1968) Relative and absolute terrestrial abundances of the rare earths. In: Arhens, L.H. (ed.) *Origin and distribution of the elements, vol 1*. Pergamon, Oxford., pp. 889-911.
- Hauri, E.H., Whitehead, J.A. and Hart, S.R. (1994) Fluid dynamic and geochemical aspects of entrainment in mantle plumes. *Journal of Geophysical Research* **99**, 24275-24300.
- Hawkesworth, C.J. and Vollmer, R. (1979) Crustal contamination versus enriched mantle: $^{143}\text{Nd}/^{144}\text{Nd}$ and $^{87}\text{Sr}/^{86}\text{Sr}$ evidence from the Italian volcanics. *Contributions to Mineralogy and Petrology* **69**, 151-165.
- Hippolyte, J.-C., Angelier, J. and Roure, F. (1994) A major geodynamic change revealed by Quaternary stress patterns in the Southern Apennines (Italy). *Tectonophysics* **230**, 199-210.

- Hoernle, K., Zhang, Y-S. and Graham, D. (1995) Seismic and geochemical evidence for large-scale mantle upwelling beneath the eastern Atlantic and western and central Europe. *Nature* **374**, 34-39.
- Hofmann, A.W., Jochum, K.P., Seufert, M. and White, W.M. (1986) Nb and Pb in oceanic basalts: new constraints on mantle evolution. *Earth and Planetary Science Letters* **79**, 33-45.
- Holik, J.S., Rabinowitz, P.D. and Austin, J.A., Jr. (1991) Effects of Canary hotspot volcanism on structure of oceanic crust off Morocco. *Journal of Geophysical Research* **96**(B7), 12039-12067.
- Holm, P.M. and Munksgaard, N.C. (1982) Evidence for mantle metasomatism: an oxygen and strontium isotope study of the Vulsinian District, Central Italy. *Earth and Planetary Science Letters* **60**, 376-388.
- Holm, P.M., Lou, S. and Nielson, A. (1982) The geochemistry and petrogenesis of the Vulsinian district, Roman Province, Central Italy. *Contributions to Mineralogy and Petrology* **80**, 367-378.
- Hunziker, J.C. (1971) Rb-Sr and K-Ar Age determinations and the Alpine Tectonic History of the Western Alps. *Annales de la Societe Geologique de Belgique* **94**, 116-117.
- Hunziker, J.C. and Martinotti, G. (1984) Geochronology and evolution of the Western Alps. *Memorie della Società Geologica Italiana* **29**, 43-56.
- Hunziker, J.C., Desmons, J. and Martinotti, G. (1989) Alpine thermal evolution in the Central and Western Alps. In: Coward, M.P., Dietrich, D. and Park, R.G. (eds) *Alpine Tectonics. Geological Society of London Special Publication* **45**, 353-367.
- Hurford, A.J., Hunziker, J.C. and Stockhert, B. (1991) Constraints on the late thermotectonic evolution of the Western Alps: evidence for episodic rapid uplift. *Tectonics* **10**, 758-769.
- Hurley, P.M., Fairbairn, H.W. and Pinson, W.H. (1966) Rb-Sr isotopic evidence in the origin of potash-rich lavas of western Italy. *Earth and Planetary Science Letters* **1**, 301-306.
- Innocenti, F., Serri, G., Ferrara, P. and Manetti, P. (1992) Genesis and classification of the rocks of the Tuscan Magmatic Province: thirty years after Marinelli's model. *Acta Vulcanologica* **2**, 247-265.
- Ionov, D.A., Dupuy, C., O'Reilly, S.Y., Kopylova, M. and Genshaft, Y.S. (1993) Carbonated peridotite xenoliths from Spitsbergen: implications for trace element signature of mantle carbonate metasomatism. *Earth and Planetary Science Letters* **119**, 283-297.

- Ionov, D.A., Bodinier, J.-L., Mukasa, S.B. and Zanetti, A. (2002) Mechanisms and sources of mantle metasomatism: Major and trace element compositions of peridotite xenoliths from Spitsbergen in the context of numerical modeling. *Journal of Petrology* **43**, 2219-2259.
- Johannsen, A. (1931) The average chemical composition of various rock types. *Neues Jahrbuch fuer Mineralogie, Geologie und Palaeontologie, Abhandlungen, Abteilung A: Mineralogie, Petrographie*, 505-516.
- Johnson, M.C. and Plank, T. (1999) Dehydration and melting experiments constrain the fate of subducted sediments. *Geochemistry Geophysics Geosystems* **1**, 1999GC000014.
- Joron, J.L., Metrich, N., Rosi, M., Santacroce, R. and Sbrana, A. (1987) Chemistry and petrography. In: Santacroce, R. (ed) *Somma-Vesuvius*. Quaderni de la ricerca scientifica, CNR, Roma **8**, 105-171.
- Juteau, M., Michard, A. and Albarede, F. (1986) The Pb-Sr-Nd isotope geochemistry of some recent circum-Mediterranean granites. *Contributions to Mineralogy and Petrology* **92**, 331-340.
- Kagami, H., Fischer, H. and Steiger, R.H. (1985) Nd and Sr isotopic evidence for the crustal origin of the Western Periadriatic plutons. *Terra Cognita* **5**, 324.
- Kagami, H., Ulmer, P., Hansmann, W., Dietrich, V. and Steiger, R.H. (1991) Nd-Sr isotopic and geochemical characteristics of the southern Adamello (Northern Italy) intrusives: implications for crustal versus mantle origin. *Journal of Geophysical Research* **96**(B9), 14331-14346.
- Karato, S. (1993) Importance of anelasticity in the interpretation of seismic tomography. *Geophysical Research Letters* **20**, 1623-1626.
- Keller, J. (1980) The island of Vulcano. *Rendiconti della Società Italiana di Mineralogia e Petrologia* **36**, 369-414.
- Keller, J.V.A., Minelli, G. and Pialli, G. (1994) Anatomy of late orogenic extension: the Northern Apennines case. *Tectonophysics* **238**, 275-294.
- Keyser, M., Ritter, J.R.R. and Jordan, M. (2002) 3D shear-wave velocity structure of the Eifel plume, Germany. *Earth and Planetary Science Letters* **203**, 59-82.
- Kushiro, I., Syono, Y. and Akimoto, S. (1967) Stability of phlogopite at high pressures and possible presence of phlogopite in the Earth's upper mantle. *Earth and Planetary Science Letters* **3**, 197-203.

- Laruenzi, M., Stoppa, F. and Villa, I. (1994) Eventi ignei monogenici e depositi piroclastici nel Distretto Ultra-alcalino Umbro-laziale (ULUD): revisione, aggiornamento e comparazione dei data cronologici. *Plinius* **12**, 61-65.
- Laubscher, H.P. (1970) Bewegung und Wärme in der alpinen Orogenese. *Schweizerische Mineralogische und Petrographische Mitteilungen* **50**, 565-596.
- Laubscher, H.P. (1971) The large scale kinematics of the western Alps and the northern Apennines and its palinspastic implications. *American Journal of Science* **271**, 193-226.
- Laubscher, H.P. (1974) The tectonics of subduction in the Alpine system. *Memorie della Società Geologica Italiana* **13**, 275-283.
- Laubscher, H.P. (1983) Detachment, shear and compression in the central Alps. *Geological Society of America Memoir* **158**, 19-211.
- Laubscher, H.P. (1988) The arcs of the Western Alps and the Northern Apennines: an updated view. *Tectonophysics* **146**, 67-78.
- Laurora, A., Mazzucchelli, M., Rivalenti, G., Vannucci, R., Zanetti, A., Barbieri, M.A. and Cingolani, C.A. (2001) Metasomatism and melting in carbonated peridotite xenoliths from the mantle wedge: The Gobernador Gregores Case (Southern Patagonia). *Journal of Petrology* **42**, 69-87.
- Lavecchia, G. and Stoppa, F. (1996) The tectonic significance of Italian magmatism: an alternative view to the popular interpretation. *Terra Nova* **8**, 435-446.
- Lavecchia, G. and Boncio, P. (2000) Tectonic setting of the carbonatite-melilitite association of Italy. *Mineralogical Magazine* **64**, 583-592.
- Lavecchia, G. and Creati, N. (in press) A mantle plume pinched in the transition zone beneath the Mediterranean: A preliminary idea. *Annali di Geophysica*.
- La Volpe, L., Patella, D., Rapisardi, L. and Tramacere, A. (1984) The evolution of the Monte Vulture volcano (Southern Italy): inferences from volcanological, geological and deep dipole electrical soundings data. *Journal of Volcanology and Geothermal Research* **22**, 147-162.
- Leake, B.E., Woolley, A., Arps, C.E.S., Birch, W.D., Gilbert, M.C., Grice, J.D., Hawthorne, F.C., Kato, A., Kisch, A., Krivovichev, V.G., Linthout, K., Laird, J., Mandarino, J.A., Maresch, W.V., Nickel, E.H., Rock, N.M.S., Schumacher, J.C., Smith, D.C., Stephenson, N.C.N., Ungaretti, L., Whittaker, E.J.W. and Youzhi, G. (1997) Nomenclature of amphiboles: report of the subcommittee on amphiboles of the International Mineralogical Association, Commission on new minerals and mineral names. *The Canadian Mineralogist* **35**, 219-246.

- Le Maitre, R.W. (ed.), Streckeisen, A., Zanettin, B., Le Bas, M.J., Bonin, B., Bateman, P., Bellieni, G., Dudek, A., Efremova, S., Keller, J., Lameyre, J., Sabine, P.A., Schmid, R., Sorenson, H. and Woolley, A.R. (2002) *Igneous Rocks. A Classification and Glossary of Terms*. Cambridge University Press, Cambridge, UK. pp. 1-39.
- Lemoine, M. and Trümpy, R. (1987) Pre-oceanic rifting in the Alps. *Tectonophysics* **133**, 305-320.
- Le Roex, A.P., Cliff, R.A. and Adair, B.J.I. (1990) Tristan da Cunha, South Atlantic: geochemistry and petrogenesis of a basanite-phonolite lava series. *Journal of Petrology* **31**, 779-812.
- Lima, A. (2000) Experimental study on silicate-melt inclusions in clinopyroxene phenocrysts from Roccamonfina lavas (Italy). *Mineralogy and Petrology* **70**, 199-220.
- Lloyd, F.E. (1981) Upper mantle metasomatism beneath a continental rift: clinopyroxenes in alkali mafic lavas and nodules from South West Uganda. *Mineralogical Magazine* **44**, 315-323.
- Lucente, F.P., Chiarabba, C., Cimini, G.B. and Giardini, D. (1999) Tomographic constraints on the geodynamic evolution of the Italian region. *Journal of Geophysical Research* **104**(B9), 20307-20327.
- Luhr, J.F. and Giannetti, B. (1987) The Brown Leucitic Tuff of Roccamonfina Volcano (Roman Region, Italy). *Contributions to Mineralogy and Petrology* **95**, 420-436.
- Lustrino, M. (2000) Phanerozoic geodynamic evolution of the circum-Italian realm. *International Geology Review* **42**, 724-757.
- Lustrino, M., Melluso, L. and Morra, V. (2000) The role of lower continental crust and lithospheric mantle in the genesis of Plio-Pleistocene volcanic rocks from Sardinia (Italy). *Earth and Planetary Science Letters* **180**, 259-270.
- Macera, P., Gasperini, D., Piromallo, C., Blichert-Toft, J., Bosch, D., Del Moro, A. and Martin, F. (2003) Geodynamic implications of deep mantle upwelling in the source of Tertiary volcanics from the Veneto region (South-Eastern Alps). *Journal of Geodynamics* **36**, 563-590.
- Malinverno, A. and Ryan, W.B.F. (1986) Extension in the Tyrrhenian Sea and shortening in the Apennines as result of arc migration driven by sinking of the lithosphere. *Tectonics* **5**, 227-245.
- Mantovani, E., Albarello, D., Tamburelli, C., Babbucci, D. and Viti, M. (1997) Plate convergence, crustal delamination, extrusion tectonics and minimization of shortening work as main controlling factors of the recent Mediterranean deformation pattern. *Annali di Geofisica* **40**, 611-643.

- Marchant, R. (1993) The underground of the Western Alps. *Memoires de Geologie Lausanne* **15**, pp. 137.
- Marchant, R.H. and Stampfli, G.M. (1997) Subduction of continental crust in the Western Alps. *Tectonophysics* **269**, 217-235.
- Marty, B., Trull, T., Lussiez, P., Basile, I. and Tanguy, J-C. (1994) He, Ar, O, Sr and Nd isotope constraints on the origin and evolution of Mount Etna magmatism. *Earth and Planetary Science Letters* **126**, 23-39.
- McCulloch, M.T. and Gamble, J.A. (1991) Geochemical and geodynamical constraints on subduction zone magmatism. *Earth and Planetary Science Letters* **102**, 358-374.
- McDonough, W.F., Sun, S.S., Ringwood, A.E., Jagoutz, E., Hofmann, A.W. (1992) Potassium, rubidium, and cesium in the Earth and Moon and the evolution of the mantle of the Earth. *Geochimica et Cosmochimica Acta* **56**, 1001-1012.
- McKenzie, D. (1984) The generation and compaction of partially molten rock. *Journal of Petrology* **25**, 713-765.
- Meen, J.K., Eggler, D.H. and Ayers, J.C. (1989) Experimental evidence for very low solubility of rare-earth elements in CO₂-rich fluids at mantle conditions. *Nature* **340**, 301-303.
- Middlemost, E.A.K. (1975) The basalt clan. *Earth Science Reviews* **11**, 337-364.
- Middlemost, E.A.K. (1989) Iron oxidation ratios, norms and the classification of volcanic rocks. *Chemical Geology* **77**, 19-26.
- Milani, L., Beccaluva, L., and Coltorti, M. (1999) Petrogenesis and evolution of the Euganean magmatic complex, Veneto Region, North-East Italy. *European Journal of Mineralogy* **11**, 379-399.
- Mirnejad, H. (2002) Isotope geochemistry, petrology, and source evaluation of the Leucite Hills lamproites, Wyoming. *Ph.D. Thesis*, Carleton University, Ottawa, pp. 253.
- Mitchell, R.H. (1986) *Kimberlites: mineralogy, geochemistry and petrology*. Plenum Press, New York, pp. 442.
- Mitchell, R.H. and Bergman, S.C. (1991) *Petrology of lamproites*. Plenum Press, New York, pp. 447.
- Mongelli, F., Zito, G., Della Vedova, B., Pellis, G., Squarci, P. and Taffi, L. (1991) Geothermal Regime of Italy and surrounding Seas. In: *Exploration of the the Deep Continental Crust*. Springer-Verlag, Berlin, pp. 381-394.

- Montone, P., Amato, A., Chiarabba, C., Buonasorte, G. and Fiordelisi, A. (1995) Evidence of active extension in the Quaternary volcanoes of Central Italy from breakout analysis and seismicity. *Geophysical Research Letters* **22**, 1909-1912.
- Morimoto, N., Fabries, J., Ferguson, A.K., Ginzburg, I.V., Ross, M., Seifert, F.A., Zussman, J., Aoki, K. and Gottardi, G. (1989) Nomenclature of pyroxenes. *The Canadian Mineralogist* **27**, 143-156.
- Morra, V., Secchi, F.A.G., Melluso, L. and Franciosi, L. (1997) High-Mg subduction-related Tertiary basalts in Sardinia, Italy. *Lithos* **40**, 69-91.
- Morris, J.D. and Hart, S.R. (1983) Isotopic and incompatible element constraints on the genesis of island arc volcanics from Cold Bay and Amak Island, Aleutians, and implications for mantle structure. *Geochimica et Cosmochimica Acta* **47**, 2015-2030.
- Morris, J.D., Leeman, W.P. and Tera, F. (1990) The subducted component in island arc lavas: constraints from Be isotopes and B-Be systematics. *Nature* **344**, 31-36.
- Morris, J.D., Ryan, J. and Leeman, W.P. (1993) Be isotope and B-Be investigations of the historic eruptions of Mt. Vesuvius. *Journal of Volcanology and Geothermal Research* **58**, 345-358.
- Morris, J.D., Gosse, J., Brachfeld, S. and Tera, F. (2002) Cosmogenic Be-10 and the solid earth: Studies in geomagnetism, subduction zone processes, and active tectonics. In: Grew, E.S. (ed.) *Beryllium: Mineralogy, Petrology, and Geochemistry. Reviews in Mineralogy and Geochemistry* **50**, 207-270.
- Mostardini, F. and Merlini, S. (1986) Appennino centro meridionale: Sezioni geologiche e proposta di modello strutturale. *Memorie della Societe Geologica Italiana* **35**, 177-202.
- Muttoni, G., Argnani, A., Kent, D.V., Abrahamsen, N. and Cibin, U. (1998) Paleomagnetic evidence for Neogene tectonic rotations in the northern Apennines, Italy. *Earth and Planetary Science Letters* **154**, 25-40.
- Nakamura, N. (1974) Determination of REE, Ba, Fe, Mg, Na and K in carbonaceous and ordinary chondrites. *Geochimica et Cosmochimica Acta* **38**, 757-775.
- Nelson, D.R. (1992) Isotopic characteristics of potassic rocks: evidence for the involvement of subducted sediments in magma genesis. *Lithos* **28**, 403-420.
- Nicoletti, M., Petrucciani, C., Piro, R. and Trigila, R. (1979) Nuove datazioni Vulsinee per uno schema di evoluzione dell'attivita vulcanica. Il quadrante Nort-Occidentale. *Periodico di Mineralogia* **48**, 153-165.
- Nimis, P. (1995) A clinopyroxene geobarometer for basaltic systems based on crystal-structure modeling. *Contributions to Mineralogy and Petrology* **121**, 115-125.

- Nimis, P. (1999) Clinopyroxene geobarometry of magmatic rocks Part 2. Structural geobarometers for basic to acid, tholeiitic and mildly alkaline magmatic systems. *Contributions to Mineralogy and Petrology* **135**, 62-74.
- Nimis, P. and Ulmer, P. (1998) Clinopyroxene geobarometry of magmatic rocks Part 1: An expanded structural geobarometer for anhydrous and hydrous, basic and ultrabasic systems. *Contributions to Mineralogy and Petrology* **133**, 122-135.
- Nixon, P.H. and Hornung, G. (1973) The carbonatite lavas and tuffs near Fort Portal, western Uganda. *Institute of Geological Science Overseas Geology and Mineral Resources* **41**, 168-179.
- Nixon, P.H., Thirlwall, M.F., Buckley, F. and Davies, C.J. (1984) Spanish and Western Australian lamproites: aspects of whole rock geochemistry. In: Kornprobst, J. (ed), *Kimberlites I: Kimberlites and Related Rocks*. Elsevier, Amsterdam, pp. 285-296.
- Oldow, J.S., Ferranti, L., Lewis, D.S., Campbell, J.K., D'Argenio, B., Catalano, R., Pappone, G., Carmignani, L., Conti, P. and Aiken, C.L.V. (2002) Active fragmentation of Adria, the north African promontory, central Mediterranean orogen. *Geology* **30**, 779-782.
- Oschidari, v.H. and Ziegler, U.R.F. (1992) Vergleichende Sm-Nd und Rb-Sr-untersuchungen an Gergeller Gerollen aus der Gonfolite Lombardia ("sudalpine molasse") und an Bergeller und Novate granitoiden des ursprungsgebietes. *Eclogae. Geol. Helv.* **85**, 375-384.
- Owen, J.P. and Bell, K. (2004) Trace element and isotopic constraints on the origin and age of upper mantle metasomatism in central-southern Italy. *GAC-MAC Abstract volume*, pp. 421.
- Owen, J.P., Bell, K., and Peccerillo, A. (2004) Trace element and Sr, Nd, and Pb isotope geochemistry of potassium-rich volcanics from Roccamonfina and Ernici, Southern Latium Transition Zone, Italy: Implications for mantle mixing. *IGC Abstract volume*, 291-27.
- Owen, J.P. and Bell, K. (2005) Mineral chemistry of potassium-rich volcanic rocks from Central-Southern Italy: Implications for crystallization conditions and magma genesis. *GAC-MAC Abstract volume*, pp. 146.
- Parello, F., Allard, P., D'Alessandro, W., Federico, C., Jean-Baptiste, P. and Catani, O. (2000) Isotope geochemistry of Pantelleria volcanic fluids, Sicily Channel rift: a mantle volatile end-member for volcanism in southern Europe. *Earth and Planetary Science Letters* **180**, 325-339.

Patacca, E., Sartori, R. and Scandone, P. (1990) Tyrrhenian basin and Apenninic arcs: Kinematic relations since late Tortonian times. *Memorie della Società Geologica Italiana* **45**, 425-451.

Pearce, J.A. (1982) Trace element characteristics of lavas from destructive plate boundaries. In: Thorpe, R.S. (ed) *Andesites*. Wiley, Chichester, pp. 525-548.

Peccerillo, A. (1985) Roman comagmatic province (central Italy): Evidence for subduction-related magma genesis. *Geology* **13**, 103-106.

Peccerillo, A. (1990) On the origin of the Italian potassic magmas – Comments. *Chemical Geology* **85**, 183-196.

Peccerillo, A. (1992) Potassic and ultrapotassic rocks: Compositional characteristics, petrogenesis, and geologic significance. *Episodes* **15**, 243-251.

Peccerillo, A. (1998) Relationships between ultrapotassic and carbonate-rich volcanic rocks in central Italy: petrogenetic and geodynamic implications. *Lithos* **43**, 267-279.

Peccerillo, A. (1999) Multiple mantle metasomatism in central-southern Italy: geochemical effects, timing and geodynamic implications. *Geology* **27**, 315-318.

Peccerillo, A. (2001) Geochemistry and petrogenesis of Quaternary magmatism in central-southern Italy. *Geochemistry International* **39**, 2001.

Peccerillo, A. and Taylor, S.R. (1976) Geochemistry of Eocene calc-alkaline volcanic rocks from the Kastamonu area, northern Turkey. *Contributions to Mineralogy and Petrology* **58**, 63-81.

Peccerillo, A. and Manetti, P. (1985) The potassium alkaline volcanism of central Southern Italy: a review of the data relevant to petrogenesis and geodynamic significance. *Transactions of the Geological Society of South Africa* **88**, 379-394.

Peccerillo, A., Poli, G. and Serri, G. (1988) Petrogenesis of orenditic and kamafugitic rocks from central Italy. *The Canadian Mineralogist* **26**, 45-65.

Peccerillo, A., Kempton, P.D., Harmon, R.S., Wu, T.-W., Santo, A.P., Boyce, A.J. and Tripodo, A. (1993) Petrological and geochemical characteristics of the Alicudi volcano, Aeolian Islands, Italy: Implications for magma genesis and evolution. *Acta Vulcanologica* **3**, 235-249.

Peccerillo, A. and Panza, G.F. (1999) Upper mantle domains beneath central-southern Italy: petrological, geochemical and geophysical constraints. *Pure and Applied Geophysics* **156**, 421-443.

- Peccerillo, A. and Turco, E. (2004) Petrological and geochemical variations of Plio-Quaternary volcanism in the Tyrrhenian Sea area: regional distribution of magma types, petrogenesis and geodynamic implications. *Periodico di Mineralogia* **73**, 231-251.
- Pialli, G. and Alvarez, W. (1997) Tectonic setting of the Miocene Northern Apennines; the problem of contemporaneous compression and extension. *Developments in Palaeontology and Stratigraphy* **15**, 167-185.
- Piromallo, C. and Morelli, A. (1997) Imaging the Mediterranean upper mantle by P-wave travel time tomography. *Annali di Geofisica* **40**, 963-979.
- Piromallo, C. and Morelli, A. (2003) P-wave tomography of the mantle under the Alpine-Mediterranean area. *Journal of Geophysical Research* **108**(B2), pp. 23.
- Piromallo, C. and Faccenna, C. (2004) How deep can we find traces of Alpine subduction? *Geophysical Research Letters* **31**, L06605.
- Plank, T. and Langmuir, C.H. (1998) The chemical composition of subducting sediment and its consequences for the crust and mantle. *Chemical Geology* **145**, 325-394.
- Poli, G. (1992) Geochemistry of Tuscan Archipelago granitoids, Central Italy: the role of hybridization processes in their genesis. *Journal of Geology* **100**, 41-56.
- Poli, G., Frey, F.A. and Giorgi, F. (1984) Geochemical characteristics of the South Tuscany (Italy) volcanic province: constraints on lava petrogenesis. *Chemical Geology* **43**, 203-221.
- Polyack, B.G., Fernandez, M. and FLUCALB Group. (1996) Heat flow in the Alboran Sea, western Mediterranean. *Tectonophysics* **263**, 191-218.
- Principe, C. and Stoppa, F. (1994) Caratteristiche litologiche delle piroclastiti associate alla genesi dei maar di Monticchio: prima segnalazione di depositi carbonatitico-melilitici al Mt. Vulture. *Plinius* **12**, 86-90.
- Putirka, K., Johnson, M., Kinzler, R., Longhi, J. and Walker, D. (1996) Thermobarometry of mafic igneous rocks based on clinopyroxene-liquid equilibria, 0-30 kbar. *Contributions to Mineralogy and Petrology* **123**, 992-108.
- Puxeddu, M. (1971) Studio chimico-petrografico delle vulcaniti del M. Cimino (Viterbo). *Atti Soc. Toscana Sci. Nat. Mem.* **78**, 329-394.
- Ranalli, G. (1996) *Seismic tomography and mineral physics*. Editrice Compositori, Bologna, Italy, pp. 443-461.

- Ranalli, G. (2000) Rheology and subduction of continental lithosphere. In: Ranalli, G., Ricci, C.A. and Trommsdorff, V. (eds.) *Crust Mantle Interactions, Siena, 24 September – 3 October 1999: Proceedings of the International School of Earth and Planetary Sciences*, pp. 21-40.
- Rieder, M., Cavazzini, G., D'Yakonov, Y.S., Frank-Kamenetskii, V.A., Gottardi, G., Guggenheim, S., Koval, P.V., Müller, G., Neiva, A.M.R., Radoslovich, E.W., Robert, J.-L., Sassi, F.P., Takeda, H., Weiss, Z. and Wones, D.R. (1998) Nomenclature of the micas. *The Canadian Mineralogist* **36**, 41-48.
- Regard, V.C., Faccenna, C., Martinod, J., Bellier, O. and Thomas, J.-C. (2003) From subduction to collision: Control of deep processes on the evolution of convergent plate boundary. *Journal of Geophysical Research* **108**(B4), pp.16.
- Renzulli, A., Serri, G., Santi, P., Mattioli, M. and Holm, P.M. (2001) Origin of high-silica liquids of Stromboli volcano (Aeolian Islands, Italy) inferred from crustal xenoliths. *Bulletin of Volcanology* **62**, 400-419.
- Ritter, R.R., Jordan, M., Christensen, U.R. and Achauer, U. (2001) A mantle plume below the Eifel volcanic fields, Germany. *Earth and Planetary Science Letters* **186**, 7-14.
- Rock, N.M.S. (1991) *Lamprophyres*. Van Nostrand Reinhold, New York, USA. pp. 1-102.
- Rogers, N.W., Hawkesworth, C.J., Parker, R.J. and Marsh, J.S. (1985) The geochemistry of potassic lavas from Vulcini, central Italy and implications for mantle enrichment processes beneath the Roman region. *Contributions to Mineralogy and Petrology* **90**, 244-257.
- Rogers, N.W., De Mulder, R. and Hawkesworth, C.J. (1992) An enriched mantle source for potassic basanites: evidence from Karisimbi volcano, Virunga volcanic province, Rwanda. *Contributions to Mineralogy and Petrology* **111**, 543-556.
- Romano, R. and Villari, L. (1973) Caratteri petrologici e magmatologici del vulcanismo ibleo. *Rendiconti della Societe Italiana di Mineralogia e Petrologia* **29**, 453-484.
- Rollinson, H. (1993) *Using geochemical data: evaluation, presentation, interpretation*. Pearson Education Limited, England, pp. 352.
- Rosi, M., Sbrana, A. and Principe, C. (1983) The Phlegraean Fields: structural evolution, volcanic history and eruptive mechanism. *Journal of Volcanology and Geothermal Research* **17**, 273-288.

- Rossi, G., Oberti, R. and Smith, D.C. (1989) The crystal structure of a K-poor Ca-rich silicate with the nepheline framework, and crystal-chemical relationships in the compositional space $(K, Na, Ca)_8(Al, Si)_{16}O_{32}$. *European Journal of Mineralogy* **1**, 59-70.
- Royden, L., Patacca, E., and Scandone, P. (1987) Segmentation and configuration of subducted lithosphere in Italy: An important control on thrust-belt and foredeep-basin evolution. *Geology* **15**, 714-717.
- Rudnick, R.L., McDonough, W.F. and Chappell, B.W. (1993) Carbonatite metasomatism in the northern Tanzanian mantle: petrographic and geochemical characteristics. *Earth and Planetary Science Letters* **114**, 463-475.
- Rutter, M.J. (1987) Evidence for crustal assimilation by turbulently convection mafic alkaline magmas: geochemistry of mantle xenolith-bearing lavas from northern Sardinia. *Journal of Volcanology and Geothermal Research* **32**, 343-354.
- Ryan, J.G. (2002) Trace-element systematics of beryllium in terrestrial materials. In: Grew, E.S. (ed.) *Beryllium: Mineralogy, Petrology, and Geochemistry. Reviews in Mineralogy and Geochemistry* **50**, 121-146.
- Ryan, J.G. and Langmuir, C.H. (1993) The systematics of boron abundances in young volcanic rocks. *Geochimica et Cosmochimica Acta* **57**, 1489-1498.
- Santo, A.P., Chen, Y., Clark, A.H., Farrar, E. and Tsegaye, A. (1995) $^{40}\text{Ar}/^{39}\text{Ar}$ ages of the Filicudi Island volcanics: implications for the volcanological history of the Aeolian Arc, Italy. *Bulletin of Volcanology* **7**, 13-18.
- Sartori, R. (1990) The main results of ODP Leg 107 in the frame of Neogene to Recent geology of Peri-Tyrrhenian area. *Proceedings of Science and Research of the Ocean Drilling Program* **107**, 715-730.
- Saunders, A.D. and Tarney, J. (1984) Geochemical characteristics of basaltic volcanism within back-arc basins. In: Kokelarr, B.P. and Howells, M.F. (eds) *Marginal basin geology. Geological Society of London Special Publication* **16**, 59-76.
- Saunders, A.D., Norry, M.J. and Tarney, J. (1988) Origin of MORB and chemically depleted mantle reservoirs: trace element constraints. *Journal of Petrology* **1988**, 415-445.
- Savelli, C. (1967) The problem of rock assimilation by Somma-Vesuvio magma, I, Composition of Somma and Vesuvius lavas. *Contributions to Mineralogy and Petrology* **16**, 328-353.

- Savelli, C. (1988) Late Oligocene to Recent episodes of magmatism in and around the Tyrrhenian Sea: implications for the processes of opening in a young inter-arc basin of intra-orogenic (Mediterranean) type. *Tectonophysics* **146**, 163-181.
- Savelli, C. and Gasparotto, G. (1994) Calc-alkaline magmatism and rifting of the deep-water volcano of Marsili (Aeolian back-arc, Tyrrhenian Sea). *Marine Geology* **199**, 137-157.
- Scarascia, S., Lozej, A. and Cassinis, R. (1994) Crustal structure of the Ligurian, Tyrrhenian and Ionian seas and Adjacent onshore areas interpreted from wide-angle seismic profiles. *Bolletino di Geofisica et Teoretica Applicata* **36**, 5-19.
- Schiano, P., Clocchiatti, R., Ottolini, L. and Busa, T. (2001) Transition of Mount Etna lavas from a mantle-plume to an island-arc magmatic source. *Nature* **412**, 900-904.
- Schmid, S.M., Pfiffner, O.A., Froitzheim, N., Schonborn, G. and Kissling, E. (1996) Geophysical-geological transect and tectonic evolution of the Swiss-Italian Alps. *Tectonics* **15**, 1036-1064.
- Schoales, D.Y., Rutherford, N.J. and Sigurdsson, H. (1987) Conditions in the magma chamber prior to the 79 A.D. eruption of Mt. Somma-Vesuvius. *EOS* **68**, 434.
- Selli, R., Lucchini, F., Rossi, P.L., Savelli, C. and Del Monte, M. (1977) Dati geologici, petrochimici e radiometrici sui vulcani centro-tirrenici. *G. Geol.* **42**, 221-246.
- Selvaggi, G. and Chiarabba, C. (1995) Seismicity and P-wave velocity image of the southern Tyrrhenian subduction zone. *Geophysical Journal International* **121**, 818-826.
- Serri, G. (1991) Neogene-Quaternary magmatism of the Tyrrhenian region: characterization of the magma sources and geodynamical implications. *Memorie della Società Geologica Italiana* **44**, 219-242.
- Serri, G., Innocenti, F. and Manetti, P. (1993) Geochemical and petrological evidence of the subduction of delaminated Adriatic continental lithosphere in the genesis of the Neogene-Quaternary magmatism of central Italy. *Tectonophysics* **223**, 117-147.
- Shannon, R.D. (1976) Revised effective ionic radii and systematic studies of interatomic distances in halides and chalcogenides. *Acta Crystallogica* **A32**, 751-767.
- Shaw, D.M., Truscott, M.G., Gray, E.A. and Middleton, T.A. (1988) Boron and lithium in high-grade rocks and minerals from the Wawa-Kapuskasing region, Ontario. *Canadian Journal of Earth Sciences* **25**, 1485-1502.

- Shen, Y., Solomon, S.C., Bjarnason, I.T. and Purdy, G.M. (1996) Hot mantle transition zone beneath Iceland and the adjacent Mid-Atlantic Ridge inferred from P-to-S conversions at the 410 and 660 discontinuities. *Geophysical Research Letters* **23**, 3527–3530.
- Sims, K.W.W. and DePaolo, D.J. (1997) Inferences about mantle magma sources from incompatible element concentration ratios in oceanic basalts. *Geochimica et Cosmochimica Acta* **61**, 765-784.
- Sinclair, H.D. (1997) Flysch to molasse transition in peripheral foreland basins: The role of the passive margin versus slab breakoff. *Geology* **25**, 1123-1126.
- Sleep, N.H. (1990) Hotspots and mantle plumes: some phenomenology. *Journal of Geophysical Research* **95**, 6715–6736.
- Snoke, A.W., Kalakay, T.J., Quick, J.E. and Sinigoi, S. (1999) Development of a deep-crustal shear zone in response to syntectonic intrusion of mafic magma into the lower crust, Ivrea-Verbano zone, Italy. *Earth and Planetary Science Letters* **166**, 31-45.
- Sobolev, S.V., Achauer, U. and Granet, M. (1997) Mineral physics and dynamic interpretation of high resolution mantle tomographic images. *EOS Transactions* **78**, pp.466.
- Somma, R., Ayuso, R.A., De Vivo, B. and Rolandi, G. (2001) Major, trace element and isotope geochemistry (Sr-Nd-Pb) of interplinian magmas from Mt. Somma-Vesuvius (southern Italy). *Mineralogy and Petrology* **73**, 121-143.
- Spakman, W., Van Der Lee, S. and Van Der Hilst, R. (1993) Travel-time tomography of the European-Mediterranean mantle down to 1400 km. *Physics of the Earth and Planetary Interior* **79**, 3-74.
- Stoppa, F. (1995) The San Venanzo maar and tuff ring, Umbria, Italy: eruptive behavior of a carbonatite-melilitite volcano. *Bulletin of Volcanology* **57**, 563-578.
- Stoppa, F. and Lavecchia, G. (1992) Late Pleistocene ultra-alkaline magmatic activity in the Umbria Latium region (Italy): An overview. *Journal of Volcanology and Geothermal Research* **52**, 227-293.
- Stoppa, F. and Lupini, L. (1993) Mineralogy and petrology of the Polino monticellite calcite carbonatite (Central Italy). *Mineralogy and Petrology* **49**, 213-231.
- Stoppa, F. and Cundari, A. (1995) A new Italian carbonatite occurrence at Cupaello (Rieti) and its genetic significance. *Contributions to Mineralogy and Petrology* **122**, 275-288.

Stoppa, F. and Principe, C. (1997) Eruption style and petrology of a new carbonatite suite from the Mt. Vulture, Southern Italy: The Monticchio Lakes Formation. *Journal of Volcanology and Geothermal Research* **78**, 251-265.

Stoppa, F. and Woolley, A.R. (1997) The Italian carbonatites: field occurrence, petrology and regional significance. *Mineralogy and Petrology* **59**, 43-67.

Stünitz, H. (1989) Partitioning of metamorphism and deformation in the boundary region of the "Seconda Zona Diorito-Kinzigitica", Sesia Zone, Western Alps. *Ph.D. thesis*, Swiss Federal Polytechnic, Zürich, pp. 255.

Suhadolc, P. and Panza, G.F. (1989) Physical properties of the lithosphere-asthenosphere system in Europe from geophysical data. In: Boriani, A., Bonafede, M., Piccardo, G.B. and Vai, G.B. (eds) *The Lithosphere in Italy, Advances in Earth Science Research*. Acc. Nazionale Lincei, Roma, pp. 15-40.

Sun, S.S. (1980) Lead isotopic study of young volcanic rocks from mid-ocean ridges, ocean islands and island arcs. *Philosophical Transactions of the Royal Society of London* **A297**, 409-445.

Sun, S. S. and Hanson, G. N. (1975). Evolution of the mantle: geochemical evidence from alkali basalt. *Geology* **3**, 297-302.

Sun, S.S. and McDonough, W.F. (1989) Chemical and isotopic systematics of oceanic basalts: implications for mantle composition and processes. In: Saunders, A.D. and Norry, M.J. (eds) *Magmatism in ocean basins. Geological Society of London Special Publication* **42**, 313-345.

Taylor, H.P. Jr. (1980) The effects of assimilation of country rocks by magmas on $^{18}\text{O}/^{16}\text{O}$ and $^{87}\text{Sr}/^{86}\text{Sr}$ systematics in igneous rocks. *Earth and Planetary Science Letters* **47**, 243-254.

Taylor, H.P. and Turi, B. (1976) High ^{18}O igneous rocks from the Tuscan magmatic province, Italy. *Contributions to Mineralogy and Petrology* **55**, 33-54.

Taylor, H.P. Jr., Giannetti, B. and Turi, B. (1979) Oxygen isotope geochemistry of the potassic igneous rocks from the Roccamonfina volcano, Roman Co-magmatic Region, Italy. *Earth and Planetary Science Letters* **46**, 81-106.

Taylor, S.R. and McLennan, S.M. (1981) The composition and evolution of the continental crust: rare earth element evidence from sedimentary rocks. *Philosophical Transactions of the Royal Society of London* **A301**, 381-399.

Taylor, S.R. and McLennan, S.M. (1985) *The continental crust: its composition and evolution*. Blackwell, Oxford.

Tera, F., Brown, L., Morris, J., Sacks, I.S., Klein, J. and Middleton, R. (1986) Sediment incorporation in island-arc magmas: Inferences from ^{10}Be . *Geochimica et Cosmochimica Acta* **50**, 535-550.

Tilton, G.R., Schreyer, W. and Schertl, H.-P. (1989) Pb-Sr-Nd isotopic behavior of deeply subducted crustal rocks from the Dora Maira Massif, Western Alps, Italy. *Geochimica et Cosmochimica Acta* **53**, 1391-1400.

Thompson, R.N. (1974) Some high-pressure pyroxenes. *Mineralogical Magazine* **39**, 768-787.

Thompson, R.N. (1977) Primary basalts and magma genesis, III. Alban Hills, Roman Comagmatic Province, Central Italy. *Contributions to Mineralogy and Petrology* **60**, 91-108.

Thompson, R.N. (1982) British Tertiary volcanic province. *Scottish Journal of Geology* **18**, 49-107.

Thompson, R.N., Morrison, M.A., Hendry, G.L. and Parry, S.J. (1984) An assessment of the relative roles of a crust and mantle in magma genesis: an elemental approach. *Philosophical Transactions of the Royal Society of London* **A310**, 549-590.

Tonarini, S., D'Orazio, M., Armienti, P., Innocenti, F. and Scribano, V. (1996) Geochemical features of eastern Sicily lithosphere as probed by Hyblean xenoliths and lavas. *European Journal of Mineralogy* **8**, 1153-1173.

Tonarini, S., Armienti, P., D'Orazio, M. and Innocenti, F. (2001) Subduction-like fluids in the genesis of Mt. Etna magmas: evidence from boron isotopes and fluid mobile elements. *Earth and Planetary Science Letters* **192**, 471-483.

Trua, T., Esperança, S. and Mazzuoli, R. (1998) The evolution of the lithospheric mantle along the N. African Plate: geochemical and isotopic evidence from the tholeiitic and alkaline volcanic rocks of the Hyblean plateau, Italy. *Contributions to Mineralogy and Petrology* **131**, 307-322.

Trümpy, R. (1980) *Geology of Switzerland, a Guide Book. Part A, an outline of the geology of Switzerland*. Wepf and Co., Basel.

Turi, B. and Taylor, H.P. (1976) Oxygen isotope studies of potassic volcanic rocks of the Roman Province, Central Italy. *Contributions to Mineralogy and Petrology* **55**, 1-31.

Turi, B., Taylor, H.P. and Ferrara, G. (1986) A criticism of the Holm-Munksgaard oxygen and strontium isotope study of the Vulsinian district, Central Italy. *Earth and Planetary Science Letters* **78**, 447-453.

- Turpin, L., Velde, D. and Pinte, G. (1988) Geochemical comparison between minettes and kersantites from the Western European Hercynian orogen: trace element and Pb-Sr-Nd isotope constraints on their origin. *Earth and Planetary Science Letters* **87**, 73-86.
- Van Bergen, M.J., Ghezzo, C. and Ricci, C.A. (1983) Minette inclusions in the rhyodacitic lavas of Mt. Amiata (Central Italy): mineralogical and chemical evidence of mixing between Tuscan and Roman type magmas. *Journal of Volcanology and Geothermal Research* **19**, 1-35.
- Van der Voo, R. (1993) *Paleomagnetism of the Atlantic Tethys and Iapetus oceans*. Cambridge University press, Cambridge, pp. 411.
- Varne, R. (1985) Ancient subcontinental mantle: A source for K-rich orogenic volcanics. *Geology* **13**, 405-408.
- Varne, R. and Foden, J.D. (1986) Geochemical and isotopic systematics of eastern Sunda arc volcanics: implications for mantle sources and mantle mixing processes. In: F. Wezel (ed) *The Origin of Arcs*. Elsevier, Amsterdam, pp.159-189.
- Venturelli, G., Thorpe, R.S., Dal Piaz, G.V., Del Moro, A. and Potts, P.J. (1984) Petrogenesis of calc-alkaline, shoshonitic and associated ultrapotassic Oligocene volcanic rocks from the Northwestern Alps, Italy. *Contributions to Mineralogy and Petrology* **86**, 209-220.
- Verwoerd, W.J. (1967) The carbonatites of South Africa and South West Africa. *Geological Survey of South Africa Handbook* **6**, pp. 452.
- Villemant, B. (1988) Trace element evolution in Phlegraean Fields (Central Italy): fractional crystallization and selective contamination. *Contributions to Mineralogy and Petrology* **98**, 169-183.
- Vollmer, R. (1976) Rb-Sr and U-Th-Pb systematics of alkaline rocks: the alkaline rocks from Italy. *Geochimica et Cosmochimica Acta* **40**, 283-295.
- Vollmer, R. (1977) Isotopic evidence for genetic relations between acid and alkaline rocks in Italy. *Contributions to Mineralogy and Petrology* **60**, 109-118.
- Vollmer, R. (1990) On the origin of the Italian potassic magmas – Reply. *Chemical Geology* **85**, 191-196.
- Vollmer, R. and Hawkesworth, C.J. (1980) Lead composition of the potassic rocks from Roccamonfina (South Italy). *Earth and Planetary Science Letters* **47**, 91-101.

- Vollmer, R., Johnston, K., Ghiara, M.R., Lirer, L. and Munno, R. (1981) Sr isotope geochemistry of megacrysts from continental rift and converging plate margin alkaline volcanism in South Italy. *Journal of Volcanology and Geothermal Research* **11**, 317-327.
- von Blanckenburg, F., Fruh-Green, G., Diethelm, K. and Stille, P. (1992) Nd-, Sr-, O-isotopic and chemical evidence for a two-stage contamination history of mantle magma in the Central-Alpine Bergell intrusion. *Contributions to Mineralogy and Petrology* **110**, 33-45.
- von Blanckenburg, F. and Davies, J.H. (1995) Slab breakoff: A model for syncollisional magmatism and tectonics in the Alps. *Tectonics* **14**, 120-131.
- von Blanckenburg, F., Kagami, H., Deutsch, A., Oberli, F., Meier, M., Wiedenbeck, M., Barth, S. and Fischer, H. (1998) The origin of Alpine plutons along the Periadriatic Lineament. *Schweizerische Mineralogische und Petrographische Mitteilungen* **78**, 55-66.
- Washington, H.S. (1906) The Roman Comagmatic Region. *Carnegie Institute of Washington* **36**, 1-220.
- Weaver, B.L. (1991) The origin of ocean island basalt end-member compositions: trace element and isotopic constraints. *Earth and Planetary Science Letters* **104**, 3810-3897.
- Weaver, B. and Tarney, J. (1984) Empirical approach to estimating the composition of the continental crust. *Nature* **310**, 575-577.
- Wheller, G.E., Varne, R., Foden, J.D. and Abbott, M.J. (1987) Geochemistry of Quaternary volcanism in the Sunda-Banda Arc, Indonesia, and three-component genesis of island-arc basaltic magmas. *Journal of Volcanology and Geothermal Research* **32**, 137-160.
- Wilson, M. (1989) *Igneous Petrogenesis*. Chapman & Hall, London, pp. 466.
- Wilson, M. and Downes, H. (1991) Tertiary-Quaternary extension-related alkaline magmatism in western and central Europe. *Journal of Petrology* **32**, 811-849.
- Wilson, M. and Downes, H. (1992) Mafic alkaline magmatism associated with the European Cenozoic rift system. *Tectonophysics* **208**, 173-182.
- Wilson, M., Rosenbaum, J.M. and Dunworth, E.A. (1995) Melilitites: partial melts of a thermal boundary layer? *Contributions to Mineralogy and Petrology* **119**, 181-196.

- Wilson, M. and Bianchini, G. (1999) Tertiary-Quaternary magmatism within the Mediterranean and surrounding regions. In: Durand, B., Jolivet, L., Horvath, F. and Seranne, M. (eds) *The Mediterranean Basins: Tertiary Extension within the Alpine Orogen*. *Geological Society of London Special Publication* **156**, 141-168.
- Wilson, M. and Patterson, R. (2001) Intra-plate magmatism related to hot fingers in the upper mantle: Evidence from the Tertiary-Quaternary volcanic province of western and central Europe. In: Ernst, R. and Buchan, K. (eds.) *Mantle Plumes: Their identification through time*. *Geological Society of America Special Paper* **352**, 37-58.
- Wong, A., Ton, S.Y.M. and Wortel, M.J.R. (1997) Slab detachment in continental collision zones: An analysis of controlling parameters. *Geophysical Research Letters* **24**, 2095-2098.
- Wörner, G., Zindler, A., Staudiget, H. and Schmincke, H.-U. (1986) Sr, Nd, and Pb isotope geochemistry of Tertiary and Quaternary alkaline volcanics from West Germany. *Earth and Planetary Science Letters* **79**, 107-119.
- Wortel, M.J.R. and Spakman, W. (1992) Structure and dynamics of subducted lithosphere in the Mediterranean region. *Proc. Kon. Ned. Akad. V. Wetensch* **95**, 325-347.
- Wortel, M.J.R. and Spakman, W. (2000) Subduction and slab detachment in the Mediterranean-Carpathian region. *Science* **290**, 1910-1917.
- Yang, H.-J., Kinzler, R.J. and Grove, T.L. (1996) Experiments and models of anhydrous, basaltic olivine-plagioclase-augite saturated melts from 0.001 to 10 kbar. *Contributions to Mineralogy and Petrology* **124**, 1-18.
- Yoder, H.S. and Tilley, C.E. (1962) Origin of basalt magmas: an experimental study of natural and synthetic rock systems. *Journal of Petrology* **3**, 342-532.
- Zampieri, D. (1995) Tertiary extension in the Southern Trento Platform, Southern Alps, Italy. *Tectonics* **14**, 645-657.
- Zartman, R.E. and Doe, B.R. (1981) Plumbotectonics – the model. *Tectonophysics* **75**, 135-162.
- Zeck, H.P. (1999) Alpine plate kinematics in the western Mediterranean: a westward-directed subduction regime followed by slab roll-back and slab detachment. In: Durand, B., Jolivet, L., Horvath, F. and Seranne, M. (eds) *The Mediterranean Basins: Tertiary Extension within the Alpine Orogen*. *Geological Society of London Special Publication* **156**, 109-120.
- Zhang, Y.-S. and Tanimoto, T. (1992) Ridges, hotspots and their interaction as observed in seismic velocity maps. *Nature* **355**, 45-49.

APPENDIX A
ISOTOPE REFERENCES

Magmatic Province	Individual Magmatic Centre	Reference
Tuscan Province	Mt. Amiata	Hawkesworth and Vollmer (1979)
		Vollmer (1977)
	Cimino	Hawkesworth and Vollmer (1979)
		Vollmer (1977)
	Montecatini	De Astis et al. (2000)
		Conticelli et al. (2002)
	Orciatico	De Astis et al. (2000)
		Conticelli et al. (2002)
	Roccastrada	Hawkesworth and Vollmer (1979)
		Vollmer (1977)
	Radicofani	Hawkesworth and Vollmer (1979)
		Vollmer (1977)
De Astis et al. (2000)		
San Vincenzo	Hawkesworth and Vollmer (1979)	
	Vollmer (1977)	
Torre Alfina	De Astis et al. (2000)	
	Conticelli (1998)	
Sisco	Conticelli et al. (2002)	
Roman Province	Alban Hills	D'Antonio et al. (1996)
		Hawkesworth and Vollmer (1979)
		Vollmer and Hawkesworth (1980)
		Federico et al. (1994)
	Sabatini	Hawkesworth and Vollmer (1979)
		Vollmer (1976)
	Vico	Hawkesworth and Vollmer (1979)
		Vollmer (1976)
	Vulsini	Hawkesworth and Vollmer (1979)
		Vollmer and Hawkesworth (1980)
		Vollmer (1976)
		Battistini et al. (2001)
		Rogers et al. (1985)
Conticelli et al. (2002)		
Southern Latium Transition Zone	Ernici	D'Antonio et al. (1996)
	Roccamonfina	Gianetti and Luhr (1990)
		D'Antonio et al. (1996)
		Hawkesworth and Vollmer (1979)
		Vollmer and Hawkesworth (1980)

Table A.1. References for Sr, Nd, and Pb isotopic data used in regional diagrams.

Internal Apennines Zone	Cupaello	Castorina et al. (2000)
		Bell (2000) (unpublished data)
		Battistini et al. (2001)
		Conticelli et al. (2002)
	Polino	Castorina et al. (2000)
		Bell (2000) (unpublished data)
	San Venanzo	Castorina et al. (2000)
		Bell (2000) (unpublished data)
		Battistini et al. (2001)
	Colle Fabbri	Castorina et al. (2000)
		Bell (2000) (unpublished data)
	Campanian Province	Ischia
Vollmer and Hawkesworth (1980)		
Hawkesworth and Vollmer (1979)		
Phlegrean Fields		Civetta et al. (1991)
Vesuvius		D'Antonio et al. (1996)
		Ayuso et al. (1998)
		Hawkesworth and Vollmer (1979)
		Vollmer and Hawkesworth (1980)
		Vollmer (1976)
Aeolian Arc		Alicudi
	Lipari	Esperanca et al. (1992)
	Salina	Gertisser and Keller (2000)
		Ellam et al. (1988)
	Stromboli	Renzulli et al. (2001)
		Fancalanci et al. (1993)
		Ellam et al. (1988)
	Vulcano	De Astis et al. (2000)
		Del Moro et al. (1998)
	Mount Vulture	Downes et al. (2002)
Hawkesworth and Vollmer (1979)		
Vollmer and Hawkesworth (1980)		
Vollmer (1976)		
Bell (2000) (unpublished data)		
Pietre Nere	Hawkesworth and Vollmer (1979)	
	Vollmer and Hawkesworth (1980)	
Tyrrhenian Sea	Gasperini et al. (2002)	
Sardinia	Lustrino et al. (2000)	
Mount Etna	Carter et al. (1978)	
	Armienti et al. (1995)	
	Carter and Civetta (1977)	
	Marty et al. (1994)	
Iblean Plateau	Carter and Civetta (1977)	
	Trua et al. (1998)	
Pantelleria	Esperanca and Crisci (1995)	

Table A.1. *Continued.*

Sample Number	Longitude	Latitude	Altitude (m)	Comments
WA 100	7°51'12" E	45°40'06" N	307	Gressoney Valley, at road junction between Fontainemore and Issime. Mica-rich dyke 2 m wide.
WA 101	7°52'11" E	45°39'17" N	1130	Gressoney Valley, between Fontainemore and Issime. Altered, amphibole-rich dyke.
WA 102		no GPS reading		Gressoney Valley, between Pont St. Martin and Lillianes, near bridge at Nantay. West-dipping dyke 3 m wide, located in river.
WA 103	7°48'48" E	45°37'21" N	770	Gressoney Valley, on road between Perloz and Marine. Altered dyke with visible sulphides.
WA 104	7°48'34" E	45°35'41" N	778	Gressoney Valley, between Carema and Pont St. Martin. Mica-rich, narrow 0.75 m wide dyke by roadside.
WA 105	7°49'32" E	45°36'45" N	914	Gressoney Valley, on road 2.5 km N of Carema, near Ciamp da Las. Mica-rich 2.5 m wide dyke with banded texture.
WA 106		no GPS reading		Approximately 7 km W of Biella, 1.8 km N of Netro, along river near Bossola. Mica-rich 2.5 m wide dyke.
WA 107		no GPS reading		Approximately 7 km W of Biella, 1.7 km N of Netro, along river near Bossola. Altered, amphibole-rich 5 m wide dyke with xenoliths.

Table B.1. Western Alps sample localities.

Sample Number	Series	Type	Longitude	Latitude	Altitude (m)	Comments
RC 100	HKS	lava	13°58'52" E	41°19'04" N	600	Lava flow, rich in 0.5-1.0 cm leucite phenocrysts.
RC 101	HKS	lava	13°58'20" E	41°19'20" N	582	Phenocryst-poor.
RC 102	HKS	lava	13°58'07" E	41°19'26" N	559	Leucite phenocrysts visible.
RC 103	HKS	dyke	13°57'39" E	41°19'40" N	511	Vertical 2m wide dyke, phenocryst-poor, glassy texture.
RC 104	KS	lava	13°59'24" E	41°22'09" N	255	Vesicular and glassy with dark grey groundmass, no visible leucite.
RC 105	KS	lava	13°59'46" E	41°19'37" N	440	Possible landslide deposit of large (0.5m) angular lava blocks.
RC 106	KS	lava	13°59'10" E	41°18'04" N	723	Lava dome, grey fine-grained groundmass with no visible leucite.
RC 107	KS	lava	13°58'26" E	41°18'08" N	720	Vesicular texture with visible olivine phenocrysts.
RC 108	HKS	lava	13°59'51" E	41°19'48" N	492	Lava dome, fresh leucite phenocrysts.
RC 109	HKS	lava	14°00'31" E	41°19'49" N	471	Lava flow with rare visible clinopyroxene phenocrysts.
RC 110	KS	lava	13°58'53" E	41°21'32" N	345	Located outside main caldera, banded texture.
RC 111	KS	lava	13°56'29" E	41°19'39" N	438	Lava flow about 5m thick, overlying HKS lava flow.
RC 112	HKS	lava	13°56'30" E	41°19'38" N	435	Lava flow with abundant leucite phenocrysts.
RC 113	HKS	lava	13°56'03" E	41°19'32" N	423	Similar to RC 112, very fine-grained.
RC 114	HKS	lava	13°55'43" E	41°19'13" N	404	Slightly altered with visible leucite phenocrysts.
RC 115	HKS	lava	13°55'24" E	41°18'50" N	380	Lava flow with thin white banding and no visible phenocrysts.
RC 116	KS	lava	13°55'18" E	41°18'16" N	431	Leucite and pyroxene phenocrysts, banded texture.
RC 117	HKS	lava	13°56'54" E	41°16'18" N	461	Phenocryst-poor lava flow, overlain by another HKS flow.
RC 118	HKS	lava	13°56'55" E	41°16'16" N	459	Similar to RC 117, but more vesicular.
RC 119	KS	lava	13°58'24" E	41°17'02" N	570	Fine-grained with visible mica.
RC 120	KS	lava	13°57'20" E	41°17'25" N	605	Vesicular, grey groundmass, no visible leucite.
RC 121	KS	lava	13°57'22" E	41°17'21" N	578	Similar to RC 120 but with reddish groundmass.
RC 122	KS	lava	13°57'08" E	41°17'43" N	762	Phenocryst-rich lava flow with very fresh mica and clinopyroxene.
RC 123	HKS	lava	13°56'54" E	41°18'28" N	795	Thin (1-2m) lava flow on caldera rim.
RC 124	HKS	lava	13°56'48" E	41°18'14" N	842	Lava flow on caldera rim, large 0.5-1.5 cm leucite phenocrysts.
RC 125	HKS	lava bomb	13°57'54" E	41°16'22" N	570	Juvenile lava bomb in welded spatter deposit, phenocryst-poor.
RC 126	KS	scoria	13°59'31" E	41°16'37" N	535	Scoria from scoria and ash flow, very fine-grained.
RC 127	KS	lava bomb	13°59'09" E	41°16'45" N	575	Located in possible mudflow related to caldera collapse.
RC 128	KS	lava	13°59'30" E	41°17'43" N	590	Large (7m) lava boulder just inside caldera rim.

Table B.2. Roccamonfina sample localities.

Sample Number	Series	Type	Longitude	Latitude	Altitude (m)	Comments
ER 100	HKS	lava	13°19'11" E	41°40'33" N	282	Lava flow from most northerly eruptive centre, likely not in situ.
ER 101	HKS	lava	13°19'42" E	41°40'56" N	262	Located in house excavation near northerly eruptive centre.
ER 102	-	pyroclastic	13°17'13" E	41°35'39" N	156	Pyroclastic material from building site, contains visible phlogopite.
ER 103	HKS	lava	13°17'04" E	41°35'22" N	161	Boulders of unaltered lava under rail track (near Patrica).
ER 104	HKS	lava	13°17'16" E	41°35'08" N	174	Beside tunnel entrance, lava flow covered by lapilli (near Patrica).
ER 105	HKS	lava	13°16'35" E	41°32'24" N	308	Fresh lava flow (S of Giuliano di Roma).
ER 106	HKS	lava	13°16'49" E	41°32'14" N	275	Fresh lava flow by roadside (S of Giuliano di Roma).
ER 107	HKS	lava	13°16'30" E	41°32'31" N	283	Lava flow from house excavation (S of Giuliano di Roma).
ER 108	KS	scoria	13°18'35" E	41°33'43" N	179	Altered (<10cm diameter) scoria from fall deposit (W of Ceccano).
ER 109	KS	lava bomb	13°18'34" E	41°33'44" N	192	Rounded fine-grained lava bomb in surge deposit (W of Ceccano).
ER 110	HKS	lava	13°18'15" E	41°33'52" N	229	Lava block from top of small cone (W of Ceccano).
ER 111	HKS	lava	13°18'17" E	41°33'54" N	238	Lava block from top of small cone (W of Ceccano).
ER 112	KS	scoria	13°18'31" E	41°31'00" N	175	Large (25x25cm) scoria in fall deposit (near S. Stefano).
ER 113	KS	scoria	13°18'27" E	41°31'06" N	166	Scoria 3-8 cm in size with fresh cpx visible (near S. Stefano).
ER 114	KS	lava bomb	13°20'33" E	41°32'36" N	170	Lava bomb (12x20cm) in surge dep, beside rail track (S of Ceccano).
ER 115	HKS	lava bomb	13°19'22" E	41°33'27" N	155	Lava bomb (10x20cm) in surge deposit (SE of Ceccano).
ER 116	KS	lava bomb	13°21'31" E	41°33'55" N	192	Lava bomb (20x25cm) in scoria fall (ENE of Ceccano).
ER 117	KS	lava bomb	13°23'24" E	41°35'13" N	271	Lava bomb with visible cpx in scoria fall (Arnara).
ER 118	HKS	lava	13°25'03" E	41°34'34" N	199	Lava fragment from lapilli fall (Pofi).
ER 119	HKS	lava	13°24'49" E	41°34'01" N	240	Lava autobreccia wall, likely very close to vent location (Pofi).
ER 120	HKS	lava bomb	13°25'24" E	41°34'16" N	247	Lava bomb in surge deposit (Pofi)
ER 121	KS	lava	13°21'18" E	41°33'28" N	150	Lava fragment (30x30cm) in pyroclastic deposit (ESE of Ceccano).
ER 122	KS	scoria	13°21'32" E	41°33'42" N	152	Scoria in spatter deposit, likely close to vent (ESE of Ceccano).

Table B.3. Ernici sample localities.

APPENDIX C

LAMPROPHYRE CLASSIFICATION

Light-coloured constituents		Predominant mafic minerals		
<i>feldspar</i>	<i>foid</i>	<i>biotite > hornblende, ± diopsidic augite, (± olivine)</i>	<i>hornblende, diopsidic augite, (± olivine)</i>	<i>brown amphibole, Ti-augite, olivine, biotite</i>
or > pl	-	minette	vogesite	-
pl > or	-	kersantite	spessartite	-
or > pl	feld > foid	-	-	sannaite
pl > or	feld > foid	-	-	camptonite
-	glass or foid	-	-	monchiquite

Table C.1. Lamprophyre classification based on predominant felsic and mafic silicate mineralogy (Le Maitre et al., 2002). or = alkali feldspar; pl = plagioclase; feld = feldspar; foid = feldspathoid.

APPENDIX D
MINERALOGY AND TEXTURE OF RC AND ER SAMPLES

D.1. Roccamonfina

Sample RC100

Groundmass (48%)

Mineral	Percent	Description
leucite	10%	small, subrounded, not really straight sided, more irregular
feldspar	28%	plag, shows poly twinning, some w/ sieve texture, some without, many with ragged ends
clinopyroxene	10%	small higher birefringence crystals, strongly suspect px, shows px cleavage and crystal shape
opagues	trace	abundant cubic disseminated

Overall texture and comments

-fine-grained, much of groundmass is cryptocrystalline with low xp (likely feldspar, included with feldspar %).

Phenocrysts (52%)

Mineral	Percent	Description
leucite	40%	abundant, ranging from 2 mm to 8 mm, a few are euhedral, most are sub to anhedral, rounded, not fractured, some porous zones, some with thin cryptocrystalline rim, some with needle-like apatite inclusions
feldspar	8%	plagioclase with sieve texture
clinopyroxene	4%	euhedral, low yellow xp, concentric zoning, light green in ppl, up to 2 mm in length

Overall texture and comments

-porphyritic, lots of leucite.

Sample RC101

Groundmass (75%)

Mineral	Percent	Description
leucite	50%	abundant small round, sub to anhedral, some with apatite inclusions
feldspar	20%	euhedral, slight trachytic texture, plag, abundant
glass	5%	dark in ppl, between feldspar
opagues	trace	abundant tiny
clinopyroxene?	small	low-med xp material, not sure if cpx

Overall texture and comments

-fine-grained, some glass.

Phenocrysts (25%)

Mineral	Percent	Description
leucite	20%	some subhedral, most small (< 3 mm) but several about 1 cm, some with apatite inclusions, clean sides, slightly fractured. A number of small growths of multiple crystals.
clinopyroxene	5%	low grey-yellow xp, green in ppl, fairly small, some broken and fractured, some simple twinned, some elongate
relict amph?	trace	strong cleavage (in photo), with holes, brown in ppl, dark brown-blue xp, concentric zoning, inclined extinction

Overall texture and comments

-porphyritic with abundant leucite. Lack of feldspar phenocrysts. Lack of different mineral types as phenocrysts.

Sample**RC102****Groundmass (65%)**

Mineral	Percent	Description
leucite	20%	abundant small round
feldspar	40%	euhedral laths in random texture, suspect plag, some aligned to 'flow' around leucite
opagues	trace	abundant tiny
apatite	trace	rims and as inclusions in leucite
clinopyroxene	5%	suspect, many broken small fragments of light brown-green mineral, variable xp but usually low yellow xp

Overall texture and comments

-fine-grained, fair amount of groundmass is dark-coloured cryptocrystalline

Phenocrysts (35%)

Mineral	Percent	Description
leucite	28%	some with porous zones, rimmed by apatite, most med-size (about 1 mm), some broken
clinopyroxene	7%	green-brown, cleavage visible, slight pleochroism, blue-pink xp, inclined extinction, some show simple twinning, 1 seen as inclusion in larger leucite. Some anhedral and quite fractured, concentric zoning.

Overall texture and comments

-contains large (1.2 cm) leucite phenocrysts (2 on slide). Small amount of brown material, isotopic: glass. Lack of many types of phenocrysts. Some light brown alteration, fine-grained, isotropic, beside leucite phenocryst.

Sample**RC103****Groundmass (88%)**

Mineral	Percent	Description
leucite	40%	abundant skeletal, variety of cross, star, circle shapes
opagues	trace	very small, abundant
feldspar	28%	likely plag, laths, euhedral but with jagged ends and fish-tails, tiny
apatite	trace	
glass	20%	devitrified

Overall texture and comments

-fine-grained, glassy, with skeletal crystals, cryptocrystalline, dark in ppl, some reddish areas

Phenocrysts (12%)

Mineral	Percent	Description
leucite	6%	med-size, rounded, most in small clumps, non-skeletal, sparse larger leucite (up to 1 mm)(trace)
chlorite?	1%	light green in ppl, no pleochroism
clinopyroxene	3%	most is anhedral, without strong cleavage, quite small, fractured, weak brown-green pleochroism
amphibole	2%	mass of green amp near one end of slide, quite badly fragmented, with many holes, randomly oriented

Overall texture and comments

-not many mineral types present
-no apparent reaction between amp cluster and main rock

Sample RC104**Groundmass (80%)**

Mineral	Percent	Description
feldspar	45%	very tiny plag laths/needles, grey xp
amphibole?	25%	abundant sub to euhedral clear, low yellow-grey xp, mod-high relief, elongate but usually < 90 degree angle, some show swallow-tail
opagues	trace	tiny disseminated
glass	10%	
olivine	trace	bright blue xp, anhedral to subhedral

Overall texture and comments

*Highly vesicular, fine-grained to glassy. Some areas have a weak trachytic texture.

Phenocrysts (20%)

Mineral	Percent	Description
clinopyroxene	5%	fairly clear with slightly brown rims, indistinct cleavage, bright pink to med yellow xp, possibly olivine, some is euhedral, largest about 2 mm, simple twinning
amphibole (1)	13%	strong cleavage, same as seen in groundmass, clear/pale green, yellow xp
feldspar	2%	resorbed phenocryst, unhappy feldspar (plag?), undulose extinction, all are broken, rough ends
amphibole (2)	trace	small brown crystals, not abundant, not isotropic, diff amphibole type

Overall texture and comments

*No leucite observed.

Sample RC105**Groundmass (70%)**

Mineral	Percent	Description
opagues	trace	abundant, very small, cubic to irregular
feldspar	40%	likely plag, not in nice laths
glass	30%	

Overall texture and comments

-fine-grained to cryptocrystalline groundmass, abundant very tiny unknown laths (plag or apatite?)

Phenocrysts (30%)

Mineral	Percent	Description
clinopyroxene	7%	zoned, light brown centre, dark brown edge in ppl, euhedral but corroded, quite small, some green in ppl, appear altered, anhedral, anomalous bright xp
tabulate black area	1%	fuzzy edges, small, relict mica?
altered feldspar?	6%	clear in ppl, anomalous light brown to grey xp, some w/ simple twinning, undulose extinction (sanidine?), broken, some glomeroporphyritic
amphibole?	13%	greenish edges, many broken, core altered
altered olivine	2%	in dark area only, cored by hole, no cleavage, bright xp

Overall texture and comments

-sort of fresh, definitely needs probing for correct mineral ID, appears to be magma mingling, can clearly see dark (75% of slide) and light (25% of slide) of areas on slide with naked eye (see rough notes for description of dark and light areas separately), some areas quite messy looking, altered with reddish-brown coloration, some chloritization, 1.5 mm clear crystal in ppl, triangular (1%), no cleavage, corroded edges, light yellow in xp, suspect quartz. Most phenocrysts are quite altered and difficult to identify. Central blob contains 2.5 mm hole that is rimmed by clear crystals, tabulate, euhedral, 1st order xp, some with simple twinning – suspect sanidine.

* No reaction or difference mineralogy/texture at contact of 2 magmas.

Sample RC106**Groundmass (40%)**

Mineral	Percent	Description
feldspar	40%	plag, some with swallow-tails, tabulate euhedral, unaltered, strong trachytic texture, 'flow' around phenocrysts
apatite	trace	small laths in groundmass
opagues	trace	disseminated very small

Overall texture and comments

-fine-grained with trachytic texture

Phenocrysts (60%)

Mineral	Percent	Description
mica	10%	dark-light brown pleochroism, euhedral but with holes, strong cleavage
relict amph?	trace	skinny elongate dark fuzzy
opagues	trace	larger cubic corroded
feldspar	30%	most show simple twins, 1 st order xp, concentric zoning. Plag, some are broken, sieve texture & included opagues and ap, up to 2 mm, abundant, some med and many larger crystals, most euhedral, some glomeroporphyritic (5%). A few are quite rounded
clinopyroxene	9%	highly fractured, light green/brown, broken, light yellow xp, suspect px (opx?)
amphibole	6%	may be 2 types, light green, included opagues, no pleochroism

Overall texture and comments

*phenocryst-rich. Large (1.5 mm) brown fragment, resembles c-axis mica flake, brown in xp, undulose extinction. A few holes.

*No leucite observed.

Sample RC107**Groundmass (50%)**

Mineral	Percent	Description
feldspar	50%	euhedral, trachytic texture, small to med size, suspect sanidine, shows simple twinning, some may be fish-tail
opagues	trace	very small, disseminated

Overall texture and comments

-fine-grained with distinct trachytic texture of small-medium size groundmass feldspars. Vesicular, vesicles elongated parallel to trachytic texture. Cryptocrystalline, dark.

Phenocrysts (50%)

Mineral	Percent	Description
clinopyroxene	10%	good cleavage, light brown in ppl, 1 st and 2 nd order xp, subhedral, some are glomeroporphyritic, xp a bit anom.
feldspar	28%	continuous size distribution from groundmass to phenocrysts, suspect sanidine. Euhedral, med-size, slightly porous, max size 0.9 mm. Sieve-textured cores.
nepheline (?)	4%	1 st order xp, euhedral, not sure on ID, with exsolution lamellae, near edge of slide.
olivine	8%	small, suspect, bright xp, clear in ppl, fractured with no cleavage, seen under high power, anhedral

Overall texture and comments

-contains black area 2 mm wide, rimmed by reddish material and with hole in centre. Rock is dominated by feldspar laths of various sizes.

*No leucite observed.

Sample RC108**Groundmass (73%)**

Mineral	Percent	Description
leucite	25%	abundant, small, round, not skeletal, commonly rimmed by very tiny apatite
amphibole	15%	elongate, green fairly abundant
opagues		tiny, ubiquitous
feldspar	28%	low grey xp, fairly cryptocrystalline. Some are more well-formed laths also
pyroxene?	5%	hard to tell, quite small

Overall texture and comments

-seen well on medium power

Phenocrysts (27%)

Mineral	Percent	Description
clinopyroxene	5%	weak brown-green pleochroism, euhedral, some with strong cleavage, some glomeroporphyritic, weak concentric zoning. 2 crystals are heavily altered isotropic, anhedral. May be 2 types present.
dark masses	1%	unknown – clump of opagues or relict mineral
amphibole	10%	suspect, green-brown pleochroic, elongate, with holes & opaque inclusions
unknown	trace	clear, cleavage about 120 degrees, bright anom. yellow xp, strong reaction rim of opagues + cryptocrystalline material
feldspar	5%	suspect sanidine + plag. low xp, broken on ends, subhedral, some plag with oscillatory zoning
mica	trace	a few long thin relict black mica
leucite	6%	1.2 cm large phenocrysts + a few smaller crystals, some broken

Overall texture and comments

-Two most striking feature: 1.2 cm very large leucite, and 1 cm 'green blob'. Closer inspection of the blob reveals... subhedral but broken at edges light green cpx, fractured, prominent cleavage. Diff type of cpx, light brown, anhedral. Mica, small brown pleochroic, 1 cleavage, suspect. Elongate green mineral surrounding blob – possibly amphibole. A few cubic to rounded opagues as inclusions in cpx. Unknown highly altered red-brown patches, some are rounded, some tabulate, no xp colour. Some small rounded inclusions in cpx also, low grey xp, qtz or likely feldspar, some look porous. Apatite also present.

Strong disequilibrium evidence

Sample RC109**Groundmass (92%)**

Mineral	Percent	Description
leucite	27%	very small, rounded, abundant
opagues	trace	abundant, very small, cubic
feldspar	65%	euhedral laths, show random alignment, jagged ends – rapid cooling, simple twins. Suspect sanidine.
apatite	trace	tiny stubs
relict mica?	trace	light-dark brown pleochroism, anom. xp, strong cleavage

Overall texture and comments

-fine-grained. Vesicular: some show aligned elongation. Very small bright xp mineral in groundmass - mica or cpx.

Phenocrysts (8%)

Mineral	Percent	Description
clinopyroxene (1)	1%	light green, slightly darker green rim, indistinct cleavage, anhedral, fractured, low xp (light brown-yellow)
clinopyroxene (2)	5%	subhedral-euhedral, light brown with darker rim, bright pink-yellow xp, strong concentric zoning
relict amph	trace	suspect, green, weak pleochroism (light-dark green), displays amph cleavage, fairly altered, especially in core
mica	2%	strong suggestion of small mica scattered throughout, most sub to anhedral, brown w/ pleochroism, not isotropic, anom blue-pink xp

Overall texture and comments

*phenocryst-poor. Some larger cpx rimming vesicle – suggests plucking of clump of cpx.

No leucite phenocrysts observed.

Sample RC110**Groundmass (78%)**

Mineral	Percent	Description
feldspar	60%	strongly trachytic plag laths, euhedral
clinopyroxene	18%	small cored, euhedral, good cleavage, clear to light brown, low to anom. xp.
opagues	trace	abundant very tiny

Overall texture and comments

-very fine-grained, strongly aligned trachytic feldspar, some glassy areas.

Phenocrysts (22%)

Mineral	Percent	Description
clinopyroxene	14%	light brown, euhedral, reddish rim on some larger crystals, concentric zoning, good cleavage, low grey xp, some cored lengthwise, many quite broken
feldspar	4%	euhedral with rounded edges, plag, grey xp, others quite rounded. Possible nepheline present (trace)
mica	2%	light-dark brown pleochroic with parallel extinction, some broken chunks, have darker rims
olivine	2%	rounded, relatively unfractured, clear, bright yellow xp

Overall texture and comments

-clear dark and light banding of the very fine-grained groundmass, some reddish-brown alteration. Some small vesicles. Long edge of cpx aligned with trachytic flow direction.

*No leucite observed.

Sample RC111**Groundmass (80%)**

Mineral	Percent	Description
feldspar	55%	trachytic, lath-shaped, euhedral, many show simple twinning
clinopyroxene	15%	fairly abundant, small, sub-rounded to slightly elongate, low yellow xp, suspect
opagues	trace	moderate amount, tiny
glass	10%	isotropic

Overall texture and comments

-fine-grained, trachytic, glassy

Phenocrysts (20%)

Mineral	Percent	Description
mica	trace	may have small reaction rim, 3 mm, broken, good cleavage, brown pleochroism, parallel extinction, irregular edges, located adjacent to several holes
clinopyroxene	8%	subhedral, shows simple twinning, some glomeroporphyritic, brown in ppl, low brown-grey xp but has inclined extinction, some weak concentric zoning, some fairly euhedral, some broken
feldspar	9%	low grey anhedral to euhedral, some simple twinned, suspect sanidine, elongate, with some fractures. Plag phenocryst 1mm shows polysynthetic twinning, holes, subhedral, low grey xp.
olivine	3%	bright orange xp, rounded, clear in ppl, reddish rim, high relief

Overall texture and comments

-medium to low amount of phenocrysts, some black patchy areas.

*No leucite observed.

Sample RC112**Groundmass (62%)**

Mineral	Percent	Description
leucite	15%	small round
opaques	trace	abundant disseminated
feldspar	32%	plag laths
amphibole	15%	small green, fairly abundant
apatite	trace	needles

Overall texture and comments

-fine-grained

Phenocrysts (38%)

Mineral	Percent	Description
leucite	25%	large, pseudo-isometric to rounded, w/ apatite inclusions in core, size up to 1 cm, some elongated, w/ porous zones. Some strongly rimmed by apatite (also seen in Gm lc).
clinopyroxene	6%	green, irregular concentric zoning, euhedral, some fairly strong green, weak green-brown pleochroism. Large cpx and leucite together. May be more than 1 type present.
amphibole	6%	green, more green than px, euhedral but broken, brighter xp (blue)
feldspar	1%	some plag observed in large mass, but not much other free feldspar phenocrysts seen
mica	trace	inside a leucite phenocryst, brown

Overall texture and comments

-with fairly abundant leucite phenocrysts

Some interesting textures in leucite and plagioclase observed...lc cored by fresh plag with a rim of altered plag, plag rims on pre-existing plag, possibly pseudoleucite.

Sample RC113**Groundmass (64%)**

Mineral	Percent	Description
leucite	25%	small crystals, abundant, rounded to euhedral
apatite	trace	abundant, small stubby crystals, tabular, clear, high relief, random orientation
opaques	trace	abundant, tiny, cubic
feldspar	incl. in 38%	laths
black areas	1%	unknown

Overall texture and comments

-fine-grained, much of groundmass is cryptocrystalline (38%).

Phenocrysts (36%)

Mineral	Percent	Description
leucite	12%	larger and medium-size, up to 1.5 mm, contain ap and cpx inclusions
relict mica (?)	trace	unknown black altered relict mica or amph, shows light-dark brown pleochroism
clinopyroxene	10%	square with good cleavage, light brown in ppl, 1 st order xp, some are anhedral and quite rounded, weakly green-brown pleochroic, some quite broken
amphibole	8%	green in ppl, yellow-brown in xp, very corroded edges, suspect, largest about 1.5 mm, some quite broken
nepheline?	6%	unknown yellow-grey xp, clear ppl, some appear simple-twinned, similar to that seen in RC 105, up to 1 mm, maybe sanidine. But some show concentric zoning. Suspect a thick section.

Overall texture and comments

-porphyritic texture, a few holes (not sure if vesicles), leucite very abundant. Some mm-size black areas (1%).

Sample RC114**Groundmass (60%)**

Mineral	Percent	Description
apatite	3%	included in leucite phenocrysts and groundmass lc. In linear zones...result of fluid flow through lc? Also concentrated along edges of lc crystals.
opagues	trace	as inclusions in leucite
leucite	57%	small, rounded
feldspar	crypto	lath-shaped, randomly oriented

Overall texture and comments

-cryptocrystalline, likely feldspar + apatite + opaques + lc

Phenocrysts (40%)

Mineral	Percent	Description
leucite	25%	large (0.1-0.8 cm) many are euhedral, pseudo-isometric shapes, some are broken or have corroded rims. Many have zones of microporosity, some small fractures, especially near edges. Contain acicular needles of apatite.
clinopyroxene (suspect subcalcic)	8%	strong brown-green pleochroism, high xp, indistinct cleavage, many inclusions, some concentric zoning
amphibole	7%	weakly brown-green pleochroic, green rims, subhedral, broken ends, typical amph cleavage, some concentric zoning
unknown	trace	small thin red

Overall texture and comments

-visibly porphyritic with naked eye, dominated by large (0.1 – 0.8 cm) leucite phenocrysts. Some reddish alteration along fractures. Both cpx and amph are intergrown with leucite in some places. Some fracturing resembles olivine, but is probably px. 1 mm anhedral (px?) green, with inclusions.

Sample RC115**Groundmass (65% is cryptocrystalline)**

Mineral	Percent	Description
leucite	20%	small, contain inclusions of ap (1%) and opaques, abundant, appear almost skeletal at first but are not, some have corroded edges
feldspar	incl. in 65%	small, lath-shaped crystals, but have anomalous blue-yellow xp... due to section. Plag with polysynthetic twinning and ragged ends observed (2%).
opagues	trace	abundant tiny
clinopyroxene (?)	4%	small cluster with leucite, anomalous xp but cleavage suggests px

Overall texture and comments

-fine-grained, cryptocrystalline groundmass (65%), messy-looking, may be slightly altered

Phenocrysts (35%, but all are microphenocrysts)

Mineral	Percent	Description
feldspar	8%	microphenocrysts, euhedral, sometimes broken, may be sanidine or nepheline
lc, cpx, plag, ap	27%	see above

Overall texture and comments

*thick section

-abundant leucite, no large phenocrysts of anything. Most non-leucite minerals are difficult to identify: altered. Near end of slide, can resolve simple-twinning sanidine euhedral small laths. Appears to also have plag in groundmass. May contain olivine also, but hard to distinguish from altered cpx.

Sample RC116**Groundmass (80%)**

Mineral	Percent	Description
feldspar	80%	felty texture, likely plagioclase
mica (?)	trace	light brown both in ppl and xp
opauscs	trace	abundant, very small, cubic black, euhedral, disseminated

Overall texture and comments

-fine-grained, consists primarily of feldspar microlites, random alignment. Some dark cloudy areas, black in ppl, indistinct boundaries, unknown. Also unknown material between plag microlites: clear in ppl, almost black in xp, possibly leucite but no x-hatch pattern observed. No vesicles observed.

Phenocrysts (20%)

Mineral	Percent	Description
olivine	3%	anhedral, random fractures, reddish rim alteration
feldspar	5%	tabulate, simple twins, some 1-2 mm crystals of zoned plag, some with sieve texture
clinopyroxene (1)	9%	many euhedral, likely augite, light brown, edges very slightly corroded, larger, good cleavage
clinopyroxene (2)		smaller subhedral to euhedral, green in ppl, show simple twinning and concentric zoning, more corroded, many opaque inclusions
mica	3%	brown, pleochroic

Overall texture and comments

-some feldspar is glomeroporphyritic with cpx, possibly some 2-pyroxene intergrowth. Several high relief light grey ppl (grey xp) crystals: unknown. 3mm cluster of feldspar + cpx at one end, sieve texture obvious.

*No leucite observed.

Sample RC117**Groundmass (92%)**

Mineral	Percent	Description
leucite	60%	skeletal, clear in ppl, pseudo-isotropic in xp, variety of cross, star, and circle shapes
feldspar	4%	very small microlites, lath-shaped, euhedral
*glass	28%	
pyroxene (?)	trace	very small
opauscs	trace	scarce, very small, euhedral

Overall texture and comments

-very fine-grained, groundmass full of skeletal leucite, much is cryptocrystalline, glassy. Some irregular vesicles.

Phenocrysts (8%)

Mineral	Percent	Description
leucite	6%	rounded, size 1-1.5 mm
clinopyroxene	2%	euhedral, < 1 mm, good cleavage, light brown in ppl, some show concentric zoning, several have irregular zoning
olivine (??)	trace	suspect olivine, but prob. cpx, broken on 1 side, euhedral, cleavage indistinct, some fractures
feldspar	trace	sparse microphenocrysts, show polysynthetic twinning, euhedral

Overall texture and comments-3mm unusual patch of vesicular material w/even finer grained groundmass, contains no phenocrysts.

Sample RC118**Groundmass (95%)**

Mineral	Percent	Description
leucite	70%	skeletal, very fine-grained
feldspar	4%	very small microlites, likely plag, lath-shaped
pyroxene (?)	trace	
opaques	trace	scarce, disseminated, euhedral, cubic
*glass	21%	

Overall texture and comments

* very similar in texture and mineralogy to RC 117, but with more elongate vesicles (up to 0.8 cm).

Phenocrysts (5%)

Mineral	Percent	Description
leucite	3%	up to 0.6 cm
clinopyroxene	2%	euhedral, good cleavage visible, light brown, low birefringence (yellow-brown), some with simple twinning, some glomeroporphyritic, a few with concentric zoning
mica	trace	elongate, pleochroic: light to dark brown, dark rims

Overall texture and comments

-photo shows zoned cpx about 1 mm in length. One large hole filled with broken leucite.

Sample RC119**Groundmass (60%)**

Mineral	Percent	Description
feldspar	45%	tiny lath-shaped euhedral, suspect plag, weak alignment
opaques	trace	
apatite	trace	
amphibole	15%	small light brown, abundant, low brown-yellow xp, suspect
olivine	trace	suspect small rounded fractured, yellow xp, clear in ppl

Overall texture and comments

-fine-grained

Phenocrysts (40%)

Mineral	Percent	Description
clinopyroxene	8%	light brown-green in ppl, weak brown-green pleochroism, cleavage visible, subhedral to euhedral, fairly small, beige xp, some glomeroporphyritic
mica	6%	strong light brown-dark brown pleochroism, anom. brown xp, 2 strong cleavages, prominent dark rim
feldspar	22%	plagioclase, concentric zoning, abundant, up to 1.8 mm. Middle is altered, porous, sides are fractured. Most show altered core with preserved euhedral concentric rim. Core black in xp, some look wormy
amphibole?	4%	euhedral light green, bright blue xp, fractured w/ opaque inclusions, indistinct cleavage, slight concentric zoning, larger than cpx, suspect

Overall texture and comments

-porphyritic, irregular holes in slide, fairly abundant

*Strong disequilibrium evidence, med-high amount of phenocrysts

*No leucite observed.

Sample RC120**Groundmass (54%)**

Mineral	Percent	Description
feldspar	48%	abundant, small lath-shaped with simple twinning, moderate to strongly trachytic texture
opaques	trace	some disseminated, tiny
mica?	2%	elongate, black, opaque, black xp, relict, crystal shape reminiscent of mica, no visible internal features
clinopyroxene	4%	small euhedral to subhedral green, mod. brown xp, some cleavage visible
apatite	trace	

Overall texture and comments

-fine-grained, vesicular (8%) – most are small rounded to irregular. Are vesicles filled with a late-stage mineral?

Phenocrysts (38%)

Mineral	Percent	Description
feldspar	20%	abundant ~1 mm size plagioclase, concentrically zoned and poly twinned, sieve texture, most fairly euhedral, some anhedral, some glomeroporphyritic and complexly zoned. Many with replaced cores of light brown material in ppl.
relict mica	6%	opaque, small core of brown material left shows bird's eye parallel extinction. Some are bent.
clinopyroxene	12%	light green (up Fe), eu to anhedral, some broken, mod to high xp, some have dark rims, some are zoned but not most

Overall texture and comments

-porphyritic, fairly phenocryst-rich. Mica replaced by degassing to cpx + mag +/- plag. Some glomeroporphyritic clumps of plag and cpx.

*No leucite observed.

Sample RC121**Groundmass (60%)**

Mineral	Percent	Description
feldspar	45%	abundant trachytic plag laths, some with fish-tail
opaques	trace	disseminated, tiny
relict mica	2%	small opaque, no internal features visible
clinopyroxene	13%	small light brown, fairly anhedral (grouped with numerous small light brown fragments, too small to see features, anom. xp, suspect cpx)

Overall texture and comments

-fine-grained, with some irregular vesicles (5%)

Phenocrysts (35%)

Mineral	Percent	Description
feldspar	15%	sieve-textured plag with obvious poly twinning, about 1.5 mm in size, some glomeroporphyritic, euhedral to anhedral, broken
mica	8%	good cleavage, euhedral to subhedral, brown, parallel extinction, replaced by black material on rims, some cores preserved, some are bent
clinopyroxene	12%	light brown, good cleavage, mod-high xp, inclined extinction, simple twinning, up to 3 mm in size. Some with mica inclusions.

Overall texture and comments

-similar to RC120, porphyritic

*No leucite observed.

Sample RC122**Groundmass (66%)**

Mineral	Percent	Description
feldspar	60%	very tiny laths, some with fish-tail, slight to moderate trachytic texture
apatite	trace	very tiny
opaques	trace	very tiny, some with red edges
clinopyroxene	3%	moderate xp
mica	2%	small black elongate

Overall texture and comments

-extremely fine-grained. Vesicular – about 8% of rock.

Phenocrysts (34%)

Mineral	Percent	Description
feldspar	22%	very unhappy plag, some of euhedral shape preserved, even rim affected, edges corroding. Largest 2-3 mm. With isotropic parts.
clinopyroxene	5%	green, eu to subhedral, fractured, yellow/brown xp
mica	5%	with dark black rim, brown pleochroic eu-subhedral, also in groundmass as slender black crystals. Edges of some being absorbed. Largest ~ 2 mm.
olivine	2%	with red rim, mod yellow xp, small rounded, largest 1 mm

Overall texture and comments

-porphyritic. Several clumps (~ 4 mm) of cpx + plag contains small light brown fresh mica

*No leucite observed.

Sample RC123**Groundmass (67%)**

Mineral	Percent	Description
feldspar	20%	small plag with ragged ends and sides, subhedral laths, trachytic texture, all have poly twinning
clinopyroxene	crypto	small green low to high xp, good cleavage, euhedral to anhedral
leucite	crypto	small round
olivine	2%	small amount, rounded, clear in ppl, bright xp
muscovite	trace	

Overall texture and comments

-fine-grained. Vesicular – up to 5% of rock. Much of groundmass is dark, cryptocrystalline (45%), glassy.

Phenocrysts (33%)

Mineral	Percent	Description
leucite	25%	abundant, eu to subhedral, some fractured, with apatite inclusions, up to 2 mm.
clinopyroxene	8%	green subhedral, smaller than leucite

Overall texture and comments

-porphyritic. Small amount of light brown material – mica (?) or maybe glass. Light green-brown area in leucite, anom. low grey xp, maybe chloritoid.

Sample RC124**Groundmass (65%)**

Mineral	Percent	Description
leucite	25%	small, sub to anhedral, irregularly-shaped
feldspar	35%	laths, most tiny but some bigger, simple twins
clinopyroxene	5%	small euhedral light brown, fair amount, simple twinned
apatite	trace	fair amount scattered throughout
opaques	trace	some small black cubic

Overall texture and comments

-fine-grained. Contains circular and sub-circular areas – vesicle? have fine-grained black material inside, suspect mounting media. Some light brown isotropic material – glass?

Phenocrysts (35%)

Mineral	Percent	Description
leucite	22%	eu to subhedral, some with apatite inclusions, largest up to 0.9 cm, some look like broken fragments, some contain opaque inclusions with red rims
clinopyroxene	10%	with weak brown-green pleochroism, light yellow/brown xp, included extinction, up to 2-3 mm, concentric zoning
mica?	trace	may be present as small inclusions in cpx, not sure
feldspar	3%	sparse medium-size plag

Overall texture and comments

-porphyritic with large leucite phenocrysts. Suspect olivine with clear ppl, reddish rim, but low grey xp.

Sample RC125**Groundmass (77%)**

Mineral	Percent	Description
leucite	34%	abundant eu to subhedral, subrounded
apatite	trace	as inclusions in leucite
feldspar	3%	sparse laths, show simple twinning
clinopyroxene	40%	small anhedral brown and green (% includes much of groundmass that is dark and cryptocrystalline)
opaques	trace	small amount, scattered

Overall texture and comments

-fine-grained *about 5% of rock is composed of irregular vesicles.

Phenocrysts (23%)

Mineral	Percent	Description
leucite	15%	euhedral, subrounded, with apatite inclusions near rims, abundant, some with micropores. Largest 3-4 mm contains plag inclusions + brown-green pleochroic cpx)
clinopyroxene	6%	green, zoned, largest 3mm, broken and partially resorbed. In cracks can see brown material, isotropic – glass? Smaller green cpx, subhedral, are throughout sample, some concentrically zoned.
mica	trace	small amount of brown mica seen as inclusions in cpx near edge of slide
feldspar	2%	sparse, unhappy, subhedral with holes, less than 1mm

Overall texture and comments

-porphyritic with leucite phenocrysts. Some larger opaques in cluster with cpx + plag. Fluid inclusions visible in leucite phenocrysts.

Sample RC126**Groundmass (81%)**

Mineral	Percent	Description
mica	5%	small kinked brown pleochroic, some with fish-tails
apatite	trace	very tiny
feldspar	3%	very small amount of laths
cpx	2%	
unknown	trace	small red-brown mineral

Overall texture and comments

-extremely fine-grained. Much of groundmass is cryptocrystalline (71%), glassy. In general, the groundmass consists of dark areas with white interstices, not able to positively identify. Some irregular holes (may have mineral-like outlines). Rounded areas of darker groundmass.

Phenocrysts (19%)

Mineral	Percent	Description
mica	10%	brown pleochroic, bird's eye parallel extinction. Up to 1.5 mm, euhedral, some broken and bent. No dark rims, but some zoned with darker core.
opagues	trace	larger than groundmass opagues
feldspar	3%	3-4 mm very relict plag (?), low xp grey, very unhappy, very broken up, no intact rim, clear in ppl, looks isotropic now. Some simple twins.
apatite	1%	med-size, high relief
clinopyroxene	5%	light green in ppl, mod-low xp, no pleochroism, eu to subhedral

Overall texture and comments

-porphyritic. *No leucite confirmed, but may be in groundmass.

Sample RC127**Groundmass (45%)**

Mineral	Percent	Description
feldspar	15%	laths, euhedral, many show simple twinning, weak to no trachytic texture, some skeletal
olivine	2%	subrounded, bright xp
clinopyroxene	6%	light brown, non-pleochroic, low xp, eu to subhedral

Overall texture and comments

-fine-grained, glassy, vesicular – quite high, about 35% of rock. Much of groundmass is dark brown glassy (22%). Brown fresh glass – isotropic.

Phenocrysts (20%)

Mineral	Percent	Description
clinopyroxene	12%	light brown, low xp, inclined extinction, euhedral, some are broken, some subhedral, simple twinning. Up to 1.5 mm. Some larger anhedral cpx with small amount of mica inclusions.
feldspar	8%	k-spar? eu to subhedral, med-size, << 1 mm, simple twinned

Overall texture and comments

-porphyritic. Not such a good thin section, very low xp everything. No large phenocrysts with high xp, not sure if olivine phenocrysts are present.

*No leucite observed.

Sample RC128**Groundmass (64%)**

Mineral	Percent	Description
feldspar	56%	strongly trachytic with some small fish-tail plag laths, very abundant
opaques	trace	disseminated
cpx, mica?	8%	very small broken pieces of mod xp material

Overall texture and comments

-fine-grained

Phenocrysts (36%)

Mineral	Percent	Description
feldspar	18%	plagioclase, shows simple and poly twinning, most euhedral, some fresh. Many completely resorbed with sieve texture core – almost isotropic. Concentrically zoned, complex growths.
mica	7%	brown pleochroic, some broken, some kinked, bird's eye parallel extinction, show general alignment with groundmass feldspars, subhedral (may be 2 generations).
clinopyroxene	10%	green (up Fe), subhedral to euhedral, broken, mod xp, inclined extinction. May be 2 types (1 has some pleochroism).
opaques	1%	fair amount of larger opaques, some with reddish rim

Overall texture and comments

-porphyritic with zoned plagioclase. Some unknown dark brown-black areas, broken, can see lighter areas inside, no change in xp. Some glomeroporphyritic clumps of plag + cpx.

*No leucite observed.

D.2. Ernici**Sample ER100****Groundmass (93%)**

Mineral	Percent	Description
leucite	40%	small rounded, anhedral, abundant
clinopyroxene	20%	light green, subhedral, mod yellow-brown xp, no pleochroism
opaques	trace	disseminated
feldspar	crypto	very tiny

Overall texture and comments

-fine-grained. One large vesicle 0.8 cm in length, some smaller vesicles << 1 mm present also. Fair amount of groundmass is cryptocrystalline (33%): likely composed of very fine-grained feldspar laths. Small amount of light brown isotropic glass.

Phenocrysts (7%)

Mineral	Percent	Description
clinopyroxene	7%	nice green core in photo, zoning, most cpx phenocrysts do not show this strong zoning, some rounded cores. Largest < 1 mm. Good cleavage, eu to subhedral, some broken, low grey-yellow xp, some smaller crystals have cores slightly resorbed.

Overall texture and comments

-porphyritic, phenocryst-poor. Some larger cpx crystal are broken and resorbed, with cores eaten away. Only cpx phenocrysts observed. No leucite or feldspar phenocrysts. No olivine observed.

Sample ER101**Groundmass (85%)**

Mineral	Percent	Description
leucite	27%	subrounded to anhedral
apatite	trace	as inclusions in leucite
opauques	2%	abundant disseminated tiny
feldspar	2%	small amount, lath-shaped
clinopyroxene	25%	light green non-pleochroic, abundant, some with rounded green cores
amphibole	4%	

Overall texture and comments

-fine-grained. Some light brown isotropic glass. Cryptocrystalline very fine-grained dark material, mod-low xp, likely cpx+ feldspar, composes 25% of rock.

Phenocrysts (15%)

Mineral	Percent	Description
clinopyroxene	8%	light green, weak trachytic-like texture of long axes, non-pleochroic, eu to subhedral, some broken, up to 1 mm.
amphibole	7%	zoned, strong green-brown pleochroism, subhedral, most are small and zoned with green core. One 3 mm quite relict amphibole observed.

Overall texture and comments

-porphyritic, quite phenocryst-poor. One crystal is suspect cpx, but not sure. Has wavy but intact edge, center is very fine-grained altered, anomalous xp. No leucite or feldspar phenocrysts observed. No olivine observed.

Sample ER102**Crystals (10%)****Overall texture and comments**

Mineral	Percent	Description
quartz?	N/A	suspect, anhedral
mica		brown, pleochroic, < 1 mm, bird's eye parallel extinction, euhedral, a little broken
clinopyroxene		strong cleavage, anhedral, mod-high xp, light brown, non-pleochroic, up to 1.5 mm.
apatite		some in clumps, stubby crystals, low xp, clear
feldspar?		felsic, anhedral, likely k-spar
olivine?		small, clear, bright xp but no usual red rim

-did not observe % of each mineral type.

Lithics (30%)

Rock Type	Percent	Description
carbonate	N/A	0.8 cm rounded piece of limestone, can see individual calcite crystals
mudrock		dark subrounded clasts

Overall texture and comments

-pyroclastic sample, heterogeneous mix of broken crystals, lithics, matrix and holes. Contains 3 cm long calcite vein – evidence of likely some secondary alteration. No alignment of components. Most lithics are subrounded to rounded, a few are angular.

Matrix (60%)

Overall texture and comments -very fine-grained, composed of ash +/- glass.

Sample ER103**Groundmass (70%)**

Mineral	Percent	Description
leucite	34%	subrounded to anhedral
apatite	trace	as inclusions in leucite
clinopyroxene	28%	sub to anhedral, concentric zoning in some, simple twins
amphibole	8%	less abundant, strong brown-green pleochroism, very anhedral, some with green cores
opaques	trace	disseminated

Overall texture and comments

-fine-grained, fairly equigranular mix of leucite and cpx (similar to ER105 and ER104).

Phenocrysts (30%)

Mineral	Percent	Description
clinopyroxene	10%	slight zoning (greener rim), some with resorbed cores, leucite in cre, most are euhedral, up to 1.5 mm
amphibole	7%	very anhedral, green-brown pleochroism, low yellow-brown xp
feldspar	10%	very unhappy, not recognizable in ppl but in xp some patches have low xp and uniform extinction (see photo)
olivine	3%	rounded with red rim, slightly fractured, up to 1 mm

Overall texture and comments

-porphyritic. No leucite phenocrysts.

Sample ER104**Groundmass (79%)**

Mineral	Percent	Description
leucite	42%	sub to anhedral
apatite	trace	as inclusions in leucite
clinopyroxene	25%	light green subhedral, non-pleochroic. Some euhedral with rounded green cores.
amphibole	5%	small amount, anhedral, strong brown-green pleochroism
feldspar	7%	very unhappy, broken up, overgrown by other minerals, space-fillers in groundmass, not nice laths

Overall texture and comments

-fine-grained, groundmass fairly equigranular, mostly cpx + leucite. Small amount of brown isotropic material – glass.

Phenocrysts (21%)

Mineral	Percent	Description
amphibole	5%	zoned, greener at core, intact, strong green to yellow-tan pleochroism, < 1 mm, euhedral but with rough edges. Suspect diff type than gm: diff pleochroism. Some are quite resorbed.
clinopyroxene	13%	light green, some with conspicuous green subrounded cores, non-pleochroic, most very fresh, but some with resorbed cores. Up to 1-2 mm, some simple twins, some glomeroporphyritic, eu to subhedral.
olivine	3%	about 1 mm, clear ppl, red rim, very small reaction corona?, rounded, anhedral

Overall texture and comments

-porphyritic. Trace amount of ~ 2 mm wide cluster of small anhedral apatite, with holes and glass + feldspar. No olivine observed in groundmass. No leucite phenocrysts.

*Similar to ER105

Sample ER105**Groundmass (84%)**

Mineral	Percent	Description
leucite	48%	sub to anhedral, very abundant
apatite	trace	as inclusion in leucite
opagues	trace	disseminated
clinopyroxene	24%	light green, non-pleochroic, eu to subhedral, some have been cored
amphibole	6%	strong brown-light green pleochroism, broken crystal, low yellow-grey xp, subhedral
olivine	2%	small, reddish rims, not abundant, rounded, high xp
unknown	4%	black very small material with red borders

Overall texture and comments

-fine-grained, fairly equigranular mix of cpx + leucite. May be small amount of glass.

Phenocrysts (16%)

Mineral	Percent	Description
clinopyroxene	7%	green, broken with resorbed middle, non-pleochroic, with concentric zoning, up to 2 mm, eu to subhedral
feldspar	8%	heavily resorbed feldspar (plag?), good example in photo, new fresh minerals inside, low xp
olivine	1%	sparse, anhedral, slight red tm, fractured

Overall texture and comments

-porphyritic. Leucite inside pink phenocryst in photo. Fairly phenocryst-poor. No leucite phenocrysts observed.

Sample ER106**Groundmass (90%)**

Mineral	Percent	Description
leucite	42%	abundant, anhedral, appears more like space-filler
feldspar	5%	resorbed plag, not in nice laths
opagues	trace	abundant disseminated
apatite	trace	some as inclusions in leucite
clinopyroxene	40%	light green, eu to subhedral, mod-high xp, some with cores slightly eaten, some with brown-green pleochroism
olivine	3%	rounded, high xp, reddish rim, fractured

Overall texture and comments

-fine-grained

Phenocrysts (10%)

Mineral	Percent	Description
clinopyroxene	6%	light green non-pleochroic, mod-high xp, eu to subhedral, up to 2 mm. Some larger cpx are broken, but with clean edges.
leucite	trace	rare small crystals, subrounded
olivine	2%	rare small clear, subrounded, red rims
amphibole	2%	brown-green pleochroic, small, euhedral, not common

Overall texture and comments

-porphyritic, phenocryst-poor. No big leucite.

Sample ER107**"Groundmass" (55%)**

Mineral	Percent	Description
leucite	55%	small subrounded, very abundant
apatite	trace	some as inclusions in leucite
opaques	trace	abundant disseminated tiny

Overall texture and comments

-fine-grained. Space between leucite is cryptocrystalline, light green in ppl, mod-low brown/yellow/grey xp, suspect fine-grained cpx. Some small brown isotropic areas – maybe glass.

"Phenocrysts" (45%)

Mineral	Percent	Description
olivine	10%	rounded to subhedral, relatively unfractured, about 1 mm in size, easily distinguished by pearly white colour, red rime and high pink-blue xp
clinopyroxene	35%	light green, most euhedral to subhedral, inclined extinction, mod brown xp, some show zoning. Some larger cpx with resorbed cored, some glomeroporphyritic.
unknown	small	irregular areas of clear ppl, light grey xp, has extinction, no cleavage, appears as lc in ppl but much lighter xp, not rounded

Overall texture and comments

-fairly equigranular with no large phenocrysts. Both olivine and cpx are roughly same size (a little larger) as leucite.

Sample ER108**Groundmass (65%)**

Mineral	Percent	Description
feldspar	3%	scattered, simple twinning, suspect sanidine, low xp, laths, show slight trachytic texture, some with fish-tail. Some have poly twinning: may be plag also present.
apatite	trace	
clinopyroxene	6%	small green, sub to anhedral, mod-high xp
mica	2%	small brown, bird's eye parallel extinction, ragged ends
glass	54%	

Overall texture and comments

-glassy and vesicular. Vesicles are about 30% of rock, most are < 1 mm, quite small, all are irregular, not rounded. Some devitrified glass, dark brown-black.

Phenocrysts (5%)

Mineral	Percent	Description
olivine	1%	highly suspect ol, ~ 1 mm, sparse, high relief, clear in ppl, but low grey xp
clinopyroxene	4%	light green, non-pleochroic, high xp, subhedral, up to 1.5 mm. Some glomeroporphyritic.
feldspar	-	med-size plag with poly twinning (included with groundmass feldspar)

Overall texture and comments

-porphyritic. High glass content precludes full mineral ID of rock.

*No leucite observed.

Sample ER109**Groundmass (84%)**

Mineral	Percent	Description
feldspar	14%	random to weak trachytic texture, laths, show simple twinning and poly twinning
mica	4%	small brown pleochroic
analcite	16%	small round
apatite	trace	as inclusions in leucite
clinopyroxene	6%	eu to subhedral, light green
unknown	trace	scattered red material

Overall texture and comments

-fine-grained. Much of groundmass is cryptocrystalline (44%). Many small holes (?), some with reddish rims, actually tricky to distinguish from small leucite. Some small clumps of groundmass feldspar.

Phenocrysts (16%)

Mineral	Percent	Description
clinopyroxene	12%	green, good cleavage, some with greener core, non-pleochroic, largest 0.5 cm, low to mod. xp, some concentrically zoned. Large 1-2 mm broken clumps.
mica	4%	light brown (in photo), largest 0.5 cm, straight, good cleavage, edges fresh, smaller pieces scattered.

Overall texture and comments

-porphyritic, phenocryst-poor. * No leucite phenocrysts observed. No large feldspar observed. May be some nepheline, low xp, clear ppl, however some show simple twinning.

Sample ER110**Groundmass (74%)**

Mineral	Percent	Description
leucite	28%	abundant small round, subhedral
apatite	trace	as inclusions in leucite
clinopyroxene	8%	light green, mod xp, non-pleochroic, subhedral to anhedral
mica	2%	small broken, brown pleochroic
feldspar	4%	hard to determine type, skeletal
unknown	2%	small red bits – glass?

Overall texture and comments

-fine-grained with some vesicles. Cryptocrystalline material (likely cpx + feldspar) makes up 30% of groundmass.

Phenocrysts (26%)

Mineral	Percent	Description
leucite	16%	eu to anhedral, with apatite inclusions, abundant, up to ~ 1 mm. Gradation in size from groundmass leucite.
relict amph?	2%	suspect, crystal shape suspicious, not abundant, dark rim, but clear in ppl and no pleochroism, low grey xp. << 1 mm. Another crystal is ~ 2mm, no features visible, altered to opaques, anom. xp.
clinopyroxene	7%	green, non-pleochroic, mod yellow xp, up to 1.5 mm. Some larger crystals are slightly embayed and broken.
mica	1%	3 mm mica, very relict, replaced by black material

Overall texture and comments

-porphyritic, leucite-rich. * No olivine observed, no feldspar phenocrysts.

Sample **ER111****Groundmass (85%)**

Mineral	Percent	Description
leucite	25%	small, rounded
apatite	trace	as inclusions in leucite
clinopyroxene	4%	green, sub to anhedral, non-pleochroic
mica	3%	small, broken, bird's eye parallel extinction, brown pleochroic
feldspar	trace	not many visible, laths
unknown	1%	small bits of clear ppl, grey xp material, no distinct crystal shape

Overall texture and comments

-fine-grained, vesicular, glassy – devitrified, with small irregular holes. Groundmass is quite messy-looking. Much of groundmass is cryptocrystalline and dark (52%).

Phenocrysts (15%)

Mineral	Percent	Description
leucite	8%	many with apatite as radial inclusions, crystals are eu to anhedral
clinopyroxene	7%	large 0.8 cm bright green cpx, no pleochroism, no strong cleavage, bright orange xp, only 1 this size on slide, inclined extinction.

Overall texture and comments

-porphyritic. Aligned minerals on slide are pyroxene even though they look like mica in photo: no pleochroism, inclined extinction. Not much feldspar observed in this sample. Weak alignment of long axes of cpx. No olivine observed.

Sample **ER112****Groundmass (60%)**

Mineral	Percent	Description
feldspar	8%	laths, euhedral, some skeletal, plag?, not aligned
olivine	6%	rounded with red rims
clinopyroxene	14%	light green, eu to subhedral, non-pleochroic
unknown	trace	sparse red mineral
glass	32%	devitrified

Overall texture and comments

-fine-grained, vesicular, glassy, irregular holes up to 0.9 cm compose 15% of rock.

Phenocrysts (25%)

Mineral	Percent	Description
clinopyroxene	18%	light greenish-brown, non-pleochroic, strong cleavage, eu to subhedral, mod-high xp, some simple twins, about 1.5 mm in size. Some with resorbed cored, some glomeroporphyritic, some fairly fractured.
olivine	7%	eu to subhedral, bright xp, red rim, < 1 mm, slightly fractured, some quite unfractured

Overall texture and comments

-porphyritic. No feldspar phenocrysts observed.

*No leucite observed.

Sample ER113**Groundmass (74%)**

Mineral	Percent	Description
feldspar	2%	very small lath-shaped plag, not abundant, moderately trachytic
glass	52%	
clinopyroxene	12%	small green subhedral
zeolite?	6%	small circular areas of possible zeolite, likely small infilled vesicles
opaques	trace	small amount, tiny
olivine	2%	small amount, clear in ppl, bright xp

Overall texture and comments

-glassy groundmass, vesicular (irregular vesicles) all rimmed by fine-grained late magmatic mineral – likely zeolites. Amygdules (8%).

Phenocrysts (18%)

Mineral	Percent	Description
olivine	4%	clear in ppl, high pink xp, up to 2-3 mm, slightly fractured, euhedral – subhedral, very fresh
clinopyroxene	14%	good cleavage, green in ppl, many have high bright xp, non-pleochroic, euhedral to subhedral, some are slightly glomeroporphyritic, some greener in core. Up to 3-4 mm, some show slight concentric zoning.

Overall texture and comments

-porphyritic, altered.
*No feldspar phenocrysts.
*No leucite observed.

Sample ER114**Groundmass (62%)**

Mineral	Percent	Description
feldspar	5%	plag laths, some may have swallow-tails, in random arrangement, not too abundant
opaques	trace	abundant tiny
apatite	trace	in clusters, acicular
olivine	2%	small, clear in ppl, bright xp, eu to subhedral
clinopyroxene	15%	fairly abundant light green strong cleavage, inclined extinction, many are broken and fractured
glass	40%	dark, much of groundmass

Overall texture and comments

-dark and glassy

Phenocrysts (18%)

Mineral	Percent	Description
olivine	4%	small amount, fractured, subhedral, pink zp, clear ppl
clinopyroxene	12%	highly fractured, brown in ppl, low-med xp, abundant, some very broken cpx in holes
unknown	trace	odd rounded mineral bright xp, no cleavage, located in hole, very light brown ppl
unknown	2%	no cleavage, low xp, unfractured, light green ppl, in hole, pieces broken apart

Overall texture and comments

-quite fragmented: is this a result of thin section making or inherent to rock? Series of connected holes, rounded, with fine-grained black material inside. Could this be rock dust from the sample itself. Holes compose about 20% of slide, and are up to 4 mm each. Visible to naked eye.

Sample ER115**Groundmass (65%)**

Mineral	Percent	Description
leucite	15%	abundant, look like vesicles in ppl, rounded, anhedral
apatite	trace	
feldspar	5%	plag laths
glass	30%	dark, constitutes most of groundmass
clinopyroxene	15%	suspect, small light green, comparable to lc in abundance, mod-high xp (pink-blue), subhedral to irregular, rounded, cleavage indistinct

Overall texture and comments

-Vesicular (20%), glassy, circular vesicles with no alignment. Most vesicles are just bigger than leucite and cpx groundmass.

Phenocrysts (15%)

Mineral	Percent	Description
clinopyroxene	15%	light green in ppl, high xp, numerous concentric zoning, Fe-rich?, with irregular holes in centre. Some elongate, some euhedral to subhedral or more stubby, fairly abundant. Larger cpx have cores eaten away. Slight fracturing, some glomeroporphyritic, cleavage indistinct on some. Largest about 4 mm.

Overall texture and comments

*No leucite phenocrysts observed.

Sample ER116**Groundmass (53%)**

Mineral	Percent	Description
feldspar	3%	small laths, show poly twinning in some, no alignment
clinopyroxene	18%	light green, subhedral, non-pleochroic
olivine	4%	subhedral to rounded, unfractured, bright xp, no reddish rim

Overall texture and comments

-fine-grained, glassy, very vesicular: irregular to rounded, with fine black infill, composes 35% of rock. Some fresh glass seen on edges of vesicles. Much of the groundmass is dark brown-black, glassy (28%).

Phenocrysts (12%)

Mineral	Percent	Description
clinopyroxene	8%	light green, irregular zoning with greener core, fractured, mod-high xp, up to 1.5 mm, some glomeroporphyritic
olivine	3%	< 1 mm, euhedral-subhedral, broken, high xp, slight reddish rim
unknown	trace	small amount of clear, low grey xp, su-rectangular, parallel extinction, no twinning <<1 mm, nepheline?

Overall texture and comments

-porphyritic. About 1% of the rock is composed of ~ 1 mm-sized areas of very fine-grained feldspar + px + opaques. Origin unsure, several of these areas, another is ~ 2 mm, appears to be replacement. No feldspar phenocrysts.

*No leucite observed.

Sample ER117**Groundmass (62%)**

Mineral	Percent	Description
analcite	17%	abundant, small, sub to anhedral
mica	5%	brown pleochroic euhedral but broken, bird's eye extinction
amphibole	8%	strong tan-yellow to green pleochroism, subhedral, concentric zoned with green core
clinopyroxene	8%	light green non-pleochroic, green cores, subhedral, some euhedral with cores eaten away.
olivine	2%	clear, bright pink xp, anhedral

Overall texture and comments

-fine-grained, glassy. Much of the groundmass is dark, cryptocrystalline (22%), some devitrified glass – light brown ppl, anom. xp.

Phenocrysts (38%)

Mineral	Percent	Description
olivine	4%	clear, bright xp, sub to anhedral with some slight alteration
mica	9%	brown pleochroic, strong cleavage, 1 macrocryst ~ 1.1 cm, most < 1 mm
clinopyroxene	7%	many broken with green eaten away cores, mod-high xp, concentric zoning, inclined extinction (in photo)
feldspar	1%	rare, anhedral, low grey xp (plag?), with reaction rim of clear isotropic material, some concentric zoning observed, sides are not straight, extinction irregular
amphibole	13%	zoned with strong tan-dark green pleochroism, eu to anhedral, some with reaction rim of fine-grained material
unknown	3%	fibrous material near edge, suspect at first foreign thread or clothing or tissue. Clear in ppl, low anom. xp. Suspect muscovite, seems to have parallel extinction.

Overall texture and comments

-somewhat fresh. Porphyritic, quite complex. Contains light brown-black lithic fragment (?) with reaction rim of clear low xp fine-grained material, isotropic, rounded but irregular (1%). No leucite phenocrysts observed.

Sample ER118**Groundmass (71%)**

Mineral	Percent	Description
leucite	30%	small, rounded, anhedral
apatite	trace	as inclusions in leucite
clinopyroxene	14%	subhedral, light green
opaques	trace	disseminated
olivine	3%	med-small with heavy red rim
feldspar	trace	very small amount, laths, plag?
unknown	trace	small red mineral, nearly isotropic

Overall texture and comments

-fine-grained, some vesicles – elongate, 5% of rock. Much of groundmass is cryptocrystalline, between leucite, likely rich in cpx (24%). Devitrified glass seen by vesicle walls.

Phenocrysts (24%)

Mineral	Percent	Description
olivine	4%	2-3 mm large olivine, quite embayed/resorbed, with red rim
clinopyroxene	16%	light greenish-brown, some with eaten-away cored, most are fresh, non-pleochroic, mod-high xp, eu to subhedral, some simple twins, some with concentric zoning. Up to 2 mm.
amphibole	4%	with dark green pleochroic cores, subrounded, med-small size, some with eaten away cores

Overall texture and comments

-porphyritic. Trace amount of small subrounded black patchy area. No leucite phenocrysts observed, not much feldspar at all seen.

Sample ER119**Groundmass (63%)**

Mineral	Percent	Description
leucite	17%	subrounded to anhedral
apatite	trace	as inclusions in leucite
feldspar	6%	laths, quite small and thin, scattered, not aligned, k-spar?
olivine	2%	slight red rim, small, clear, bright xp, embayed, subhedral
clinopyroxene	15%	light green, subhedral to anhedral

Overall texture and comments

-fine-grained, vesicular, similar phenomena to that seen in ER114 (holes with fine-grained black material inside + fine-grained speckled appearance under xp: may be some tiny clear minerals), but not as connected – compose 20% of rock. Vesicles up to 0.7 cm, all are irregular, not rounded. Much of groundmass is fairly dark in ppl – glassy (23%).

Phenocrysts (17%)

Mineral	Percent	Description
clinopyroxene	10%	light green eu to subhedral, up to ~1 mm, some with concentric zoning
olivine	7%	red rims, fairly large, rounded, with reddish alteration, larger than most cpx, moderately fractured, bright xp

Overall texture and comments

-porphyritic. No feldspar phenocrysts, no leucite phenocrysts observed. Possible amph but don't think so.

Sample ER120**Groundmass (82%)**

Mineral	Percent	Description
leucite	42%	sub to anhedral
apatite	trace	as inclusions in leucite
clinopyroxene	28%	eu to subhedral, light green, non-pleochroic
opagues	trace	disseminated
amphibole	8%	brown-green pleochroism, anhedral
feldspar	4%	quite small, scattered, not obvious

Overall texture and comments

-fine-grained. Area between leucite is dark and cryptocrystalline, mod xp, suspect devitrified glass + cpx.

Phenocrysts (18%)

Mineral	Percent	Description
clinopyroxene	10%	light greenish-brown, eu to anhedral, non-pleochroic, high xp, some glomeroporphyritic, some with resorbed cores. Up to 1 mm. Clumps of smaller cpx are ~ 1 mm in size.
olivine	2%	red rim, slightly fractured, subhedral, some very rounded. About 1 mm in size.
amphibole	4%	med-size, green core, slight pleochroism
unknown	2%	felsic material, anhedral, no cleavage, low grey xp, clear in ppl, most are broken. Feldspar? << 1 mm

Overall texture and comments

-porphyritic. No leucite phenocrysts.

Sample ER121**Groundmass (74%)**

Mineral	Percent	Description
feldspar	15%	laths, very small, skeletal, fairly abundant, sanidine?
opagues	trace	disseminated
clinopyroxene	25%	small green, mod-low xp, subhedral
olivine	4%	rounded, red rim, slightly fractured
analcite	30%	isotropic, abundant

Overall texture and comments

-fine-grained, some of the groundmass is cryptocrystalline, maybe some glass.

Phenocrysts (26%)

Mineral	Percent	Description
olivine	8%	clear in ppl, eu to subhedral, red rim, stand out clearly, up to 1-2 mm, a few are quite rounded
clinopyroxene	16%	light green, eu to subhedral, fairly large, up to 0.6 cm, good cleavage, some with resorbed cores, broken, concentric zoning. Many are fairly fractured and some are glomeroporphyritic.

Overall texture and comments

-porphyritic with large cpx and olivine. 2% of the rock is composed of ~ 1 mm dark patchy areas, very fine-grained: unknown material. No feldspar phenocrysts.

*No leucite observed.

Sample ER122**Groundmass (59%)**

Mineral	Percent	Description
olivine	5%	small clear, reddish rim, subhedral
feldspar	3%	laths, euhedral
clinopyroxene	10%	light green, non-pleochroic, low-med xp, su to anhedral
apatite		
glass	41%	dark

Overall texture and comments

-glassy, very vesicular: irregular vesicles, rounded to oval, up to 3-4 mm in size (most ~ 1 mm). Up to 30% of rock. Some vesicles with thick dark rim – glass.

Phenocrysts (11%)

Mineral	Percent	Description
clinopyroxene	7%	light green, some show zoning, no pleochroism, inclined extinction, eu to subhedral. Largest ~ 1 mm.
olivine	3%	reddish rim, < 1 mm, eu to subhedral, high bright xp

Overall texture and comments

-contains 1% fine-grained globular structures, composed of tiny feldspar + ol + cpx + ap, several seen in section, about 1 mm in size. No feldspar phenocrysts.

*No leucite observed.

APPENDIX E

ELECTRON MICROPROBE ANALYSES

E.1. Olivine

	KS RC111-4 gm	KS RC111-11 gm	KS RC111-16 pheno	HKS RC100-5 gm	HKS RC100-16 gm	HKS RC109-1 pheno	HKS RC109-2 pheno	HKS RC109-15 gm
SiO ₂	35.76	36.90	41.18	37.02	37.00	39.24	37.10	34.12
Al ₂ O ₃	0.07	0.09	0.03	0.07	0.00	0.01	0.03	0.06
FeO	37.74	30.50	11.53	30.86	32.18	17.82	28.27	44.18
MgO	25.67	31.49	47.86	31.37	30.31	42.68	33.47	20.06
MnO	0.71	0.59	0.19	1.00	0.00	0.37	0.91	1.74
CaO	0.36	0.30	0.24	0.53	0.72	0.40	0.43	0.51
NiO	0.09	b.d.	0.20	b.d.	0.31	0.12	b.d.	b.d.
Total	100.40	99.87	101.23	100.85	100.52	100.64	100.21	100.67

Olivine formulae calculated on the basis of 4 oxygen

Si ⁴⁺	1.004	1.002	1.005	0.999	1.006	0.994	0.996	0.994
Al ³⁺	0.002	0.003	0.001	0.002	0.000	0.000	0.001	0.002
Total	1.006	1.005	1.006	1.001	1.006	0.994	0.997	0.996
Fe ²⁺	0.886	0.693	0.235	0.697	0.732	0.378	0.634	1.077
Mg ²⁺	1.074	1.275	1.740	1.262	1.228	1.612	1.339	0.871
Mn ²⁺	0.017	0.014	0.004	0.023	0.000	0.008	0.021	0.043
Ca ²⁺	0.011	0.009	0.006	0.015	0.021	0.011	0.012	0.016
Ni ²⁺	0.002	0.000	0.004	0.000	0.007	0.002	0.000	0.000
Total	1.990	1.991	1.989	1.997	1.988	2.011	2.006	2.007
Mg#	55	65	88	64	63	81	68	45

	HKS RC109-16 gm	HKS RC123-4 gm	HKS RC123-6 gm	HKS RC123-7 gm	KS ER109-14 gm	KS ER109-21 gm	KS ER112-8 pheno	KS ER112-11 pheno
SiO ₂	34.29	34.58	34.38	35.60	38.11	38.90	40.96	41.57
Al ₂ O ₃	0.09	0.05	0.12	0.10	0.13	0.13	0.03	0.02
FeO	41.96	38.90	44.99	37.88	22.36	23.24	12.01	11.59
MgO	20.09	23.31	19.66	25.87	38.56	36.98	47.29	47.83
MnO	1.64	1.02	1.30	0.97	0.40	0.49	0.23	0.22
CaO	0.59	2.20	0.77	0.62	0.38	0.50	0.31	0.31
NiO	b.d.	0.05	b.d.	b.d.	b.d.	b.d.	0.16	0.10
Total	98.66	100.11	101.22	101.04	99.94	100.24	100.99	101.64

Olivine formulae calculated on the basis of 4 oxygen

Si ⁴⁺	1.010	0.989	0.998	0.995	0.994	1.013	1.004	1.009
Al ³⁺	0.003	0.002	0.004	0.003	0.004	0.004	0.001	0.001
Total	1.013	0.991	1.002	0.998	0.998	1.017	1.005	1.010
Fe ²⁺	1.033	0.931	1.092	0.885	0.488	0.506	0.246	0.235
Mg ²⁺	0.882	0.994	0.850	1.078	1.499	1.436	1.728	1.731
Mn ²⁺	0.041	0.025	0.032	0.023	0.009	0.011	0.005	0.004
Ca ²⁺	0.019	0.067	0.024	0.019	0.011	0.014	0.008	0.008
Ni ²⁺	0.000	0.001	0.000	0.000	0.000	0.000	0.003	0.002
Total	1.975	2.018	1.998	2.005	2.007	1.967	1.990	1.980
Mg#	46	52	44	55	75	74	88	88

E.1. *Olivine continued*

	KS ER112-3 pheno	KS ER117-17 pheno	KS ER121-3 pheno	KS ER121-4 pheno	KS ER121-5 gm	KS ER121-9 pheno	KS ER121-10 pheno	HKS ER104-8 gm
SiO ₂	40.79	41.48	40.59	38.24	36.64	40.23	39.12	33.26
Al ₂ O ₃	0.07	0.04	0.00	0.05	0.06	0.05	0.03	0.06
FeO	13.06	9.95	12.05	25.29	32.09	11.04	18.70	45.51
MgO	45.89	48.72	46.97	36.07	29.94	47.62	42.22	17.44
MnO	0.20	0.23	0.19	0.49	0.72	0.20	0.36	2.09
CaO	0.40	0.35	0.28	0.38	0.54	0.36	0.32	1.16
NiO	0.13	0.25	0.13	0.07	b.d.	0.18	0.13	b.d.
Total	100.54	101.02	100.21	100.59	99.99	99.68	100.88	99.52

Olivine formulae calculated on the basis of 4 oxygen

Si ⁴⁺	1.009	1.007	1.003	1.004	1.003	0.997	0.993	0.995
Al ³⁺	0.002	0.001	0.000	0.002	0.002	0.002	0.001	0.002
Total	1.011	1.008	1.003	1.006	1.005	0.999	0.994	0.997
Fe ²⁺	0.270	0.202	0.249	0.555	0.735	0.229	0.397	1.139
Mg ²⁺	1.692	1.763	1.730	1.411	1.222	1.758	1.597	0.778
Mn ²⁺	0.004	0.005	0.004	0.011	0.017	0.004	0.008	0.053
Ca ²⁺	0.011	0.009	0.008	0.011	0.016	0.009	0.009	0.037
Ni ²⁺	0.003	0.005	0.003	0.001	0.000	0.004	0.003	0.000
Total	1.980	1.984	1.994	1.989	1.990	2.004	2.014	2.007
Mg#	86	90	87	72	62	88	80	41

	HKS ER104-12 pheno	HKS ER104-18 gm	HKS ER110-18 gm	HKS ER118-6 gm	HKS ER118-7 gm	HKS ER118-17 gm	HKS ER118-18 gm	HKS ER118-20 gm
SiO ₂	41.18	33.12	36.85	37.63	34.95	36.61	33.19	39.63
Al ₂ O ₃	0.04	0.06	0.09	0.13	0.06	0.08	0.04	0.03
FeO	9.85	48.72	29.74	29.38	41.31	33.44	52.35	18.50
MgO	49.21	13.98	30.61	32.54	22.53	28.99	12.52	42.36
MnO	0.21	2.41	1.35	0.84	1.69	1.07	2.00	0.54
CaO	0.35	1.39	1.21	0.76	0.88	0.85	1.22	0.40
NiO	0.27	b.d.	0.06	b.d.	0.09	b.d.	b.d.	0.08
Total	101.11	99.68	99.91	101.28	101.51	101.04	101.32	101.54

Olivine formulae calculated on the basis of 4 oxygen

Si ⁴⁺	1.000	1.008	1.004	1.003	0.994	1.001	1.007	0.998
Al ³⁺	0.001	0.002	0.003	0.004	0.002	0.003	0.002	0.001
Total	1.001	1.010	1.007	1.007	0.996	1.004	1.009	0.999
Fe ²⁺	0.200	1.240	0.678	0.655	0.983	0.764	1.328	0.389
Mg ²⁺	1.780	0.634	1.243	1.292	0.955	1.181	0.566	1.590
Mn ²⁺	0.004	0.062	0.031	0.019	0.041	0.025	0.051	0.012
Ca ²⁺	0.009	0.045	0.035	0.022	0.027	0.025	0.040	0.011
Ni ²⁺	0.005	0.000	0.001	0.000	0.002	0.000	0.000	0.002
Total	1.998	1.981	1.988	1.988	2.008	1.995	1.985	2.004
Mg#	90	34	65	66	49	61	30	80

E.2. Pyroxene

	WA100-1 gm	WA100-2 gm	WA100-3 gm	WA100-7 pheno	WA100-8 pheno	WA100-13 pheno	WA100-15 pheno	WA100-17 pheno	WA100-18 pheno	WA102-5 pheno	WA102-6 pheno	WA102-8 pheno
SiO ₂	54.78	53.48	48.23	53.11	47.30	53.65	53.65	48.68	52.90	54.97	53.31	51.41
Al ₂ O ₃	1.19	1.35	3.97	0.75	4.58	0.04	0.99	3.95	1.19	0.46	0.92	0.76
TiO ₂	0.35	0.32	0.81	0.21	0.90	0.06	0.23	0.56	0.22	0.24	0.30	0.38
Cr ₂ O ₃	0.12	b.d.	0.05	b.d.	b.d.	b.d.	0.18	b.d.	0.21	b.d.	b.d.	b.d.
Fe ₂ O ₃ *	0.00	1.06	4.55	2.64	5.78	1.99	2.62	6.29	3.62	0.00	0.97	4.28
FeO*	4.80	5.22	7.18	3.52	7.52	6.50	2.02	4.90	0.90	3.95	5.74	0.82
MgO	17.39	16.23	11.30	17.63	11.21	15.67	17.89	11.63	17.93	18.10	15.56	17.06
MnO	0.15	0.25	0.38	0.24	0.31	0.33	0.14	0.29	0.10	0.13	0.22	0.12
CaO	22.33	22.31	22.65	21.45	21.69	22.18	22.86	23.35	22.97	22.14	22.94	23.38
Na ₂ O	0.25	0.27	0.36	0.22	0.38	0.22	0.22	0.62	0.23	0.24	0.20	0.11
Total	101.36	100.49	99.49	99.77	99.67	100.64	100.80	100.27	100.26	100.23	100.16	98.32
Pyroxene formulae calculated on the basis of 6 oxygen												
Si ⁴⁺	1.973	1.957	1.835	1.949	1.803	1.978	1.942	1.830	1.924	1.993	1.965	1.916
ivAl ³⁺	0.027	0.043	0.165	0.032	0.197	0.002	0.042	0.170	0.051	0.007	0.035	0.033
ivFe ³⁺	0.000	0.000	0.000	0.019	0.000	0.020	0.016	0.000	0.025	0.000	0.000	0.051
Total	2.000	2.000	2.000	2.000	2.000	2.000	2.000	2.000	2.000	2.000	2.000	2.000
viAl ³⁺	0.024	0.015	0.013	0.000	0.009	0.000	0.000	0.005	0.000	0.013	0.005	0.000
Ti ⁴⁺	0.009	0.009	0.023	0.006	0.026	0.002	0.006	0.016	0.006	0.007	0.008	0.011
Cr ³⁺	0.003	0.000	0.002	0.000	0.000	0.000	0.005	0.000	0.006	0.000	0.000	0.000
viFe ³⁺	0.000	0.029	0.130	0.054	0.166	0.035	0.055	0.178	0.074	0.000	0.027	0.069
Fe ²⁺	0.145	0.160	0.229	0.108	0.240	0.200	0.061	0.154	0.027	0.120	0.177	0.026
Mg ²⁺	0.934	0.885	0.641	0.965	0.637	0.861	0.965	0.652	0.972	0.978	0.855	0.948
Mn ²⁺	0.005	0.008	0.012	0.007	0.010	0.010	0.004	0.009	0.003	0.004	0.007	0.004
Ca ²⁺	0.862	0.875	0.923	0.843	0.886	0.876	0.887	0.941	0.895	0.860	0.906	0.934
Na ⁺	0.017	0.019	0.027	0.016	0.028	0.016	0.015	0.045	0.016	0.017	0.014	0.008
Total	1.999	2.000	2.000	1.999	2.002	2.000	1.998	2.000	1.999	1.999	1.999	2.000
Molecular percentages												
ΣFeO	7.7	9.4	16.4	7.8	17.9	12.1	5.2	13.7	4.1	6.3	10.1	4.5
MgO	48.0	45.6	34.3	49.2	34.3	43.6	49.4	35.3	49.9	49.9	43.7	48.1
CaO	44.3	45.0	49.4	43.0	47.7	44.3	45.4	51.0	46.0	43.8	46.3	47.4
Mg#	86	82	63	84	60	76	88	66	88	89	80	86

E.2. *Pyroxene continued*

	WA102-19	WA102-20	WA102-21	WA102-22	WA104-6	WA104-10	WA104-12	WA104-13	WA104-15	WA105-3	WA105-6	WA105-7
	pheno	pheno	pheno	pheno	gm	pheno	pheno	pheno	gm	gm	pheno	pheno
SiO ₂	53.24	52.61	53.91	52.69	54.34	55.37	52.72	55.09	55.08	54.02	54.31	50.42
Al ₂ O ₃	0.68	0.73	0.38	0.60	0.62	0.33	1.40	0.30	0.26	0.86	0.78	2.94
TiO ₂	0.41	0.37	0.43	0.49	0.73	0.36	0.13	0.31	0.27	0.33	0.39	0.35
Cr ₂ O ₃	b.d.	b.d.	0.31	b.d.	b.d.	0.13	b.d.	b.d.	0.11	b.d.	0.22	b.d.
Fe ₂ O ₃ *	1.86	1.71	0.80	1.50	0.23	0.00	1.01	0.00	0.00	0.00	0.00	1.76
FeO*	3.17	3.56	3.74	4.48	4.68	3.11	8.35	3.89	2.66	4.61	3.93	9.44
MgO	16.96	16.48	17.33	15.71	16.75	17.80	11.98	17.16	17.61	16.36	16.74	10.78
MnO	0.15	0.23	0.16	0.17	0.18	0.08	0.32	0.15	0.13	0.13	0.09	0.30
CaO	23.35	23.11	22.95	23.49	23.08	23.46	24.16	23.84	23.42	23.46	23.76	22.96
Na ₂ O	0.12	0.10	0.14	0.15	0.29	0.20	0.47	0.15	0.10	0.14	0.18	0.48
Total	99.94	98.90	100.15	99.28	100.90	100.84	100.54	100.89	99.64	99.91	100.40	99.43
Pyroxene formulae calculated on the basis of 6 oxygen												
Si ⁴⁺	1.953	1.953	1.970	1.957	1.974	1.995	1.968	1.993	2.004	1.980	1.977	1.917
ivAl ³⁺	0.029	0.032	0.016	0.026	0.026	0.005	0.032	0.007	0.000	0.020	0.023	0.083
ivFe ³⁺	0.018	0.015	0.014	0.017	0.000	0.000	0.000	0.000	0.000	0.000	0.000	0.000
Total	2.000	2.000	2.000	2.000	2.000	2.000	2.000	2.000	2.004	2.000	2.000	2.000
viAl ³⁺	0.000	0.000	0.000	0.000	0.001	0.009	0.030	0.006	0.011	0.017	0.010	0.049
Ti ⁴⁺	0.011	0.010	0.012	0.014	0.020	0.010	0.004	0.008	0.007	0.009	0.011	0.010
Cr ³⁺	0.000	0.000	0.009	0.000	0.000	0.004	0.000	0.000	0.003	0.000	0.006	0.000
viFe ³⁺	0.033	0.033	0.008	0.025	0.006	0.000	0.028	0.000	0.000	0.000	0.000	0.050
Fe ²⁺	0.097	0.111	0.114	0.139	0.142	0.094	0.261	0.118	0.081	0.141	0.120	0.300
Mg ²⁺	0.927	0.912	0.944	0.870	0.907	0.956	0.667	0.925	0.955	0.894	0.909	0.611
Mn ²⁺	0.005	0.007	0.005	0.005	0.006	0.002	0.010	0.005	0.004	0.004	0.003	0.010
Ca ²⁺	0.918	0.919	0.898	0.935	0.898	0.905	0.967	0.924	0.913	0.921	0.927	0.935
Na ⁺	0.009	0.007	0.010	0.011	0.020	0.014	0.034	0.011	0.007	0.010	0.013	0.035
Total	2.000	1.999	2.000	1.999	2.000	1.994	2.001	1.997	1.981	1.996	1.999	2.000
Molecular percentages												
ΣFeO	6.5	7.2	6.6	8.4	7.7	4.9	14.9	6.2	4.3	7.4	6.3	17.8
MgO	47.0	46.2	47.8	44.1	46.4	48.8	34.8	46.9	48.9	45.6	46.4	32.5
CaO	46.5	46.6	45.5	47.5	45.9	46.3	50.4	46.9	46.7	47.0	47.3	49.7
Mg#	86	85	87	82	85	91	69	88	92	86	88	63

E.2. *Pyroxene continued*

	WA105-10	KS RC111-1	KS RC111-2	KS RC111-5	KS RC111-6	KS RC111-7	KS RC111-8	KS RC111-9	KS RC111-10	KS RC119-1	KS RC119-11	KS RC119-12
	pheno	pheno	pheno	pheno	pheno	pheno	pheno	pheno	gm	pheno	gm	pheno
SiO ₂	54.35	54.20	46.80	50.76	46.20	54.72	53.92	51.20	47.42	52.04	48.79	52.55
Al ₂ O ₃	0.63	1.69	7.31	5.60	8.31	1.54	2.09	3.51	7.12	2.58	6.79	2.08
TiO ₂	0.39	0.27	1.80	0.78	1.71	0.20	0.26	0.85	1.71	0.48	1.22	0.38
Cr ₂ O ₃	0.33	0.33	b.d.	0.10	b.d.	0.61	0.39	b.d.	0.06	b.d.	0.10	b.d.
Fe ₂ O ₃ *	0.00	0.00	2.61	0.07	2.79	0.00	0.00	0.78	2.42	0.67	0.97	0.00
FeO*	3.44	2.95	7.31	5.50	6.50	3.16	3.79	7.92	7.31	9.12	7.06	10.05
MgO	16.99	17.20	11.98	14.37	12.00	17.39	17.08	14.18	12.18	12.11	13.19	11.59
MnO	0.09	0.06	0.16	0.08	0.18	0.07	0.09	0.16	0.19	0.51	0.15	0.61
CaO	23.46	23.31	21.65	22.81	21.76	22.76	22.48	21.69	21.86	22.91	21.51	22.47
Na ₂ O	0.19	0.15	0.22	0.21	0.18	0.13	0.14	0.18	0.22	0.45	0.25	0.62
Total	99.87	100.16	99.83	100.29	99.63	100.58	100.24	100.48	100.49	100.87	100.03	100.35
Pyroxene formulae calculated on the basis of 6 oxygen												
Si ⁴⁺	1.984	1.965	1.758	1.862	1.735	1.974	1.957	1.895	1.769	1.937	1.811	1.968
ivAl ³⁺	0.016	0.035	0.242	0.138	0.265	0.026	0.043	0.105	0.231	0.063	0.189	0.032
ivFe ³⁺	0.000	0.000	0.000	0.000	0.000	0.000	0.000	0.000	0.000	0.000	0.000	0.000
Total	2.000	2.000	2.000	2.000	2.000	2.000	2.000	2.000	2.000	2.000	2.000	2.000
viAl ³⁺	0.011	0.037	0.082	0.104	0.103	0.039	0.046	0.048	0.082	0.050	0.108	0.060
Ti ⁴⁺	0.011	0.007	0.051	0.022	0.048	0.005	0.007	0.024	0.048	0.013	0.034	0.011
Cr ³⁺	0.010	0.009	0.001	0.003	0.000	0.017	0.011	0.000	0.002	0.000	0.003	0.001
viFe ³⁺	0.000	0.000	0.074	0.002	0.079	0.000	0.000	0.022	0.068	0.019	0.027	0.000
Fe ²⁺	0.105	0.089	0.229	0.169	0.204	0.095	0.115	0.245	0.228	0.284	0.219	0.315
Mg ²⁺	0.924	0.930	0.671	0.786	0.672	0.935	0.924	0.782	0.677	0.672	0.730	0.647
Mn ²⁺	0.003	0.002	0.005	0.002	0.006	0.002	0.003	0.005	0.006	0.016	0.005	0.019
Ca ²⁺	0.917	0.906	0.871	0.897	0.875	0.880	0.874	0.860	0.874	0.914	0.856	0.901
Na ⁺	0.013	0.011	0.016	0.015	0.013	0.009	0.010	0.013	0.016	0.032	0.018	0.045
Total	1.994	1.991	2.000	2.000	2.000	1.982	1.990	1.999	2.001	2.000	2.000	1.999
Molecular percentages												
ΣFeO	5.5	4.7	15.0	9.3	13.9	5.1	6.1	13.7	14.7	16.3	13.0	17.7
MgO	47.4	48.3	37.0	42.4	37.4	48.9	48.2	41.1	37.2	35.5	40.0	34.4
CaO	47.1	47.0	48.0	48.3	48.7	46.0	45.6	45.2	48.0	48.2	46.9	47.9
Mg#	90	91	69	82	70	91	89	74	69	68	74	66

E.2. Pyroxene *continued*

	KS RC119-18	KS RC-106-1	KS RC-106-2	KS RC-106-3	KS RC-106-4	KS RC106-11	KS RC106-14	KS RC106-15	KS RC106-16	KS RC106-17	HKS RC109-3	HKS RC109-4
	gm	pheno	pheno	gm (opx)	gm	gm	gm (opx)	pheno	pheno	pheno	pheno	pheno
SiO ₂	48.45	51.59	52.51	53.67	50.50	52.09	53.24	53.68	52.02	51.00	45.82	49.48
Al ₂ O ₃	6.23	3.40	2.56	0.81	4.12	1.53	0.66	2.53	2.95	4.01	7.73	4.76
TiO ₂	1.30	0.59	0.34	0.23	0.94	0.25	0.20	0.27	0.38	0.58	1.50	0.78
Cr ₂ O ₃	b.d.	0.29	b.d.	b.d.	b.d.	0.15						
Fe ₂ O ₃ *	0.14	0.00	0.00	0.00	0.00	2.04	0.00	0.00	0.74	2.09	4.28	1.68
FeO*	9.68	10.13	8.69	20.28	10.40	8.12	21.42	4.87	8.40	6.01	4.47	4.27
MgO	12.28	11.29	12.70	21.46	12.08	12.21	21.38	16.65	14.52	14.43	11.67	13.91
MnO	0.29	0.63	0.48	1.39	0.59	0.72	1.41	0.15	0.29	0.24	0.15	0.14
CaO	20.10	21.85	21.89	2.04	20.09	22.91	1.64	22.39	21.14	22.22	23.18	23.24
Na ₂ O	0.32	0.54	0.42	0.08	0.40	0.55	0.04	0.13	0.19	0.23	0.22	0.19
Total	98.79	100.02	99.59	99.96	99.14	100.43	99.95	100.96	100.63	100.81	99.02	98.61
Pyroxene formulae calculated on the basis of 6 oxygen												
Si ⁴⁺	1.834	1.936	1.963	1.994	1.908	1.950	1.988	1.944	1.922	1.876	1.732	1.854
ivAl ³⁺	0.166	0.064	0.037	0.006	0.092	0.050	0.012	0.056	0.078	0.124	0.268	0.146
ivFe ³⁺	0.000	0.000	0.000	0.000	0.000	0.000	0.000	0.000	0.000	0.000	0.000	0.000
Total	2.000											
viAl ³⁺	0.112	0.086	0.076	0.029	0.091	0.017	0.017	0.052	0.050	0.050	0.076	0.064
Ti ⁴⁺	0.037	0.017	0.010	0.006	0.027	0.007	0.006	0.007	0.011	0.016	0.043	0.022
Cr ³⁺	0.000	0.000	0.000	0.000	0.000	0.000	0.000	0.008	0.000	0.000	0.000	0.004
viFe ³⁺	0.004	0.000	0.000	0.000	0.000	0.057	0.000	0.000	0.021	0.058	0.122	0.047
Fe ²⁺	0.307	0.318	0.272	0.630	0.329	0.254	0.669	0.147	0.260	0.185	0.141	0.134
Mg ²⁺	0.693	0.632	0.708	1.188	0.680	0.681	1.190	0.899	0.800	0.791	0.658	0.777
Mn ²⁺	0.009	0.020	0.015	0.044	0.019	0.023	0.045	0.005	0.009	0.007	0.005	0.004
Ca ²⁺	0.815	0.879	0.877	0.081	0.813	0.919	0.066	0.869	0.837	0.876	0.939	0.933
Na ⁺	0.023	0.039	0.030	0.006	0.029	0.040	0.003	0.009	0.014	0.016	0.016	0.014
Total	2.000	1.991	1.988	1.984	1.988	1.998	1.996	1.996	2.002	1.999	2.000	1.999
Molecular percentages												
ΣFeO	17.4	18.3	15.3	34.7	18.9	16.0	36.2	7.9	14.6	11.7	11.5	8.7
MgO	37.9	34.2	37.8	61.1	37.0	35.7	60.4	46.8	41.7	41.9	36.5	41.5
CaO	44.6	47.5	46.9	4.2	44.2	48.2	3.3	45.3	43.7	46.4	52.1	49.8
Mg#	68	65	71	64	66	67	63	86	73	76	71	81

E.2. *Pyroxene continued*

	HKS RC109-5 pheno	HKS RC109-8 pheno	HKS RC109-9 pheno	HKS RC100-1 pheno	HKS RC100-4 gm	HKS RC100-6 gm	HKS RC100-7 pheno	HKS RC100-8 pheno	HKS RC100-11 pheno	HKS RC100-12 pheno	HKS RC100-1 pheno	HKS RC123-1 pheno
SiO ₂	49.70	50.30	44.88	46.94	49.00	45.64	46.83	48.10	46.26	51.17	47.78	47.83
Al ₂ O ₃	4.39	3.80	8.97	7.16	5.31	8.95	6.71	6.73	8.00	4.01	6.88	6.76
TiO ₂	1.00	0.84	1.72	1.27	1.10	1.93	1.13	1.21	1.59	0.60	1.12	1.05
Cr ₂ O ₃	b.d.	b.d.	b.d.	b.d.	b.d.	b.d.	b.d.	b.d.	b.d.	0.19	b.d.	b.d.
Fe ₂ O ₃ *	2.03	0.64	4.14	3.37	0.61	3.94	5.16	3.31	4.36	1.02	4.08	3.73
FeO*	7.21	8.30	5.06	5.49	8.22	6.09	4.59	5.63	4.77	4.59	4.80	5.96
MgO	12.70	12.49	11.24	11.31	11.96	10.52	11.07	11.78	11.09	14.40	11.72	11.92
MnO	0.26	0.36	0.15	0.16	0.21	0.16	0.22	0.13	0.17	0.15	0.20	0.23
CaO	22.21	21.80	22.59	23.58	23.14	23.17	24.15	23.77	23.74	23.79	23.79	22.84
Na ₂ O	0.38	0.44	0.22	0.27	0.04	0.35	0.33	0.30	0.35	0.18	0.38	0.31
Total	99.88	98.97	98.98	99.55	99.59	100.74	100.18	100.96	100.33	100.10	100.76	100.62
Pyroxene formulae calculated on the basis of 6 oxygen												
Si ⁴⁺	1.860	1.898	1.700	1.767	1.843	1.706	1.759	1.784	1.730	1.886	1.775	1.781
ivAl ³⁺	0.140	0.102	0.300	0.233	0.157	0.294	0.241	0.216	0.270	0.114	0.225	0.219
ivFe ³⁺	0.000	0.000	0.000	0.000	0.000	0.000	0.000	0.000	0.000	0.000	0.000	0.000
Total	2.000	2.000	2.000	2.000	2.000	2.000	2.000	2.000	2.000	2.000	2.000	2.000
viAl ³⁺	0.054	0.067	0.100	0.085	0.078	0.100	0.056	0.078	0.083	0.060	0.076	0.078
Ti ⁴⁺	0.028	0.024	0.049	0.036	0.031	0.054	0.032	0.034	0.045	0.017	0.031	0.029
Cr ³⁺	0.000	0.001	0.000	0.000	0.001	0.001	0.000	0.000	0.000	0.006	0.000	0.001
viFe ³⁺	0.057	0.018	0.118	0.096	0.017	0.111	0.146	0.092	0.123	0.028	0.114	0.104
Fe ²⁺	0.226	0.262	0.160	0.173	0.259	0.190	0.144	0.175	0.149	0.142	0.149	0.185
Mg ²⁺	0.709	0.703	0.635	0.635	0.671	0.586	0.620	0.651	0.618	0.791	0.649	0.662
Mn ²⁺	0.008	0.012	0.005	0.005	0.007	0.005	0.007	0.004	0.005	0.005	0.006	0.007
Ca ²⁺	0.891	0.881	0.917	0.951	0.933	0.928	0.972	0.944	0.951	0.939	0.947	0.911
Na ⁺	0.028	0.032	0.016	0.020	0.003	0.025	0.024	0.022	0.025	0.013	0.027	0.022
Total	2.001	2.000	2.000	2.001	2.000	2.000	2.001	2.000	1.999	2.001	1.999	1.999
Molecular percentages												
ΣFeO	14.1	15.1	12.6	12.5	14.6	14.2	12.3	12.4	12.1	8.5	11.7	13.5
MgO	38.1	37.6	35.7	35.0	35.7	33.2	34.1	35.8	34.6	41.8	35.9	36.4
CaO	47.8	47.2	51.6	52.5	49.7	52.6	53.5	51.9	53.3	49.7	52.4	50.1
Mg#	71	71	69	70	70	66	68	71	69	82	71	69

E.2. Pyroxene *continued*

	HKS RC123-2	HKS RC123-3	HKS RC123-11	HKS RC123-13	KS ER109-1	KS ER109-9	KS ER109-10	KS ER109-11	KS ER109-16	KS ER109-17	KS ER109-18	KS ER109-19
	pheno	gm	pheno	gm	pheno	pheno	pheno	gm	gm	pheno	pheno	gm
SiO ₂	48.57	50.15	48.83	46.68	45.47	44.02	46.15	47.49	45.88	53.27	48.14	50.64
Al ₂ O ₃	6.82	5.03	6.50	7.33	9.45	8.62	9.76	8.11	9.85	2.53	7.14	4.99
TiO ₂	1.04	0.96	1.32	1.91	1.47	1.44	1.70	1.26	1.88	0.40	0.92	0.81
Cr ₂ O ₃	0.09	b.d.	b.d.	b.d.	0.06	b.d.	b.d.	b.d.	b.d.	0.65	b.d.	b.d.
Fe ₂ O ₃ *	2.27	1.48	2.56	4.23	4.73	7.56	3.22	3.17	3.60	0.38	3.83	2.07
FeO*	5.04	7.29	6.77	7.81	3.34	6.05	4.28	4.32	4.22	3.02	5.11	4.45
MgO	13.01	13.02	12.37	11.13	11.71	8.38	12.09	12.99	11.92	16.68	11.84	14.24
MnO	0.18	0.17	0.16	0.25	0.08	0.44	0.10	0.10	0.10	0.05	0.16	0.17
CaO	23.12	22.42	22.79	21.75	23.28	23.16	23.01	22.56	23.06	23.42	23.47	23.69
Na ₂ O	0.21	0.31	0.30	0.38	0.34	0.61	0.28	0.31	0.31	0.27	0.42	0.20
Total	100.36	100.83	101.61	101.47	99.92	100.28	100.59	100.31	100.82	100.67	101.02	101.26
Pyroxene formulae calculated on the basis of 6 oxygen												
Si ⁴⁺	1.797	1.854	1.798	1.740	1.696	1.679	1.705	1.755	1.694	1.930	1.781	1.849
ivAl ³⁺	0.203	0.146	0.202	0.260	0.304	0.321	0.295	0.245	0.306	0.070	0.219	0.151
ivFe ³⁺	0.000	0.000	0.000	0.000	0.000	0.000	0.000	0.000	0.000	0.000	0.000	0.000
Total	2.000	2.000	2.000	2.000	2.000	2.000	2.000	2.000	2.000	2.000	2.000	2.000
viAl ³⁺	0.094	0.073	0.080	0.062	0.111	0.066	0.130	0.108	0.123	0.038	0.092	0.064
Ti ⁴⁺	0.029	0.027	0.037	0.054	0.041	0.041	0.047	0.035	0.052	0.011	0.026	0.022
Cr ³⁺	0.003	0.000	0.000	0.000	0.002	0.000	0.000	0.000	0.000	0.019	0.000	0.000
viFe ³⁺	0.063	0.041	0.071	0.119	0.133	0.217	0.090	0.088	0.100	0.010	0.107	0.057
Fe ²⁺	0.156	0.225	0.209	0.244	0.104	0.193	0.132	0.134	0.130	0.091	0.158	0.136
Mg ²⁺	0.718	0.717	0.679	0.618	0.651	0.476	0.666	0.716	0.656	0.901	0.653	0.775
Mn ²⁺	0.006	0.005	0.005	0.008	0.003	0.014	0.003	0.003	0.003	0.002	0.005	0.005
Ca ²⁺	0.916	0.888	0.899	0.868	0.930	0.946	0.911	0.893	0.912	0.909	0.930	0.927
Na ⁺	0.015	0.022	0.021	0.027	0.025	0.045	0.020	0.022	0.022	0.019	0.030	0.014
Total	2.000	1.998	2.001	2.000	2.000	1.998	1.999	1.999	1.998	2.000	2.001	2.000
Molecular percentages												
ΣFeO	10.6	13.5	13.6	17.3	9.9	18.2	10.3	10.1	10.5	5.1	12.0	9.1
MgO	39.3	38.6	37.2	34.4	37.1	27.4	37.9	40.0	37.4	47.2	36.3	41.4
CaO	50.2	47.8	49.2	48.3	53.0	54.4	51.8	49.9	52.1	47.6	51.7	49.5
Mg#	76	73	70	62	73	53	75	76	74	90	71	80

E.2. *Pyroxene continued*

	KS ER117-5	KS ER117-6	KS ER117-12	KS ER117-13	KS ER117-15	KS ER117-16	KS ER112-1	KS ER112-2	KS ER112-5	KS ER112-9	KS ER112-13	KS ER112-14
	gm	gm	pheno	pheno	pheno	pheno	pheno	pheno	gm	gm	pheno	pheno
SiO ₂	48.50	50.92	46.22	53.37	41.30	48.53	53.79	53.41	50.87	43.41	54.61	47.56
Al ₂ O ₃	7.21	4.41	8.56	2.76	12.13	6.15	2.48	2.92	4.89	8.06	2.04	7.38
TiO ₂	1.00	0.54	1.16	0.45	1.37	0.98	0.34	0.33	0.79	1.14	0.19	1.48
Cr ₂ O ₃	b.d.	b.d.	b.d.	0.12	b.d.	b.d.	0.07	0.54	0.31	b.d.	b.d.	b.d.
Fe ₂ O ₃ *	3.73	1.44	5.69	0.29	8.76	3.39	0.00	0.00	1.50	7.01	0.00	3.05
FeO*	4.26	5.13	3.80	3.78	6.91	3.90	4.45	3.88	4.11	10.60	3.16	6.34
MgO	12.46	13.64	11.07	16.13	6.42	12.82	16.10	15.99	14.59	6.15	16.85	11.87
MnO	0.19	0.15	0.11	0.11	0.19	0.09	0.09	0.14	0.09	0.25	0.08	0.13
CaO	24.29	24.01	24.30	24.07	23.73	24.27	23.89	23.85	23.80	23.82	24.59	22.92
Na ₂ O	0.24	0.22	0.33	0.16	0.36	0.21	0.16	0.17	0.18	0.13	0.14	0.26
Total	101.87	100.45	101.24	101.24	101.17	100.34	101.37	101.23	101.13	100.56	101.66	101.01
Pyroxene formulae calculated on the basis of 6 oxygen												
Si ⁴⁺	1.774	1.877	1.713	1.929	1.576	1.799	1.943	1.930	1.855	1.685	1.957	1.764
ivAl ³⁺	0.226	0.123	0.287	0.071	0.424	0.201	0.057	0.070	0.145	0.315	0.043	0.236
ivFe ³⁺	0.000	0.000	0.000	0.000	0.000	0.000	0.000	0.000	0.000	0.000	0.000	0.000
Total	2.000	2.000	2.000	2.000	2.000	2.000	2.000	2.000	2.000	2.000	2.000	2.000
viAl ³⁺	0.085	0.069	0.087	0.047	0.121	0.068	0.049	0.054	0.065	0.054	0.043	0.087
Ti ⁴⁺	0.028	0.015	0.032	0.012	0.039	0.027	0.009	0.009	0.022	0.033	0.005	0.041
Cr ³⁺	0.000	0.000	0.001	0.003	0.000	0.000	0.002	0.015	0.009	0.000	0.001	0.001
viFe ³⁺	0.103	0.040	0.159	0.008	0.251	0.095	0.000	0.000	0.041	0.205	0.000	0.085
Fe ²⁺	0.130	0.158	0.118	0.114	0.220	0.121	0.134	0.117	0.125	0.344	0.095	0.197
Mg ²⁺	0.680	0.750	0.612	0.869	0.365	0.708	0.867	0.861	0.793	0.356	0.900	0.656
Mn ²⁺	0.006	0.005	0.003	0.003	0.006	0.003	0.003	0.004	0.003	0.008	0.002	0.004
Ca ²⁺	0.952	0.948	0.965	0.932	0.970	0.964	0.925	0.923	0.930	0.991	0.944	0.911
Na ⁺	0.017	0.016	0.024	0.011	0.027	0.015	0.011	0.012	0.013	0.010	0.010	0.019
Total	2.001	2.001	2.001	1.999	1.999	2.001	2.000	1.995	2.001	2.001	2.000	2.001
Molecular percentages												
ΣFeO	10.3	9.7	11.3	6.3	20.9	9.3	7.1	6.4	7.9	25.2	5.0	13.4
MgO	37.4	39.9	34.4	45.2	21.6	38.4	44.9	45.2	42.4	19.8	46.4	36.2
CaO	52.3	50.4	54.3	48.5	57.5	52.3	47.9	48.4	49.7	55.0	48.6	50.3
Mg#	74	79	69	87	43	76	86	88	82	39	90	70

E.2. *Pyroxene continued*

	KS ER112-15 pheno	KS ER121-1 pheno	KS ER121-2 pheno	KS ER121-12 gm	KS ER121-13 gm	KS ER121-16 pheno	KS ER121-17 pheno	KS ER121-18 gm	HKS ER110-1 gm	HKS ER110-2 gm	HKS ER110-7 pheno	HKS ER110-8 pheno
SiO ₂	53.14	54.02	46.73	50.04	48.20	51.84	48.39	44.88	52.72	48.12	53.04	45.15
Al ₂ O ₃	2.76	2.04	9.07	4.45	5.86	2.97	5.57	9.52	2.25	5.60	1.85	6.81
TiO ₂	0.32	0.25	1.55	0.75	1.20	0.44	1.12	1.59	0.60	1.54	0.35	2.24
Cr ₂ O ₃	b.d.	0.27	b.d.	0.17	0.05	0.43	b.d.	b.d.	b.d.	b.d.	b.d.	b.d.
Fe ₂ O ₃ *	0.69	0.36	3.68	3.50	3.74	0.31	3.22	5.41	0.69	3.87	1.31	6.92
FeO*	5.48	2.99	5.16	2.20	5.06	3.47	5.57	3.96	4.23	3.79	3.05	2.33
MgO	15.94	16.86	11.66	14.86	12.51	15.64	12.46	11.29	15.26	12.67	15.73	11.61
MnO	0.17	0.08	0.10	0.16	0.19	0.10	0.14	0.15	0.08	0.05	0.08	0.15
CaO	22.58	24.23	23.43	23.84	23.13	23.49	22.96	23.11	24.56	24.39	24.91	24.17
Na ₂ O	0.18	0.14	0.26	0.24	0.33	0.18	0.33	0.27	0.13	0.27	0.14	0.40
Total	101.26	101.25	101.64	100.21	100.26	98.87	99.76	100.18	100.52	100.30	100.46	99.78
Pyroxene formulae calculated on the basis of 6 oxygen												
Si ⁴⁺	1.929	1.946	1.719	1.840	1.796	1.919	1.812	1.679	1.929	1.790	1.937	1.702
ivAl ³⁺	0.071	0.054	0.281	0.160	0.204	0.081	0.188	0.321	0.071	0.210	0.063	0.298
ivFe ³⁺	0.000	0.000	0.000	0.000	0.000	0.000	0.000	0.000	0.000	0.000	0.000	0.000
Total	2.000	2.000	2.000	2.000	2.000	2.000	2.000	2.000	2.000	2.000	2.000	2.000
viAl ³⁺	0.047	0.033	0.112	0.033	0.053	0.049	0.058	0.099	0.026	0.035	0.017	0.004
Ti ⁴⁺	0.009	0.007	0.043	0.021	0.034	0.012	0.032	0.045	0.017	0.043	0.010	0.063
Cr ³⁺	0.001	0.008	0.000	0.005	0.001	0.013	0.000	0.000	0.001	0.001	0.000	0.000
viFe ³⁺	0.019	0.010	0.102	0.097	0.105	0.009	0.091	0.152	0.019	0.108	0.036	0.196
Fe ²⁺	0.166	0.090	0.159	0.068	0.158	0.108	0.174	0.124	0.129	0.118	0.093	0.074
Mg ²⁺	0.863	0.905	0.639	0.815	0.695	0.863	0.696	0.630	0.833	0.702	0.857	0.652
Mn ²⁺	0.005	0.002	0.003	0.005	0.006	0.003	0.004	0.005	0.002	0.002	0.002	0.005
Ca ²⁺	0.878	0.935	0.923	0.939	0.924	0.932	0.921	0.926	0.963	0.972	0.975	0.976
Na ⁺	0.013	0.010	0.019	0.017	0.024	0.013	0.024	0.020	0.009	0.019	0.010	0.029
Total	2.001	2.000	2.000	2.000	2.000	2.002	2.000	2.001	1.999	2.000	2.000	1.999
Molecular percentages												
ΣFeO	9.4	5.0	12.0	6.5	11.8	6.0	12.2	11.6	7.3	9.4	5.8	9.8
MgO	44.9	46.7	36.0	43.4	37.9	45.2	37.8	35.8	43.0	38.0	44.0	36.1
CaO	45.7	48.3	52.0	50.1	50.3	48.8	50.0	52.6	49.7	52.6	50.1	54.1
Mg#	82	90	71	83	72	88	72	69	85	75	87	70

E.2. *Pyroxene continued*

	HKS ER110-11 pheno	HKS ER110-12 pheno	HKS ER110-13 pheno	HKS ER110-14 pheno	HKS ER118-1 pheno	HKS ER118-2 pheno	HKS ER118-3 pheno	HKS ER118-5 gm	HKS ER118-12 pheno	HKS ER118-13 pheno	HKS ER118-14 pheno	HKS ER118-15 pheno
SiO ₂	51.51	50.33	52.61	48.89	53.43	52.76	45.31	43.71	52.34	46.40	51.31	52.76
Al ₂ O ₃	3.22	2.96	1.75	4.54	2.64	2.79	9.19	9.08	3.67	8.29	3.84	3.32
TiO ₂	0.65	0.92	0.37	1.27	0.42	0.37	1.63	1.86	0.55	1.42	1.05	0.44
Cr ₂ O ₃	b.d.	b.d.	0.07	b.d.	0.13	0.13	b.d.	b.d.	0.22	b.d.	b.d.	0.18
Fe ₂ O ₃ *	2.00	3.34	2.09	4.29	0.95	1.04	5.82	9.27	1.45	4.71	0.00	0.23
FeO*	2.92	3.31	2.08	3.24	2.93	3.40	3.04	4.07	3.17	3.95	11.30	3.90
MgO	14.89	13.61	15.96	13.23	16.40	15.72	11.45	11.18	15.59	11.48	12.00	15.71
MnO	0.03	0.23	0.06	0.10	0.05	0.14	0.09	0.22	0.07	0.23	0.17	0.09
CaO	24.86	24.65	24.98	24.42	24.44	24.32	24.30	21.82	24.22	23.87	21.35	23.85
Na ₂ O	0.18	0.35	0.14	0.30	0.16	0.15	0.21	0.38	0.22	0.33	0.32	0.20
Total	100.26	99.70	100.11	100.29	101.54	100.82	101.04	101.59	101.49	100.68	101.34	100.68
Pyroxene formulae calculated on the basis of 6 oxygen												
Si ⁴⁺	1.891	1.875	1.927	1.816	1.924	1.919	1.680	1.631	1.892	1.725	1.904	1.918
ivAl ³⁺	0.109	0.125	0.073	0.184	0.076	0.081	0.320	0.369	0.108	0.275	0.096	0.082
ivFe ³⁺	0.000	0.000	0.000	0.000	0.000	0.000	0.000	0.000	0.000	0.000	0.000	0.000
Total	2.000	2.000	2.000	2.000	2.000	2.000	2.000	2.000	2.000	2.000	2.000	2.000
viAl ³⁺	0.030	0.005	0.003	0.015	0.036	0.039	0.082	0.030	0.048	0.088	0.072	0.060
Ti ⁴⁺	0.018	0.026	0.010	0.035	0.011	0.010	0.045	0.052	0.015	0.040	0.029	0.012
Cr ³⁺	0.000	0.000	0.002	0.000	0.004	0.004	0.000	0.000	0.006	0.000	0.001	0.005
viFe ³⁺	0.055	0.094	0.058	0.120	0.026	0.029	0.162	0.260	0.039	0.132	0.000	0.006
Fe ²⁺	0.090	0.103	0.064	0.101	0.088	0.104	0.094	0.127	0.096	0.123	0.351	0.119
Mg ²⁺	0.815	0.756	0.872	0.733	0.880	0.852	0.633	0.622	0.840	0.636	0.664	0.851
Mn ²⁺	0.001	0.007	0.002	0.003	0.002	0.004	0.003	0.007	0.002	0.007	0.005	0.003
Ca ²⁺	0.978	0.984	0.980	0.972	0.943	0.948	0.965	0.872	0.938	0.951	0.849	0.929
Na ⁺	0.013	0.025	0.010	0.022	0.011	0.011	0.015	0.027	0.015	0.024	0.023	0.014
Total	2.000	2.000	2.001	2.001	2.001	2.001	1.999	1.997	1.999	2.001	1.994	1.999
Molecular percentages												
ΣFeO	6.2	8.3	4.8	8.8	5.3	6.3	10.0	15.0	6.2	11.0	19.1	6.5
MgO	42.6	39.8	44.8	39.2	45.7	44.3	35.6	35.4	44.3	35.7	35.5	44.7
CaO	51.2	51.9	50.4	52.0	49.0	49.3	54.3	49.6	49.5	53.3	45.4	48.8
Mg#	85	79	88	77	88	86	71	61	86	71	65	87

E.2. Pyroxene *continued*

	HKS ER118-16	HKS ER104-1	HKS ER104-2	HKS ER104-3	HKS ER104-4	HKS ER104-5	HKS ER104-9	HKS ER104-10	HKS ER104-11	HKS ER104-13
	pheno	pheno	pheno	pheno	pheno	pheno	pheno	pheno	pheno	gm
SiO ₂	46.18	50.42	44.84	40.02	47.65	42.85	41.53	48.35	42.58	50.77
Al ₂ O ₃	8.92	6.00	9.88	13.01	7.24	10.53	11.09	6.67	10.51	3.66
TiO ₂	1.60	0.77	1.51	1.96	1.22	2.24	1.56	1.04	1.58	0.70
Cr ₂ O ₃	b.d.	b.d.	b.d.	b.d.	b.d.	b.d.	b.d.	0.12	b.d.	b.d.
Fe ₂ O ₃ *	2.97	2.17	5.23	9.56	4.32	8.01	9.41	4.66	9.36	3.23
FeO*	5.98	3.30	4.93	5.10	3.11	2.87	3.65	1.46	1.42	2.74
MgO	10.94	14.17	9.99	6.98	12.65	10.18	8.42	13.73	10.26	14.51
MnO	0.14	0.04	0.21	0.15	0.07	0.12	0.08	0.09	0.19	0.11
CaO	22.96	24.70	23.73	23.83	24.63	24.23	24.07	24.49	24.01	24.88
Na ₂ O	0.35	0.16	0.35	0.30	0.17	0.23	0.32	0.29	0.36	0.16
Total	100.04	101.73	100.67	100.91	101.06	101.26	100.13	100.91	100.28	100.76
Pyroxene formulae calculated on the basis of 6 oxygen										
Si ⁴⁺	1.729	1.827	1.679	1.525	1.755	1.601	1.583	1.772	1.603	1.863
ivAl ³⁺	0.271	0.173	0.321	0.475	0.245	0.399	0.417	0.228	0.397	0.137
ivFe ³⁺	0.000	0.000	0.000	0.000	0.000	0.000	0.000	0.000	0.000	0.000
Total	2.000	2.000	2.000	2.000	2.000	2.000	2.000	2.000	2.000	2.000
viAl ³⁺	0.123	0.083	0.115	0.109	0.069	0.065	0.081	0.060	0.069	0.021
Ti ⁴⁺	0.045	0.021	0.043	0.056	0.034	0.063	0.045	0.029	0.045	0.019
Cr ³⁺	0.000	0.000	0.000	0.000	0.000	0.000	0.000	0.003	0.000	0.000
viFe ³⁺	0.084	0.059	0.147	0.274	0.120	0.225	0.270	0.129	0.265	0.089
Fe ²⁺	0.187	0.100	0.154	0.163	0.096	0.090	0.116	0.045	0.045	0.084
Mg ²⁺	0.611	0.765	0.557	0.397	0.695	0.567	0.478	0.750	0.576	0.794
Mn ²⁺	0.004	0.001	0.007	0.005	0.002	0.004	0.003	0.003	0.006	0.003
Ca ²⁺	0.921	0.959	0.952	0.973	0.972	0.970	0.983	0.961	0.968	0.978
Na ⁺	0.025	0.011	0.025	0.022	0.012	0.017	0.024	0.021	0.026	0.011
Total	2.000	1.999	2.000	1.999	2.000	2.001	2.000	2.001	2.000	1.999
Molecular percentages										
ΣFeO	13.2	7.1	13.5	18.2	8.7	11.8	14.8	6.1	10.6	6.9
MgO	34.6	41.3	32.0	23.7	38.1	32.5	27.9	41.1	33.3	41.7
CaO	52.2	51.7	54.6	58.1	53.3	55.6	57.3	52.7	56.1	51.4
Mg#	69	83	64	47	76	64	55	81	65	82

E.3. Amphibole

	WA101-1	WA101-5	WA101-7	WA101-9	WA101-11	WA101-12	WA103-2	WA103-7
	mghs	mghs	mghbl	act	tsch	act	mghs	mghs
SiO ₂	41.51	40.41	50.78	53.80	41.07	53.95	41.29	41.63
Al ₂ O ₃	13.12	11.54	5.34	1.51	13.02	1.88	13.07	12.76
TiO ₂	2.73	2.48	0.67	0.02	2.49	0.02	2.53	2.58
Cr ₂ O ₃	b.d.	0.09	b.d.	0.06	b.d.	0.05	b.d.	0.07
FeO*	3.22	5.56	11.99	13.53	7.27	12.14	6.74	4.90
Fe ₂ O ₃ *	8.60	5.95	2.32	0.16	6.45	0.00	3.84	6.03
MnO	0.13	0.17	0.23	0.33	0.21	0.02	0.13	0.08
MgO	14.70	14.26	14.09	14.97	11.99	15.20	14.25	14.94
K ₂ O	0.82	0.95	0.40	0.07	0.88	0.04	0.85	0.95
CaO	11.48	11.99	12.56	13.13	10.82	12.98	12.00	12.02
Na ₂ O	2.11	1.77	0.66	0.08	2.01	0.07	2.39	2.15
Cl	b.d.	b.d.	b.d.	b.d.	0.03	b.d.	b.d.	0.04
F	0.08	0.10	0.05	b.d.	b.d.	b.d.	0.10	0.17
H ₂ O*	2.04	1.95	2.06	2.07	1.99	2.04	1.99	1.98
O=Cl	0.00	0.00	0.00	0.00	-0.01	0.00	0.00	-0.01
O=F	-0.03	-0.04	-0.02	0.00	0.00	0.00	-0.04	-0.07
Total	100.50	97.17	101.14	99.72	98.22	98.38	99.17	100.22
Amphibole formulae calculated on the basis of 24(O, OH, F, Cl)								
Si ⁴⁺	5.981	6.075	7.290	7.800	6.115	7.846	6.067	6.037
ivAl ³⁺	2.019	1.925	0.710	0.200	1.885	0.154	1.933	1.963
ivTi ⁴⁺	0.000	0.000	0.000	0.000	0.000	0.000	0.000	0.000
Total	8.000	8.000	8.000	8.000	8.000	8.000	8.000	8.000
viAl ³⁺	0.209	0.120	0.194	0.058	0.400	0.168	0.330	0.218
viTi ⁴⁺	0.296	0.280	0.072	0.002	0.279	0.002	0.280	0.281
Cr ³⁺	0.000	0.011	0.000	0.007	0.000	0.006	0.000	0.008
Fe ²⁺	0.387	0.699	1.440	1.640	0.906	1.477	0.828	0.594
Fe ³⁺	0.932	0.673	0.251	0.017	0.723	0.000	0.425	0.658
Mn ²⁺	0.016	0.022	0.028	0.041	0.026	0.002	0.016	0.010
Mg ²⁺	3.157	3.196	3.016	3.235	2.661	3.296	3.122	3.230
Total	4.997	5.001	5.001	5.000	4.995	4.951	5.001	4.999
Ca ²⁺	1.772	1.931	1.932	2.039	1.726	2.023	1.889	1.868
Na ⁺	0.228	0.069	0.068	0.000	0.274	0.000	0.111	0.132
Total	2.000	2.000	2.000	2.039	2.000	2.023	2.000	2.000
Na ⁺	0.361	0.447	0.116	0.022	0.306	0.020	0.57	0.473
K ⁺	0.151	0.182	0.073	0.013	0.167	0.007	0.159	0.176
Total	0.512	0.629	0.189	0.035	0.473	0.027	0.729	0.649
OH ⁻	1.961	1.952	1.977	1.998	1.978	1.986	1.949	1.912
Cl ⁻	0.000	0.000	0.000	0.000	0.008	0.000	0.000	0.010
F ⁻	0.036	0.048	0.023	0.000	0.000	0.000	0.046	0.078
O ²⁻	23.961	23.952	23.977	23.998	23.978	23.986	23.949	23.912
Mg#	89	82	68	66	75	69	79	84

Abbreviations for amphibole names: mghs = magnesiohastingsite, mghbl = magnesiohornblende, act = actinolite, tsch = tschermakite, ferich = ferrichterite, rich = richterite, eden = edenite, f-fepar = fluoro-ferropargasite, f-hast = fluorohastingsite

E.3. *Amphibole continued*

	WA103-10	WA103-13	WA103-14	WA104-4	WA104-5	WA104-7	WA104-8	WA107-1
	mghs	tsch	mghs	ferich	rich	ferich	rich	tsch
SiO ₂	41.20	42.56	41.81	48.83	49.17	48.21	50.38	43.07
Al ₂ O ₃	12.26	11.79	13.71	0.63	0.52	0.89	0.40	11.53
TiO ₂	2.76	3.04	2.68	3.33	2.87	3.31	2.12	1.37
Cr ₂ O ₃	b.d.	b.d.	0.06	b.d.	b.d.	b.d.	b.d.	b.d.
FeO*	5.13	8.36	6.30	21.49	14.46	20.52	11.38	2.53
Fe ₂ O ₃ *	7.76	5.76	4.59	3.59	5.38	3.38	3.98	9.74
MnO	0.09	0.21	0.14	0.50	0.31	0.44	0.35	0.16
MgO	14.16	12.80	14.37	6.90	10.56	7.03	13.60	15.07
K ₂ O	0.79	0.82	0.81	2.52	2.30	2.31	1.92	0.75
CaO	11.70	11.59	12.14	3.57	3.50	3.77	4.55	11.18
Na ₂ O	2.10	1.87	2.35	5.89	5.99	5.47	6.18	2.08
Cl	0.05	0.11	0.05	b.d.	b.d.	b.d.	b.d.	0.06
F	0.06	0.24	0.16	0.61	0.68	0.41	0.70	0.30
H ₂ O*	2.01	1.92	1.99	1.63	1.61	1.70	1.64	1.91
O=Cl	-0.01	-0.02	-0.01	0.00	0.00	0.00	0.00	-0.01
O=F	-0.03	-0.10	-0.07	-0.26	-0.29	-0.17	-0.29	-0.13
Total	100.03	100.94	101.09	99.23	97.06	97.27	96.90	99.63
Amphibole formulae calculated on the basis of 24(O, OH, F, Cl)								
Si ⁴⁺	6.014	6.193	6.020	7.606	7.602	7.615	7.656	6.239
ivAl ³⁺	1.986	1.807	1.980	0.116	0.095	0.166	0.072	1.761
ivTi ⁴⁺	0.000	0.000	0.000	0.278	0.303	0.219	0.242	0.000
Total	8.000	8.000	8.000	8.000	8.000	8.000	7.970	8.000
viAl ³⁺	0.123	0.215	0.346	0.000	0.000	0.000	0.000	0.207
viTi ⁴⁺	0.303	0.333	0.290	0.112	0.031	0.174	0.000	0.149
Cr ³⁺	0.000	0.000	0.007	0.000	0.000	0.000	0.000	0.000
Fe ²⁺	0.626	1.017	0.758	2.799	1.870	2.710	1.446	0.307
Fe ³⁺	0.852	0.631	0.497	0.421	0.626	0.402	0.455	1.062
Mn ²⁺	0.011	0.026	0.017	0.066	0.041	0.059	0.045	0.020
Mg ²⁺	3.082	2.777	3.084	1.602	2.434	1.655	3.081	3.254
Total	4.997	4.999	4.999	5.000	5.002	5.000	5.027	4.999
Ca ²⁺	1.830	1.807	1.873	0.596	0.580	0.638	0.741	1.735
Na ⁺	0.170	0.193	0.127	1.404	1.420	1.362	1.259	0.265
Total	2.000	2.000	2.000	2.000	2.000	2.000	2.000	2.000
Na ⁺	0.424	0.335	0.529	0.375	0.376	0.313	0.562	0.319
K ⁺	0.147	0.152	0.149	0.501	0.454	0.465	0.372	0.139
Total	0.571	0.487	0.678	0.876	0.830	0.778	0.934	0.458
OH ⁻	1.960	1.862	1.915	1.697	1.665	1.793	1.658	1.848
Cl ⁻	0.012	0.027	0.012	0.000	0.000	0.000	0.000	0.015
F ⁻	0.028	0.110	0.073	0.301	0.332	0.205	0.336	0.137
O ²⁻	23.960	23.862	23.915	23.697	23.665	23.793	23.658	23.848
Mg#	83	73	80	36	57	38	68	91

E.3. *Amphibole continued*

	WA107-2	WA107-3	WA107-5	WA107-6	WA107-8	WA107-9	WA107-10	WA107-12
	eden	mghs	act	act	mghs	mghs	act	act
SiO ₂	46.18	43.70	57.30	58.00	43.08	43.56	56.74	57.26
Al ₂ O ₃	9.38	11.16	0.69	0.49	11.29	10.98	1.31	1.12
TiO ₂	1.77	2.05	0.14	0.01	2.14	2.10	0.02	0.05
Cr ₂ O ₃	0.13	0.08	0.06	b.d.	b.d.	0.05	0.35	0.23
FeO*	2.40	4.64	5.22	6.42	5.38	4.29	6.69	5.96
Fe ₂ O ₃ *	6.89	5.57	1.71	0.00	6.49	5.78	0.00	0.00
MnO	0.08	0.11	0.14	0.13	0.16	0.03	0.14	0.19
MgO	17.48	15.72	20.12	20.21	14.71	16.10	19.63	20.14
K ₂ O	0.82	0.85	0.05	0.04	0.74	0.92	0.04	0.02
CaO	11.62	11.80	12.72	13.57	11.54	11.90	13.30	13.15
Na ₂ O	2.17	2.21	0.20	0.21	2.25	2.22	0.37	0.25
Cl	b.d.	b.d.	b.d.	b.d.	0.05	b.d.	b.d.	b.d.
F	0.39	0.33	0.04	b.d.	0.19	0.36	0.06	b.d.
H ₂ O*	1.93	1.92	2.15	2.17	1.96	1.90	2.13	2.15
O=Cl	0.00	0.00	0.00	0.00	-0.01	0.00	0.00	0.00
O=F	-0.16	-0.14	-0.02	0.00	-0.08	-0.15	-0.03	0.00
Total	101.08	100.00	100.52	101.24	99.89	100.04	100.75	100.54
Amphibole formulae calculated on the basis of 24(O, OH, F, Cl)								
Si ⁴⁺	6.526	6.308	7.922	7.975	6.261	6.286	7.869	7.916
ivAl ³⁺	1.474	1.692	0.078	0.025	1.739	1.714	0.131	0.084
ivTi ⁴⁺	0.000	0.000	0.000	0.000	0.000	0.000	0.000	0.000
Total	8.000	8.000	8.000	8.000	8.000	8.000	8.000	8.000
viAl ³⁺	0.088	0.207	0.034	0.054	0.195	0.153	0.083	0.098
viTi ⁴⁺	0.188	0.223	0.015	0.001	0.234	0.228	0.002	0.005
Cr ³⁺	0.015	0.009	0.007	0.000	0.000	0.006	0.038	0.025
Fe ²⁺	0.284	0.560	0.604	0.738	0.654	0.517	0.776	0.689
Fe ³⁺	0.733	0.605	0.178	0.000	0.710	0.628	0.000	0.000
Mn ²⁺	0.010	0.013	0.016	0.015	0.020	0.004	0.016	0.022
Mg ²⁺	3.683	3.383	4.147	4.143	3.187	3.464	4.058	4.151
Total	5.001	5.000	5.001	4.951	5.000	5.000	4.973	4.990
Ca ²⁺	1.759	1.825	1.884	1.999	1.797	1.840	1.976	1.948
Na ⁺	0.241	0.175	0.054	0.001	0.203	0.160	0.024	0.052
Total	2.000	2.000	1.938	2.000	2.000	2.000	2.000	2.000
Na ⁺	0.354	0.444	0.000	0.055	0.431	0.461	0.075	0.015
K ⁺	0.148	0.157	0.009	0.007	0.137	0.169	0.007	0.004
Total	0.502	0.601	0.009	0.062	0.568	0.630	0.082	0.019
OH ⁻	1.823	1.847	1.983	1.995	1.900	1.831	1.974	1.985
Cl ⁻	0.000	0.000	0.000	0.000	0.012	0.000	0.000	0.000
F ⁻	0.174	0.151	0.017	0.000	0.087	0.164	0.026	0.000
O ²⁻	23.823	23.847	23.983	23.995	23.900	23.831	23.974	23.985
Mg#	93	86	87	85	83	87	84	86

E.3. *Amphibole continued*

	WA107-13	WA107-15	WA107-16	WA107-17	WA107-23	WA107-24	WA107-25	WA107-26
	mghs	act	mghs	act	tsch	fepar	mghbl	tsch
SiO ₂	44.91	57.03	43.82	57.15	44.02	42.11	45.54	43.68
Al ₂ O ₃	9.86	0.84	10.79	0.54	9.97	13.08	9.87	10.60
TiO ₂	1.72	0.00	1.98	0.03	1.85	0.77	1.61	1.21
Cr ₂ O ₃	0.14	0.39	0.06	b.d.	b.d.	b.d.	0.05	b.d.
FeO*	1.96	5.01	3.42	7.99	4.31	17.22	2.49	4.73
Fe ₂ O ₃ *	7.72	0.65	8.03	0.00	5.93	0.60	6.06	7.87
MnO	0.09	0.21	0.14	0.17	0.17	0.39	0.16	0.22
MgO	17.15	20.64	15.63	19.31	15.25	7.90	17.02	14.57
K ₂ O	0.81	0.02	0.80	0.02	0.64	1.68	0.82	0.69
CaO	11.60	13.18	11.42	13.24	11.31	11.56	11.50	11.38
Na ₂ O	2.17	0.22	2.14	0.19	1.79	1.40	2.02	1.99
Cl	b.d.	b.d.	b.d.	b.d.	b.d.	0.08	b.d.	0.04
F	0.41	0.08	0.31	0.04	0.07	0.09	0.27	0.13
H ₂ O*	1.91	2.13	1.94	2.14	2.00	1.90	1.96	1.98
O=Cl	0.00	0.00	0.00	0.00	0.00	-0.02	0.00	-0.01
O=F	-0.17	-0.03	-0.13	-0.02	-0.03	-0.04	-0.11	-0.05
Total	100.28	100.36	100.34	100.80	97.28	98.73	99.24	99.02
Amphibole formulae calculated on the basis of 24(O, OH, F, Cl)								
Si ⁴⁺	6.414	7.891	6.302	7.952	6.494	6.435	6.536	6.390
ivAl ³⁺	1.586	0.109	1.698	0.048	1.506	1.565	1.464	1.610
ivTi ⁴⁺	0.000	0.000	0.000	0.000	0.000	0.000	0.000	0.000
Total	8.000	8.000	8.000	8.000	8.000	8.000	8.000	8.000
viAl ³⁺	0.074	0.028	0.131	0.041	0.228	0.791	0.206	0.218
viTi ⁴⁺	0.185	0.000	0.214	0.003	0.205	0.088	0.174	0.133
Cr ³⁺	0.016	0.043	0.007	0.000	0.000	0.000	0.006	0.000
Fe ²⁺	0.235	0.580	0.411	0.930	0.532	2.201	0.298	0.579
Fe ³⁺	0.830	0.067	0.869	0.000	0.658	0.069	0.655	0.866
Mn ²⁺	0.011	0.025	0.017	0.020	0.021	0.050	0.019	0.027
Mg ²⁺	3.651	4.258	3.351	4.006	3.354	1.800	3.642	3.177
Total	5.002	5.001	5.000	5.000	4.998	4.999	5.000	5.000
Ca ²⁺	1.775	1.954	1.760	1.974	1.788	1.893	1.769	1.784
Na ⁺	0.225	0.046	0.240	0.026	0.212	0.107	0.231	0.216
Total	2.000	2.000	2.000	2.000	2.000	2.000	2.000	2.000
Na ⁺	0.376	0.013	0.357	0.025	0.3	0.308	0.331	0.348
K ⁺	0.148	0.004	0.147	0.004	0.120	0.328	0.150	0.129
Total	0.524	0.017	0.504	0.029	0.420	0.636	0.481	0.477
OH ⁻	1.815	1.965	1.859	1.982	1.967	1.936	1.873	1.930
Cl ⁻	0.000	0.000	0.000	0.000	0.000	0.021	0.000	0.010
F ⁻	0.185	0.035	0.141	0.018	0.033	0.043	0.123	0.060
O ²⁻	23.815	23.965	23.859	23.982	23.967	23.936	23.873	23.930
Mg#	94	88	89	81	86	45	92	85

E.3. *Amphibole continued*

	WA107-27	WA107-28	WA107-29	WA107-30	ER104-14	ER104-15	ER104-17
	act	mghbl	mghbl	tsch	f-hast	f-feapar	f-hast
SiO ₂	57.22	45.23	48.84	43.63	39.28	39.00	38.87
Al ₂ O ₃	1.12	9.49	8.87	10.76	11.57	12.39	12.08
TiO ₂	0.04	1.83	0.64	1.86	1.07	1.33	1.16
Cr ₂ O ₃	0.08	b.d.	0.41	b.d.	b.d.	b.d.	b.d.
FeO*	5.99	2.51	0.08	4.21	15.36	17.35	16.20
Fe ₂ O ₃ *	0.00	7.68	6.13	7.80	4.16	1.61	4.06
MnO	0.16	0.08	0.03	0.15	0.51	0.54	0.69
MgO	19.94	16.43	18.96	14.97	8.70	8.07	8.09
K ₂ O	0.01	0.73	0.47	0.71	1.97	1.92	1.84
CaO	13.06	11.08	12.14	11.32	11.58	11.93	11.77
Na ₂ O	0.23	2.05	1.31	2.06	1.85	1.84	1.91
Cl	b.d.	b.d.	b.d.	0.04	0.16	0.18	0.12
F	0.04	0.21	b.d.	0.18	2.66	2.69	2.68
H ₂ O*	2.14	1.98	2.13	1.97	0.61	0.59	0.62
O=Cl	0.00	0.00	0.00	-0.01	-0.04	-0.04	-0.03
O=F	-0.02	-0.09	0.00	-0.08	-1.12	-1.13	-1.13
Total	100.01	99.20	100.02	99.58	98.34	98.26	98.94
Amphibole formulae calculated on the basis of 24(O, OH, F, Cl)							
Si ⁴⁺	7.944	6.515	6.822	6.334	6.145	6.123	6.071
ivAl ³⁺	0.056	1.485	1.178	1.666	1.855	1.877	1.929
ivTi ⁴⁺	0.000	0.000	0.000	0.000	0.000	0.000	0.000
Total	8.000	8.000	8.000	8.000	8.000	8.000	8.000
viAl ³⁺	0.127	0.126	0.282	0.175	0.278	0.416	0.295
viTi ⁴⁺	0.004	0.198	0.067	0.203	0.126	0.157	0.136
Cr ³⁺	0.009	0.000	0.045	0.001	0.000	0.000	0.000
Fe ²⁺	0.695	0.302	0.010	0.511	2.010	2.277	2.117
Fe ³⁺	0.000	0.832	0.645	0.852	0.490	0.190	0.478
Mn ²⁺	0.019	0.010	0.004	0.018	0.068	0.072	0.091
Mg ²⁺	4.127	3.528	3.948	3.240	2.029	1.889	1.884
Total	4.981	4.996	5.001	5.000	5.001	5.001	5.001
Ca ²⁺	1.943	1.710	1.817	1.761	1.941	2.007	1.970
Na ⁺	0.057	0.290	0.183	0.239	0.059	0.000	0.030
Total	2.000	2.000	2.000	2.000	2.000	2.007	2.000
Na ⁺	0.005	0.283	0.172	0.341	0.502	0.560	0.548
K ⁺	0.002	0.134	0.084	0.131	0.393	0.385	0.367
Total	0.007	0.417	0.256	0.472	0.895	0.945	0.915
OH ⁻	1.982	1.899	1.986	1.908	0.642	0.616	0.644
Cl ⁻	0.000	0.000	0.000	0.010	0.042	0.048	0.032
F ⁻	0.018	0.096	0.000	0.083	1.316	1.336	1.324
O ²⁻	23.982	23.899	23.986	23.908	22.642	22.616	22.644
Mg#	86	92	100	86	50	45	47

E.4. Mica

	WA100-4	WA100-5	WA100-6	WA100-16	WA100-20	WA100-21	WA100-22	WA100-23	WA100-25	WA102-1	WA102-2	WA102-3
SiO ₂	40.78	36.20	35.51	36.12	34.71	35.44	37.65	36.40	33.42	39.23	37.16	37.88
Al ₂ O ₃	13.99	14.62	15.84	15.42	18.17	18.60	15.45	14.24	14.66	14.12	13.72	13.96
TiO ₂	1.57	3.82	5.45	2.35	0.80	0.13	1.56	3.51	2.74	3.36	3.36	3.29
Cr ₂ O ₃	0.86	b.d.	b.d.	b.d.	b.d.	0.05	0.21	b.d.	b.d.	0.11	b.d.	b.d.
FeO	5.12	18.57	12.77	17.51	15.41	15.61	5.47	14.97	18.49	6.83	17.84	10.67
MgO	23.81	12.69	14.87	13.84	14.12	15.32	21.95	15.25	13.13	21.06	13.57	18.80
MnO	0.03	0.16	0.06	0.20	0.12	0.15	0.03	0.14	0.14	0.04	0.18	0.05
K ₂ O	10.14	9.43	8.53	9.48	8.92	9.71	9.39	8.99	8.29	9.50	8.97	9.42
CaO	b.d.	0.04	b.d.	0.10	0.02	b.d.	0.07	0.07	0.08	0.04	0.03	b.d.
Na ₂ O	0.25	0.10	0.51	0.05	0.33	0.21	0.32	0.15	0.08	0.25	0.16	0.25
BaO	0.48	1.08	1.48	0.61	1.39	0.20	0.75	0.95	1.14	0.73	0.86	0.82
F	1.21	0.37	0.48	0.50	0.34	0.41	0.48	0.53	0.39	0.82	0.41	0.60
Cl	b.d.	0.04	b.d.	0.03	0.05	b.d.	0.05	0.04	0.08	b.d.	0.05	b.d.
Total	98.24	97.12	95.50	96.21	94.41	95.83	93.38	95.24	92.64	96.09	96.31	95.75
Mica formulae calculated on the basis of 22 oxygen												
Si ⁴⁺	5.738	5.487	5.328	5.484	5.325	5.321	5.552	5.525	5.331	5.664	5.631	5.594
ivAl ³⁺	2.262	2.513	2.672	2.516	2.675	2.679	2.448	2.475	2.669	2.336	2.369	2.406
Total	8.000											
viAl ³⁺	0.058	0.099	0.128	0.242	0.611	0.613	0.237	0.073	0.087	0.067	0.082	0.025
Ti ⁴⁺	0.166	0.435	0.615	0.269	0.093	0.015	0.173	0.400	0.328	0.365	0.383	0.366
Cr ³⁺	0.096	0.000	0.000	0.000	0.000	0.006	0.024	0.000	0.000	0.013	0.000	0.000
Fe ²⁺	0.602	2.354	1.603	2.223	1.977	1.960	0.675	1.900	2.467	0.825	2.261	1.317
Mg ²⁺	4.993	2.867	3.326	3.132	3.228	3.428	4.825	3.451	3.122	4.532	3.065	4.138
Mn ²⁺	0.003	0.021	0.007	0.026	0.015	0.019	0.004	0.018	0.018	0.005	0.023	0.006
Total	5.918	5.776	5.679	5.892	5.924	6.041	5.938	5.842	6.022	5.807	5.814	5.852
K ⁺	1.819	1.824	1.632	1.836	1.746	1.861	1.767	1.740	1.686	1.750	1.734	1.775
Ca ²⁺	0.000	0.006	0.000	0.015	0.003	0.001	0.011	0.011	0.013	0.006	0.005	0.000
Na ⁺	0.068	0.031	0.147	0.014	0.098	0.061	0.092	0.044	0.025	0.071	0.046	0.071
Ba ²⁺	0.027	0.064	0.087	0.036	0.084	0.012	0.043	0.057	0.071	0.042	0.051	0.048
Total	1.914	1.925	1.866	1.901	1.931	1.935	1.913	1.852	1.795	1.869	1.836	1.894
F ⁻	0.536	0.177	0.227	0.238	0.166	0.195	0.224	0.252	0.198	0.374	0.197	0.278
Cl ⁻	0.000	0.011	0.000	0.009	0.012	0.000	0.013	0.011	0.022	0.000	0.014	0.000
Mg#	89	55	67	58	62	64	88	64	56	85	58	76

E.4. *Mica continued*

	WA102-4	WA102-7	WA102-11	WA102-12	WA102-13	WA102-14	WA102-15	WA103-13	WA103-14	WA104-1	WA104-2	WA104-3
SiO ₂	35.54	37.69	38.70	37.16	37.16	38.42	34.46	47.81	46.91	35.47	36.40	41.58
Al ₂ O ₃	14.23	13.83	13.96	13.70	13.56	13.93	14.51	30.81	35.43	14.34	14.26	11.69
TiO ₂	3.95	3.52	3.09	3.35	3.27	3.33	4.27	b.d.	0.05	3.82	3.42	2.26
Cr ₂ O ₃	b.d.	0.22	0.14	0.29	0.11	0.05	b.d.	b.d.	b.d.	b.d.	b.d.	b.d.
FeO	19.50	6.34	6.83	12.85	16.58	6.83	20.02	2.92	1.25	20.95	20.28	5.28
MgO	11.62	21.68	21.72	17.48	14.87	21.40	11.36	1.23	0.29	10.20	10.98	23.89
MnO	0.24	0.01	0.03	0.13	0.19	0.07	0.28	0.00	0.03	0.35	0.20	0.04
K ₂ O	8.83	9.22	9.54	9.24	9.18	9.22	8.76	8.57	9.83	9.48	9.71	10.72
CaO	0.03	0.05	0.04	b.d.	b.d.	0.11	0.07	0.26	0.08	b.d.	0.07	0.04
Na ₂ O	0.19	0.18	0.20	0.21	0.18	0.15	0.18	0.18	0.54	0.21	0.29	0.14
BaO	1.31	0.79	0.52	0.82	0.84	0.83	1.23	0.35	0.59	1.86	0.37	0.36
F	0.22	0.81	0.84	0.58	0.44	0.84	0.18	0.06	b.d.	0.36	0.26	1.46
Cl	0.03	b.d.	b.d.	b.d.	b.d.	b.d.	0.06	b.d.	b.d.	0.25	0.21	b.d.
Total	95.69	94.34	95.61	95.81	96.38	95.18	95.38	92.19	95.00	97.29	96.45	97.46
Mica formulae calculated on the basis of 22 oxygen												
Si ⁴⁺	5.492	5.549	5.619	5.551	5.604	5.610	5.368	6.555	6.248	5.494	5.586	5.922
ivAl ³⁺	2.508	2.400	2.381	2.412	2.396	2.390	2.632	1.445	1.752	2.506	2.414	1.962
Total	8.000	7.949	8.000	7.963	8.000	7.884						
viAl ³⁺	0.083	0.000	0.007	0.000	0.013	0.007	0.031	3.534	3.810	0.112	0.165	0.000
Ti ⁴⁺	0.459	0.390	0.338	0.377	0.371	0.366	0.500	0.000	0.005	0.445	0.395	0.242
Cr ³⁺	0.000	0.025	0.017	0.034	0.013	0.006	0.000	0.000	0.000	0.000	0.000	0.000
Fe ²⁺	2.519	0.780	0.829	1.606	2.090	0.834	2.608	0.335	0.139	2.714	2.603	0.628
Mg ²⁺	2.676	4.758	4.700	3.893	3.343	4.656	2.637	0.252	0.058	2.355	2.511	5.072
Mn ²⁺	0.031	0.001	0.003	0.016	0.025	0.009	0.036	0.000	0.003	0.046	0.026	0.005
Total	5.769	5.954	5.894	5.926	5.855	5.878	5.812	4.122	4.015	5.672	5.700	5.947
K ⁺	1.740	1.731	1.768	1.760	1.765	1.718	1.741	1.500	1.670	1.873	1.902	1.948
Ca ²⁺	0.005	0.008	0.006	0.000	0.000	0.017	0.011	0.038	0.011	0.000	0.011	0.006
Na ⁺	0.057	0.052	0.056	0.062	0.053	0.043	0.055	0.048	0.140	0.062	0.087	0.038
Ba ²⁺	0.079	0.045	0.029	0.048	0.050	0.047	0.075	0.019	0.031	0.113	0.022	0.020
Total	1.881	1.836	1.859	1.870	1.868	1.825	1.882	1.605	1.852	2.048	2.022	2.012
F ⁻	0.107	0.375	0.384	0.273	0.211	0.387	0.087	0.026	0.000	0.174	0.124	0.655
Cl ⁻	0.008	0.000	0.000	0.000	0.001	0.000	0.015	0.000	0.000	0.066	0.053	0.000
Mg#	52	86	85	71	62	85	50	43	29	46	49	89

E.4. *Mica continued*

	WA104-4	WA104-7	WA104-8	WA104-9	WA104-16	WA104-17	WA104-18	WA105-1	WA105-2	WA105-8	WA105-9	WA105-13
SiO ₂	39.06	36.21	41.56	41.44	41.95	37.45	35.83	38.28	36.68	38.40	36.90	38.41
Al ₂ O ₃	12.00	15.35	12.67	12.32	11.48	12.56	14.49	13.99	13.74	14.17	13.85	14.24
TiO ₂	4.06	4.46	1.74	1.52	1.87	4.80	3.68	3.41	3.01	3.10	3.05	3.29
Cr ₂ O ₃	b.d.	b.d.	0.33	0.70	0.24	b.d.	b.d.	b.d.	b.d.	0.15	0.05	0.07
FeO	11.90	12.41	3.32	3.02	4.24	12.84	19.87	7.49	16.46	7.39	16.29	6.54
MgO	17.68	16.45	25.21	25.07	23.71	16.97	11.15	20.82	14.63	20.93	14.34	21.42
MnO	0.12	0.09	0.00	0.03	0.00	0.09	0.35	0.06	0.18	0.00	0.25	0.04
K ₂ O	10.18	10.14	10.87	10.68	9.48	9.24	8.96	9.98	9.51	10.17	9.47	10.06
CaO	b.d.	0.02	0.02	0.08	0.67	b.d.	0.02	b.d.	0.02	0.02	0.02	0.05
Na ₂ O	0.15	0.20	0.08	0.09	0.18	0.14	0.26	0.27	0.20	0.22	0.28	0.27
BaO	0.87	1.25	0.37	0.35	0.42	1.33	0.77	1.02	0.98	0.98	0.97	1.08
F	0.94	0.51	1.32	1.39	1.39	0.83	0.35	1.02	0.56	1.02	0.67	1.07
Cl	0.05	b.d.	b.d.	b.d.	b.d.	0.03	0.15	b.d.	b.d.	b.d.	b.d.	b.d.
Total	97.01	97.09	97.49	96.69	95.63	96.28	95.88	96.35	95.97	96.55	96.14	96.54
Mica formulae calculated on the basis of 22 oxygen												
Si ⁴⁺	5.772	5.366	5.859	5.889	6.021	5.605	5.526	5.583	5.581	5.588	5.604	5.575
ivAl ³⁺	2.091	2.634	2.105	2.064	1.942	2.215	2.474	2.404	2.419	2.412	2.396	2.425
Total	7.863	8.000	7.964	7.953	7.963	7.820	8.000	7.987	8.000	8.000	8.000	8.000
viAl ³⁺	0.000	0.047	0.000	0.000	0.000	0.000	0.161	0.000	0.045	0.019	0.083	0.010
Ti ⁴⁺	0.452	0.497	0.184	0.162	0.202	0.540	0.427	0.374	0.344	0.339	0.349	0.359
Cr ³⁺	0.000	0.000	0.037	0.079	0.027	0.000	0.000	0.000	0.000	0.017	0.006	0.008
Fe ²⁺	1.471	1.538	0.392	0.359	0.509	1.607	2.562	0.913	2.094	0.899	2.070	0.794
Mg ²⁺	3.896	3.634	5.298	5.311	5.073	3.785	2.564	4.525	3.317	4.541	3.246	4.632
Mn ²⁺	0.015	0.011	0.000	0.003	0.001	0.011	0.046	0.007	0.023	0.000	0.033	0.005
Total	5.834	5.729	5.911	5.914	5.812	5.943	5.760	5.819	5.823	5.815	5.787	5.808
K ⁺	1.919	1.917	1.955	1.935	1.735	1.764	1.763	1.858	1.846	1.889	1.836	1.863
Ca ²⁺	0.000	0.003	0.003	0.012	0.103	0.000	0.003	0.000	0.003	0.003	0.003	0.007
Na ⁺	0.043	0.057	0.023	0.024	0.050	0.042	0.079	0.076	0.058	0.061	0.082	0.075
Ba ²⁺	0.051	0.073	0.020	0.019	0.024	0.078	0.046	0.058	0.058	0.056	0.057	0.062
Total	2.013	2.050	2.001	1.990	1.912	1.884	1.891	1.992	1.965	2.009	1.978	2.007
F ⁻	0.442	0.239	0.587	0.624	0.629	0.391	0.171	0.469	0.268	0.470	0.321	0.492
Cl ⁻	0.012	0.000	0.000	0.000	0.000	0.007	0.040	0.000	0.000	0.000	0.000	0.000
Mg#	73	70	93	94	91	70	50	83	61	83	61	85

E.4. *Mica continued*

	WA105-14	WA105-15	WA105-16	WA106-2	WA106-3	WA106-4	WA106-5	WA106-7	WA106-8	WA106-9	WA106-10	WA106-11
SiO ₂	36.24	38.59	36.08	39.57	38.84	41.75	40.77	40.67	39.83	40.76	40.79	41.03
Al ₂ O ₃	15.04	13.72	14.64	11.94	10.57	12.48	12.26	12.44	12.13	12.54	12.33	12.35
TiO ₂	3.58	2.95	3.38	2.25	2.67	2.00	2.42	1.82	2.39	1.62	2.36	2.10
Cr ₂ O ₃	b.d.	b.d.	b.d.	0.10	b.d.	0.08	0.07	0.40	b.d.	0.80	0.05	0.05
FeO	18.59	10.75	17.45	7.72	13.65	5.95	12.66	4.88	10.40	5.21	11.09	6.31
MgO	12.80	18.84	13.45	22.07	16.93	23.54	18.32	23.70	19.80	23.30	18.81	22.46
MnO	0.25	0.07	0.15	0.01	0.20	0.00	0.09	0.05	0.08	0.00	0.10	0.06
K ₂ O	9.17	9.65	9.13	9.82	9.10	9.93	9.54	10.45	10.19	10.28	9.64	10.20
CaO	b.d.	0.08	0.04	0.10	0.13	0.06	0.08	b.d.	0.06	0.05	0.06	0.05
Na ₂ O	0.27	0.24	0.34	0.15	0.03	0.18	0.02	0.07	0.07	0.20	0.13	0.16
BaO	1.35	0.75	1.25	0.47	0.61	0.34	0.54	0.38	0.57	0.32	0.53	0.47
F	0.37	0.72	0.52	0.52	0.30	0.68	0.34	0.79	0.40	0.58	0.38	0.63
Cl	b.d.	b.d.	b.d.	b.d.	0.04	b.d.	0.03	b.d.	b.d.	0.04	0.03	b.d.
Total	97.66	96.36	96.43	94.72	93.07	96.99	97.14	95.65	95.92	95.70	96.30	95.87
Mica formulae calculated on the basis of 22 oxygen												
Si ⁴⁺	5.462	5.669	5.490	5.811	5.959	5.908	5.928	5.853	5.846	5.857	5.946	5.907
ivAl ³⁺	2.538	2.331	2.510	2.067	1.910	2.082	2.072	2.110	2.098	2.124	2.054	2.093
Total	8.000	8.000	8.000	7.878	7.869	7.990	8.000	7.963	7.944	7.981	8.000	8.000
viAl ³⁺	0.134	0.044	0.116	0.000	0.000	0.000	0.029	0.000	0.000	0.000	0.064	0.002
Ti ⁴⁺	0.406	0.325	0.387	0.248	0.307	0.213	0.265	0.197	0.264	0.175	0.259	0.227
Cr ³⁺	0.000	0.000	0.000	0.012	0.000	0.009	0.008	0.046	0.000	0.091	0.005	0.005
Fe ²⁺	2.344	1.320	2.220	0.948	1.752	0.705	1.539	0.587	1.276	0.627	1.352	0.760
Mg ²⁺	2.877	4.125	3.050	4.830	3.870	4.965	3.970	5.083	4.332	4.991	4.086	4.820
Mn ²⁺	0.031	0.009	0.019	0.001	0.026	0.001	0.011	0.006	0.010	0.000	0.012	0.007
Total	5.792	5.823	5.792	6.039	5.955	5.893	5.822	5.919	5.883	5.884	5.778	5.821
K ⁺	1.764	1.808	1.772	1.839	1.781	1.793	1.769	1.918	1.908	1.885	1.793	1.873
Ca ²⁺	0.000	0.013	0.006	0.015	0.022	0.010	0.012	0.001	0.010	0.008	0.009	0.008
Na ⁺	0.080	0.067	0.100	0.043	0.009	0.050	0.007	0.018	0.019	0.057	0.036	0.046
Ba ²⁺	0.080	0.043	0.074	0.027	0.037	0.019	0.031	0.022	0.033	0.018	0.030	0.027
Total	1.924	1.931	1.952	1.924	1.849	1.872	1.819	1.959	1.970	1.968	1.868	1.954
F ⁻	0.178	0.335	0.252	0.242	0.146	0.304	0.157	0.359	0.184	0.265	0.178	0.285
Cl ⁻	0.000	0.000	0.000	0.000	0.009	0.000	0.008	0.000	0.000	0.011	0.008	0.000
Mg#	55	76	58	84	69	88	72	90	77	89	75	86

E.4. *Mica continued*

	WA106-12	WA107-2	WA107-5	KS RC119-6	KS RC119-7	KS RC106-7	KS RC106-10	HKS RC109-11	HKS RC109-12	HKS RC109-13	KS ER109-2	KS ER109-3
SiO ₂	41.36	48.41	45.86	37.89	37.07	36.34	36.79	40.99	40.34	40.62	35.93	37.89
Al ₂ O ₃	12.39	33.32	34.69	14.47	15.50	16.27	14.41	11.83	12.36	12.09	16.82	16.83
TiO ₂	2.53	0.04	0.03	4.06	3.66	2.92	4.13	2.81	2.73	2.73	3.54	3.31
Cr ₂ O ₃	b.d.	b.d.	b.d.	b.d.	b.d.	b.d.	b.d.	b.d.	b.d.	b.d.	b.d.	b.d.
FeO	11.89	1.59	1.75	14.30	14.22	13.08	17.62	8.71	9.33	8.86	10.76	7.68
MgO	18.04	1.11	1.04	16.08	15.34	16.16	13.83	20.74	20.21	20.26	17.17	19.03
MnO	0.06	0.00	0.00	0.18	0.15	0.13	0.30	0.25	0.17	0.18	0.07	0.11
K ₂ O	9.79	7.20	8.16	9.74	9.39	9.32	9.34	9.07	9.03	9.28	8.81	8.94
CaO	0.10	0.44	0.12	b.d.	b.d.	b.d.	b.d.	0.02	0.02	0.26	0.13	0.12
Na ₂ O	0.12	1.16	0.94	0.31	0.57	0.62	0.52	0.90	0.86	0.88	0.40	0.40
BaO	0.59	2.17	2.96	0.11	0.34	0.29	0.05	0.55	0.60	0.48	0.36	0.37
F	0.34	b.d.	b.d.	0.82	0.52	1.37	0.65	6.06	6.01	5.67	0.23	0.39
Cl	0.04	b.d.	b.d.	0.08	0.06	0.03	0.12	0.05	0.04	b.d.	b.d.	b.d.
Total	97.25	95.44	95.55	98.04	96.82	96.53	97.76	101.98	101.70	101.31	94.22	95.07
Mica formulae calculated on the basis of 22 oxygen												
Si ⁴⁺	5.986	6.423	6.170	5.554	5.488	5.415	5.493	5.916	5.855	5.888	5.346	5.493
ivAl ³⁺	2.014	1.577	1.830	2.446	2.512	2.585	2.507	2.012	2.114	2.066	2.654	2.507
Total	8.000	8.000	8.000	8.000	8.000	8.000	8.000	7.928	7.969	7.954	8.000	8.000
viAl ³⁺	0.100	3.634	3.671	0.053	0.193	0.273	0.029	0.000	0.000	0.000	0.295	0.368
Ti ⁴⁺	0.275	0.004	0.004	0.447	0.407	0.327	0.463	0.305	0.298	0.298	0.396	0.361
Cr ³⁺	0.000	0.000	0.000	0.000	0.000	0.000	0.000	0.000	0.000	0.000	0.000	0.000
Fe ²⁺	1.439	0.176	0.197	1.753	1.761	1.630	2.200	1.051	1.132	1.074	1.339	0.931
Mg ²⁺	3.891	0.219	0.208	3.513	3.385	3.588	3.078	4.462	4.372	4.377	3.808	4.111
Mn ²⁺	0.007	0.000	0.000	0.022	0.019	0.016	0.038	0.030	0.021	0.022	0.008	0.014
Total	5.712	4.033	4.080	5.788	5.765	5.834	5.808	5.848	5.823	5.771	5.846	5.785
K ⁺	1.808	1.218	1.400	1.821	1.772	1.772	1.779	1.669	1.671	1.716	1.673	1.653
Ca ²⁺	0.016	0.063	0.017	0.000	0.000	0.000	0.001	0.003	0.003	0.041	0.021	0.019
Na ⁺	0.033	0.299	0.245	0.087	0.162	0.178	0.151	0.252	0.241	0.248	0.116	0.112
Ba ²⁺	0.034	0.113	0.156	0.006	0.020	0.017	0.003	0.031	0.034	0.027	0.021	0.021
Total	1.891	1.693	1.818	1.914	1.954	1.967	1.934	1.955	1.949	2.032	1.831	1.805
F ⁻	0.157	0.000	0.000	0.381	0.243	0.644	0.309	2.766	2.759	2.598	0.110	0.177
Cl ⁻	0.010	0.000	0.000	0.020	0.015	0.009	0.030	0.012	0.011	0.000	0.000	0.000
Mg#	73	55	51	67	66	69	58	81	79	80	74	82

E.4. *Mica continued*

	KS ER109-20	KS ER117-1	KS ER117-8	KS ER117-11	KS ER117-18	HKS ER110-5	HKS ER110-9	HKS ER110-16
SiO ₂	36.93	37.90	36.52	37.04	37.85	33.11	33.60	33.61
Al ₂ O ₃	17.03	16.54	16.59	16.40	15.96	13.68	13.90	14.14
TiO ₂	3.48	3.04	3.04	3.04	1.57	2.66	2.51	2.57
Cr ₂ O ₃	b.d.	b.d.	b.d.	b.d.	b.d.	b.d.	b.d.	b.d.
FeO	8.28	8.36	10.62	8.78	7.46	7.82	7.26	7.75
MgO	18.71	19.74	17.84	18.62	20.33	18.61	19.41	19.30
MnO	0.14	0.07	0.11	0.10	0.13	0.14	0.16	0.23
K ₂ O	9.74	9.76	9.69	9.99	9.69	6.48	6.38	6.42
CaO	0.05	0.05	0.13	0.05	0.05	0.33	0.04	0.02
Na ₂ O	0.46	0.18	0.27	0.28	0.23	0.19	0.25	0.25
BaO	0.35	0.34	0.48	0.39	0.17	9.31	9.76	9.62
F	0.32	0.60	0.55	0.52	0.61	5.20	5.27	5.23
Cl	b.d.	b.d.	b.d.	b.d.	b.d.	0.03	0.04	b.d.
Total	95.49	96.58	95.84	95.21	94.05	97.56	98.58	99.13
Mica formulae calculated on the basis of 22 oxygen								
Si ⁴⁺	5.381	5.459	5.382	5.444	5.571	5.312	5.323	5.295
ivAl ³⁺	2.619	2.541	2.618	2.556	2.429	2.586	2.595	2.624
Total	8.000	8.000	8.000	8.000	8.000	7.898	7.918	7.919
viAl ³⁺	0.305	0.268	0.264	0.286	0.340	0.000	0.000	0.000
Ti ⁴⁺	0.382	0.330	0.337	0.336	0.173	0.320	0.299	0.304
Cr ³⁺	0.000	0.000	0.000	0.000	0.000	0.000	0.000	0.000
Fe ²⁺	1.009	1.007	1.309	1.080	0.918	1.050	0.962	1.021
Mg ²⁺	4.064	4.239	3.919	4.079	4.461	4.451	4.583	4.532
Mn ²⁺	0.018	0.009	0.013	0.012	0.016	0.019	0.022	0.031
Total	5.778	5.854	5.842	5.793	5.908	5.840	5.866	5.888
K ⁺	1.811	1.794	1.822	1.873	1.818	1.325	1.289	1.290
Ca ²⁺	0.008	0.008	0.021	0.008	0.008	0.057	0.007	0.004
Na ⁺	0.129	0.051	0.076	0.080	0.066	0.059	0.078	0.076
Ba ²⁺	0.020	0.019	0.028	0.022	0.010	0.585	0.606	0.594
Total	1.968	1.872	1.947	1.983	1.902	2.026	1.980	1.964
F ⁻	0.147	0.274	0.259	0.241	0.286	2.638	2.639	2.608
Cl ⁻	0.000	0.000	0.000	0.000	0.000	0.007	0.010	0.000
Mg#	80	81	75	79	83	81	83	82

E.5. Feldspar

	WA100-4	WA100-9	WA100-12	WA100-14	WA100-19	WA101-3	WA101-8	WA101-10
SiO ₂	69.63	62.50	64.56	63.90	62.78	66.88	64.88	63.33
Al ₂ O ₃	18.79	18.92	18.61	18.97	18.98	20.56	18.87	22.65
Fe ₂ O ₃	0.09	0.12	0.31	0.12	0.21	0.07	0.41	0.07
K ₂ O	0.29	15.35	15.80	14.88	14.78	0.10	15.74	0.10
CaO	1.77	0.09	0.03	0.13	0.53	0.89	0.09	3.71
Na ₂ O	9.46	0.41	0.37	0.64	0.48	11.21	0.51	9.51
BaO	b.d.	1.27	0.23	1.29	0.94	0.14	0.60	0.09
Total	100.03	98.66	99.91	99.93	98.70	99.85	101.10	99.46

Feldspar formulae calculated on the basis of 16 oxygen

Si ⁴⁺	6.060	5.906	5.976	5.937	5.904	5.876	5.954	5.627
Al ³⁺	1.928	2.107	2.031	2.078	2.104	2.129	2.042	2.372
Fe ³⁺	0.006	0.009	0.024	0.009	0.017	0.005	0.031	0.005
Total	7.994	8.022	8.031	8.024	8.025	8.010	8.027	8.004
K ⁺	0.033	1.851	1.866	1.763	1.773	0.011	1.843	0.011
Ca ²⁺	0.165	0.009	0.003	0.013	0.054	0.084	0.009	0.353
Na ⁺	1.597	0.075	0.066	0.115	0.087	1.910	0.091	1.638
Ba ²⁺	0.000	0.047	0.008	0.047	0.035	0.005	0.021	0.003
Total	1.795	1.982	1.943	1.938	1.949	2.010	1.964	2.005
Molecular percentages								
Or	1.8	95.6	96.4	93.2	92.6	0.6	94.9	0.6
An	9.2	0.5	0.2	0.7	2.8	4.2	0.5	17.6
Ab	89.0	3.9	3.4	6.1	4.6	95.3	4.7	81.8

	WA101-11	WA102-9	WA102-10	WA102-16	WA102-17	WA102-18	WA102-23	WA102-24
SiO ₂	63.34	64.42	68.44	67.40	64.85	63.33	67.97	63.21
Al ₂ O ₃	18.84	18.78	20.75	19.90	18.71	19.42	20.00	18.49
Fe ₂ O ₃	0.22	b.d.	b.d.	0.07	b.d.	0.02	0.02	0.02
K ₂ O	15.92	15.81	0.22	0.19	15.97	14.71	0.08	15.61
CaO	0.07	b.d.	0.83	0.52	0.05	0.05	0.55	0.01
Na ₂ O	0.35	0.39	11.06	11.28	0.34	0.50	10.93	0.44
BaO	0.77	0.88	0.15	0.08	0.41	2.18	0.00	0.88
Total	99.51	100.28	101.45	99.44	100.33	100.21	99.55	98.66

Feldspar formulae calculated on the basis of 16 oxygen

Si ⁴⁺	5.925	5.963	5.907	5.936	5.981	5.898	5.957	5.954
Al ³⁺	2.077	2.049	2.111	2.065	2.033	2.132	2.066	2.053
Fe ³⁺	0.017	0.000	0.000	0.005	0.000	0.002	0.002	0.001
Total	8.019	8.012	8.018	8.006	8.014	8.032	8.025	8.008
K ⁺	1.900	1.867	0.025	0.021	1.878	1.748	0.008	1.876
Ca ²⁺	0.007	0.000	0.076	0.049	0.004	0.005	0.052	0.001
Na ⁺	0.064	0.070	1.852	1.927	0.061	0.090	1.857	0.081
Ba ²⁺	0.028	0.032	0.005	0.003	0.015	0.080	0.000	0.033
Total	1.999	1.969	1.958	2.000	1.958	1.923	1.917	1.991
Molecular percentages								
Or	96.4	96.4	1.2	1.1	96.6	94.8	0.5	95.8
An	0.4	0.0	3.9	2.5	0.3	0.3	2.7	0.1
Ab	3.2	3.6	94.8	96.5	3.1	4.9	96.8	4.1

E.5. *Feldspar continued*

	WA103-5	WA103-8	WA103-9	WA103-12	WA103-15	WA104-5	WA104-11	WA104-14
SiO ₂	64.56	64.44	66.54	63.08	66.62	65.21	64.48	63.89
Al ₂ O ₃	21.30	18.55	20.33	18.11	21.26	18.44	18.11	18.39
Fe ₂ O ₃	0.13	0.13	0.17	0.08	0.05	0.23	1.28	0.97
K ₂ O	0.12	15.52	0.15	15.32	0.15	16.82	15.20	14.87
CaO	2.40	0.06	1.65	0.19	2.36	0.35	b.d.	0.03
Na ₂ O	10.28	0.37	10.49	0.43	10.46	0.39	1.01	1.17
BaO	0.02	1.30	b.d.	1.28	b.d.	0.79	b.d.	1.81
Total	98.81	100.37	99.33	98.49	100.90	102.23	100.08	101.13

Feldspar formulae based on 16 oxygen

Si ⁴⁺	5.755	5.973	5.876	5.967	5.804	5.960	5.960	5.918
Al ³⁺	2.237	2.027	2.115	2.019	2.183	1.986	1.973	2.007
Fe ³⁺	0.009	0.010	0.012	0.006	0.004	0.016	0.089	0.068
Total	8.001	8.010	8.003	7.992	7.991	7.962	8.022	7.993
K ⁺	0.013	1.836	0.017	1.848	0.017	1.961	1.792	1.757
Ca ²⁺	0.230	0.006	0.156	0.019	0.221	0.034	0.000	0.003
Na ⁺	1.777	0.066	1.797	0.080	1.767	0.069	0.181	0.210
Ba ²⁺	0.001	0.047	0.000	0.047	0.000	0.028	0.000	0.066
Total	2.021	1.955	1.970	1.994	2.005	2.092	1.973	2.036

Molecular percentages

Or	0.7	96.2	0.9	95.0	0.8	95.0	90.8	89.2
An	11.3	0.3	7.9	1.0	11.0	1.7	0.0	0.2
Ab	88.0	3.5	91.2	4.1	88.2	3.3	9.2	10.7

	WA105-4	WA105-5	WA105-11	WA105-12	WA106-1	WA106-6	WA107-1	WA107-4
SiO ₂	64.85	68.94	64.75	68.23	69.35	69.73	67.79	59.82
Al ₂ O ₃	18.61	19.99	18.69	19.85	20.01	19.74	20.23	25.24
Fe ₂ O ₃	0.07	0.16	0.06	0.11	b.d.	0.12	0.07	0.35
K ₂ O	16.42	0.17	16.17	0.12	0.19	0.12	0.05	1.44
CaO	b.d.	0.31	0.01	0.31	0.02	0.01	0.63	5.71
Na ₂ O	0.44	11.82	0.21	11.55	11.66	11.97	11.40	6.76
BaO	0.65	b.d.	0.23	b.d.	b.d.	b.d.	b.d.	0.52
Total	101.04	101.39	100.12	100.17	101.23	101.69	100.17	99.84

Feldspar formulae calculated on the basis of 16 oxygen

Si ⁴⁺	5.969	5.953	5.980	5.956	5.981	5.993	5.921	5.363
Al ³⁺	2.019	2.034	2.035	2.042	2.034	2.000	2.083	2.667
Fe ³⁺	0.005	0.010	0.004	0.007	0.000	0.009	0.005	0.023
Total	7.993	7.997	8.019	8.005	8.015	8.001	8.009	8.053
K ⁺	1.929	0.019	1.906	0.013	0.021	0.014	0.005	0.165
Ca ²⁺	0.000	0.028	0.001	0.029	0.001	0.001	0.059	0.549
Na ⁺	0.078	1.980	0.038	1.955	1.951	1.996	1.931	1.175
Ba ²⁺	0.023	0.000	0.008	0.000	0.000	0.000	0.000	0.018
Total	2.030	2.027	1.953	1.997	1.973	2.011	1.995	1.907

Molecular percentages

Or	96.1	0.9	98.0	0.7	1.1	0.7	0.3	8.7
An	0.0	1.4	0.1	1.5	0.1	0.0	3.0	29.0
Ab	3.9	97.7	1.9	97.9	98.8	99.3	96.8	62.2

E.5. *Feldspar continued*

	WA107-7	WA107-14	KS RC-106-5	KS RC-106-6	KS RC106-8	KS RC106-9	KS RC106-1	KS RC106-13
SiO ₂	69.49	70.18	50.11	55.46	47.20	54.47	68.16	66.16
Al ₂ O ₃	19.55	19.28	32.71	29.32	33.67	29.46	18.97	19.50
Fe ₂ O ₃	0.24	0.15	0.63	0.55	0.79	0.61	0.66	0.34
K ₂ O	0.05	0.05	0.19	0.58	0.12	0.60	9.15	9.98
CaO	0.40	0.32	15.10	10.94	16.86	11.48	0.95	0.93
Na ₂ O	11.55	11.62	2.37	4.64	1.71	4.39	4.19	3.81
BaO	b.d.	b.d.	0.05	0.04	b.d.	b.d.	b.d.	0.11
Total	101.28	101.60	101.16	101.53	100.35	101.01	102.08	100.83

Feldspar formulae calculated on the basis of 16 oxygen

Si ⁴⁺	5.997	6.030	4.520	4.930	4.326	4.879	6.008	5.937
Al ³⁺	1.988	1.953	3.478	3.073	3.636	3.109	1.971	2.063
Fe ³⁺	0.017	0.011	0.043	0.037	0.054	0.041	0.044	0.023
Total	8.003	7.993	8.041	8.040	8.016	8.029	8.023	8.023
K ⁺	0.005	0.006	0.022	0.066	0.014	0.069	1.029	1.142
Ca ²⁺	0.037	0.030	1.459	1.042	1.655	1.102	0.090	0.090
Na ⁺	1.933	1.936	0.415	0.799	0.303	0.762	0.716	0.663
Ba ²⁺	0.000	0.000	0.002	0.001	0.000	0.000	0.000	0.004
Total	1.975	1.972	1.898	1.908	1.972	1.933	1.835	1.899

Molecular percentages

Or	0.3	0.3	1.2	3.4	0.7	3.5	56.1	60.3
An	1.9	1.5	77.0	54.6	83.9	57.0	4.9	4.7
Ab	97.8	98.2	21.9	41.9	15.4	39.4	39.0	35.0

	KS RC111-3	KS RC111-12	KS RC111-14	KS RC111-17	KS RC119-2	KS RC119-3	KS RC119-5	KS RC119-9
SiO ₂	45.99	48.07	65.21	48.35	48.28	58.18	59.49	58.92
Al ₂ O ₃	34.75	33.22	20.04	33.41	33.26	27.46	24.93	26.99
Fe ₂ O ₃	0.73	0.85	0.54	0.98	0.62	0.53	0.76	0.39
K ₂ O	0.10	0.33	10.43	0.30	0.24	0.94	3.16	0.95
CaO	18.25	16.63	1.45	16.41	16.19	9.12	7.76	8.58
Na ₂ O	0.83	1.73	3.67	1.76	1.94	5.43	4.42	5.98
BaO	b.d.	b.d.	b.d.	0.01	b.d.	0.06	0.07	0.05
Total	100.65	100.83	101.34	101.22	100.53	101.72	100.59	101.86

Feldspar formulae calculated on the basis of 16 oxygen

Si ⁴⁺	4.213	4.382	5.854	4.386	4.403	5.138	5.331	5.191
Al ³⁺	3.752	3.569	2.120	3.572	3.575	2.858	2.633	2.803
Fe ³⁺	0.051	0.059	0.037	0.067	0.043	0.036	0.051	0.026
Total	8.016	8.010	8.011	8.025	8.021	8.032	8.015	8.020
K ⁺	0.012	0.038	1.195	0.035	0.028	0.105	0.361	0.107
Ca ²⁺	1.791	1.624	0.139	1.595	1.582	0.863	0.745	0.810
Na ⁺	0.148	0.305	0.639	0.310	0.343	0.930	0.767	1.021
Ba ²⁺	0.000	0.000	0.000	0.001	0.000	0.002	0.002	0.002
Total	1.951	1.967	1.973	1.941	1.953	1.900	1.875	1.940

Molecular percentages

Or	0.6	1.9	60.5	1.8	1.4	5.6	19.3	5.5
An	91.8	82.5	7.1	82.2	81.0	45.5	39.8	41.8
Ab	7.6	15.5	32.4	16.0	17.6	49.0	41.0	52.7

E.5. *Feldspar continued*

	KS RC119-10	KS RC119-1	KS RC119-15	HKS RC109-7	HKS RC109-10	HKS RC100-3	HKS RC100-9	HKS RC100-9
SiO ₂	57.80	50.53	63.74	48.95	50.82	45.21	46.33	46.28
Al ₂ O ₃	27.15	32.40	21.62	32.05	31.05	34.49	33.78	34.62
Fe ₂ O ₃	0.41	0.55	0.69	1.20	1.30	0.76	0.75	0.80
K ₂ O	0.69	0.27	7.07	0.12	0.26	0.14	b.d.	0.19
CaO	8.97	14.32	3.24	14.98	13.72	18.07	17.95	18.05
Na ₂ O	5.88	2.95	4.29	2.88	3.25	1.07	1.12	1.05
BaO	b.d.	0.38	0.10	0.10	b.d.	0.11	b.d.	b.d.
Total	100.90	101.40	100.75	100.28	100.40	99.85	99.93	100.99

Feldspar formulae calculated on the basis of 16 oxygen

Si ⁴⁺	5.143	4.555	5.708	4.479	4.620	4.186	4.271	4.228
Al ³⁺	2.847	3.442	2.282	3.456	3.326	3.765	3.670	3.727
Fe ³⁺	0.027	0.038	0.046	0.083	0.089	0.053	0.052	0.055
Total	8.017	8.035	8.036	8.018	8.035	8.004	7.993	8.010
K ⁺	0.078	0.031	0.808	0.014	0.030	0.017	0.000	0.023
Ca ²⁺	0.855	1.383	0.311	1.469	1.336	1.793	1.773	1.767
Na ⁺	1.014	0.516	0.745	0.510	0.573	0.193	0.201	0.187
Ba ²⁺	0.000	0.013	0.003	0.004	0.000	0.004	0.000	0.000
Total	1.947	1.943	1.867	1.997	1.939	2.007	1.974	1.977
Molecular percentages								
Or	4.0	1.6	43.3	0.7	1.6	0.8	0.0	1.1
An	43.9	71.7	16.7	73.7	68.9	89.6	89.9	89.5
Ab	52.1	26.7	40.0	25.6	29.5	9.6	10.1	9.4

	HKS RC100-15	HKS RC123-9	HKS RC123-15	KS ER112-6	KS ER112-10	KS ER112-1	KS ER121-7	KS ER121-8
SiO ₂	45.06	50.58	49.99	48.21	49.09	47.85	48.25	58.81
Al ₂ O ₃	34.46	32.16	32.36	32.83	32.88	33.22	32.06	24.92
Fe ₂ O ₃	0.55	0.86	1.03	1.04	1.08	1.01	1.03	0.84
K ₂ O	0.28	0.66	0.47	0.28	0.23	0.23	0.20	1.23
CaO	18.01	14.59	15.09	16.83	16.73	16.99	15.92	6.45
Na ₂ O	0.84	2.54	2.43	1.73	1.79	1.64	2.30	6.86
BaO	0.38	0.10	0.08	b.d.	b.d.	b.d.	0.02	0.53
Total	99.58	101.49	101.45	100.92	101.80	100.94	99.78	99.64

Feldspar formulae calculated on the basis of 16 oxygen

Si ⁴⁺	4.189	4.558	4.513	4.395	4.429	4.362	4.443	5.311
Al ³⁺	3.776	3.416	3.444	3.527	3.496	3.569	3.479	2.653
Fe ³⁺	0.039	0.059	0.070	0.071	0.073	0.070	0.071	0.057
Total	8.004	8.033	8.027	7.993	7.998	8.001	7.993	8.021
K ⁺	0.033	0.076	0.054	0.033	0.026	0.027	0.024	0.142
Ca ²⁺	1.794	1.409	1.460	1.644	1.618	1.659	1.571	0.624
Na ⁺	0.151	0.445	0.424	0.306	0.314	0.291	0.411	1.202
Ba ²⁺	0.014	0.004	0.003	0.000	0.000	0.000	0.001	0.019
Total	1.992	1.934	1.941	1.983	1.958	1.977	2.007	1.987
Molecular percentages								
Or	1.7	3.9	2.8	1.6	1.4	1.4	1.2	7.2
An	90.7	73.1	75.3	82.9	82.6	84.0	78.3	31.7
Ab	7.7	23.0	21.9	15.4	16.0	14.7	20.5	61.1

E.5. Feldspar *continued*

	KS ER121-15	KS ER121-19	KS ER109-4	KS ER109-12	KS ER109-15	KS ER117-7	KS ER117-9	KS ER117-10
SiO ₂	47.63	55.82	49.15	47.80	47.11	49.09	49.50	49.68
Al ₂ O ₃	32.53	27.98	32.64	32.34	34.11	31.22	29.16	30.84
Fe ₂ O ₃	1.20	0.65	0.90	0.83	0.67	0.91	1.58	0.99
K ₂ O	0.16	0.46	0.41	0.31	0.23	0.57	0.64	0.59
CaO	15.88	9.68	16.39	16.94	18.06	14.93	13.68	14.50
Na ₂ O	2.19	5.92	2.06	1.88	1.33	2.28	2.73	2.47
BaO	b.d.	0.27	0.03	b.d.	0.02	0.14	0.23	0.13
Total	99.59	100.78	101.58	100.10	101.53	99.14	97.52	99.20
Feldspar formulae calculated on the basis of 16 oxygen								
Si ⁴⁺	4.396	5.008	4.446	4.399	4.281	4.540	4.655	4.585
Al ³⁺	3.538	2.958	3.481	3.508	3.653	3.403	3.232	3.355
Fe ³⁺	0.083	0.044	0.062	0.057	0.046	0.063	0.112	0.069
Total	8.017	8.010	7.989	7.964	7.980	8.006	7.999	8.009
K ⁺	0.019	0.053	0.048	0.037	0.026	0.067	0.076	0.069
Ca ²⁺	1.570	0.930	1.589	1.670	1.759	1.479	1.378	1.434
Na ⁺	0.392	1.030	0.361	0.335	0.234	0.409	0.498	0.443
Ba ²⁺	0.000	0.010	0.001	0.000	0.001	0.005	0.008	0.005
Total	1.981	2.023	1.999	2.042	2.020	1.960	1.960	1.951
Molecular percentages								
Or	1.0	2.6	2.4	1.8	1.3	3.4	3.9	3.6
An	79.3	46.2	79.5	81.8	87.1	75.7	70.6	73.7
Ab	19.8	51.2	18.1	16.4	11.6	20.9	25.5	22.7

E.6. Nepheline

	ER104-7	ER104-16	ER110-10	ER110-15	ER110-17	ER118-9	ER118-19
SiO ₂	43.77	45.00	42.56	41.54	42.33	47.53	48.50
Al ₂ O ₃	34.18	34.10	32.72	32.65	33.93	32.73	31.96
Fe ₂ O ₃	0.63	0.63	1.42	1.40	3.27	0.84	0.44
K ₂ O	4.06	3.80	9.25	10.18	6.49	3.60	3.07
CaO	2.70	2.61	0.25	0.24	0.32	1.23	1.25
Na ₂ O	15.24	15.17	14.37	13.60	13.72	15.98	16.21
BaO	0.02	b.d.	0.09	0.02	0.08	0.04	b.d.
Total	100.6	101.31	100.66	99.63	100.14	101.95	101.43
Nepheline formulae calculated on the basis of 32 oxygen							
Si ⁴⁺	8.290	8.425	8.268	8.189	8.153	8.792	8.971
Al ³⁺	7.630	7.524	7.493	7.586	7.702	7.136	6.966
Fe ³⁺	0.090	0.089	0.208	0.207	0.473	0.117	0.062
K ⁺	0.982	0.909	2.292	2.559	1.594	0.850	0.723
Ca ²⁺	0.548	0.524	0.052	0.051	0.066	0.243	0.247
Na ⁺	5.597	5.505	5.414	5.200	5.125	5.732	5.815
Ba ²⁺	0.002	0.000	0.007	0.002	0.006	0.003	0.000
Total	23.139	22.976	23.734	23.794	23.119	22.873	22.784
Molecular percentages							
Ne	81.5	80.5	67.9	65.4	74.6	77.7	77.4
Ks	14.3	13.3	28.7	32.2	23.2	11.5	9.6
Q	4.2	6.2	3.4	2.4	2.2	10.7	12.9

E.7. Leucite

	RC100-2	RC100-14	RC109-6	RC123-8	RC123-14	ER104-6	ER110-3	ER110-4
SiO ₂	56.12	56.34	56.56	56.82	56.80	54.41	55.37	54.87
Al ₂ O ₃	23.32	22.55	22.88	23.13	23.41	23.07	23.12	23.05
Fe ₂ O ₃	0.38	0.29	0.48	0.43	1.82	0.57	0.53	0.74
CaO	b.d.	b.d.	b.d.	b.d.	0.17	b.d.	b.d.	b.d.
Na ₂ O	0.60	0.36	0.15	0.12	0.22	0.26	0.03	b.d.
K ₂ O	20.86	20.71	21.20	21.00	19.03	21.20	21.35	21.24
Total	101.28	100.25	101.27	101.50	101.45	99.51	100.40	99.90

Leucite formulae calculated on the basis of 6 oxygen

Si ⁴⁺	2.007	2.031	2.023	2.023	2.010	1.990	2.003	1.997
Total	2.007	2.031	2.023	2.023	2.010	1.990	2.003	1.997
Al ³⁺	0.983	0.958	0.964	0.970	0.976	0.995	0.986	0.989
Fe ³⁺	0.010	0.008	0.013	0.012	0.048	0.016	0.015	0.020
Ca ²⁺	0.000	0.000	0.000	0.000	0.006	0.000	0.000	0.000
Total	0.993	0.966	0.978	0.982	1.030	1.011	1.001	1.009
Na ⁺	0.042	0.025	0.010	0.008	0.015	0.018	0.002	0.000
K ⁺	0.952	0.952	0.967	0.954	0.859	0.989	0.985	0.986
Total	0.994	0.977	0.977	0.962	0.874	1.007	0.987	0.986

APPENDIX F

SAMPLE PREPARATION

F.1. Petrography

Polished thin sections (30 μm thick) were produced from 1" x 1.5" slabs of fresh rock for each sample listed in Appendix B. Sections were photographed using 35mm film in a Nikon FX-35WA camera mounted on a Nikon optical microscope at Carleton University.

F.2. Electron microprobe

Representative silicate minerals in polished thin sections of selected samples were circled with permanent marker, and slides were carbon coated prior to analysis.

F.3. Whole-rock geochemistry

Samples were hand-split into thumbnail-sized pieces using a hydraulic splitter to remove any alteration and obtain appropriate size for pulverization. Samples from the Western Alps were crushed in an agate ring mill, while samples from Roccamonfina and Ernici were crushed in a tungsten carbide ring mill. Both procedures produced a fine powder (<200 mesh). Possible contaminants in the agate mill include Si (up to 0.3%) and trace amounts of Al, Na, Fe, K, Ca, Mg, and Pb, and possible contaminants in the tungsten carbide include W (up to 0.1%) and trace amounts of Co, C, Ta, Nb, and Ti. The ring mills were rinsed with distilled water, dried with ethanol, and pre-contaminated between each sample. Approximately 10g of powdered sample was sent to Activation

Laboratories Ltd. in Ancaster, Ontario, for major and trace element analysis.

F.4. Isotope geochemistry

The amount of powdered material required for isotopic analyses was calculated based on the concentration of Sr, Nd, or Pb in each sample (as analyzed by Activation Laboratories), assuming that 5 µg of Nd, 2-5 µg of Pb and 10-15 µg of Sr are required for mass spectrometer analyses. The lab procedure for all samples is as follows:

1. The calculated amount of powdered whole-rock sample was weighed and transferred to a Savillex vial.
2. 1.5 ml of concentrated HNO₃ and 4.5 ml concentrated HF were added to each vial. Sealed vials were heated on a hotplate for a minimum of 24 hours.
3. After cooling, the caps of the vials were removed and rinsed with nanopure water. The samples were then evaporated to dryness.
4. 4 ml of 6 M HCl was added to each sample. The samples were heated for 1 hour to re-dissolve, and then evaporated to dryness and completely cooled. Repeat.
5. The calculated amount of ultrapure 2.5 M HCl was then added to each sample. Usually 3.0 ml was added, with 1.5 ml to be used for the Sr and Nd columns, and 1.5 ml for the Pb procedure. Occasionally, in samples with relatively low Pb content (< 12 ppm), 4.5 ml was added and 3.0 ml of that was used for the Pb procedure.
6. The Sr, Nd, and Pb column procedures are described individually below.

Sr separation procedure

- a. 1.5 ml of solution from Step 5 was transferred to a centrifuge tube, covered with parafilm and centrifuged for 10 minutes at high speed.
- b. The Sr columns were drained and the centrifuged sample was added to the column. The Sr columns are 20 cm x 0.7 cm and are filled with 3.5 ml of Bio-Rad AG50W-X8 cation exchange resin (200-400 mesh) in H⁺ form. The Sr column procedure began (see section F.5a.)
- c. 6 ml of Sr solution was collected from the column at the appropriate time. The calculated amount was removed and transferred to a small Teflon container, evaporated and covered with parafilm. The sample was now ready for loading in the mass spectrometer.

Note: The concentration of Sr in the sample is generally much higher than required for analysis, therefore only a small portion of the Sr solution is necessary. Most samples required only 1 ml of Sr solution; the remaining 5 ml was evaporated and stored.

Nd separation procedure

- a. REE solution was collected from the Sr column at the appropriate time and then evaporated to dryness.
- b. The REE solution was re-dissolved in 0.2 ml 0.15 M HCl. The solution was added to REE column and the REE column procedure began (see section F.5b.). The REE columns are individually calibrated 20 cm Bio-Rad Vycor (quartz) columns of 0.7 mm diameter filled with compressed Teflon powder coated with di-hexyl orthophosphoric acid.

c. Nd solution was collected from the column at the appropriate time, evaporated until approximately 1 ml remained, then transferred to a small Teflon container and evaporated completely. The sample was covered with parafilm, ready for loading in the mass spectrometer.

Pb separation procedure

- a. The calculated amount for Pb analysis (from Step 5) was evaporated to dryness and cooled completely.
- b. 3 ml 1 M HBr were added to re-dissolve the sample, which was then transferred to a centrifuge tube and centrifuged for 10 minutes at high speed.
- c. The 0.50 ml column procedure began (see section F.5c.), and the column was loaded with centrifuged material at the appropriate time. The Pb columns are filled with new Bio-Rad AG1-X8 anion exchange resin (100-200 mesh) in Cl⁻ form for each sample.
- d. The column solution was collected prior to Pb collection: this is sample material without Pb (but with Sr and Nd) and was stored to use later if necessary.
- e. Pb solution was collected from column and evaporated to dryness.
- f. The sample was re-dissolved in 1 ml 1 M HBr. The 0.20 ml column procedure began (see section G.5.), and the sample was loaded at the appropriate time.
- g. 1 ml Pb solution was collected, transferred to a small Teflon container, and evaporated to dryness. The sample was covered with parafilm, ready for loading in the mass spectrometer.

F.5. Ion exchange column procedures

The following tables summarize the Sr, Nd, and Pb column procedures:

Table F.5.a Elution chart for Rb-Sr column

	ml	M HCl
Load Sample	1.5	2.5
Wash	1	2.5
Wash	7	2.5
Collect <u>Rb</u>	3	2.5
Wash	5	2.5
Collect <u>Sr</u>	6	2.5
Wash	3	6.2
Collect <u>REE</u>	9	6.2
Clean	11	6.2
Wash	8	2
Condition	10	2.5

Table F.5.b Elution chart for REE column

	ml	M HCl	Column Number							
			3	5	6	7	9	11	13	14
Load Sample	0.2	0.15								
Wash	0.2	0.15								
Wash	0.2	0.15								
Wash	1	0.3								
Wash		0.3	3	2	3	2	3	3	5	1
Collect Nd		0.3	5	5	3.5	3.5	3.5	4	5.5	3.5
Wash		0.3	3	3	2.5	3.5	1.5	2	2.5	1.5
Wash		0.3	2	2	2	4	0	4	0	2
Wash		0.5	2	2	1	0	3	2	6	0
Collect Sm		0.5	4	4	4	4	5	6	7	4
Wash	5	0.5								
Clean	25	6								
Condition	25	0.15								

Tables F.5.c and F.5.d

c) Elution chart for 0.50 ml Pb column

Wash	2 ml	6 M HCl
	2 ml	H ₂ O
	2 ml	1 M HBr
Load Sample		
Collect U	4 x 1 ml	1 M HBr
	1 ml	1 M HCl
Collect Pb	3 ml	6 M HCl

d) Elution chart for 0.20 ml Pb column

Wash	1 ml	6 M HCl
	1 ml	H ₂ O
	1 ml	1 M HBr
Load Sample		
Wash	1.2 ml	1 M HBr
	0.8 ml	H ₂ O
Collect Pb	1 ml	6 M HCl

F.5.d. Blank values

Maximum procedural blank values were determined by Mirnejad (2002) as 1.5 ng Sr, 0.26 ng Nd, and 1 ng Pb. Blank corrections were not applied to the isotope results in this study as the blank values were insignificant in comparison with the trace element contents of all samples analyzed.

APPENDIX G

ANALYTICAL METHODS

G.1. Electron Microprobe

Major element abundances of silicate minerals in polished thin sections were determined by a wavelength-dispersive x-ray analysis method (WDX) using an automated Camebax MBX electron microprobe in the Department of Earth Sciences, Carleton University. Operating conditions were 15 kV accelerating voltage, 20 nA beam current and peak counting times of about 30 seconds or 40,000 counts. Background measurements were made at 50% peak counting time on each side of the analyzed peak. Beam sensitive minerals such as feldspar were analyzed with the electron beam rastered over an area of 5 x 5 to 10 x 10 microns. A suite of calibrated natural and synthetic minerals and compounds were used as standards. Raw data were converted to elemental wt% by the Cameca PAP matrix correction program, and into mineral formulae using the FORMULA program by T.S. Ercit, Canadian Museum of Nature. Analyses are accurate to 1-2% of the quoted values for major elements, and 3-5% for minor elements.

Digital BSE (back-scattered electron) images were collected at 512 x 512 resolution with a Lamont 4 element solid state BSE detector and BSE Quad Summing Amplifier interfaced to a 4Pi Analysis Inc. digital imaging system and Power Macintosh computer.

G.2. Whole-rock geochemistry

Major and trace element analyses of selected samples were completed by

Activation Laboratories Ltd. in Ancaster, Ontario, using a combination of Inductively Coupled Plasma (ICP), Inductively Coupled Plasma Mass Spectrometry (ICP-MS), Instrumental Neutron Activation Analysis (INAA), Prompt Gamma Neutron Activation Analysis (PGNAA), and Ion Specific Electrode (ISE) techniques.

For ICP and ICP-MS, samples are taken into solution using a fusion technique in which samples are mixed with a flux of lithium metaborate and lithium tetraborate and fused in an induction furnace. The melt is poured into a 5% nitric acid solution and mixed continuously until completely dissolved (~ 30 minutes). The advantage of this fusion method is that the same solution can be analyzed by ICP and ICP-MS.

Major elements were determined by ICP using a simultaneous/sequential Thermo Jarrel-Ash Enviro II machine. Calibration is performed using eight certified USGS and Canmet certified reference materials, one of which is used during the analysis for every group of ten samples. In the ICP method, the sample solution is introduced into a radio frequency excited plasma (~8000 K), and atoms are excited to the point that they emit characteristic wavelength-specific photons. The number of photons produced is directly related to the concentration of that element in the sample. ICP is a multi-element technique that is more versatile and sensitive than X-Ray Fluorescence (XRF), which is limited by sample dilution from the fusion matrix.

Trace elements determined by ICP-MS were spiked with internal standards, further diluted, and introduced into a Perkin Elmer SCIEX ELAN 6000 machine. The ICP-MS instrument employs an argon plasma as the ionization source and a quadrupole mass spectrometer to detect the ions produced. During analysis, the sample solution is nebulized into flowing argon gas and passed into an inductively coupled plasma. The

positive ions in the plasma are then focused into the mass spectrometer and separated according to mass. Calibration is performed using ten prepared USGS and Canmet certified reference materials.

INAA is used for a number of trace elements, including Au, As, Sb, Ta, U, and Th, that can be difficult and expensive to determine by conventional chemical procedures. Samples are irradiated with international reference material and NiCr flux wires at a thermal neutron flux of $7 \times 10^{12} \text{ ncm}^{-2}\text{s}^{-1}$ in the McMaster Nuclear Reactor, Hamilton. Following a 7-day decay period, the primary gamma radiation of the sample is measured on an Ortec high purity Ge detector with a resolution of 1.67 KeV. Activities for each element are decay and weight corrected to multiple certified reference materials. Selected samples are re-measured and compared to the original as part of the quality assurance procedure.

The element Cl was determined by INAA only for the samples from the Western Alps. For this procedure, 1 g samples are weighed into polyethylene vials and are irradiated for 20-60 seconds depending on the nature of the material. After an appropriate decay time of 1,000 to 1,800 seconds to allow aluminum and other very short lived isotopes to decay, the samples are counted sequentially for the Cl-38 induced ratio isotope [Cl-37 (n, γ) Cl-38, $t_{1/2}$ 37.24 min] gamma-rays 1642.69 and 2167.68 KeV. Values are corrected for decay and compared to a standard calibration.

PGNAA is a multi-element technique that measures gamma radiation emitted during neutron capture, instead of delayed gamma rays which are measured by INAA. The neutron flux during a typical PGNAA determination is several orders of magnitude lower than for conventional INAA. This method was used for boron analyses of the

samples from Roccamonfina and Ernici. Samples are encapsulated in a polyethylene vial and placed in a thermalized beam of neutrons produced from a nuclear reactor, and then measured for the doppler broadened prompt gamma ray at 478 KeV using a high purity Ge detector. Samples are compared to certified reference materials used to calibrate the system.

An ISE is a cylindrical tube with an ion-selective membrane fixed at one end together with a separate, external reference electrode that can be immersed in an aqueous solution containing the ions to be measured. A measurable potential difference is developed across the ISE membrane when the target ions diffuse through from the high concentration side to the lower concentration side. Fluorine in the Western Alps samples was measured using a fluorine ISE, which is a single crystal of Lanthanum Fluoride (LaF_3) doped with Europium Fluoride (EuF_2) which produces holes in the crystal lattice through which F ions can pass. In this method, 0.5 g samples are fused with sodium hydroxide in an oven at 580°C for 1 hour to release the fluoride ions from the sample matrix. The fuseate is dissolved in sulphuric acid with ammonium citrate buffer. The fluorine ISE is immersed in this solution to measure the fluoride-ion activity directly. Standard solutions are diluted sequentially to produce concentrations of 1000 ppm, 100 ppm, 10 ppm, 1 ppm and 0.1 ppm for complete calibration.

Accuracy and precision values for major and trace elements, calculated based on repeated runs of the MRG standard, are given in Tables G.1. and G.2.

Table G.1. Reported precision and accuracy of standard MRG used for major element analysis.

	Mean (ppm)	Std Dev.	Precision (%)	Accuracy (%)	MRG Certified Value (ppm)	Detection Limit
SiO ₂	38.74	0.31	0.80	-0.90	39.09	0.01%
Al ₂ O ₃	8.43	0.06	0.68	-0.35	8.46	0.01%
Fe ₂ O ₃	17.69	0.19	1.06	-1.34	17.93	0.01%
MnO	0.166	0.000	0.760	-2.350	0.170	0.01%
MgO	13.56	0.12	0.92	0.07	13.55	0.01%
CaO	14.52	0.17	1.14	-1.29	14.71	0.01%
Na ₂ O	0.73	0.01	0.82	-1.35	0.74	0.01%
K ₂ O	0.19	0.02	8.73	5.56	0.18	0.01%
TiO ₂	3.825	0.040	0.950	1.460	3.770	0.01%
P ₂ O ₅	0.08	0.00	0.00	0.00	0.08	0.01%
LOI	N/A	N/A	N/A	N/A	N/A	0.01%

Table G.2. Reported precision and accuracy of standard MRG used for trace element analysis (N/A = not available).

	Mean (ppm)	Std Dev.	Precision (%)	Accuracy (%)	MRG Certified Value (ppm)	Detection Limit (ppm)
V	514.74	33.23	6.46	-2.14	526.00	5
Cr	440.97	28.16	6.39	2.55	430.00	0.5
Co	85.04	5.37	6.32	-2.26	87.00	0.1
Ni	184.98	24.78	13.40	-4.15	193.00	1
Cu	127.13	15.11	11.88	-5.13	134.00	1
Zn	185.34	29.08	15.69	-2.96	191.00	1
Sc	55.00	0.00	0.00	0.00	55.00	0.01
Be	1.00	N/A	N/A	N/A	0.62	1
Ga	18.31	1.24	6.78	7.71	17.00	1
Ge	1.41	0.36	25.26	40.96	1.00	0.5
As	-2.80	10.28	0.00	0.00	0.73	1
B	136.00	N/A	N/A	N/A	136.00	0.5
Rb	7.48	0.77	10.25	-12.00	8.50	2
Sr	266.22	14.76	5.55	0.08	266.00	2
Y	13.12	0.81	6.18	-6.25	14.00	1
Zr	99.15	9.05	9.13	-8.20	108.00	1
Nb	19.81	2.21	11.15	-0.95	20.00	0.5
Mo	1.20	0.46	38.29	37.66	0.87	2
Ag	-0.18	0.69	0.00	0.00	0.11	0.5
In	-0.06	0.09	0.00	0.00	N/A	0.1
Sn	3.58	0.65	18.23	-0.53	3.60	1
Sb	0.65	0.23	34.97	-24.00	0.86	0.1
Cs	0.63	0.12	19.47	9.67	0.57	0.1
Ba	49.15	5.31	10.81	-19.42	61.00	1
La	9.53	0.76	7.93	-2.75	9.80	0.05
Ce	26.50	2.02	7.63	1.94	26.00	0.1

Table G.2. continued

Pr	3.59	0.36	10.15	5.63	3.40	0.02
Nd	18.61	1.09	5.86	-3.09	19.20	0.05
Sm	4.59	0.24	5.25	4.40	4.40	0.01
Eu	1.43	0.08	5.64	2.63	1.39	0.005
Gd	4.00	0.32	8.10	-0.06	4.00	0.02
Tb	0.60	0.04	6.16	18.33	0.51	0.1
Dy	2.99	0.15	5.15	3.15	2.90	0.02
Ho	0.50	0.02	4.41	2.15	0.49	0.01
Er	1.27	0.07	5.65	12.95	1.12	0.01
Tm	0.15	0.01	8.23	32.61	0.11	0.01
Yb	0.81	0.09	11.21	34.92	0.60	0.01
Lu	0.11	0.01	7.62	-5.40	0.12	0.01
Hf	3.78	0.24	6.45	0.64	3.76	0.1
Ta	0.84	0.09	10.38	5.14	0.80	0.1
W	0.50	0.73	146.23	66.63	0.30	1
Tl	0.00	0.11	2439.10	-91.47	0.06	0.05
Pb	7.88	3.06	38.81	-21.20	10.00	5
Bi	0.24	0.22	89.81	85.81	0.13	0.1
Th	0.89	0.15	16.80	-4.25	0.93	0.05
U	0.28	0.06	19.91	17.80	0.24	0.05
F	0.01%	N/A	N/A	N/A	0.02%	0.01%
Cl	N/A	N/A	N/A	N/A	N/A	0.01%

G.3. Thermal Ionization Mass Spectrometry (TIMS)

Radiogenic isotopic analyses were performed using a Finnigan-MAT 261 multicollector solid source mass spectrometer operated in static mode at Carleton University. Loading procedures for mass spectrometry are provided below in Table G.3. The conditions for running the samples on the TIMS such as optimum analysis temperature, evaporation current, ionization current, and minimum intensity required are shown in Table G.4.

A magazine of filaments for the TIMS contains 12 samples and 1 standard. Based on numerous runs over the past 12 years at Carleton University, the following average values have been obtained for the standards: NBS-987 $^{87}\text{Sr}/^{86}\text{Sr} = 0.71025 \pm 0.00003$, La Jolla $^{143}\text{Nd}/^{144}\text{Nd} = 0.51187 \pm 0.00003$, NBS-981 $^{206}\text{Pb}/^{204}\text{Pb} = 16.890 \pm 0.010$, $^{207}\text{Pb}/^{204}\text{Pb} = 15.429 \pm 0.013$, $^{208}\text{Pb}/^{204}\text{Pb} = 36.498 \pm 0.042$. Uncertainties are given at the 2σ level. The measured Sr and Nd isotopic ratios for all samples were corrected for fractionation to $^{88}\text{Sr}/^{86}\text{Sr} = 8.3752$ and $^{146}\text{Nd}/^{144}\text{Nd} = 0.7219$. Sr and Nd isotopic ratios exceeding $\pm 1\%$ of the fractionation correction values were considered unacceptable. Fractionation corrections of 0.27%, 0.39%, and 0.55% were applied to the measured $^{206}\text{Pb}/^{204}\text{Pb}$, $^{207}\text{Pb}/^{204}\text{Pb}$, and $^{208}\text{Pb}/^{204}\text{Pb}$ ratios, respectively, based on a 7-year average of NBS-981 at Carleton University.

Table G.3. Loading procedures for Sr, Nd, and Pb for TIMS analysis.

Element	Filament	Loading acid	Drying current
Sr	single Ta	H ₃ PO ₄	1.5 A
Nd	double Re	HNO ₃	2 A
Pb	single Re	H ₃ PO ₄ + silica gel	1.3 A

Table G.4. Running conditions for TIMS.

Element	Analysis temp.	Evaporation current	Ionization current	Minimum intensity
Sr	1500 °C	2.5-3.5 A		⁸⁸ Sr 1.5 V
Nd	1800 °C	0.5-1.5 A	4.5-5.5 A	¹⁴⁴ Nd 0.35 V
Pb	1300 °C	1.5-2.0 A		²⁰⁸ Pb 1.5 V

APPENDIX H
FURTHER SUBDIVISIONS OF FIELDS A, B, AND C ON THE TAS DIAGRAM

	A	B	C
Further Subdivisions of Fields A, B, and C	trachybasalt	basaltic trachyandesite	trachyandesite
$\text{Na}_2\text{O} - 2.0 \geq \text{K}_2\text{O}$	hawaiite	mugearite	benmorite
$\text{Na}_2\text{O} - 2.0 \leq \text{K}_2\text{O}$	potassic trachybasalt	shoshonite	latite

Table H.1. Further subdivisions of fields A, B, and C on the Total Alkalis-Silica diagram (Le Maitre et al., 2002).

APPENDIX I
CIPW NORMATIVE COMPOSITIONS

I.1. Roccamonfina

Normative Minerals	HKS RC 100	HKS RC 103	KS RC 104	KS RC 106	KS RC 107	HKS RC 109	KS RC 110
Quartz	0	0	0	4.63	3.93	0	0
Plagioclase	14.86	17.73	43.13	48.84	50.17	28.05	45.10
Orthoclase	43.58	36.48	18.79	26.89	18.20	34.33	25.41
Nepheline	10.50	11.41	0	0	0	7.53	0
Leucite	15.59	9.48	0	0	0	0	0
Kalsilite	0	0	0	0	0	0	0
Corundum	0	0	0	0	0	0	0
Diopside	5.67	12.67	14.79	6.63	7.69	17.54	15.79
Hypersthene	0	0	15.63	6.98	13.99	0	6.75
Wollastonite	0	0	0	0	0	0	0
Olivine	3.60	4.40	0.15	0	0	5.19	1.58
Larnite	0	0	0	0	0	0	0
Acmite	0	0	0	0	0	0	0
K ₂ SiO ₃	0	0	0	0	0	0	0
Na ₂ SiO ₃	0	0	0	0	0	0	0
Rutile	0	0	0	0	0	0	0
Ilmenite	1.16	1.56	1.50	1.31	1.56	1.71	1.29
Magnetite	3.44	4.34	4.07	3.76	3.76	4.41	3.32
Hematite	0	0	0	0	0	0	0
Apatite	0.90	1.23	0.58	0.60	0.60	0.95	0.46
Zircon	0	0	0	0	0	0	0
Perovskite	0	0	0	0	0	0	0
Chromite	0	0	0	0	0	0	0
Sphene	0	0	0	0	0	0	0
Pyrite	0	0	0	0	0	0	0
Halite	0	0	0	0	0	0	0
Fluorite	0	0	0	0	0	0	0
Anhydrite	0	0	0	0	0	0	0
Na ₂ SO ₄	0	0	0	0	0	0	0
Calcite	0.68	0.71	1.34	0.36	0.11	0.27	0.30
Na ₂ CO ₃	0	0	0	0	0	0	0
Total	99.98	100.01	99.98	100.00	100.01	99.98	100.00

I.1. Roccamonfina *continued*

Normative Minerals	KS RC 111	HKS RC 113	HKS RC 118	KS RC 119	KS RC 121	HKS RC 123	KS RC 127
Quartz	0	0	0	6.36	2.16	0	3.14
Plagioclase	44.60	23.10	19.66	40.67	50.78	28.39	45.26
Orthoclase	19.09	53.36	45.50	23.70	22.52	41.43	16.31
Nepheline	0	9.03	11.48	0	0	5.96	0
Leucite	0	0	0	0	0	0	0
Kalsilite	0	0	0	0	0	0	0
Corundum	0	0	0	3.28	0	0	0
Diopside	14.59	7.60	10.22	0	2.35	8.58	14.96
Hypersthene	10.68	0	0	14.96	13.62	0	14.44
Wollastonite	0	0	0	0	0	0	0
Olivine	3.95	1.87	5.57	0	0	7.38	0
Larnite	0	0	0	0	0	0	0
Acmite	0	0	0	0	0	0	0
K ₂ SiO ₃	0	0	0	0	0	0	0
Na ₂ SiO ₃	0	0	0	0	0	0	0
Rutile	0	0	0	0	0	0	0
Ilmenite	1.84	1.06	1.52	1.58	1.54	1.48	1.46
Magnetite	3.99	3.06	4.13	4.03	3.99	4.00	3.68
Hematite	0	0	0	0	0	0	0
Apatite	0.70	0.58	1.09	0.72	0.72	1.04	0.53
Zircon	0	0	0	0	0	0	0
Perovskite	0	0	0	0	0	0	0
Chromite	0	0	0	0	0	0	0
Sphene	0	0	0	0	0	0	0
Pyrite	0	0	0	0	0	0	0
Halite	0	0	0	0	0	0	0
Fluorite	0	0	0	0	0	0	0
Anhydrite	0	0	0	0	0	0	0
Na ₂ SO ₄	0	0	0	0	0	0	0
Calcite	0.57	0.34	0.82	4.71	2.32	1.73	0.23
Na ₂ CO ₃	0	0	0	0	0	0	0
Total	100.01	100.00	99.99	100.01	100.00	99.99	100.01

I.2. Ernici

Normative Minerals	HKS ER 101	HKS ER 104	HKS ER 105	HKS ER 107	KS ER 109	HKS ER 110	KS ER 112
Quartz	0	0	0	0	0	0	0
Plagioclase	16.38	15.03	15.01	14.59	56.14	7.88	45.35
Orthoclase	26.27	6.93	9.31	2.74	7.27	14.30	4.08
Nepheline	11.32	8.85	9.12	8.57	2.99	7.84	0
Leucite	10.49	27.52	22.86	28.58	0	30.40	0
Kalsilite	0	0	0	0	0	0	0
Corundum	0	0	0	0	0	0	0
Diopside	24.84	30.97	31.04	33.43	15.91	24.32	28.42
Hypersthene	0	0	0	0	0	0	8.35
Wollastonite	0	0	0	0	0	0	0
Olivine	3.26	3.07	4.62	4.38	9.15	4.28	6.59
Larnite	0	0	0	0	0	0	0
Acmite	0	0	0	0	0	0	0
K ₂ SiO ₃	0	0	0	0	0	0	0
Na ₂ SiO ₃	0	0	0	0	0	0	0
Rutile	0	0	0	0	0	0	0
Ilmenite	1.65	1.63	1.65	1.67	2.15	2.07	1.69
Magnetite	3.89	3.97	4.20	4.28	3.76	4.52	2.80
Hematite	0	0	0	0	0	0	0
Apatite	0.88	1.02	0.95	1.00	0.81	2.36	0.49
Zircon	0	0	0	0	0	0	0
Perovskite	0	0	0	0	0	0	0
Chromite	0	0	0	0	0	0	0
Sphene	0	0	0	0	0	0	0
Pyrite	0	0	0	0	0	0	0
Halite	0	0	0	0	0	0	0
Fluorite	0	0	0	0	0	0	0
Anhydrite	0	0	0	0	0	0	0
Na ₂ SO ₄	0	0	0	0	0	0	0
Calcite	1.02	1.00	1.23	0.75	1.82	2.05	2.23
Na ₂ CO ₃	0	0	0	0	0	0	0
Total	100.00	99.99	99.99	99.99	100.00	100.02	100.00

I.2. *Ernici continued*

Normative Minerals	KS ER 114	HKS ER 115	KS ER 116	KS ER 117	HKS ER 118	KS ER 121	KS ER 122
Quartz	0	0	0	0	0	0	0
Plagioclase	28.74	17.88	48.59	46.15	15.42	38.55	47.18
Orthoclase	16.31	5.39	2.13	6.50	13.33	2.95	2.72
Nepheline	6.30	6.37	0	5.90	9.31	4.41	0
Leucite	0	27.24	0	0	19.95	0	0
Kalsilite	0	0	0	0	0	0	0
Corundum	0	0	0	0	0	0	0
Diopside	33.95	29.97	31.34	27.45	30.64	37.96	24.64
Hypersthene	0	0	1.76	0	0	0	13.45
Wollastonite	0	0	0	0	0	0	0
Olivine	7.94	5.24	9.31	5.87	3.99	10.75	4.75
Larnite	0	0	0	0	0	0	0
Acmite	0	0	0	0	0	0	0
K ₂ SiO ₃	0	0	0	0	0	0	0
Na ₂ SiO ₃	0	0	0	0	0	0	0
Rutile	0	0	0	0	0	0	0
Ilmenite	1.60	1.86	1.75	1.71	1.61	1.56	1.88
Magnetite	3.68	3.64	2.83	3.58	4.18	2.51	3.03
Hematite	0	0	0	0	0	0	0
Apatite	0.58	1.16	0.51	1.00	1.04	0.53	0.51
Zircon	0	0	0	0	0	0	0
Perovskite	0	0	0	0	0	0	0
Chromite	0	0	0	0	0	0	0
Sphene	0	0	0	0	0	0	0
Pyrite	0	0	0	0	0	0	0
Halite	0	0	0	0	0	0	0
Fluorite	0	0	0	0	0	0	0
Anhydrite	0	0	0	0	0	0	0
Na ₂ SO ₄	0	0	0	0	0	0	0
Calcite	0.91	1.27	1.77	1.84	0.55	0.80	1.84
Na ₂ CO ₃	0	0	0	0	0	0	0
Total	100.01	100.02	99.99	100.00	100.02	100.02	100.00